Nanoparticles: Synthesis, Stabilization, Passivation and Functionalization

Molecules → Nuclei → Nanoparticles → Agglomerate / Aggregate

Passivation   Stabilization   Functionalization

EDITED BY

Ramanathan Nagarajan
and T. Alan Hatton

Nanoparticles: Synthesis, Stabilization, Passivation, and Functionalization

Nanoparticles: Synthesis, Stabilization, Passivation, and Functionalization

R. Nagarajan, Editor
Natick Soldier Research, Development, and Engineering Center

T. Alan Hatton, Editor
Massachusetts Institute of Technology

Sponsored by the
ACS Division of Colloid and Surface Chemistry

The paper used in this publication meets the minimum requirements of American National Standard for Information Sciences—Permanence of Paper for Printed Library Materials, ANSI Z39.48–1984.

Foreword

The ACS Symposium Series was first published in 1974 to provide a mechanism for publishing symposia quickly in book form. The purpose of the series is to publish timely, comprehensive books developed from ACS sponsored symposia based on current scientific research. Occasionally, books are developed from symposia sponsored by other organizations when the topic is of keen interest to the chemistry audience.

Before agreeing to publish a book, the proposed table of contents is reviewed for appropriate and comprehensive coverage and for interest to the audience. Some papers may be excluded to better focus the book; others may be added to provide comprehensiveness. When appropriate, overview or introductory chapters are added. Drafts of chapters are peer-reviewed prior to final acceptance or rejection, and manuscripts are prepared in camera-ready format.

As a rule, only original research papers and original review papers are included in the volumes. Verbatim reproductions of previously published papers are not accepted.

ACS Books Department

Preface

This book is a result of the symposium *Nanoparticles: Synthesis, Stabilization, Passivation, and Functionalization* held at the 233rd American Chemical Society (ACS) National Meeting in Chicago, Illinois on March 25–29, 2007. The symposium was sponsored by the ACS Division of Colloid and Surface Chemistry as part of its continuing series of symposia focusing on various aspects of nanoscience and nanotechnology. Approximately 100 papers were presented at this symposium and the papers included in this book contain a sampling of various problems addressed in this symposium.

Every chapter in this book emphasizes one or more of the themes— synthesis, stabilization, passivation, and functionalization of nanoparticles. The shapes of nanoparticles considered are diverse and include spheres, cubes, nanorods, nanowires, nanopyramids, and so on. Equally diverse are the methods to synthesize, stabilize, passivate, and functionalize the nanomaterials described in these chapters. Most of the chapters also provide discussion of many nanoparticle characterization methods, identify novel properties displayed by the functionalized nanoparticles, and provide the scientific basis for potential applications of these nanoparticles. The book is divided into sections that are based on the chemical feature of the nanoparticles emphasized; for example, antibody conjugated gold nanorods are included under bionanoparticles rather than under metal nanoparticles. Clearly, the chapters can be moved from one grouping to another and the classification is not rigid.

Chapter 1 presents a general introduction to nanoparticles as building blocks for nanotechnology, emphasizing the diversity of nanoparticles and drawing attention to the growing activity in scientific studies as well as providing practical applications.

The first section describes metal nanoparticles, with gold nanoparticles being predominant. Chapter 2 describes the colloidal approach to synthesize gold nanoparticles and the performance of various

stabilizing agents as they impact on the near infrared surface-enhanced Raman scattering activity of the nanoparticles. Chapter 3 shows how a controlled number of functional groups can be attached to gold nanoparticles by the solid phase place exchange reaction. Methods to synthesize thiol surfactants of various lengths are outlined in Chapter 4. These thiols can spontaneously assemble as monolayers on gold nanoparticles and can act as stabilizers of gold nanoparticle dispersions in organic solvents. In Chapter 5, the use of a mixture of thiols and charged thiols that self–assemble on gold nanoparticles is shown to lead to phase separation of the thiols on the particle surface and to provide water dispersibility of the nanoparticles essential for many biological and medical applications. Chapter 6 demonstrates ways to tune plasmon resonance of metal nanoparticles by changes in the shape of gold nanoparticles with gold nanorods and bipyramids and by the synthesis of gold/silver or gold/silver sulfide core/shell particles. The formation of nanotubes and nanocapsules from silver using wet chemical methods are described in Chapter 7. Chapter 8 describes the synthesis of tannic acid-functionalized, iron tannate magnetic nanoparticles, their surface characterization, and their ability to complex with other metal atoms. In Chapter 9 time-dependent density functional theory is used to evaluate the adsorption properties of passivating ligands on a 20-atom gold nanoparticle.

The second section focuses on metal oxide nanoparticles. The formation of iron oxide nanoparticles and their size are shown to be affected by a surfactant added as the stabilizing agent, in Chapter 10. The synthesis of titania nanotubes and growth of anatase thin films are described in Chapter 11. It is shown that the amorphous and poly-crystalline surfaces lead to marked differences in the thermal desorption of various molecules, indicating a structure-binding activity relationship relevant for catalytic applications. Chapter 12 describes a hydrothermal condensation method to prepare nanowires of vanadium pentoxide.

The third section of the book (Chapters 13 to 19) deals with semi-conductor and other inorganic nanoparticles. The preparation of quantum dot surfactants and their properties as Langmuir–Blodgett films with controlled nanoparticle separations are described in Chapter 13. The synthesis of composite nanoparticles with fluoroalkyl end-capped acrylic acid oligomers grafted on silica nanoparticles is described in Chapter 14, which also shows that antimicrobial agents can be encapsulated in this composite particle to provide efficient antibacterial activity. Chapter 15 presents a kinetic study of silver sulfide nanoparticle formation using

stopped flow technique. The preparation of ultrabright silica nanoparticles, which have potential applications in tagging, tracing, and labeling by physical entrapment of a fluorescent dye, is described in Chapter 16. Chapter 17 presents a comprehensive view of the microwave irradiation method to produce passivated and stabilized nanoparticles, nanowires, and nanorods from metals, metal oxides, and various semiconductors and rare earth oxides. The creation of nanoporous membranes using silica nanoparticle crystalline films and their permeability properties to ions are discussed in Chapter 18. In Chapter 19, the convectional, sedimentation and drying patterns of nanoparticle dispersions showing the nanoparticle assemblies that can be generated by different means are described.

The fourth section of the book concentrates on polymeric and polymer-stabilized nanoparticles. A general strategy to synthesize ferromagnetic nanoparticles coated with end–functionalized polystyrene surfactants is described in Chapter 20. Using ligand exchange, a versatile approach to the functionalization of the ferromagnetic nanoparticles is achieved. Chapter 21 describes the synthesis of amphiphilic polymer conetworks and the characterization and swelling properties of the resulting nanodomains. Ring-opening metathesis polymerization methods to produce polymer overlayers on solid nanoparticles are discussed in Chapter 22. Four different methods of preparing polysaccharide-covered polymer nanoparticles using amphiphilic polysaccharides and the properties of the synthesized nanoparticles are correlated to the methods of their preparation are covered in Chapter 23. Chapter 24 describes ways to produce stable polymer nanoparticles of controlled size from amphiphilic block copolymers, using a binary solvent mixture of a good solvent and a selective solvent.

The last section focuses on organic, carbon, and biofunctionalized nanoparticles. A novel method to crystallize organic nanorods of arachidic acid as branches on cadmium selenide nanoparticles is described in Chapter 25. In Chapter 26, the use of a biological nanoparticle, tobacco mosaic virus, as a template to prepare composite nanofibers as well as to carryout polymerization of aniline are described. The potential to surface modify the tobacco mosaic virus in order to manipulate the assembly and structural patterns of the composite material are explored. The synthesis of gold nanorods of various aspect ratios and their functionalization with antibodies are discussed in Chapter 27. Biosensing based on surface plasmon resonance with these biofunctionalized nanoparticles is modeled. Chapter 28 presents an

experimental and simulation study of stabilization of aqueous dispersions of single wall carbon nanotubes using gamma cyclodextrins. The stabilizing interaction forces are estimated using AFM and compared to the simulations.

The reviewers of individual chapters contributed prompt critical reviews that have helped improve the quality of the manuscripts. The Editors acknowledge the support from their institutions, Natick Soldier Research, Development, and Engineering Center and Massachusetts Institute of Technology, that allowed them to organize the symposium and develop this book based on selected contributions.

R. Nagarajan
Molecular Sciences and Engineering Team
Natick Soldier Research, Development, and Engineering Center
Natick, MA 01760
ramanthan.nagarajan@us.army.mil

T. Alan Hatton
Department of Chemical Engineering
Massachusetts Institute of Technology
Cambridge, MA 02139
tahatton@mit.edu

# Chapter 1

Nanoparticles: Building Blocks for Nanotechnology

R. Nagarajan

Molecular Sciences and Engineering Team, Natick Soldier Research, Development and Engineering Center, Kansas Street, Natick, MA 01760

Nanoparticles are defined as particles with size in the range of 1 to 100 nm at least in one of the three dimensions. Because of this very small size scale, they possess an immense surface area per unit volume, a high proportion of atoms in the surface and near surface layers, and the ability to exhibit quantum effects. The resulting unique properties of nanoparticles cannot be anticipated from a simple extrapolation of the properties of bulk materials. Nanoparticles exist with great chemical diversity in the form of metals, metal oxides, semiconductors, polymers, carbon materials, organics or biological. They also exhibit great morphological diversity with shapes such as spheres, cylinders, disks, platelets, hollow spheres and tubes, etc. Nanoparticles can be generated via a number of synthetic routes based on gas, liquid or solid phase approaches. The synthesized nanoparticles have to be surface modified in most cases, in order to passivate and stabilize them since their nanoscale renders them chemically very reactive and/or physically aggregative. The nanoparticles are also surface functionalized in order to meet the needs of specific applications. Nanoparticles serve as the fundamental building blocks for various nanotechnology applications.

Introduction

The term 'nanoparticle' is used to describe a particle with size in the range of 1 to 100 nm, at least in one of the three possible dimensions. In this size range, the physical, chemical and biological properties of the nanoparticle change in fundamental ways from the properties of both individual atoms/molecules and of the corresponding bulk material. Nanoparticles can be made of materials of diverse chemical nature, the most common being metals, metal oxides, silicates, non-oxide ceramics, polymers, organics, carbon and biomolecules. Nanoparticles exist in several different morphologies such as spheres, cylinders, platelets, tubes, etc. Generally, they are designed with surface modifications tailored to meet the needs of specific applications they are going to be used for. The enormous diversity of the nanoparticles (Figure 1) arising from their wide chemical nature, shapes and morphologies, the medium in which the particles are present, the state of dispersion of the particles and most importantly, the numerous possible surface modifications the nanoparticles can be subjected to make this an important active field of science.
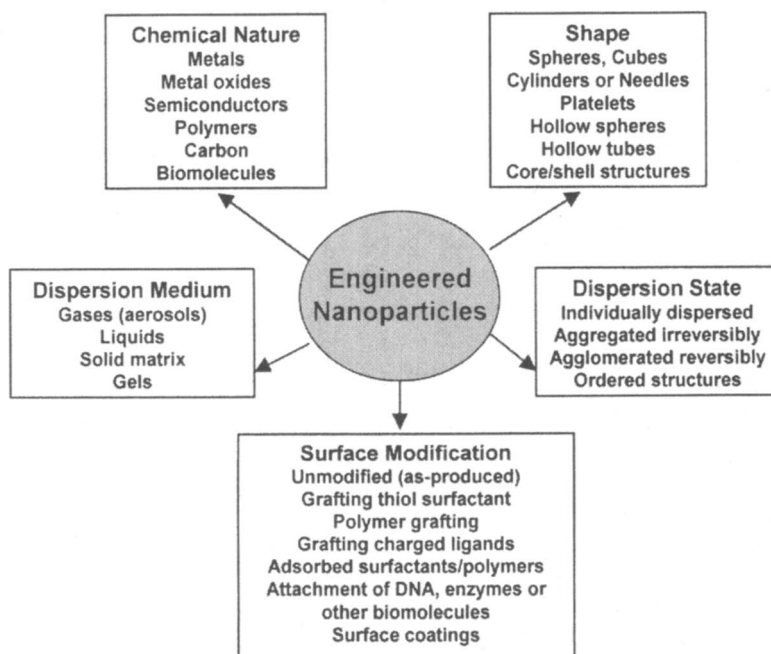
Figure 1. Various features contributing to the diversity of engineered nanoparticles. The same chemical can generate a wide variety of nanoparticles.

Nanoscale Properties and Relevance

The most significant consequences of the nanoscale are the presence of a high fraction of atoms/molecules constituting the nanoparticle on the particle surface rather than in the particle interior (Figure 2) and the immense surface area available per unit volume of the material (Figure 3). Both of these properties increase in magnitude with a decreasing particle size. The unique physical, chemical and biological properties of nanomaterials originate from these two features. In some nanoscale materials quantum effects are exhibited allowing for a number of interesting applications. Further, unusual morphologies such as carbon nanotubes (CNT) and dendrimers contribute to morphology dependent novel applications.
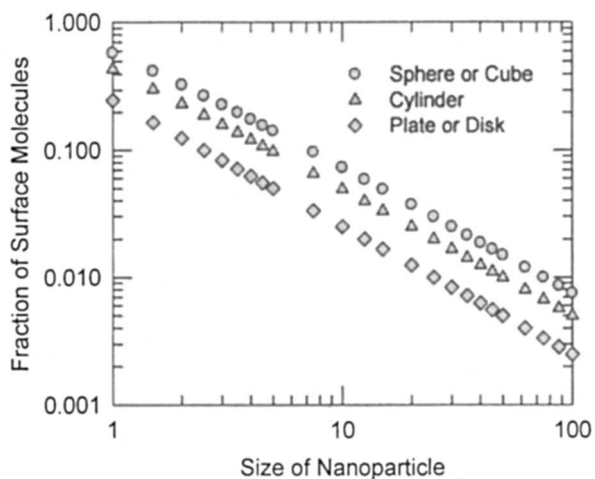
Figure 2. Calculated fraction of molecules at the surface as a function of nanoparticle size for particles of various shapes. The assumed atomic/molecular size is 0.5 nm. The size of nanoparticle refers to the diameter in the case of a sphere and a cylinder, the side for a cube and the thickness for a plate and a disk. The sphere and cube have all three dimensions in the nanoscale, the cylinder has two dimensions in the nanoscale and the plate and disk have one dimension in the nanoscale.

The small particle size leads to many unique properties of nanoparticles. Nanoparticles display interesting optical properties since the absorption and/or emission wavelengths can be controlled by particle size and surface functionalization. If the nanoparticle size is below the critical wavelength of

light, then transparency can be attained. The chemical nature and the size of the nanoparticle control the ionic potential or the electron affinity and thereby the electron transport properties. For metals, with decreasing size of nanoparticles, the sintering and melting temperatures decrease. Nanoparticles may be incorporated into a solid matrix to provide better thermal conduction. For some metals and metal oxides, the decrease of the particle size results in improved magnetic behavior. Individual metallic magnetic nanoparticles can exhibit super-paramagnetic behavior.
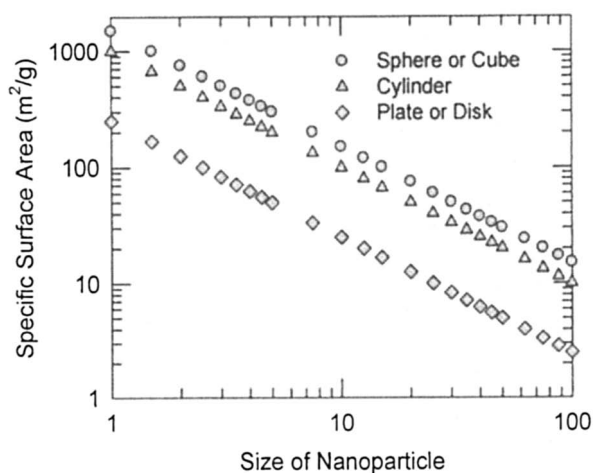
Figure 3. Calculated surface area per unit volume as a function of nanoparticle size for particles of various shapes. The assumed atomic/molecular size is 0.5 nm and the particle density is 1 g/cm³.

The large specific surface area of nanoparticles is the origin of a number of their unique applications. Catalysis is enhanced by high surface area per unit volume and the homogenous distribution of nanoparticles. High surface areas give strong interactions between the nanoparticles and the solid matrix in which they may be incorporated. In composites, depending on the chemistry of the nanoparticle, its aspect ratio, extent of dispersion and interfacial interactions with the polymer matrix (which can be modified by surface functionalization), it is possible to obtain different levels of mechanical properties for the final composites. In particular, a high elastic modulus can be achieved without a proportional loss in impact strength that is commonly observed when larger particles are used. The platelet morphology and large specific surface areas of silicate particles enhance the barrier properties of polymer membranes by vastly increasing the pathway for molecular transport of permeating substances.

Nanoparticles can also influence the flammability of polymers by increasing the glass transition temperature and the heat deflection temperature.

Nanoparticle Synthesis Methods

Nanoparticles can be synthesized by a variety of methods using gas, liquid or solid phase processes. These include gas phase processes of flame pyrolysis, high temperature evaporation, and plasma synthesis; microwave irradiation; physical and chemical vapor deposition synthesis; colloidal or liquid phase methods in which chemical reactions in solvents lead to the formation of colloids; molecular self-assembly; and, mechanical processes of size reduction including grinding, milling and alloying.

Gas phase synthesis approaches are based on homogeneous nucleation of a supersaturated vapor and subsequent particle growth by condensation, coagulation and capture (Figure 4).
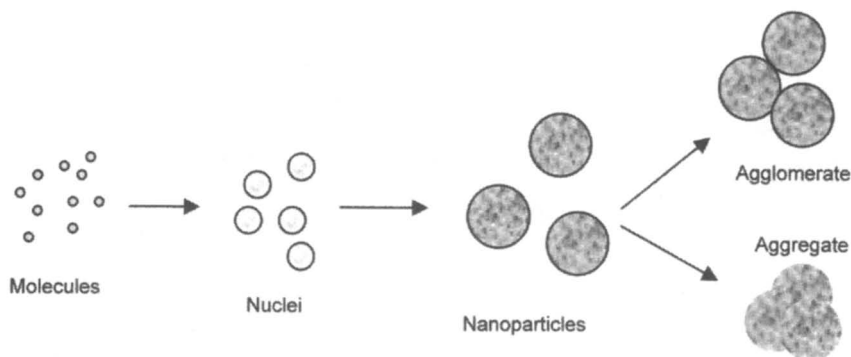
Figure 4. Mechanism of nanoparticle production using vapor phase or liquid phase/ colloidal methods. The methods differ in the way the starting molecules are generated by vaporization or by chemical reaction/precipitation. The nuclei may be amorphous or crystalline and lead to amorphous or crystalline nanoparticles. Because of their intrinsic instability, the nanoparticles may form agglomerates that can be easily redispersed or form non-dispersible aggregate clusters.

The supersaturated vapor can be generated in many ways depending on the chemical nature of the material, but typically by heating a solid and evaporating it into a carrier gas phase. The supersaturation is achieved by cooling or by chemical reaction or by some combination of these. The supersaturated vapor

can nucleate homogeneously in the gas phase and also heterogeneously by contact with surfaces. The nuclei grow by collision and condensation to give rise to a distribution of particle sizes and morphologies. Depending on the heating and cooling processes used, a wide range of gas phase methods such as flame pyrolysis (fumed silica, TiO_2), furnace flow reactors (Ag, Ga, Al, PbS, Pb, Si, Ge), laser induced vaporization and pyrolysis (silica and iron), thermal and microwave plasmas (metals and metal oxides), sputtering (metals), and laser ablation have been employed.

Vapor deposition methods are based on forming a vapor by pyrolysis, followed by reduction, oxidation and allowing the deposition of the vapor on a surface. Starting from initial nuclei existing as islands on a surface, the growth is controlled by various ways to produce nanoparticles (TiO_2, ZnO, SiC). An important example of this approach is the production of carbon nanotubes.

Colloidal methods are based on precipitation processes in solutions. For example, solutions of different ions can be mixed under controlled conditions of temperature and pressure to form insoluble precipitates. By controlling the nucleation and growth kinetics, particles of various sizes and morphologies can be produced. The method has been implemented in bulk solutions and also in confined systems such as reverse micelles. To control the process of nucleation, ultrasonic or sonochemical effects have also been employed. A wide range of metal, metal oxide and organic nanoparticles have been produced by colloidal wet chemical approach.

The molecular self assembly method is a spontaneous process by which nanoparticles are created starting from molecules. This is a particularly effective method for the production of polymeric nanoparticles starting from amphiphilic block copolymer molecules. An added advantage of this approach is the ability to produce thermodynamically stable nanoparticles whose size and shape can be controlled by the choice of the block copolymer (type, block composition and molecular weight) and the choice of the solvent and self-assembly conditions.

In addition to the nanoparticle synthesis approaches in gas or liquid phases, it is also possible to use solid substrates as heterogeneous nucleating sites to build up nanoparticles at solid-liquid interfaces. Indeed, by using patterned surfaces, one may be able to control the nucleation and growth processes thereby affecting the nature of nanoparticles produced.

All of the above synthesis approaches start at the molecular level to build up or create the nanoparticles. In the opposite direction, mechanical size reduction methods such as grinding and milling have also been employed to generate nanoparticles. These methods are the traditional approaches to produce fine particles and they have been able to generate nanoparticles from minerals such as clay, coal and metals. To avoid particle aggregation in the course of the size reduction process, the grinding and milling operations are often carried out with colloidal stabilizers.

Surface Modification of Nanoparticles

Once the nanoparticles are produced and purified to a satisfactory level it is often necessary to introduce surface modifications. The surface modifications can be for the purposes of (a) passivating a very reactive nanoparticle, (b) stabilizing a very aggregative nanoparticle in a medium (which may be a solvent or a polymer melt) where the nanoparticles are to be dispersed, (c) functionalizing the nanoparticle for applications such as molecular recognition, or (d) promoting the assembly of nanoparticles (Figure 5). Most commonly used surface modification methods include grafting thiolated surfactants or polymers, adsorption of charged surfactants, charged ligands or polymer brushes, attachment of biological molecules such as DNA, peptides, proteins, antigens, streptavidin or coating a continuous polymer film on nanoparticles.

a   b   c
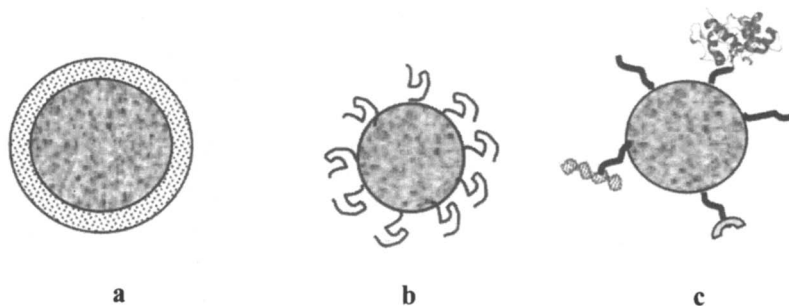
Figure 5. Different approaches to surface modifications. (a) Surface treatment to make the interfacial tension at the nanoparticle-medium interface close to zero allowing for thermodynamic stability of the nanoparticle dispersion. The treatment could be the charging of the surface or coating with ligands. (b) Surface adsorption of a surfactant or a block copolymer to provide inter-particle electrostatic and/or steric repulsions that would provide kinetic stability of the nanoparticle dispersion. (c) Surface modification to make the nanoparticle functional in one of many ways including hydrophobic or hydrophilic, the ability to bind to specific molecular recognition elements, DNA, enzymes, bridge to other nanoparticles, etc. The surface modification may involve a linker molecule.

Much of this book is devoted to a description of various types of surface modifications performed on metal, metal oxide, semiconductor, polymer, carbon, organic and biological nanoparticles and specific examples can be found in the different book chapters.

Assembling Nanoparticles

For most practical applications, the nanoparticles have to be assembled in one, two or three dimensions, similar to how atoms and molecules are assembled into matter. For example, a sensing device may require that nanoparticles be arranged with specified inter–particle separation. An optoelectronic device may require the nanoparticles to be assembled to create a patterned surface. In general, it will be necessary to place the nanoparticles in specified locations on a substrate so that addressing and connecting them to the macroscopic outside world will be possible.
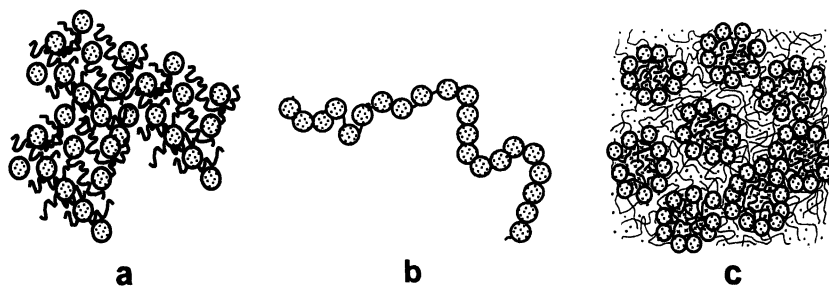
Figure 6. Assembling nanoparticles for applications. (a) Nanoparticles with stabilizing polymer molecules around them in a random three dimensional arrangement to create a porous nanoparticle system for catalytic or adsorption applications. (b) Nanoparticles assembled on a polyelectrolyte or a DNA molecule to serve as a nanoelectrical wire. (c) Nanoparticles assembled on a block copolymer patterned surface with nanoparticles located at the domain boundaries for a sensor application. (Adapted from reference 1.)

A number of approaches have been developed to accomplish this objective. For example, surface patterning has been used to direct polymer and silica nanoparticles to specific surface locations. Self-assembled surfactant and block copolymer nanostructures have been used as templates to direct the nanoparticle assembly of metal oxide particles to generate mesoporous materials. Cationic (or anionic) polyelectrolytes have been used to direct the assembly of oppositely charged nanoparticles such as negatively charged gold particles or silica particles. Nanoparticles can also self-assemble into nano-crystalline materials. A variety of molecular recognition methods such as antigen-antibody interactions have been used to direct the assembly of nanoparticles that have the recognition molecules bound to their surfaces. The binding of DNA to the nanoparticle surface has been used to create particle assemblies dictated by nucleic acid interactions. Nanoparticles have also been self-assembled at air-liquid and

liquid-liquid interfaces taking advantage of surface tension effects. Also the dewetting of a solid surface by a polymer solution has been exploited to attain nanoparticle self-assembly. Biological nanoparticles such as viruses can self-assemble to yield ordered nanoparticle assemblies in one, two or three dimensions.

Nanoparticle Commercial Applications

Existing and potential applications involving nanoparticles are almost endless. The following list from Ref.(*2*), with additions, provides examples in various fields of technology. The amount of nanoparticles usage in different applications may vary significantly.

The Project on Emerging Nanotechnologies (*3*) lists more than 470 products in May 2007, that are verified to include some form of nanotechnology, the number being double that was reported the same time in 2006. Many of the products address consumer needs in health care and fitness, home and garden, electronics and computers, food and beverage, automotive, appliances and products for children. The positive view with which the nanoproducts are being greeted is reflected in the explicit choice of the term 'nano' in the names of many commercial products, for example, Nano & UV Artificial Teeth Cleaner, Nano Air Filter, Nano Anti Aging Cream, Nano B-12 Vitamin Spray, Nano Bag, Nano Breast Cream, Nano Cold Catalyst Air Purifier, Nano Pacifier, Nano Trousers, Nanoceuticals Artichoke Nanoclusters, Nanodesu X Bowling Ball. The preponderant nanomaterials in these 470 commercial products are shown on Figure 7.

In 2005, over US $32 billion of products sold claimed to have incorporated some nanotechnology (3). The global investment in nanotechnology research and development is approximately US $9 billion. There are more than 4,000 US Patents filed to-date. The growing interest in nanoparticles and their importance can also be measured by the increase in the number of scientific publications (Figure 8).

Conclusions

Nanoparticles constitute the building blocks for nanotechnology and thus for numerous potential applications in energy and power, health and biomedicine, electronics and computers, environmental applications, new engineering materials, consumer goods, personal care products, food and transportation. To perform these functions nanoparticles have to be synthesized, passivated to control their chemical reactivity, stabilized against particle aggregation, and functionalized to achieve specific performance goals. The individual nano-

Table 1. Examples of Present and Potential Applications of Nanoparticles

Biomedicine	• Antibacterial creams and powders (Ag) • Biocompatible coatings for implants • Biolabeling and detection (Au, Ag, Quantum dots) • Biosensors (metal oxide, polymer nanoparticles, CNT) • Bone growth promoters (hypoxyapatite ceramics) • Cancer diagnostics and targeted drug delivery (magnetic nanoparticles) • Cell, receptor, antigen, enzyme imaging (Quantum dots) • Fungicides (ZnO, Cu_2O) • Gene delivery (CNT) • MRI contrast agents (Fe_2O_3, Fe_3O_4) • Dental composites
Consumer Goods and Personal Care Products	• Anti-bleaching, scratch resistance additives in paints • Anti-scratch coated tiles (alumina) • Barrier packaging (silicates) • Glass coatings for anti-glare, anti-misting mirrors (TiO_2) • Skin creams with antioxidant vitamins (nanocapsules) • Sunscreens (ZnO and TiO_2) • Tennis balls, rackets (nanoclays, carbon nanotubes)) • Water- and stain-repellent textiles
Electronics and Computers	• Chemical mechanical planarization (alumina, silica, ceria) • Coatings and joining materials for optical fibers (Si) • Conductive coatings/fabrics (rare-earth-doped ceramics) • Display technologies (conducting oxides) • Electronic circuits (Cu, Al) • EMI shielding using conducting and magnetic materials • Ferro-fluids (Fe, FeCo, Fe_3O_4) • Magnetic particles for high-density data storage (Fe) • Optoelectronics devices (Gd_2O_3, Y_2O_3 doped with rare-earth metals)
Engineering Materials	• Anti-scattering layers in photographic film • Chemical sensors • Conducting/magnetic inks (metal powders) • Cutting tool bits (Al_2O_3, ZrO_2,WC, TaC) • Thermal spray coating techniques (TiO_2, TiC-Co) • Flame retardant polymer formulations (nanoclay) • Lubricants and sealants/hydraulic additives (Cu MoS_2) • Molecular sieves • Pigments (metals and metal oxides) • Polymer composites (nanoclays, TiO_2, SiO_2) • Spark plugs (metal and ceramic powders) • Wear/abrasion-resistant coatings (alumina, Y-Zr_2O_3)

Table 1. *Continued.*

Environmental	• Controlled delivery of herbicides and pesticides • Self-cleaning glass (TiO_2 based coatings) • Soil remediation (Fe) • Water treatment (photo-catalyst treatments, TiO_2)
Food	• Flavors and colors in food and beverages (nanocapsules) • Frying oil refining catalysis (ceramics) • Food packaging materials (nanoclays, SiO2, TiO2, Ag) • Neutraceutical delivery (liposomes, block copolymer micelles) • Food pathogen sensing
Power and Energy	• Anode and cathode materials for solid oxide fuel cells (nanoclays, CNT) • Catalysts for various fuel technologies (metals and metal oxides) • Conducting polymers for bipolar plates in fuel cells • Dye-sensitized solar cells (TiO_2, ZnO, Au) • Environmental catalysts (TiO_2, CeO_2 as diesel additive) • Fuel cell catalysts (Pt in PEM cells) • Hydrogen storage (metal hydrides) • Improved electrodes in batteries and supercapacitors • Thermal control fluids (Cu)
Transportation	• Automated highways • Battery technology • High strength, light weight composites for increasing fuel efficiency • High temperature sensors • Improved displays • Thermal barrier and wear resistant coatings • Wear-resistant tires
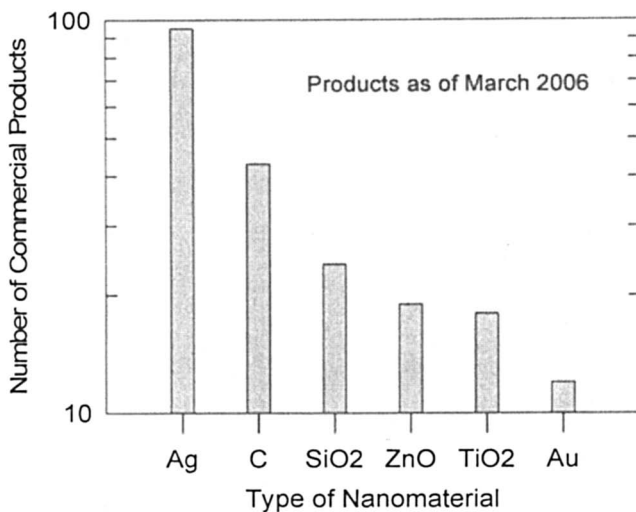
Figure 7. The use of nanoparticles of the specified kind in commercial products. C refers to fullerenes and carbon nanotubes (2).
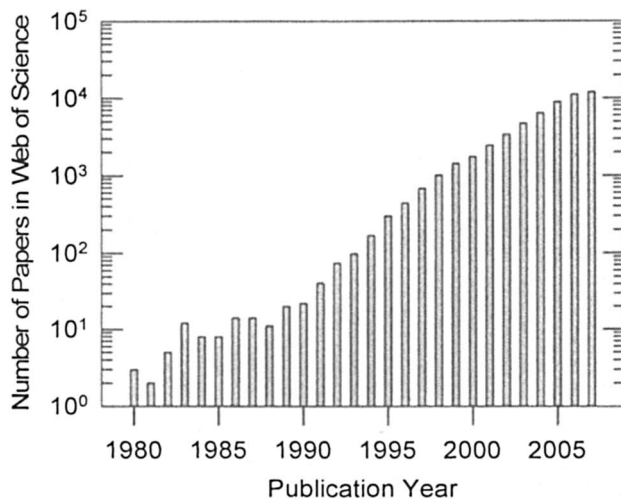
Figure 8. Number of publication entries in the Web of Science for the keyword 'nanoparticles'. The number for 2007 covers only eleven months.

particles then have to be assembled into devices or integrated into other solid matrices to create the final nanoproducts. The tremendous diversity of nanoparticles possible because of their wide chemical nature, shape and morphology, medium in which they are present, their state of dispersion and the nature of surface modifications make this a rich field for scientific investigations.

Acknowledgements

References

1. Shenhar, R.; Norsten, T.B.; Rotello, V.M. **2005**, Adv. Mater. 17, 657-669.
2. Perez, J.; Baxc, L.; Escolano, C. *Roadmap Report on Nanoparticles*; Nano Road Map Project, European Commission (2005)
3. Project on Emerging Nanotechnologies, Woodrow Wilson International Center for Scholars, Washington, DC (2007).

Chapter 2

Synthesis and Stabilization of Colloidal Gold Nanoparticle Suspensions for SERS

Paul H. Davis[1], Cody P. Morrisey[1], Sean M. V. Tuley[1,2,*], and Chris I. Bingham[1]

[1]Department of Chemistry, Pacific Lutheran University, Tacoma, WA 98447
[2]Current address: School of Veterinary Medicine, St. George's University, Grenada, West Indies

Colloidal gold nanoparticles were synthesized by thiosulfate reduction of aqueous $HAuCl_4$. Nanoparticle flocculation was controlled by addition of a stabilizing agent (e.g., Na_2SO_4 or NaCl) 5 minutes into the reaction. Synthesis kinetics were followed by monitoring the growth in intensity of the surface plasmon resonance (SPR) at ~535 nm using visible-NIR absorption spectroscopy. In addition to the SPR, the time-dependent spectra also exhibited an extended plasmon band (EPB) in the NIR that initially increased in intensity and red-shifted with time before blue-shifting and eventually disappearing due to changes in nanoparticle flocculation. TEM and x-ray diffraction measurements showed that the resultant nanoparticles were predominantly spherical in shape and ~20-30 nm in diameter. Surface chemistry was confirmed using XPS. The stabilizing agent was found to play a key role in the subsequent SERS activity of the nanoparticles by adsorbing to their surface, preventing premature nanoparticle aggregation and mediating the analyte-nanoparticle interaction.

Introduction

Gold nanoparticles have a long and storied history dating back for millennia. In the Middle Ages, colloidal gold was used for a diverse assortment of purposes including as a colorant in stained glass windows and as a purported curative for a wide variety of diseases (*1*). Probably the earliest scientific investigation into the synthesis of colloidal gold was carried out by Michael Faraday, who in 1857 reported a method for preparing colloidal gold by electrochemical reduction of aqueous tetrachloroaurate ions, $AuCl_4^-$ (*2*). Almost a century later, in 1951, Turkevich et al. developed a method for producing spherical gold nanoparticles via citrate reduction of tetrachloroauric acid, $HAuCl_4$ (*3*). The beauty of the citrate reduction method was that it was simple and resulted in a relatively monodisperse distribution of particle sizes. Further work by Frens in 1973 afforded control over average particle size by varying the ratio of gold salt to citrate reducing agent (*3,4*). Since then, numerous other methods of producing gold nanoparticles have been developed as interest has grown due to the myriad applications of gold nanoparticles, including cell labeling (*5*). SPR (surface plasmon resonance) spectroscopy (*6-8*), and SERS (surface enhanced Raman scattering) (*9,10*). In general, however, most synthesis methods have relied on *in situ* reduction of a gold (III) salt such as $HAuCl_4$ or $HAuBr_4$ via chemical means (*1,11,12*).

The use of gold nanoparticles as substrates for plasmonic spectroscopy and SERS has stimulated interest in tuning the location of the SPR by controlling the size, shape, morphology, and local environment of nanoparticles. Several groups have developed methods for synthesizing nanorods, nanocubes, and nanoprisms, to name a few shapes (*11-13*). Others have created hollow gold nanospheres (*14,15*) or core/shell type structures consisting of, for example, a silica core with a gold shell (*16,17*). For spherical nanoparticles, flocculation of the nanoparticles greatly increase the SERS effect due to a resultant enhancement of the local electric field at the interparticle junction (*18,19*). In addition, because of the relative inertness of gold, it has been necessary to find ways to make gold nanoparticles more attractive to analytes. Because of this, researchers have investigated ways to stabilize nanoparticle suspensions while creating favorable electrostatic or hydrophilic/hydrophobic interactions to induce adsorption of analytes onto gold nanoparticles.

Much of the interest in gold nanoparticles as SERS substrates centers on the fact that the SPR of gold nanoparticles is significantly red-shifted relative to that of silver nanoparticles. This makes gold nanoparticles ideal candidates for NIR-SERS, a promising technique for biomedical diagnostic and monitoring applications due to the ability of near-IR radiation to penetrate the skin (*9,20*). In 1994, Zhou et al. reported a new method of synthesizing spherical nanoparticles based on sulfide reduction of tetrachloroauric acid (*21*). Based in large part on the absorption spectra obtained (which exhibited two peaks, one in

the visible and another in the NIR) they postulated that Au_2S/Au core/shell nanoparticles were being formed. Subsequently, Zhang et al. showed that Zhou's results could be explained instead by flocculation of spherical nanoparticles resulting in the appearance of a transverse SPR in the visible and an extended plasmon band (EPB) in the NIR (22-24). In their attempts to reproduce the work of Zhou et al., however, Zhang and coworkers found that freshly prepared solutions of sodium sulfide did not work. Instead, they found it necessary to first allow the sulfide solution to "age" by leaving it open to the air for several weeks, suggesting that in fact it was not sulfide ions *per se* that were acting as the reducing agent (23,25).

In this paper, we describe a new method of synthesizing and stabilizing SERS-active gold nanoparticles by thiosulfate reduction of $HAuCl_4$. This method grew out of attempts to discern the identity of the actual reducing agent present in the "aged" sulfide solutions employed by Zhang's group in their investigations of Zhou's method. Throughout this article, the term "flocculation" will be used to refer to both reversible and irreversible processes resulting in the close association of nanoparticles (26). However, a distinction will be made between agglomerates and aggregates. Agglomerates will be used to refer specifically to loose, reversible associations of nanoparticles, as occurs during the course of synthesizing the nanoparticles. Agglomerates tend to remain in suspension, and can typically be resuspended by sonication should they fall out of suspension. The term "aggregates" will be reserved for irreversible associations of nanoparticles, as per the definitions of Ross and Morrison (27). Aggregates are found to form upon addition of an analyte to our SERS-active gold nanoparticles. Formation of aggregates leads to the nanoparticles falling out of suspension, usually within 1-2 hours.

Experimental Section

Chemicals

Hydrogen tetrachloroaurate trihydrate ($HAuCl_4 \cdot 3H_2O$) was purchased from either Aldrich (99.9+%) or GFS Chemicals (ACS reagent grade). Anhydrous ACS reagent grade sodium acetate ($NaC_2H_3O_2$, ≥99.0%), sodium chloride (NaCl, ≥99.0%), sodium sulfate (Na_2SO_4, ≥99.0%), sodium sulfite (Na_2SO_3, ≥99.0%), and sodium thiosulfate ($Na_2S_2O_3$, ≥98.0%) were all purchased from J. T. Baker, along with rhodamine 6G (R6G) and biochemical research grade DL-alanine and L-methionine. Sodium dodecylsulfate (SDS, 98%), 11-mercaptoundecanoic acid (11-MUA, 95%), and L-lysine monohydrochloride (99+%) were purchased from Aldrich. All reagents were used as received, and

all solutions were prepared using 18.2 MΩ water purified by a Millipore Synergy 185 UV ultrapure water system.

Synthesis of Gold Nanoparticles

Aqueous suspensions of gold nanoparticles were prepared in a manner similar to the method of Norman et al. (*22*) with the exception that sodium thiosulfate was used as the reducing agent, and a variety of stabilizing agents were employed to control nanoparticle flocculation. Prior to use, glassware was filled with freshly prepared aqua regia (3:1 concentrated $HCl:HNO_3$) to dissolve any gold or other contaminants present from prior syntheses. The glassware was then thoroughly rinsed at least twice with Milli-Q water to remove any traces of aqua regia. During the cleaning process particular care was taken to ensure complete removal of any soap or salt residues to prevent premature nanoparticle aggregation during synthesis. The basic synthesis procedure was as follows: 1.0 mL of 0.02 M $HAuCl_4$ was added to 40 mL of gently stirred Milli-Q water, resulting in a gold concentration of ~5 x 10^{-4} M. Immediately following addition of the gold solution, a variable amount (typically 60 µL) of 0.10 M $Na_2S_2O_3$ solution was injected into the stirred reaction mixture. Addition of the thiosulfate caused the solution to immediately turn from a pale golden yellow to a light yellow-brown. As the reaction progressed, the solution rapidly darkened to a deep golden brown color. Five minutes after addition of the thiosulfate, an aliquot (typically 20 µL) of a 0.10 M solution of stabilizing agent (e.g., Na_2SO_4, NaCl, SDS, or an amino acid) was injected. Successful syntheses were characterized by a continued darkening of the solution, which over time changed in color from deep golden brown to dark purple to a milky rusty red. Nanoparticle suspensions that remained purple and did not turn rusty red in color were found to have formed aggregates that rapidly fell out of suspension and exhibited no SERS activity.

Characterization of Gold Nanoparticles

Time-dependent UV-Visible-NIR absorption spectra of the nanoparticle suspensions were taken over a period of 48 hours during the course of the synthesis reaction using a Cary 5000 UV-Vis-NIR dual beam scanning spectrophotometer. Transmission electron microscopy images of selected nanoparticles were obtained using a JEOL 2010 high-resolution TEM after the synthesis was completed. Samples were prepared by placing a single drop of nanoparticle solution on a standard TEM grid and allowing the water to evaporate. Size and shape distributions determined from TEM images were confirmed in solution via dynamic light scattering (DLS) using a Brookhaven

Instruments BI-200SM Research Goniometer and Laser Light Scattering System. The excitation source for the DLS system was a 40 mW, 632.8 nm He:Ne laser whose output was filtered to prevent detector saturation. Detection of scattered light was carried out at 90° relative to the incident beam. Asymmetric grazing-incidence x-ray diffraction (GI-XRD) data to characterize sample structure and crystalline domain size were collected on a Philips X'Pert PRO MPD system with $\omega = 5.00°$ and $2\theta = 30.00°\text{-}100.00°$. XPS data for surface chemistry studies were obtained using a Physical Electronics Instruments (PHI) Quantum 2000 X-Ray Photoelectron Spectrometer. Both XRD and XPS samples were prepared by placing several drops of nanoparticle solution on a silicon wafer and allowing the solvent to evaporate. SERS activity of the nanoparticles was tested using either a Delta Nu Advantage NIR Raman spectrometer or a refurbished Renishaw Research Raman microscope (80 mW, 785 nm diode laser excitation) and rhodamine 6G as the analyte.

Results and Discussion

Nanoparticle Synthesis and Stabilization

The oxidation reduction reaction believed responsible for the formation of the nanoparticles is

$$8\ Au^{3+} + 3\ S_2O_3^{2-} + 15\ H_2O \rightarrow 8\ Au + 6\ SO_4^{2-} + 30\ H^+.$$
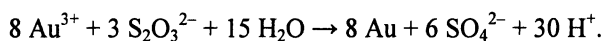
The reaction equation above dictates a gold to thiosulfate molar ratio of 8:3. However, after varying the amount of reducing agent solution used (40-100 µL), it was found empirically that a slightly sub-stoichiometric amount of thiosulfate (60 µL aliquot of 0.1 M $Na_2S_2O_3$ added to 40 mL of 5×10^{-4} M $HAuCl_4$) was the optimal amount for nanoparticle formation. Thus the actual molar ratio of gold to thiosulfate under the reaction conditions employed was 10:3. Despite the slight excess of gold, XPS studies showed no evidence of residual Au^{3+} (see Figure 4a). It is therefore thought that the actual Au^{3+} concentration in solution is slightly less than the nominal $HAuCl_4$ concentration. The most likely reason for this is that $HAuCl_4$ is extremely hygroscopic, and it is therefore highly likely that the solid absorbed moisture from the atmosphere during the weighing process, leading to an overestimation of the amount of gold in solution. Further possible contributing factors will be described in detail below in the context of discussing the long-term stability of the tetrachloroaurate solution. Returning to the chemical reaction equation above, an examination of the right hand side of the equation shows that as the reaction progresses, the solution should become more acidic. This is in fact the case, as the pH drops from approximately 3.1 to

2.8 during the course of the reaction, as would be predicted. Although it is possible for thiosulfate, $S_2O_3^{2-}$, to be partially oxidized to tetrathionate, $S_4O_6^{2-}$, via the following reaction,

$$2 \, Au^{3+} + 6 \, S_2O_3^{2-} \rightarrow 2 \, Au + 3 \, S_4O_6^{2-},$$
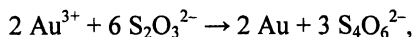
this would not lead to the experimentally observed decrease in pH. In addition, the experimental stoichiometry more closely agrees with full oxidation of the thiosulfate to sulfate, and the XPS spectrum of the nanoparticles provides confirmation of the production of sulfate during the course of the reaction, with no evidence of other sulfur species (see Figure 4b).

Numerous variations on the basic synthesis method described above were tried and evaluated. Purging of the water and/or gold solution with argon prior to synthesis did not appear to have a discernable effect, in agreement with the observations of Norman et al (22). In addition, neither carrying out the synthesis under a constant flow of argon nor saturation of the water with oxygen appeared to affect the reaction. However, the reaction was found to be extremely sensitive to the presence of contaminants on the glassware, leading to the precautions detailed above in the Experimental Section. Freshly prepared concentrated gold solution (0.02 M HAuCl₄) was found to be good for approximately 2-3 weeks, but upon dilution of the gold solution to ~0.5 mM it was necessary to start the reaction immediately. The precise reason(s) for this behavior are unknown. One possible contributing factor to the short lifetime of the gold solutions (particularly the dilute solution) is adsorption of a portion of the gold ions onto the glassware. In addition, it is surmised based on the Pourbaix diagram for aqueous gold chloride solutions that the increase in pH upon dilution may decrease the amount of tetrachloroaurate ion, $AuCl_4^-$, in solution as the ion is only stable in an acidic, oxidative environment.(28) This would also serve to explain the relatively short useful lifetime of the concentrated gold solution, as the concentration of $AuCl_4^-$ in solution would be expected to decrease with time due to reduction of Au^{3+} to Au.

In contrast to the gold solution, the thiosulfate solution was found to be stable for months. Because all of the solutions were prepared using ultrapure UV-sterilized water, it was not necessary to employ a bactericidal agent such as sodium carbonate to stabilize the thiosulfate solution (29). In addition, use of stabilized thiosulfate solution was avoided because it could potentially affect the nanoparticle synthesis by introducing unwanted ions into the solution. However, care was taken to minimize exposure of the thiosulfate solution to light when not in use, due to the known photodecomposition of thiosulfate, particularly in acidic solutions (29). Air oxidation of thiosulfate is known to be a relatively slow process, even under conditions of oxygen saturation, with the predominant decomposition products being sulfate, sulfite, and possibly tetrathionate ($S_4O_6^{2-}$, a polythionate species) (29-31). As sulfate contains sulfur in its fully oxidized

(+6) state, the presence of a small number of sulfate ions in the thiosulfate solution should not significantly affect the gold reduction process. Polythionates such as tetrathionate are expected to compose only a minor fraction of any decomposition products. Although sulfite (SO_3^{2-}) can act as a reducing agent, particularly in basic solution, control experiments carried out using a 60 µL aliquot of 0.1 M sodium sulfite solution as the reducing agent showed no evidence of nanoparticle growth. This was not surprising, given that the pH of the 0.5 mM gold (tetracholorauric acid) solution was quite acidic (pH ≈ 3.1), and sulfite was therefore not expected to be a particularly strong reducing agent under the conditions. As a result, air oxidation of thiosulfate in solution was not found to be a major concern, although it is surmised to be the major contributor to the eventual (>6 months) decomposition of the thiosulfate solutions used.

To prevent premature aggregation of the nanoparticles, a stabilizing agent was added to the reaction mixture 5 minutes into the reaction. A variety of stabilizing agents were employed and evaluated. Initially, sodium sulfate was used as the stabilizing agent to supplement the sulfate produced by the electrochemical reaction. Subsequently, several halides (in particular Cl⁻) were evaluated because of their ready availability and known ability to stabilize metal nanoparticles, and were found to work equally well. Due to our interest in employing these nanoparticles as SERS substrates, several other species representing various chemical functionalities were also evaluated as possible stabilizing agents for the purpose of potentially rendering the nanoparticles attractive to different classes of analytes. The species evaluated as possible stabilizing agents included a carboxylate (acetate), a thiol/mercapto compound (11-mercaptoundecanoic acid), a surfactant (SDS, sodium dodecylsulfate), and several amino acids (DL-alanine, L-lysine, and L-methionine). Of these, all but lysine and methionine served to stabilize the nanoparticle suspensions.

In contrast with the other species investigated as possible stabilizing agents, addition of lysine and methionine caused the nanoparticles to immediately aggregate and fall out of suspension. Further investigations are currently underway with these and other amino acids in an attempt to determine why lysine and methionine behaved as they did. In the case of lysine, the monohydrochloride was used, so it is possible that the further acidification of the reaction mixture upon addition of the amino acid solution led to the observed loss of stability of the nanoparticle suspension. We are therefore investigating both the stability of the nanoparticle suspensions as a function of pH as well as the use of a less acidic preparation of lysine. Another possible explanation of lysine's behavior is that it contains a terminal amine group in its side chain that will be protonated at the pH of the nanoparticle solution. If adsorption of amino acids occurs via the amine group, the presence of this second amine group would allow lysine to serve as a chemical "linker" between two adjacent nanoparticles. Experiments involving arginine, which also contains a terminal amine group, will help to test this hypothesis. In the case of methionine, its side chain contains

a sulfur atom. Because sulfur has a high affinity for gold, it is possible that aggregation of the nanoparticles upon addition of methionine was due to the presence of an additional (sulfur) adsorption site in the amino acid that would allow it to serve as a "linker" molecule between nanoparticles, in analogy to the lysine behavior postulated above. If this is in fact the case, then cysteine should exhibit similar behavior.

Nanoparticle Formation and Flocculation Kinetics

Nanoparticle growth was followed by monitoring the change in intensity of the surface plasmon resonance (SPR) at ~535 nm using visible absorption spectroscopy. As expected, the SPR increased in intensity with time, indicating an increase in the number of nanoparticles (see Figure 1). The SPR reached its maximum intensity approximately 50 minutes after the start of the reaction, at which point it is presumed that all of the gold had been consumed to form nanoparticles and the synthesis reaction had reached completion. The location of the peak absorbance of the SPR changed slightly with time, red-shifting by approximately 4 nm over the course of the reaction (see Figure 1). As the SPR peak absorption wavelength is proportional to the size of the nanoparticles, this red shift was most likely due to a gradual increase in the average size of the nanoparticles, although it is also possible that it was instead due to a change in the local dielectric environment of the nanoparticles caused by buildup of surface charge. The fact that the SPR exhibited a single peak suggested that the nanoparticles were spherical in nature, which was subsequently confirmed via TEM.

In addition to the SPR, the time-dependent spectra also exhibited an extended plasmon band (EPB) in the NIR (see Figure 2) due to temporary flocculation (i.e., agglomeration) of the nanoparticles during synthesis. For the first ~15 minutes of the reaction, the EPB increased in intensity and red-shifted with time, then abruptly began to blue-shift while still increasing in intensity for the next ~15 minutes (see Figure 2). By ~30 minutes into the reaction, the EPB reached its maximum intensity, and remained approximately constant in intensity for the next ~15 minutes while continuing to blue-shift. At this point, ~45 minutes into the reaction, the SPR was nearing its peak intensity, and the EPB began a long gradual decline in intensity (while continuing to blue-shift), as shown in Figure 2. By 3 hours into the reaction, the EPB had virtually disappeared, and 24 hours later it was completely gone due to redispersal of the nanoparticles. Visually, the flocculated nanoparticles present between ~15 minutes and ~1 hour into the reaction corresponded to the deep purple suspension described above in the Experimental Section. Redispersal of the nanoparticles led to the final milky rusty red color. Evidence that this visually apparent color change was related to nanoparticle flocculation was provided by
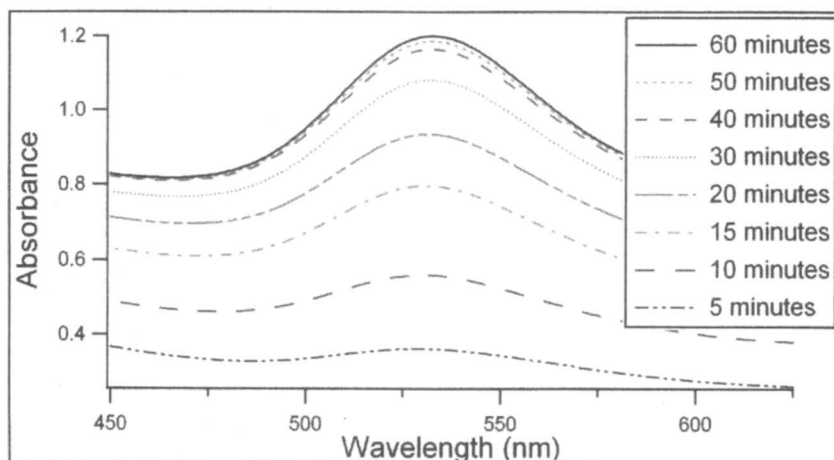
Figure 1. Time-dependent visible absorption spectra (450-625 nm) of an aqueous nanoparticle suspension taken during the course of the synthesis reaction. Note how the surface plasmon resonance (SPR) peak at ~535 nm increases in intensity and red-shifts slightly (~4 nm) with time.
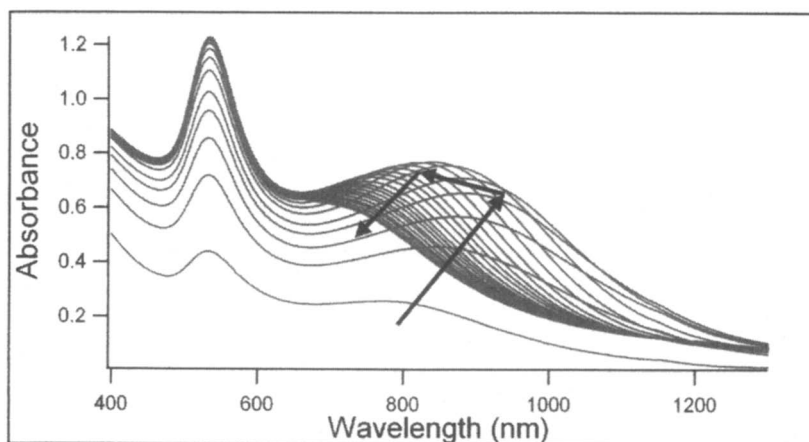
Figure 2. Time-dependent visible-NIR absorption spectra (400-1300 nm) of aqueous nanoparticle suspensions taken at ~5 minute intervals for the first 2 hours of the synthesis reaction. Note the arrows highlighting the changes in intensity and location of the near infrared (NIR) extended plasmon band (EPB) at ~850 nm with time. These changes are indicative of transient nanoparticle flocculation (i.e., agglomeration), followed by redispersal.

the fact that upon addition of a SERS-active analyte (which induces nanoparticle aggregation), the suspensions turned deep purple again and exhibited an EPB. In addition, TEM images of nanoparticles taken both during the synthesis at times when an EPB was present and after 48 hours (when the EPB had disappeared) showed the same distribution of nanoparticle sizes and shapes: predominantly spherical nanoparticles, with only occasional (<<1%) rod-shaped or triangular nanoparticles. However, TEM images of nanoparticle from suspensions exhibiting an EPB displayed large numbers of extensive aggregates, whereas images from suspensions lacking an EPB showed predominantly individual nanoparticles.

Nanoparticle Characterization

To date, only nanoparticles produced by the above method and stabilized with either sulfate or chloride have been fully characterized. TEM images of these nanoparticles show that the nanoparticles are predominantly spherical in shape and ~20-30 nm in diameter (see Figure 3), irrespective of whether they were stabilized with sulfate or chloride. Preliminary dynamic light scattering measurements have confirmed the TEM results, although a detailed statistical
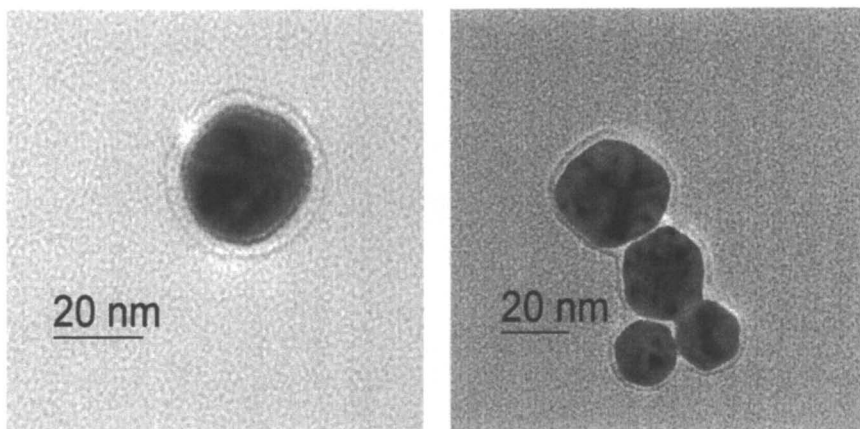
Figure 3. TEM images taken 48 hours into the reaction (no EPB). (a) Individual spherical gold nanoparticle. (b) Image showing several representative nanoparticles. Although mainly individual, non-aggregated nanoparticles were observed following loss of the EPB, a small number of aggregates such as this were also seen. These were most likely an artifact due to convective concentration of the nanoparticles as the solvent evaporated during TEM sample preparation.

analysis of the TEM images is necessary to carry out a more rigorous comparison of the results from the two methods. Asymmetric GI-XRD showed that the gold nanoparticles exhibited a diffraction pattern typical of bulk gold, suggesting that the nanoparticles are crystalline in nature. Analysis of the (111) peak provided further confirmation of nanoparticles size, indicating crystalline domain sizes on the order of 10-25 nm, depending upon the sample.

The surface chemistry of the nanoparticles and the nature of the oxidation-reduction reaction that formed them were confirmed using XPS (see Figure 4). Analysis of the Au $4f$ region showed a doublet at energies corresponding to Au^0 (see Figure 4a), indicating complete reduction of Au^{3+} to Au^0. Analysis of the S $2s$ region for nanoparticles stabilized with chloride (see Figure 4b) showed a single peak at 233.5 eV, corresponding to S^{6+} (i.e., sulfate), while analysis of a sample of sodium thiosulfate in the same region yielded two peaks, one at 226.6 eV (corresponding to S^{2-}) and the other at 232.5 eV (corresponding to S^{6+}). Since no sulfate was added to the chloride-stabilized nanoparticles, this indicates that the thiosulfate reducing agent is fully oxidized to sulfate, as postulated in the proposed electrochemical oxidation-reduction reaction. The slight offset between the S^{6+} peaks in the nanoparticle and thiosulfate spectra is thought to be due to charging of the sample substrate with the nanoparticles.
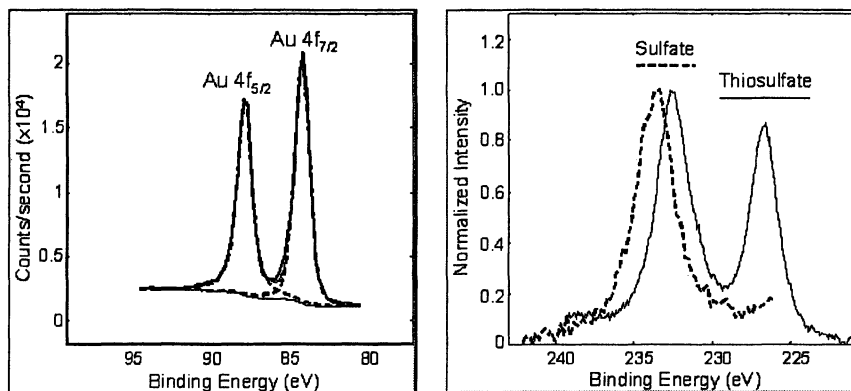
Figure 4. (a) High resolution XPS spectrum of the gold 4f region. The peaks at 87.6 eV and 84.1 eV are due to the $f_{5/2}$ and $f_{7/2}$ spin states of Au^0, respectively. The corresponding peaks for Au^{3+} would be ~3 eV higher in energy. (b) High resolution XPS spectrum of the sulfur 2s region. The doublet (solid line) is from a sample of sodium thiosulfate, demonstrating the two different sulfur oxidation states (6+ and 2–) present in thiosulfate. The overlaid singlet at 233.5 eV (dotted line) is from sulfate (S^{6+}) adsorbed on the surface of chloride stabilized nanoparticles.

SERS Activity

Nanoparticles were tested for SERS activity using 200 nM rhodamine 6G (R6G) as the analyte (see Figure 5), as R6G has typically been difficult to detect using gold nanoparticles (*25*). Although results with the SDS-stabilized nanoparticles were inconclusive (there appeared to be some contamination in the samples), all of the other nanoparticle preparations proved to be SERS active. Further SERS studies with other analytes are currently underway, and preliminary results suggest that all of the anionic stabilizing agents employed thus far permit detection of a wide range of cationic analytes. Consequently, the stabilizing agent is thought to play a key role in the SERS activity of the nanoparticles by adsorbing to their surface, preventing premature nanoparticle aggregation and mediating the analyte-nanoparticle interaction.
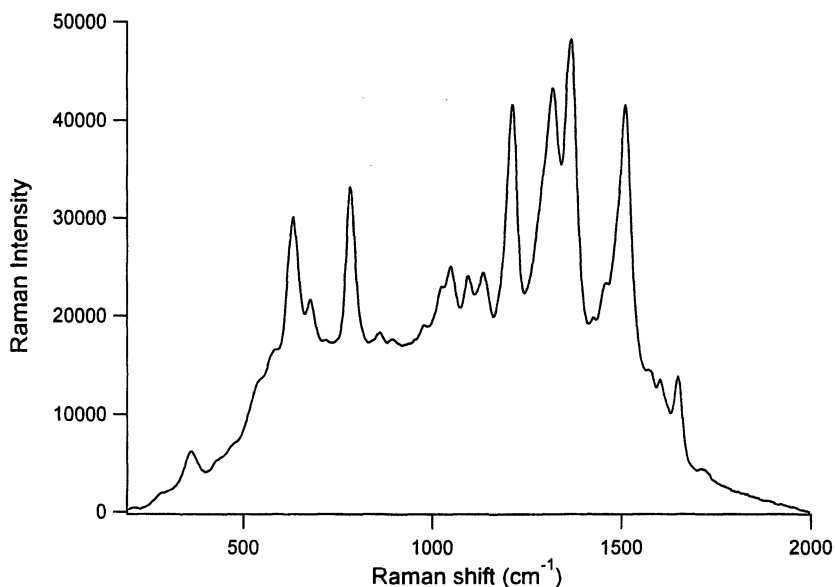
Figure 5. Representative SERS spectrum of 200 nM rhodamine 6G obtained using gold nanoparticles synthesized via the procedure described in this paper.

Conclusions

Highly stable aqueous suspensions of SERS-active spherical gold nanoparticles (15-20 nm diameter) have been prepared by thiosulfate reduction of tetrachloroauric acid ($HAuCl_4$). The reaction proceeds via reduction of Au

(III) to Au (0) with concurrent oxidation of thiosulfate to sulfate. Time-dependent absorption spectra of the nanoparticle suspensions exhibit both the expected visible SPR as well as an EPB in the NIR that initially increases in intensity and red-shifts with time, then blue-shifts and decreases in intensity, before eventually disappearing. The behavior of the EPB is thought to be due to changes in nanoparticle flocculation because of competition between agglomeration of nanoparticles (which minimizes their surface energy) and electrostatic repulsion due to charge buildup on the surface of the nanoparticles. The sulfate produced in the course of the reaction appears to adhere to the surface of the nanoparticle, but is insufficient to prevent nanoparticle aggregation, necessitating the addition of a stabilizing agent. A wide variety of stabilizing agents were found to work, including sulfate, several halides, a carboxylate anion (acetate), a surfactant (SDS), and an amino acid (alanine). The stabilizing agent appears to play a key role in the subsequent SERS activity of the nanoparticles by adsorbing to their surface and mediating the analyte-nanoparticle interaction.

Acknowledgements

References

1. Daniel, M.-C.; Astruc, D. *Chem. Rev.* **2004**, *104*, 293-346.
2. Faraday, M. *Philos. Trans. R. Soc. London, A* **1857**, *147*, 145-181.
3. Turkevich, J.; Stevenson, P. C.; Hillier, J. *Disc. Faraday Soc.* **1951**, *No. 11*, 55-75.
4. Frens, G. *Nature: Phys. Sci.* **1973**, *241*, 20-22.
5. Slot, J. W.; Geuze, H. J. *Eur. J. Cell Biol.* **1985**, *38*, 87-93.
6. Zhao, J.; Das, A.; Zhang, X.; Schatz, G. C.; Sligar, S. G.; Van Duyne, R. P. *J. Am. Chem. Soc.* **2006**, *128*, 11004-11005.

7. Haes, A. J.; Zou, S.; Zhao, J.; Schatz, G. C.; Van Duyne, R. P. *J. Am. Chem. Soc.* **2006**, *128*, 10905-10914.
8. Sherry, L. J.; Jin, R.; Mirkin, C. A.; Schatz, G. C.; Van Duyne, R. P. *Nano. Lett.* **2006**, *6*, 2060-2065.
9. Haynes, C. L.; McFarland, A. D.; Van Duyne, R. P. *Anal. Chem.* **2005**, *77*.
10. Eustis, S.; El-Sayed, M. A. *Chem. Soc. Rev.* **2006**, *35*, 209-217.
11. Murphy, C. J.; Gole, A. M.; Hunyadi, S. E.; Orendorff, C. J. *Inorg. Chem.* **2006**, *45*, 7544-7554.
12. Murphy, C. J.; Sau, T. K.; Gole, A. M.; Orendorff, C. J.; Gao, J.; Gou, L.; Hunyadi, S. E.; Li, T. *J. Phys. Chem. B* **2005**, *109*, 13857-13870.
13. Burda, C.; Chen, X.; Narayanan, R.; El-Sayed, M. A. *Chem. Rev.* **2005**, *105*, 1025-1102.
14. Schwartzberg, A. M.; Olson, T. Y.; Talley, C. E.; Zhang, J. Z. *J. Phys. Chem. B* **2006**, *110*, 19935-19944.
15. Schwartzberg, A. M.; Oshiro, T. Y.; Zhang, J. Z.; Huser, T.; Talley, C. E. *Anal. Chem.* **2006**, *78*, 4732-4736.
16. Hirsch Leon, R.; Gobin Andre, M.; Lowery Amanda, R.; Tam, F.; Drezek Rebekah, A.; Halas Naomi, J.; West Jennifer, L. *Annals of Biomedical Engineering* **2006**, *34*, 15-22.
17. Nehl, C. L.; Grady, N. K.; Goodrich, G. P.; Tam, F.; Halas, N. J.; Hafner, J. H. *Nano. Lett.* **2004**, *4*, 2355-2359.
18. Hao, E.; Li, S.; Bailey, R. C.; Zou, S.; Schatz, G. C.; Hupp, J. T. *J. Phys. Chem. B* **2004**, *108*, 1224-1229.
19. Hao, E.; Schatz, G. C. *J. Chem. Phys.* **2004**, *120*, 357-366.
20. Stuart, D. A.; Yuen, J. M.; Shah, N.; Lyandres, O.; Yonzon, C. R.; Glucksberg, M. R.; Walsh, J. T.; Van Duyne, R. P. *Anal. Chem.* **2006**, *78*, 7211-7215.
21. Zhou, H. S.; Honma, I.; Komiyama, H.; Haus, J. W. *Phys. Rev. B* **1994**, *50*, 12052-12057.
22. Norman, T. J.; Grant, C. D.; Magana, D.; Zhang, J. Z.; Liu, J.; Cao, D.; Bridges, F.; Van Buuren, A. *J. Phys. Chem. B* **2002**, *106*, 7005-7012.
23. Schwartzberg, A. M.; Grant, C. D.; Wolcott, A.; Bogomolni, R.; Zhang, J. Z. In *Proc. SPIE-Int. Soc. Opt. Eng.*; Halas, N. J., Ed.; SPIE: Bellingham, WA, 2003; Vol. 5221, pp 100-107.
24. Zhang, J. Z.; Schwartzberg, A. M.; Norman, T., Jr.; Grant, C. D.; Liu, J.; Bridges, F.; Van Buuren, T. *Nano. Lett.* **2005**, *5*, 809-810.
25. Schwartzberg, A. M.; Grant, C. D.; Wolcott, A.; Talley, C. E.; Huser, T. R.; Bogomolni, R.; Zhang, J. Z. *J. Phys. Chem. B* **2004**, *108*, 19191-19197.
26. Weisbecker, C. S.; Merritt, M. V.; Whitesides, G. M. *Langmuir* **1996**, *12*, 3763-3772.
27. Ross, S.; Morrison, I. D. *Colloidal Systems and Interfaces*; John Wiley & Sons: New York, 1988.
28. Schweitzer, G. K. In *Descriptive Inorganic Chemistry*: Knoxville, TN, 1993, pp 50-55.

29. Blaedel, J.; Meloche, V. W. In *Elementary Quantitative Analysis: Theory and Practice*; 2nd ed.; Harper and Row: New York, 1963, pp 464-465.

30. Cotton, F. A.; Wilkinson, G. In *Advanced Inorganic Chemistry*; 3rd ed.; John Wiley & Sons: New York, 1972, pp 446-453.

31. Shriver, D. F.; Atkins, P. W.; Langford, C. H. In *Inorg. Chem.*; W. H. Freeman: New York, 1990, pp 391-392.

Chapter 3

Controlled Chemical Functionalization of Gold Nanoparticles

Jianhua Zou[1], Qiu Dai[1], Ramakrishna Guda[2], Xiong Liu[1],
James G. Worden[1], Theodore Goodson III[2], and Qun Huo[1,*]

[1]Nanoscience Technology Center, Department of Chemistry,
Department of Mechanical, Materials, and Aerospace Engineering,
University of Central Florida, 12424 Research Parkway,
Suite 400, Orlando, FL 32826
[2]Department of Chemistry, University of Michigan, Ann Arbor, MI 48109

Controlled chemical functionalization of gold nanoparticles through solid-phase place exchange reactions was demonstrated as an efficient approach toward particles with a single chemical group attached on the nanoparticle surface. The as-synthesized monofunctional gold nanoparticles were used as a versatile building blocks in bottom-up approach to prepare various particle assemblies through coupling reaction with other chemicals, molecules, and nanoparticles. Unique optical properties such as enhanced nonlinear optical property and electromagnetic coupling interactions between nanoparticles were observed from a nanoparticle necklace structure prepared by this approach.

Introduction

Gold nanoparticle (AuNP) is among one of the most interesting nanomaterials with a broad application potential (*1-5*). Most AuNPs are covered with a monolayer of ligands to ensure their stability and solubility. To date, most synthetic methods (*6, 7*) or place exchange reaction (*8-11*) without any control can only lead to nanoparticles with either no functional groups or unknown numbers of functional groups which distribute uniformly on the particle. AuNPs

with accurately controlled functionality (i.e. number and distribution of functional groups) are highly demanded for two reasons: first, with a known number of functional groups, AuNPs can be treated as molecules to react with other chemicals, molecules, or nanoparticles to form well defined complex nanodevice in bottom-up approach; second, new properties and applications will derive from the asymmetric distribution of functional groups around AuNPs (*12-15*). So far only a few approaches have been demonstrated for controlled functionalization of AuNPs including separation of AuNPs with discrete numbers of DNA molecules by electrophoresis (*16, 17*) and confined interfacial place exchange reaction by Langmuir film technique (*18*). Recently, a solid phase place exchange reaction was reported for the controlled chemical functionalization of AuNPs (*19-21*) and has been further developed since then. Solid phase synthesis is a synthetic strategy in which chemical reactions are conducted on a solid support such as a polymer resin. This technique has been used extensively in peptide and combinatorial library synthesis (*22, 23*). When applied in controlled chemical functionalization of AuNPs, place exchange reaction (*8-11*) was conducted between AuNPs and ligands supported on polymer beads. By modulating the density of ligands on polymer beads, functional groups can be attached to AuNPs with controlled amount and distribution.

Controlled Chemical Functionalization of AuNPs by Solid-Phase Place Exchange Reaction

A representative procedure of solid-phase place exchange reaction towards controlled functionalization of AuNPs is outlined in Figure 1 (*19-21*). Bifunctional thiol ligands with a carboxyl end group were first immobilized on a solid support such as a polymer resin with a controlled density. The density was tuned according to quantity of functional groups on the final AuNP. If AuNPs with one functional group is expected, the density is controlled low enough that neighboring thiol ligands were far apart from each other. When the modified polymer support was incubated in an alkanethiolate-protected AuNP solution, a one-to-one place exchange reaction took place between the polymer-bound thiol ligands and nanoparticles as depicted in Figure 1. After cleaving off from the solid support, nanoparticles with a single carboxyl group were obtained as the major product. Comparison study on the solution phase versus solid phase place exchange reaction showed that in solution phase reaction, even after strict stoichiometric control of incoming ligand ratio versus the nanoparticle-bound ligands, AuNPs with even distribution of one, two, three, and other discrete numbers of functional groups were obtained (*19*).

A further investigation on controlled chemical functionalization of AuNPs by solid phase modification was carried out to simplify the procedure and
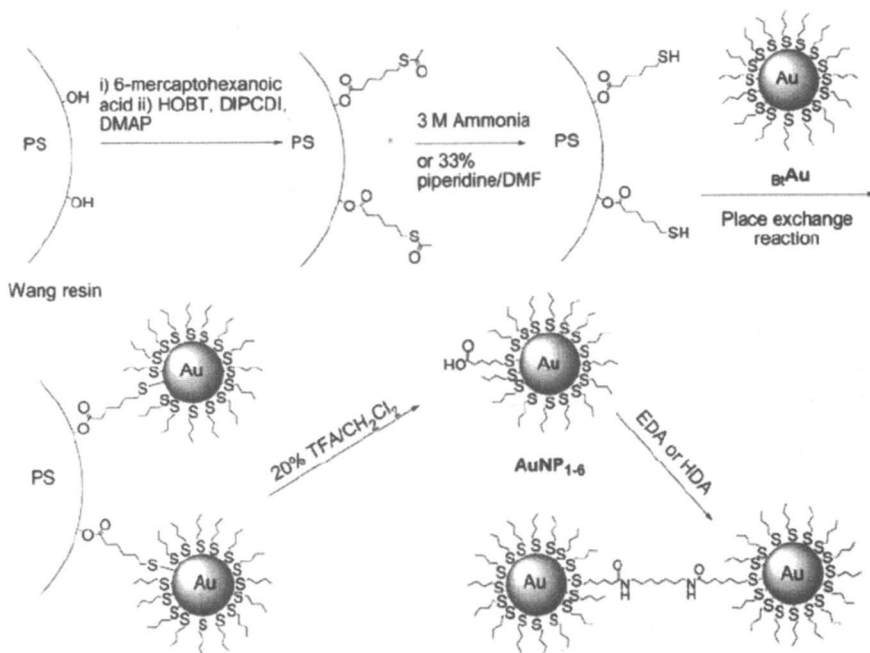
Figure 1. A representative synthetic procedure for monofunctional AuNPs through a solid phase place exchange reaction. (Reprinted with permission from reference 21. Copyright 2004 American Chemical Society.)

improve the yield of monofunctional nanoparticle product. Initially the bifunctional thiol ligands were loaded to polymer support by covalent bond. Multiple reaction steps including protection and deprotection of chemical groups were required to complete the synthesis, which is rather time consuming and costly. An improved procedure of using noncovalent bond to "catch and release" AuNPs was investigated (24, 25). Amino-functionalized silica gel, Rink resin, and anionic resin were used as solid support to conduct the solid phase modification of AuNPs. As depicted in Figure 2, thiol ligands with carboxyl groups were loaded onto amine-functionalized polymer beads directly as a result of electrostatic interactions. Then the surface bound thiol groups underwent a one-to-one place-exchange reaction with AuNPs. Finally, AuNPs with a single carboxyl group attached to the surface were cleaved from polymer beads with a 5% acetic acid solution in a few minutes.

Compared to covalent bond-based solid phase controlled functionalization, the noncovalent bond approach shows advantages including fewer reaction steps and reduced cost. It can be seen that in noncovalent approach, very few chemicals are needed compared to covalent approach. Although with several advantages, special attention needs to be paid to the noncovalent approach
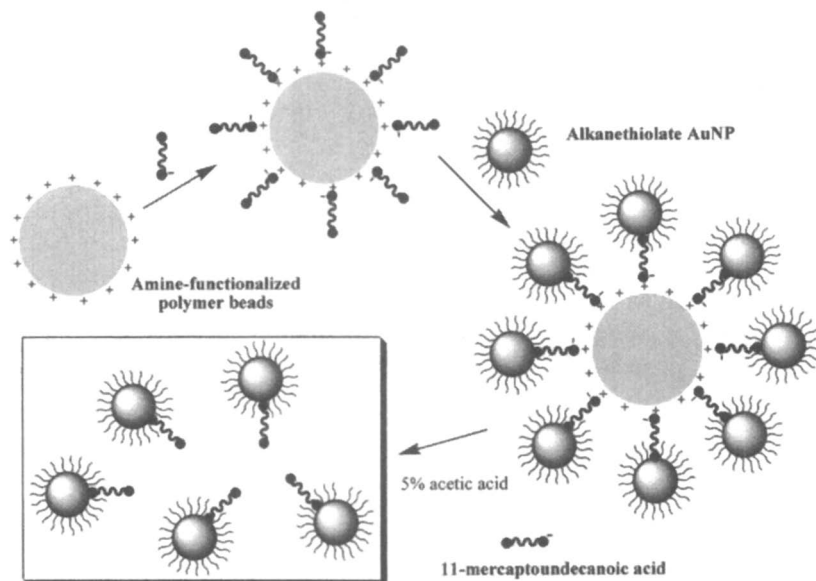
Figure 2. Noncovalent bond-based solid phase synthesis of monofunctional AuNPs. (Reprinted with permission from ref 24. Copyright 2006 John Wiley & Sons, Inc.)

because the electrostatic interaction is a rather weak interaction. Reaction conditions such as polarity of solvents used in each step, thiol ligands loading concentration, and solid phase place exchange reaction time have to be carefully controlled to avoid reversible thiol ligands release from polymer beads back into solution, leading to uncontrolled functionalization product.

Monofunctional AuNPs as Building Blocks to Synthesize AuNPs Assemblies

The first example of a bottom up approach using monofunctional AuNPs was demonstrated on the synthesis of AuNP dimers by coupling two particles with diamine molecules. Shown in Figure 3 is a TEM image of the nanoparticle product after diamine coupling. AuNP dimers were indicated by circles and AuNP trimers or tetramers as indicated by arrows were also observed because of the presence of a small percentage of multifunctional AuNPs. The distance between two particles in dimer can be tuned by the length of diamine. This dimer structure may find potential use in the study of surface enhanced Raman scattering (SERS) effect, as it has been reported that the site sandwiched between two metal nanoparticles is the hot spot for SERS effect (*26*).
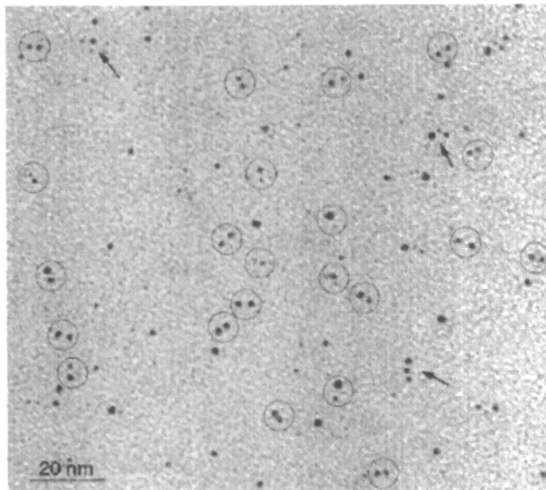
Figure 3. AuNP dimers by coupling single functional AuNPs with diamine.
(Reprinted with permission from ref 20. Copyright 2004 The Royal Society
of Chemistry.)

Another more complicated example was demonstrated through the synthesis of a AuNP nanonecklace assembly using polylysine as a templating skeleton (*27*). Polylysine is a linear polypeptide with side amino groups from lysine residues available for coupling with the monocarboxylic AuNPs. The nanonecklace structures were formed by first covalent attachment of AuNPs to the polylysine backbone followed by ring closure of the polylysine chain as shown in Figure 4. Because each polylysine chain has a carboxylic acid end group, with the presence of amide coupling agent, DIPCDI, the carboxylic end group could have reacted with the end or one of the side amino groups from the same polylysine to form a cyclic polypeptide. The average length of the nanonecklaces correlates to the molecular weight of polylysine. Higher molecular weight of polylysine leads to necklace with longer average length.

Interparticle interactions play a critical role in the optical and electrical properties of nanoparticle material (*28*). Recently, the electromagnetic coupling interaction in gold nanonecklace has been investigated (*29*) using a time-resolved spectroscopy (*30,31*). Figure 5 shows the kinetic traces of surface plasmon bleach for individual AuNPs and gold nanonecklace. The kinetics shown in Figure 5A revealed a considerably slower electron-electron scattering from gold nanonecklace versus individual nanoparticles. In addition, the recovery of bleach (Figure 5B) was also found to be substantially slower for the gold nanonecklace over AuNPs. These observations indicated an efficient dipolar coupling between the plasmons of two neighboring particles. This interparticle electromagnetic coupling can have vital implications in linear,
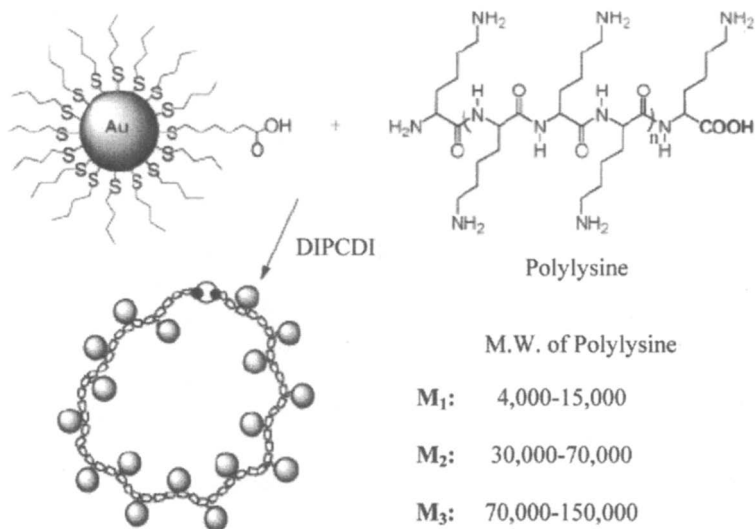
Figure 4. Schematic outline showing the nanonecklace formation by coupling monofunctional AuNPs with polylysine. (Reprinted with permission from reference 27. Copyright 2005 American Chemical Society.)
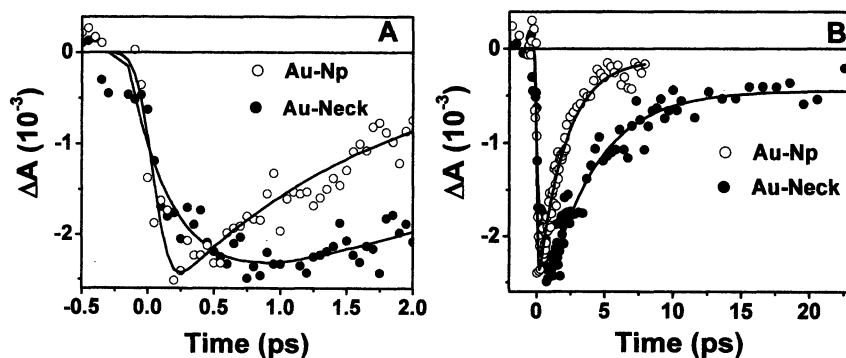
Figure 5. Kinetics decay profiles for Au-Np and at the peak of their bleach wavelengths (A) in short time window and (B) long time window after intraband excitation at 390 nm (Reprinted with permission from reference 29. Copyright 2007 American Chemical Society.)

nonlinear optics, and surface enhanced Raman scattering effect of nanoparticles. One of the interesting properties already observed from the gold nanonecklace is the enhanced optical limiting effect (*32*). AuNPs are known to exhibit nonlinear optical properties for both nanosecond and picosecond laser pulses (*33-35*). Compared to individual AuNPs, gold nanonecklace demonstrates an

enhanced optical limiting effect as shown in Figure 6. The limiting threshold, defined as the incident fluence at which the transmittance drops to 90% of the linear transmission, is as low as ~0.08 J/cm^2 for nanonecklace compared to 0.63 J/cm^2 for individual AuNPs. The transmission drops to 25% when the incident fluence increased to ~1.7 J/cm^2 for gold nanonecklace, while the transmission only drops to 50% for uncoupled AuNPs. The enhanced optical limiting of gold nanonecklace is attributed to the electromagnetic interaction between nanoparticles in close proximity.
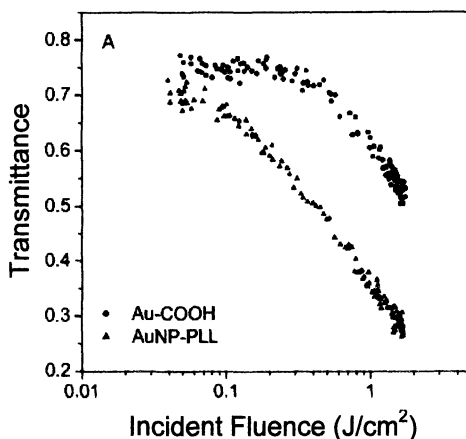
Figure 6. Optical limiting curves for monofunctional AuNPs (Au-COOH) and the gold nanonecklace (AuNP-PLL). (Reprinted with permission from reference 32. Copyright 2005 American Chemical Society.)

The approach to prepare AuNPs assemblies from single functional AuNPs was further demonstrated by the synthesis of a AuNP-dendrimer conjugate cluster (*33*). AuNPs with a single carboxyl group on the surface were coupled to a generation 5 PAMAM dendrimer through amide coupling. After coupling reaction, AuNP clusters ranging in size from 4-10 particles per cluster and with a diameter of 10-13 nm were formed (Figure 7). Interestingly, the AuNP cluster shows no apparent change in the wavelength of the SPR band when compared to the uncoupled monofunctional AuNPs. This may be because the distance between adjacent particles in clusters is not short enough in solution to induce strong interparticle interactions. It is known that the size of a PAMAM dendrimer increases with decreasing pH value (*34-36*), and the polarity of solvents and ionic concentration also have a strong effect on the size of PAMAM dendrimer. Therefore it may be possible to tune the interparticle interaction between AuNPs attached to the dendrimer by adjusting the pH, ionic strength or solvent polarity of the solution. This study is currently under investigation.

38
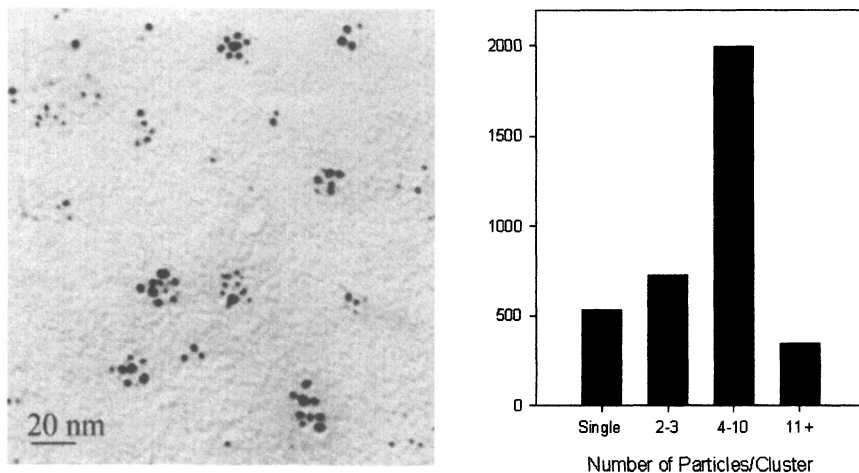
Figure 7. TEM image of AuNP-dendrimer conjugate clusters, and histogram showing the number of particles per cluster. (Reprinted with permission from reference 33. Copyright 2006 The Royal Society of Chemistry.)

Conclusions and Perspectives

Controlled chemical functionalization of AuNPs is a very important area of nanoparticle research. As demonstrated in our and other groups study (*37-41*), monofunctional AuNPs can be successfully synthesized through a solid phase reaction approach. AuNPs with bifunctional or multifunctional groups asymmetrically distributed on the particle surface may also be synthesized either through multicycle of solid phase synthesis or through other controlled synthesis (*42*). AuNPs with controlled chemical functionality may be used as versatile building blocks to synthesize particle assemblies through simple chemical reactions. Further development of assembles using more structurally complicated polymers (e.g. star shape, comb shape polymers and block copolymers) and functional polymer (e.g. thermosensitive (*43, 44*), light sensitive (*45, 46*), and pH sensitive) may lead to new materials with interesting optical and electrical properties.

Acknowledgement

References

1. Templeton, A. C.; Wuelfing, W. P.; Murray, R. W. *Acc. Chem. Res.* **2000**, *33*, 27.
2. Shenhar, R.; Rotello, V. M. *Acc. Chem. Res.* **2003**, *36*, 549.
3. Storhoff, J. J.; Mirkin, C.A. *Chem. Rev.* **1999**, *99*, 1849.
4. Daniel, M. C.; Astruc, D. *Chem. Rev.* **2004**, *104*, 293.
5. Rosi, N. L.; Mirkin, C. A. *Chem. Rev.* **2005**, *105*, 1547.
6. Brust, M.; Walker, M.; Bethell, D.; Schiffrin, D. J.; Whyman, R. *J. Chem. Soc., Chem. Commun.* **1994**, 801.
7. Hostetler, M. J.; Wingate, J. E.; Zhong, C.-J.; Harris, J. E.; Vachet, R. W.; Clark, M. R.; Londono, J. D.; Green, S. J.; Stokes, J. J.; Wignall, G. D.; Glish, G. L.; Porter, M. D.; Evans, N. D.; Murray, R. W. *Langmuir* **1998**, *14*, 17.
8. Hostetler, M. J.; Templeton, A. C.; Murray, R. W. *Langmuir* **1999**, *15*, 3782.
9. Templeton, A. C.; Hostetler, M. J.; Warmoth, E. K.; Chen, S.; Hartshorn, C. M.; Krishnamurthy, V. M.; Forbes, M. D. E.; Murray, R. W. *J. Am. Chem. Soc.* **1998**, *120*, 4845.
10. Templeton, A. C.; Chen, S.; Gross, S. M.; Murray, R. W. *Langmuir* **1999**, *15*, 66.
11. Templeton, A. C.; Cliffel, D. E.; Murray, R. W. *J. Am. Chem. Soc.* **1999**, *121*, 7081.
12. Glaser, N.; Adams, D. J.; Böker, A.; Krausch, G. *Langmuir,* **2006**, *22*, 5227.
13. Perro, A.; Reculusa, S.; Pereira, F.; Delville, M.; Mingotaud, C.; Duguet, E.; Bourgeat-lami, E.; Ravaine, S. *Chem. Commun.* **2005**, 5542.
14. Roh, K.; Martin, D. C.; Lanann, A. J. *Nature Mater.* **2005**, *4*, 759.
15. Perro, A.; Reculusa, S.; Ravaine, S.; Bourgeat-Lami, E.; Duguet, E. *J. Mater. Chem.* **2005**, *15*, 3745.
16. Zanchet, D.; Micheel, C. M.; Parak, W. J. Gerion, D.; Alivisatos, A. P. *Nano Lett.* **2001**, *1*, 32.
17. Zanchet, D.; Micheel, C. M.; Parak, W. J.; Gerion, D.; Williams, S. C.;Alivisatos, A. P. *J. Phys. Chem. B* **2002**, *106*, 11758.
18. Pradhan, S.; Xu, L.; Chen, S. *Adv. Funct. Mater.* **2007** (accepted).
19. Shaffer, A. W.; Worden, J. G.; Huo, Q. *Langmuir* **2004**, *20*, 8343.
20. Worden, J. G.; Shaffer, A. W.; Huo, Q. *Chem. Commun.* **2004**, 518.
21. Worden, J. G.; Dai, Q.; Shaffer, A. W.; Huo, Q. *Chem. Mater.* **2004**, *16*, 3746.
22. *Combinatorial Peptide and Nonpeptide Libraries: A Handbook*; Jung Ed. G; John Wiley & Sons, New York, 1997.
23. *Molecular Diversity and Combinatorial Chemistry*; Chaiken, I. M.; Janda, K. D.; American Chemical Society, Washington, DC, 1996.

24. Liu, X.; Worden, J. G.; Dai, Q.; Zou, J.; Wang, J.; Huo, Q. *Small* **2006**, *2*, 1126.

25. Zou, J.; Dai, Q.; Wang, J.; Liu, X.; Huo, Q. *J. Nanosci. Nanotechnol.* **2007** (in press).

26 Hao, E.; Schatz, G. *J. Chem. Phys.* **2004**, *120*, 357.

27. Dai, Q.; Worden, J. G.; Trullinger, J.; Huo, Q. *J. Am. Chem. Soc.* **2005**, *127*, 8008.

28. Lazarides, A. A.; Schatz, G. C. *J. Phys. Chem. B* **2000**, *104*, 460.

29. Ramakrishna, G.; Dai, Q.; Zou, J.; Huo, Q.; Goodson III, T. *J. Am. Chem. Soc.* **2007**, *129*, 1848.

30. Goodson, T., III. *Acc. Chem. Res.* **2005**, *38*, 99.

31. Goodson, T., III. *Annu. Rev. Phys. Chem.* **2005**, *56*, 581.

32. Sun, W.; Dai, Q.; Worden, J. G.; Huo, Q. *J. Phys. Chem. B* **2005**, *109*, 20854.

33. Francüois, L.; Mostafavi, M.; Belloni, J.; Delois, J.-F.; Delaire, J.; Feneyrou, P. *J. Phys. Chem. B* **2000**, *104*, 6133.

34. Francüois, L.; Mostafavi, M.; Belloni, J.; Delaire, J. A. *Phys. Chem. Chem. Phys.* **2001**, *3*, 4965.

35. Qu, S.; Du, C.; Song, Y.; Wang, Y.; Gao, Y.; Liu, S.; Li, Y.; Zhu, D. *Chem. Phys. Lett.* **2002**, *356*, 403.

33. Worden, J. G.; Dai, Q.; Huo, Q. *Chem. Commun.* **2006**, 1536.

34. Maiti, P. K.; Goddard III, W. A. *J. Phys. Chem. B* **2006**, *110*, 25628.

35. Topp, A.; Bauer, B. J.; Tomalia, D. A.; Amis, E. J. *Macromolecules* **1999**, *32*, 7232.

36. Welch, P.; Muthukumar, M. *Macromolecules* **1998**, *31*, 5892.

37. Sung, K. M.; Mosley, D. W.; Peelle, B. R.; Zhang S.; Jacobson, J. M. *J. Am. Chem. Soc.* **2004**, *126*, 5064.

38. Abed, O.; Vaskevich, A.; Arad-Yelin, R.; Shanzer, A.; Rubinstein, I. *Chem. Eur. J.* **2005**, *11*, 2836.

39. Abed, O.; Wanunu, M.; Vaskevich, A.; Arad-Yelin, R.; Shanzer, A.; Rubinstein, I. *Chem. Mater.* **2006**, *18*, 1247.

40. Huo, F.; Lytton-Jean, A. K. R.; Mirkin, C. A.; *Adv. Mater.* **2006**, *18*, 2304.

41. Xu, X.; Rosi, N. L.; Wang, Y.; Huo, F.; Mirkin, C. A. *J. Am. Chem. Soc.* **2006**, *128*, 9286.

42. DeVries, G. A.; Brunnbauer, M.; Hu, Y.; Jackson, A. M.; Long, B.; Nelter, B. T.; Uzun, O.; Wunsch, B. H.; Stellacci, F. *Science* **2007**, *315*, 358.

43. Hay, D. N. T.; Rickert, P. G.; Seifert, S.; Firestone, M. A. *J. Am. Chem. Soc.* **2004**, *126*, 2290.

44. Zhu, P. W.; Napper, D. H. *Macromolecules* **1999**, *32*, 2068.

45. Sidhaye, D. S.; Kashyap, S.; Sastry, M.; Hotha, S.; Prasad, B. L. V. *Langmuir* **2005**, *21*, 7979.

46. Callari, F.; Petralia, S.; Sortino, S. *Chem. Commun.* **2006**, 1009.

Chapter 4

Synthesis of Thiol Surfactant with Tunable Length as a Stabilizer of Gold Nanoparticles

Quan Li[1], Jouliana M. El Khoury[1], Xiaoli Zhou[1], Augustine Urbas[2], Liangti Qu[3], and Liming Dai[3]

[1]Liquid Crystal Institute, Kent State University, Kent, OH 44242
[2]Materials and Manufacturing Directorate, Air Force Research Laboratory, Wright-Patterson Air Force Base, OH 45433
[3]Department of Chemical and Materials Engineering, University of Dayton, Dayton, OH 45469

The discovery of spontaneous assemblies of thiols on the surface of gold nanoparticles has proven to be a major advance for chemists, physicists and materials scientists in the disciplines ranging from electronics to biomedicine. However, the lack of availability of new thiols with diverse structure has been a barrier to wide investigation on monolayer-protected gold nanoparticles. This chapter describes our recent progress on synthesizing the new thiol surfactants as a stabilizer of gold nanoparticles in organic solvents. Two efficient and mild methods were established for synthesizing the tunable length thiols by reacting alkyl bromide with hexamethyldisilathiane, and by the deprotection of thioacetate into thiol in the presence of tetrabutylammonium cyanide. The approaches are very versatile and effective, and provide an easy access for the direct synthesis of various different length thiols with aliphatic or aromatic structural moieties, which play a crucial role in stabilizing gold nanoparticles and tuning their properties for various technological applications. Gold nanoparticles encapsulated with our synthetic thiols, i.e. thiol monolayer-protected gold nanoparticles, were prepared and well characterized by ^{1}H NMR, UV-vis, FT-IR and TEM. The hybrid nanoparticles are stable in both organic solvents and solid media without irreversible aggregation or decomposition.

Introduction

Gold particles in the nanometer size regime have attracted tremendous attention due to their unusual behaviors compared with corresponding bulk materials (*1*), and hold a great promise in the area of ferrofluids (*2*), catalysis (*3*), electronics (*4*), and biomedical applications (*5*). One of the major challenges is to prevent the aggregation propensity of nanoparticles and control their size, and to organize them into nanostructured devices and composite materials. Dispersing gold particles in organic solvents is appealing since the low interfacial energies should allow for a high degree of control during solution and surface processing. The recent progress on thiol monolayer-protected gold nanoparticles as a result of the strong Au-thiol interaction, i.e. very small clusters of gold atoms coated with thiol monolayers, provides an intriguing pathway to address the challenge (*6a-f*), since the gold nanoparticles prepared by other non-thiol methods such as the citrate method for gold colloids and the reverse micelle method are prone to aggregation to revert back to the bulk gold and do not have good solubility in organic solvents.

Thiol monolayer-protected gold nanoparticles can be prepared following a straightforward procedure that normally involves the wet-chemical reduction of a gold salt in the presence of a stabilizing thiol surfactant usually in a two phase system (*6a*). The resulting gold nanoparticles are different from the conventional colloids and the nanoparticles prepared by micelle, polymer stabilization and stabilization with other small organic ligands in that they are stable and isolable without irreversible aggregation or decomposition in organic solvents (*7*). The thiol surfactants binding to the gold surface by Au-S linkage can not only impart the stability of gold nanoparticles but also tune the properties of the resulting hybrid nanoparticles. To date, thiols have widely been used to stabilize dispersions of gold nanoparticles in organic solvents, however studies on the spontaneous assemblies of organic thiols to form a monolayer on the surface of gold nanoparticle have mainly relied on the availability of a relatively few commercially available unbranched alkanethiols. Recently Zhong et al. (*8*) demonstrated that the size of gold nanoparticles can be tuned molecularly by manipulating different length alkanethiols. By using the commercially available alkanethiols $C_NH_{2N+1}SH$ from N=5 to N=17, gold nanoparticle sizes ranging from 5 to 8 nm with good monodispersity were obtained. Interestingly, an increase in the alkanethiol chain length leads to a gain in stabilization energy due to additional interchain cohesive interactions. Furthermore, it is well known that gold nanoparticles possess size-dependent optical, electrical and magnetic properties with the most significant size effects occurring for nanoparticles 1-10 nm in diameter (*9*). The nanoparticles below 5 nm are thought to be of great practical value for numerous applications (*10*). In order to obtain stable and monodispersed gold nanoparticles with a desired particle size, it is important to

synthesize thiol surfactants with tunable length. A logical way is to connect two length-controllable linear chains via ester group as a linker (Figure 1). The length of the resultant surfactant will be controlled by the combination of different length aliphatic alcohols and aliphatic acids.

In the synthesis of thiols, a protecting group is often employed since organic thiol has the propensity to be oxidized into corresponding disulfide. The most common protecting group is acetyl which can be deprotected by using harsh reaction conditions such as strong acids or bases (e.g. sulfuric acid, hydrochloride, potassium hydroxide, potassium carbonate and lithium aluminum hydride) (11). However, the strong acidic or basic condition results in the formation of by-products or the decomposition of the target thiols containing the group (e.g. ester and amide) sensitive to acid or base. An ideal synthetic procedure to prepare thiol surfactant should involve an efficient transformation to form a protected but conveniently activated thiol precursor under a mild reaction condition.

Here we describe our recent progress on synthesizing the new thiol surfactants as a stabilizer of gold nanoparticles in organic solvents (12). Two efficient and mild methods have been established for the synthesis of the tunable length thiols. These approaches provide an easy access for the direct synthesis of various different length thiols which play a crucial role in stabilizing gold nanoparticles and tuning their properties. The easily synthesized thiols can be spontaneously assembled on the surface of gold nanoparticles. Gold nanoparticles encapsulated with our synthetic thiols, i.e. thiol monolayer-protected gold nanoparticles, were prepared and well characterized by H NMR, UV-vis, FT-IR and TEM. The hybrid nanoparticles are stable in both organic solvents and solid media without irreversible aggregation or decomposition.
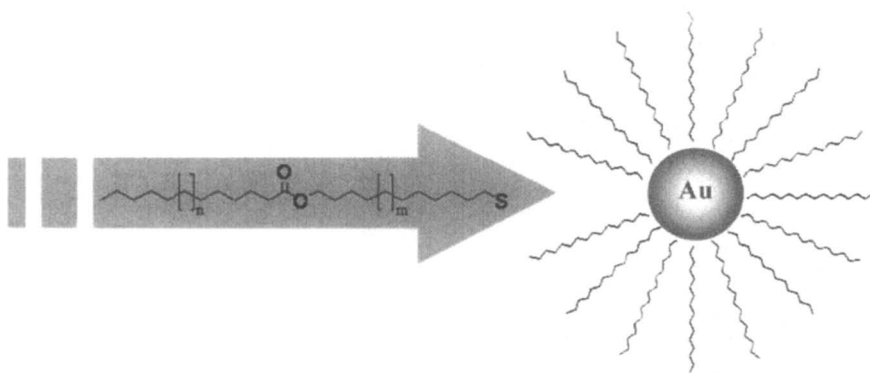
Figure 1. Schematic diagram of thiol monolayer protected gold nanoparticles.

Experimental

All chemicals and solvents were purchased from commercial suppliers and used without further purification. Deionized water was used in the preparation of the gold nanoparticles. $HAuCl_4$ is a 30 wt % in diluted HCl solution. ^{1}H and ^{13}C NMR spectra were recorded in $CDCl_3$. Chemical shifts are in δ units (ppm) with the residual solvent peak as the internal standard. The coupling constant (J) is reported in hertz (Hz). NMR splitting patterns are designated as follows: s, singlet; d, doublet; t, triplet; and m, multiplet. Analytical thin layer chromatography (TLC) was performed on commercially coated 60 mesh F_{254} glass plates. Spots were rendered visible by exposing the plate to UV light or colour agent. Column chromatography was carried out on silica gel (60-200 mesh). Infrared FT-IR spectra were recorded with a KBr pellet. UV-vis spectra were measured in CH_2Cl_2. TEM images were taken on a Hitachi H-7600 transmission electron microscope.

Method 1: synthesis of thiols. The thiol was introduced by a convenient (trimethylsilyl)thioxy-dehalogention reaction (*12*). The target thiols **4a-d** were synthesized starting from aliphatic acid **1** which was reacted with aliphatic alcohol **2** under N, N′-dicyclohexylcarbodiimide (DCC) and 4-dimethylaminopyrindine (DMAP) at room temperature to get aliphatic bromide **3**. The intermediate **3** was reacted with hexamethyldisilathiane in the presence of tetrabutyl ammonium fluoride (Bu_4NF) to get thiol **4** (Scheme 1). The structures of thiols **4a-d** were well identified by ^{1}H NMR, ^{13}C NMR, FT-IR, MS and elemental analysis.

Dodecanoic acid 11-bromo-undecyl ester (3a, m = 1, n = 1): The mixture of 11-bromo-undecan-1-ol (1 g, 3.98 mmol), lauric acid (0.88 g, 4.38 mmol), DCC (0.90 g, 4.38 mmol), and DMAP (0.097 g 0.796 mmol) in CH_2Cl_2 was stirred at room temperature for 12 h. The resulting reaction mixture was extracted with CH_2Cl_2. The organic layer was washed three times with brine, dried over anhydrous magnesium sulfate and evaporated. The residue was purified by flash silicon chromatography using 3% ethyl acetate in hexane as eluent to afford the product. Clear liquid, yield: 72%; ^{1}H NMR: 0.88 (t, 3H) 1.26 (m, 30H) 1.61 (m, 4H) 1.82 (m, 2H) 2.29 (t, 2H, J = 7.6 Hz) 3.41 (t, 2H, J = 6.8 Hz) 4.05 (t, 2H, J = 6.8 Hz).

Tetradecanoic acid 11-bromo-undecyl ester (3b, m = 1, n = 3): White solid, yield: 84%; ^{1}H NMR: δ 0.88 (t, 3H) 1.25 (m, 32H) 1.42 (m, 2H) 1.61 (m, 4H) 1.85 (m, 2H) 2.29 (t, 2H, J = 7.6 Hz) 3.41 (t, 2H, J = 6.8 Hz) 4.05 (t, 2H, J = 6.6 Hz).

Octadecanoic acid 11-bromo-undecyl ester (3d, m = 1, n = 7): White solid, yield: 85%; ^{1}H NMR: δ 0.88 (t, 3H), 1.25 (m, 40H), 1.42 (m, 2H), 1.61 (m, 4H), 1.85 (m, 2H), 2.28 (t, 2H, J = 7.5 Hz), 3.40 (t, 2H, J = 6.8 Hz), 4.05 (t, 2H, J = 6.6 Hz); ^{13}C NMR: δ 14.10, 28.18, 28.76, 29.18, 29.24, 29.29, 29.38,
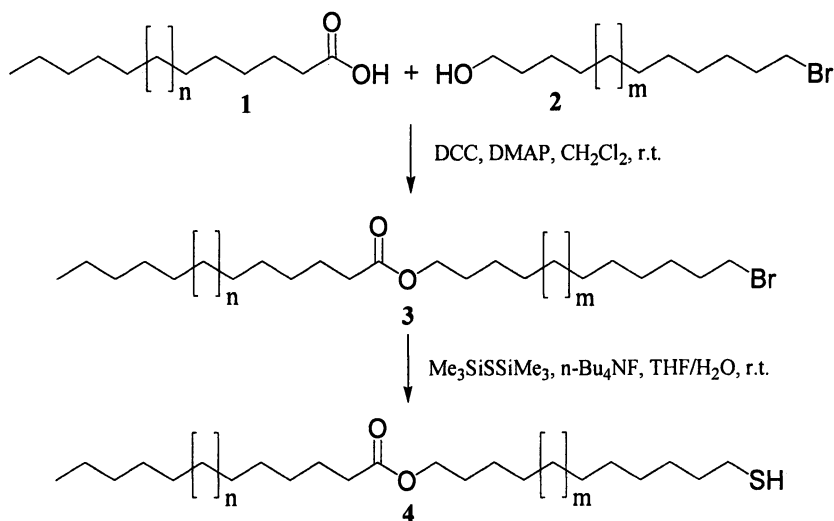
Scheme 1. Synthesis of the tunable length thiols (Method 1)

29.41, 29.45, 29.48, 29.62, 29.67, 29.71, 31.94, 32.84, 34.01, 34.43, 64.38, 174.04.

Dodecanoic acid 11-mercapto-undecyl ester (4a, m = 1, n = 1): White solid; IR (KBr) v_{max} (cm^{-1}): 2920, 2851, 1736, 1177; ^{1}H NMR: δ 0.88 (t, 3H), 1.33 (m, 30H), 1.63 (m, 6H), 2.28 (t, 2H, J = 7.6 Hz), 2.52 (q, 2H), 4.04 (t, 2H, J = 6.6 Hz); ^{13}C NMR: δ 14.07, 22.66, 24.60, 25.03, 25.92, 28.35, 28.67, 29.04, 29.16, 29.21, 29.26, 29.31, 29.46, 29.59, 31.90, 34.03, 34.41, 64.32, 173.87; MALDI-TOF MS calcd for $C_{23}H_{46}O_2SNa$ (M+Na): 409.3116, found: 409.3108; Anal. calcd for $C_{23}H_{46}O_2S$: C, 71.44; H, 11.99; S, 8.29. Found: C, 71.19; H, 12.01; S, 8.08.

Tetradecanoic acid 11-mercapto-undecyl ester (4b, m = 1, n = 3): White solid; IR (KBr) v_{max} (cm^{-1}): 2918, 2850, 1736, 1182; ^{1}H NMR: δ 0.88 (t, 3H), 1.31 (m, 34H), 1.60 (m, 6H), 2.27 (t, 2H, J = 7.6 Hz), 2.51 (q, 2H), 4.04 (t, 2H, J = 6.8 Hz); ^{13}C NMR: δ 14.05, 22.65, 24.58, 25.02, 25.92, 28.35, 28.66, 29.04, 29.15, 29.21, 29.24, 29.32, 29.45, 29.62, 31.90, 34.01, 34.39, 64.30, 173.84; MALDI-TOF MS calcd for $C_{25}H_{50}O_2SNa$ (M+Na): 437.3429, found: 437.3426; Anal. calcd for $C_{25}H_{50}O_2S$: C, 72.40; H, 12.15; S, 7.73. Found: C, 72.68; H, 12.48; S, 7.27.

Hexadecanoic acid 11-mercapto-undecyl ester (4c, m = 1, n = 5): White solid; IR (KBr) v_{max} (cm^{-1}): 2917, 2849, 1735, 1472, 1463, 1179; ^{1}H NMR: δ 0.88 (t, 3H), 1.31 (m, 38H), 1.61 (m, 6H), 2.29 (t, 2H, J = 7.3 Hz), 2.52 (q, 2H), 4.05 (t, 2H, J = 6.7 Hz); ^{13}C NMR: δ 14.10, 22.69, 24.63, 25.05, 25.94, 28.38, 28.68, 29.06, 29.17, 29.24, 29.27, 29.36, 29.48, 29.61, 29.66, 29.69, 31.93, 34.04, 34.43, 64.30, 173.90.

Octadecanoic acid 11-mercapto-undecyl ester (4d, m = 1, n = 7): White solid; IR (KBr) v_{max} (cm^{-1}) : 2918, 2850, 1737, 1464, 1175, 1193; ^{1}H NMR: δ 0.87 (t, 3H), 1.31 (m, 42H), 1.60 (m, 6H), 2.28 (t, 2H, J = 7.6 Hz), 2.52 (q, 2H), 4.04 (t, 2H, J = 6.8 Hz); ^{13}C NMR: δ 14.05, 22.70, 24.64, 25.04, 25.93, 28.38, 28.66, 28.89, 29.07, 29.17, 29.24, 29.28, 29.38, 29.49, 29.62, 29.67, 29.71, 31.94, 34.06, 34.41, 64.36, 173.98; MALDI-TOF MS calcd for $C_{29}H_{58}O_2SNa$ (M+Na): 493.4055, found: 493.4048; Anal. calcd for $C_{29}H_{58}O_2S$: C, 73.98; H, 12.42; S, 6.81. Found: C, 74.03; H, 12.55; S, 6.91.

Method 2: the synthesis of thiols. The thiol was conveniently activated by deprotection of thioacetate in the presence of tetrabutylammonium cyanide [*13*]. The target thiols **4a-d** were synthesized starting from bromoalkanol **2** which was treated with thiolacetic acid in the presence of triethylamine to get **5**. The intermediate **5** was reacted with aliphatic acid **1** under DCC and DMAP at room temperature to get thioacetate **6** followed by the deprotection in the presence of tetrabutyl ammonium cyanide (Bu$_4$NCN) to get thiol **4** (Scheme 2) (*12*).
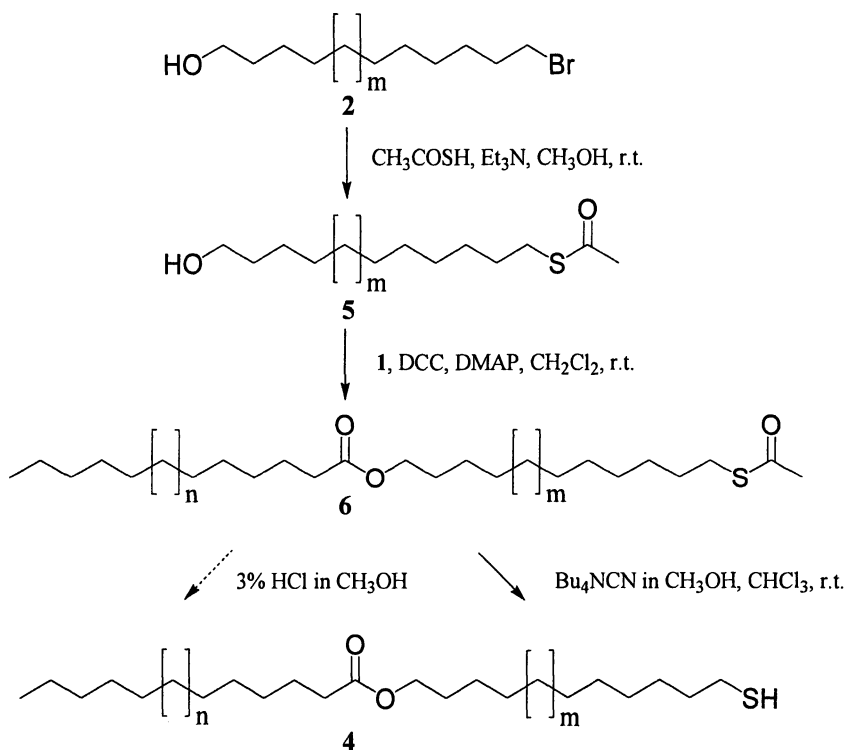
Scheme 2. Synthesis of the tunable length thiols (Method 2)

Thioacetic acid S-(11-hydroxy-undecyl) ester (5, m = 1): A solution of triethylamine(7.96 mmol ,0.81 g) and 20 mL methanol was cooled to 0 °C using ice bath. Then a solution of thiolacetic acid (9.55 mmol, 0.73 g) diluted in 1.5 mL of methanol was added dropwise. The resulting solution was stirred at 0 °C for 10 min, and then added to a room temperature solution of 11-bromo-undecan-1-ol (7.96 mmol, 2 g) in 30 ml of methanol dropwise. The resulting solution was refluxed for 3 h. The reaction mixture was extracted with CH_2Cl_2. The organic layer was washed three times with brine, dried over anhydrous magnesium sulfate and evaporated. The residue was purified by flash silicon chromatography using 10% ethyl acetate in hexane as eluent to afford the product. White solid, yield: 76%; ^1H NMR: δ 1.27 (m, 14H), 1.56 (m, 4H), 2.32 (s, 3H), 2.86 (t, 2H, J = 7.2 Hz), 3.63 (t, 2H, J = 6.6 Hz); ^{13}C NMR: δ 29.16, 29.39, 29.42, 29.46, 29.47, 29.52, 29.54, 29.55, 29.57, 30.63, 32.77, 62.98, 196.20.

Dodecanoic acid 11-acetylsulfanyl-undecyl ester (6a, m = 1, n = 1): The mixture of thioacetic acid S-(10-hydroxy-decyl)ester (1 g, 4.3 mmol), Lauric acid (0.86 g, 4.3 mmol), DCC (0.98 g, 4.73 mmol), and DMAP (0.11 g, 0.86mmol) in CH_2Cl_2 was stirred at room temperature for 12 h. After the reaction complete, the mixture was extracted with CH_2Cl_2. The organic layer was washed three times with brine, dried over anhydrous magnesium sulfate and evaporated. The residue was purified by flash silicon chromatography using 5% ethyl acetate in hexane as eluent to afford the product as white solid, Yield: 91%; IR (KBr) v_{max} (cm^{-1}): 2914, 2849, 1725, 1691, 1653; ^1H NMR: δ 0.88 (t, 3H), 1.29 (m, 30H), 1.58 (m, 6H), 2.28 (t, 2H), 2.32 (s, 3H), 2.86 (t, 2H, J = 7.2 Hz), 4.05 (t, 2H, J = 6.6 Hz); ^{13}C NMR: δ 14.09, 22.66, 25.01, 25.91, 28.64, 28.78, 29.08, 29.10, 29.14, 29.21, 29.26, 29.32, 29.41, 29.45, 29.49, 29.59, 30.57, 31.89, 34.37, 64.32, 173.90, 195.86; MALDI-TOF MS calcd for $C_{25}H_{48}O_3SNa$ (M+Na): 451.3222, found: 451.3222.

Tetradecanoic acid 11-acetylsulfanyl-undecyl ester (6b, m = 1, n = 3): White solid, yield: 84%; IR (KBr) v_{max} (cm^{-1}): 2917, 2849, 1736, 1725, 1694, 1202, 1183; ^1H NMR: δ 0.87 (t, 3H), 1.25 (m, 34H), 1.59 (m, 6H), 2.28 (t, 2H), 2.31 (s, 3H), 2.85 (t, 2H, J = 7.4 Hz), 4.05 (t, 2H, J = 6.8 Hz); ^{13}C NMR: δ 14.10, 22.70, 25.04, 25.94, 28.66, 28.82, 29.11, 29.16, 29.24, 29.28, 29.36, 29.44, 29.48, 29.61, 29.66, 29.68, 30.64, 31.93, 34.43, 64.39, 174.04, 196.07; MALDI-TOF MS calcd for $C_{27}H_{52}O_3SNa$ (M+Na): 479.3535, found: 479.3537.

Hexadecanoic acid 11-acetylsulfanyl-undecyl ester (6c, m = 1, n = 5): White solid, yield: 88%; IR (KBr) v_{max} (cm^{-1}): 2918.02, 2849.84, 1721.47, 1679.05, 1470.86, 1179.02; ^1H NMR: δ 0.86 (t, 3H), 1.24 (m, 38H), 1.59 (m, 6H), 2.27 (t, 2H), 2.30 (s, 3H), 2.84 (t, 2H, J = 7.4 Hz), 4.03 (t, 2H, J = 6.8 Hz); ^{13}C NMR: δ 14.10, 22.70, 25.03, 25.93, 28.65, 28.81, 29.10, 29.13, 29.16, 29.23, 29.28, 29.36, 29.43, 29.47, 29.61, 29.66, 29.69, 30.60, 31.93, 34.40, 64.36, 173.97, 195.97. MALDI-TOF MS (M+Na) calcd for $C_{29}H_{56}O_3SNa$: 507.3848, found: 507.3847.

Octadecanoic acid 11-acetylsulfanyl-undecyl ester (6d, m = 1, n = 7): White solid; Yield: 90%; IR (KBr) v_{max} (cm^{-1}): 2918, 2850, 1721, 1697, 1471, 1179; ^{1}H NMR: δ 0.87 (t, 3H), 1.24 (m, 42H), 1.60 (m, 6H), 2.28 (t, 2H), 2.31 (s, 3H), 2.85 (t, 2H, J = 7.4 Hz), 4.04 (t, 2H, J = 6.8 Hz); ^{13}C NMR: δ 14.10, 22.70, 25.03, 25.93, 28.66, 28.82, 29.10, 29.14, 29.17, 29.24, 29.29, 29.37, 29.44, 29.48, 29.62, 29.67, 29.70, 30.63, 31.93, 34.41, 64.37, 174.00, 196.00; MALDI-TOF MS calcd for $C_{31}H_{60}O_3SNa$ (M+Na): 535.4161, found: 535.4160. Anal. calcd for $C_{31}H_{60}O_3S$: C, 72.60; H, 11.79; S, 6.25. Found: C, 72.50; H, 11.94; S, 6.14.

Thiols 4a-d: The mixture of thioacetate **6** (1.60 mmol) and tetrabutylammonium cyanide (0.16 mmol) in CHCl$_3$ (16 mL) and CH$_3$OH (16 mL) was stirred at room temperature under the protection of nitrogen. The resulting reaction mixture was extracted, washed with water and ammonium chloride, dried over anhydrous sodium sulphate. The organic solvent was removed under reduced pressure to get a pure thiol in a high yield without further purification. Their structures are consistent with those in method 1.

Synthesis of the gold nanoparticles encapsulated with the thiol 4. Gold nanoparticle solutions were prepared following the procedure described by Brust, et al. (*7a*) with slight modification. The thiol **4** was used as a stabilizer to synthesize the gold nanoparticles in a ratio of 2:1 for Au:S. In a typical procedure, 15 mL of 0.015 M aqueous solution of HAuCl$_4$ was mixed with 10 mL of 0.05 M solution of tetraoctylammonium bromide (TOAB) in toluene. The mixture was vigorously stirred for 0.5 h until the gold solution was extracted into the organic layer completely. The top orange red toluene layer was separated from the aqueous layer, and washed twice with water. The solution of thiol **4** (0.09 mmol) in toluene was quickly added to the above mixture with stirring. Freshly prepared aqueous NaBH$_4$ solution (12 mL, 0.2 M) was added slowly. The resulting mixture was continued to stir for 3 h at room temperature. The toluene layer was separated and concentrated with a rotary evaporator under reduced pressure. The gold colloids were precipitated in ethanol and kept overnight in the refrigerator, then filtered with Millipore filter paper (0.5 μm pore size) and washed with ethanol. The precipitation procedure was done twice in order to get rid of free thiol and TOAB impurities. The black precipitate was collected for IR, UV-vis, ^{1}H NMR and TEM studies.

Results and Discussion

We have established two efficient and mild methods for synthesizing the tunable length thiols. In method 1, the thiols were synthesized by reacting alkyl bromide with hexamethyldisilathiane (Scheme 1). In method 2, the thiols were

synthesized by the deprotection of thioacetate into thiol in the presence of tetrabutylammonium cyanide (Scheme 2). The common characteristics of the two methods are 1) very mild reaction condition in which some groups (e.g. ester and amide) sensitive to acid or base are still stable, and 2) their precursors (bromide and thioacetate) are stable to air, moisture and light. However, the advantage of method 1 is that thiol synthesis can be done within a relatively very short time compared with that in method 2. In method 2, we tried to convert the thioacetate **6** into free thiol using 3% HCl/CH$_3$OH (*14*). Unfortunately, it was not successful. Meanwhile, its hydrolyzed products were obtained. This is not surprising since the ester group as the linker might be easily hydrolyzed under the acidic reaction condition.

Although we synthesized four thiols, the general principle of the two methods is applicable to other thiols with aliphatic or aromatic structural moieties. We can use the two approaches to synthesize different length thiols or functional thiols by introducing some functional group into the molecular structure. Interestingly, our synthetic thiols are not easily oxidized into disulfides, as evidenced by the proton-proton coupling between -CH$_2$- and -SH in the NMR spectra recorded from samples even after having been kept for a long time under ambient condition. So the thiols can be purified by flash chromatography on silica gel with 1% ethyl acetate in hexane as the eluent.

Using the thiol **4b** and **4d** respectively as the stabilizer, gold nanoparticles were prepared by reducing HAuCl$_4$ in the presence of TOAB in an organic/aqueous two phase solution (*6a, 15*). As expected, the two resulting hybrid gold nanoparticles encapsulated with the thiol **4b** and **4d** were stable in both organic solvent such as CH$_2$Cl$_2$, THF, toluene or ether and the solid state. These nanoparticles did not show any sign of aggregation or precipitation with time, and they could be re-dispersed in organic solvent after complete removal of solvent (*16*). Size distribution and particle size can be obtained from the TEM which shows almost uniform size and shape of the nanoparticles which is consistent with the literature. Their sizes were 2-4 nm, and TEM images in Figures 2 and 3 also clearly show isolated nanoparticles without aggregation. It is interesting that the length of thiol **4b** and **4d** is approximately 3.4 nm and 3.9 nm, respectively (Figure 4). Since the distance of the hybrid gold nanoparticles in Figure 2 and Figure 3 is less than 6.8 (2x3.4) nm and 7.8 (2x3.9) nm, we can deduce that the intercalation of the surfactant chain might exist (A in Figure 5). It seems that the longer surfactant **4d** in hybrid nanoparticle has a more intercalation than the shorter **4b**.

It is worthy noting here that a unique property of the gold nanoparticles encapsulated with thiol surfactants is that they can be handled and characterized as a simple chemical compound. Therefore, NMR, UV-vis and FT-IR are useful tools to characterize them. The ^{1}H NMR spectra of the gold nanoparticle samples in CDCl$_3$ were similar to the free thiols spectra, but with broadened peaks and the disappearance of the α-methylene quartet at 2.55 ppm close to the
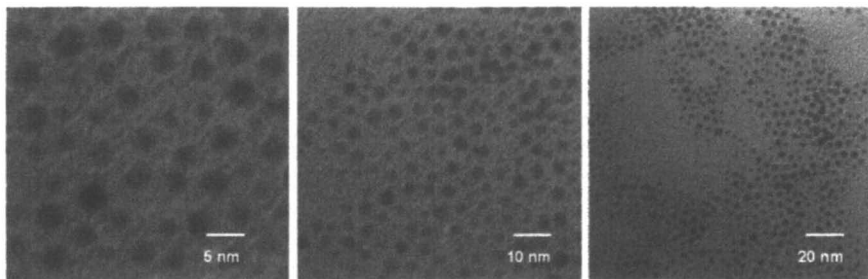
*Figure 2. TEM images (left, middle and right) of gold nanoparticles encapsulated with the thiol **4b** under different magnification.*
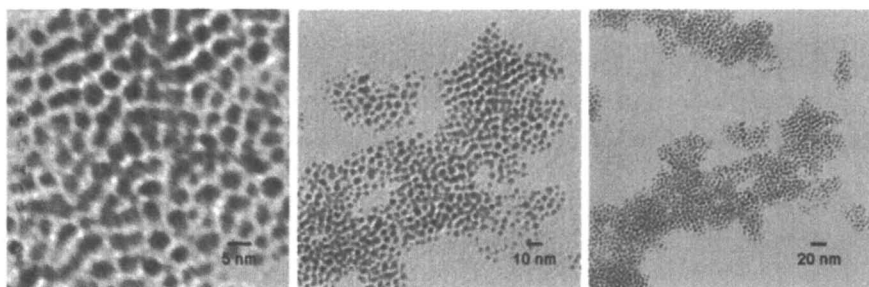
*Figure 3. TEM images (left, middle and right) of gold nanoparticles encapsulated with the thiol **4d** under different magnification.*

~ 3.4 nm

~ 3.9 nm
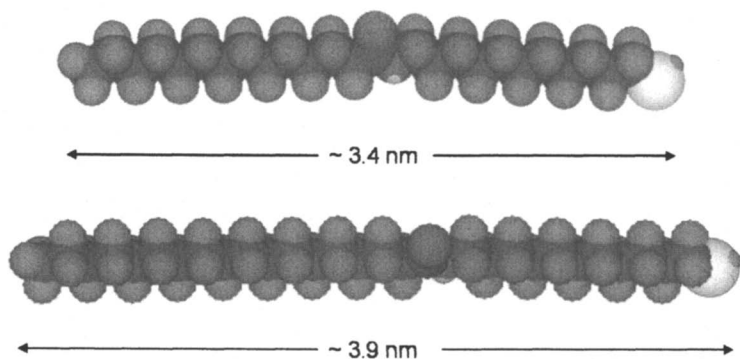
*Figure 4. Space filling model of the thiols **4b** and **4d** by 3D-ChemDraw.*
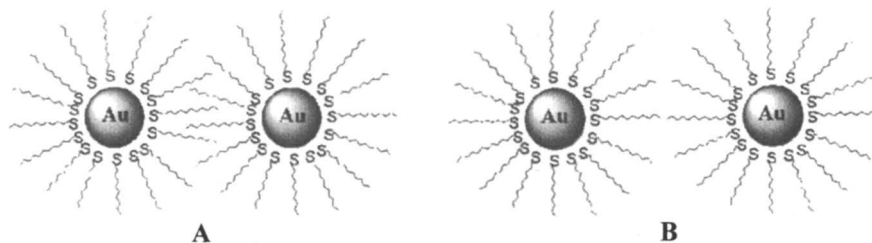
Figure 5. Schematic diagram of the intercalation of thiol surfactants in monolayer protected gold nanoparticles (A: with intercalation; B: without intercalation).

thiol group (Figure 6) (*17*). Also the ^{1}H NMR spectra showed the disappearance of any TOAB residual after the precipitation and washing with ethanol for two times. The FT-IR spectra of the free thiol ligands and of the Au-thiol nanoparticles are similar which indicates that the thiol is part of the composite and the gold nanoparticles are effectively stabilized with these ligands. The ester peak at 1736 cm^{-1} indicates that there is no reduction of the ester group in the thiols ligands during the preparation of the gold nanoparticles. The UV-vis spectra of the gold nanoparticles encapsulated with thiols **4b** and **4d** in CH$_2$Cl$_2$ (Figure 7) are similar and show a broad plasmon band around 510 nm which originates from the formation of the gold colloids (*6d,18*).
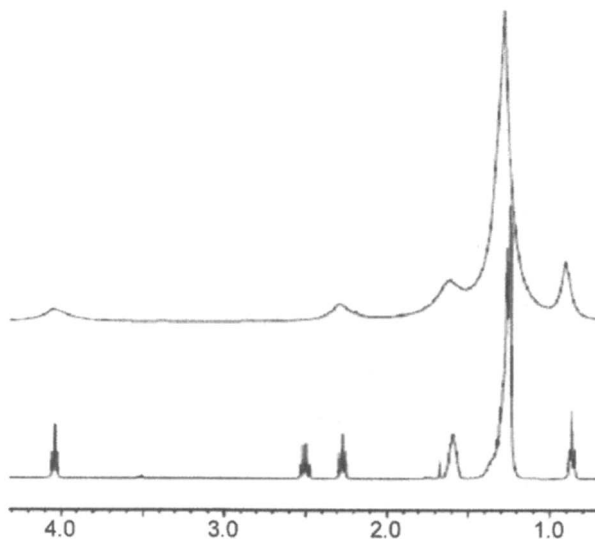
*Figure 6. ^{1}H NMR spectra of the hybrid gold nanoparticles encapsulated with thiol **4b** (above) and the free thiol **4b** (bottom).*
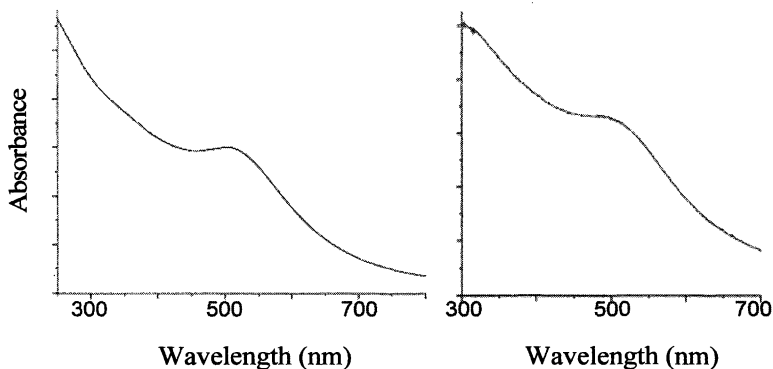
*Figure 7. UV-vis spectra of the gold nanoparticles encapsulated with thiol **4b** (left) and **4d** (right)*

Conclusion

Two efficient and mild methods for the synthesis of the tunable length thiols were established. The ester group as a linker in the thiol-functionalized aliphatic esters is stable under the mild reaction condition. The two synthetic methods are very versatile and effective for constructing many other different length thiol surfactants with aliphatic or aromatic structural moieties, which play a crucial role in stabilizing gold nanoparticles and tuning their properties for various technological applications. Gold nanoparticles encapsulated with some of our synthetic thiols are stable in both organic solvent and the solid state. The hybrid gold nanoparticles did not show any sign of aggregation or precipitation with time, and they could be re-dispersed in organic solvent after complete removal of solvent.

Acknowledgement

References

1. (a) El-Sayed, M. A. *Acc. Chem. Res.* **2001**, *34*, 257; (b) *Metal Nanoparticles: Synthesis, Characterization, and Applications*; Feldheim, D. L.; Foss, Jr., C. A., Eds.; Marcel Dekker: New York, 2002; (c) Lerme, J.

Eur. Phys. D **2000**, *10*, 265; (d) Daniel, M.-C.; Astruc, D. *Chem. Rev.* **2004**, *104*, 293.

2. Rankin, P. J.; Ginder, J. M.; Klingenberg, D. J. *Curr. Opin. Colloid Interface Sci.* **1998**, *3*, 372.

3. Bönnemann, H.; Brijoux, W. R. In *Advanced Catalysts and Nanostructured Materials*; W. R. Moster, Ed.; Academic Press: San Diego, **1996**.

4. (a) Hasobe, T.; Imahori, H.; Kamat, P. V.; Ahn, T. K.; Kim, S. K.; Kim, D.; Fujimoto, A.; Hirakawa, T.; Fukuzumi, S. *J. Am. Chem. Soc.* **2005**, *127*, 1216; (b) Maisch, S.; Buckel, F.; Effenberger, F. *J. Am. Chem. Soc.* **2005**, *127*, 17315; (c) Gu, T.; Whitesell, J. K.; Fox, M. A. *J. Org. Chem.* **2004**, *69*, 4075.

5. (a) Schultz, D. A. *Curr. Opin. Biotechnol.* **2003**, *14*, 13; (b) Salem, A. K.; Searson, P. C.; Leong, K. W. *Nature Mater.* **2003**, *2*, 668; (c) Sandhu, K. K.; McIntosh, C. M.; Simard, J. M.; Smith, S. W.; Rotello, V. M. *Bioconjugate Chem.* **2002**, *13*, 3.

6. (a) Brust, M.; Walker, M.; Bethell, D.; Schiffrin, D. J.; Whyman, R. *J. Chem. Soc. Chem. Commun.* **1994**, 801; (b) Templeton, A. C.; Wuelfing, W. P.; Murrray, R. W. *Acc. Chem. Res.* **2000**, *33*, 27; (c) Maye, M. M.; Luo, J.; Han, L.; Kariuk, N. N.; Zhong, C.-J. *Gold Bulletin* **2003**, *36*, 75; (d) Hussain, I.; Wang, Z.; Cooper, A. I.; Burst, M. *Langmuir* **2006**, *22*, 2938; (e) Waters, C. A.; Mills, A. J.; Johnson, K. A.; Schiffrin, D. J. *Chem. Comm.* **2003**, 540; (f) Chen, S. *J. Phys. Chem.* **2000**, *104*, 4.

7. (a) *Colloidal Gold: Principles, Methods, and Applications*; Hayat, M. A., Ed.; Academic Press: San Diego, **1989**; (b) Cole, D. H.; Shull, K. R.; Baldo, P.; Rehn, L. *Macromolecules* **1999**, *32*, 771; (c) *Clusters and Colloids*; Schmid, G., Ed.; VCH: Weinheim, **1994**; (d) Burda, C.; Chen, X.; Narayanan, R.; El-Sayed, M. A. *Chem. Rev.* **2005**, *105*, 1025; (e) Gascon, I.; Marty, J.-D.; Gharsa, T.; Mingotaud, C. *Chem. Mater.* **2005**, 17, 5228.

8. Schadt, M. J.; Cheung, W.; Luo, J.; Zhong, C.-J. *Chem. Mater.* **2006**, *18*, 5147.

9. Jana, N. R.; Gearheart, L.; Murphy, C. J. *Langmuir* **2001**, *17*, 6782.

10. Hussain, I.; Graham, S.; Wang, Z.; Tan, B.; Sherrington, D. C.; Rannard, S. P.; Cooper, A.; Brust, M. *J. Am. Chem. Soc.* **2005**, *127*, 16398.

11. (a) Shepherd, J. L.; Kell, A.; Chung, E.; Sinclair, C. W.; Workentin, M. S.; Bizzotto, D. *J. Am. Chem. Soc.* **2004**, *126*, 8329; (b) Ciszek, J. W.; Stewart, M. P.; Tour, J. M. *J. Am. Chem. Soc.* **2004**, *126*, 13172; (c) Inman, C. E.; Reed, S. M.; Hutchison, J. E. *Langmuir* **2004**, *20*, 9144.

12. Zhou, X.; El Khoury, J. M.; Qu, L.; Dai, L.; Li, Q. *J. Colloid Interface Sci.* **2007**, 308, 381.

13. (a) Han, C.-C.; Balakumar, R. *Tetrahedron Lett.* **2006**, *47*, 8255; (b) Holmes, B. T.; Snow, A. W. *Tetrahedron* **2005**, *61*, 12339.

14. (a) Steliou, K.; Salama, P.; Corriveau, J. *J. Org. Chem.* **1985**, *50*, 4969; (b) Hu, J.; Fox, M. A. *J. Org. Chem.* **1999**, *64*, 4959; (c) Abel, E. W.; Armitage, D. A.; Bush, R. P. *J. Chem. Soc.* **1964**, 2455; (d) Shiao, M.-J.;

Lai, L.-L.; Ku, W.-S.; Lin, P.-Y.; Hwu, J. R. *J. Org. Chem.* **1993**, *58*, 4742; (e) Strijtveen, B.; Kellogg, R. *J. Org. Chem.* **1986**, *51*, 3664.

15. Jiang, P.; Xie, S.; Yao, J.; Pang, S.; Gao, H. J. *Phys. D: Appl. Phys.* **2001**, *34*, 2255.

16. Balasubramanian, R.; Kim, B.; Tripp, S. L.; Wang, X.; Lieberman, M. Wei, A. *Langmuir* **2002**, *18*, 3681.

17. Hasan, M.; Bethell, D.; Brust, M. *J. Am. Chem. Soc.* **2002**, *124*, 1132.

18. Link, S.; Wang, Z. L.; El-Sayed, M. A. *J. Phys. Chem. B* **1999**, *103*, 3529.

Chapter 5

"Rippled" Mixed Monolayer Protected Nanoparticles with Charged Ligands

Suelin Chen, Oktay Uzun, Alicia Jackson, and Francesco Stellacci[*]

Department of Materials Science and Engineering, Massachusetts Institute of Technology, Cambridge, MA 02139

We present here the first molecular-level resolution STM images of water-soluble nanoparticles with a sulfonate group. We show that when mixed self-assembled monolayers (SAMs) of mercaptoundecasulfonic acid (MUS) and octanethiol (OT) in a 1:1 ratio are assembled on gold nanoparticles, they spontaneously phase-separate into highly ordered ribbon-like phases ("ripples"). These MUS:OT 1:1 nanoparticles have unprecedented solubility in aqueous environments and are thus ideal for use in biological applications. Their water solubility and net negative charge prevented traditional sample preparation methods from being viable and we present new methods for characterization. This new family of water-soluble nano-structured nano-materials may demonstrate new properties due to this novel and unique morphology in their ligand shell.

Introduction

Monolayer protected metal nanoparticles (MPMNs) are composed of a metallic nanocrystal coated by a 'three dimensional' self-assembled monolayer (SAM) of thiolated molecules (*1,2*) This ligand shell determines a large fraction of the particles' properties, ranging from their electro-optical behavior (*3*) to biological catalysis (*4,5*). Due to the easy synthetic approaches used to form these particles (*1*) and to the dynamic equilibrium of the molecules on the nanoparticle core (*6*), a large variety of thiolated ligands have been used to coat these particles (*2*). In some cases nanoparticles are directly synthesized with these ligand shell molecules; in other cases these molecules are placed in the ligand shell via place-exchange reactions. Increasingly, mixtures of molecules are used in the ligand shell where each molecule imparts a different property to the particle. Recently we addressed the problem of ligand shell morphology in mixed ligand coated metal nanoparticles (*7,8*). It has been known that in some, if not most, cases mixed SAMs phase separate into domains on flat gold surfaces (*9*). We used Scanning Tunneling Microscopy (STM) to show that when these same mixed SAMs are assembled onto gold nanoparticles, they spontaneously phase separate into highly ordered ribbon-like domains (*7,8*). The size of these domains is small enough (~0.5 nm) to be comparable to the size of a small molecule. This unique nanostructure confers unexpected properties to the nanoparticles such as non-monotonic dependence of solubility on ligand shell composition as well as some demonstrated resistance to non-specific adsorption of proteins (*8*).

It has been shown that metal nanoparticles display various useful properties when interacting with biological materials, including bio-catalytic activity (*4,10*), excellent light-scattering properties (*11*), and penetration into brain tissues (*12*). These biological applications can only be probed with water soluble nanoparticles. At present the strategies to produce these particles include the use of charged ligands (*4*), ligands terminated with ethylene glycol moieties (*13*), or the use of both biological and non-biological macromolecules (*14*). The latter two strategies employ ligands whose conformational freedom prevents them from forming ordered SAMs on flat surfaces (*15*), let alone on nanocrystals. In such cases there is a negligible enthalpic contribution to mixing, and we thus expect perfect mixing behavior when the ligand shell has two components or more. On the other hand, charged thiolated molecules can indeed form ordered SAMs on flat gold (*15*), and thus it is possible that they can phase separate into ordered domains on gold nanoparticles. Our previous studies dealt exclusively with water insoluble particles and did not address this question (7,8).

Here we show the first study that proves that ribbon-like domains are present in the ligand shell of gold nanoparticles coated with a mixture of mercaptoundecasulfonic acid and octanethiol. These particles are extremely

water soluble—up to 33 wt% for several weeks in solution---even when there is a relatively low fraction of mercaptoundecasulfonic acid. While water solubility and a negative net charge were the targeted properties, they also presented significant challenges towards the characterization of these particles. First, our sample preparation procedure (based on organic solvents) had to be changed; second, the net charge of the particles prevented the formation of dense particle layers; third, residual water molecules on the particles made imaging difficult. We will present a path to overcome all of these problems.

Experimental

Sample Preparation

All materials were purchased from Sigma Aldrich and used as received. Mercaptoundecasulfonic acid was synthesized using a procedure that will be published elsewhere.

200 mL abs. ethanol (EtOH) was stirred in a 500 mL round bottom flask on an ice bath for 10 min. 0.9 mM $HAuCl_4 \cdot H_2O$ (355 mg) was dissolved in EtOH, and after 10 min 0.9 mM of thiol was added to the reaction mixture. After stirring the reaction mixture for another 10 min, 200 ml of a supersaturated solution of $NaBH_4$ in ethanol was added all at once, causing the solution to turn black. The solution was then stirred for another 3 h and refrigerated overnight to precipitate. The supernatant solution was removed, and the remaining solution containing the nanoparticles (~5 ml) was filtered through quantitative filter paper. After filtration, the nanoparticles were rinsed with 200 mL ethanol followed by 200 mL methanol, and then dried thoroughly under air.

Throughout this paper we assume that the stoichiometric ratio used in the reaction is also the ratio found on the particles' ligand shell. Further study to confirm this assumption in this particular system is underway.

The synthesis resulted in nanoparticles polydisperse in size, with core diameters ranging from ~2 to 10 nm, as determined by TEM and confirmed with STM.

Bare Au (111) thermally evaporated on freshly cleaved mica substrates (Molecular Imaging) were used for imaging of the particles. Approximately 1 mg of nanoparticles was dissolved in 1 ml of DI water. ~3 µl of this solution was cast onto the substrate that had been previously (~5 min) placed onto a hotplate kept at ~120°C. The heat causes the water to evaporate quickly (~2-3 s), effectively 'freezing' the solution distribution of nanoparticles onto the substrate.

Imaging

STM images were obtained using a Digital Instruments Multimode Nanoscope IIIa equipped with an E scanner. Pt/Ir tips were purchased from Veeco and mechanically cut. Typically a bias voltage of -1.2 to -1.4 V, a set current value of ~600 pA, and a tip speed of 0.3-1.3 μm/s were used. Integral gains and proportional gains had typical values of ~0.6 and ~0.8, respectively.

Results and Discussion

Our standard sample preparation techniques were developed for nanoparticles dissolved in organic solvents (7). The basic procedure is to expose a gold substrate coated with an alkanedithiol monolayer to a solution of nanoparticles. We used this technique as a starting point for the preparation of samples of these water soluble particles, but found that few particles, if any, were transferred to the substrate. Additionally, because the nanoparticles were not directly attached to or interdigitated into the dithiol monolayer (due to the hydrophobic nature of the SAM and the hydrophilic nature of the nanoparticles), the particles were not stabilized on the surface. Thus the effective tunneling barrier from the particle core to the gold substrate was extremely large, requiring high voltages that could drive particles away from the tip and make imaging nearly impossible. Another difficulty was that we were not able to solubilize dithiol molecules in the aqueous solution of nanoparticles to crosslink them together, which is a strategy that we commonly use to obtain stable nanoparticle networks that are easier to image (7). We also tried electrostatically attracting the particles to the surface by forming a cysteamine hydrochloride ($HSCH_2CH_2NH_2 \cdot HCl$) SAM on the gold on mica. These SAMs were formed from solutions of either water or ethanol, at concentrations of 100μM, 1mM and 10 mM. Unfortunately, STM images showed the tendency of this molecule to form three dimensional aggregates on these surfaces. We thus settled on casting the nanoparticles on bare Au (111).

Our sample preparation procedure consisted of placing a drop of nanoparticle solution on the substrate and allowing the solvent to evaporate under ambient conditions. However, we found that the relatively slow evaporation of water at room temperature caused large aggregates of nanoparticles to form that made the samples difficult to image. This led us to cast the nanoparticles onto a heated substrate to accelerate the evaporation of the water, allowing for the formation of sparse sub-monolayers of these particles on the gold surface. This enabled the achievement of the first STM images of these nanoparticles.

STM images, in agreement with the TEM images, showed a nanoparticle population polydisperse in diameter, ranging from about 2 nm to about 10 nm. Since ripple spacing has been found to vary with nanoparticle diameter (7), we

tried to limit our ripple analyses to nanoparticles with diameters in the range of 3-5 nm for this study.

Figure 1a shows an STM height image that has two nanoparticles with defined ribbon-like domains (or ripples) of about 0.59 nm in spacing. The nanoparticle on the left has ripples that are roughly vertical, while the one on the right has ripples that are roughly horizontal. For comparison, homoligand nanoparticles coated only with mercaptoundecasulfonic acid ligands are shown in Figure 1b. Some streaks are visible due to nanoparticle movement caused by the STM during imaging. Indeed, the nanoparticles are not covalently attached to the substrate and have only weak interactions with the surface; nor are they packed tightly enough to have stabilizing interactions with each other. When examining these rippled nanoparticles, we preliminarily assign the higher, lighter domains to the mercaptoundecasulfonic acid and the darker domains to the octanethiol molecules. The observed striations (ripples) are similar in appearance to our previous images of octanethiol:mercaptopropionic acid (OT:MPA) (7,8).
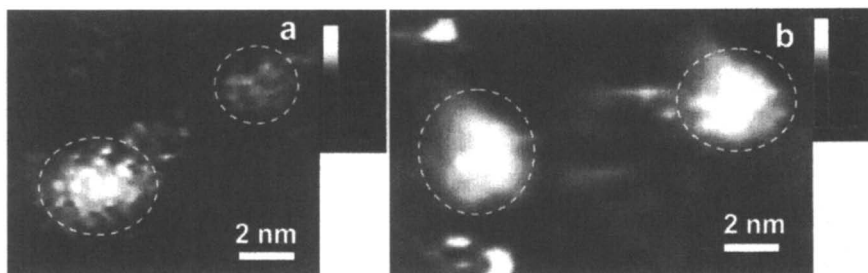
Figure 1. STM height images. (a) Gold nanoparticles coated with a 1:1 molar ratio of mercaptoundecasulfonic acid and octanethiol (MUS:OT 1:1), cast on bare Au on mica, showing nanostructuring in their ligand shell due to the phase separation of the two ligands. These "ripples" are evident in the nanoparticles outlined with dashed circles. (b) Homoligand gold nanoparticles coated with mercaptoundecasulfonic acid only (all-MUS), cast on bare Au on mica. Nanoparticles are outlined with dashed circles. No ripples are visible.

However, as shown in Figure 2, their average spacing is smaller than that measured in OT:MPA and is close to the spacing of headgroups in homoligand nanoparticles. We attribute this phenomenon to the formation of fine monomolecular domains, an effect that we have observed in 1:1 mixtures.[7] Charge and dipole balances in this system may be the driving force for a further narrowing of the domain sizes. As usual, attention was paid to distinguish noise from true domains in our images. Figure 3 displays measurements of ripple spacing with respect to tip velocity. The linear fit clearly does not go through
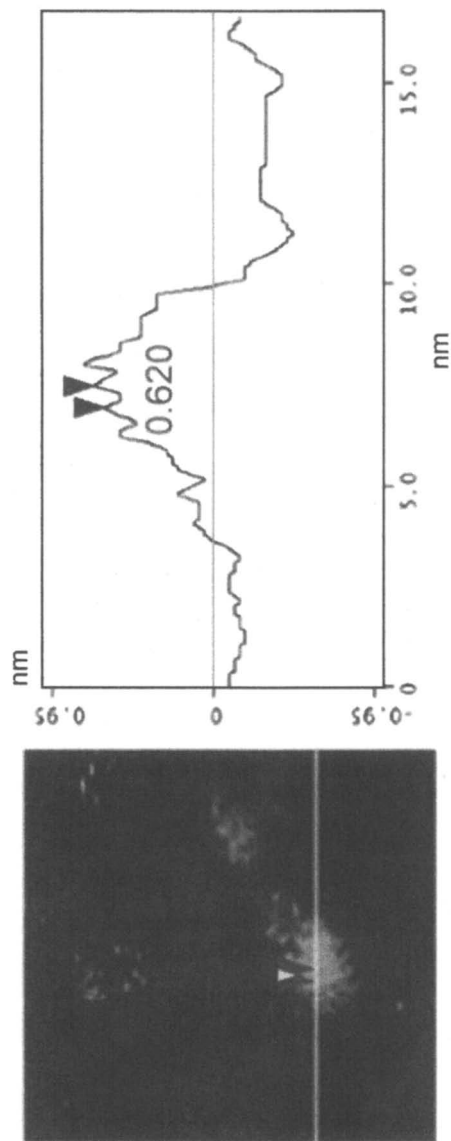
Figure 2. Line scan through one rippled nanoparticle, showing a peak-to-peak spacing between ripples of ~0.620 nm.

the origin, and is only weakly dependent on tip speed; we are thus confident that the ripples in the image are real and not imaging artifacts.
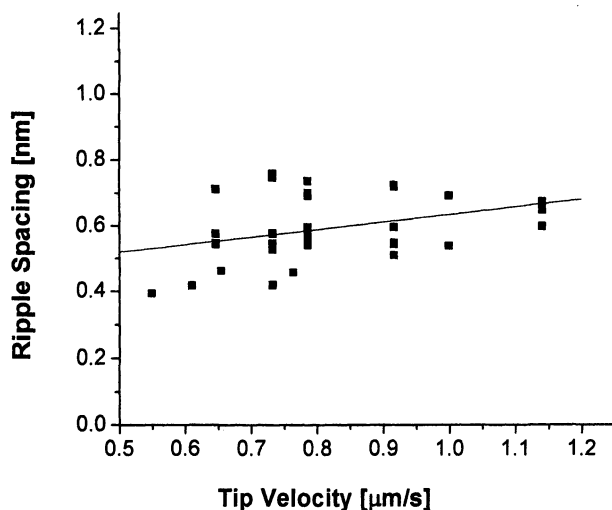
Figure 3. STM ripple spacing data of MUS:OT 1:1 nanoparticles with diameters between ~3-5 nm, imaged at tip velocities between 0.55-1.14 μm/s. The line is a linear fit to the data and has an equation of y = 0.406 + 0.228x. The spread is likely due to measurement error, the polydispersity of the nanoparticles, as well as convolution with noise.

Conclusions

In conclusion, we have presented here high resolution STM images of 'rippled' nanoparticles with charged ligands. Their unique nanostructure will determine how they interact with their environment, which we will further investigate. The hydrophilicity of these nanoparticles makes them ideal for use in biological applications.

Acknowledgements

References

1. Daniel, M. C.; Astruc, D., *Chem. Rev.* **2004**, *104*, *1*, 293-346.
2. Templeton, A. C.; Wuelfing, M. P.; Murray, R. W., *Accounts Chem. Res.* **2000**, *33*, *1*, 27-36.
3. Thomas, K. G.; Kamat, P. V., *Accounts Chem. Res.* **2003**, *36*, *12*, 888-898.
4. Verma, A.; Simard, J. M.; Worrall, J. W. E.; Rotello, V. M., *J. Am. Chem. Soc.* **2004**, *126*, *43*, 13987-13991.
5. Pasquato, L.; Pengo, P.; Scrimin, P., *Supramolecular Chemistry* **2005**, *17*, *1-2*, 163-171.
6. DeVries, G. A.; Brunnbauer, M.; Hu, Y.; Jackson, A. M.; Long, B.; Neltner, B. T.; Uzun, O.; Wunsch, B. H.; Stellacci, F., *Science* **2007**, *315*, 5810, 358-361. Ingram, R. S.; Hostetler, M. J.; Murray, R. W., *J. Am. Chem. Soc.* **1997**, *119*, *39*, 9175-9178.
7. Jackson, A. M.; Jacob Silva, P.; Hu, Y.; Stellacci, F., *J. Am. Chem. Soc.* **2006**, *128*, 11135-11149.
8. Jackson, A. M.; Myerson, J. W.; Stellacci, F., *Nat. Mater.* **2004**, *3*, *5*, 330-336.
9. Cygan, M. T.; Dunbar, T. D.; Arnold, J. J.; Bumm, L. A.; Shedlock, N. F.; Burgin, T. P.; Jones, L.; Allara, D. L.; Tour, J. M.; Weiss, P. S., *J. Am. Chem. Soc.* **1998**, *120*, *12*, 2721-2732. Smith, R. K.; Reed, S. M.; Lewis, P. A.; Monnell, J. D.; Clegg, R. S.; Kelly, K. F.; Bumm, L. A.; Hutchison, J. E.; Weiss, P. S., *J. Phys. Chem. B* **2001**, *105*, *6*, 1119-1122. Stranick, S. J.; Atre, S. V.; Parikh, A. N.; Wood, M. C.; Allara, D. L.; Winograd, N.; Weiss, P. S., *Nanotechnology* **1996**, *7*, *4*, 438-442. Weiss, P. S.; Bumm, L. A.; Dunbar, T. D.; Burgin, T. P.; Tour, J. M.; Allara, D. L., Probing electronic properties of conjugated and saturated molecules in self-assembled monolayers. In *Molecular Electronics: Science and Technology*, 1998; Vol. 852, pp 145-168.
10. Manea, F.; Houillon, F. B.; Pasquato, L.; Scrimin, P., *Angew. Chem.-Int. Edit.* **2004**, *43*, *45*, 6165-6169.
11. El-Sayed, I. H.; Huang, X. H.; El-Sayed, M. A., *Cancer Letters* **2006**, *239*, *1*, 129-135.
12. Kohler, N.; Sun, C.; Fichtenholtz, A.; Gunn, J.; Fang, C.; Zhang, M. Q., *Small* **2006**, *2*, *6*, 785-792.
13. Zheng, M.; Li, Z. G.; Huang, X. Y., *Langmuir* **2004**, *20*, *10*, 4226-4235.
14. Taton, T. A.; Mirkin, C. A.; Letsinger, R. L., *Science* **2000**, *289*, 5485, 1757-1760.
15. Love, J. C.; Estroff, L. A.; Kriebel, J. K.; Nuzzo, R. G.; Whitesides, G. M., *Chem. Rev.* **2005**, *105*, *4*, 1103-1169.

Chapter 6

Synthesis and Optical Properties of 1D Metal and Core/Shell Colloidal Nanostructures

Mingzhao Liu and Philippe Guyot-Sionnest

James Franck Institute, The University of Chicago, Chicago, IL 60637

The plasmon resonance of noble metal nanoparticles provides interesting optical properties in the visible and near-infrared region, and is highly tunable by varying the shape and the composition of the nanoparticles. This chapter describes the synthesis of gold nanorods and monodisperse gold bipyramids, as well as their growth mechanism. These rod-like nanostructures have pronounced plasmon resonance varying in the 1~2 eV range. These nanostructures also have extraordinary near-field behavior. It is shown by FDTD (finite-difference time-domain) simulation that there is significant field enhancement (> 100 fold) in the vicinity of the nanoparticle at its plasmon resonance. This chapter also covers the synthesis and optical properties of core/shell nanostructures, such as metal/metal or metal/semiconductor nanorods. These composite material gives more tunability to the plasmon and may present interesting nonlinear optical properties.

Noble metal nanocrystals have interesting optical properties which come from the excitation of free electron surface plasmon by the electromagnetic field (*1,2*). The surface plasmon drastically disturbs the near-field at its resonance and gives strong light scattering and absorption, in addition of large local field enhancement. The plasmon modes of a metal particle are determined by its shape, composition, size and surrounding media (*2*). Although spherical nanoparticles can be synthesized easily, the tunability of the plasmon is small, since its frequency is independent of the size as long as $R \ll \lambda$. However, the resonance frequency is very sensitive to the shape of the nanoparticles. In recent years, metal nanoparticles with different shapes and compositions have been synthesized, with their spectra covering the whole visible and near-infrared range (Figure 1). The shapes explored include prisms (*3*), spherical shells (*4*), cubes (*5*), rods (*6–9*), bipyramids (*9*), and wires (*10*).
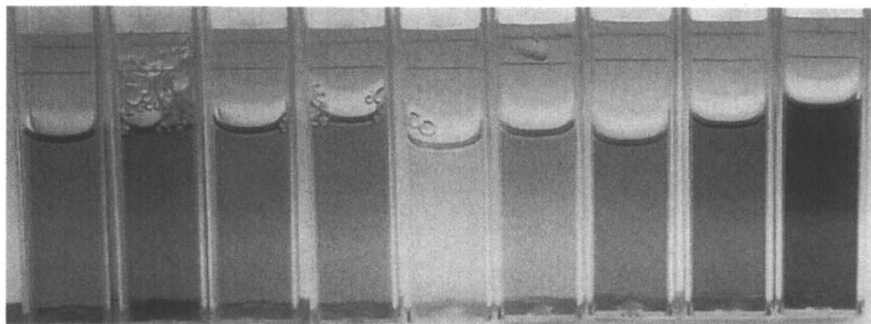
Figure 1.Colloid solutions of Gold and Silver nanoparticles of different sizes, composition and with sphere or rod-like shape. (Reproduced from reference 11. Copyright 2004 American Chemical Society)

As a noble metal nanosphere is distorted into prolate spheroid (or rod), its single plasmon resonance mode splits into two modes with one blue-shifted (transverse) and another red-shifted (longitudinal). The rod-like nanoparticles are therefore promising systems for optical studies as the spectrum is easily tunable by varying the aspect ratio. For example, we reported on gold nanorods, where the longitudinal plasmon resonance is tunable from 2.4 eV to 0.6 eV by increasing the aspect ratio from 1 (sphere) to 13 (*11*). Compared to spheres, the quasi-one-dimensional structure gives a larger curvature at the tips for the same volume. Since the local field enhancement is proportional to the curvature of the surface (*12*), significant field enhancement is expected for the nanorods.

The enhancement of near-field at the plasmon resonance allows the electromagnetic energy to be localized more tightly than the diffraction limit, i.e., half of the optical wavelength, which restricts the miniaturization of

conventional photonic devices. Preliminary steps have been made, for example, towards using surface plasmons in nanoparticles to construct subwavelength waveguides (13). The active control of the light propagation in such structures requires the presence of units with optical nonlinearities, acting as switches and logic gates. Significant optical nonlinearity has been observed from single gold nanorod when its longitudinal plasmon mode was excited, although it is mainly due to the thermalization of the conduction electrons and phonons (14).

Another way of introducing enhanced nonlinearities is to immerse the metal nanoparticles into a nonlinear medium. As the dielectric constant of the medium changes, the plasmon resonance shifts, as seen in Mie's solution (15). This nonlinearities may lead to optical bistability under certain conditions. Practically, core/shell structures are developed for such purpose, where the shell can be considered as an effective medium of the core. Different types of materials, either metal or semiconductor, can be coated over the gold nanorods in a homogenous way, and tune the plasmon resonance to different directions. In the case of metal coating, the free electrons can travel between two metals, leading to extra damping associated with the electron scattering at the interface, which is another interesting aspect of the plasmon dynamics (11).

Synthesis of Gold Nanorods by Seed-Mediated Method

During the past decade, several methods have been developed to synthesize gold nanorods. Gold nanorods were synthesized by Van der Zande et al., using porous alumina as a hard template (16). However, this method only yields very small amount of nanorods for each synthesis. The electrochemical reduction method developed by Yu et al provided higher yield of gold nanorods with aspect ratio 2 – 7 (6). This method consists in electrochemically reducing $HAuCl_4$ in an aqueous solution of cetyltrimethylammonium bromide (CTAB), a cationic surfactant. The seed-mediated method was developed by Murphy and coworkers, inspired by the idea that CTAB may act as a "soft template".

General Approach of the Seed-Mediated Method

In Murphy's method, nanorods are produced in reasonable yield by chemically reducing $HAuCl_4$ with L-ascorbic acid in a CTAB solution, where small "seed" gold nanoparticles were added as nucleation centers (Figure 2) (7). Using selective area electron diffraction (SAED) and high resolution transmission electron microscopy (HRTEM), Johnson et al showed that the nanorods are isometric penta-fold twinned around their growth axis, which is along the [011] direction (17). Each section is separated by (111) planes. In an idealized model, each nanorod has five {100} side faces and ten {111} end

faces. The elongation along the twinning axis was naturally explained by the different growth rates of the {100} facets and {111} facets. Therefore, a previous assumption that CTAB acts as a "soft template" by forming cylindrical micelles, is not needed. By varying the experimental conditions, including seeds concentration and pH of the growth solution, gold nanorods with aspect ratio 2~20 have been reported (7). However, the method also produces significant amount of spherical gold nanoparticles as by-products, leaving certain difficulties for the separation.

Later, El-Sayed and coworkers developed an alternative procedure to produce gold nanorods in nearly quantitative yield, by adding silver nitrate into the growth solution (8). The aspect ratio of the nanorods is well controlled by the concentration of silver. In one of our reports, we found that by increasing the Ag/Au ratio from 0.04 to 0.2, the longitudinal plasmon resonance red-shifts from 2 eV to 1.4 eV (Figure 3a), corresponding to an increase of the aspect ratio from 2 to 5, as confirmed by the TEM (9). The spectra can be nearly quantitatively explained by treating the rod as a prolate spheroid in the quasi-static approximation (Gans' solution). We note that the gold nanorods grown to such different aspect ratios nevertheless preserve approximately similar volume, which is consistent with the gold seeds nucleating the growth. It was observed by us and others that the freshly prepared nanorods can further grow into a dumbbell shape, causing the longitudinal plasmon resonance to blue-shift by up to 100 nm over the first few hours (18,19). We found that reducing the pH to about 3 allowed to significantly improve the method and product stability (Figure 3b).

Followed by HRTEM studies, we found that the gold nanorods prepared with the assistance of silver are single crystals with no observable stacking faults or twins. The axis of growth is along the [100] direction. For a fresh sample, the ends of the nanocrystals are nearly flat, which must be the {100} facets. The aged samples generally develop more truncated ends. For a fully grown nanorods sample, both {011} and {001} were found as the side facets. The structure is totally different from the seed-mediated grown gold nanorods in the absence of Ag(I) (17), suggesting a different growth mechanism. The growth reaction can be terminated at anytime, by adding n-dodecanethiol to the solution, leaving the smaller, "unfinished" nanorods capped by thiol. Most of these nanorods have their side facets as {011}, indicating its dominance during the growth process. Therefore, the {100} facets observed for the fully grown nanorods are more likely to have appeared during the aging.

Growth Mechanism: Role of the Seeds and Silver(I)

The gold seeds used for the growth are very small in size, with average diameter 2~3 nm. However, it does not mean that they have a simple structure,
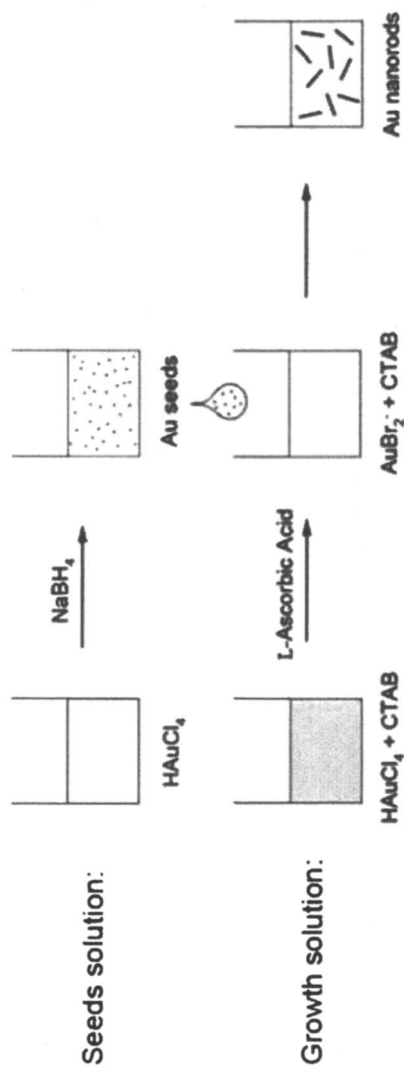
Figure 2. The sketch shows the typical procedure followed in the seed-mediated synthesis of the gold nanorod. The size of the seeds are about 2-3 nm in diameter. For the growth solution, excess L-ascorbic acid is added, but only reducing Au^{III} to Au^{I} in the first step. Au^{I} is further reduced to the elemental form in the second step, when Au seeds are introduced as nucleation centers.
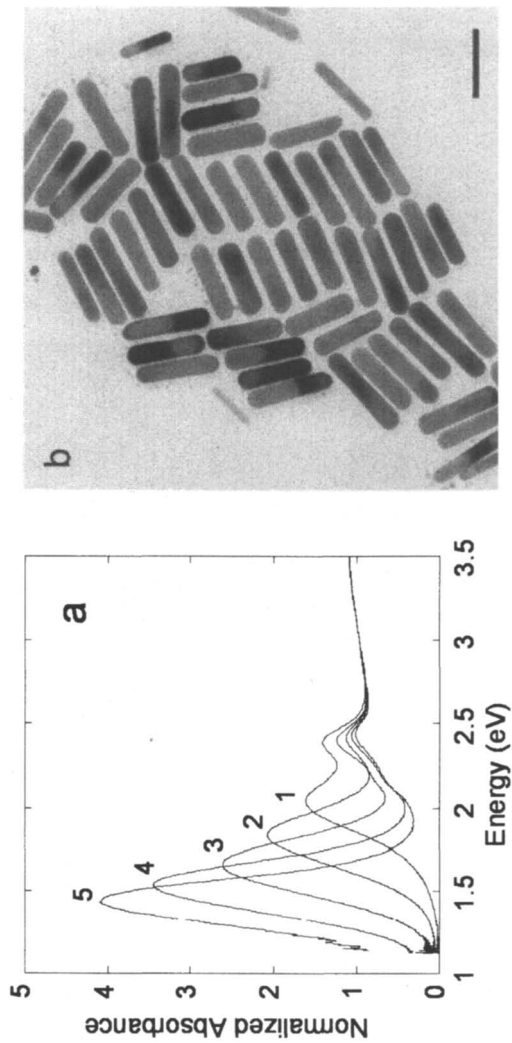
Figure 3. (a) UV-Vis spectra of gold nanorods synthesized by Ag(I). The Ag/Au ratios are 0.04, 0.08, 0.12, 0.16, 0.2 for the samples 1 to 5. (Reproduced from reference 9. Copyright 2005 American Chemical Society) (b) The TEM image of the gold nanorods synthesized at pH 3. (Scale bar = 56.25 nm)

instead, their structure can be complex and not necessarily single crystalline. We revealed that there are at least two basic types of seeds obtained in different preparations, namely seeds *I* and seeds *II* (*9*). Both seeds are prepared by reducing HAuCl$_4$ with NaBH$_4$, the difference is that the first one is performed in CTAB solution and the second one in sodium citrate solution. Seeds *I* are very tiny in size, with an average diameter of 1.5 nm, and appear to be single crystalline in majority (Figure 4a). Seeds *II* are larger, with the diameter 2~3 nm, and quite monodisperse. However, seeds *II* are mostly twinned, in contrast to seeds *I*. The twinned crystals, if oriented properly, can be seen to have pentagonal symmetry (Figure 4b). Seeds *II* were used for the original procedure developed by Murphy et al (*7*) and seed *I* were used for the silver-assisted method developed by El-Sayed et al (*8*). It should be noticed that the twinned gold nanorods can actually be grown from both seed *II* and single crystalline seeds *I*, when no silver(I) presents in the growth solution. Single crystalline gold nanorods can be made only when using seeds *I* together with silver(I) in the growth solution, suggesting a non-trivial role of silver in the growth.

Gold Bipyramids, a Novel Product from Silver-Assisted Growth

However, when seeds *II* are used for the silver-assisted growth, a novel gold nanostructure with bipyramid-shape emerged with well-defined facets, as shown in Figure 5(a) (*9*). The yield of the bipyramids is estimated to be about 30%, with the rest part being spherical-like particles. The bipyramids have a strikingly pronounced near-IR absorption peak around 1.5 eV (Figure 5(b)), which corresponds to the longitudinal surface plasmon mode. The linewidth is as narrow as 0.12 eV, which is unheard of in metal colloid solution and it deserves further discussion. For comparison, the inhomogeneous linewidth of a gold nanorods solution with a similar plasmon resonance is at least 0.3 eV as shown in Figure 3(a). The white light scattering spectra from single bipyramids were studied by dark-field microscopy, finding the homogeneous linewidth of the longitudinal plasmon resonance to be ~94 meV. Therefore the inhomogeneous broadening is as little as 30 meV, suggesting that the bipyramids have a very small variance on their shape.

Indeed the TEM images show that the variance of the tip angles is as small as ±1° within each sample. For different samples, the average tip angle varies only from 26° to 30°. It is confirmed by HRTEM and its Fourier transform, i.e. the power spectrum, that the bipyramid is penta-fold twinned around its growth axis. The growth axis is [011] and the twinning planes are (111), as shown in the inset of Figure 5(a). The bipyramids actually have exactly the same twinning structure as the gold nanorods synthesized by Murphy's method (*17*). This similarity gives them similar surfaces, which are {100} facets. For the nanorods, each {100} facet is flat along the growth direction. For the bipyramids, the {100} facet has to be stepped periodically along the growth direction to fit the
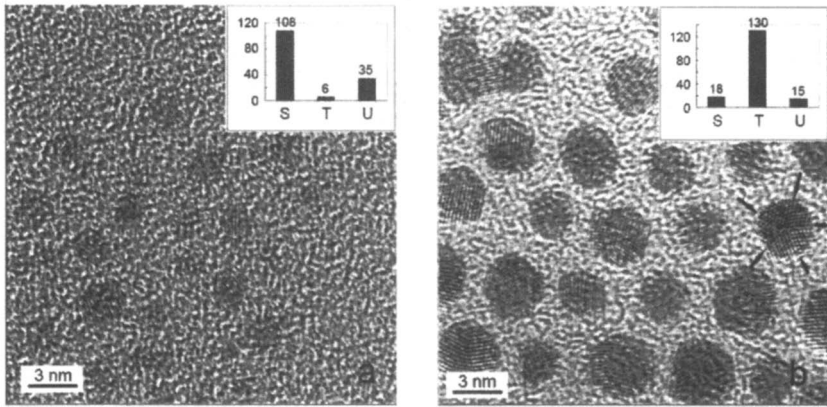
Figure 4. (a) High-Resolution TEM image of gold seeds I. (b) High-Resolution TEM image of gold seeds II. In the histograms, S, T, and U stand for single crystalline, twinned, and unidentified nanoparticles, respectively. (Reproduced from reference 9. Copyright 2005 American Chemical Society)
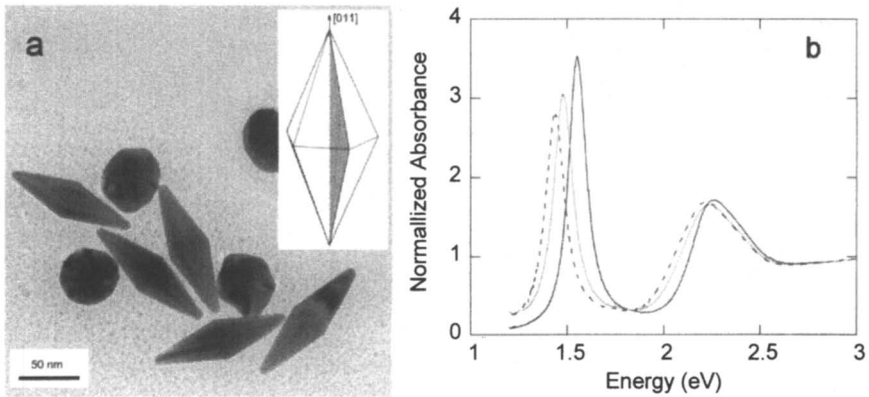
Figure 5. (a) TEM image of gold bipyramids. Inset: The idealized model showing the twinning structure. (Reproduced from reference 9. Copyright 2005 American Chemical Society.) (b) UV-Vis spectra of different gold nanobipyramids solutions. The broad peak around 2.3 eV is mostly due to the spherical-like particles.

geometry, and is indexed as ~{117}. The monodispersity and therefore the narrow ensemble spectrum may increase the sensitivity for sensing the modification of the near-field environment, i.e., adsorption of biomolecules, without having to resort to single particle measurements.

The gold bipyramids are larger than the nanorods, with the length about 90 nm and the equator diameter about 30 nm. However, they have a much sharper apex where the curvature radius is smaller than 4 nm. The sharp apex provides larger near-field enhancement at the plasmon resonance. As shown by the finite-difference time-domain (FDTD) simulation, the enhancement on the electric field amplitude $|E/E_0|$ of up to 200 times can be achieved at the vicinity of the tips, much larger than that of the nanorods which is about 60 times (Figure 6(a), (b)). Local field enhancement as large as that would display strong SERS activity and provide strong coupling to other electronic transitions such as fluorescence spectroscopy by the antenna effect. Further studies on this aspect is in progress.
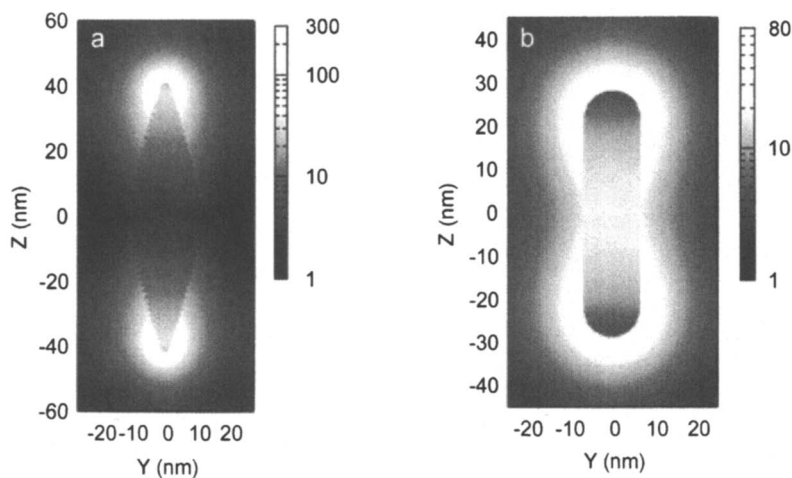
Figure 6. Electric field enhancement $|E/E_0|$ distributions simulated by three-dimensional-FDTD at the longitudinal plasmon resonance of a gold bipyramid (a) and a gold nanorod (b). The light propagation is along the x-axis and the polarization is along the z-axis.

Shaping Nanoparticles by Underpotential Deposition

It is found that the silver-assisted growth creates no more stacking fault from the seeds. For example, the single crystalline seeds *I* grow into single crystalline nanorods, while in the same growth solution, the multiply twinned gold seeds *II* grow into multiply twinned structures, and in particular into the

penta-twinned bipyramids. From the high resolution TEM studies, it is also concluded that the growth assisted by silver(I) leads to a priori energy unfavorable surface structures (9). Indeed, the single crystalline nanorod has its four side surfaces as {110} facets, which rarely appear in gold nanocrystals. The {110} facet is not a densely packed surface, and it has higher energy than the {100} and {111} facets (19). For the bipyramids, the stepped {11n} side facets must be of higher energy as well, because the atoms on the edge of the step are very open. No other noble metal nanostructures have been reported to exhibit such highly stepped dominant facets.

To explain the nontrivial role of silver in the growth, it was proposed by us that a monolayer of silver (0) can be selectively deposited onto the high-energy sites of gold nanocrystals by an electrochemical process called underpotential deposition (UPD). It is known that silver (I) cannot be reduced by ascorbic acid at the experimental condition (pH = 3). However, a metal submonolayer or monolayer can be deposited onto a different metal substrate with higher work function at a potential significantly less negative than for bulk deposition. This is called underpotential deposition (UPD) (20,21). The work function of silver is lower than that of gold by more than 0.5 eV, therefore the UPD of silver over gold is expected. It is also known that the UPD shift depends on the surface of the metal substrate. Usually, larger UPD shift is seen at more open surface, since the adatom on a more open surface has more neighbors, and therefore experiences stronger attractive potential.

From the analysis above, we found that the UPD process allows a compact silver monolayer to be formed preferably on the {110} facets of the gold nanocrystals, but not the other facets. The growth rate of gold on {110} facets will be significantly slowed down. The top of the nanorods, i.e., Au{100} facets, are only partially covered by silver, and therefore grow faster, which leads to the one-dimensional growth along the [100] direction. The ratio of growth rates between Au{100} and Au{110} is adjustable by varying the Ag(I) concentration, which naturally explains the fact that the aspect ratio is controlled by the Ag(I) concentration. Recently, it has been confirmed by Murphy et al that silver is found on the surface of the nanorods (22). The formation of gold bipyramids can be explained in a similar way. For the growth from seed *II*, penta-fold twinned gold nanorods with {100} side facets are expected, when silver(I) is not involved. However, as silver(I) is added into the growth solution, the steps formed during the growth will be stabilized by the UPD of silver, since the steps are also open surface structures.

Core/shell Structures: More Tunability for the Plasmon

It is well known that the plasmon resonance of a metal nanoparticle can be easily tuned by the medium surrounding it. Although most solvents have refractive indexes between 1.3 and 1.5, other materials can be coated onto the

surface of metal nanocrystals to provide more spectral tunability. We have been able to coat different types of materials, including silver and silver chalcogenides, over the gold nanorods (*11,23*).

Gold/silver core/shell nanorods can be made by reducing silver nitrate with ascorbic acid at pH ≥ 8. Usually, the initial solution is slightly acidic therefore the reaction does not happen. Sodium hydroxide solution is then titrated into the nanorods solution to slowly increase the pH. By doing that, silver ions can be slowly reduced and deposited over the gold nanorods surfaces in a very homogeneous way (Figure 7(a)). As the silver layer gets thicker, the longitudinal plasmon band of gold nanorods gradually shifts toward blue (Figure 8(a)), making the color of the solution vary from green, bluish green, to purplish red. Since silver and gold have little lattice mismatch (< 0.5%), the silver layer can be more than 5 nm thick (*11*).
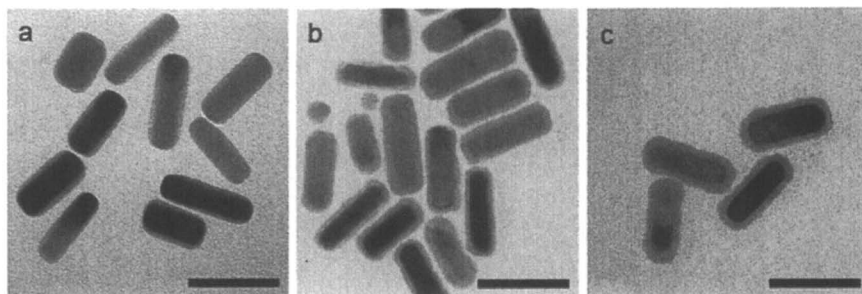
Figure 7. TEM image of Au/Ag core/shell nanorods (a), Au/Ag$_2$S core/shell nanorods(b) and Au/Ag$_2$Se core/shell nanorods (c). Scale bars = 50 nm. (Reproduced from reference 21. Copyright 2006 Royal Society of Chemistry)

The silver layer can be further converted into semiconductor materials such as silver sulfide or silver selenide, by a simple chemical method. In the method, Au/Ag core/shell nanorods is mixed with an excess of a freshly prepared sodium sulfide aqueous solution. By exposing the mixture to air, the reaction was completed within a few hours, with the solution turned from greenish to brownish. It is important for the solution to be in contact with air, as seen in the balanced reaction:

$$4 \, Ag + 2 \, S^{2-} + O_2 + 2 \, H_2O \rightarrow 2 \, Ag_2S + 4 \, OH^-.$$
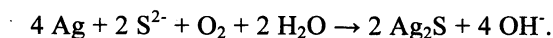
To make the silver selenide layer instead, the sodium sulfide solution was replaced by selenourea ((NH$_2$)$_2$CSe). Selenourea is quickly hydrolyzed and releases free Se^{2-} *in situ*. A similar reaction as above then leads to the formation of silver selenide. The solution of the silver selenide coated gold nanorods is

dark brown. As the silver layer is converted into silver sulfide or selenide, the layer is still homogeneous but significantly thicker (Figure 8), due to the insertion of S^{2-} or Se^{2-} anions. The formation of the silver chalcogenides layers was confirmed by studying the selective area electron diffraction (SAED) of the samples. Silver sulfide was found as monoclinic Acanthite and silver selenide as orthorhombic Naumannite, both in their low-temperature phases. The chemical procedures described here is not only restricted to gold nanorods but also applicable to other gold nanostructures.

Both silver compounds are narrow band gap semiconductors (~1 eV for silver sulfide (24) and ~0.15 eV for silver selenide (25)) with large refractive indexes at optical frequencies. Therefore, the longitudinal plasmon resonance significantly red-shifts once the silver chalcogenides layer is coated over the gold nanorods, as seen in Figure 8(a). The longitudinal plasmon resonance is also attenuated as the silver layer is converted to silver sulfide or silver selenide, due to the screening by the silver chalcogenide layer which have high refractive indexes. The optical nonlinearity of silver chalcogenides is expected to be enhanced due the local field enhancement by the plasmon resonance.

The spectrum of the core/shell nanorods can be nearly quantitatively explained by a simple electrodynamics model, without the reference to any "averaged" optical constant. The model is to treat the core/shell nanorods as a ellipsoid (core) confocally coated by another ellipsoid (shell). In the quasi-static approximation, the polarizability tensor of the composite ellipsoidal particle can
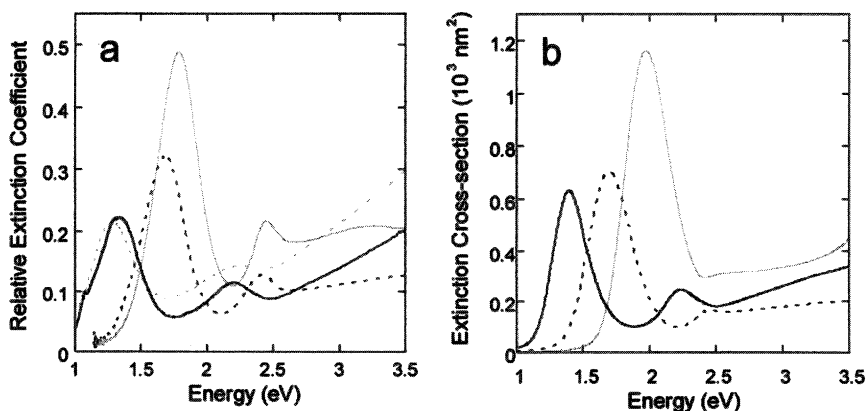
Figure 8. (a) UV-Vis-NIR spectra of Au nanorods (dotted black), Au/Ag nanorods (gray), Au/Ag₂S nanorods (black), and Au/Ag₂Se nanorods (dotted gray). (b) Simulated extinction spectra of Au nanorods (dotted black), Au/Ag nanorods (gray), and Au/Ag₂S nanorods (black) immersed a medium with $\varepsilon_m = 1.77$ (water). (Reproduced from reference 21. Copyright 2006 Royal Society of Chemistry)

be expressed analytically, in a similar form as Gans' solution. The optical cross-sections of the particle are then calculated using the optical theorem. The details of the solution can be found elsewhere and are not discussed here (2,23). In Figure 8(b), the spectra of the core/shell nanorods are calculated using optical constants from other experiments. A rather good agreement with the experimental result is seen.

Conclusion

In summary, quasi-one-dimensional metal nanostructures have highly interesting and tunable plasmonic properties. The novel gold bipyramids have a sharp structural feature, which is responsible for its huge local field enhancement. The chemistry in the silver-assisted growth was discussed, revealing that the UPD process led to a selective Ag(0) deposition over high energy surface sites, which assisted the gold nanocrystals growth into specific shapes. The underpotential deposition of impurity metals may provide a general mechanism to control shape evolution in other metallic nanostructures. In addition, thin layers of different type of materials can be coated homogeneously to the surface of the gold nanorods, which tunes the plasmonic properties further. The metal/semiconductor composite also provides an interesting avenue to enhanced nonlinear optical properties of nanomaterials.

Acknowledgements

References

1. Kreibig, U.; Vollmer, M. *Optical properties of metal clusters*; Springer: Berlin ; New York, 1995.
2. Bohren, C. F.; Huffman, D. R. *Absorption and scattering of light by small particles*; Wiley: New York, 1983.
3. Jin, R. C.; Cao, Y. W.; Mirkin, C. A.; Kelly, K. L.; Schatz, G. C.; Zheng, J. G. *Science* **2001**, *294*, 1901-1903.
4. Averitt, R. D.; Sarkar, D.; Halas, N. J. *Phys. Rev. Lett.* **1997**, *78*, 4217-4220.
5. Sun, Y. G.; Xia, Y. N. *Science* **2002**, *298*, 2176-2179.
6. Yu, Y. Y.; Chang, S. S.; Lee, C. L.; Wang, C. R. C. *J. Phys. Chem. B* **1997**, *101*, 6661-6664.

7. Murphy, C.; Jana, N. *Adv. Mater.* **2002**, *14*, 80-82.
8. Nikoobakht, B.; El-Sayed, M. A. *Chem. Mater.* **2003**, *15*, 1957-1962.
9. Liu, M. Z.; Guyot-Sionnest, P. *J. Phys. Chem. B* **2005**, *109*, 22192-22200.
10. Sun, Y. G.; Mayers, B.; Herricks, T.; Xia, Y. N. *Nano Lett.* **2003**, *3*, 955-960.
11. Liu, M. Z.; Guyot-Sionnest, P. *J. Phys. Chem. B* **2004**, *108*, 5882-5888.
12. Gersten, J.; Nitzan, A. *J. Chem. Phys.* **1980**, *73*, 3023-3037.
13. Zia, R.; Selker, M. D.; Brongersma, M. L. *Physical Review B* **2005**, *71*, -.
14. Pelton, M.; Liu, M. Z.; Park, S.; Scherer, N. F.; Guyot-Sionnest, P. *Phys. Rev. B* **2006**, *73*, 155419.
15. Mie, G. *Ann. Phys.* **1908**, *25*, 377-445.
16. Van der Zande, B. M. I.; Bohmer, M. R.; Fokkink, L. G. J.; Schonenberger, C. *J. Phys. Chem. B* **1997**, *101*, 852-854.
17. Johnson, C. J.; Dujardin, E.; Davis, S. A.; Murphy, C. J.; Mann, S. *J. Mater. Chem.* **2002**, *12*, 1765-1770.
18. Zweifel, D. A.; Wei, A. *Chem. Mater.* **2005**, *17*, 4256-4261.
19. Wang, Z. L.; Gao, R. P.; Nikoobakht, B.; El-Sayed, M. A. *J. Phys. Chem. B* **2000**, *104*, 5417-5420.
20. Kolb, D. M. In *Advances in electrochemistry and electrochemical engineering*; Gerisher, H., Tobias, C. W., Eds.; Wiley: New York, 1978; Vol. 11; pp 125.
21. Herrero, E.; Buller, L. J.; Abruna, H. D. *Chem. Rev.* **2001**, *101*, 1897-1930.
22. Orendorff, C. J.; Murphy, C. J. *J. Phys. Chem. B* **2006**, *110*, 3990-3994.
23. Liu, M. Z.; Guyot-Sionnest, P. *J. Mater. Chem.* **2006**, *16*, 3942-3945.
24. Bennett, J. M.; Stanford, J. L.; Ashley, E. J. *J. Opt. Soc. Am.* **1969**, *59*, 499.
25. Dalven, R.; Gill, R. *Phys. Rev.* **1967**, *159*, 645.

Chapter 7

Functional Nanostructures by Wet Chemistry: A Tool to Ordered 1D and 3D Nanostructures

Lidiany Gonzalez[1], Eunice Mercado[1], Priscila Santiago[1], Madeline Leon[1], Marissa Morales[1], Roberto Irizarry[2], and Miguel E. Castro[1]

[1]Chemical Imaging Center, University of Puerto Rico at Mayaguez, Mayaguez, Puerto Rico 00680
[2]DuPont Electronic Technologies, 14 T. W. Alexander Drive, Research Triangle Park, NC 27709

Hollow nanostructures are functional structures suitable for high energy material storage, controlled drug release, light weight structural materials, catalysts and filters. We present evidence, based on scanning and transmission electron microscopy measurements, for the formation of one and three dimensional hollow nanostructures from chemically modified silver particles. One dimensional structures form in acid media while an increase in the solution ionic strength result in the formation of hollow nanostructures that exhibit three dimensional order. Such structures can find applications in high energy material storage, catalysis, electrochemistry and biomedicine.

Introduction

There is a tremendous interest in the synthesis of nanostructures suitable for the storage of high energy materials. This interest drives from the need to replace our dependence on fossil fuels with environmentally friendly alternatives (1,2). Hydrogen is the most abundant element in the universe and does not create environmental pollution when used as a fuel. Overcoming hydrogen storage is among the important steps toward widespread commercialization and implementation of fuel cells in vehicles. Organic and inorganic molecules with high hydrogen content and which can release the hydrogen in their decomposition reactions are as important as hydrogen itself. Depending of the application, storage of hydrogen and hydrogen containing molecules in adequate structures is central to find green solutions to our energy needs. The use of nanotechnology for this task promises to result in a reduction of space required for high energy materials storage and transport, which can trickle down to the miniaturization of fuel cells. The broader impact of cost effective and efficient functional nanostructures for hydrogen and hydrogen materials storage resides in (i) facilitation of fuel transportation and (ii) the miniaturization of fuel cells and the (iii) acceleration in the implementation of environmentally friendly energy alternatives in vehicles.

Nanotubes and hollow nanospheres are excellent candidates for hydrogen storage. Short diffusion distances and surface sites to dissociate hydrogen are among the characteristics of ideal nanostructures for hydrogen storage materials. The low density and high strength of nanotubes has made them ideal for their exploration as hydrogen storage material. Research in this area has been very active since the end of the last decade and the beginning of the new millennium. The availability of new methods for the synthesis of carbon nanotubes (3–6), as well as our energy needs, accelerated work in the area. Recent work suggests that titanium decorated SWCN may be able to store about 8 % H_2 per weight, slightly higher than the 6 % per weigh minimum required by the Freedom Car Research Partnership Act set forth by the Department of Energy and major American car manufacturers (7).

The synthesis of hollow nanostructures has received considerable less attention than pure metal or semiconductor counterparts (8–12). Ideal hollow nanostructure synthesis platforms should take advantage of methods to functionalize nanoparticles into structures suitable for high energy storage. As illustrated in Figure 1 below, such structures may include nanotubes and nanospheres. In the case of nanotubes with a very thin diameter and decorated with metal nanoparticles, new effects may be brought about such as electron conduction across their wall, resulting in nanoscaled electrochemical cells suitable for hydrogen generation from electrolysis of water or other chemicals.

In the last few years, we have worked in the ensemble of silver into hollow nanostructures like those displayed in Figures 1a, b and 1c. From the perspective

of a starting material that consists of silver nanoparticles, we can think about the hollow nanostructures in 1a and 1b as one and three dimensional constructions from nanoparticle building blocks. These are already functional nanostructures, suitable for high energy material storage. The nanostructure displayed on Figure 1c, on the other hand, is clearly a step ahead in complexity and is suitable for energy conversion chemistry thru electrochemical processes.
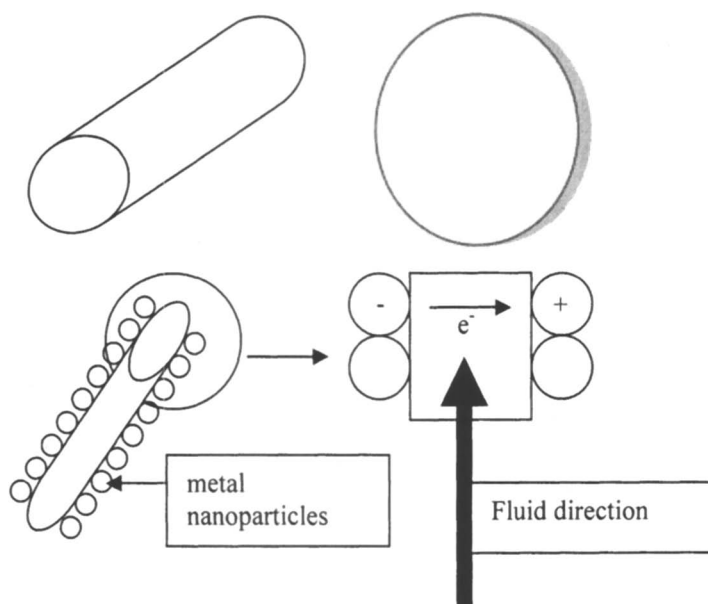
Figure 1. The scheme shows possible hollow nanostructure suitable for hydrogen storage in (a) and (b). A more specialized hollow nanostructure is displayed in (c), where metal nanoparticles added to the outside wall of a hollow nanotube can be used as electrodes for the electrochemistry of fluids moving inside the tube. The inset at the right illustrates the electron flow from the - to a + charged nanoparticle.

Results

The approach to the synthesis of one dimensional nanostructures, like the one displayed on Figure 1b, is based on wet chemistry. Wet chemical approaches methods are a promising tool to the mass production of functional nanostructures. The thiol itself must have several structural restrictions, besides just simply a sulfur atom to bond to the silver surface.
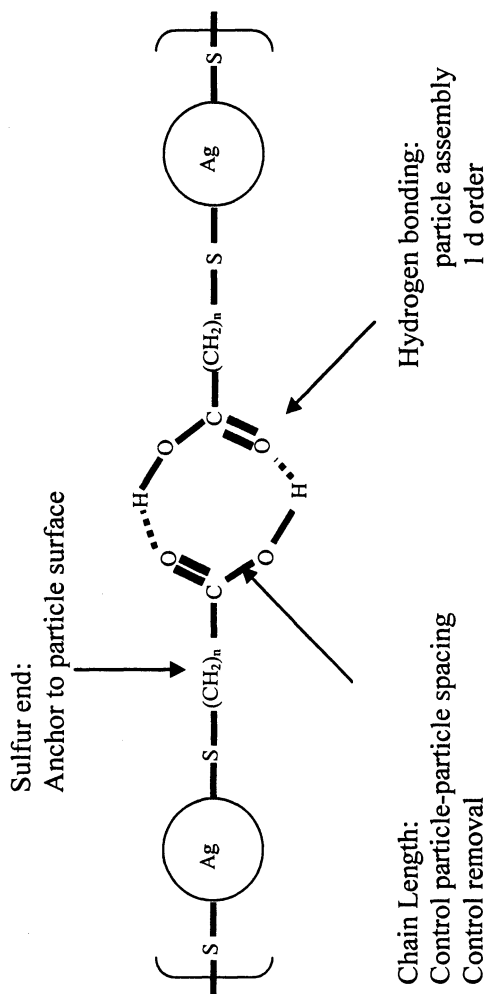
Figure 2. General approach employed to the synthesis of one dimensional nanostructures. A thiol capped silver particle is assembled into one dimensional nanostructure.

The terminal group is also important. Carboxylic acids are ideal for this purpose: hydrogen bonding interactions can be used for inter-particle links while pH control may be used to turn such links "on" and "off". We have demonstrated that mercapto acetic acid ($HOOCCH_2SH$) capped silver nanoparticles is capable of driving such order. As displayed on Figure 3, hydrogen bonding interactions among the carboxylic acid terminal group in $HOOCCH_2S$- Ag can be used as a linker.
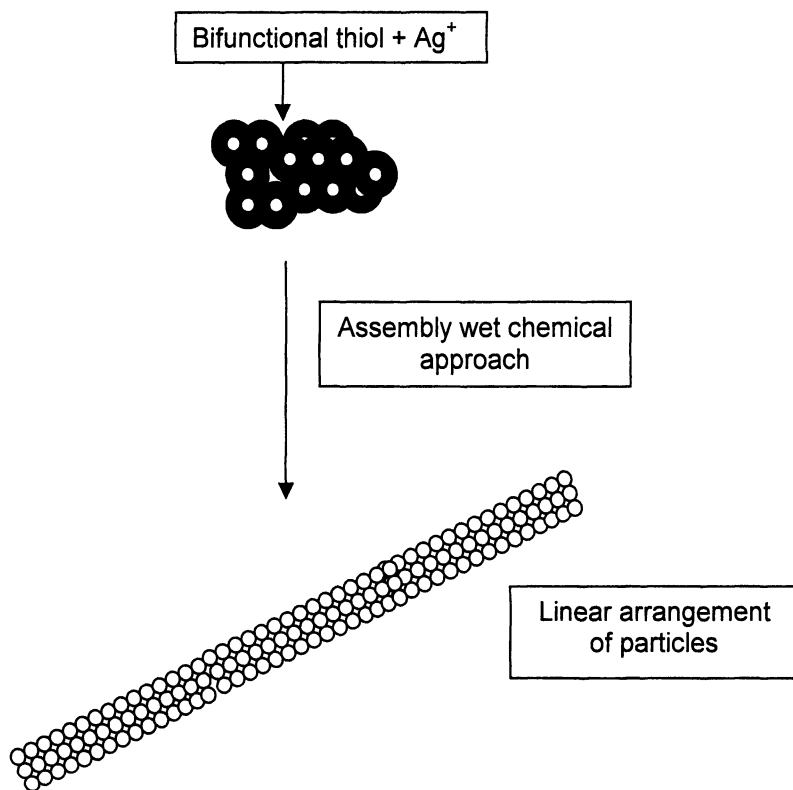
Figure 3. Cartoon illustrating the concept of hydrogen bonding interactions among carboxylic acid end of alkyl thiols bonded to silver surfaces.

The synthesis of the precursors is made by adding $HSCH_2COOH$ to silver nitrate in water. Scanning electron microscopy (SEM) measurements of the wet solution are summarized in Figure 4. Large micelles, like the one displayed on Figure 4a, are the dominant structure observed. Once in a while we will observe

some of these micelles broken and some one dimensional structure inside the area as displayed on Figures 4b to 4f. In favorable cases, we can observe the formation of tubes in some of the micelles, as displayed in the inset of Figure 4f. The large amount of water present solvates the carboxylic acid ends of the thiol molecules and prevents the formation of links and one dimensional structures, although there are enough fluctuations to allow their occasional detection.

Typical scanning and transmission electron microscopy images of dry deposits of a mixture of $AgNO_3$ and thiol diluted with 10.0 mL of water are displayed on Figures 5 and 6, respectively. A bundle of nanofibers is identified in SEM. These one dimensional structures are readily identified in the TEM image. The primary beam energy of the TEM employed for the measurements reported here allowed us to obtain clear images of the edge of the deposits. The TEM does allow imaging these nanostructures in greater detail than in SEM measurements. The nanostructures are between 15 and 30 nm in diameter while their length varied from about 230 nm up to several micrometers.

It is interesting that, not a single "free" particle is observed in TEM images of dry deposits of aqueous dispersions of thiol-silver mixtures, despite the fact that their existence is suggested in independent UV-visible absorption measurements (λ_{max} 3240-380 nm). The particles, if present, must be inside the nanofibers. Inspection of the regions indicated by the arrows at higher magnifications confirms the presence of small particles inside the fibers. We were able to observe these formations in all the nanofibers examined in the TEM. The size of the particles is very difficult to determine from the images. We estimate an upper limit of 1 nm for the diameter of the particles that can be distinguished in the image. This particle size is considerable smaller than those reported in the literature for silver nanoparticle synthesis in basic media. Smaller structures are observed on the edges of the walls of the nanofibers, but the images are not resolved well enough to interpret them in terms of the silver dimer, Ag_2.

In passing, we note that the pH of the solution is below 3.0 . The density of one dimensional nanostructures decreases with solution pH and disappear when a pH>7 is attained, indicating that hydrogen bonding interactions are responsible for the formations displayed in Figures 5 and 6.

If particles are inside the one dimensional structures, we hypothesized that the one dimensional structures must be hollow and a strong binding molecule should be able to remove the particles from the inner volume of the formation. Figure 7 shows SEM images of dry deposits of the thiol-silver mixture treated with a cysteine solution. The nanoparticles are displaced to the outside walls of the one dimensional formation, a result that confirms the hollow nature of the formation, consistent with the images displayed in Figure 4f, which shows the formation of a hollow nanotube. These particles have probably undergone several chemical processes and their sizes are likely to be different from those of the particles contained in the original nanostructure.
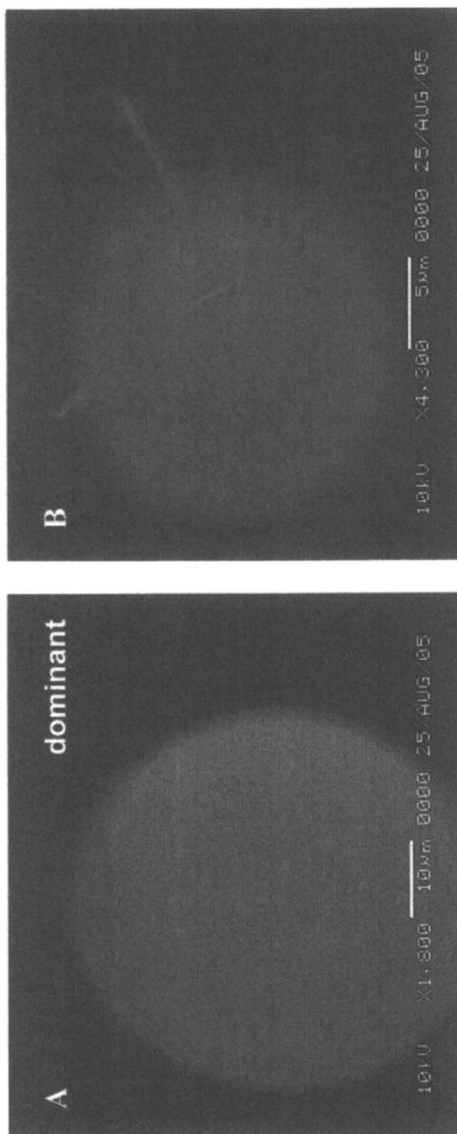
Figure 4. From (a) to (f) illustrate wet SEM measurements of aqueous colloidal solutions containing of mercapto acetic acid and silver. Continued on next page.
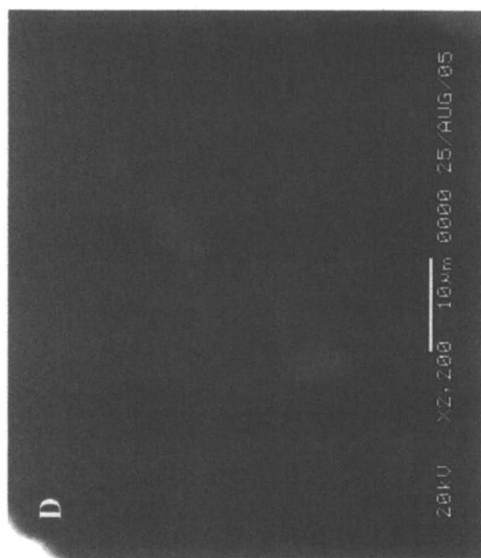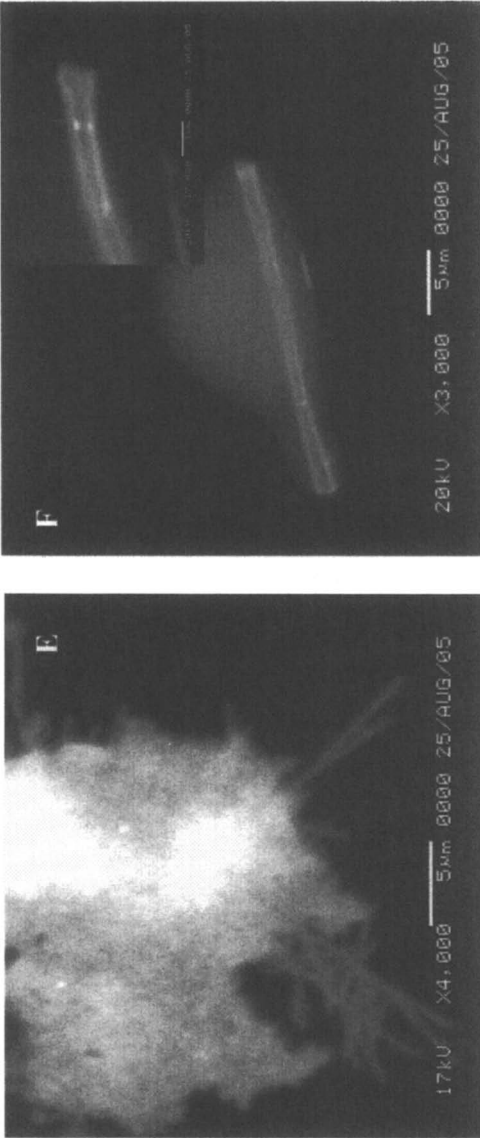
Figure 4. Continued.
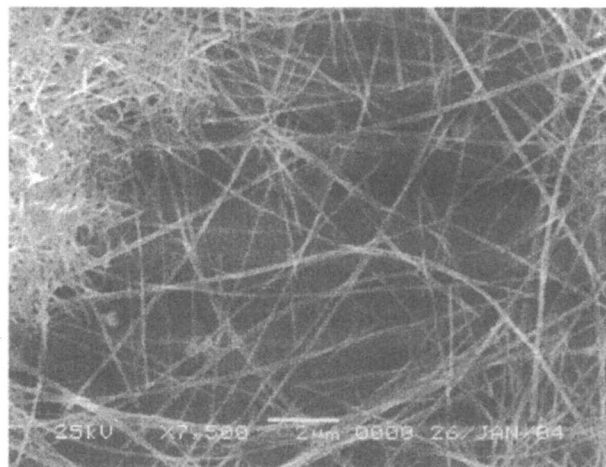
Figure 5. Scanning electron microscopy image of a dry deposits of a silver-thiol mixture diluted with 10.0 mL of water.
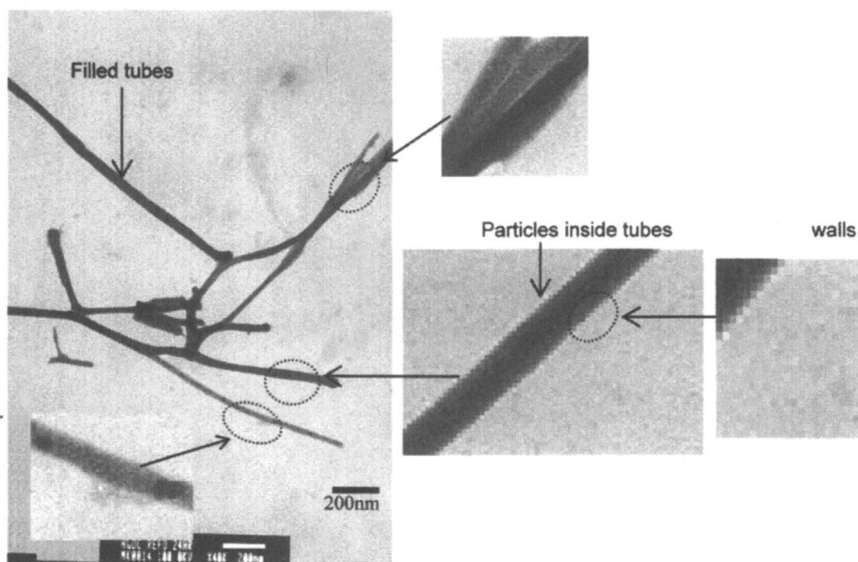
Figure 6. Transmission electron microscopy images of dry deposits of a silver-thiol mixture diluted with 10.0 mL of water. The insets corresponds to the regions indicated by the arrows magnified by a factor of 500 to indicate the formation of the particles. The region of a wall magnified 1000 times is also displayed in the inset.
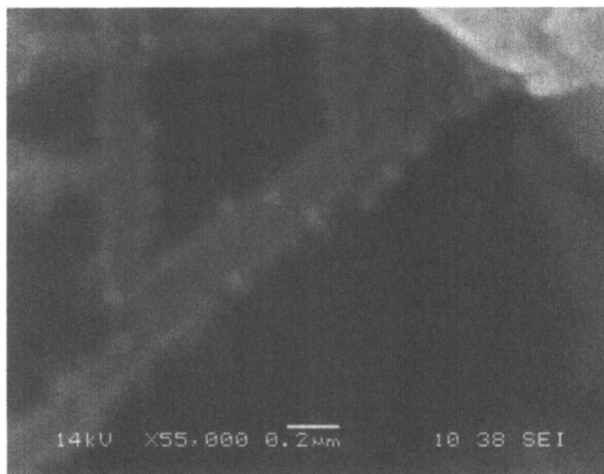
Figure 7. SEM image of a dry deposit of a thiol-silver material treated with cysteine. The particles are observed on the walls of the tube and the inner volume of the tube is now empty.

There are several approaches to bring three dimensional order to colloidal solutions. For instance, electrostatic or magnetic interactions among particles may result in specific long range order among particles in solution.

To test this possibility, a few micro liters of an aqueous sodium nitrate ($NaNO_3$) solution were added to the colloidal solution of the thiol and silver. Wet SEM measurements performed on the colloid are summarized in Figure 9. The first thing to note is the order that is exhibited by the micelles. Nearly linear formations are clearly distinguished in the image. When the electron beam is

disordered   **ordered**
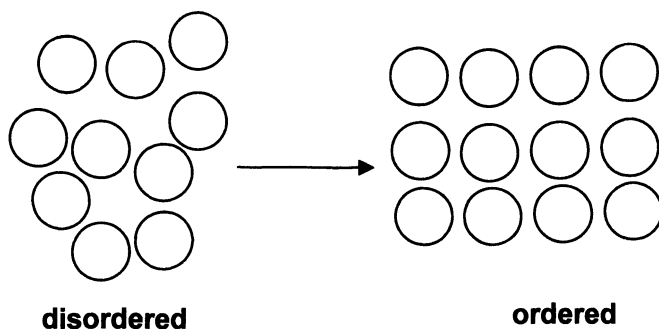
Figure 8. Bringing order to a disordered array in solution.

focused on one of the micelles it is easy to see that they are hollow spheres. The size of each sphere is comparable to the size of the dominant nanostructures found in solution (see Figure 4), which are several micrometers in diameter. The formation of spheres is a surprising result, since we expect the electrostatic interactions to affect only the long range order and have little or no effect on internal structure of the micelle Vibrational spectroscopy work is needed to fully characterize the chemical composition of these micelles and learn on the tools that can be used to bring one and two dimensional order at the nanoscale.
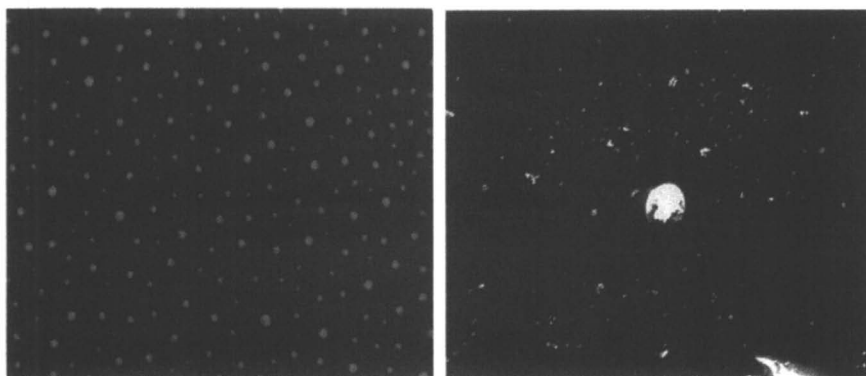
Figure 9. Three dimensional ordered silver-thiol colloids. The SEM image at the right hand side shows the electron beam burned hole in one of the hollow nanospheres.

Conclusions

Hydrogen bonding interactions among the carboxylic acid end of the thiol on Ag drive 1 dimensional order of nanoparticles while longer range electrostatic interactions may be effective in driving the 3D order of suspension. The hollow nanostructures presented here may be useful for applications in materials storage, for fuel cell applications, dug delivery and nanostructured batteries.

References

1. Liu, C.; Fan, Y. Y.; Liu, M.; Cong, H. T.; Cheng, H. M.; Dresselhaus, S. Hydrogen Storage in Single-Walled Carbon Nanotubes at Room Temperature. *Science* **1999**, *285*, 1127.

2. Ye, Y.; Ahn, C. C.; Witham, C.; Fultz, B.; Liu, J.; Rinzler, A. G.; Colbert, D.; Smith, K. A.; Smalley, R. E. Hydrogen Adsorption and Cohesive Energy of Single-Walled Carbon Nanotubes. *Appl. Phys. Lett.* **1999**, *74*.

3. Wand, Q. Y.; Johnson, J. K. Optimization of Carbon Nanotubes Arrays for Hydrogen Adsorption. *J. Phys. Chem. B* **1999**, *103*, 4809.

4. Lee, S. M.; Lee, Y. H. Hydrogen Storage in Single Wall Carbon Nanotubes. *Appl. Phys. Lett.* **2000**, *76*, 2877.

5. Smith Jr., M. R.; Bittner, E. W.; Shi, W.; Johnson, J. K.; Bockrath, B. C. Chemical Activation of Single-Walled Carbon Nanotubes for Hydrogen Adsorption. *J. Phys. Chem. B* **2003**, *107*, 3752.

6. Beyaz-Kayiran, S.; Darkrim-Lamari, F.; Levesque, D. Adsorption Properties and Structural Characterization of Activated Carbons and Nanocarbons. *J. Phys. Chem. B* **2004**, *108*, 15211.

7. Dillon, A. C.; Jones, K. M.; Bekkedahl, T. A.; Kiang, C. H.; Bethune, . S.; Heben, M. J. Storage of Hydrogen in Single-Walled Carbon Nanotubes. *Nature* **1997**, *386*, 377.

8   Zhang, D.; Qi, L.; Yang, J.; Ma, J.; Cheng, H.; Huang , L. Wet Chemical Synthesis of Silver Nanowire Thin Films at Ambient Temperature. *Chem. Mater.* **2004**, *16*, 872-876.

9. Ma, Y.; Qi, L.; Ma, J.; Cheng, H. Facile Synthesis of Hollow ZnS Nanospheres in Block Copolymer Solutions, *Langmuir* **2003**, *19*, 4040-4042.

10. Ma, Y.; Qi, L.; Ma, J.; Cheng, H,; Shen, W. Synthesis of Submicrometer-Sized CdS Hollow Spheres in Aqueous Solutions of a Triblock Copolymer. *Langmuir* **2003**, *19*, 9079-9085

11. Kuznetsova, A.; Mawhinney, D. B.; Naumenko, V.; Yates Jr., J. T.; Liu, C.; Smalley, R. E. Enhancement of Adsorption inside of Single-Walled Nanotubes. *Chem. Phys. Lett.* **2000**, *321*, 292.

12. Zhang, D.; Qi, L.; Ma, J.; Cheng, H. Synthesis of submicrometer-sized silver spheres in in mixed polymer-surfactants solutions. *Adv. Mat.* **2002**, 14, 1499-1502..

13 Hernandez, E.; Posada, B.; Irizarry, R.; Castro, M. The role of hydrogen bonding interactions in directing one dimensional-thiol assited growth of silver nanofibers. *J. Phys. Chem.* **2005**, *109*, 7251-7257.

Chapter 8

Synthesis and Characterization of Tannic Acid Functionalized Magnetic Nanoparticles

Anselm Omoike

Department of Chemistry and Biochemistry, University of Michigan at Flint, 303 East Kearsley Street, Flint, MI 48502–1950

Magnetic nanoparticles containing tannic acid have been synthesized using coprecipitation and post-precipitation methods. The synthesized products were characterized using transmission electron microscopy (TEM), diffused reflectance Fourier transform infrared spectroscopy (DRIFTS) and X-ray photoelectron spectroscopy (XPS). FTIR and XPS results reveal the presence of metal complexing groups in the solid-phases. The application of the novel nanoparticles was demonstrated in the separation of Cu^{2+} ions from a synthetic mixture of $Cu^{2+}-Zn^{2+}$ solution (pH 4.5 and ionic strength of 10 mM). Nanoparticles synthesized by post-precipitation method demonstrate higher binding capacity for Cu^{2+} ions in the presence of Zn^{2+} ions relative to nanoparticles synthesized by coprecipitation method. The novel nanoadsorbents have potential applications for the removal and recovery of toxic metal ions from aqueous systems.

Introduction

Metals are natural constituents of the environment. However, their inputs into the environment through human use of metal-enriched chemicals and discharge of industrial effluents pose a major problem for the environment as well as treatment processes. Most existing methods for treating metal ions are either economically unfavorable, or too technically complicated or ineffective at low metal ion concentration (*1 – 3*).

Adsorption is the most favored method of metal ion removal at low concentration. The choice of adsorbents depends on adsorption capacity, cost and availability. Among the different promising adsorbents for adsorption or recovery of contaminants from aqueous systems, nanoparticles of iron oxide ferrites such as magnetite (Fe_3O_4) or its oxidized form maghemite (γ- Fe_2O_3) continues to arouse great interest because they possesses unique sizes and are magnetic, which means they can be easily manipulated using an external magnetic field gradient. Fe_3O_4 and γ- Fe_2O_3 are easy to synthesize, exist in the environment as crystalline minerals and their reported point of zero charge (pzc) usually range from 6.4-7.1 (*4*). It is often necessary to functionalize nanoparticles in order to ensure effective control of the dispersion and /or increase the affinity of the nanoparticles for some specific substances. Surface functionalized magnetic nanoparticles using ligand-bearing inorganic silica and ligand-bearing synthetic / natural polymeric organic materials have been utilized to tether different functional groups on magnetite for use in immobilization of biomaterials and contaminants, bioseparation, drug delivery, and magnetic resonance contrasting reagent (*5–8*).

In industrial effluents and natural aqueous systems, complex multi-component metal systems are commonly encountered, and studies evaluating the effect of binary metal mixtures in various combinations are more representative of the actual field environmental problems. Therefore, there is need to develop cost effective treatment methods capable of removing low concentration of toxic metal ions particularly from multi-component environmental samples. Several studies have demonstrated the excellent metal binding capacity of tannic acid, a hydrolysable tannin (*9–11*). It is composed of naturally occurring esters of gallic acid with glucose and belongs to a group of complex plant polyphenolic compounds known as gallotannins. Recently, the adsorption behavior of several metal ions on tannic acid coated activated carbon was reported and the authors remarked that the immobilization procedure optimized metal removal capacity of activated carbon (*11*). Unlike activated carbon, nanomagnetic particles with tailored surface properties can be separated, recovered, and recycled from water and wastewater after the adsorption process utilizing high gradient magnetic force field. In order to develop magnetic nanomaterials with reactive functionalities for metal ion removal in multi-metal aqueous systems, we

synthesized magnetic nanoparticles in the presence of tannic acid using coprecipitation and post-precipitation methods. The nanoparticles were characterized using a suite of analytical methods and the potential application of these particles as sorbents in metal ion removal from aqueous solutions was evaluated.

Experimental

Materials and Reagents

Ferric (III) chloride ($FeCl_3$), ferrous (II) chloride ($FeCl_2$), ammonia (NH_3), nitric acid (HNO_3), sodium hydroxide (NaOH), copper (II) nitrate [Cu $(NO_3)_2$], zinc (II) nitrate [Zn $(NO_3)_2$], and tannic acid ($C_{76}H_{52}O_{46}$) were of analytical grade, and used without further purification. All aqueous solutions and suspensions were made using nanopure water (18 MΩ cm resistance). All glassware and polypropylene tubes used for metal uptake studies were soaked in 10 % nitric acid for 24 h and then thoroughly rinsed with metal free water.

Synthesis of Magnetic Nanoparticles

Magnetic nanoparticles were synthesized in the presence and absence of tannic acid using coprecipitation and post-precipitation methods.

In a typical coprecipitation method (Scheme 1), $FeCl_3$ (2.0 g) and $FeCl_2$ (1.3 g) were dissolved in nitrogen gas (N_2) purged 2.0 M hydrochloric acid solution and magnetically stirred under a continuous flow of N_2. The mixture was heated at 70 $^{\circ}$C for 30 min. Tannic acid was added and the mixture was heated for another 5 min under a blanket of N_2. Ammonia was added to precipitate the magnetic nanoparticles and the black product formed was treated hydrothermally at 70°C for 30 min. The final product, magnetic-iron tannate nanoparticles (noted as MTAC) was thus obtained.

$$FeCl_2 + FeCl_3 + C_{76}H_{52}O_{46}$$

(a) pH 2.0 using HCl
(b) N_2 purged; 70° C
(c) Ammonia

Magnetic—iron tannate nanoparticles (MTAC)
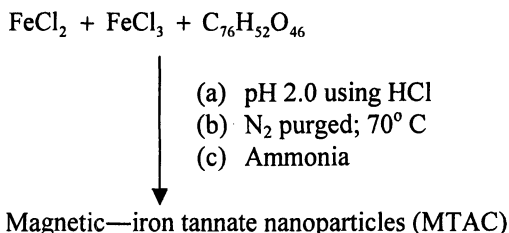
Scheme 1. Synthesis of magnetic nanoparticles coprecipitated with tannic acid (MTAC).

Similarly, in a typical post-precipitation method (Scheme 2), $FeCl_3$ (2.0 g) and $FeCl_2$ (1.3 g) were dissolved in N_2 purged 2.0 M hydrochloric acid solution and magnetically stirred under a continuous flow of N_2. The mixture was heated to 70 °C for 30 min before addition of ammonia. The black product obtained was heated for another 5 min under a blanket of N_2. Tannic acid was added followed by hydrothermal treatment of the black product at 70°C for 30 min. The final product, magnetic-iron tannate nanoparticles (noted as MTAP) was thus obtained.

$$FeCl_2 \; + \; FeCl_3$$

    (a) pH 2.0 using HCl
    (b) N_2 purged; 70° C
    (c) Ammonia
    (d) Tannic acid ($C_{76}H_{52}O_{46}$)

Magnetic—iron tannate nanoparticles (MTAP)
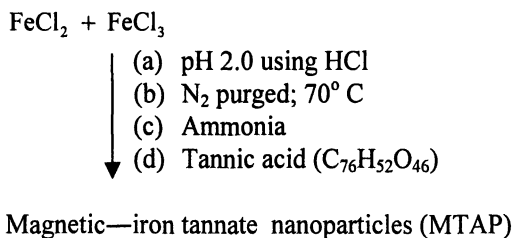
Scheme 2. Synthesis of magnetic nanoparticles post-precipitated with tannic acid (MTAP).

Magnetic nanoparticles were synthesized using the same conditions as above in the absence of tannic acid (Scheme 3). The final product, magnetic nanoparticles (noted as M) was thus obtained.

$$FeCl_2 \; + \; FeCl_3$$

    (a) pH 2.0 using HCl
    (b) N_2 purged; 70° C
    (c) Ammonia

Magnetic nanoparticles (M)
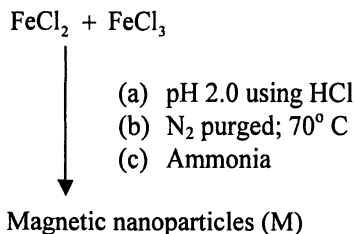
Scheme 3. Synthesis of magnetic nanoparticles in the absence of tannic acid (M)

The resulting nanoparticles from each synthetic method were subsequently separated from the reaction media under magnetic field, and washed three times with nanopure water before freeze drying.

Characterization of Magnetic Nanoparticles

The XPS analysis was carried out using a Kratos Axis Ultra 165 X-ray photoelectron spectrometer fitted with a 300W monochromatized Al Kα radiation (1486.6 eV). All spectra were recorded at a base pressure of ~ 5 x 10^{-9} Torr and normal (90°) take-off angle. Samples were prepared by immobilizing a thin layer of the nanoparticles onto an indium foil. Survey scan spectra (1.0 eV step and 160 eV pass energy) and select high-resolution spectra (0.1 eV step and 20 eV pass energy) were recorded. Surface charging effects were corrected with C1s peak at 284.6 eV as a reference. The diffused reflectance spectra in the region 4000-400 cm^{-1} of the nanoparticles were recorded at room temperature on a Perkin Elmer GX spectrometer fitted with DRIFTS accessories. Two-milligram of the nanoparticles was mixed with KBr to a total weight per sample of 400 mg, and then lightly mixed in an agate mortar using a pestle. The milled sample was immediately transferred into a DRIFTS sample cell and its surface was smoothed with a microscope slide. To obtain the DRIFTS data 150 scans at 1 cm^{-1} resolution were collected relative to a KBr background. A transmission electron microscope (TEM, JOEL 2010F) was used to acquire images of the nanoparticles at an accelerated voltage of 200 kV.

Metal Uptake Experiment

Cu^{2+} and Zn^{2+} solutions were prepared from $Cu(NO_3)_2$ and $Zn(NO_3)_2$ respectively and the pH was adjusted to 4.5. Known masses (50 mg or 150 mg) of pre-equilibrated nanoparticles (24 h; pH 4.5) were added to the Cu^{2+} + Zn^{2+} mixed system (pH 4.5) containing 10 mg/L each in 50 mL tubes. The ionic strength of all solutions and suspensions were kept at 10 mM (using KNO_3) and the pH adjustments was carried out using 0.1 M NaOH and 0.1 M HNO_3. The reaction tubes were allowed to equilibrate for 24 h on an end-over-end shaker at 20 ± 2° C and the solid phases separated from the suspensions using magnetic field. Blank tests without magnetic nanoparticles were performed to ensure that precipitation did not occur during the metal uptake experiments. The pH measurements of the solutions and suspensions were made with a Denver instrument pH/ion/ conductivity meter (Model 250). A Varian SpectrAA-20 atomic absorption spectrophotometer, equipped with hallow cathode lamps and an air-acetylene flame was used for the determination of zinc and copper, before and after contact with the nanoparticles.

Results and Discussion

In this work two novel magnetic nanoparticles functionalized with tannic acid were synthesized, freeze-dried and characterized using a suite of analytical

methods. The chemical functionalization of the nanoparticles synthesized in the presence of tannic acid was confirmed by XPS and DRIFT spectroscopy.

XPS survey scans revealed Fe, O, and C species on the surface of the nanoparticles and in addition, traces of impurities of nitrogen probably from ammonia in MTAC and MTAP nanoparticles (Figure 1). The small CIs peak detected on the surface of M nanoparticles (Figure 1) is attributed to adventitious carbon contaminant arising from exposure to air during sample preparation for XPS analysis. Compared with the spectrum of M, the spectra of MTAC and MTAP, were qualitatively the same, although differences in the relative intensities of the C Is and O 1s peaks were observed (Figure 1). The surface atomic concentration results from the XPS survey scan are presented in Table 1.

Table 1. Elemental Composition of Magnetic Nanoparticles from XPS Survey Spectra.

Sample	Surface elemental composition (Atomic %)			Ratio		
	C	Fe	O	C/O	C/Fe	O/Fe
TA (tannic acid)	68.48		31.50	2.17		
M (no TA)	8.87	40.64	50.48	0.18	0.22	1.25
MTAC (coprecipitation)	42.56	15.23	42.21	1.01	2.78	2.77
MTAP (post-precipitation)	25.22	25.76	46.16	0.55	0.98	1.79

Evidences for the successful incorporation of tannic acid into MTAC and MTAP (Table 1) are (i) the attenuation of the C1s signals, (ii) the decrease in surface % atomic oxygen atoms due to the lower oxygen content of incorporated tannic acid relative to magnetic nanoparticles with TA, and (iii) the decrease in the % surface Fe atoms due to screening of the nanoparticles surface by incorporated tannic acid. The band appearing at 711 eV assigned to Fe2p3 (Figure 1), is consistent with the binding energy of magnetic iron nanoparticles (12). It is worth noting that both C/Fe and O/Fe ratios for MTAC are higher than those for MTAP. In addition, MTAC has the highest % surface atomic carbon and the lowest % surface Fe atoms, which probably suggest that the mechanism of interaction is different.

The data obtained from curve fitting and deconvolution of the C1s and O1s regions of the XPS spectra are shown in Tables 2 and 3 respectively. It is evident from Table 2 that there are new surface functional groups (C–OH, O–C–O– and C=O,/ –COOH) in the core C1s spectra of MTAC and MTAP due to
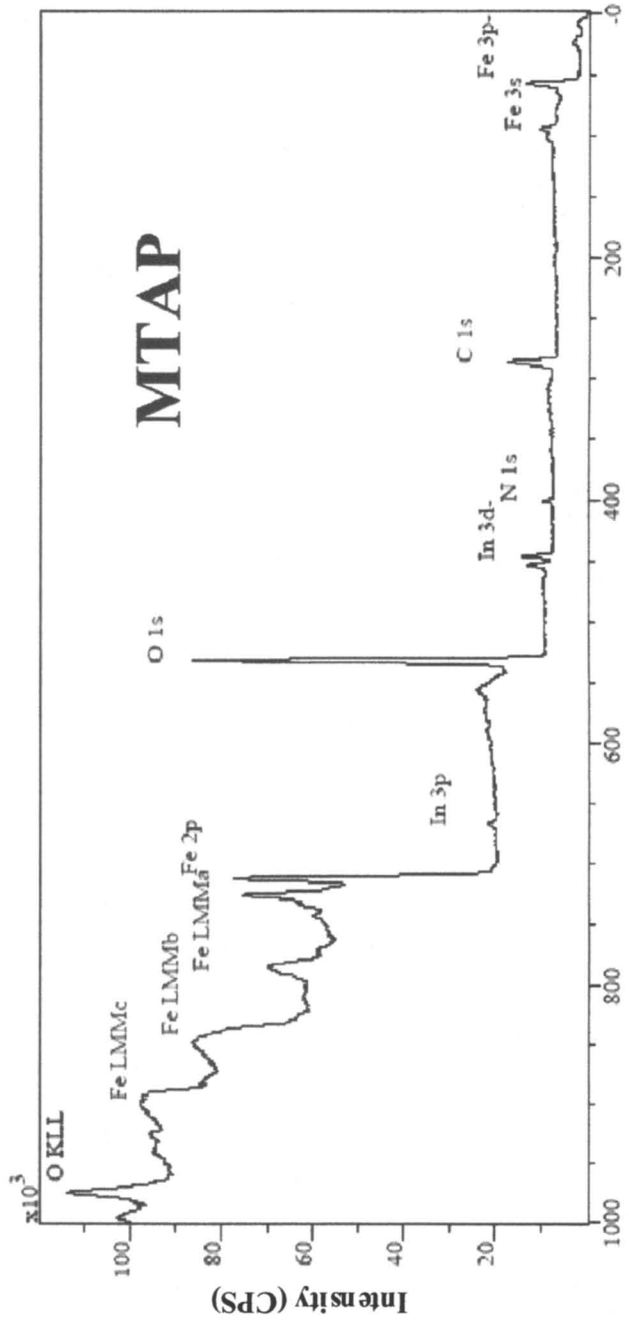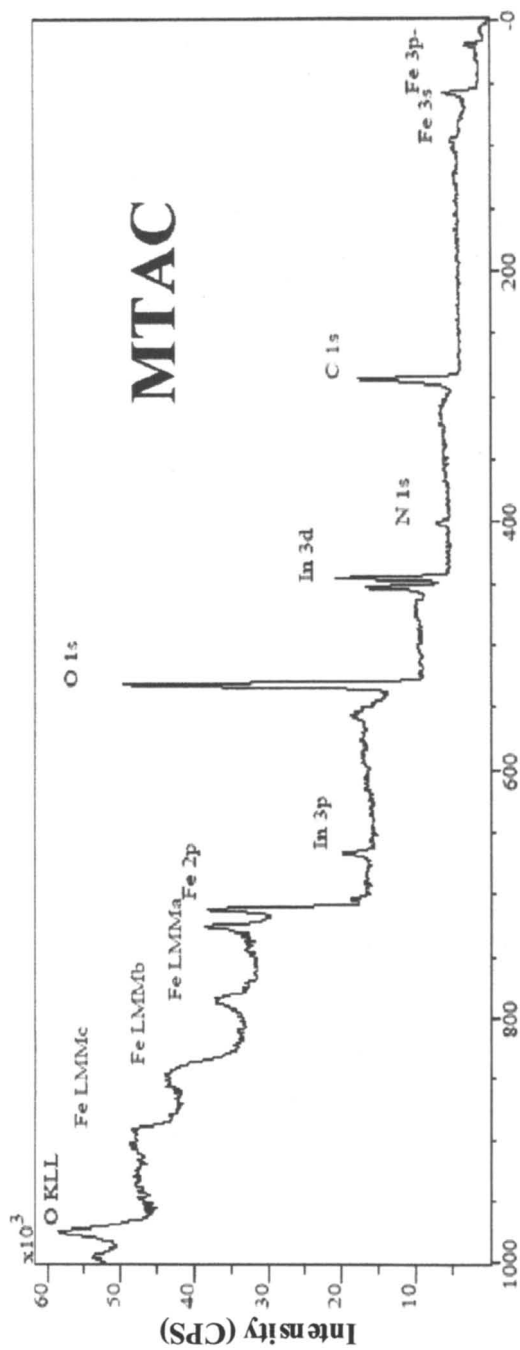
Figure 1. XPS spectra of tannic acid (TA), magnetic nanoparticles (M), magnetic-iron tannate nanoparticles produced by coprecipitation (MTAC) method, and magnetic-iron tannate nanoparticles produced by post-precipitation method (MTAP). Continued on next page.
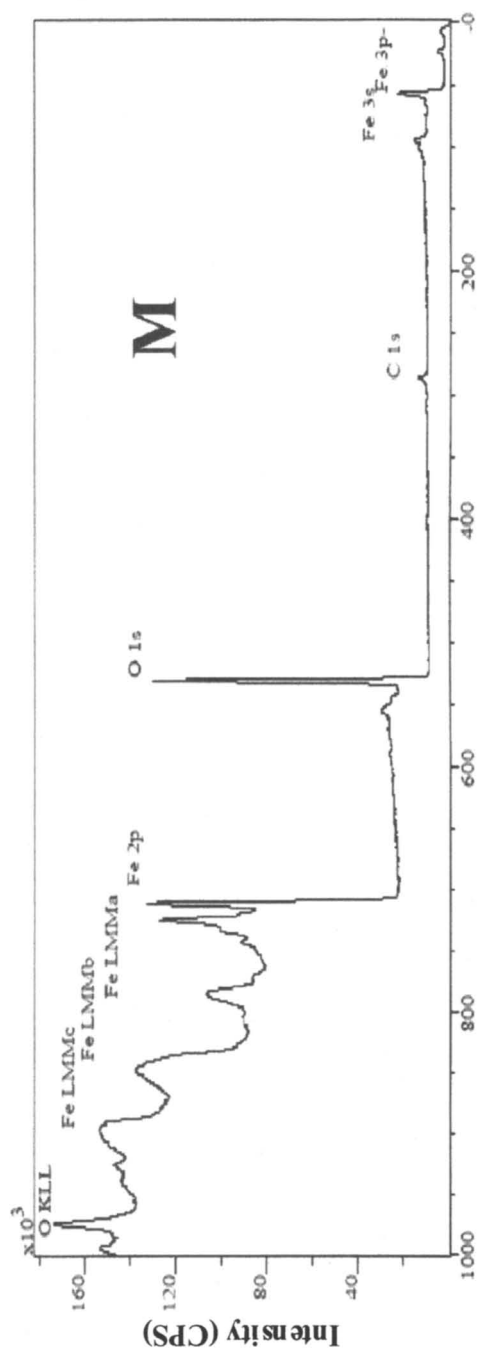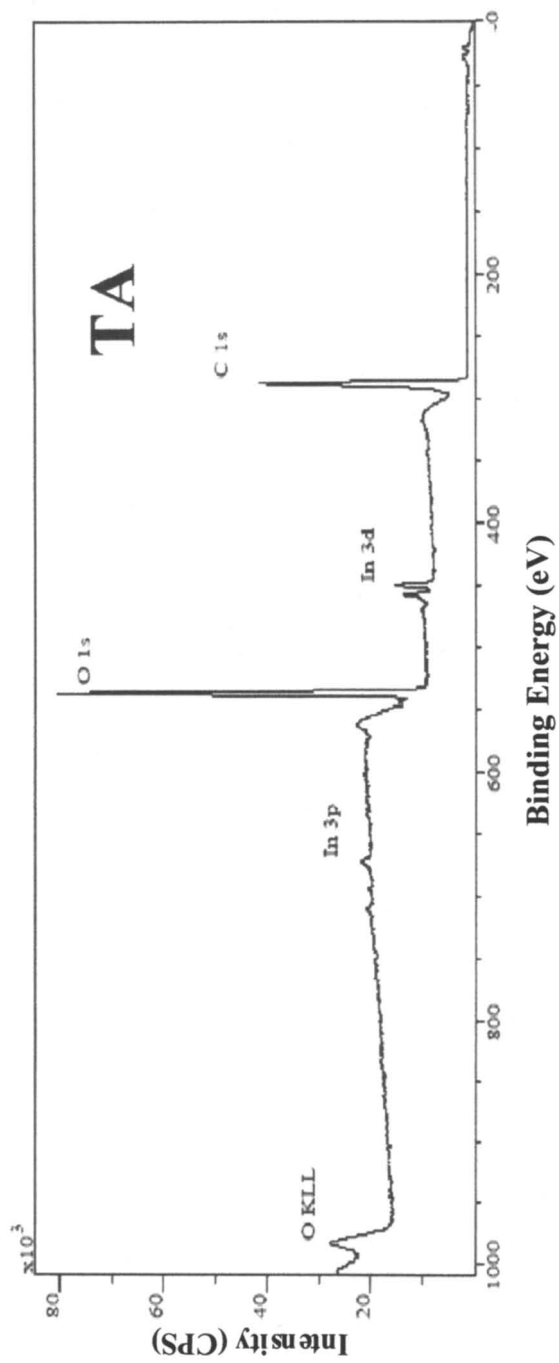
Figure 1. Continued.

incorporated tannic acid; which are absent in the core C1s spectra of M. The C_3/C_4 ratio (Table 2) is higher in MTAC relative to MTAP, indicating more $\underline{C}$–OH or O–$\underline{C}$–O functionality in the former. The data presented in Figure 2 show that all the nanoparticles contain a high binding energy signal at 290 eV that is undoubtedly a carbonate adventitious carbon from sample handling. The O1s fitted data (Table 3) reveal that oxygen-containing functionalities such as C=$\underline{O}$, – C$\underline{O}$OH and C–$\underline{O}$–C bridging sites characteristic of tannic acid are incorporated in MTAC and MTAP nanoparticles. The $\underline{O}$H $^-$/ $\underline{O}^{2-}$ ratios for M, MTAC and MTAP are 0.30, 1.04, and 0.44 respectively, which imply that in MTAC hydroxyl ($\underline{O}$H$^-$) species are the dominant surface oxygen species.

Table 2. Contribution of Different Types of Carbon in the XPS C1s Core Spectra of Magnetic Nanoparticles.

Sample	C_1 ($\underline{C}$-C) ($\underline{C}$-H) (Aromatic)	C_2 ($\underline{C}$-H) ($\underline{C}$-H) (Aliphatic)	C_3 ($\underline{C}$-O) ($\underline{C}$-O-C)	C_4 ($\underline{C}$ = O) ($\underline{C}$OOH)	C_5 (CO_3^{2-})	C_6 (π-π*)
	eV (%)	eV (%)	eV (%)	eV (%)	eV (%)	eV (%)
TA	284.6 (45.9)		286.3 (36.3)	288.7 (11.2)		291.5 (6.6)
M		285.1 (68.2)			289 (31.8)	
MTAC	284.6 (29.7)	285.7 (28.0)	286.8 (15.9)	288.2 (11.0)	289.3 (10.3)	290.9 (5.3)
MTAP	284.6 (24.9)	285.7 (24.4)	286.8 (21.7)	288.6 (16.5)	289.6 (8.9)	291.7 (3.6)

DRIFTS spectra of the magnetic nanoparticles before and after contact with tannic acid are shown in Figures 2 and 3. All the spectra (Figure 2) in the region 400–850 cm^{-1} exhibit bands due to Fe–O stretching modes (v_1 and v_2) of magnetite nanoparticles (11). Depending on the Fe(II) content the broad band located 526–840 cm^{-1} and 520– 610 cm^{-1} are assigned to magnetite and maghemite respectively (12, 13). The DRIFT data also provided results that complement XPS data. MTAC and MTAP exhibit significant spectral changes upon incorporation of tannic acid (Figures 2 and 3). Most of the tannic acid peaks such as hydrogen bonded OH stretching, C=O stretching, and C–O stretching

Table 3. Contribution of Different Types of Carbon in the XPS O1s Core Spectra of Magnetic Nanoparticles.

Sample	O_1 ($\underline{O}^{2-}$)	O_2 ($\underline{O}H^-$)	O_3 (C–$\underline{O}$; C–$\underline{O}$–C)	$\underline{O}H^-/\underline{O}^{2-}$ ratio
	eV (%)	eV (%)	eV (%)	
TA		531.3 (86.2)	532.9 (13.8)	
MG	529.7 (77.1)	531.1 (22.9)		0.30
MGTAC	530.1 (36.9)	531.4 (38.5)	532.9 (24.6)	1.04
MGTAP	530.2 (59.1)	531.4 (26.2)	532.8 (14.7)	0.44

vibrations appeared at frequencies shifted in the spectra of MTAC and MTAP (Table 4; Figures 2 and 3).

In MTAC and MTAP, the stretching band of C=O shifted from 1709 cm^{-1} in tannic acid by 6 and 24 cm^{-1} to a lower wavenumber in MTAC and MTAP respectively, indicating that some of the carboxylic groups were involved in the formation of magnetic-iron tannate complexes. Additional confirmation of the involvement of carboxyl functional groups in the magnetic-iron tannate complex formation is the appearance of two new bands at 1399 ± 1 cm^{-1} and 1572 ± 2 cm^{-1} attributed to asymmetrical and symmetric stretching vibrations of carboxyl group complexed with iron oxide (13). We also observed frequency shifts from 3347 cm^{-1} to 3134/3128 cm^{-1} and from ~ 1086 cm^{-1} to 1071± 9 cm^{-1}. Similar shifts were attributed to the interaction of CO stretching vibration of –COH or CH$_2$OH groups with iron oxide (15, 16). Interestingly, the band located at 1206 cm^{-1} was also observed in studies of tannic acid with various iron oxides and assigned as ferric tannate peak (17). Thus, the nanoparticles synthesized in the presence of tannic acid can be considered magnetic-iron tannate nanoparticles.

The TEM images of M and MTAP nanoparticles are shown in Figure 4. The interaction of preformed magnetic nanoparticles in alkaline media with tannic acid for 30 min did not significantly alter the morphology of the particles. The morphology of both types of nanoparticles are fairly spherical with diameters between 10 nm and 15 nm.

The uptake of Cu and Zn from solutions containing 10 mg/L of each metal ion was determined using the nanoparticles synthesized as adsorbents at pH 4.5
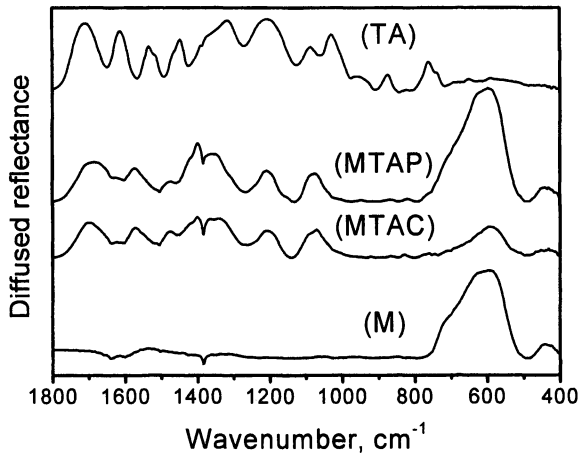
Figure 2. DRIFT spectra in the region 1800-450 cm^{-1} of magnetite nanoparticles (M), magnetic nanoparticles produced by coprecipitation, (MTAC), magnetic nanoparticles produced by post-precipitation (MTAP), and tannic acid (TA).
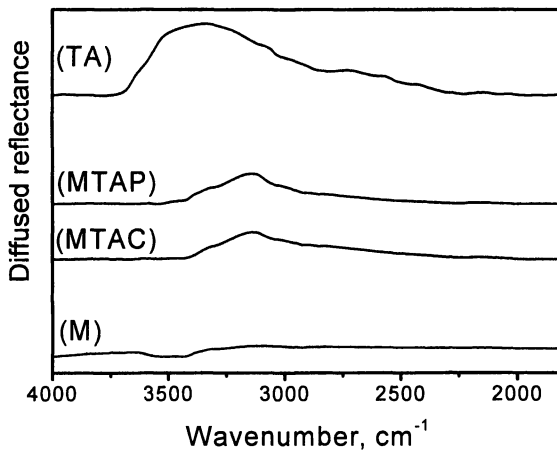
Figure 3. DRIFT spectra in the region 4000-1800 cm^{-1} of magnetite nanoparticles (M), magnetic nanoparticles produced by coprecipitation, (MTAC), magnetic nanoparticles produced by post-precipitation (MTAP), and tannic acid (TA).

Table 4. DRIFTS Spectra for Tannic Acid and Magnetic Nanoparticles.

IR band position (cm^{-1})				Peak assignments (*14–18*)
TA	M	MTAC	MTAP	
3347		3124	3124	OH stretching vibrations
1712				C=O stretching vibrations
		1702	1685	Weakened C=O stretching vibrations
1613		1572	1574	C–C ring stretching , COO^-
1534				asymmetric stretching vibrations
1447				C–C ring stretching, C–H bending
1351				vibrations
		1400	1399	COO^- symmetric stretching vibrations
1318		1208	1209	Phenolic C–O(H) stretching and bending vibrations
1083		1071	1079	C–O (H) stretching vibrations of
1027				sugar moiety; CC bending vibrations
	599	597	598	Fe–O stretching vibrations
	441	431	440	Fe–O stretching vibrations

and ionic strength of 10 mM. All the nanoparticles showed no significant adsorption for zinc in the binary mixture. The % uptake of Cu^{2+} ions using 50 and 150 mg of magnetic adsorbents are shown in Figure 5. It evident that Cu^{2+} ions uptake increases in the order M < MTAC < MTAP at the two adsorbent doses investigated. The Cu^{2+} ions removal capacity at pH 4.5 and ionic strength of 10 mM using M, MTAC and MTAP nanoparticles was 1.8, 3.90, and 6.21 mg per gram of nanoparticles, respectively. It is interesting to note that MTAC containing more carbon than MTAC based on XPS analysis showed lower metal uptake compare with MTAP. The higher metal uptake observed with MTAP relative to MTAC could be due to differences in the nature of functionalities at the adsorbent surface (Table 2 and 3). The C_3/C_4 ratios (Table 2) for MTAC and
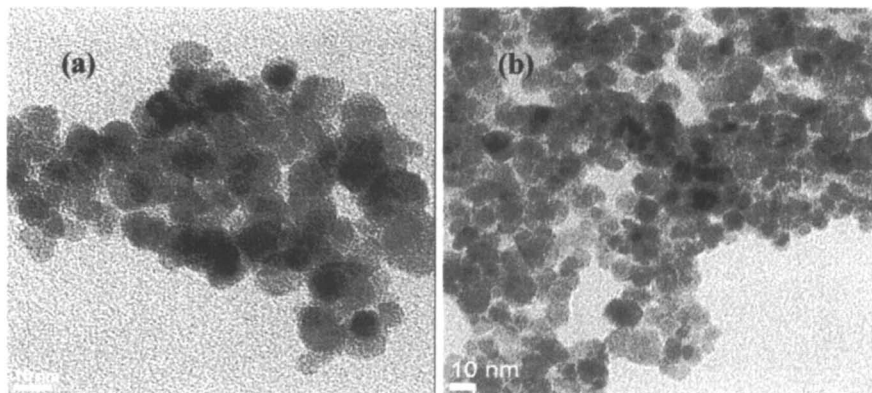
Figure 4. TEM images of magnetic nanoparticles produced in the presence and absence of tannic acid. (a) magnetic nanoparticles (no tannic acid), and (b) magnetic nanoparticles produced by post-precipitation (MTAP) method.

MTAP are 1.45 and 1.31 respectively, indicating more surface COOH functionality in the latter. Unlike in the formation of MTAP nanoparticles, where the tannic acid was adsorbed onto pre-formed magnetic nanoparticles; in MTAC, tannic acid was incorporated into the magnetic nanoparticles. The novel nanoparticles affinity follows the order Cu > Zn consistent with affinity order reported for more complex systems (*19*). We are currently examining the effects of variation of solution pH, ionic strength, and concentration of the constituents in the mixture on uptake capacity of the novel functionalized magnetic nanoparticles.

Conclusions

The following conclusions may be drawn from the characterization and preliminary metal uptake results of the tannic acid functionalized magnetic nanoparticles.

1. Two different novel magnetic-iron tannate nanoparticles can be synthesized by changing the sequence of tannic acid addition during magnetic nanoparticles synthesis.
2. DRIFTS results demonstrate that the formation of the magnetic-iron tannate complexes involve carboxylate and hydroxyl functionalities.
3. The functionalized nanoparticles have high sorption capacity for Cu^{2+} relative to Zn^{2+} in a binary $Cu^{2+}-Zn^{2+}$ system.
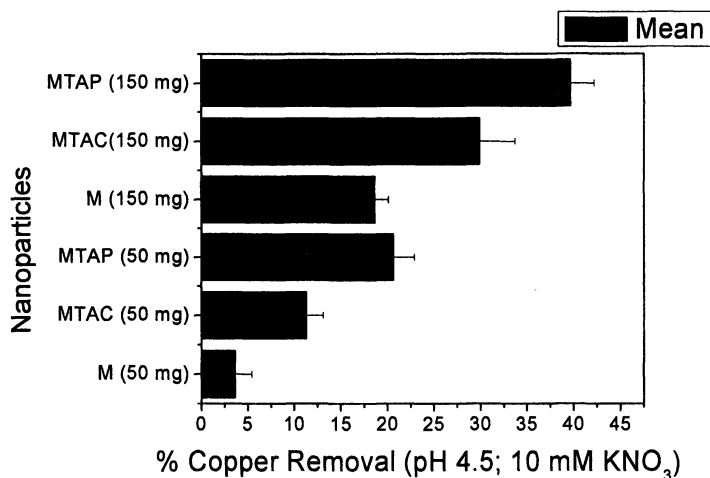
Figure 5. The % uptake of Cu^{2+} ions from aqueous binary solutions of Cu^{2+} ions and Zn^{2+} ions at different nanoparticles concentration. Initial metal ion concentration =10 mg/L each, pH= 4.5, total volume = 200 mL, temperature = 22 ±° C, and ionic strength = 10 mM KNO_3)

4. Magnetic-iron tannate complexes synthesized using post-precipitation method display higher copper ion sorption capacity than magnetic-iron tannate complexes synthesized using coprecipitation method.

Acknowledgements

References

1. Brown, P. A.; Jefcoat, I. A.; Parrish, D.; Gill, S.; Graham, E. Evaluation of the adsorptive capacity of peanut hull pellets for heavy metals in solution. *Adv. Environ. Res.* **2000**, *4*, 19-29.

2. Brown, P. A.; Gill, S. A.; Allen, S. J. Metal removal from wastewater using peat. *Water Res.* **2000**, *16*, 3907-3916.
3. Panayotova, M. I. Kinetics and thermodynamics of copper ions removal from wastewater by use of zeolite. *Waste Manage.* **2001**, *21*, 671-676.
4. Cornell, R. M,; Schwertmann, U. *The Iron Oxide: Structure, Properties, Reactions, Occurrence and Uses*; VCH: Weinheim, 1996; 573 pp.
5. Aurich, K.; Schwalbe, M.; Clement, J. H.; Weitschies, W.; Buske, N. Polyaspartate coated magnetite nanoparticles for biomedical application. *J. Magn. Magn. Mater.* **2007**, *311*, 1-5.
6. Goa, X.;Yu, K. M. K.; Tam, K. Y.; Tsang, S. C. Colloidal stable silica encapsulated nano-magnetite composite as a novel bio-catalyst carrier. *Chem. Commum.* **2003**, 2998-2999.
7. Bruce, I. J.; Taylor, J.; Todd, M.; Davies, M. J.; Borioni, E.; Sangregorio, C.; Sen, T. Synthesis, characterization and application of silica-magnetite nanocomposites. *J. Magn. Magn. Mater.* **2004**, *284*, 145-160.
8. Robinson, P. J.; Dunnill, P.; Lilly, M. D. The properties of magnetic supports in relation to immobilized enzyme reactors. *Biotechnol, Bio-eng.* **1973**, *15*, 603-606.
9. Kraal, P.; Jansen, B.; Nierop, K. G. J.; Verstraten, J. M. Copper complexation by tannic acid in aqueous solution. *Chemosphere* **2006**, *65*, 2193-2198.
10. Haslam, E.; Lilley, T. H.; Warminski, E.; Lioa, H.; Cai, Y.; Martin, R.; Gaffney, S. H.; Goulding, P. N.; Luck, G. Polyphenol complexation: A study in Molecular Recognition, In: *Phenolic compounds in Food and Their Effects on Health II*, M. J. Comstock (Ed),; ACS Symposium Series 507, 1992 (Chapter 2).
11. Ucer, A.; Uyanik, A.; Aygun, S. F. Adsorption of Cu (II), Cd (II), Zn (II) and Fe (III) ions by tannic acid immobilized activated carbon. *Separation and Purification Technology*, **2006**, *47*, 113-118.
12. Yamaura, M.; Camilo, R. L.; Sampaio, L. C.; Macedo, M. A.; Nakamura, M.; Toma, H. E. Preparation and characterization of (3-aminopropyl) triethoxysilane-coated magnetic nanoparticles. *J. Magn. Magn. Mater.* **2004**, *279*, 210-217.
13. Gomez, J. A. G.; Daida, P.; Kesmez, M.; Weir, M.; Moreno, H.; Parga, J. R.; Irwin, G.; MacWhinney, G.; Grady, T.; Peterson, E.; Cocke, D. L. Arsenic removal by electrocoagulation using combined Al–Fe electrode system and characterization of products. *Journal of Hazardous Materials.* **2007**, *B139*, 220-231.
14. Nyquist, R. A.; Kapal, R. O. *Infrared Spectra of Inorganic Compounds* Academic Press, New York, 1971.
15. Gu, B.; Schmitt, J.; Chen, Z.; Liang, L.; McCarthy, J. F. Adsorption and desorption of different organic matter fraction on iron oxide. *Geochim. Cosmochim. Acta.* **1995**, *59* (2), 219-229.

16. Subramania, S.; Nataragan, K. A. Some studies of adsorption behavior of an oxidized starch on hematite. *Minerals Engineering* **1988**, *1*(3), 241-254.

17. Socrates, G. I*nfrared and Raman characteristic group frequencies: Tables and Charts,* 3rd edition, John Wiley: Chichester, UK, 2001; 347p.

18. Nasrazadani, S. The application of infrared spectroscopy to a study of phosphoric and tannic acid interactions with magnetite (Fe_3O_4), goethite (α-FeOOH), and lepidocrocite (γ-FeOOH). *Corrosion Science.* **1997**, *39*(10-11), 1845-1859.

19. Hammaini, A.; Ballester, A.; Gonzalez, F.; Blazquez, M. L.; Munoz, J. A. Activated sludge as biosorbent of heavy metals. In *Biohydrometallurgy and the environment towards the mining of the 21st century*; Amils, R.; Ballester, A. (Eds) Part B, Elsevier science: Amsterdam, **1999**. p 185-192.

Time-Dependent Density Functional Theory Examination of the Effects of Ligand Adsorption on Metal Nanoparticles

Christine M. Aikens and George C. Schatz

Department of Chemistry, Northwestern University, 2145 Sheridan Road, Evanston, IL 60208

Metal nanoparticles have attracted intense interest due to their remarkable optical, catalytic, and electronic properties. The passivating ligands have a significant impact on the physical properties of the particle in addition to stabilizing the metal core. In this work, the binding energies, structures, and changes in electron density are assessed for the adsorption of ligands such as PH_3 and NH_3 to a representative Au_{20} cluster. Time-dependent density functional theory is employed to examine the effects of passivating ligands on the optical absorption of the metal particle.

Introduction

Bare metal clusters can be isolated in the gas-phase. However in solution phase, these clusters tend to aggregate unless ligands are used to passivate the nanoparticles. Typical passivating ligands include thiol(ate)s and phosphines. Primary amine ligands have also been used in exchange reactions, and the use of these ligands has been shown to lead to expanded metal cores (1). The addition of passivating ligands to bare metal clusters involves potential structural changes induced by the ligands as well as changes in the physical properties such as the optical absorption. For example, the HOMO-LUMO gap of Au_{11} clusters increases from 1.4 eV to 1.8 eV when the surface-protecting ligands are varied from triphenylphosphines to alkanethiolates (2).

One system of interest contains an Au_{20} core. In the gas phase, this cluster is predicted to be tetrahedral based on the agreement between experimental and theoretical photoelectron spectra (*3*). The structure of this cluster looks like a fragment of bulk gold with (111) surfaces on all sides of the tetrahedron. As a consequence, Au_{20} has been used as a model of the Au(111) surface for surface-enhanced Raman scattering calculations (*4*).

As mentioned above, passivating ligands are needed so that the gold nanoparticles do not aggregate in solution. The triphenylphosphine (PPh_3) ligand has recently been shown to coordinate with the Au_{20} particle to yield a $Au_{20}(PPh_3)_8$ complex (*5*). High-resolution mass spectrometry data confirms the existence of $Au_{20}(PPh_3)_8{}^{2+}$ dications, and collision-induced dissociation experiments show that four PPh_3 ligands can be readily dissociated (*5*). Numerous triangular particles with edges less than 1 nm can be seen in high-resolution transmission electron microscopy images, which suggest that the tetrahedral Au_{20} core remains essentially tetrahedral upon addition of triphenylphosphine ligands (*5*).

In this work, the differences between the binding of phosphine and amine ligands and the consequent effects on the optical absorption spectra are investigated.

Computational Details

All calculations discussed in this work were performed with the Amsterdam Density Functional (ADF) 2006.01 program (*6*). The structures of the species studied were determined at the density functional (DFT) level of theory using the gradient-corrected Becke-Perdew (BP86) exchange-correlation functional (*7,8*). A triple-zeta with polarization functions (TZP) Slater type basis set was employed with a $[1s^2\text{-}4f^{14}]$ frozen core for Au and a $[1s^2]$ frozen core for the first row elements. Scalar relativistic effects were included by utilizing the zeroth-order regular approximation (ZORA) (*9*). The highest molecular symmetry possible for each structure was considered (T_d for Au_{20}, $Au_{20}(PH_3)_n$, and $Au_{20}(NH_3)_n$ with $n = 4$ and 8, C_{3v} for $Au_{20}(PH_3)_n$ and $Au_{20}(NH_3)_n$ with $n = 5$ and 7, and C_{2v} for $Au_{20}(PH_3)_n$ and $Au_{20}(NH_3)_n$ with $n = 6$). The numbering for the molecular orbitals starts from one for each symmetry representation, and include orbitals formed from the $5s^25p^65d^{10}6s^1$ electrons on gold and the valence electrons on phosphorus, nitrogen, and hydrogen that are treated explicitly. The SCF convergence was tightened to 10^{-8}. A gradient convergence criterion of 10^{-4} and an energy convergence criterion of 10^{-5} were used in order to obtain well-converged geometries.

Time-dependent DFT (TDDFT) was used to determine energetics and composition of the excited states. The tolerance was set to 10^{-8} and the

orthonormality was set to 10^{-10}. (Information about these technical parameters is available in the online ADF manual (*10*).) Excitations to the lowest 1800 states of all symmetries were evaluated for the optical absorption spectra. The absorption spectra were fit with a Lorentzian function with a width at half-maximum of 0.2 eV.

Results

Binding Energies

The tetrahedral Au_{20} cluster has three sites available for binding: vertex, edge, and surface atoms (Figure 1). The vertex atoms have the lowest coordination number and may be expected to be the most reactive. At the BP86/TZP level of theory, the first PH_3 ligand is predicted to have a binding energy of 0.82 eV to a vertex site. Previous theoretical results for $Au_{20}(PH_3)_4$ using the PW91 functional and a TZ2P basis set for Au and P and a DZP basis set for H predicted $Au-PH_3$ bond energies of ~1 eV (*5*). In the present calculations, the average binding energy for the first four PH_3 ligands to vertex sites is predicted to be 0.81 eV. In contrast, a single PH_3 ligand is predicted to bind to a surface site on the bare Au_{20} cluster with a binding energy of 0.47 eV, and the average binding energy to the surface sites is predicted to be 0.43 eV. In general, the binding energies of NH_3 ligands are lower. The first binding energy and the average binding energy to the vertex sites are predicted to be 0.69 and
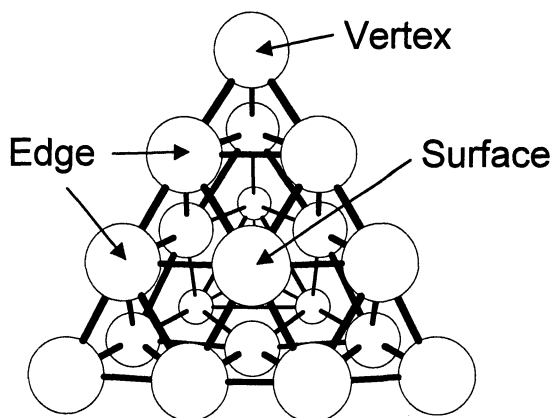
Figure 1. Tertrahedral Au_{20} structure illustrating locations of vertex, edge and surface sites.

0.61 eV, respectively, while the first binding energy and average binding energy to the surface sites are predicted to be 0.24 and 0.19 eV, respectively. These binding energies support the idea that the first four ligands are bound to vertex sites. Once four ligands are bound to vertex sites, the binding energy of additional PH_3 ligands to the surface sites ranges from 0.27-0.30 eV. However, the binding energy of additional NH_3 ligands ranges from 0.00-0.05 eV. At typical reaction temperatures, these NH_3 ligands are essentially unbound. The labile nature of the amine ligands may explain why ligand exchange reactions involving these ligands resulted in the growth of the cluster cores as seen in Ref. (1). With fewer passivating ligands attached to the cluster, more metal atoms would be accessible, which could lead to cluster-cluster aggregation.

Binding energies predicted by density functional theory may not be quantitatively accurate. In general, DFT tends to overbind. Since dispersion effects are not incorporated in DFT, which would lead to an underestimation of the binding energy, this may offset the error to some extent. Thus, it is instructive to compare density functional results with other levels of theory. The binding energy of NH_3 with a single gold atom is predicted to be 0.516 eV at the CCSD/BS10 level of theory (11). The binding energy for NH_3 with a single gold atom at the BP86/TZP level of theory is predicted to be 0.490 eV (12).

Bond Lengths

The trends in the bond lengths echo the trends observed for the binding energies. The distance between the gold atom and the phosphorus atom is longer at the vertex sites than at the surface sites (Table 1), which agrees with the weaker binding energies predicted at the surface sites. The distance between nitrogen and gold at the vertex sites is slightly (0.022 Å) shorter than the distance between phosphorus and gold at the vertex sites, but this decrease is less than expected due to the relative sizes of N and P. The distance between nitrogen and gold at the surface sites is predicted to be 2.550 Å, which is 0.154 Å longer than the analogous distance between phosphorus and gold. These amine groups are very weakly bound.

Optical Absorption Spectra

In Au_{20}, intraband transitions from occupied sp conduction orbitals to unoccupied sp orbitals occur at low energies (Figure 2). Interband transitions between the d band and the sp conduction band contribute a broad background to the spectrum. The addition of PH_3 ligands to the Au_{20} core causes the appearance of a large peak at 3.27 eV and the disappearance of the Au_{20}

Au$_{20}$ excitation spectrum

Distorted Au$_{20}$ excitation spectrum
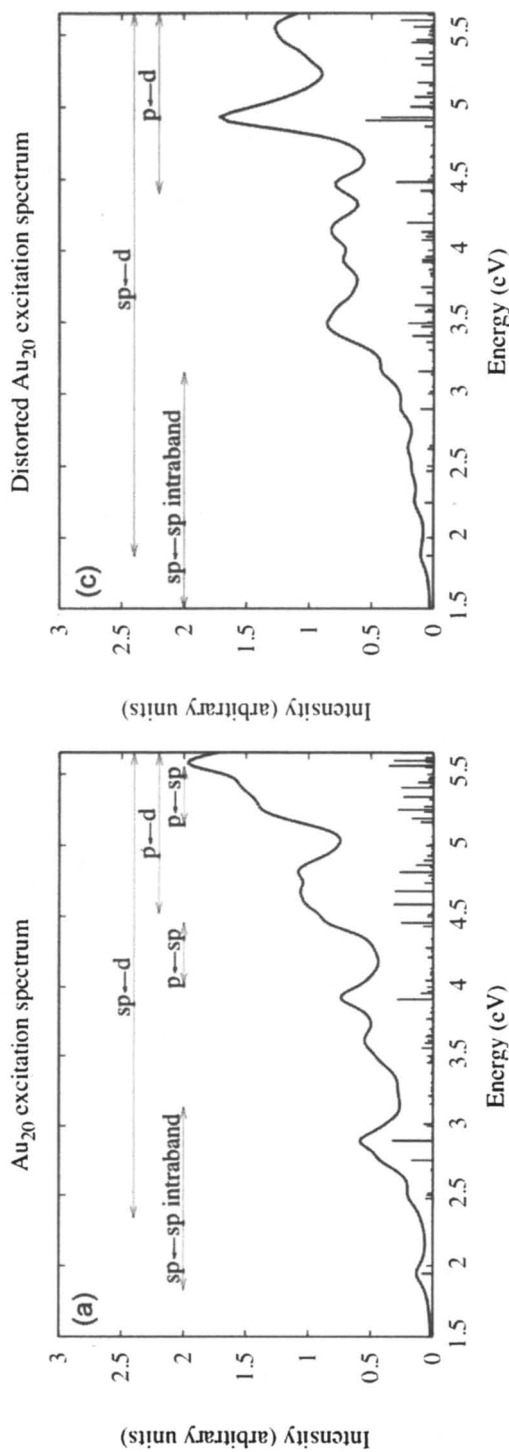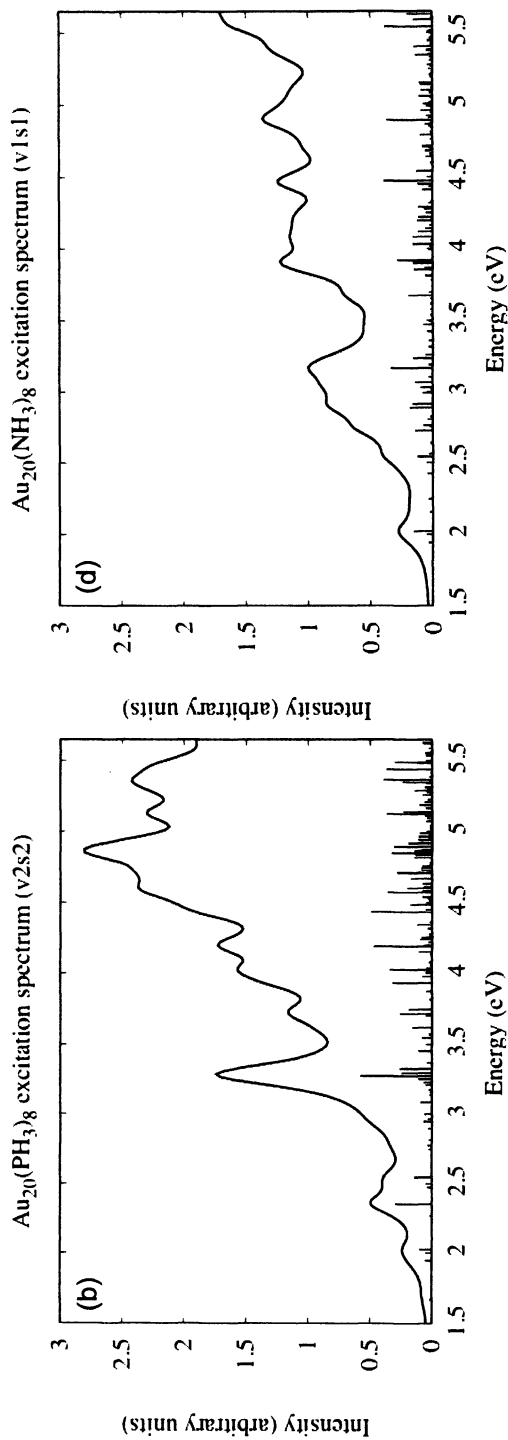
Figure 2. Calculated optical absorption spectra for (a) the bare Au_{20} cluster, (b) the $Au_{20}(PH_3)_8$ complex, (c) the distorted Au_{20} cluster (see text), and (d) the $Au_{20}(NH_3)_8$ complex. (Figure 2(a) reproduced from reference 4. Copyright 2006 American Chemical Society.)

Table 1. Distance from Ligand to Gold in $Au_{20}L_8$ (L = PH_3, NH_3) Clusters

Gold-ligand distance	$\mathring{A}$
Au-P distance (surface)	2.396
Au-P distance (vertex)	2.371
Au-N distance (surface)	2.550
Au-N distance (vertex)	2.349

intraband peak at 2.89 eV in the absorption spectrum (Figure 2). Potential causes for these changes include geometrical distortions in the metal core induced by the ligands, ground state charge transfer from the ligands to the metal cluster, and changes in the orbital energies due to the metal-ligand interaction.

Geometrical Distortion

When the ligands adsorb on the cluster, they induce dramatic changes to the geometrical structure of the metal core. When the PH_3 ligands adsorb, the surface atoms expand by 0.935 Å relative to the center of mass (COM) (Table 2). The vertex atoms expand slightly (0.058 Å) relative to the center of mass, while the edge atoms contract somewhat (0.153 Å). As a result, nearest neighbor (edge to surface/vertex atom) Au-Au distances increase by approximately 0.07-0.13 Å. When NH_3 ligands adsorb to the cluster, the same trends are followed; however, the magnitude of each change is reduced. The surface atoms expand by 0.706 Å relative to the COM, while the vertex atoms expand by 0.030 Å and the edge atoms contract by 0.122 Å. The nearest neighbor Au-Au distances increase by 0.04-0.06 Å.

Figure 2c shows an optical absorption spectrum of an Au_{20} cluster whose geometry has been distorted as though eight PH_3 ligands have been adsorbed. Of note, the intraband peak at 2.89 eV with relatively high oscillator strength in the Au_{20} spectrum is not apparent in the distorted Au_{20} spectrum. In addition, the peak at 3.27 eV in the $Au_{20}(PH_3)_8$ spectrum is also not apparent in the distorted Au_{20} spectrum. The geometrical distortion induces changes in the absorption spectrum, but is not sufficient to explain the ligand effects on the absorption spectrum. Thus, even the addition of PH_3 ligands changes the absorption spectrum relative to that of a bare metal cluster.

An analysis of the excitations in the distorted Au_{20} cluster shows that intraband transitions occur in the 1.54 – 3.15 eV range. The interband transitions become important after 1.87 eV. Even so, the six strongest transitions below 3.0 eV that are evident in Figure 2c have primarily intraband character. In contrast, both the intraband and interband transitions occur at slightly higher

**Table 2. Distance Between Gold Atom and Center of Mass (COM)
or Other Gold Atoms**

	Au_{20}	$Au_{20}(PH_3)_8$	$Au_{20}(NH_3)_8$
Distance (Å) from COM to:			
edge atoms	3.337	3.184	3.215
vertex atoms	4.993	5.051	5.023
surface atoms	1.944	2.879	2.650
Distance (Å) between:			
edge and surface atoms	2.839	2.965	2.897
edge and vertex atoms	2.735	2.808	2.777
surface and vertex atoms	4.716	4.910	4.835

energies in the bare Au_{20} cluster. The excitations are also more mixed than the excitations for the distorted cluster; the peak at 2.89 eV in Figure 2a has both significant intraband and interband character. For the distorted complex, the interband transitions are required to describe the absorption spectrum above 3.1 eV, while the intraband transitions are responsible for the broad featureless region below 3.0 eV.

Ground State Charge Transfer

When ligands such as PH_3 and NH_3 adsorb to a gold nanoparticle, they donate electron density to the metal core. Soft acids such as PH_3 would be expected to have a low electronegativity, whereas harder acids such as NH_3 would be expected to have a higher electronegativity. Voronoi deformation density (VDD) and Hirschfeld charges predict that NH_3 transfers more electron density to the gold cluster than PH_3, while a Mulliken charge analysis shows the opposite trend (Table 3).

Each charge analysis method predicts that approximately one electron total is transferred from the eight ligands to the metal core. Although charge analysis based on VDD or Hirschfeld charges would be preferred (13), subsequent analysis in this paper focuses on Mulliken charges because the atomic electron density per angular momentum number is available within ADF. One difference between the PH_3 and NH_3 ligands is that the each phosphorus atom is predicted to have approximately 0.18 electrons in d orbitals, whereas each nitrogen atom is predicted to have only 0.03 electrons in d orbitals based on the Mulliken charge analysis (Table 4).

Table 3. Charge Transferred (Electrons) from Ligands to Gold Cluster

Charge Method	$Au_{20}(PH_3)_8$	$Au_{20}(NH_3)_8$
Voronoi Deformation Density	1.18	1.28
Hirschfeld	1.05	1.14
Mulliken	1.14	0.70

Table 4. Mulliken Atomic Electron Density in d Orbitals (Electrons)

	$Au_{20}(PH_3)_8$	$Au_{20}(NH_3)_8$
Vertex atoms	0.1853	0.0331
Surface atoms	0.1853	0.0318

The Mulliken charge analysis can be used to analyze the amount of s, p, and d character on the gold atoms at various locations and to analyze how this changes upon adsorption of ligands (Table 5). Relative to occupations of $5s^2 5p^6 5d^{10} 6s^1$ for an isolated gold atom, the edge atoms in the tetrahedral Au_{20} cluster have gained 0.38 electrons in p orbitals and have lost 0.35 electrons from the d orbitals. This may be expected as a consequence of the interaction of the partially occupied sp orbitals with the occupied d orbitals, which is pronounced in gold because of close $6sp$ and $5d$ orbital energies due to relativistic effects. The vertex atoms in the tetrahedral Au_{20} cluster gain 0.17 and 0.19 electrons in s and p orbitals, respectively, while losing 0.27 electrons from the d orbitals. These atoms are predicted to be slightly negatively charged. The surface atoms lose about 0.18 electrons from the s orbitals, gain about 0.36 electrons from the p orbitals, and lose about 0.34 electrons from the d orbitals. As a result, these atoms are predicted to be slightly positively charged.

Orbital Energies

The HOMO-LUMO gap for Au_{20} at the BP86/TZP level of theory is 1.787 eV. When eight PH_3 ligands bind to the cluster, the HOMO-LUMO gap is predicted to decrease to 1.597 eV (in reasonable agreement with a HOMO-LUMO gap of 1.55 eV predicted by Ref. (5)). However, when eight NH_3 ligands bind to the metal core, the HOMO-LUMO gap is predicted to increase to 1.828 eV. If four ligands bind to the vertex sites of the cluster, the HOMO-LUMO gaps are predicted to increase from 1.787 eV for the bare cluster to 1.827 eV for $Au_{20}(PH_3)_4$ (in good agreement with the 1.82 eV gap predicted in

Ref. (*5*)) or 1.963 eV for $Au_{20}(NH_3)_4$. However, the binding of four ligands to surface sites is predicted to decrease the HOMO-LUMO gap to 1.587 eV for $Au_{20}(PH_3)_4$ or 1.418 for $Au_{20}(NH_3)_4$. So, the binding of phosphine or amine ligands to vertex sites increases the HOMO-LUMO gap, while the binding of these ligands to surface sites decreases the HOMO-LUMO gap. For the phosphine ligands, the effects of the binding to the surface sites dominate the total change in the HOMO-LUMO gap. For the amine ligands, the change to the HOMO-LUMO gap is dominated by the effects of the ligands at the vertex sites, as may be expected due to the weak binding of the surface ligands.

In general, the mixing of the PH_3 orbitals with the Au_{20} orbitals increases the energies of both the occupied and unoccupied metal orbitals. The phosphine ligands are electron donors, and the increase in the energy of the highest occupied orbitals suggests that the ionization energy of the complex is lowered relative to the bare cluster (*5*). Upon inspection of the molecular orbitals of the complex, ten occupied orbitals (two A_1, two E, two T_1, and four T_2) containing 48 electrons clearly arise from PH_3 orbitals. The remaining 16 electrons originally associated with the PH_3 ligands are now located in mixed orbitals comprised of phosphorus *p* character and gold *sp* and *d* character. The unoccupied orbitals have a significant amount of PH_3 character, whereas unoccupied orbitals in the $Au_{20}(NH_3)_8$ system have negligible NH_3 character.

The strong excitation at 3.27 eV in the optical absorption spectrum for $Au_{20}(PH_3)_8$ is primarily interband (sp - d), with approximately 15% metal-to-ligand charge-transfer behavior (PH_3 - sp) (Table 6). Since density functional theory fails for long-range charge-transfer states (*14*), the accuracy of these transitions in the theoretical calculations must be considered. The proximity of the ligands to the metal core and the minor degree of charge-transfer in the transition at 3.27 eV may mean that this issue does not greatly affect this peak in the TDDFT spectrum of $Au_{20}(PH_3)_8$. Other metal-to-ligand charge transfer states appear in the 3.7-4.1 eV range in the calculated TDDFT absorption spectrum; it is possible that these transitions actually occur at higher energies.

For $Au_{20}(NH_3)_8$, the strongest peak below 3.5 eV occurs at 3.17 eV. The composition of this transition is presented in Table 7. Interband transitions are responsible for most of the composition of this excitation, although approximately 20% of the character of the excitation arises from excitations out of the conduction band into the H *s* orbitals on the ligands.

The occupied orbitals in the *d* band for $Au_{20}(NH_3)_8$ differ from those for $Au_{20}(PH_3)_8$.

Summary

The binding of phosphine and amine groups to the tetrahedral Au_{20} cluster has been examined, and the effects of the ligands on the geometrical structure

Table 5. Mulliken Atomic Electron Density (Electrons) and Total Charge on Gold Atoms

	Atoms	S	P	D	Overall
	Edge	2.9799	6.3804	9.6513	-0.0115
T_d Au_{20}	Vertex	3.1659	6.1853	9.7307	-0.0819
	Surface	2.8227	6.3987	9.6618	0.1165
	Edge	2.9804	6.4287	9.6454	-0.0545
$Au_{20}(PH_3)_4$	Vertex	3.1088	6.3260	9.6513	-0.0861
(vertex)	Surface	2.9273	6.3196	9.6923	0.0607
	Edge	3.0295	6.3919	9.6613	-0.0828
$Au_{20}(PH_3)_4$	Vertex	3.1964	6.1457	9.7368	-0.0789
(surface)	Surface	2.6801	6.5398	9.6320	0.1481
	Edge	3.0522	6.4092	9.6416	-0.1030
$Au_{20}(PH_3)_8$	Vertex	3.1459	6.3084	9.6481	-0.1025
	Surface	2.7129	6.5133	9.6470	0.1268
	Edge	3.0466	6.4212	9.6532	-0.1210
$Au_{20}(NH_3)_8$	Vertex	3.0684	6.2544	9.6892	-0.0120
	Surface	2.6740	6.3997	9.7257	0.2007

and absorption spectrum of the complex have been considered. PH_3 ligands bind more strongly than NH_3 ligands. The first four ligands bind preferentially to the vertex sites of the tetrahedral cluster. For the first four ligands, the average binding energy of PH_3 is 0.81 eV, and the average binding energy of NH_3 is 0.61 eV. After four ligands bind to the vertex sites, additional PH_3 ligands have a binding energy of approximately 0.3 eV, while additional NH_3 ligands are essentially unbound.

The absorption spectra of Au_{20}, $Au_{20}(PH_3)_8$, and $Au_{20}(NH_3)_8$ vary dramatically. The binding of phosphine or amine ligands to vertex sites increases the HOMO-LUMO gap, while the binding of these ligands to surface sites decreases the HOMO-LUMO gap. Mixing of the ligand orbitals with the metal

Table 6. Composition of the Au$_{20}$(PH$_3$)$_8$ Transition at 3.27 eV

occupied orbital (assignment)		unoccupied orbital (assignment)	weight
33t$_2$ (d)	->	36t$_2$ (sp)	0.3989
17e (d)	->	21t$_1$ (sp)	0.0832
2a$_2$ (d)	->	21t$_1$ (sp)	0.0562
35t$_2$ (sp)	->	20a$_1$ (PH$_3$)	0.0523
20t$_1$ (d)	->	37t$_2$ (sp)	0.0768
17a$_1$ (d)	->	36t$_2$ (sp)	0.0370
18a$_1$ (sp)	->	38t$_2$ (PH$_3$)	0.0363
35t$_2$ (sp)	->	19a$_1$ (PH$_3$)	0.0131
35t$_2$ (sp)	->	22t$_1$ (PH$_3$)	0.0244
32t$_2$ (d)	->	21t$_1$ (sp)	0.0191
33t$_2$ (d)	->	21t$_1$ (sp)	0.0188
18t$_1$ (d)	->	36t$_2$ (sp)	0.0187
17t$_1$ (d)	->	36t$_2$ (sp)	0.0077

Table 7. Composition of the $Au_{20}(NH_3)_8$ Transition at 3.17 eV

occupied orbital (assignment)		unoccupied orbital (assignment)	weight
$19t_1$ (d)	->	$37t_2$ (sp)	0.1567
$35t_2$ (sp,d)	->	$38t_2$ (H s)	0.1489
$33t_2$ (d)	->	$37t_2$ (sp)	0.1390
$16e$ (d)	->	$36t_2$ (sp)	0.0905
$18a_1$ (sp)	->	$38t_2$ (H s)	0.0586
$18t_1$ (d)	->	$37t_2$ (sp)	0.0400
$18e$ (sp,d)	->	$37t_2$ (sp)	0.0188
$34t_2$ (d)	->	$37t_2$ (sp)	0.0376
$3a_2$ (d)	->	$21t_1$ (sp)	0.0175
$33t_2$ (d)	->	$19a_1$ (sp)	0.0150
$17a_1$ (d)	->	$37t_2$ (sp)	0.0146
$34t_2$ (d)	->	$21t_1$ (sp)	0.0244
$17t_1$ (d)	->	$36t_2$ (sp)	0.0116

core orbitals changes the orbital energies. A number of the low energy unoccupied orbitals for the passivated $Au_{20}(PH_3)_8$ complex have significant PH_3 character, whereas the low energy orbitals for $Au_{20}(NH_3)_8$ do not have significant NH_3 character. Note that the present results show no connection with what would be expected from electromagnetic modeling, in which one would expect a simple red-shift in the spectral features due to the presence of a nonabsorbing dielectric layer of adsorbed molecules. This shows the complexity that can arise as a result of chemical interactions between the adsorbed molecules and the gold particle, and it points to the importance of electronic structure calculations in properly modeling adsorbate effects on nanoparticle spectra.

Acknowledgements

References

1. Brown, L. O.; Hutchison, J. E. *J. Am. Chem. Soc.* **1999**, *121*, 882.
2. Yang, Y.; Chen, S. *Nano Lett.* **2003**, *3*, 75.
3. Li, J.; Li, X.; Zhai, H.-J.; Wang, L.-S. *Science* **2003**, *299*, 864.
4. Aikens, C. M.; Schatz, G. C. *J. Phys. Chem. A* **2006**, *110*, 13317.
5. Zhang, H.-F.; Stender, M.; Zhang, R.; Wang, C.; Li, J.; Wang, L.-S. *J. Phys. Chem. B* **2004**, *108*, 12259.
6. te Velde, G.; Bickelhaupt, F. M.; Baerends, E. J.; Fonseca Guerra, C.; van Gisbergen, S. J. A.; Snijders, J. G.; Ziegler, T. *J. Comp. Chem.* **2001**, *22*, 931.
7. Becke, A. D. *Phys. Rev. A* **1988**, *38*, 3098.
8. Perdew, J. P. *Phys. Rev. B* **1986**, *33*, 8822.
9. van Lenthe, E.; Baerends, E. J.; Snijders, J. G. *J. Chem. Phys.* **1993**, *99*, 4597.
10. http://www.scm.com/Doc/Doc2006.01/Welcome.html
11. Lambropoulos, N. A.; Reimers, J. R.; Hush, N. S. *J. Chem. Phys.* **2002**, *116*, 10277.
12. Roden, J. M.; Aikens, C. M.; Schatz, G. C., to be published.
13. Fonseca Guerra, C.; Handgraaf, J.-W.; Baerends, E. J.; Bickelhaupt, F. M. *J. Comp. Chem.* **2004**, *25*, 189.
14. Dreuw, A.; Head-Gordon, M. *J. Am. Chem. Soc.* **2004**, *126*, 4007.

Chapter 10

Surfactant Effects on the Particle Size and Formation of Iron Oxides via a Sol–Gel Process

Erin Camponeschi[1], Jeremy Walker[1], Hamid Garmestani[1], and Rina Tannenbaum[1,2]

[1]School of Materials Science and Engineering, Georgia Institute of Technology, Atlanta, GA 30332
[2]Department of Chemical Engineering, Technion, Haifa 32000, Israel

This work illustrates the effects of adding a common surfactant, sodium dodecylbenzene sulfonate (NaDDBS), to the reaction mixture used in the formation of iron (III) oxide nanoparticles via a modified sol-gel process. In order to elucidate the role of the surfactant on the control of the resulting iron oxide particle size, experiments were conducted with two different metal salt precursors: $Fe(NO_3)_3 \cdot 9H_2O$ and $FeCl_3 \cdot 6H_2O$. The average particle size of the dried iron oxide gels, in the absence of the surfactant, was 4.5 nm and 3.6 nm for $Fe(NO_3)_3 \cdot 9H_2O$ and $FeCl_3 \cdot 6H_2O$ as precursors, respectively. The addition of a surfactant inhibited gel formation in the $Fe(NO_3)_3 \cdot 9H_2O$ system, while in the $FeCl_3 \cdot 6H_2O$ system the gelation process was delayed. The resultant particle sizes were 3.2 nm and 4.9 nm, respectively. It appears that even though the $Fe(NO_3)_3 \cdot 9H_2O$ system was unable to gel the surfactant was able to stabilize the nanoparticles to form even smaller particles than the gel counterpart.

Introduction

The study of nanomaterials is a very active research area that is constantly being fuelled by new ideas, new strategies, new insight and new methods for their design and applications (*1-17*). Nanomaterials represent a novel class of materials that possess distinctive physical and chemical properties that are very different than their bulk counterparts (*2,4-8,10-17*). For example, nanometer sized iron oxide exhibits exceptionally strong magnetic properties and as such, may have a wide number of applications in pigments, magnetic materials, catalysts, sensors, data storage, and medical devices. This is one of many systems that have recently become highly attractive and extensively explored (*2, 5-8,10-13,15-17*).

The facile and reproducible creation of nanoparticles is the ultimate goal for their incorporation and utilization in specific devices, thus promoting the development of new technologies (*15,17-19*). There are several avenues for the formation metal oxide nanoparticles, including iron oxide nanoparticles, which, as stated before, present a particular interest: sol gel processing, synthesis in microemulsions, hydrothermal synthesis, and high temperature solution processing (*2,5,8,10–13,15,17*). All these methods generate iron oxide nanoparticles, but require well-controlled environments that may prohibit the scale-up efforts of these processes from the lab bench to bulk production (*2,17,20,21*), with the exception of the sol gel processing method. Sol-gel synthesis provides an extremely easy method of creating a large variety of metal oxides from their metal salts at ambient conditions and at low temperatures. However, the drawback of the method is that it generates 3D oxide networks , and hence, it is limited in its efficiency regarding the formation of independent, disconnected nanosized particles. Therefore, the advantages of a relatively simple synthesis method for the creation of nanosized particles, in which the probability for the formation of a 3D network would be diminished, might prove useful for the functionalization of iron oxide particles designated to be incorporated in magnetic nanostructures and in drug targeting and delivery nanoplatforms (*20–24*).

In this work we describe the development of a modified sol gel processing method that was used to create iron (III) oxide nanoparticles. We was found that with the addition of a common surfactant, e.g. sodium dodecyl benzene sulfonate (NaDDBS), iron oxide nanoparticles can easily be synthesized at room temperature in just a few minutes without the formation of 3D iron oxide network. Moreover, in order to comply with aqueous compatibility requirements imposed by the potential use of these materials in conjunction with medical application, the sol gel method was also performed in a water-based environment.

Experimental Procedure

Ferric nitrate nonahydrate, $Fe(NO_3)_3 \cdot 9H_2O$, ferric chlorate hexahydrate, $FeCl_3 \cdot 6H_2O$, propylene oxide, C_3H_6O, and stock absolute ethanol, were purchased from Fisher Scientific and used as received. Sodium dodecyl benzene sulfonate (NaDDBS, molecular weight of 348.48 g/mol, purchased from TCI) was used in the same concentrations and methods as described in Matarredona et al. (19). The syntheses were performed at room temperature in glass scintillation vials. Six separate solutions were made in order to test the effects of the surfactant on the final iron oxide particle size.

Solution 6 was formed by completely dissolving 0.65 g $Fe(NO_3)_3 \cdot 9H_2O$ in 3.5 mL of ethanol. Then, 1.2 mL of propylene oxide was added as the gelation agent. Solutions 2 and 4 followed the same procedures as solution 6, but 3.5 mL of a 1.2 mM solution of NaDDBS was added before the addition of the propylene oxide. Solution 5 was formed by completely dissolving 0.42 g $FeCl_3 \cdot 6H_2O$ in 3.5 mL of ethanol. Then, 1.2 mL of propylene oxide was added. Solutions 1 and 3 followed the same procedures as solution 5, but 3.5 mL of a 1.2 mM solution of NaDDBS was added before the addition of the propylene oxide. Upon gelation, an additional amount of 1.2 mM NaDDBS was added to solutions 1 and 2. All solutions were then placed in a Fisher Scientific isotemp oven to dry for several days at 100°C. After this time, water was added to solutions 3, 4, 5, and 6 (see Table 1).

All the solutions were placed in a dismembrator (Fisher Scientific., 20 kHz) at 35 % amplification for 30 minutes, followed by the removal of small samples for transmission electron microscopy (TEM) imaging and analysis in order to determine particle size. A droplet from each solution was placed on a grid (Ted Pella, Inc. carbon coated copper, PELCO® Center-Marked Grids, 400 mesh, 3.0 mm O.D.) and dried in air. These samples were then analyzed using a Hitachi HF2000, 200kV transmission electron microscope.

X-ray diffraction (XRD) was performed on the samples in order to determine composition. The samples were prepared and tested in the same manner as previously reported (20). The dried samples were then placed on a zero background holder and analyzed using a Philips PW 1800 X-ray diffractometer. Patterns from 20° to 90° were examined with a step size of 0.02° using monochromatic Cu Kα X-rays with a wavelength of 1.54056 Å.

Results and Discussion

The main insight gained from this work showed that the surfactant used, NaDDBS, has the potential of altering the particle size of the resulting iron oxide nanoparticles formed via the modified sol gel processing method. Propylene oxide was used as a gelation agent because it is known to promote the formation

Table 1. Solution Parameters

Solution #	Metal Salt	Gelation Agent	NaDDBS Addition	Water Addition
1	$FeCl_3\ 6H_2O$	C_3H_6O	Before gelation & before drying	None
2	$Fe(NO_3)_3\ 9H_2O$	C_3H_6O	Before gelation & before drying	none
3	$FeCl_3\ 6H_2O$	C_3H_6O	Before gelation	After drying
4	$Fe(NO_3)_3\ 9H_2O$	C_3H_6O	Before gelation	After drying
5	$FeCl_3\ 6H_2O$	C_3H_6O	None	After drying
6	$Fe(NO_3)_3\ 9H_2O$	C_3H_6O	None	After drying

of a monolithic wet gel in a very short amount of time (a few minutes) (*5,17*). Moreover, the presence of water, which was also introduced in the modified sol-gel process, is known to change gelation time in some metal salt systems (*5*). The experiments conducted in this study involved two metal salts: Ferric nitrate nonahydrate, $Fe(NO_3)_3 \cdot 9H_2O$ and ferric chlorate hexahydrate, $FeCl_3 \cdot 6H_2O$. These were chosen based on their previous use as precursors in classical sol-gel processes (*2,5,17*).

The presence of NaDDBS increased the gel time for the $FeCl_3 \cdot 6H_2O$ system from minutes to hours, and prevented $Fe(NO_3)_3 \cdot 9H_2O$ from forming a gel altogether. There may be several reasons for this behavior: (a) The relative concentrations of the propylene oxide, iron salt and coordinated water may play a pivotal role in determining the gelation time. Gash et al. (*5*) showed that there was a 2 minute gelation time for the $FeCl_3 \cdot 6H_2O$ precursor in water, while the precursor with a higher water content required several hours to gel; (b) The presence of NaDDBS molecules in the solution has the additional effect of delaying the onset of gelation in the $FeCl_3 \cdot 6H_2O$ system, and preventing it altogether in the $Fe(NO_3)_3 \cdot 9H_2O$ system. These surfactant molecules tend to organize themselves in the vicinity of the water molecules, preferentially through their ionic groups, as shown in Figure 1, thus creating a stabilization layer that would either delay or completely inhibit the accessibility of the coordinated water molecules to the propylene oxide and hence, prevent the gelation process.

Solutions that gelled follow the same general procedure of hydrolysis, condensation, and heating. This process allows for the formation of iron (III) oxide particles through a series of reactions where *A* is an intermediate reaction
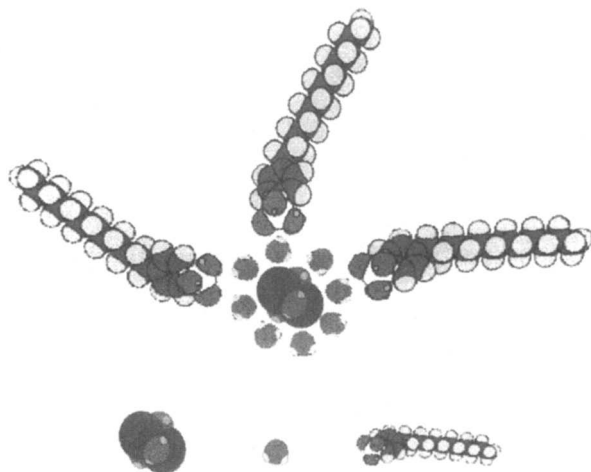
Figure 1. A schematic representation of the dipole-dipole attractions between the metal cations (Fe^{3+}) and the oxygen (O$^{\delta}$) in the surrounding water molecules, and the subsequent attraction with the hydrophilic group in the surfactant NaDDBS.

Table 2. Particle Size Results

Solution #	Metal Salt	Gel Formation	Average Particle Size (nm)	Sample Color
1	FeCl$_3$ · 6H$_2$O	Yes	4.9	Brown
2	Fe(NO$_3$)$_3$ · 9H$_2$O	No	3.2	Light brown
3	FeCl$_3$ · 6H$_2$O	Yes	84.6	Orange
4	Fe(NO$_3$)$_3$ · 9H$_2$O	No	5.1	Light brown
5	FeCl$_3$ · 6H$_2$O	Yes	3.6	Brown
6	Fe(NO$_3$)$_3$ · 9H$_2$O	Yes	4.5	Light Brown

product with a metal hydroxide reactive group. In the presence of polypropylene oxide the reaction is as follows:

$$C_3H_6O + Fe(H_2O)_6^{3+} \rightarrow C_3H_7O^+ + Fe(OH)(H_2O)_5^{2+} \xrightarrow{\Delta} Fe_2O_3$$
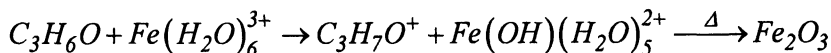
In the presence of water the reaction is as follows:

$$Fe(H_2O)_6^{3+} + H_2O \rightleftharpoons Fe(OH)(H_2O)_5^{2+} + H_3O^+$$

$$Fe(OH)(H_2O)_5^{2+} + H_2O \rightarrow \cdots \rightarrow A \rightarrow \cdots \xrightarrow{\Delta} Fe_2O_3$$
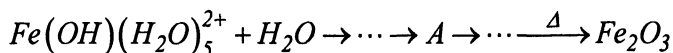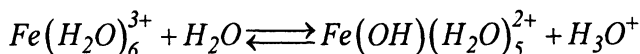
It is expected that the presence of NaDDBS was essential in the early stages of the process, impeding the reaction with the epoxide and hydroxo ligand, thus preventing the gelation process. In the last step of this process, the material is heated to 100°C in order to remove all excess water and drive the formation of the iron (III) oxide.

The change in particle size and color of the solutions is illustrated in Table 2 and Figure 2. It appears that the color of the solution is directly related to the size of the particles formed in solution. To determine the average particle size, high-resolution TEM imaging was used. The TEM images and histograms are shown in Figures 3 – 8. Due to the low molecular weight of the iron oxide particles, the surfactant and the epoxide molecules, which can cloud transmission electron images, obtaining clear TEM images was difficult.

The NaDDBS addition prior to gelation to the $FeCl_3 \cdot 6H_2O$ system did not appear to have a large effect on the particle sizes compared to the same system in the absence of NaDDBS. However, upon drying, the system having NaDDBS that was added in the final stages of the synthesis (solution 1) appears to generate significantly smaller particle size than that of the system without NaDDBS added at this stage (solution 3). This leads to the conclusion that the NaDDBS molecules inhibit the growth of the particle by replacing water molecules in the coordination sphere of the growing oxide particles, thus preventing their aggregation.

As for the $Fe(NO_3)_3 \cdot 9H_2O$ systems, the changes in particle size is negligible in most samples, however, the smallest particle sizes were obtained in the solutions containing NaDDBS. This supports the realization that the addition of NaDDBS inhibits the growth of the iron oxide nanoparticles, even though these system do not form gels. The coupling of a high number of coordinated water molecules with the presence of a surfactant, inhibits gel formation on one hand, and stabilizes small nanoparticles on the other hand. Hence, a distribution of particle sizes in the 3-5 nm range that is characteristic to the primary particles
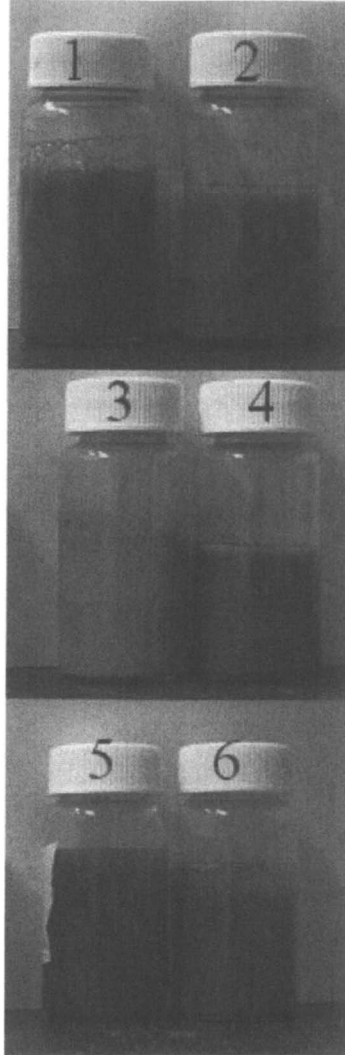
Figure 2. Color variations in solutions
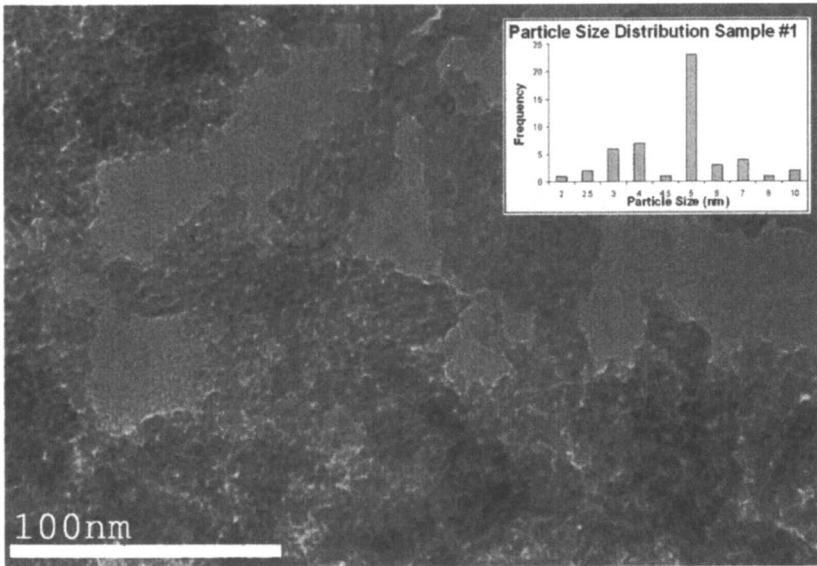
Figure 3. (a) High resolution TEM image of solution 1 (b) Particle size distribution for solution 1
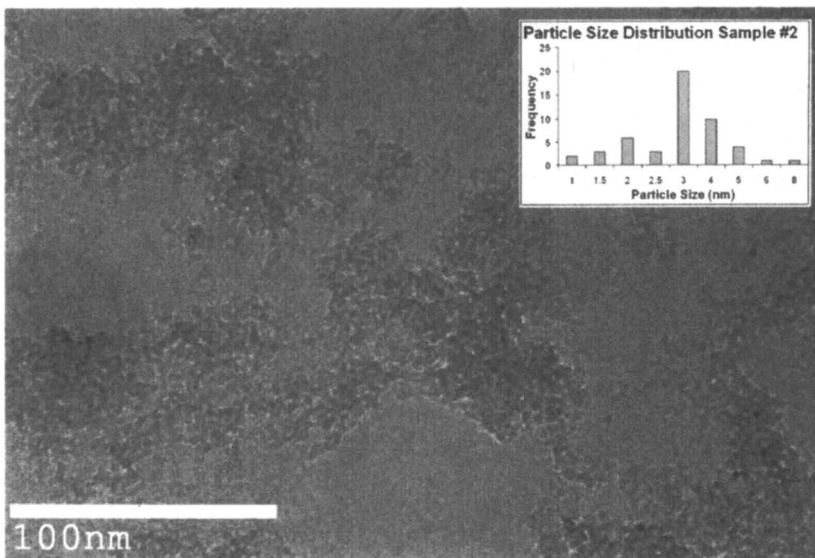
Figure 4. (a) High resolution TEM image of solution 2 (b) Particle size distribution for solution 2
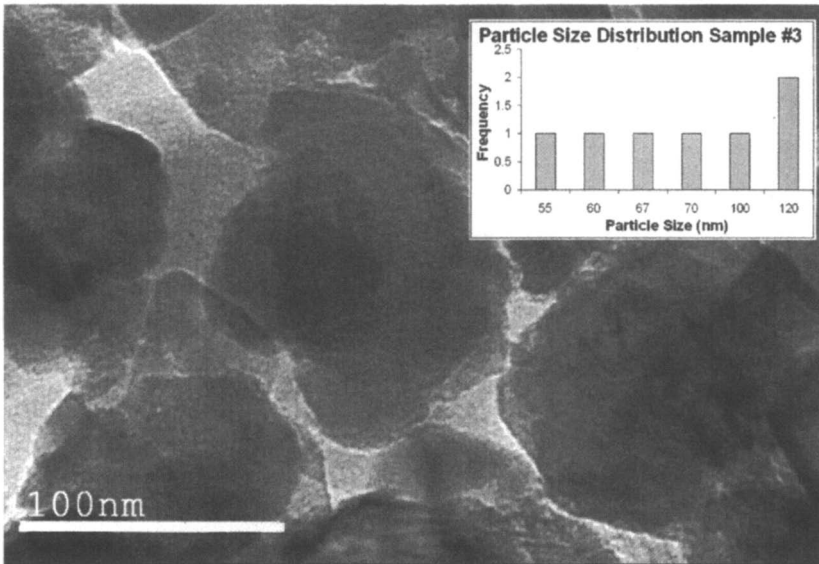
Figure 5. (a) High resolution TEM image of solution 3 (b) Particle size distribution for solution 3
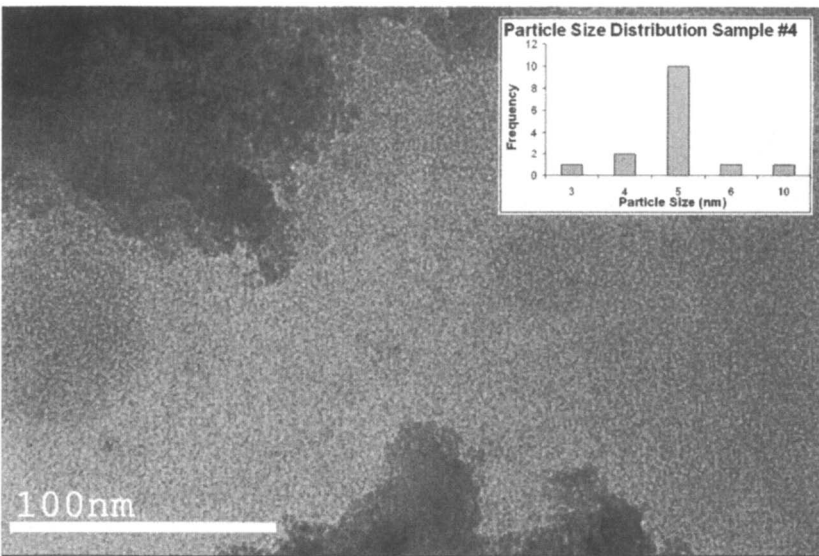
Figure 6. (a) High resolution TEM image of solution 4 (b) Particle size distribution for solution 4
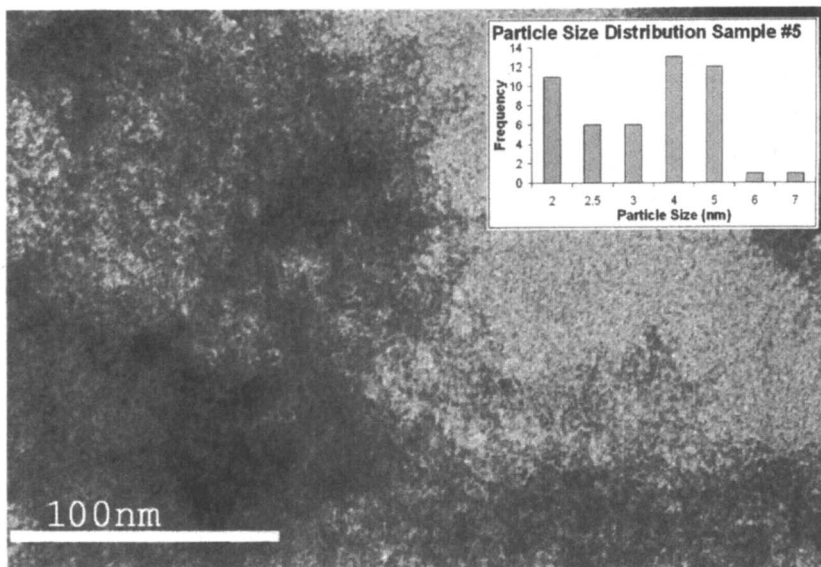
Figure 7. (a) High resolution TEM image of solution 5 (b) Particle size distribution for solution 5
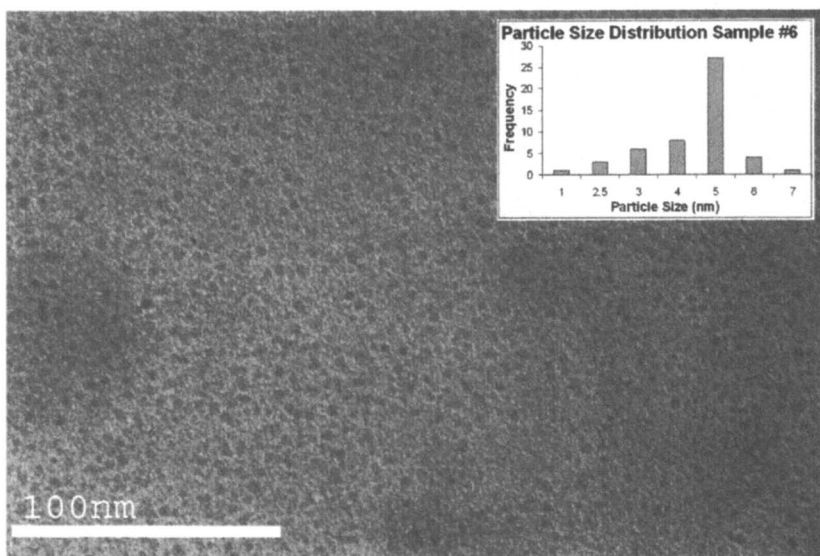
Figure 8. (a) High resolution TEM image of solution 6 (b) Particle size distribution for solution 6
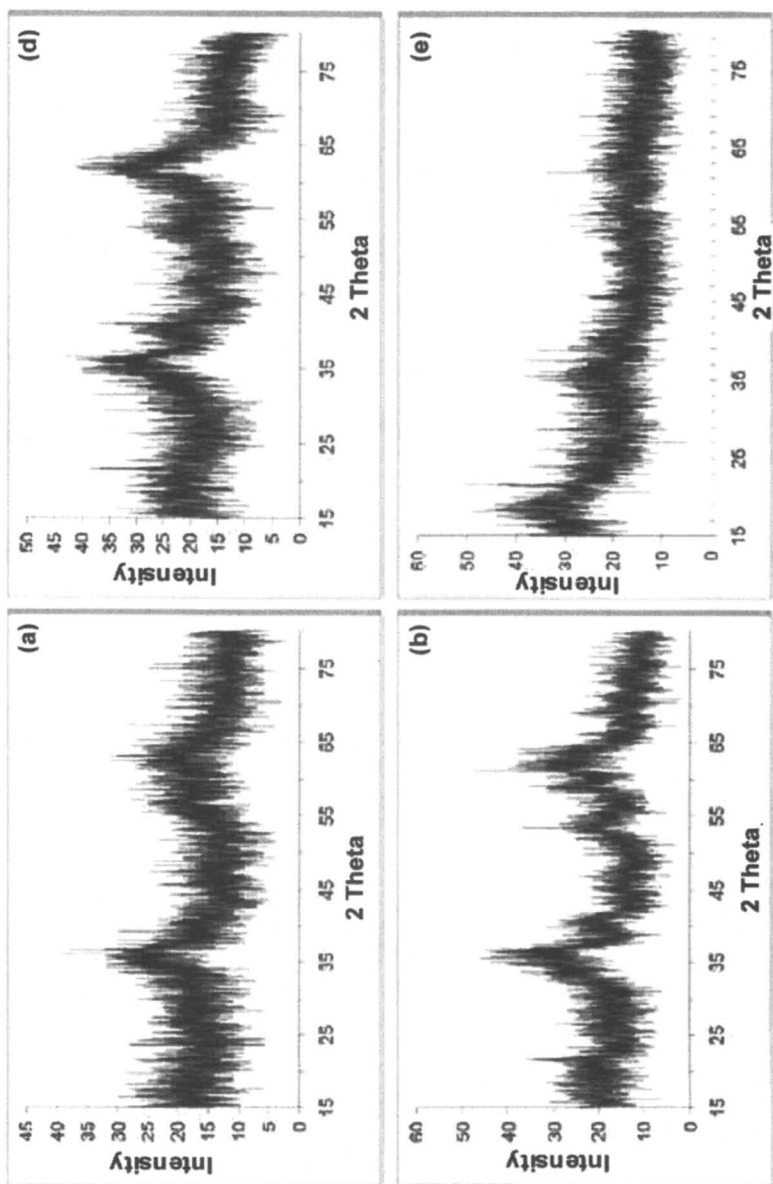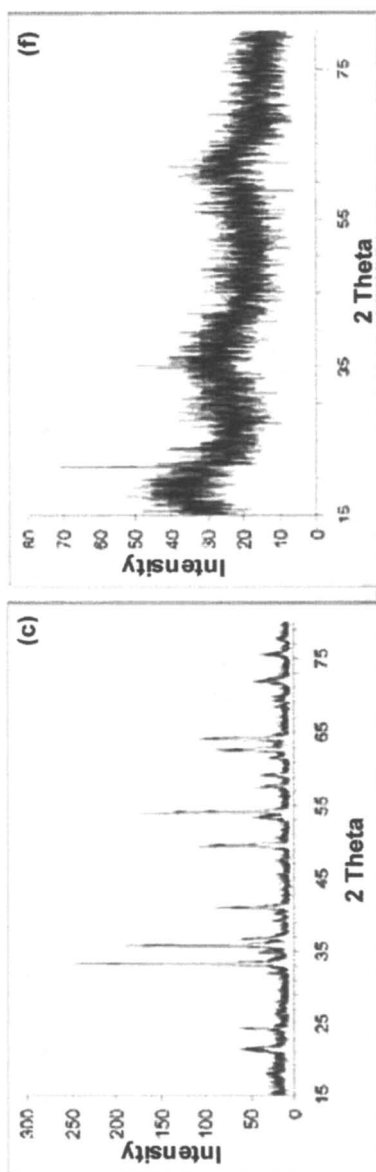
Figure 9(i). X-ray diffraction patterns for (a) Sample 1, (b) Sample 2, (c) Sample 3, (d) Sample 4, (e) Sample 5, (f) Sample 6

formed by the sol-gel process, may be achieved also in a system in which surfactants are present but the gelation is inhibited.

X-ray diffractions of the iron oxide nanoparticles are shown in Figure 9 a-f for the as-synthesized samples. The diffraction patterns for samples 1, 2, 4, 5 and 6 are largely amorphous in character, having large diffraction peaks resulting from the nanoscale features of the material. Figure 9 g-l illustrates possible alternative phases that may have formed; iron (III) oxide, hydroxide and oxyhydroxide phases: α-Fe_2O_3 (hematite), $Fe(OH)_3$, α-FeO(OH) (ferrihydrite), γ-Fe_2O_3, γ-FeO(OH); and δ-FeO(OH). Since the samples are largely amorphous, the analysis is mainly qualitative. The broad peaks that can be seen in the diffraction patterns largely overlap with all of the main peaks in most of the spectra shown in Figure 9 g-l. In samples 5 and 6 it appears that there is an additional peak at low angles, but this could be due to beam noise while the samples were analyzed. In contrast, the XRD analysis of sample 3, shown in Figure 9c, exhibited a diffraction pattern that is characteristic of a crystalline material. The crystalline character of this spectrum is commensurate with the average particles size of 80 nm calculated from TEM images. This sample, like the others tested, exhibits peaks that correspond to a variety of iron oxide compounds, as mentioned above. Based on this analysis, we cannot ascertain that the particles formed consist of Fe_2O_3 exclusively. The XRD data confirms that the particles are mostly nanocrystalline (except sample 3) iron oxide particles, similar to the results obtained from TEM imaging. In related previous studies, it was determined that the material could be assigned an empirical formula of $Fe^{(III)}_xO_yH_z$, but nevertheless, throughout this paper, it will be referred to as "iron oxide" (25). This leads to the conclusion that iron oxide particles may be present along with other oxyhyrdoxide phases.

Despite the fact that a mixture of iron oxide compounds is formed by this method, it still provides an easy and economical method for the formation of nanoscale iron (III) oxide particles with the addition of NaDDBS as a surfactant.

Conclusions

This work has illustrated that adding a common surfactant to the iron oxide sol gel processing method resulted in the decrease of the free energy of the system and allowed the creation of stable nanosized iron oxide particles without generating a 3D gel network. The $Fe(NO_3)_3 \cdot 9H_2O$ and $FeCl_3 \cdot 6H_2O$ precursors gave rise to a gel with nanosized primary particles, according to the classic sol-gel process. However, the addition of NaDDBS prior to gelation, affected the particle size of the resulting iron oxide particles. The $Fe(NO_3)_3 \cdot 9H_2O$ system did not form a gel in the presences of the NaDDBS, but was still able to support the formation of nanosized particles, similar to the nanoscale particles formed in the gel counterpart.
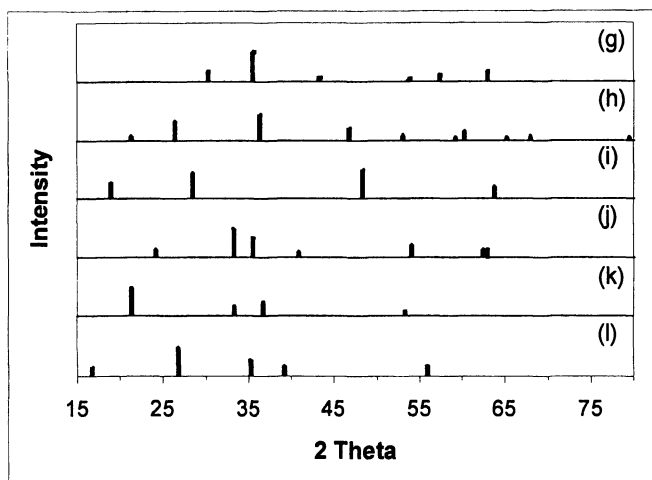
Figure 9(ii). X-ray diffraction patterns for various iron oxide/oxyhydroxide phases: (g) α-Fe2O3, (h) Fe(OH)₃, (i) α-FeO(OH) i.e. ferrihydrite, (j) γ-Fe₂O₃, (k) γ-FeO(OH), and (l) δ-FeO(OH).

Acknowledgements

References

1. Bacon, R. *Journal of Applied Physics* **1960**, *31*, 283-290.
2. Battisha, I. K.; Afify, H. H.; Hamada, I. M. *Journal of Magnetism and Magnetic Materials* **2005**, *292*, 440-446.
3. Colbert, D. T., Smalley, R. E. *Perspectives on Fullerene Nanotechnology* **2002**, 3-10.
4. Edelstein, A. S., *Nanomaterials : Synthesis, Properties, and Applications* ed.; Philadelphia Institute of Physics Publishing: Bristol, 1998; 'Vol.' p.
5. Gash, A. E.; Tillotson, T. M.; Satcher, J. H., Jr.; Poco, J. F.; Hrubesh, L. W.; Simpson, R. L. *Chemistry of Materials* **2001**, *13*, (3), 999-1007.

6. Iijima, S. *Nature (London, United Kingdom)* **1991**, *354*, (6348), 56-8.
7. Iijima, S.; Ichihashi, T. *Nature (London, United Kingdom)* **1993**, *363*, (6430), 603-5.
8. Koutzarova, T.; Kolev, S.; Ghelev, C.; Paneva, D.; Nedkov, I. *Physica Status Solidi C: Current Topics in Solid State Physics* **2006**, *3*, (5), 1302-1307.
9. Kroto, H. W.; Heath, J. R.; O'Brien, S. C.; Curl, R. F.; Smalley, R. E. *Nature (London, United Kingdom)* **1985**, *318*, (6042), 162-3.
10. Lai, J.-I.; Shafi, K. V. P. M.; Ulman, A.; Loos, K.; Lee, Y.; Vogt, T.; Lee, W.-L.; Ong, N. P. *Journal of Physical Chemistry B* **2005**, *109*, (1), 15-18.
11. Liu, S.; Wei, X.; Chu, M.; Peng, J.; Xu, Y. *Colloids and Surfaces, B: Biointerfaces* **2006**, *51*, (2), 101-106.
12. Lovely, G. R.; Brown, A. P.; Brydson, R.; Kirkland, A. I.; Meyer, R. R.; Chang, L. Y.; Jefferson, D. A.; Falke, M.; Bleloch, A. *Micron* **2006**, *37*, (5), 389-395.
13. Nassar, N.; Husein, M. *Physica Status Solidi A: Applications and Materials Science* **2006**, *203*, (6), 1324-1328.
14. Park, Y. K.; Tadd, E. H.; Zubris, M.; Tannenbaum, R. *Materials Research Bulletin* **2005**, *40*, (9), 1506-1512.
15. Vargas, J. M.; Zysler, R. D. *Nanotechnology* **2005**, *16*, (9), 1474-1476.
16. Park, Y. K.; TAdd, E. H.; Zubris, M.; Tannenbaum, R. *Materials Research Bulletin* **2005**, *40*, 1506-1512.
17. Walker, J. D.; Tannenbaum, R. *Chem. Mater.* **2006**.
18. Hilger, I.; Kiebling, A.; Romanus, E.; Hiergeist, R.; Hergt, R.; Andrea, W.; Roskos, M.; Linss, W.; Weber, P.; Weitschies, W.; Kaiser, W. A. *Nanotechnology* **2004**, *15*, (8), 1027.
19. Zhao, X.; Xiao, B.; Fletcher, A. J.; Thomas, K. M.; Bradshaw, D.; Rosseinsky, M. J. *Science* **2004**, *306*, (5698), 1012.
20. Salazar-Alvarez, G.; Muhammed, M.; Zagorodni, A. A. *Chemical Engineering Science* **2006**, *61*, (14), 4625-4633.
21. Cao, H.; Zhu, M.; Li, Y. *Journal of Solid State Chemistry* **2006**, *179*, (4), 1208-1213.
22. Du, G.; Liu, Z.; Xia, X.; Jia, L.; Chu, Q.; Zhang, S. *Nanoscience* **2006**, *11*, (1), 49-54.
23. Can, M. M.; Ozcan, S.; Firat, T. *Physica Status Solidi C: Current Topics in Solid State Physics* **2006**, *3*, (5), 1271-1278.
24. Correa-Duarte, M. A.; Grzelczak, M.; Salgueirino-Maceira, V.; Giersig, M.; Liz-Marzan, L. M.; Farle, M.; Sierazdki, K.; Diaz, R. *Journal of Physical Chemistry B* **2005**, *109*, (41), 19060-19063.
25. Walker, J. D.; Tannenbaum, R. *Chemistry of Materials* **2006**, *18*, (20), 4793-4801.

Chapter 11

Reactivity Screening of Anatase TiO_2 Nanotubes Array and Anatase Thin Films: A Surface Chemistry Point of View

S. Funk[1], B. Hokkanen[1], T. Nurkic[1], J. Goering[1], E. Kadossov[1], U. Burghaus[1,*], A. Ghicov[2], P. Schmuki[2], Z. Q. Yu[3,4], S. Thevuthasan[3], and L. V. Saraf[3]

[1]Department of Chemistry, North Dakota State University, Fargo, ND 58105
[2]Department of Materials Science, University of Erlangen-Nuremberg, Erlangen 91058, Germany
[3]Pacific Northwest National Laboratory, Richland, WA 99352
[4]Current address: Department of Chemistry, Nanjing Normal University, Nanjing, 210097 China

As a reactivity screening we collected thermal desorption spectroscopy (TDS) data of iso-butane, O_2, CO_2, and CO adsorbed on an ordered TiO_2 nanotubes (TiNTs) array. As a reference system iso-butane adsorption on an anatase TiO_2 thin film has been considered as well. The as-grown TiNTs are vertically aligned and amorphous. Polycrystalline (poly.) anatase or poly. anatase/rutile mixed nanotubes are formed by annealing confirmed by x-ray diffraction (XRD) and scanning electron microscopy (SEM). The anatase thin film was grown on $SrTiO_3(001)$ and characterized by XRD and atomic force microscopy (AFM). Surprisingly, oxygen distinctly interacts with the TiNTs whereas this process is not observed on fully oxidized single crystal rutile $TiO_2(110)$. Desorption temperatures of 110-150 K and 100-120 K were observed for CO_2 and CO, respectively, on the TiNTs. Variations in the binding energies of the alkanes on TiNTs and anatase thin films also were present, i.e., a kinetic structure-activity relationship (SAR) is evident.

139

Introduction

Motivation for this Study on Anatase TiO₂ Samples

Titanium dioxide has a wide range of applications that are as diverse as photo catalysis and cosmetics. TiO_2 is used for the design of gas sensors (*1*), for solar cells (*2*), batteries (*3*), water decomposition (*4*), as a pigment in paints and cosmetics, as a protective coating (*5*), and as a catalyst for a number of surface reactions including CO oxidation (*6*) and the selective catalytic reduction (*7*) of NO_x. TiO_2 exists in three different crystallographic phases. Due to technical difficulties to obtain anatase samples, most surface science studies have focused on rutile $TiO_2(110)$ although technical titania powder catalysts consist of rutile and anatase crystallites. Furthermore, it has been proposed that the catalytically more active component for a number of reactions in these powders is the anatase polymorph (*8*). In addition, the surface energy of anatase crystallites is smaller than for rutile (*9*) consistent with the fact that most TiO_2 nanostructures are of the anatase polymorph (*10-12*). Therefore, anatase thin films also can be considered as the planar counterpart of TiNTs and nanoparticles which has motivated our study to directly compare anatase thin films and TiNTs.

Information about what particular crystallographic orientation dominates industrial TiO_2 power catalysts is quite diverse. According to a transmission electron microscopy study (*13*), TiO_2 P25 and TiO_2 Merck powder catalysts are dominated by (001) and (010) anatase surface planes. Furthermore, it has been proposed that anatase (001) is the active phase for photocatalytic water decomposition (*14*). Thus, anatase thin films with a (001) surface orientation, as studied here, are relevant for technical applications.

TiO₂ Nanotubes for Catalysis Applications

Most projects on TiNTs focus on characterizing their morphology as well as materials science applications such as sensor design and photovoltaics (*11,15-18*). To the best of our knowledge no ultra-high vacuum (UHV) surface chemistry studies have been published. However, the great potential of planar TiO_2 for surface science and catalysis applications promises fascinating potential of TiNTs in heterogeneous catalysis. Depending on the preparation procedures, a large variety of TiNT morphologies can be obtained making them a perfect model system. Data have been collected for amorphous, poly. anatase, and poly. mixed 80%-anatase/20%-rutile TiNTs.

Nanotubes generally have the following advantages as compared with powder or planar model catalysts:

- Large surface-to-volume ratio.

- The micro-porous structure of powder catalysts can lead to transport limitations for surface reactions. Nanotubes minimize this limitation (*19*).

- Deactivation of catalysts is caused by sintering of the active metal nanoclusters. Trapping metal clusters on/inside the tubes can prevent sintering (*20-22*).

- Large diffusion coefficients for gas/liquid transport through nanotubes can prevent catalyst poisoning (*19*).

- High purity avoids self-poisoning and leads to consistent and easily reproducible properties.

- High mechanical and thermal stability.

- Functionalization allows for catalyst tailoring.

Importance of Oxygen Adsorption

The adsorption of oxygen is an important elementary reaction step for a large number of catalytic processes as well as for materials science applications.

- The gas-surface interaction of O_2 with nanotubes has been studied as a potential technique for O_2-doping of electronic devices (*23*).

- Improvements to catalytic processes for the decomposition of chemical warfare agents and pesticides are urgently needed (*24*). One promising strategy is catalytic oxidation. Efficient catalysts useful in remote locations would need to operate at ambient conditions, to require only oxygen (air), to be a non-toxic catalyst (TiO_2), and would eventually need a light source (sunlight). TiNTs are a promising candidate.

- One of the most prominent application for TiO_2 is the Au-TiO_2, low temperature CO oxidation catalyst that can be used, for example, for exhaust emission reduction (*6,25-27*). An important reaction step is the adsorption of oxygen.

- TiO_2 is important for PROX catalysts (preferential oxidation of CO in the presence of excess hydrogen) with the adsorption of oxygen as the primary reaction step (*28*). PROX is important for lean-burn gasoline engines (*29*).

- The removal of CO from syngas is required for fuel cell applications since trace amounts of CO can poison the surface of fuel cell electrodes (*30*). More efficient CO oxidation catalysts are required; for all of them, oxygen adsorption is one of the first reaction steps in the oxidation mechanism.

- A number of more exotic but important applications exist, such as closed-cycle CO_2 lasers (*31*).

Why Studying Alkane Adsorption?

The physicochemical properties of hydrocarbons have been studied extensively in surface science due to their importance for the petroleum industry as building blocks to convert raw materials into chemicals of greater value. Therefore, TDS studies characterizing the adsorption kinetics of alkanes have been conducted for a large variety of single crystal surfaces including graphite (*32*), sapphire (*33*), ZnO (*34*), Pt (*35*), Ru (*36*), Cu (*37,38*), and carbon nanotubes (12). Typically molecular and non-activated adsorption is obeyed. Analyzing TDS data reveals kinetics parameters such as coverage dependent binding energies and pre-exponential factors required for microkinetics modeling supporting catalyst development. At low adsorption temperatures, condensation in bi- and multilayers leads to additional TDS features following 0th order kinetics.

Experimental Procedures

Synthesis of the TiO$_2$ Nanotubes Array (TiNTs)

At the laboratory at Erlangen-Nuernberg University TiNT layers were produced by anodization of titanium foils. The foils were sonicated in acetone, isopropanol, and methanol, followed by rinsing with deionized water (DI) and drying in a N$_2$ stream. A three-electrode cell with a Haber-Luggin capillary, an Ag/AgCl (1M KCl) reference electrode, and platinum gauze as a counter electrode was used for the anodization. The electrolyte was 1M (NaH$_2$PO$_4$) + 0.5%w.t. HF (pH 4.5) and anodization was carried out at 300 K by ramping the potential from open circuit potential to 20 V (500 mV/s) and holding the potential at 20 V for 2 h. Afterwards, the samples were rinsed with DI and dried in a N$_2$ stream. Thermal treatments (temperature ramping from RT to 750 K at a heating/cooling rate of 30 K/min) of the initially amorphous TiNTs layers were carried out. After the ramp-up, the temperature of 750 K was held for 1 h. This procedure converts the initially amorphous nanotubes into polycrystalline anatase TiNTs on an oxidized Ti foil. Further annealing treatments result in mixed anatase/rutile TiNTs. XRD, SEM, and x-ray photoelectron spectroscopy (XPS) have been used to characterize the sample morphology and chemical cleanliness.

Growth of Anatase Thin Films

The film was grown in a custom-designed ultrahigh vacuum (UHV) chamber at PNNL as described in detail in ref.(*39*). Reflection high energy electron

diffraction (RHEED) was used to monitor the growth process. Single-crystal STO(001) substrates were ultrasonically cleaned in acetone and methanol prior to insertion into the UHV system through a load lock. In the UHV chamber, the substrates were cleaned using oxygen plasma (1.0×10^{-5} torr oxygen partial pressure, 200 W power) with a sample temperature of 900 K. During the growth, Ti was evaporated from an effusion cell in the presence of the oxygen plasma, with the substrate kept at a temperature at 900 K. The growth rate of the film was 0.01 nm/min and it was monitored by a quartz-crystal oscillator (Inficon). X-ray diffraction (XRD) and x-ray reflectivity (XRR) measurements were carried out using Philips X'pert θ-2θ diffractometer at 40 kV and 50 mA followed by data analysis using JADE 6.0 program.

Kinetics Experiments

The kinetics experiments have been conducted at North Dakota State University (NDSU) in two different UHV systems; in a TDS chamber (34) (for the TiNTs project) and in a molecular beam scattering system (for the thin film project) (40).

For TDS a number of precautions have been taken to assure that the results are not obscured by artifacts. (1) The mass spectrometer is equipped with an aperture and the sample to detector distance amounts to one mm. (2) The TiNTs samples were either mounted on a tantalum plate or directly spot welded on Ta wires. No significant differences in TDS curves have been observed for the two different setups. (3) No bulky parts have been used in designing the sample holder resulting in good cooling performance and negligible background contributions.

The reading of the thermocouple has been calibrated *in situ* by TDS using the known heat of condensation of the alkanes. The uncertainty in the temperature reading amounts to ± 5 K. The TiNTs have been cleaned by outgassing in UHV; the anatase thin films by mild sputter-anneal cycles.

The anatase thin film sample has been further characterized by Auger electron spectroscopy (AES) and low energy electron diffraction (LEED). Molecular beam scattering data have also been collected for the anatase film but will be presented elsewhere (12,41).

Sample Characterization

XRD. All samples have been characterized by XRD as summarized in Figure 1. For the amorphous TiNTs only the Ti substrate peaks are present whereas the polycrystalline TiNTs show the characteristic anatase XRD lines. Similarly, XRD of the anatase thin film sample consists of a superposition of

TiSrO$_3$(001) subtrate and anatase(001) structures. The XRD results clearly demonstrate that a high quality well oriented anatase TiO$_2$ film has been grown. The thickness of the film was determined to be 123 nm using XRR.

TiNTs. Additionally, the TiNT samples have been characterized by SEM and XPS. Figure 2 shows a SEM top view of a typical TiNT sample. Studied here have been TiNTs with a diameter of 0.1 μm and a length of 1 μm. The as-grown TiNTs show fluorine impurities (Figure 3) in XPS which can, however, be removed by annealing the samples. No desorption of fluorine has been detected in TDS after degassing the samples in UHV.

Thin film. AFM results for the anatase thin film are shown in Figure 4. On a lateral resolution scale of 200 nm, the films appear rather defect free. However, AES data indicate a nonstoichiometic sample (Ti-to-O-AES ratio of one); no LEED pattern could be observed. Some anatase particles were observed with AFM on the surface. Since the RHEED results during growth clearly showed streaks throughout the film growth, we believe the particles are well isolated. In addition, since we did not observe any other peaks except the TiO$_2$(001) peak in the XRD spectrum from the film, the particles appear to be oriented along the same direction as the film.

Kinetics of Oxygen Adsorption on TiO$_2$ Nanotubes

A detailed outline of oxygen adsorption experiments on TiNTs will be presented elsewhere (*12*). Briefly, the following data have been gathered. Oxygen distinctly interacts with the TiNTs whereas this process is not observed on fully oxidized rutile TiO$_2$ single crystals (*42*). Thus, TiNTs show intrinsically a fundamentally different catalytic behavior than TiO$_2$ single crystal model systems. Both molecularly and atomically bonded oxygen have been observed.

In the case of the mixed polycrystalline anatase/rutile TiNTs, TDS peak shifts to lower temperatures with increasing exposure (at 90 K) indicate a deviation from 1st-order kinetics. Additionally, a competing dissociative adsorption pathway for oxygen was evident at low adsorption temperatures.

For the amorphous TiNTs at low adsorption temperatures, molecular adsorption/desorption kinetics was present with a binding energy of 30.5 kJ/mol (pre-exponential 1x10^{13}/sec). Dissociative adsorption was observed above adsorption temperatures of ~150 K with a TDS peak just below 300 K.

For applications in heterogeneous catalysis the amorphous system may be better suited since oxygen adsorbs close to room temperature which will be important for oxidations of toxic compounds. For low-temperature reactions, the larger adsorption probability of O$_2$ observed on the polycrystalline TiNTs will be advantageous.
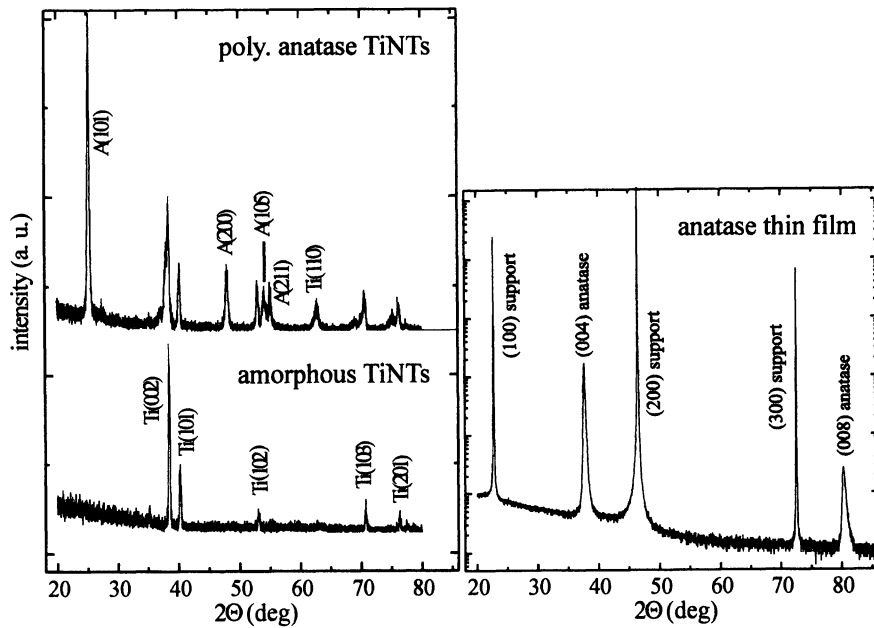
Figure 1. XRD scans of the samples studied.
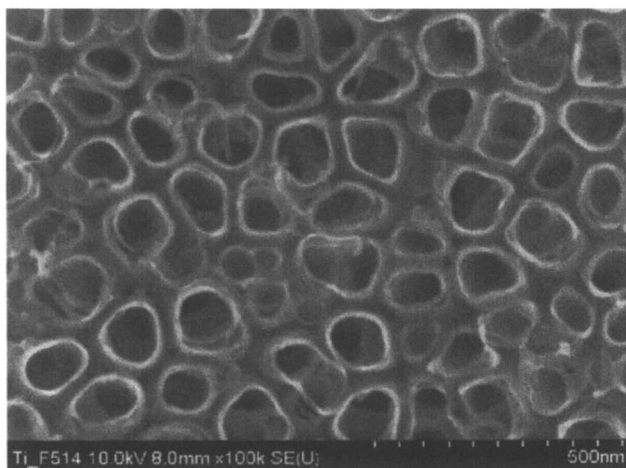
Figure 2. SEM of TiNTs.
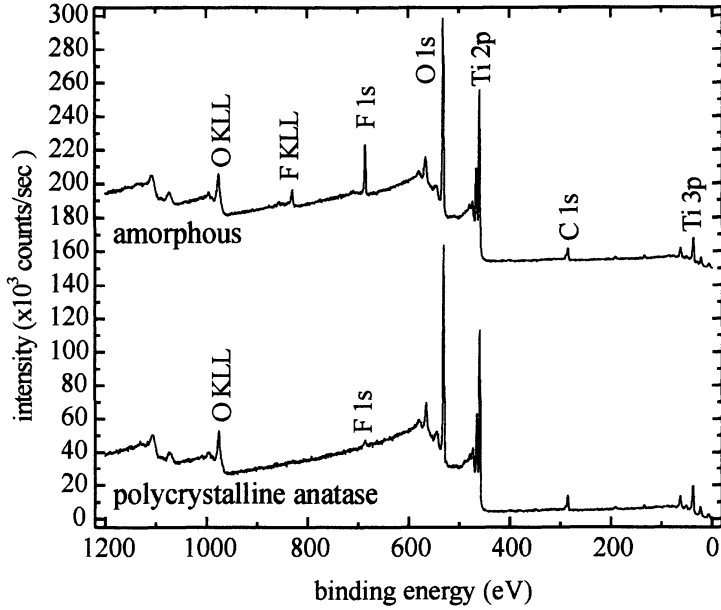
Figure 3. XPS of TiNTs (as prepared).
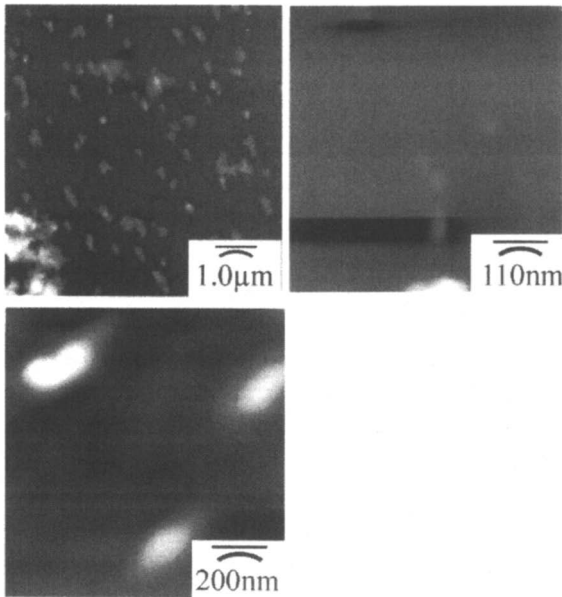
Figure 4. AFM of an anatase thin film grown on SrTiO₂(001).

Adsorption of Iso-butane on TiNTs and Anatase Thin Films

The adsorption of alkanes has been studied on amorphous, poly. anatase, and poly. mixed anatase/rutile TiNTs as well as on an anatase(001) thin film sample. Comprehensive data sets and a more detailed modeling will be presented elsewhere (10, 41). The most interesting result obtained is a clear kinetic structure activity relationship (SAR), i.e., the binding energy of iso-butane depends on the polymorph of TiO_2. Typical examples of TDS curves are shown in Figure 5. Data for small (0.1 L) and large (1 L) exposures of iso-butane are depicted. (1 L = 1 sec gas exposure at 1×10^{-6} torr.) The arrows in Figure 5 highlight the TDS peak position for small exposures which clearly depends on the particular sample studied. The reactivity decreases as anatase thin film > amorphous TiNTs > poly. anatase TiNTs > poly. mixed anatase/rutile TiNTs with zero coverage binding energies of E_d = 52, 40, 39, and 34 kJ/mol (v = 1×10^{13}/s), respectively.

Fitting (43, 44) the TDS data (10, 41) revealed the coverage dependence of the binding energy which follows the same trend. It appears that the anatase system is indeed the most reactive towards adsorption of iso-butane since in this case the largest binding energies are obtained. Although, we cannot provide an atomistic explanation, this result is intriguing concerning technical applications. The differences in the thin film data and the TiNTs may be strongly related with the density of surface defects which appears to be largest for the anatase thin film sample studied here.

The TDS peaks shift to lower desorption temperatures with increasing coverage (consistent with repulsive lateral interactions and molecular adsorption kinetics) for all samples studied. Interestingly, also for the mixed TiNTs only one TDS feature is present in the monolayer coverage range suggesting a random mixture of anatase and rutile crystallites. At large exposures (not shown), common condensation peaks have been observed allowing for a precise calibration of the temperature reading.

CO and CO_2 Adsorption on TiNTs

TDS data of CO_2 have been collected for the amorphous and poly. mixed TiNTs (Figure 6). The binding energies are systematically larger for the mixed TiNTs with E_d =35 kJ/mol. However, the deviations are smaller than 3 kJ/mol. The width of the TDS peaks is large indicating a number of kinetically distinct adsorption sites, for example, along the grain boundaries of the crystallites. Therefore it appears plausible that no pronounced defect TDS features are present as observed for rutile single crystals (45-47). CO binding energies of E_d = 30 and 38 kJ/mol were measured for amorphous and poly. anatase TiNTs, respectively.

amorphous
TiO$_2$ nanotubes

158 K

polycrystalline
rutile / anatase
TiO$_2$ nanotubes

133 K

temperature (K)

anatase thin
film

195 K

polycrystalline anatase
TiO$_2$ nanotubes

155 K

temperature (K)

Iso-butane thermal desorption spectroscopy yield (arbitray units)
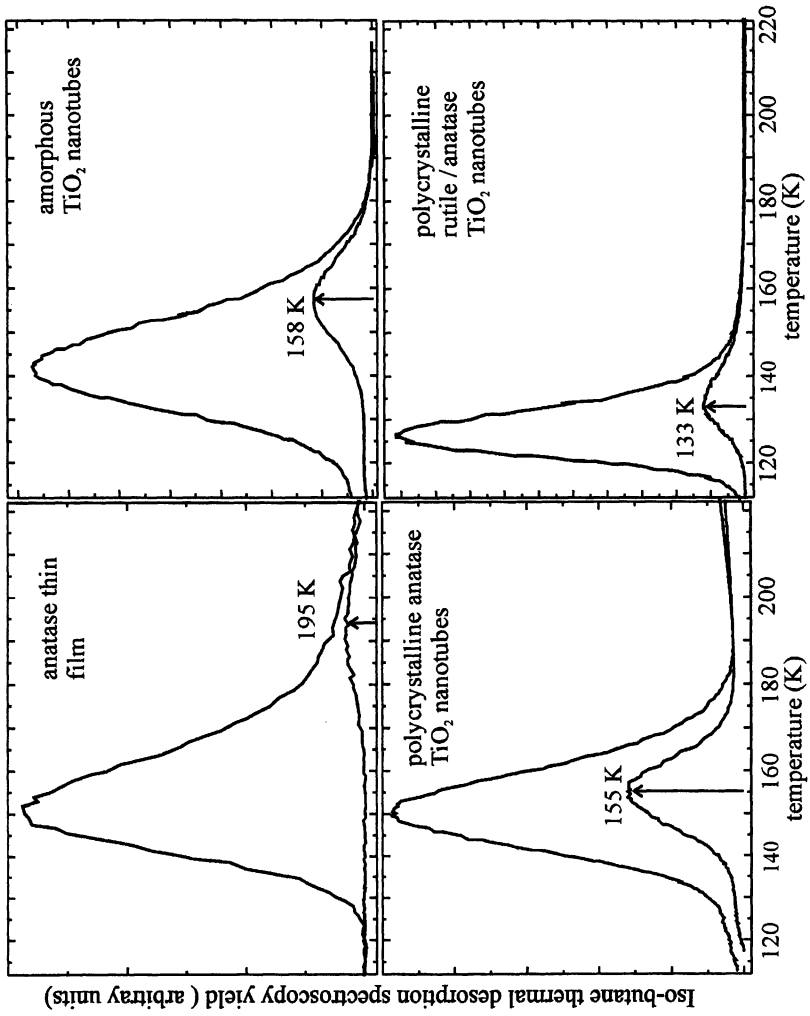
Figure 5. TDS of iso-butane for all samples studied.
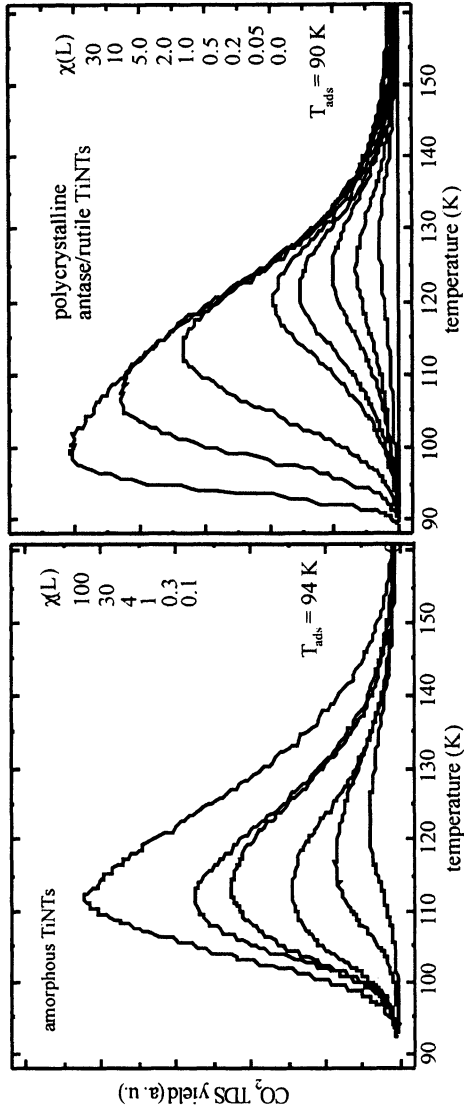
Figure 6. CO_2 TDS as a function of exposure, as indicated.

Acknowledgements

References

1. W. Goepel, J. Hesse, and J.N. Zeinel, Sensors a comprehensive survey, (Weiheim, VCH 1991).
2. B.O. Regan and M. Graetzel, *Nature* **1991**, *353*, 737.
3. S.Y. Huang, L. Kavan, I. Exnar, and M. Graetzel, *J. Electrochem.Soc.* **1995**, *142*, L142.
4. L. Kavan, M. Gratzel, S.E. Gilbert, C. Klemenz, and H.J. Scheel, *J. Am. Chem.Soc.* **1996**, *118*, 6716-6723.
5. A. Alvarez, A.J. Fort, and E. Bernabeu, *Thin Solid Films* **1999**, *349*, 212.
6. M. Haruta, *Catal. Today* **1997**, *36*, 153.
7. V.I. Parvulescu, P. Grange, and B. Delmon, *Catal. Today* **1998**, *46*, 233.
8. C.N. Satterfiled, Heterogeneous Catalysis in Industrial Practice, McGraw-Hill, Inc., New York, 1991.
9. M. Lazzeri, A. Vittadini, and A. Selloni, *Phys. Rev.B* **2001**, *63*, 155409.
10. B. Hokkanen, S. Funk, T. Nurkig, U. Burghaus, A. Ghicov, and P. Schmuki, submitted to *Surface Science*.
11. A. Ghicov, J.M. Macak, H. Tsuchiya, J. Kunze, V. Haeublein, L. Frey, and Op. Schmuki, *Nano Lett.* **2006**, *6*, 1080-1082.
12. S. Funk, B. Hokkanen, U. Burghaus, A. Ghicov, and P. Schmuki, *Nano Lett.* **2007**, *7*, 1091.
13. G. Martra, *Applied Catalysis A: General* **2000**, *200*, 275.
14. A. Fujishima and K. Honda, *Nature* **1972**, *238*, 37.
15. G.K. Mor, O.K. Varghese, M. Paulose, K. Shankar, and C.A. Grimes, *Solar Energy Materials & Solar Cells* **2006**, *90*, 2011-2075.
16. J.M. Macak, H. Tsuchiya, L. Taveira, S. Aldabergerova, and P. Schmuki, *Angew. Chem. Int. Ed.* **2005**, *44*, 7463-7465.
17. J.M. Macak, H. Tsuchiya, and P. Schmuki, *Angew. Chem. Int. Ed.* **2005**, *44*, 2100-2102.
18. D.S. Seo, J.K. Lee, and H. Kim, *J. Crystal Growth* **2001**, *229*, 428.
19. J.M. Nhut, L. Pesant, J.P. Tessonnier, G. Wine, J. Guille, C.P. Huu, and M.C. Ledoux, *Applied Catal. A: General* **2003**, *254*, 345.
20. F. Ding, A. Rosen, E. Campbell, L. Falk, and K. Bolton, *J. Phys. Chem. B* **2006**, *110*, 7666-7670.

21. J.M. Skowrosnki, P. Scharff, N. Pfaender, and S. Cui, *Adv.Mater.* **2003**, 15, 55.
22. P.M. Ajayan, T.W. Ebbesen, T. Ichihashi, S. Iljima, K. Tanigaki, and H. Hiura, *Nature* **1993**, *362*, 522.
23. H. Ulbricht, G. Moos, and T. Hertel, *Surface Science* **2003**, 532-535, 852-856.
24. L. Ember, *Chemical and Engineering News* **2006**, *24*, 9.
25. K.C. Taylor, *Catal. Rev. Sci. Eng.* **1993**, *35*, 457.
26. U. Burghaus and H. Conrad, *Surface Science* **1997**, *370*, 17.
27. T. Engel and G. Ertl, *Adv. Catal.* **1979**, *28*, 1.
28. T.V. Choudhary and D.W. Goodmann, *Topics in Catal.* **2002**, *21*, 25.
29. Y.W. Lee and E. Gulari, *Catal. Commun.* **2004**, *5*, 499.
30. J. Larminie and A. Dicks, **2003**, Wiley, ISBN 0-470-84857-X.
31. S.D. Gardner, G.B. Hoflund, D.R. Schryer, J. Schryer, U.T. Upchurch, and E.J. Kielin, *Langmuir* **1991**, *7*, 2135.
32. K.R. Paserba and A.J. Gellman, *Phys. Rev. Lett.* **2001**, *86*, 4338.
33. R.M. Slayton, C.M. Aubuchon, T.L. Camis, A.R. Noble, and N.J. Tro, *J. Phys. Chem.* **1995**, *99*, 2151.
34. J. Wang, B. Hokkanen, and U. Burghaus, *Surface Science* **2005**, *577*, 158-166.
35. M. Salmeron and G.A. Somorjai, *J. Phys. Chem.* **1981**, *85*, 3835.
36. J.L. Brand, M.V. Arena, A.A. Deckert, and S.M. George, *J. Chem. Phys.* **1990**, *92*, 5136.
37. R.Z. Lei, A.J. Gellman, and B.E. Koel, *Surface Science* **2004**, *554*, 125.
38. S. Funk, B. Hokkanen, J. Wang, U. Burghaus, G.H. Bozzolo, and J.E. Garces, *Surface Science* **2006**, *600*, 583-590.
39. S. A. Chambers, T. T. Tran, and T. A. Hileman, *J. Mat. Res.* **1994**, *9*, 2944.
40. J. Wang and U. Burghaus, *J. Chem. Phys.* **2005**, *122*, 044705-11.
41. J. Goering, E. Kadossov, U. Burghaus, Z.Q. Yu, S. Thevuthasan, and L.V. Saraf, in preparation.
42. M.A. Henderson, *Surface Science* **1995**, *343*, L1156-L1160.
43. J. Wang, B. Hokkanen, and U. Burghaus., *Surface Science* **2006**, *600*, 4855-4859.
44. U. Burghaus, J. Stephan, J.M. Rogowska, and L. Vattuone, NOVA science (New York, US), (2006), ISBN 1-59454-531-6.
45. T.L. Thompson, O. Diwald, and J.T. Yates, *J. Phys. Chem.* **2003**, *107*, 11700.
46. S. Funk and U. Burghaus, *Phys. Chem. Chem. Phys.* **2006**, *8*, 4805-4813.
47. M.A. Henderson, *Surface Science* **1998**, *400*, 203.

Chapter 12

The Facile Preparation of Partially Reduced V$_2$O$_5$ Nanowire Sheets

Chunrong Xiong[1,2], Ali E. Aliev[2], Gaurang Pant[3],
Bruce Gnade[1–3], and Kenneth J. Balkus, Jr.[1,2,*]

[1]Department of Chemistry, [2]UTD Nanotech Institute,
and [3]Department of Electrical Engineering, The University of Texas
at Dallas, Richardson, TX 75083

Hydrated and partially reduced V$_2$O$_5$ nanowires with high aspect ratios have been synthesized by the hydrothermal condensation of ammonium metavanadate. The V$_2$O$_5$ nanowires can be fabricated into free standing and flexible sheets. The V^{4+}/V^{5+} ratio in the nanowires can be increased with the hydrothermal synthesis temperature. The extremely low heat capacitance of thin V$_2$O$_{5-x}$ sheets and the high temperature gradient of resistance make them attractive materials for bolometric (IR) sensing. The current responsivity of a 30μm sheet is S = d V / d Q =178 V/W.

Introduction

V$_2$O$_5$ exhibits a layered structure, which allows the intercalation of a variety of ions (*1-8*), organic compounds (*9*), and polymeric species (*10-11*) to form functional materials that are promising for lithium batteries (*3-8*), catalysis (*12-19*), electrochromic devices (*20-24*), and supercapacitors (*25-27*). Additionally, fibrous V$_2$O$_5$ has shown some electrical properties as nanolithography templates (*28-29*), sensors for ethanol and amine (*30-33*), electric field-effect transistors (*34-36*), crossed junctions and rotational actuators (*37*). Several methods have been developed to prepare vanadium oxide 1-D nanostructures. Nesper and co-workers (*38-40*) synthesized vanadium oxide nanotubes (VO$_x$-NTs) by a sol-gel reaction of vanadium alkoxides with a primary amine, followed by hydrothermal treatment. Stucky and co-workers (*41*) synthesized mixed-valence vanadium

oxide nanorods via a nonaqueous low-temperature procedure. V_2O_5 nanorods and nanowires have been synthesized in reverse micelles (*42-43*). Cao et al. (*44*) have also developed a polyol process to self-assemble $V_2O_5 \cdot x\ H_2O$ nanorods into hollow microspheres. Takahashi et al (*22*) reported the growth of V_2O_5 nanorod arrays using electrophoretic deposition combined with templating. For these syntheses, the length of the nanowires was usually less than 10 μm. Long nanowires are expected to facilitate formation of free standing sheets. V_2O_5 sheets comprising entangled nanowires have been used as actuators (*45*), which were demonstrated to provide a high Young's modulus, high actuator-generated stress, and high actuator stroke at low applied voltage. In this case, the hydrated V_2O_5 nanowires were 10 μm long and synthesized by the polycondensation of vanadic acid in water at room temperature (*45,46*). This process requires several weeks due to the slow ion exchange between Na^+ and H^+ ions in a resin from sodium metavanadate solutions at room temperature. In this paper, we introduce a facile method to make high aspect ratio V_2O_5 nanowires within one day, and these nanowires were partially reduced. Presence of V^{+4} in nanowires may increase electrical conductivity. Furthermore, VO_2 undergoes an abrupt semiconductor-metal transition near 68°C, accompanied by dramatic changes in electrical and optical properties. These dramatic changes and the near room temperature phase transition make VO_2 an attractive material for a wide variety of applications such as optical switching and detection (*47,48*), optical storage (*49*), laser protection (*50*), smart window coatings (*51*) and bolometers (*52*).

Experimental

V_2O_5 nanowires were prepared by the hydrothermal polycondensation of ammonium metavanadate (Aldrich) in autoclave. In a typical synthesis, 0.3 g ammonium metavanadate and 0.20 g P123 ($EO_{20}PO_{70}EO_{20}$) were dissolved in 30 ml water containing 1.5 ml 2M HCl. This mixture was stirred at room temperature for 7 hours, and then transferred to 50 ml Teflon lined autoclave and heated to 130 °C and kept at this temperature for 24 hours. The resulting precipitate was dispersed in 50 ml deionized water under vigorous stirring. Subsequently, the product was suction filtered, rinsed with deionized water, and acetone. Nanowires were dried at 80 °C for 12 hours. The V_2O_5 can be peeled off the filter paper as a sheet. To increase The V^{4+}/V^{5+} ratio of V_2O_5 nanowires, the hydrothermal polycondensation of ammonium metavanadate was conducted at 160 °C and 190°C. X ray diffraction (XRD), scanning electron microscopy (SEM), transmission electron microscopy (TEM) and X ray photoelectron spectroscopy (XPS) were used to characterize the materials.

Results and Discussion

1. Preparation and Characterization of Nanowires

Figure 1a displays a digital image of a free standing V_2O_5 nanowire sheet. As can be seen in the image, the sheet can be flexed multiple times without breaking. The paper can also be cut with scissors. The resulting sheet comprises entangled nanowires as shown in the Figure 1b. The as made nanowires have high aspect ratios (> 4000). The nanowires are over 120 μm long and 29 nm wide as seen in the Figure 1b and 1c respectively. The HRTEM images in the Figure 1d shows the crystalline layered structure with a lattice spacing of 9.7 Å. The nanowires grow along the [010] direction. The green-brown color of the nanowires suggests partial reduction of the V^{+5} ions. P123 behaved as reducing agent. Without P123, the as-made wires were pure V_2O_5 wires, but with ~20 μm long and ~ 130 nm wide.

The X-ray diffraction pattern of the as-synthesized nanowires shows a characteristic peak at $2\theta = 8.8°$ as seen in Figure 2, consistent with hydrated V_2O_5 (7,11,26). The 00l reflections are consistent with the layered structure of hydrated V_2O_5. The interlayer spacing of the $V_2O_5 \cdot x\ H_2O$ nanowires was 10.1 Å, which is larger than that of $V_2O_5 \cdot 0.3\ H_2O$ (8.9 Å) and smaller than that of $V_2O_5 \cdot 1.7\ H_2O$ (11.5 Å) (53,54). Therefore, the value of x could be between 0.3 and 1.7.

To determine the content of water in the hydrated V_2O_5 layers, thermogravimetric analysis (TGA) was carried out on the nanowires. The derivative thermogravimetric curve shown in Figure 3a reveals three peaks due to removal of adsorbed and chemically coordinated water molecules, as previously reported (26). The low-temperature weight loss peak at 130 °C may be attributed to the loss of free water. The second weight loss located at ~ 270 °C is due to the loss of physically adsorbed water. For these two low temperature peaks, the weight loss percent were 2.0 % and 4.5 % respectively as seen in Figure 3b. The maximum peak temperature for weight loss was centered at 420 °C, and the weight loss was 12.3 %, which was ascribed to the loss of coordinated water. Thus, the molar ratio of the coordinated water to V_2O_5 in the hydrated V_2O_5 nanowires may be ~ 1.25. This is also consistent with the d-spacing of 10.1 Å.

The XPS spectrum of the as-made nanowires is shown in Figure 5a. The main peak ($2p_{3/2}$) located at 517.2 eV, suggests a +5 oxidation state for most of the vanadium ions. In addition, a small peak at 515.85 eV indicates that partial reduction of the V^{5+} ions to V^{4+} occurred during the hydrothermal condensation. The molar ratio of V^{4+} to V^{5+} was 0.17. The green-brown color of the nanofibers before heating is consistent with partial reduction of the V^{5+}.

If the hydrothermal condensation temperature was increased to 160 °C, the nanowires displayed an XPS spectrum with peaks at 515.85 eV and 517.2 eV as

shown in the Figure 5b, indicating that more V^{5+} ions were reduced compared to the 130 °C synthesis. The molar ratio of V^{4+} to V^{5+} was 0.38 for the 160 °C synthesis. The ratio of V^{4+} to V^{5+} was further increased to 0.49 as the hydrothermal condensation temperature was increased to 190 °C. For these two deeply reduced V_2O_5 samples, they can also be made into flexible sheets. However, when the hydrothermal condensation temperature was 160 °C, the sheet was green as seen in figure 6a, and cyan for 190 °C as seen in figure 6c. The SEM images of the deeply reduced V_2O_5 nanowires exhibited shorter length (10 ~20 μm) and bigger diameter (~ 100 nm) as shown in figure 6b, 6d.

2. Application of the Partially Reduced V_2O_5 Nanowires in a Bolometer

The high temperature gradient of resistivity of VO_2 at dielectric-metal phase transition (T_c=67°C) appear to be very attractive for thermal sensing applications. However, the high heat capacity of bulk material or thin films deposited on substrates represents the main obstacle for the thermal sensitivity response time of these type devices. Free standing VO_{5-x} nanowire paper can create new opportunities for the application of VO_{5-x} nanowires in metric sensing. The VO_{5-x} nanowire paper as a bolometric material has many advantages including extremely low heat capacity (low inertia), high absorbance coefficient in wide wave range from 0.2 to 20 μm, emissivity coefficient of paper reduced in vacuum is close to unity (black as graphite), flexibility, resistance to hard radiation damage, high resistance gradient and absorption of radiation, all of these make nanowires very attractive for bolometric materials. While we have not made pure VO_2, the reduced V_2O_5 may still provide interesting properties.

The bolometric heat balance equation in constant current mode (CCM) can be written as

$$C\frac{dT}{dt} = \eta P + I^2 R(T) - \lambda(T - T_h) \tag{1}$$

where P is the incident radiation power, η is the absorbance of the bolometer, I is the constant bias current, λ is the thermal conductivity to the heat sink, C is the heat capacity of the sensitive element, T_h is the heat sink temperature and R(T) is the temperature dependent sensor resistance.

The output voltage of the bolometer operated in CCM is determined by the responsivity which is defined as the change of output voltage for a change in incident power. Neglecting electrothermal effects the responsivity can be written as,

$$S = \frac{dV}{dQ} = 35 \text{ V/W} \tag{2}$$

20 µm

(b)

(a)
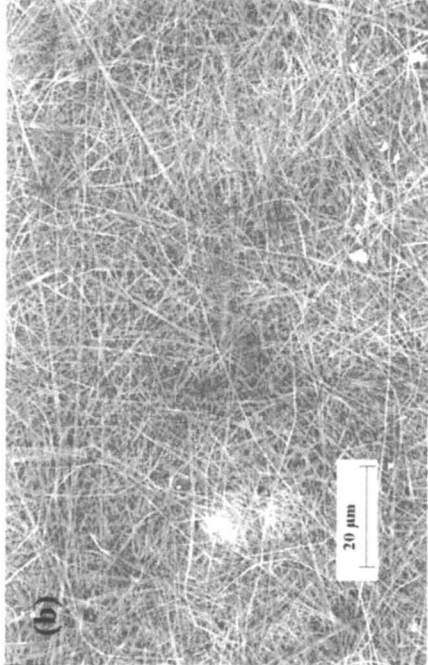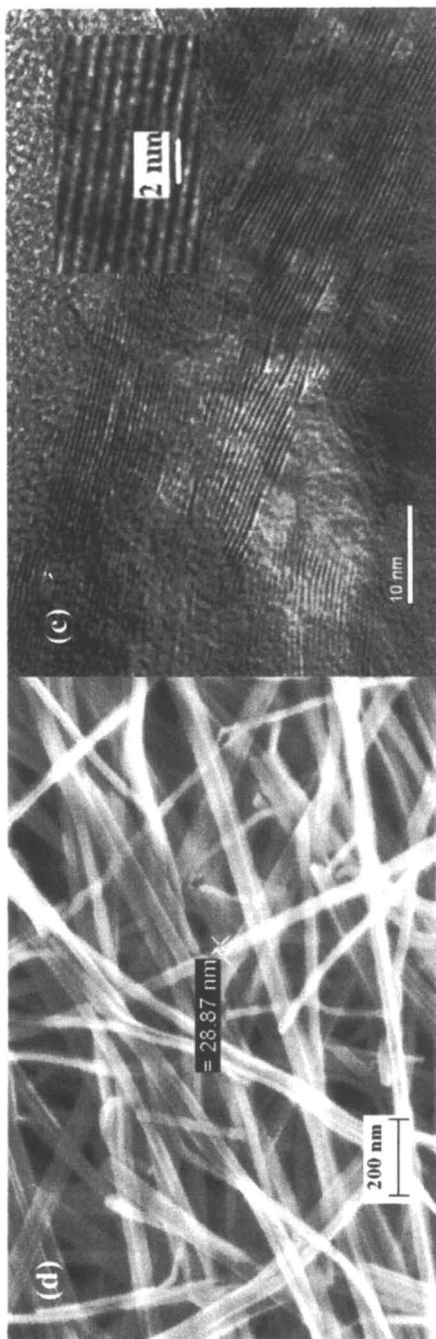
Figure 1. Nanowires prepared with hydrothermal condensation of ammonium metavanadate at 130 ℃, (a) a photo of as prepared $V_2O_5 \cdot x$ H_2O sheet, (b) and (c) SEM images of $V_2O_5 \cdot x$ H_2O nanowires with difference magnifications, (d) TEM image of $V_2O_5 \cdot x$ H_2O nanowires, and the inset is high resolution TEM image of lattice planes.
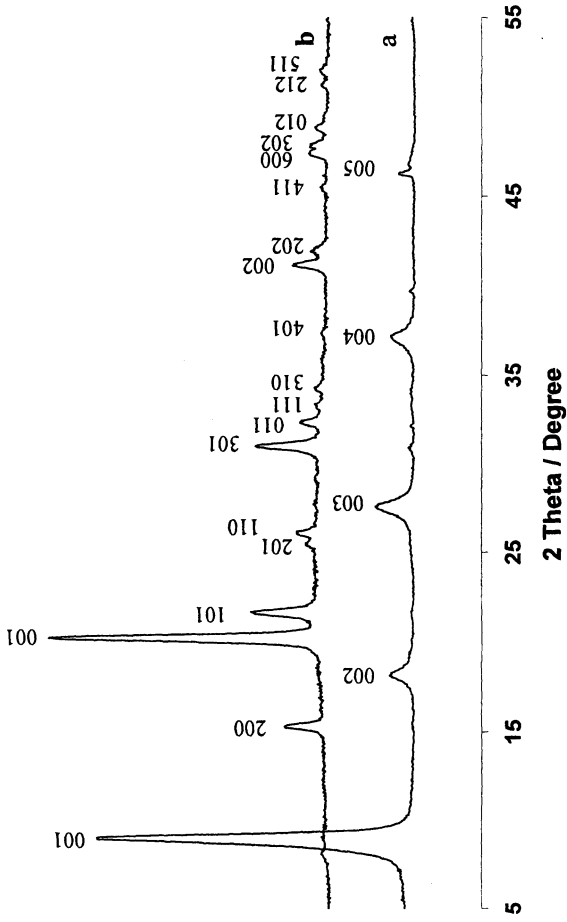
Figure 2. XRD pattern of (a) $V_2O_5 \cdot x\,H_2O$ nanowires prepared at 130 °C, (b) after annealing at 350 °C for 5 hours.
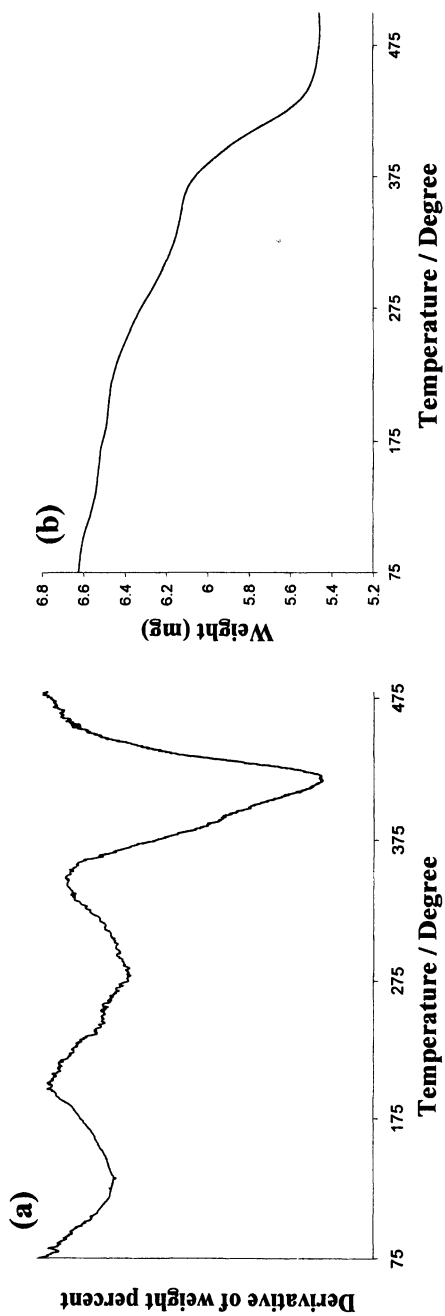
Figure 3. (a) Thermogravimetric analysis (TGA) curve for the as made $V_2O_5 \cdot x\ H_2O$ nanowires prepared at 130°C. Test conditions: N_2 flow rate, 20ml min^{-1}, heating rate, 4 $Kmin^{-1}$. (b) Weight loss curve with temperature for the as made $V_2O_5 \cdot x\ H_2O$ nanowires.
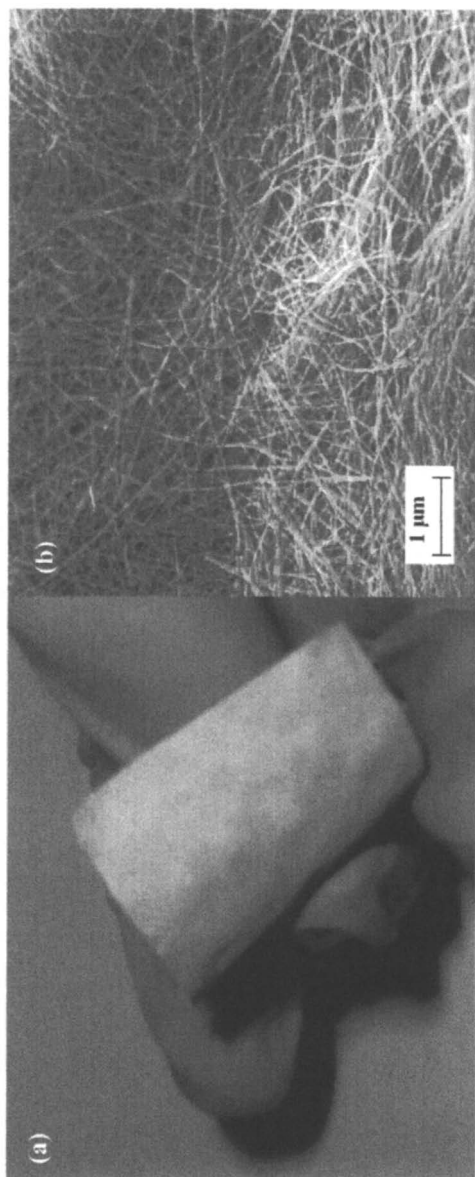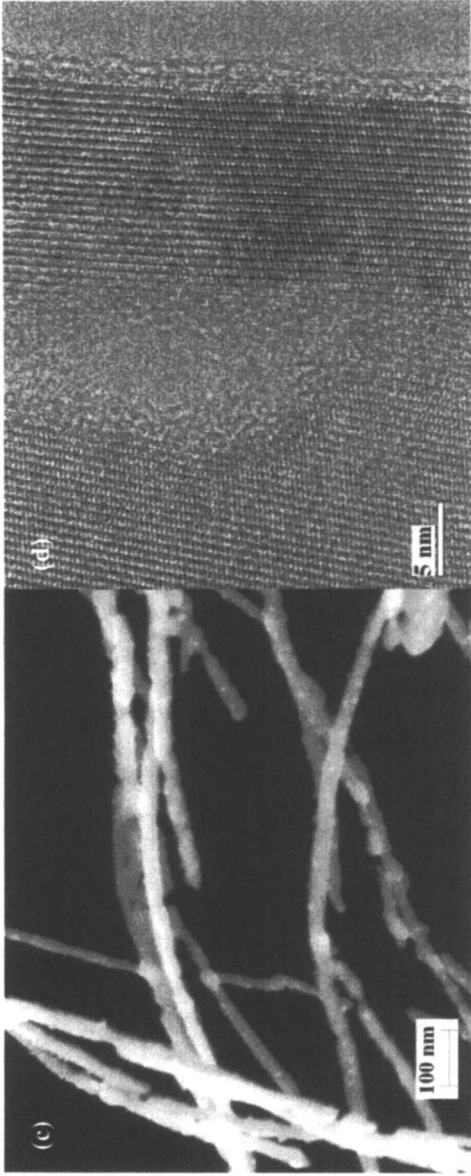
Figure 4. V_2O_5 nanowire sheet after annealing in air at 350°C for 5 hours, (a) a photo of V_2O_5 nanowire sheet, (b) and (c) SEM images of V_2O_5 nanowires with difference magnifications, (d) TEM images of V_2O_5 nanowires.

5172 eV
5159 eV

c

b

a

524   519   514

Binding Energy (eV)
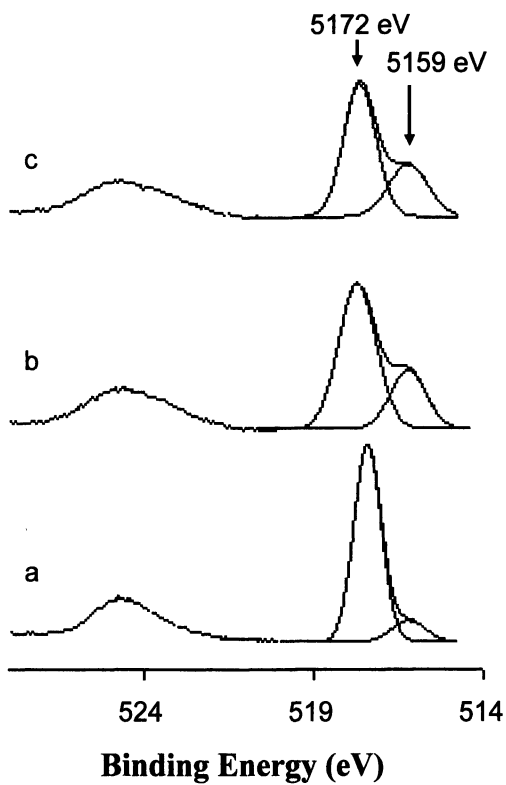
Figure 5. XPS spectra of the as made V₂O₅ nanowires, (a) hydrothermal condensation at 130 °C, (b) hydrothermal condensation at 160 °C, and (c) hydrothermal condensation at 190 °C.

where, dV = *0.37 V* is the potential change on the sample measured in chrono-potentiometry mode with constant applied current of 8 mA, R_o=1.03 kOhm is the initial resistance of the sample and P=9.8 mW is the incident light power (halogen-tungsten lamp, 15 W).

The obtained value of the responsivity for the nanowire paper prepared at 190°C is relatively low due to the low R(T) dependence at room temperature. This value can be significantly enhanced for VO_2 with pronounced metal-dielectric phase transition. This type transition at 67°C is well known for bulk and thin film VO_2. The as-made nanowire sheet has negative temperature gradient over the entire temperature range. However, if the nanowires are further reduced at 600°C in 5% hydrogen environment (or in argon atmosphere) for 4 hours, the negative slope at 240 K changed to positive. The absolute value of resistance at room temperature decreases more than one order of magnitude (see Figure 7).

The appearance of samples also changes after each thermal treatment. The pristine sample had dark cyan color. Sintering at 500°C for 4 hours in air (oxidation) turns the sample color to light yellow. Sintering in hydrogen or argon atmosphere at the same conditions (reduction) turn the sample color to black. The elemental analysis by electron microscope (LEO 1530 VP equipped with Energy Dispersive Spectrometer (EDS) for X-ray microanalysis) shows significant reduction of VO_{5-x}. It is obvious that the reflectance and transmittance spectra should also change. The oxidation substantially increases the transmittance and reflectance of the sample. At the same time the resistance of sample increased to two orders and reached of several MΩ at room temperature. The temperature dependence of resistivity resembles the behavior of wide band-gap semiconductors. The reduction decreases the transmittance and reflectance of the sample (see curve 3 in Figure 8a, 8b) and brings it to metallic behavior of resistivity at room temperature.

The obtained response time measured by electronically modulated laser beam is also relatively high (see Figure 9.). The sample thickness fabricated so far (d=15 μm) creates long thermal response and prevent the penetration of heat radiation into the sample (Eq.1). The further development of thinner free-standing VO_{5-x} film is in progress.

In summary, high aspect ratio hydrated V_2O_5 nanowires have been synthesized, which can be entangled into a flexible sheet. Hydrated and partially reduced V_2O_5 nanowires exhibit a layered structure with ~1 nm layer spacing. Upon loss of coordinated water by annealing, fibrous morphology is maintained although contraction of the lattice occurred due to dehydration, the orthorhombic V_2O_5 phase formed. V_2O_5 nanowires with a higher degree of reduction were produced by increasing the hydrothermal condensation temperature or by past synthesis of heating under H_2 or Ar. The hydrothermal polycondensation procedure is very simple and highly reproducible, and it is readily applicable to large scale synthesis for potential industrial applications.
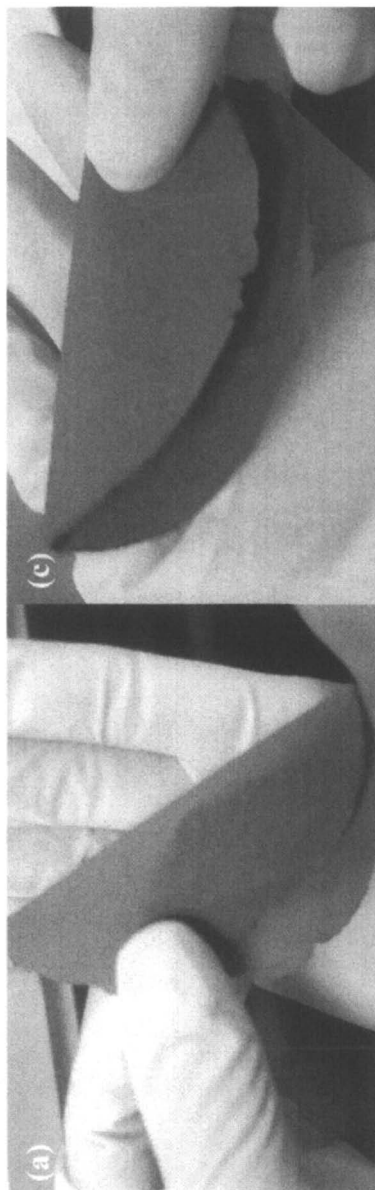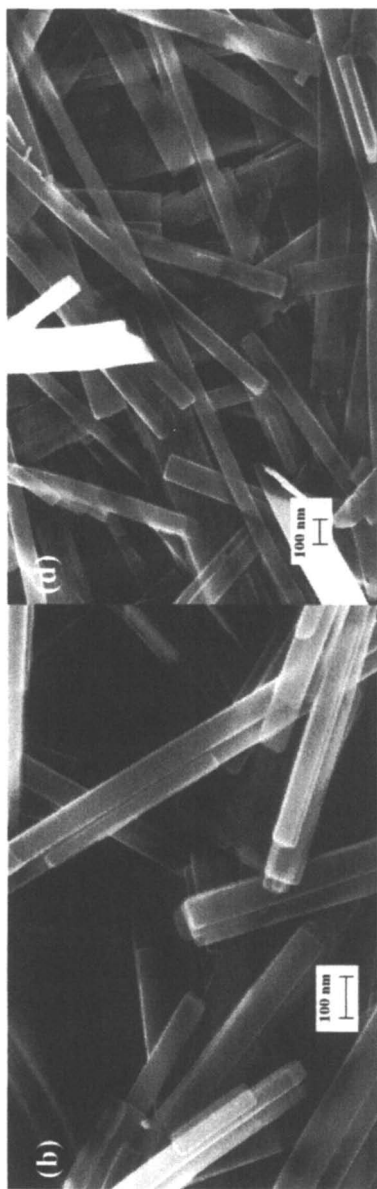
Figure 6. (a) a photo and (b) SEM images of partially reduced $V_2O_5 \cdot x\ H_2O$ sheet prepared at 160 °C, (c) a photo and (d) SEM images of partially reduced $V_2O_5 \cdot x\ H_2O$ sheet prepared at 190 °C.
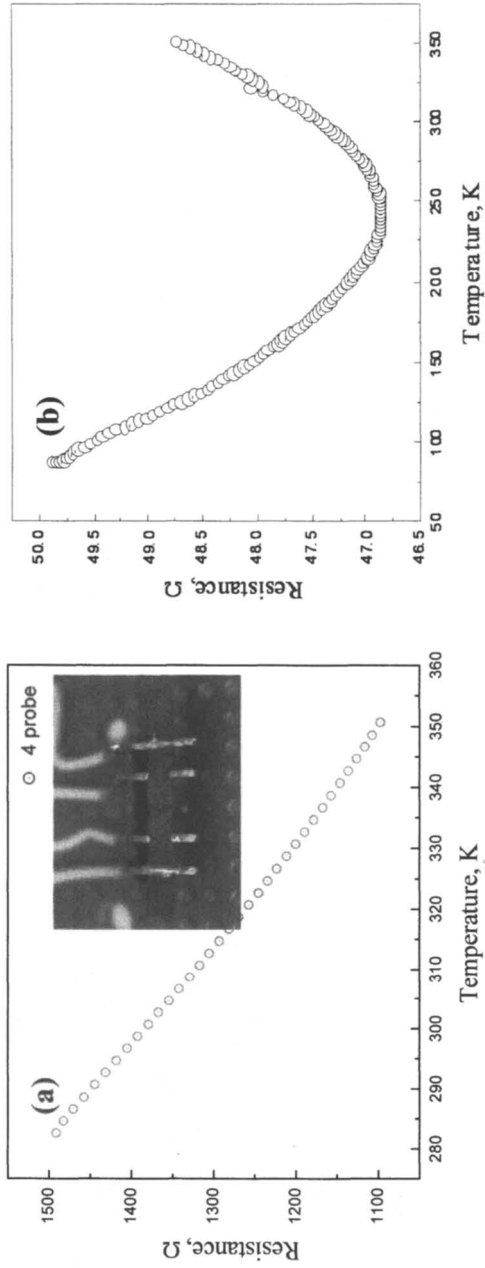
Figure 7. Temperature dependence of resistivity of (a) pristine free-standing paper of VO$_{5-x}$ nanowires, the inset shows the 4-probe resistance measurement design and (b) annealed at 400°C in air and then sintered at 600° C in 5% hydrogen environment.
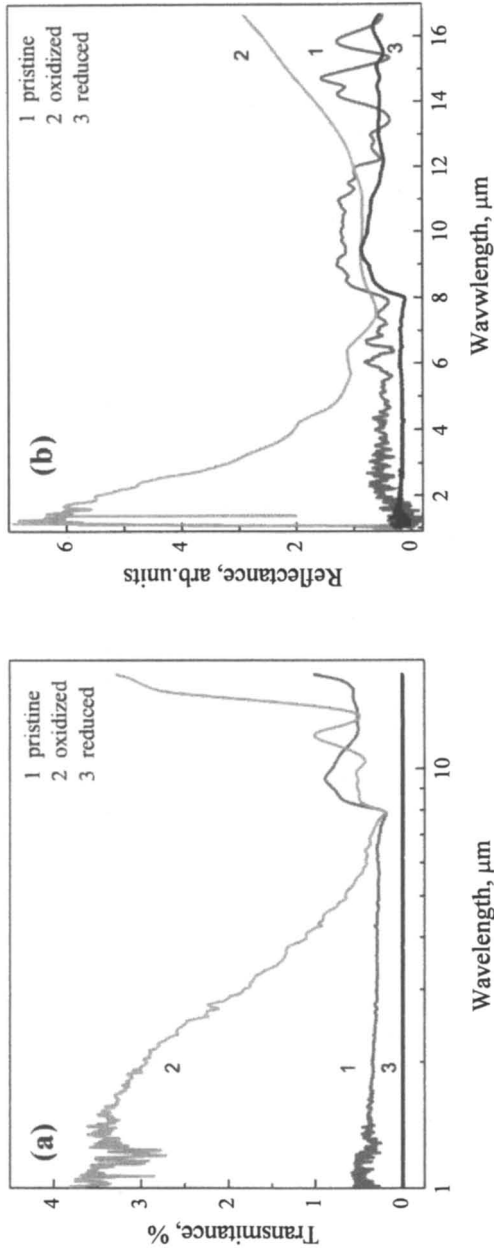
Figure 8. (a) transmittance and (b) reflectance spectra of curve 1 for pristine nanowire sheet, curve 2 for the oxidized nanowire sheet in air atmosphere at 500°C for 4 hours, curve 3 for the reduced nanowire sheet in argon atmosphere at 500°C for 4 hours, V_2O_{5-x} nanowire paper (d=15 µm).
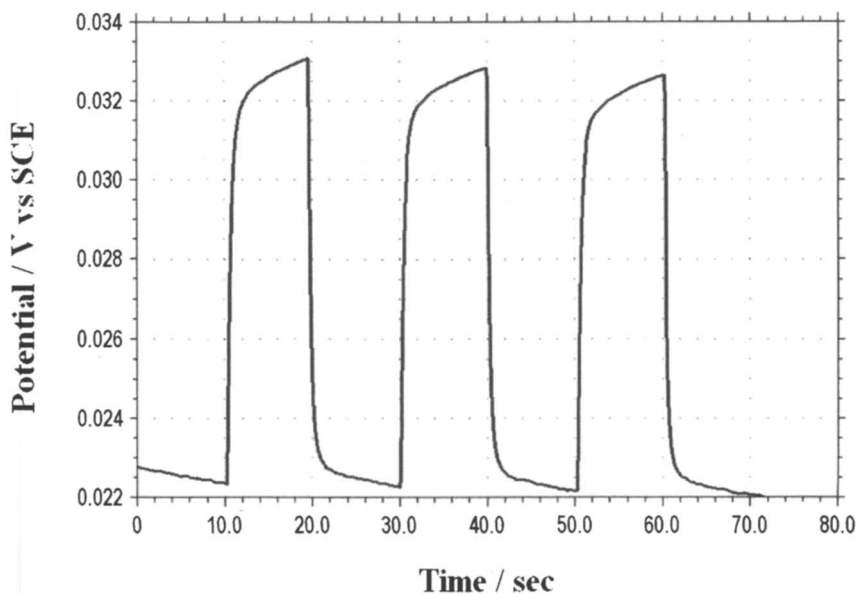
Figure 9.   Potential modulation by tungsten-halogen lamp (10mW/cm²) for fixed applied current, 8 mA.

Acknowledgments

References

1. Nordlinder, S.; Nyholm, L.; Gustafsson, T.; Edström, K. *Chem. Mater.* **2006**, *18*, 495-503.
2. Wang, Y.; Cao, G. Z. *Chem. Mater.* **2006**, *18*, 2787.
3. Poizot, P.; Grugeon, S.; Dupont, L.; Tarascon J.M. *Nature* **2000**, *407*, 496.
4. Julien, C.; Haro-Poniatowski, E.; Camacho-López, M. A.; Escobar-Alarcón, L.; Jiménez-Jarquín, J. *Mater. Sci. Eng. B* **1999**, *65*, 170.
5. Takahashi, K.; Limmer, S. J.; Wang, Y.; Cao, G. *J. Phys. Chem. B* **2004**, *108*, 9795.
6. Liu, P.; Lee, S.-H.; Tracy, C. E.; Yan, Y.; Turner, J. A. *Adv. Mater.* **2002**, *14*, 27.
7. Li, G. C.; Pang, S. P.; Jiang, L.; Guo, Z. y.; Zhang Z. K. *J. Phys. Chem. B* **2006**, *110*, 9383-9386.

8.   Wang, Y.; Takahashi, K.; Lee, K. H.; Cao, G. Z. *Adv. Funct. Mater.* **2006**, *16*, 1133

9.   Posudievsky, O. Y.; Biskulova S. A. Pokhodenko, V. D. *J. Mater. Chem.*, **2004**, *14*, 1419.

10. Pang, S. P.; Li, G.C.; Zhang, Z. K. *Macromol. Rapid Commun.* **2005**, *26*, 1262.

11. Wang, G. C.; Wang, L.; Li, X. W. *Polym. Int.* **2005**, *54*,1082.

12. Ponzi, M.; Duschatzky, C.; Carrascull, A.; Ponzi, E..*Appl. Catal. A* **1998**, *169*, 373.

13. Sun, Q.; Jehng, J. M.; Hu, H.; Herman, R. G.; Wachs, I. E.; Klier, K. *J. Catal.* **1997**, *165*, 91.

14. Banares, M. A. *Catal. Today* **1999**, *51*, 379.

15. Eon, J. G.; Olier, R.; Volta, J. C. *J. Catal.* **1994**, *209*, 318.

16. Watling, T. C.; Deo, G.; Seshan, K.; Wachs, I. E.; Lercher, J. A. *Catal. Today* **1996**, *28*, 139.

17. Khodakov, A.; Yang, J.; Su, S.; Igleasia, E.; Bell, A. T. *J. Catal.* **1998**, *177*, 343.

18. Guliants, V. V. *Catal. Today* **1999**, *51*, 255.

19. Al-Saeedi, J. N.; Guliants, V. V.; Guerrero-Perez, O.; Banares, M. A. *J. Catal.* **2003**, *215*, 108.

20. Talledo, A.; Granqvist, C. G. *J. Appl. Phys.* **1995**, *77*, 4655.

21. Liu, P.; Lee, S.H.; Tracy, C.E.; Tuener, J.A.; Pitts, J.R.; Deb, S.K. *Solid state Ionics* **2003**, *165*, 223.

22. Takahashi, K.; Limmer, S.J.; Wang, Y.; Cao, G.Z.; *Appl. Phys. Lett.* **2005**, *86*, 31

23. Cheng, K. C.; Chen F.R.; Kai J. J.; *Solar Energy Materials & Solar Cells* **2006**, *90*, 1156

24. Takahashi, K.; Wang, Y.; Cao, G. Z. *Applied Physics Letters*, **2005**,

25. Kudo, T.; Ikeda, Y.; Watanabe, T.; Hibino, M.; Miyayama, M.; Abe, H.; Kajita, K. *Sol. State Ionics* **2002**, *152*, 833.

26. Lee, H. Y.; Goodenough, J. B. *J. Sol. State Chem.* **1999**, *148*, 81.

27. Kim, Il-H.; Kim, J. H.; Cho, B. W.; Lee, Y. H. Kim, K. B. *J. Electrochem. Soc. A* **2006**, *153*, 989

28. Šordan, R.; Burghard, M.; Kern, K.. *Applied Physics Letters*, **2001**, *79*, 2073.

29. Ancona, M. G.; Kooi, S. E.; Kruppa, W. A.; Snow, W.; Foos, E. E.; Whitman, L. J.; Park, D.; Shirey L. *Nano Letters,* **2003**, *3*, 135.

30. Livage, J. *Chem. Mater.* **1991**, *3*, 578.

31. Micocci, G. *et al. J.Vac. Sci. Technol.A* **1997**, *15*, 34.

32. Liu, J.; Wang, X.; Peng, Q.; Li, Y. *Adv. Mater.* **2005**, *17*, 764.

33. Biette, L.; Carn, F.; Maugey, M.; Achard, M. F.; Maquet, J.; Steunou, N.; Livage, J.; Serier, H.; Backov, R. *Adv. Mater.* **2005**, *17*, 2970.

34. Muster, J.; Kim, G.T.; Krstic, V. *Adv. Mater.* **2000**, *12*, 420.

35. Kim, G.T.; Muster, J.; Park, J.G.; Krstic, V.; Park, Y.W. *Appl. Phys. Lett.* **2000**, *76*, 1875.

36. Davidson, P.; Lamarque-Forget, and Pelletier, O. *Adv. Mater.* **2000**, *12*, 1267.

37. Kim, Y.-K.; Park, S. J.; Koo, J. P.; Kim, G. T.; Hong, S.; Ha, J. S. *Nanotechnology* **2007**, *18*, 015304/1-015304/6.

38. Patzke, G.R.; Krumeich, F.; Nesper, R. *Angew. Chem. Int. Ed.* **2002**, *41*, 2446-2461.

39. Krumeich, F.; Muhr, H.-J.; Niederberger, M.; Bieri, F.; Schnyder, B.; Nesper, R. *J. Am. Chem. Soc.* **1999**, *121*, 8324.

40. Krumeich, F.; Schonholzer, U.P.; Bieri, F.; Niederberger, M.; Gauckler, L.J.; Nesper, R. *Adv. Mater.* **2000**, *12*, 231.

41. Niederberger, M.; Bard, M.H.; Stucky, G. D. *J. Am Chem. Soc.* **2002**, *124*, 13642–13643.

42. Pinna, N.; Wild, U.; Urban, J.; Schlögl, R. *Adv. Mater.* **2003**, *15*, 329.

43. Pinna, N.; Willinger, M.; Weiss, K.; Urban, J.; Schlögl, R.; *Nano Lett.,* **2003**, *3*, 1131-1134.

44. Cao, A. M.; Hu, J. S.; Liang, H. P.; Wan, L. J. *Angew. Chem., Int. Ed.* **2005**, *44*, 4391.

45. Gu, G.; Schmid, M.; Chiu, P. W.; Minett, A.; Fraysse, J.; Kim, G. T.; Roth, S.; Kozlov, M.; Mun~oz, E.; Baughman, R. H. *Nat. Mater.* **2003**, *2*, 316.

46. Livage, J. *Coord.Chem.Rev.***1998**, *178*, 999.

47. Chen, S.H.; Ma, H.; Yi, X.J.; Wang, H.C. *Infrared Phys. Tech.* **2004**, *45*, 239.

48. Jerominek, H.; Picard, F.; Vincent, D. *Opt. Eng.* **1993**, *32*, 2092.

49. Bugayev, A.A.; Gupta, M.C. *Opt. Lett.* **2003**, *28*, 1463.

50. Chen, S.H.; Ma, H.; Yi, X.J., *Sensor. Actuator. A 1* **2004**, *115*, 28.

51. Manning, T.D.; Parkin, I.P.; Pemble, M.E. *Chem. Mater.* **2004**, *16*, 744.

52. de Almeida, L. A. L.; Deep, G. S.; Lima, A. M. N.; Khrebtov, I. A.; Malyarov, V. G.; Neff, H. *Appl. Phys. Lett.* **2004**, *85*, 3605.

53. Yao, T.; Oka, Y.; Yamamoto, N. *Mater. Res. Bull.* **1992**, *27*, 669

54. Pan, D. Y.; Zhang, S.Y.; Chen, Y. Q.; Hou, J.G. *J. Mater. Res.,* **2002**, *17*, 1981.

55. Zhou, F.; Zhao, X.; Yuan, C.; Li, L.; Xu, H. *Chem. Lett.* **2007**, *36*, 310

Chapter 13

Langmuir and Langmuir–Blodgett Films of Quantum Dots

Jhony Orbulescu and Roger M. Leblanc[*]

Department of Chemistry, University of Miami, 1301 Memorial Drive,
Cox Science Center, Coral Gables, FL 33146

Langmuir monolayers are formed by spreading an amphiphilic molecule at the air-water interface and its interface properties are studied upon compression of the monolayer. The main requirement of the molecule is that the solvent in which is dissolved in should be immiscible with water and fairly volatile. This requirement must be fulfilled such that the solvent could evaporate within 10-15 min and the monolayer would be formed only by the amphiphilic molecules. Compression can be applied to the monolayer and a change in the surface pressure as function of the molecular area can be followed. Compression is a very convenient method to control the packing of a monolayer or in other words the intermolecular distance. This aspect is important because arrays of quantum dots (QDs) can be formed by various techniques, e.g. lithographic methods and upon deposition on metallic substrates new electronic properties given by the array could arise.

In recent years, there have been great progress in synthetic methods of quantum dot preparation, which made large scale synthesis of QDs with high quality and narrow size distribution possible. Luminescent QDs have been successfully attached to dendrimer, protein, sugar, and other biologically active agents (*1-4*). Among the various types of modifications, CdSe QDs have been studied most thoroughly due to their possible applications in biological disciplines. However, consideration of QD behavior at biological interfaces, e.g., cell membranes, is one of the most important issues requiring further study prior to implementation in real applications. Currently, few studies have been conducted regarding surface chemistry properties of quantum dots at biological interfaces.

Quantum dots of II-VI semiconductors (CdS, CdSe, and CdTe) in the 1–12 nm size range have attracted a great deal of research interest in the past few years in the field of physics, chemistry, biology, and engineering (*5-13*). Dramatically different from the bulk state, properties of QDs are dependent upon quantum confinement effects in all three spatial dimensions. These QDs demonstrate great potential in applications for optical devices, optical switches, and fluorescence labeling (*14*).

The first article focusing on the Langmuir monolayer of QDs was published by Dabbousi et al. (*15*) with the focus of controlling the QDs array deposited as a Langmuir-Blodgett film. The synthesis of QDs was based on the routine of Murray et al. (*16*). Following synthesis, the QDs were transferred into methanol to wash the excess (tri-octylphosphine oxide) TOPO capping than dried and transferred to HPLC grade chloroform that was spread on the water surface.

Following this study there was not much research published on a few years. Leblanc and co-workers (*17*) focused on the influence of ligand length on the packing of the QDs monolayer. In this case the synthetic routine was carried out using the method reported by Peng and co-workers (*18,19*). By controlling the temperature and reaction time, these experiments were reproducible, and the QDs have the same size distribution.

CdSe Quantum Dots

Modification of CdSe QDs with Alkane Thiols (QD-Cx)

Alkane thiols were directly added into pure CdSe QDs solution (molar ratio, QDs:thiol=1:300). After agitation of solution for 24 h, copper powder was added to solution in order to remove excess thiol (concentrations of QDs and modified QDs were calculated from the solution UV-vis absorption).

QDs (CdSe) have been modified with surfactants of varying chain lengths (C_6SH to $C_{18}SH$). These QD-surfactants can form a stable Langmuir monolayer at air-water interface (*17*).

Langmuir Monolayer

These modified quantum dots can form a stable monolayer (Langmuir monolayer) at the air-water interface. The surface pressure-area isotherm gives the most important indicator of the monolayer properties. A standard surface pressure- area isotherm includes three parts, the gaseous phase at large area per nanoparticle, the liquid expanded and liquid condensed phases during which surface pressure increases with compression, and the solid phase. By extrapolating the solid or liquid condensed phase part of the isotherm at zero surface pressure, a limiting nanoparticle area is measured, which is an important parameter for the Langmuir monolayer studies. The limiting nanoparticle area corresponds to the smallest area per nanoparticle at air-water interface in a 2-D arrangement. Collapse surface pressures of the modified QDs Langmuir monolayers were all higher than 25 mN/m. There are two different behaviors of modified QDs Langmuir monolayers that could be identified from these isotherms. QD-C6 (QDs modified with hexane thiol), QD-C8, QD-C10 and QD-C12 showed similar limiting nanoparticle area, when compared with pure QDs at approximately 500 $Å^2$/nanoparticle. From QD-C14 to QD-C18, the limiting nanoparticle area grew larger with increasing alkane thiol chain length. QD-C14 showed a limiting molecular area of 1200 $Å^2$/nanoparticle, whereas the limiting nanoparticle area of QD-C16 was observed to be approximately 9300 $Å^2$/nanoparticle. A limiting nanoparticle area around 9600 $Å^2$/nanoparticle was obtained from the surface pressure-area isotherm of QD-C18.

A possible explanation for the different behaviors of modified QDs may be found in the roles of TOPO on the QDs surface. The TOPO molecule contains three hydrocarbon chains that produce its hydrophobic property, and it also has a large dipole moment derived from the phosphorus-oxygen bond (16,20,21). TOPO acts as both the solvent and the capping molecules in the preparation of the CdSe QDs. After preparation, most of the TOPO molecules were removed by methanol because of its good solubility in this solvent. Hydrophobic TOPO is the capping agent responsible for CdSe's solubility in non-polar organic solvents. Therefore, TOPO molecules could not be completely washed away. In fact, the capping layer of modified QDs still contains a small amount of TOPO mixed among the alkane thiols. The limiting nanoparticle area, obtained from these isotherms, is determined by the diameter of modified QDs. Its diameter includes the diameter of the CdSe core and the length of the longest chains. Since the length of TOPO is close to C12 and greater than C6 and C8 [from the CPK model], the modified QDs (QD-C6 to QD-C10) showed limiting nanoparticle areas similar to that of pure QDs that was also covered with some TOPO molecules. From C12 to C18, the length of the alkane thiols are longer than TOPO, the modified QDs showed increased area with the increasing thiol molecule chain lengths.

In situ UV-vis Spectroscopy

The UV-vis absorption spectra of modified CdSe QDs at the air-water interface were also measured. Increasing the surface pressure revealed a linear increase of the UV-vis absorption intensity at peak maximum. All of the modified QDs from QD-C6 to QD-C18 demonstrated the same linear relationship. Therefore, there appears to be a strong linear relationship between visible absorbance (503 nm) and surface pressure.

A different approach was to use QDs Langmuir monolayers and the influence of the nature of the surfactant, particle size, surface pressure and monolayer mixing could have on the QDs engineered at the air-water interface.

Modification of CdSe QDs: TOPO/ODT Surface Cap Exchange

To replace the TOPO surface cap on the CdSe QDs by an octadecyl thiol (ODT) cap, 1 mL of the TOPO-capped QDs in chloroform was reacted with 0.287 g (1 M) of ODT for about 19 h. The reaction mixture was kept under gentle agitation, in the dark, and at room temperature. Purification of the resulting ODT-capped CdSe QDs was achieved by first evaporating all of the chloroform present in the mixture utilizing argon flow. The QDs were then washed three times with 10 mL of the anhydrous methanol/chloroform (8:2, v/v) mixture. Finally, the QDs were dispersed in 1 mL of chloroform and filtered as described above.

Molar Absorptivity of TOPO-capped QDs

The molar absorptivity (ε) of CdSe QDs at λ_{max} has been found to be dependent on nanoparticle size (Figure 1A) (*22-25*). Linear (*24*), cubic (*22,23*) and intermediate between quadratic and cubic (*25,26*) functions are implied or reported in the literature as shown in Figure 1B. Molar absorptivity of QDs has been calculated from data collected by atomic absorption spectroscopy (*22,25,26*), osmotic methods (*23*), absorption cross section (*24*) and/or controlled etching (*25,26*). These literature ε values are included in the calculations to determine the concentration of QD samples prepared for this study. The absorbance (A) values used are [1] 0.2355, [2] 0.2085, [3] 0.2701, and [4] 0.2900. To plot them within the same graph without overlapping the lines as shown in the figure, all the actual values were muliplied by 1, 2, 3, or 4, respectively.
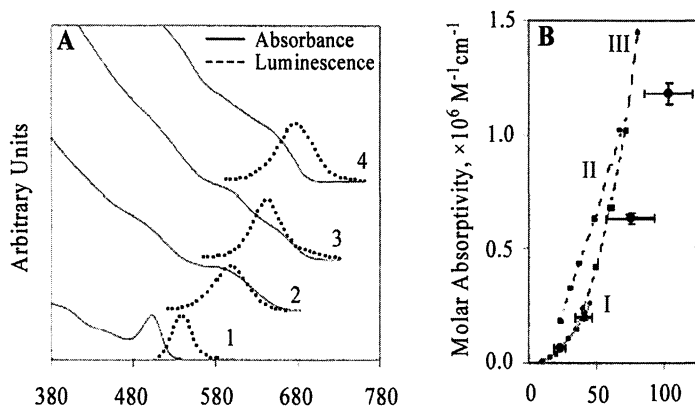
Figure 1. (A) Absorbance (solid lines) and PL (dashed lines, λ_{ex} = 400 nm) spectra of TOPO-capped CdSe QDs with average diameters of [1] 23 Å, [2] 41 Å, [3] 75 Å, and [4] 103 Å. (B) Molar absorptivity values of TOPO-capped CdSe QDs as a function of particle size (I). The error bars consist of the standard deviations for the respective axes. The lines (I, II and III) in (B) indicate the corresponding literature values (22, 24-26). (Reproduced from reference 27. Copyright 2005 American Chemical Society.)

In addition, it was found that UV-vis spectroscopy, surface pressure-area (π-A) isotherms, Langmuir monolayer properties, QD size, and Langmuir-Blodgett (LB) films could be used collectively to determine the molar absorptivity of QDs in 2D. Proposed calculations and procedures are indicated elsewhere (27). Based on these combined results, the molar absorptivity values for the 23, 41, 75, and 103 Å CdSe QDs used in this study were 6.6×10^4, 2.0×10^5, 6.3×10^5, and 1.2×10^6 $M^{-1}\cdot cm^{-1}$, respectively.

Although in close agreement with previously published calibration data, the derived ε values tend to follow a quadratic dependence (Figure 1B). This suggests that molar absorptivity is particle size-dependent and proportional to the QD surface area (Figure 1A).

TOPO-capped and ODT-capped CdSe QDs

The replacement of TOPO by ODT molecules on the surface of the QDs had a minimal effect ($\pm$ 1-3 nm) in λ_{max} of the nanocrystals' absorption and emission spectra. However, this surface cap exchange resulted in 86% quenching of PL intensity from the QDs. Introduction of S-Cd bonds on the surface of the CdSe QDs has been correlated to changes in PL properties arising from modifications of electronic states (28-31). PL intensity was 98% quenched when an equimolar mixture of N,N-diisopropylethylamine (DIEA) and ODT was utilized to

exchange the surface TOPO cap on the QDs. The non-nucleophilic base is utilized to facilitate binding of ODT to the QDs. However, utilization of DIEA during modification of the 103 Å QDs could result in a smaller average particle size, 79 Å, as imaged by TEM. This suggests that chemical "etching" of the nanoparticles could take place with prolonged reaction time.

It has been proposed that every Cd atom on the surface of the CdSe QDs may be coordinated to a TOPO molecule (32). Therefore, the degree of quenching of PL intensity could be correlated to the extent of surface ligand exchange. These changes in the QD's optical properties provide evidence of an efficient surface cap exchange. To confirm these results, energy-dispersive X-ray analysis was performed on purified dried films of QDs. Appearance of a peak at 2.3 keV revealed the presence of sulfur atoms in the purified ODT-capped nanocrystals. The phosphorus peak at 2.0 keV decreased to the noise level of the spectrum. This indicates that ODT replaced most of the TOPO molecules on the surface of the QDs. The results compare to reports in the literature in which thiol-containing organic molecules could replace 85-90% of surface TOPO/TOPSe molecules on CdSe QDs (31).

Langmuir Monolayer

The limiting nanoparticle or limiting molecular area is defined as the smallest area occupied by the nanoparticle or molecule, respectively, in 2D. It is obtained by the extrapolation of the linear portion of the π-A isotherm to zero surface pressure. First, the π-A isotherms for the pure TOPO and ODT molecules were obtained. TOPO and ODT have limiting molecular areas of 135.0 and 22.5 Å^2/molecule, respectively (Figure 2A). ODT and stearic acid are very similar in structure, both having a C18 hydrocarbon chain but a different polar group. Both compounds have comparable limiting molecular areas of 22.5 and 21.8 Å^2/molecule, respectively. No signs of ODT's thiol group oxidation were detected at the air-water interface. The ODT π-A isotherm has an additional feature. After the collapse of the monolayer film at about 15 mN/m, ODT presents a plateau region with almost constant surface pressure followed by another rapid increase in surface pressure (Figure 2A). The limiting molecular area extrapolated from this second lifting point is 7.7 Å^2/molecule. This indicates the capacity of ODT to form a stable "multilayer" film at about 1/3 of its limiting molecular area (Figure 2C). Self-assembly of ODT into a trilayer film has been reported on liquid mercury (33).

Langmuir Monolayer of TOPO-capped QDs

The π-A isotherms of QDs were recorded utilizing only fresh and purified QDs samples. This practice was utilized to minimize the presence of 3D QDs
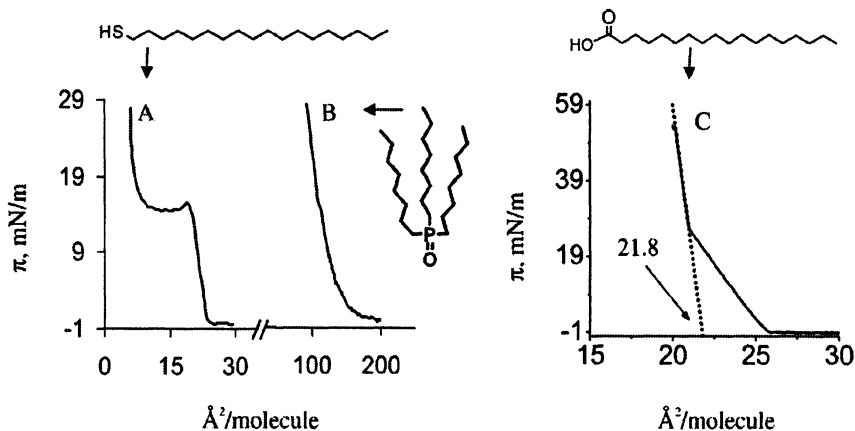
Figure 2. Characteristic π-A isotherms for (A) ODT, (B) TOPO, and (C) stearic acid molecules. (Reproduced from reference 27. Copyright 2005 American Chemical Society.)

aggregates at the air-water interface. Considering a spherical nanocrystal, the area of a single TOPO-capped CdSe QDs in 2D at the air-water interface could be predicted theoretically. Based on simple molecular modeling calculations, it has been reported that TOPO can form a monolayer on the surface of the nanocrystals (*32*). Also, TOPO Langmuir monolayer on metal surfaces has been measured at about 7 Å thick (*20*). The area per QD in 2D then should be as follows: $\pi(r + 7)^2$, where r is the QD radius in Å. The QDs used in this study had average r values of 11.5, 20.5, 37.5, and 51.5 Å. The respective theoretical area/QD values in 2D are 1075, 2376, 6221, and 10751 $Å^2$/QD. The corresponding experimental values of the limiting nanoparticle areas extrapolated from the π-A isotherms (Figure 3) of the QDs are 1086, 2375, 6370, and 10757 $Å^2$/QD, respectively. The predicted and experimentally derived limiting nanoparticle areas match very closely, with an error <3%. These results indicate minimum interdigitation of TOPO surface molecules, confirming that TOPO forms close-packed Langmuir monolayers on the surface of the QDs. These results also prove the accuracy of the molar absorptivity values that were derived previously for the respective TOPO-capped CdSe QDs.

Langmuir Monolayer of ODT-capped QDs

The limiting nanoparticle area was lower for the ODT-capped QDs than for the corresponding TOPO-capped nanoparticles. For example, the 23 Å QDs had a value of 505 or 1086 $Å^2$/QD for ODT- or TOPO-capped, respectively. This
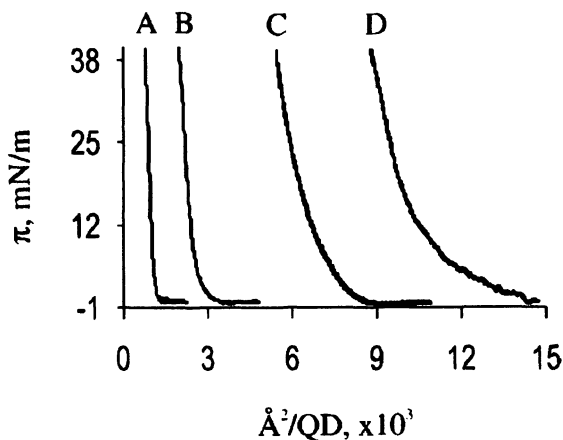
Figure 3. π-A isotherms of (A) 23 Å, (B) 41 Å, (C) 75 Å, and (D) 103 Å TOPO-capped CdSe QDs. (Reproduced from reference 27. Copyright 2005 American Chemical Society.)

suggests that replacement of the more bulky TOPO surface ligands with ODT molecules increases the packing density of the QDs through interdigitation of the longer ODT alkyl chains. However, this capacity for interdigitation facilitated 3D aggregate formation at the interface, which contributed to a smaller area/QD.

Besides surface alkyl chain interdigitation and the closest possible packing arrangement of QDs, the degree of organization at the air-water interface may also be influenced by other factors. For example, surfactants such as TOPO and the crystalline structure of the CdSe nanoparticles could bring about intrinsic dipole moments (*33-35*). Changes in surface cap and nanocrystal size may alter the direction and intensity of these polarities, which may be factors influencing the degree of nanoparticles organization at the interface.

To study the organization of the QDs at the air-water interface, TEM micrographs of LB films were taken at a surface pressure of 20 mN/m. The QDs self-assembled into domains of variable architecture as shown in Figure 4A,B. The nanoparticle organization within the 2D domains was influenced by the nature of the surface stabilizing molecule. TOPO-capped QDs had hexagonal like close-packing arrangements as shown in Figure 4C. Deviations from the hexagonal packing of QDs could be attributed in part to the large particle size distribution of the samples. The ODT-capped nanocrystals were found to have areas in which the QDs were farther apart from each other (Figure 4D). A longer interparticle distance confirmed the presence of the longer ODT on the surface of the nanoparticles. Interdigitation was then more restricted at this large particle size. Some 3D domains within the LB films were detected as darker or indistinct areas.
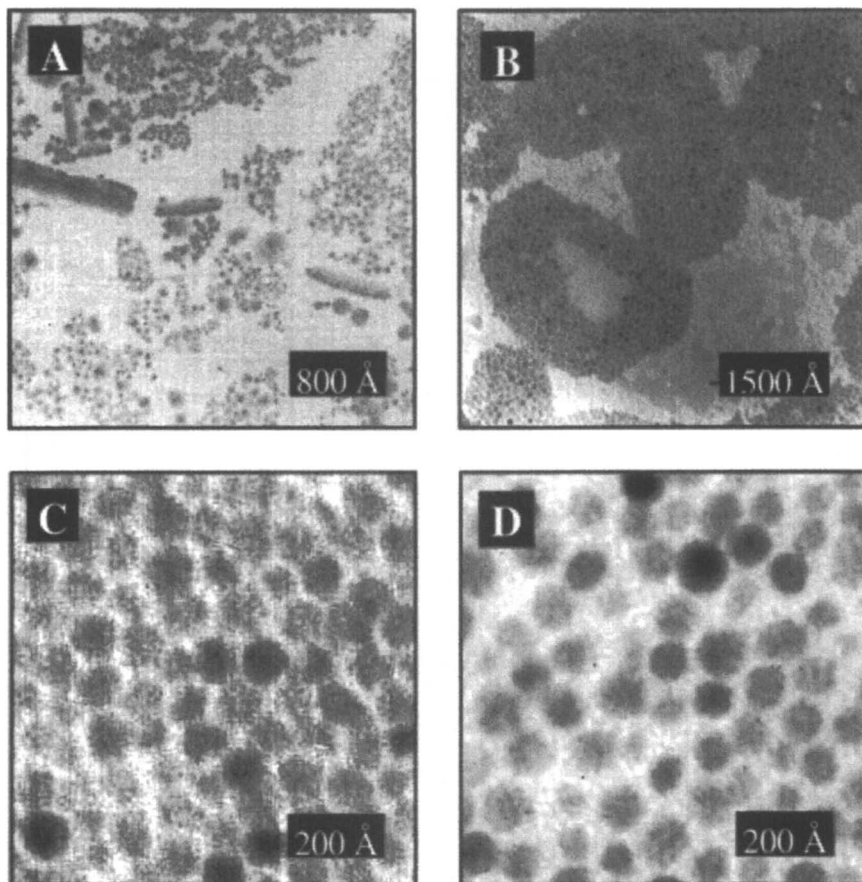
Figure 4. TEM micrographs of CdSe QD LB films deposited on carbon-coated copper grids at 20 mN/m. (A) 75 Å TOPO-capped. (B) 103 Å TOPO-capped. (C) 103 Å TOPO-capped. (D) 103 Å ODT-capped. (Reproduced from reference 27. Copyright 2005 American Chemical Society.)

Langmuir-Blodgett (LB) Film of QDs

QDs Langmuir monolayers were transferred onto hydrophilic or hydrophobic quartz slides utilizing the LB film deposition technique at different surface pressures. Deposition ratios higher than 0.8 were obtained for both substrates indicating an effective film transfer. The ratio between the area decrease at the air-water interface, that is the area of the monolayer transferred onto solid substrate, and the area of the solid substrate available for deposition is defined as "deposition ratio". A good deposition ratio has values between 0.7

and 1, which is the ideal deposition case when all the solid substrate is covered with a monolayer. Emission from a single TOPO-capped QDs LB monolayer film was detected. When deposited at higher surface pressures, the LB monolayer increased PL intensity (Figure 5). This results show the formation of more closely packed QDs domains as shown in Figure 5. When imaged with the epifluorescence microscope, the topography of the QDs LB films deposited at different surface pressures on the slides resembled that taken directly at the interface. Thus, the films were transferred nearly intact as assembled at the air-water interface.
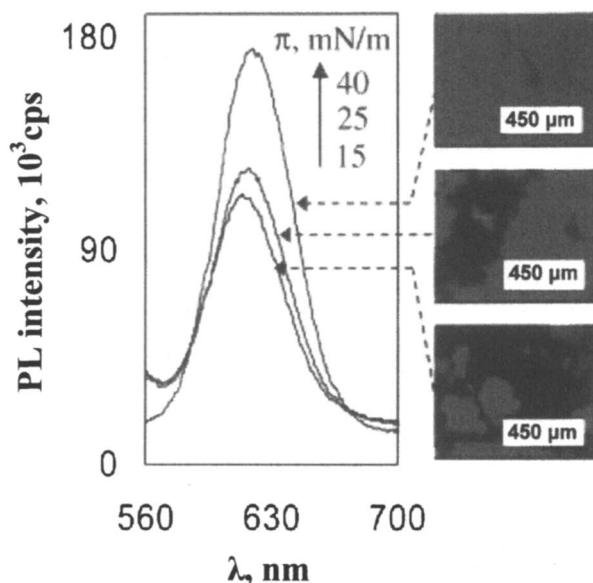
Figure 5. PL spectra and epifluorescence images (λ_{ex} = UV) of a 41 Å TOPO-capped CdSe QDs LB monolayer film at different surface pressures. (Reproduced from reference 27. Copyright 2005 American Chemical Society.)

Nature of the Substrate

Photoluminescence intensity from the LB films on the hydrophilic quartz slide increased linearly ($R^2 = 0.91$) with the number of QD monolayers. This suggested that equal amounts of QDs were transferred after each deposition cycle, which resulted in a buildup of a homogeneous film. TOPO-capped QD deposited on the hydrophobic quartz substrate had a lower correlation coefficient for linearity ($R^2 = 0.77$).

One interesting phenomena is that using these QDs no emission can be detected at the air-water interface. This is explained by the study of Cordero et al. (2). The authors were using hexadecylamine stabilized CdSe particles of 4.1 nm spread on the water surface. They have found that the water molecules are oxidizing the CdSe QDs from the interface thus affecting the luminescence properties. Further it was investigated the Langmuir film of QDs having ZnS capping.

(CdSe)ZnS Quantum Dots

The (CdSe)ZnS core-shell QDs capped with TOPO ligand were prepared through a stepwise procedure as described elsewhere [36]. The average size of the CdSe/TOPO QDs was determined by UV-vis absorption spectroscopy of its chloroform solution (25, 37). By knowing the mass of CdSe/TOPO QDs used when preparing the solution and the total volume of the stock solution, the "molecular" weight of CdSe/TOPO quantum dots could be estimated.

The common coating procedure was carried out by adding a $ZnEt_2$ and $(TMS)_2S$ mixture solution dropwise into a coordination solution (TOPO/TOP as solvent) of CdSe QDs at high temperature under argon atmosphere (36).

Photophysical Properties

UV-vis spectroscopy of QDs solutions indicated an average CdSe core size or diameter of 2.9 nm (25). The amounts of $Zn(Et)_2$ and $(TMS)_2S$ were then calculated for deposition of a 0.5 nm thick ZnS shell on the QDs. The calculated average size of (CdSe)ZnS/TOPO QDs was 3.7 nm. The QD size and the thickness of the TOPO surface cap helped to explain the limiting nanoparticle area of the QDs as derived from the surface pressure-area isotherm.

The first electronic transition peak revealed a core size of 2.9 nm according to the literature (25). The PL emission peak was found to be at 571 nm with a full width at half-maximum (fwhm) of 35 nm, which indicated a very small size distribution.

Langmuir Monolayer of TOPO-capped QDs

The surface pressure- and surface potential-area isotherms give the most important characteristics of the monolayer properties. The surface pressure-area isotherm of (CdSe)ZnS/TOPO QDs is shown in Figure 6 and three distinct phases are well displayed. The film collapsed at a surface pressure of 45 $mN \cdot m^{-1}$, indicating that the (CdSe)ZnS/TOPO QDs can form a stable Langmuir monolayer at the air-water interface.

This is similar to other amphiphilic molecules such as stearic acid, whose Langmuir monolayer usually collapses at a surface pressure between 40 and 45 $mN \cdot m^{-1}$. The limiting nanoparticle area of the QDs was obtained by extrapolating the linear part of the isotherm to zero surface pressure, i.e. 1500 $Å^2$.

As discussed before, the average particle diameter obtained from TEM measurement was 3.7 nm. The TOPO cap forms a monolayer at the surface of nanocrystals (32). The thickness of a TOPO monolayer was reported to be 0.7 nm as measured on metal surfaces (20).

Then, the diameter of the TOPO-capped CdSe(ZnS) QDs should be (2 × 0.7) + 3.7 or 5.1 nm. If assuming spherical QDs, an average diameter of 4.4 nm for a single QD was calculated from the limiting nanoparticle area of the QDs Langmuir monolayer. Obviously, at the air-water interface, the TOPO moieties were compressed and resulted in a smaller observed particle size due to interdigitation of the TOPO tails (Scheme 1).

In Situ UV-vis and Photoluminescence Spectroscopies

The *in situ* UV-vis absorption spectrum of the (CdSe)ZnS QDs Langmuir monolayer was measured at the air-water interface. The first electronic transition band was clearly observed. Although the absorbance at 533 nm showed an increasing trend with increasing surface pressure of the Langmuir monolayer, the linear fit of the absorption peak as a function of surface pressure gave poor linearity, which implied that the QDs were not uniformly distributed at the air-water interface.

The same phenomenon can be found in the *in situ* photoluminescence spectra of the QDs Langmuir monolayer. In addition, the photoluminescence intensity of the QDs Langmuir monolayer showed only a slight increase with increasing surface pressure therefore in the LB film preparation, a surface pressure greater than 15 $mN \cdot m^{-1}$ was used for the deposition of the Langmuir monolayer to ensure the homogeneity of the QDs in 2D.

Photoluminescence of Langmuir-Blodgett (LB) Films of TOPO-capped QDs

LB films were prepared at three surface pressures, namely, 15, 25, and 35 $mN \cdot m^{-1}$. This choice was based on the epifluorescence measurements, which showed homogeneity in the topography of Langmuir monolayer for surface pressures higher than 15 $mN \cdot m^{-1}$. The (CdSe)ZnS QD Langmuir monolayer was deposited onto a chemically treated hydrophobic quartz substrate. The calculated transfer ratio (barrier area swept/deposited area on the slide) was close to 1.0, indicating that the slide was completely coated by the QD monolayer. In this study, five layers were deposited at three different surface pressures. Figure 7 shows the photoluminescence spectra of LB films of (CdSe)ZnS QDs deposited
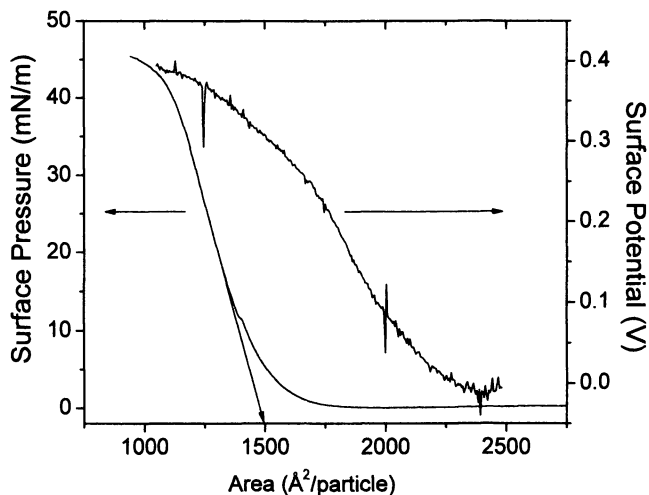
Figure 6. Surface pressure- and surface potential-area isotherms of (CdSe)ZnS/TOPO QDs.
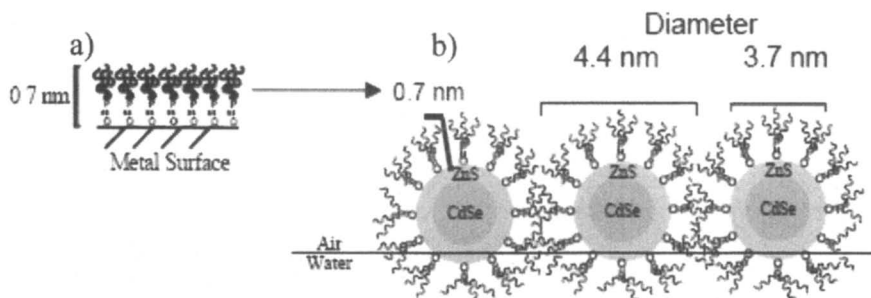
Scheme 1. Size of QDs Obtained from TEM Micrographs and Surface Pressure-Area Isotherm: (a) Reported thickness of TOPO monolayer (0.7 nm) at metal surface; (b) Model of TOPO capped QDs. The TEM measure gave a diameter of bare QD of 3.7 nm because the TOPO is nonconductive; the diameter of TOPO-capped QDs was (2×0.7) + 3.7 nm = 5.1 nm. At the air-water interface, the TOPO moieties were compressed and resulted in a smaller diameter (4.4 nm) due to the interdigitation of the TOPO tails.
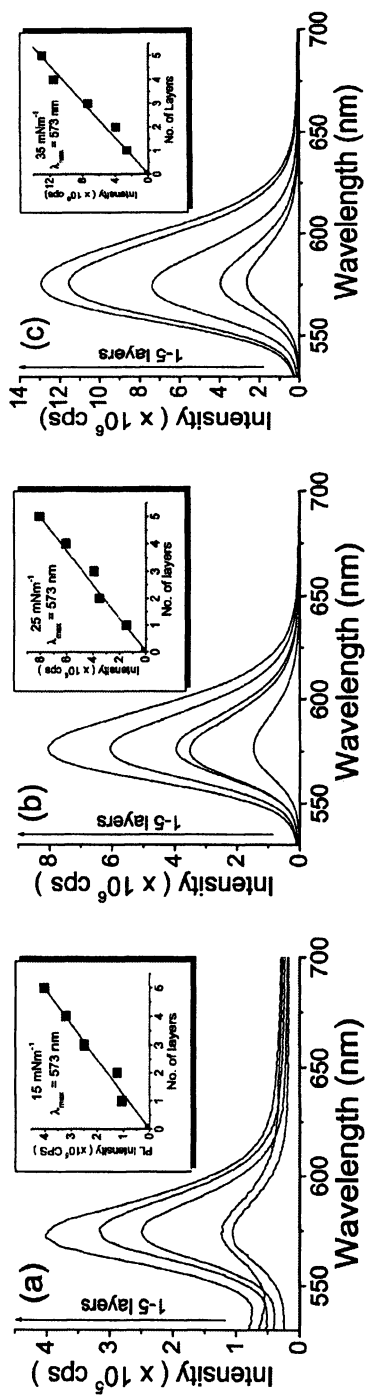
Figure 7. Photoluminescence spectra of LB films deposited at surface pressures of (a) 15, (b) 25, and (c) 35 mN·m⁻¹. The insets show the PL intensity at emission maximum (573 nm) as a function of the number of layers.

at three different surface pressures. The photoluminescent emission maximum of the QDs at 573 nm for the LB film was identical within experimental error to the value of QDs in chloroform solution (λ_{max} = 571 nm). In all three cases, the PL intensity at 573 nm increased linearly with increasing number of layers, which indicated that homogeneous Langmuir monolayers were deposited.

Recent Work

Lately, Pradhan et al. (38) investigated the electronic conductivity in Langmuir monolayers (39-42) using TOPO-protected CdSe QDs. Their experimental setup is based on the use of interdigitated arrays (IDAs) electrode that is aligned vertically at the air-water interface for *in situ* voltammetric measurements at varied interparticle distances or different surface pressures. The authors found that upon photoirradiation with photon energies higher than that of the absorption threshold, the voltammetric currents increased substantially with two of voltammetric peaks at positive potentials. Under photoirradiation, adsorption of ambient oxygen onto the particle surface leads to the efficient trapping of photogenerated electrons and hence an excess of holes in the particles (34,43-45) giving to the conductivity a dynamic profile. The authors showed that the chemical stability of the CdSe QDs and the associated photogated charge transfer mechanism were manipulated by the trapping of photogenerated electrons by adsorbed oxygen and the process is reversible just like the case of photoetching. They were able to show that the voltammetric currents can be gated by photoirradiation. The difference between the Langmuir monolayer behavior compared to the dropcast film was assigned to the presence of defects within the Langmuir monolayer and thus leading to the effects mentioned above.

Conclusions

It is clear that the use of Langmuir monolayers in controlling the interparticle distances and their application are getting more attention every day. The research on the surface engineering of quantum dots covers areas not studied in the past whether the assembly, synthetic routine, presence or absence of ZnS capping. Properties like chemical and photophysical properties are studied with various methods, e.g. UV-vis and fluorescence spectroscopies. Assemblies of QDs are studied mainly as Langmuir-Blodgett films since this technique retains most of the Langmuir monolayer properties thus giving the opportunity to investigate the films by AFM, but mainly HR-TEM. It was shown

briefly that a wide range of properties can be investigated and photophysical properties depend on factors like capping, ligand, and irradiation. Without any doubt the Langmuir and Langmuir-Blodgett film techniques are suitable tools to allow *in situ* investigation of QDs monolayers and their assembly.

Acknowledgements

References

1. Chan, W. C. W. and Nieb, S. M. *Science* **1998**, *281*, 2016.
2. Cordero, S. R.; Carson, P. J.; Estabrook, R. A.; Strouse, G. F. and Buratto S. K. *J. Phys. Chem. B* **2000**, *104*, 12137.
3. Wu, X. Y.; Liu, H. J.; Liu, J. Q.; Haley, K. N.; Treadway, J. A.; Larson, J. P. Ge; N. F.; Peale, F. and Bruchez, M. P. *Nat. Biotechnol.* **2003**, *21*, 41.
4. Coe, S.; Woo, W. K.; Bawendi, M. and Bulovic, V. *Nature* **2002**, *420*, 800.
5. Empedocles, S. and Bawendi, M. G. *Accounts Chem. Res.* **1999**, *32*, 389.
6. Heath, J. R.. *Science* **1995**, *270*, 1315.
7. Nirmal, M.; Dabbousi, B. O.; Bawendi, M. G.; Macklin, J. J.; Trautman, J. K.; Harris, T. D. and Brus, L. E. *Nature* **1996**, *383*, 802.
8. Bawendi, M. G.; Carroll, P. J.; Wilson, W. L. and Brus, L. E. *J. Chem. Phys.* **1992**, *96*, 946.
9. Bawendi, M. G.; Steigerwald, M. L. and Brus, L. E. *Annu. Rev. Phys. Chem.* **1990**, *41*, 477.
10. Nirmal, M. and Brus, L. *Accounts Chem. Res.* **1999**, *32*, 407.
11. Katari, J. E. B.; Colvin, V. L. and Alivisatos, A. P. *J. Phys. Chem.* **1994**, *98*, 4109.
12. Tittel, J.; Gohde, W.; Koberling, F.; Basche, T.; Kornowski, A.; Weller, H. and Eychmuller, A. *J. Phys. Chem. B,* **1997**, *101*, 3013.
13. Mikulec, F. V.; Kuno, M.; Bennati, M.; Hall, D. A.; Griffin, R. G. and Bawendi, M. G. *J. Amer. Chem. Soc.* **2000**, *122*, 2532.
14. Collier, C. P.; Vossmeyer, T. and Heath, J. R. *Annu. Rev. Phys. Chem.* **1998**, *49*, 371.
15. Dabbousi, B. O.; Murray, C. B.; Rubner, M. F. and Bawendi, M. G. *Chem. Mater.* **1994**, *6*, 216.
16. Murray, C. B.; Norris, D. J. and Bawendi, M. G. *J. Am. Chem. Soc.* **1993**, *115*, 8706-8715.

17. Sui, G.; Orbulescu, J.; Ji, X.; Gattas-Asfura, K. M.; Leblanc, R. M. and Micic, M. *J. Cluster Sci.* **2003**, *14*, 123.
18. Peng, Z. A. and Peng, X. G. *J. Amer. Chem. Soc.* **2001**, *123*, 183.
19. Peng, X. G.; Schlamp, M. C.; Kadavanich, A. V. and Alivisatos, A. P. *J. Amer.Chem. Soc.* **1997**, *119*, 7019.
20. Jiang, J., Krauss, T. D. and Brus, L. E. *J. Phys. Chem. B.* **2000**, *104*, 11936.
21. Alivisatos A. P. *J. Phys. Chem.* **1996**, *100*, 13226.
22. Schmelz, O.; Mews, A.; Basche, T.; Herrmann, A. and Mullen, K. *Langmuir* **2001**, *17*, 2861.
23. Striolo, A.; Ward, J.; Prausnitz, J. M.; Parak, W. J.; Zanchet, D.; Gerion, D.; Milliron, D. and Alivisatos, A. P. *J. Phys. Chem. B.* **2002**, *106*, 5500.
24. Leatherdale, C. A.; Woo, W.-K.; Mikulec, F. V. and Bawendi, M. G. *J. Phys. Chem. B* **2002**, *106*, 7619.
25. Yu, W. W.; Qu, L.; Guo, W. and Peng, X. *Chem. Mater.* **2003**, *15*, 2854.
26. Yu, W. W.; Qu, L.; Guo, W. and Peng, X. *Chem. Mater.* **2004**, *16*, 560.
27. Gattas-Asfura, K. M.; Constantine, C. A.; Lynn, M. J.; Thimann, D. A.; Ji, X. and Leblanc, R. M. *J. Am. Chem. Soc.* **2005**, *127*, 14640.
28. Seker, F.; Meeker, K.; Kuech, T. F. and Ellis, A. B. *Chem. Rev.* **2000**, *100*, 2505.
29. Wuister, S. F.; de Mello Donega, C. and Meijerink, A. *J. Phys. Chem. B* **2004**, *108*, 17393.
30. Kalyuzhny, G. and Murray, R. W. *J. Phys. Chem. B* **2005**, *109*, 7012.
31. Kuno, M.; Lee, J. K.; Dabbousi, B. O.; Mikulec, F. V. and Bawendi, M. G. *J. Chem. Phys.* **1997**, *106*, 9869.
32. Taylor, J.; Kippeny, T. and Rosenthal, S. J. *J. Cluster Sci.* **2001**, *12*, 571.
33. Kuzmenko, I.; Rapaport, H.; Kjaer, K.; Als-Nielsen, J.; Weissbuch, I.; Lahav, M. and Leiserowitz, L. *Chem. Rev.* **2001**, *101*, 1659.
34. Aldana, J.; Wang, Y. A. and Peng, X. *J. Am. Chem. Soc.* **2001**, *123*, 8844.
35. Myung, N.; Bae, Y. and Bard, A. J. *Nano Lett.* **2003**, *3*, 747.
36. Hines, M. A. and Guyot-Sionnest, P. J. *J. Phys. Chem.* **1996**, *100*, 468.
37. Harrison, M. T.; Kershaw, S. V.; Burt, M. G.; Rogach, A. L.; Kornowski, A.; Eychmuller, A. and Weller, H. *Pure Appl. Chem.* **2000**, *72*, 295.
38. Pradhan, S.; Chen, S.; Wang, S.; Zou, J.; Kauzlarich, S.M. and Louie, A.Y. *Langmuir* **2006**, *22*, 787 .
39. Chen, S. W. *Anal. Chim. Acta* **2003**, *496*, 29.
40. Greene, I. A.; Wu, F. X.; Zhang, J. Z. and Chen, S. W. *J. Phys. Chem. B* **2003**, *107*, 5733.
41. Yang, Y. Y.; Pradhan, S. and Chen, S. W. *J. Am. Chem. Soc.* **2004**, *126*, 76.
42. Yang, Y. Y.; Chen, S. W.; Xue, Q. B.; Biris, A. and Zhao, W. *Electrochim. Acta* **2005**, *50*, 3061.

43. Spanhel, L.; Haase, M.; Weller, H. and Henglein, A. *J. Am. Chem. Soc.* **1987**, *109*, 5649.
44. Koberling, F.; Mews, A. and Basche, T. *Adv. Mater.* **2001**, *13*, 672.
45. van Sark, W. G. J. H. M.; Frederix, P. L. T. M.; van den Heuvel, D. J.; Bol, A. A.; van Lingen, J. N. J.; Donega, C. D.; Gerritsen, H. C. and Meijerink, A. *J. Fluoresc.* **2002**, *12*, 69.

Chapter 14

Synthesis and Application of Fluoroalkyl End-Capped Oligomers/Silica

Hiroshi Kakehi[1,2], Masashi Muira[2], Norifumi Isu[2], and Hideo Sawada[1]

[1]Department of Materials Science and Technology, Hirosaki University, Hirosaki, Japan
[2]General Research Institute of Technology, INAX Corporation, Tokoname, Japan

Fluoroalkyl end-capped oligomers, which were prepared by the oligomerization of fluoroalkanoyl peroxides with a variety of monomers, reacted with silica nanoparticles to afford fluoroalkyl end-capped oligomer/silica nanocomposites under mild conditions. These fluoroalkyl end-capped oligomer/silica nanocomposites thus obtained have unique properties based on fluoroalkyl end-capped oligomers, such as hydrophilic-oleophobic surface characteristic and interactive activity with a variety of guest molecules. In this report, we describe two-type applications of fluorinated oligomer/silica nanocomposites. The one is the surface modification with hydrophilic-oleophobic characteristic, and the other is the encapsulation of hinokitiol possessing an antibacterial activity.

Introduction

In our research group, we have already succeeded in preparing fluoroalkyl end-capped oligomers by the oligomerization of fluoroalkanoyl peroxides with a variety of radical polymerizable monomers (*1*). These fluorinated oligomers were found to exhibit a unique surface active characteristic which can not be achieved by the corresponding traditional polysoaps. For instance, as shown in Figure 1, fluorinated oligomers were able to form the nanometer size-controlled self-assembled molecular aggregates in aqueous and organic media. These fluorinated oligomeric aggregates could interact with a variety of guest molecules such as magnetite, Au, Ag, Cu nanoparticles to afford the colloidal stable fluorinated oligomers/guest molecules nanocomposites (*2*).

Rf= -CF(CF$_3$)O[CF$_2$CF(CF$_3$)O]$_m$C$_3$F$_7$] ; m=0,1
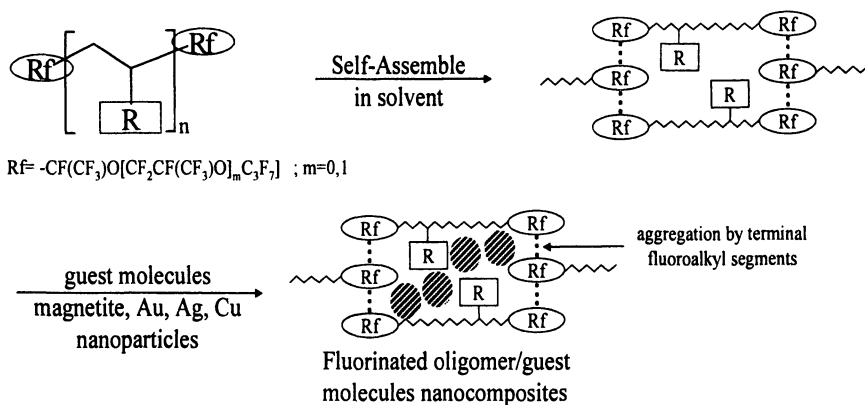
Figure 1. Formation of self-assembled molecular aggregates (2)

Additionally, as shown in Figure 2, these fluorinated oligomers were applied to the preparation of fluorinated oligomers/silica nanocomposites (*3*) and cross-linked fluorinated oligomeric nanoparticles.

Rf= -CF(CF$_3$)O[CF$_2$CF(CF$_3$)O]$_m$C$_3$F$_7$] ; m=0,1
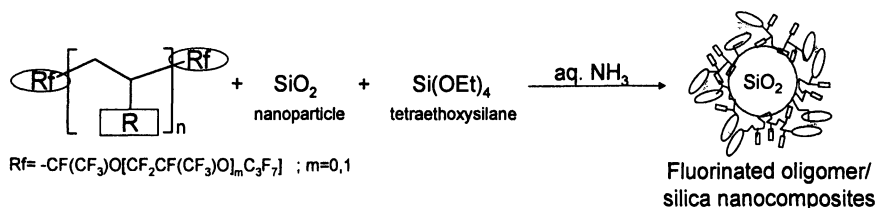
Figure 2. Synthetic approach to fluorinated oligomer/silica nanocomposites (3)

In this report, we tried to apply fluorinated oligomer/silica nanocomposites to two objectives for life space. The one is the surface modification with hydrophilic-oleophobic characteristic for anti-fouling material, and the other is the encapsulation of hinokitiol with antibacterial activity.

Application I: Surface Modification by the Use of Fluorinated Oligomer/Silica Nanocomposites

Figure 3 shows the hydrophilicity, hydrophobicity, oleophilicity and oleo-phobicity, respectively, for the surface wettability against water and oil. Traditional materials can be classified into three types of surface characters. The first is hydrophilic-oleophobic materials such as ceramics, glass and pure metal surface (4-5), the second is hydrophobic-oleophilic materials such as poly-ethylene, polystyrene and traditional organic polymers (4-5), and the third is hydrophobic-oleophobic materials such as fluorinated polymers (5-6). However, as shown in Figure 3, we can not develop the hydrophilic-oleophobic materials so far, from the surface free energytical point of view.

Figure 4a shows that relationship between surface free energy and surface wettability against water and oil. Materials possessing over around 50 mJ/m^2 surface free energy can exhibit a hydrophilic characteristic, and in contrast, materials possessing below 20 mJ/m^2 surface free energy can exhibit an oleo-phobic characteristic. Thus, ceramics possessing 60 mJ/m^2 surface free energy can exhibit a hydrophilic-oleophobic characteristic. On the other hand, fluorinated materials possessing 18 mJ/m^2 surface free energy can exhibit a hydrophobic-oleophobic characteristic. However, we can not develop new materials possessing hydrophilic-oleophobic characteristic on their surface due to the different surface free energy that is 50 mJ/m^2 and 20 mJ/m^2 (Figure 4b)).

But, fluoroalkyl end-capped oligomers have excellent surface active properties. Especially, fluoroalkyl end-capped acrylic acid oligomer (F-ACA-oligomer; Figure 5) possesses not only hydrophilic carboxyl group, but also oleophilic fluoroalkyl group. So, we tried to apply F-ACA-oligomer to the surface modification with a hydrophilic-oleophobic characteristic based on environmental responsive flip-flop mechanism (7-11).

Preparation and Characterization of Fluorinated Oligomer/Silica Nanocomposites Slurries

F-ACA-oligomer was added into aqueous alkaline silicate in the presence of silica nanoparticle as shown in Figure5. This slurry thus obtained was applied to the surface modification agent with a hydrophilic-oleophobic characteristic.
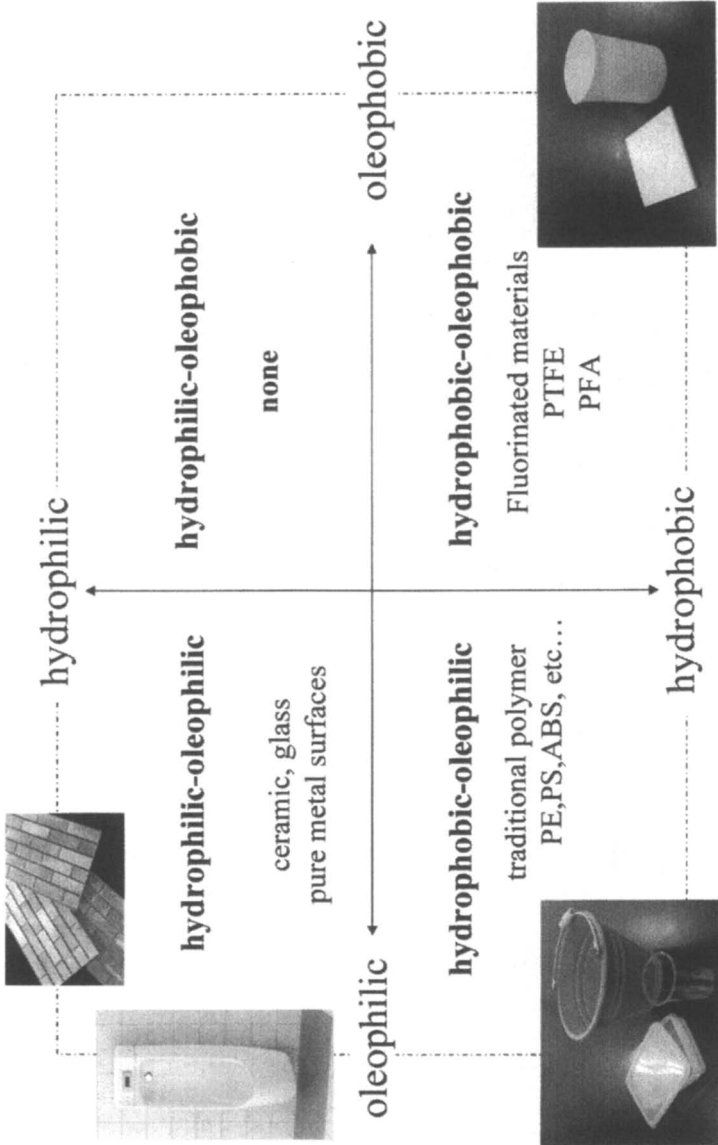
Figure 3. Surface wettability of materials

(a)

against water | against oil

higher

water 72mJ/m²

hydrophilic

⟵ ceramics with 60mJ/m²
= hydrophilic-oleophilic

50mJ/m²

oleophilic

⟵ organic polymer with 40mJ/m²
= hydrophobic-oleophilic

hydrophobic

20mJ/m²

⟵ fluorinated material with 18mJ/m²
= hydrophobic-oleophobic

oleophobic

Surface free energy

lower

air 0mJ/m²

(b)

against water | against oil

higher

hydrophilic

50mJ/m²

hydrophilic-oleophobic surface has
over 50 mJ/m² and under 20mJ/m²

can not be compatible

20mJ/m²

oleophobic

Surface free energy

lower

*Figure 4. Relationship between water or oil wettability
and surface free energy*

These F-ACA-oligomer/silica nanocomposites slurries (0 to 1.0 wt% F-ACA-oligomer) were evaluated by Dynamic Light Scattering (DLS) and Field Emission-Scanning Electron Microscopy (FE-SEM).

DLS results for these slurries (Figure 6) show that the size of these slurries nanocomposites thus obtained were found to decrease from 197 nm to 48-67 nm levels compared to the original slurry particle. Thus, it is suggested that our presented fluorinated oligomeric aggregates should strongly interact with alkaline silicate to afford a good dispersibility.

FE-SEM images show original slurry particles and fluorinated oligomer/silica nanocomposites (Figure 7). Particle size of the original slurry
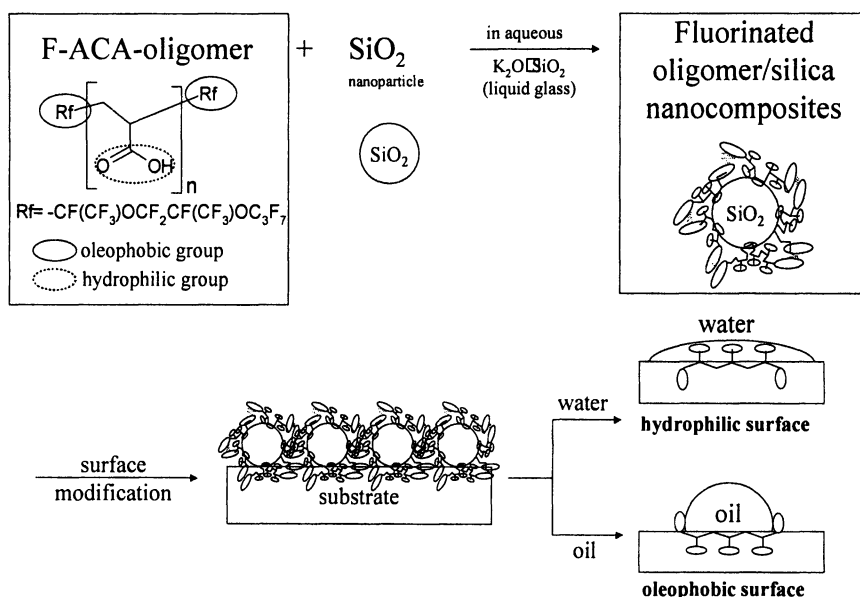
Figure 5. Application of fluorinated acrylic acid oligomer/silica nanocomposites for surface modification

was 200 nm levels due to the coagulation of silica nanoparticles, in contrast, the size of primary fluorinated oligomer/silica nanocomposites were smaller than the original slurry particles. Because these fluorinated oligomer/silica nano-composites should prevent the agglomeration of the parent slurry particle due to the presence of longer fluoroalkyl groups. In addition, it was demonstrated that these fluorinated oligomer/silica nanocomposites have a good dispersibility and stability in water.
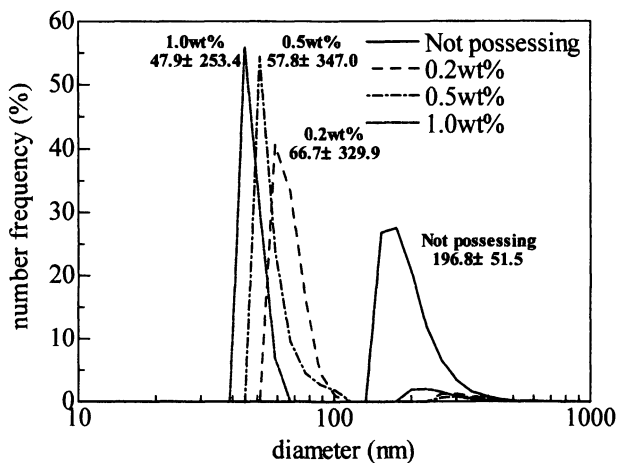
Figure 6. Particle size of fluorinated oligomer/silica
nanocomposites in slurries by DLS
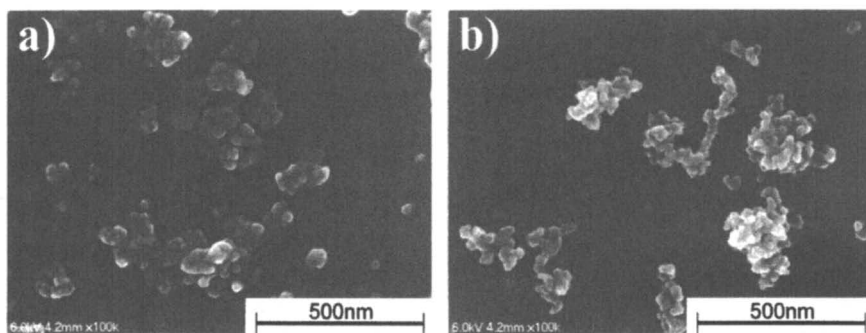
Figure 7. SEM images of fluorinated oligomer/silica nanocomposites
a) Original slurry particles without fluorinated oligomer
b) Fluorinated oligomer/silica nanocomposite possessing 1.0 wt% oligomer

Procedure

Fluorinated oligomer/silica nanocomposite slurries thus obtained were coated on the aluminum substrate surface. Firstly, slurry including silica microparticle, alkaline silicate and colorant was stirred well, and the obtained mixture was sprayed on the aluminum substrates as an undercoat. Next, fluorinated oligomer/silica nanocomposites slurries possessing 0.2, 0.5 and 1.0 wt% oligomer were sprayed on the undercoat. Similarly, we have prepared the coated aluminum substrate without fluorinated oligomer under similar conditions as the control. In addition, some of controls were modified with three type of alkoxylsilane (trimethylmethoxysilane, methyltrimethoxysilane, perfluoroalkyl-silane) as comparisons.

Measurement of Water and Oil Contact Angle

Contact angles of water and oil such oleic triglyceride were measured on these modified surfaces treated with fluorinated oligomer to evaluate surface properties (Figure 8).
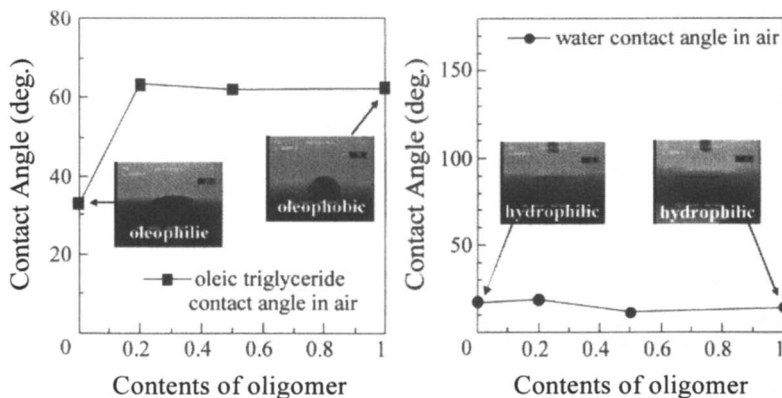
Figure 8. Contact angles of surfaces treated with fluorinated oligomer

For coated aluminum substrate with no fluorinated oligomer, the contact angle of water was 18degrees, and the contact angle of oleic triglyceride was 33.0 degree, so this surface exhibits a hydrophilic-oleo-philic characteristic. On the other hands, in the case of possessing fluorinated oligomer, contact angles of water were from 11.7 to 19.0 degrees. These values were almost same as the value of control. But, contact angles of oleic triglyceride were from 62.0 to 63.3 degrees, these values became higher than the value of the control (33.1degrees).

This result shows that the surface treated with fluorinated oligomer/silica nanocomposites should exhibit a hydrophilic and oleophobic characteristic.

On the other hand, we have measured the contact angles of water and oleic tri-glyceride on the modified surfaces treated with traditional alkoxylsilane (Figure 9). In this case, we can not have a hydrophilic-oleophobic characteristic on these surfaces. For the modified surface treated with perfluoroalkylsilane, contact angle of oleic triglyceride was 73.0 degrees and this value was almost the same as that of the surface treated with fluorinated oligomer, but contact angle of water was 108.5 degrees on this surface. This value was quite difference from the surface treated with fluorinated oligomer. Thus, such modification system should change from a hydrophilic-oleophilic to a hydrophobic-oleophobic characteristic. This result shows that fluorinated oligomer has high potential for a unique surface modification agent with a hydrophilic-oleophobic characteristic.
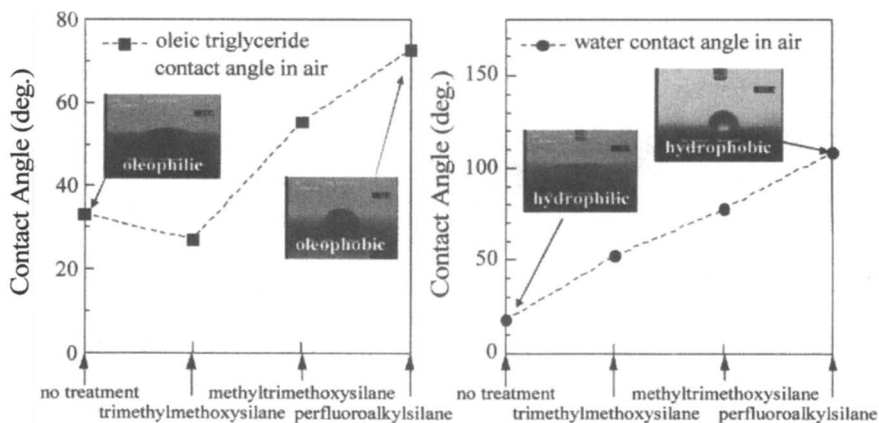
Figure 9. Contact angles of surfaces treated with alkoxylsilane

To confirm the actual effect, colored oils were dropped on surfaces treated with fluorinated oligomer, with perfluoroalkylsilane. In the case of at atmosphere, these surfaces exhibited an oil repellant characteristic against oils. Water was showered on these surfaces; the surface treated with fluorinated oligomer exhibited an extremely higher oil repellant characteristic in the presence of water. In contrast, the surface treated with perfluoroalkylsilane exhibited an oleophilic characteristic in the presence of water. This result showed that the surface treated with fluorinated oligomer has an oilrepellant property not only against air atmosphere conditions, but also in the presence of water. Therefore, the modified surface has high potential for useful anti fouling materials.

This hydrophilic-oleophobic characteristic would be due to the Flip-Flop mechanism based on hydrophilic carboxyl group and oleophobic fluoroalkyl group in fluorinated oligomer.

Application II; Preparation of Antibacterial Fluorinated Oligomer/Silica Nanocomposites Encapsulated Hinokitiol

Preparation and Characterization of Fluorinated Oligomer/Silica Nanocomposites Encapsulated Hinokitiol

Fluoroalkyl end-capped oligomers are able to form the nanometer size-controlled self-assembled molecular aggregates in aqueous and organic media (Figure 1). These fluorinated oligomeric aggregates could interact with a variety of guest molecules (2). These fluorinated oligomer/silica nanocomposites should achieve the effect on the surface. So we tried to apply the fluorinated oligomer to fluorinated oligomer/silica nanocomposites encapsulated an antibacterial activity. In fact, we have succeeded in preparing fluorinated oligomer/silica nanocomposites encapsulated hinokitiol (12). This reaction model is illustrated in Figure 10.

The preparative conditions are shown in Table I. The size of these fluorinated silica particles are nanometer size-controlled.
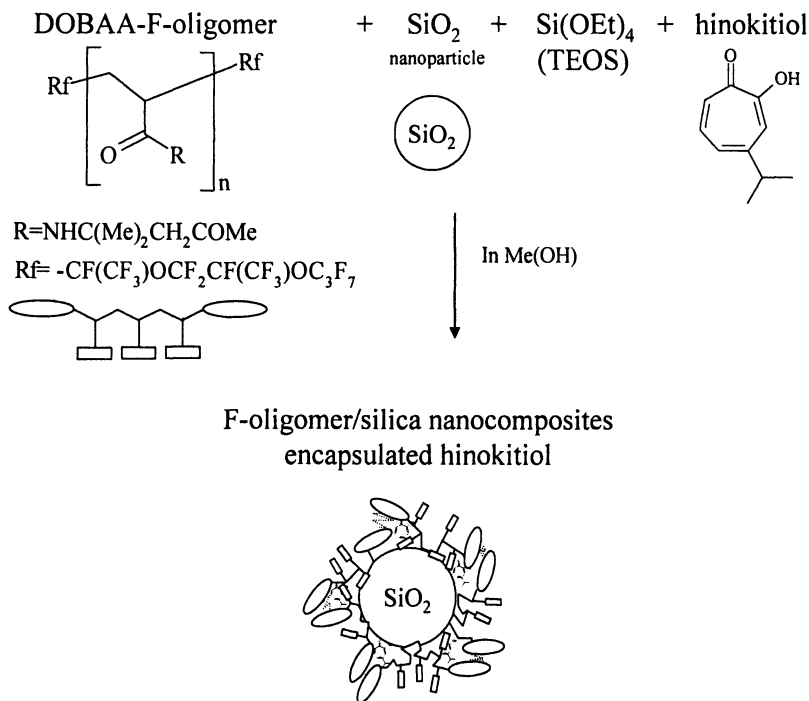
Figure 10. Formation of fluorinated oligomer/silica nanocomposites encapsulated hinokitiol

Table I. Preparation of F-Oligomer/Silica Possessing Hinokitiol

No.	oligomer (mg)	TEOS (mg)	silica (mg)	aq.-NH$_3$ (ml)	hinokitiol (mmol)	reaction time	Yield[a] (%)	Particle size[b] (nm)	Contents of hinokitiol[c](%)
a-1	80	80	80	12	0.12	4h	52	86± 12	51
a-4	80	80	80	12	0.24	4h	51	117± 25	37
a-6	80	80	80	12	0.48	4h	46	120± 23	28
a-7	80	80	80	12	0.60	4h	30	166± 30	21
a-2	80	80	80	12	0.24	1day	38	563± 104	48
a-3	80	80	80	12	0.12	1day	46	294± 50	63

a) Yield are based on Fluorinated oligomer, TEOS, SiO$_2$ and hinokitiol
b) Average particle size in MeOH was determined by DLS measurement
c) Contents of hinokitiol in nanoparticle determined by UV-vis. Spectra or TGA based on the used hinokitiol

Thermal stability of these fluorinated oligomer/silica nanocomposites encapsulated hinokitiol were measured by TGA (Figure 11). The weight loss of the nanocomposites encapsulated hinokitiol was increased compared to that of the original nanocomposites. This suggests that hinokitiol should be strongly encapsulated into fluorinated oligomer/silica nanocomposites.
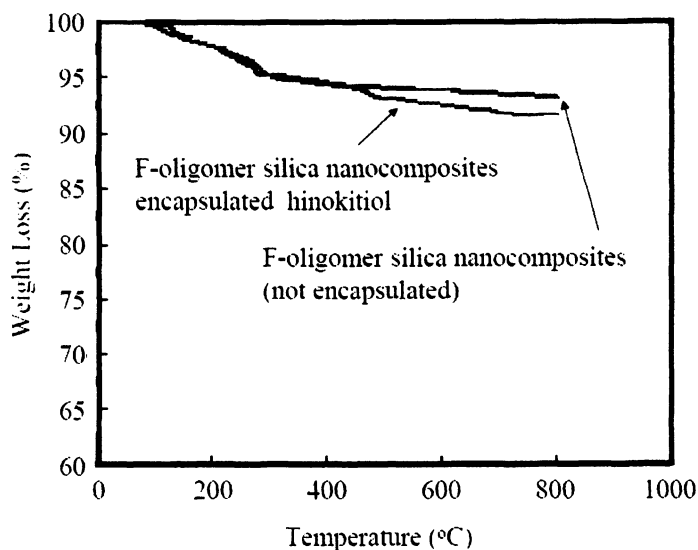
Figure 11. Thermogravimetric Analyses of fluorinated oligomer/silica nanocomposites encapsulated hinokitiol

Fluorinated oligomer/silica nanocomposites encapsulated hinokitiol were evaluated by Antibacterial examination against *Staphylococcus aureus*. Results were shown in Table II. For the fluorinated nanocomposites possessing 11.0 % hinokitiol, numbers of colonies were 1/10,000 compared with the control system, and for the nanocomposites possessing over 13.6 % hinokitiol, the bacteria completely died out. This result shows that fluorinated oligomer/silica nanocomposites encapsulated hinokitiol exhibit a good antibacterial activity.

Conclusions

Surface modification with a hydrophilic-oleophobic characteristic was achieved by using fluorinated oligomer/silica nanocomposites slurries. This modified surface exhibited a hydrophilic-oleophobic characteristic based on the environmental changes from hydrophilic to oleophobic conditions against oil on

Table II. Antibacterial Activity of Fluorinated Oligomer/Silica Nanocomposites Encapsulated Hinokitiol against *Staphylococcus aureus*

Run	Contents of Hinokitiol in Nanocomposites[a]	S. aureus (CFU)[b]
	Control	4.8×10^6
a-1	11.0%	1.0×10^2
a-4	13.6%	<10
a-6	22.0%	<10
a-2	25.2%	<10
a-7	28.8%	<10

[a] Contents of Hinokitiol based on the obtained nanocomposite (wt%)
[b] Concentration of nanocomposites : 500mg/mlb

their surface. Therefore, this surface has high potential for useful anti-fouling materials.

Fluorinated oligomer/silica nanocomposites encapsulated hinokitiol have been prepared and these nanocomposites were demonstrated to exhibit a good antibacterial activity.

References

1. Sawada, H.; Gong, Y.-F.; Minoshima, Y.; Matsumoto, T.; Nakayama, M.; Kosugi, M.; Migita, T. *J. Chem. Soc., Chem. Commun.* **1992**, 537-538.
2. Sawada, H. *Prog. Polym. Sci.* **in press**.
3. Sawada, H.; Narumi, T.; Kajiwara, A.; Ueno, K.; Hamazaki, K. *Colloid Polym. Sci.* **2006**, *284*, 551-555.
4. Erb, R. A. *J. Phys. Chem.* **1965**, *69*, 1306.
5. *Physical Surfaces*; Bikerman, J. J.; Academic Press: New York and London, **1970**; p259.
6. Yoshino, N.; Nakaseko, H.; Yamamoto, Y. *Reactive Polym.* **1994**, *23*, 157-163.
7. Vaidya, A.; Chaudhury, M. K. *J. Colloid Interface Sci.* **2002**, *249*, 235-245.
8. Rivero, M.; Rodriquez, V.; Joseph, D.; Guevara, E.; Carabano, N. U. S. Patent 5,385,175, **1995**.
9. Tarumi, Y.; Yamaguchi, H. JPN. Patent 2,877,616, **1999**. (in Japanese)
10. Sakasita, H.; Morita, M.; Kubo, M. *Sen'i Gakkai Preprints*. **1997**, 124.
11. Morita, M.; Nagasima, K.; Watanabe, T.; Huwa, T. *Journal of Society Cosmetic Chemists Japan.* **2002**, *36*, 45-49.
12. Sawada, H.; Kakehi, H.; Koizumi, M.; Katoh, Y.; Miura, M. *J. Mater. Sci.*, **in press**.

Chapter 15

Conduction in Colloidal Systems: A Kinetic Study of Ag₂S Semiconductor Nanoparticle Formation

Madeline S. León-Velázquez[1], Marissa Morales[1], Roberto Irizarry[2], and Miguel E. Castro[1]

[1]Chemical Imaging Center, University of Puerto Rico at Mayaguez, Mayaguez, Puerto Rico 00680
[2]DuPont Electronic Technologies, 14 T. W. Alexander Drive, Research Triangle Park, NC 27709

The synthesis of metal and semiconductor nanoparticles has received widespread attention by the scientific community due to the large number of technological applications they find in nanoscaled systems. The mechanism of nanoparticle growth is, in general, still an open question. The general picture that emerges from previous works is that nanostructures form from the self assembly of atoms and nuclei in solution. The driving forces involved in this self assembly are not well known. There is little doubt that electrostatic and magnetic interactions among atoms and small nuclei play an important role in the synthesis and growth of nanostructures. We have employed real time-conductivity measurements to measure the kinetics of Ag₂S nanoparticle growth. Conductivity measurements reflect the electrical stability and order of the colloid, which are well known to result from a delicate balance of electrostatic and magnetic forces. Ag₂S semiconductor nanoparticles absorb light deep in the UV (about 230-240 nm). Conductivity measurements on this synthesis are an attractive approach to study the mechanism of nucleation. In this work a stopped flow system is used to study reaction growth kinetics of the formation of Ag₂S nanoparticles. The kinetic data obtained indicates that the reaction mechanism involves multiple steps.

Conductivity and optical absorption measurements indicate that the semiconductor, nucleation and coalescence of particles occur in a time scale shorter than 5 seconds after the flow of Ag^+ and S^{-2} is brought to a stop.

Introduction

The synthesis of metal and semiconductor nanoparticles has received widespread attention by the scientific community due to the large number of technological applications they find in nanoscaled systems (1–3). The mechanism of nanoparticle growth is, in general, still an open question. Studies based on light absorption associated to silver and gold particle growth have been published (4–5). A few studies have relied on the fluorescence of semiconductor nanoparticles to monitor particle growth. These previous works have contributed significantly to the current body of knowledge related to the mechanism of nanoparticle growth.

The purpose of this work is to explore on the use real time-conductivity measurements as an alternative tool to measure the kinetics of nanoparticle growth. If successful, such studies may be extended to systems that do not have suitable optical absorption bands or do not exhibit fluorescence. For this purpose, we have focused in the synthesis of Ag_2S from the reaction of silver cations, Ag^+, with sulfide anions, S^{-2}. Ag_2S semiconductor nanoparticles absorb light deep in the UV (about 230-240 nm) and exhibit a strong fluorescence in the visible at low temperatures (6). Conductivity measurements on this synthesis are an attractive approach to study the mechanism of nucleation for the overall reaction:

$$2\,Ag^+ + S^{-2} \rightarrow Ag_2S \qquad (1)$$

results in the formation of an insoluble solid with a K_{SP} of the order of 10^{-50}. Thus a decrease in conductivity is expected to be observed in reaction mixtures of Ag^+ and S^{-2} as they form Ag_2S.

Experimental

Silver solutions were prepared by dissolving silver nitrite (ACS grade Fisher) in deionized water, obtained from a Culligam system. Sulfide solutions were prepared using ammonium sulfide solutions (Alfa Aesar) in deionized water. The concentration ranges of both solutions were from 8.0 x 10^{-2}M to 1.0 x

10^{-3}M. Reaction mixtures were studied in a Biologic Stop flow reactor model SFM 400. The reactor is equipped with cell suitable for UV-Visible light absorption measurements and two electrodes for conductivity measurements. UV-visible absorption measurements were performed with an Ocean Optic spectrometer coupled to the stop flow reactor with two UV grade fiber optics. The STM experiments where performed in a nanosurf easyscan.

Results and discussion

The dependence of molar conductivity, Λ, on the square root of $AgNO_3$ and $(NH_4)_2S$ concentration, are displayed in Figure 1. At solutions of low concentrations the molar conductivity of the electrolytes is proportional to the square root of the concentration as per the Kohlraush's law (7,8). The equation is as follows:

$$\Lambda = \Lambda_o - \alpha\, C^{1/2} \qquad (2)$$

where Λ is the molar conductivity, C is the ion concentration, α is a scaling factor, and Λ_o represents the limiting molar conductivity (6,7). The linear dependence of the silver nitrate and ammonium sulfide solutions molar conductivity on the square root of the corresponding solution concentration was verified experimentally in this work. Limiting molar conductivities of about 0.0157 and 0.0207 mS·m^2/mol are found for the silver nitrate and ammomium sulfide solutions, respectively.

The dependence of conductivity on time for a stoichiometric mixture of Ag^+ and S^{-2} is displayed on Figure 2. A flow mixture is prepared in the reactor and at time t = 0 seconds the flow is brought to a stop. The optical absorption spectra the reaction mixture is also displayed on Figure 2. The optical absorption spectra were measured at the times indicated by the arrows. There is no significant absorption of light at times t $\leq$ 0 seconds. Independent experiments on Ag^+ and S^{-2} ions exhibit absorption bands at 228 and 237 nm, respectively. The 240 nm band dominates the optical absorption spectrum about 5 seconds after the flow is stopped. This is the only band observed for reaction times as long as 135 seconds, indicating that it represents the final product of the reaction between Ag^+ and S^{-2}. We attribute this band to the formation of Ag_2S, which is the thermodynamically stable form of silver sulfide. In bulk Ag_2S, this band appears around 230 nm (6). In the reaction mixture prepared under the experimental conditions described previously, Ag_2S formed is likely to be present in colloidal form and therefore to exhibit a shift in absorption wavelength as compared to solid Ag_2S.
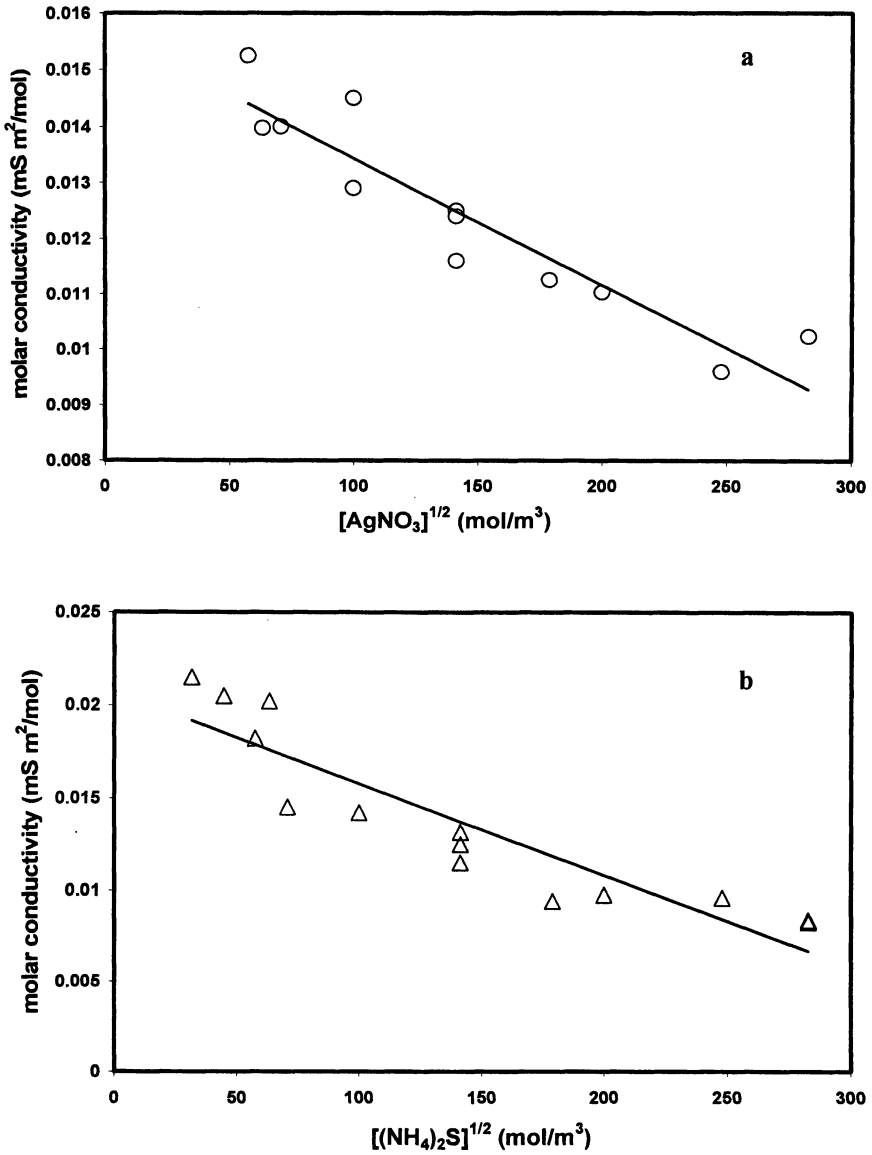
Figure 1. Dependence of molar conductivity, Λ, on (a) AgNO$_3$ and (b) (NH$_4$)$_2$S concentration.
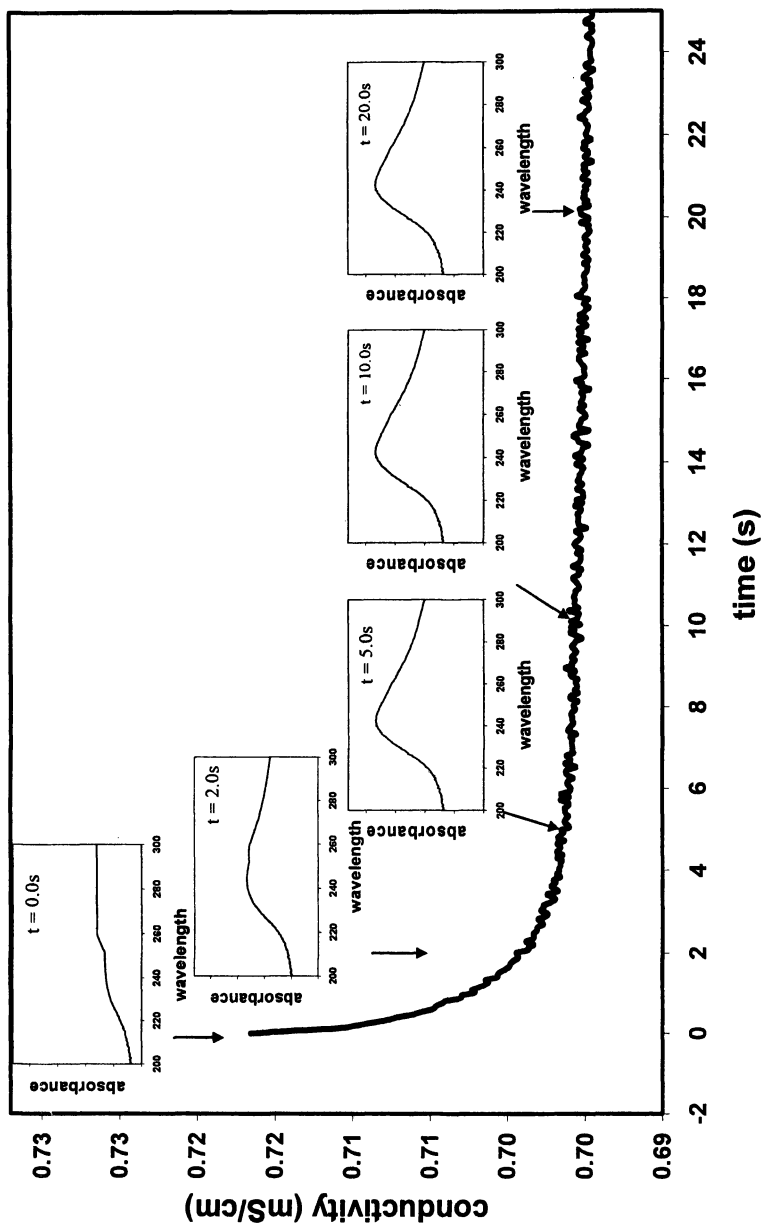
Figure 2. Dependence of conductivity on time for the reaction mixture of Ag^+ and S^{-2}. The insert represent the optical absorption spectra of the same reaction mixture obtained at the times indicated by the arrows. See text for details.

The conductivity of the equimolar reaction mixture displayed on Figure 2 exhibits an interesting dependence on time. There is a sharp decrease in the conductivity with time after the flow is brought to a stop at time t = 0 seconds and extends to about 4 seconds. There is a slow decrease in the conductivity with time after t = 4 seconds. The dependence of the conductivity on time is consistent with the observations discussed on the previous paragraphs regarding the optical absorption spectra of the reaction mixture. Accordingly, the sharp decrease in the conductivity results from the reduction in the number of Ag^+ and S^{-2} ions which forms neutral Ag_2S.

Under the conditions of our experiment, the Ag_2S is in colloidal form, i.e., it does not precipitate as a solid in the reaction cell. The absence of a solid precipitate in the cell was verified by visual observation in the optical microscope with a magnification factor of 50 X, consistent with the formation of colloidal Ag_2S. We however note that despite the fact that the Ag_2S is formed in colloidal form, the conductivity of the solution remained relatively high. This could be because (1) the Ag_2S nanoparticles are conductive instead of the semiconductor that is presumed, (2) the spectator ions are making a significant contribution to the conductivity or (3) there is an un expected conduction mechanism involved in the process. To rule out the first alternative, we performed STM and dI/dV measurements on solid deposits of the Ag_2S prepared under the experimental conditions discussed earlier.

Figure 3 shows results of STM measurements performed on dry deposits of the Ag_2S colloid. The particles are smaller than 8 nm, although agglomeration results in islands larger than 20 nm.

Measurements of the tunneling current as a function of bias voltage were performed to decide if the Ag_2S nanoparticles are conductive or a semiconductor. The dI/dV versus bias voltage is displayed on Figure 4. The inset in figure 4 shows the original I-V curves of the Ag_2S particles. The dI/dV –V curve is typical of semiconductors. We estimate a band gap of about 0.90 eV[9] across the board: detailed examination of the figure and based on the onsets reveal a band gap close to 0.70 eV. Since the data displayed on Figures 3 and 4 are consistent with the formation of a semiconductor, measurements were performed to establish if the spectator ions contribute significantly to the solution conductivity. For this purpose, reaction mixtures of Ag^+ and S^{-2} as a function of time were studied and the solution molar conductivity was determined in the limit of time going to infinity.

The results are summarized on Figure 5. The molar conductivities of these solutions (circles) are compared with that of a saturated Ag_2S solution (squares), measured under identical experimental conditions. The molar conductivity of this solution is smaller than the one observed for the colloidal Ag_2S prepared here. Also displayed on Figure 5 is the calculated molar conductivity obtained by adding the molar conductivity of all the ions in solution (triangles). In this
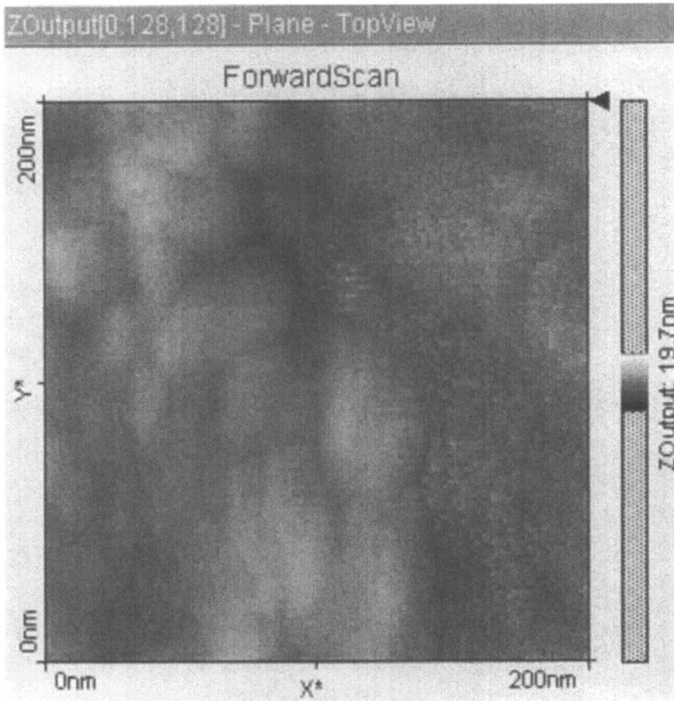
Figure 3. STM image of dry Ag₂S deposit.
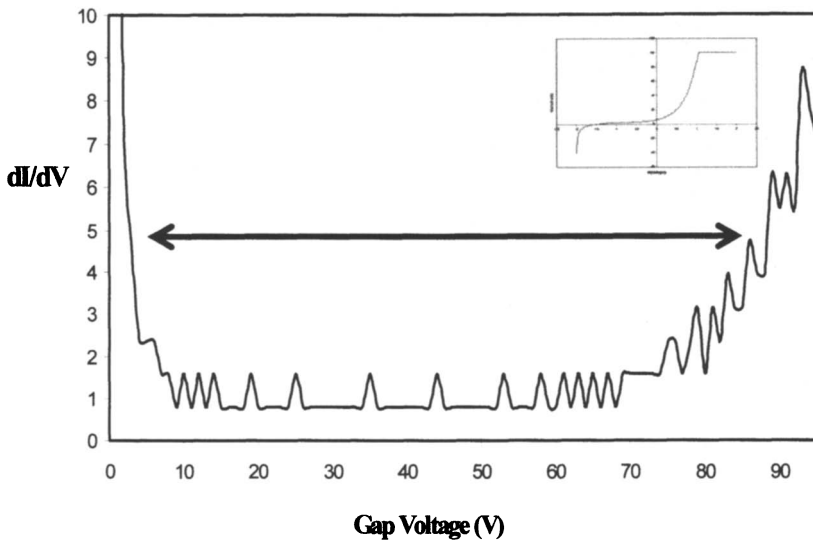
Figure 4. Plot of dI/dV vs. gap voltage for Ag₂S nanoparticles.

case, the molar conductivity measured experimentally is significantly higher than the calculated for the spectator ions in solution, indicating that they can not account for the unusually high conductivity of Ag_2S colloid.
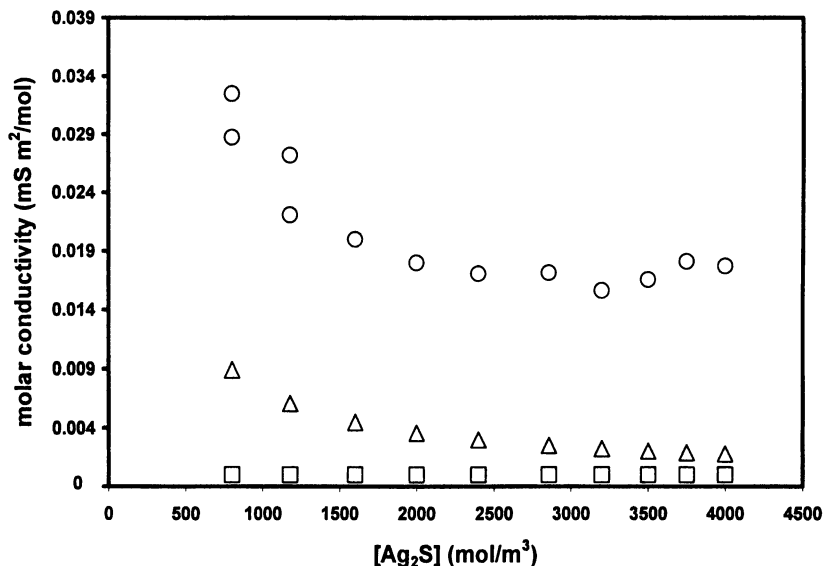
Figure 5. Molar conductivity of Ag_2S as a function of colloidal Ag_2S concentration (circles). The triangles and squares represent the ionic conductivity calculated for the spectator ions in solution and for a saturated solution of $Ag_2S_{(s)}$.

If the conductivity of the reaction mixture cannot be accounted by the metallic nature or the independent conductivities of the spectator ions in solution, why then does the Ag_2S colloid exhibit such a high conductivity? One possibility is that the ions are transported by the colloidal nanoparticles. Indeed, this is plausible since Ag_2S is a well known Ag^+ ion conductor. More recently, the contribution of free Ag_2S transport, either electronic or ionic, in thin Ag_2S films has been reported. It is possible that a similar effect takes place here, but further experiments are necessary to establish the conduction mechanism in Ag_2S colloids. Indeed, measurements of the physical properties of Ag_2S reveals that it behaves like a silver ion transport fluid. STM measurements to be published elsewhere reveal detailed ordering of Ag_2S, probably reflecting a similar ordering in solution. Further speculation is unwarranted until conductivity measurements are performed as a function of voltage to determine if there is a semiconductor to conductor transition in the material.
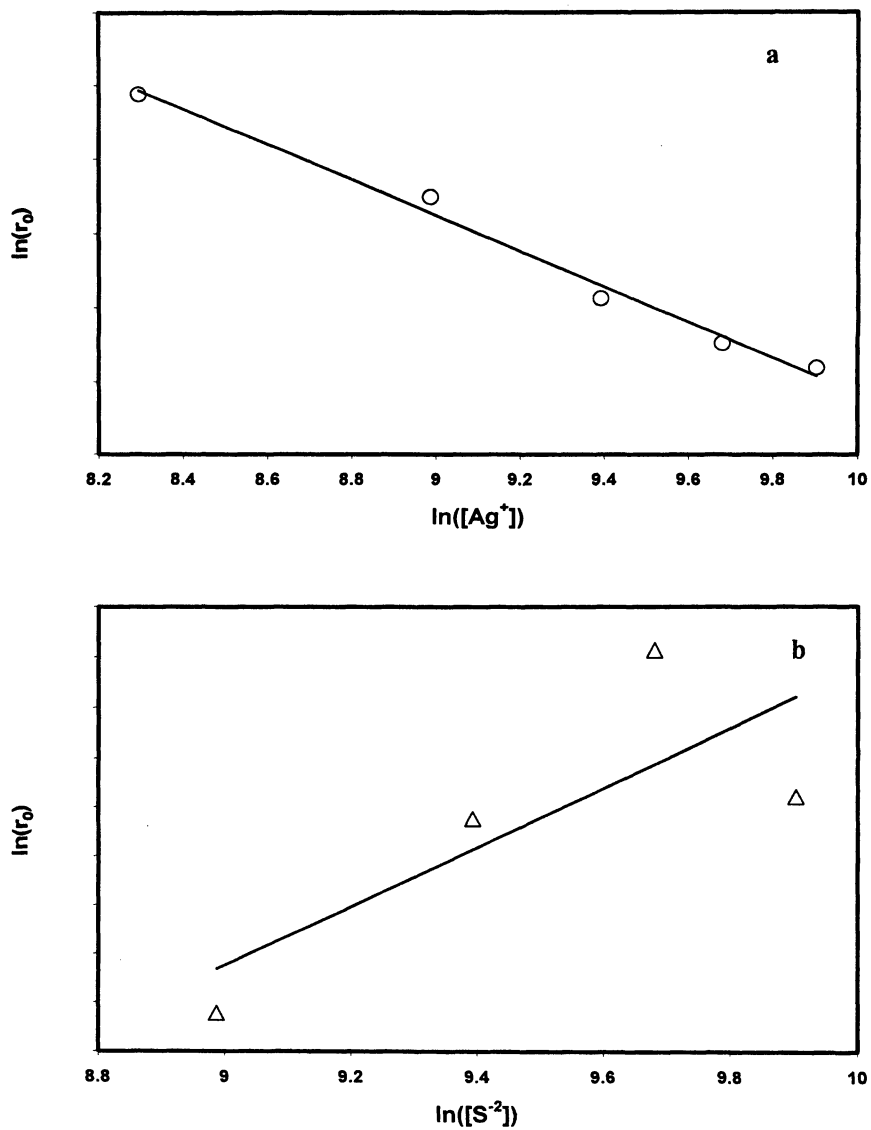
Figure 6.   ln (r_0) as a function of (a) ln ([Ag$^+$]) and (b) ln ([S^{-2}]) .

Since the solubility product or Ag_2S is of the order of 10^{-50}, the formation of silver sulfide may be regarded as irreversible. Thus the increase in concentration with time is proportional to the rate of formation of Ag_2S:

$$r \ \alpha \ dc/dt \tag{3}$$

where r is the reaction rate. To establish the reaction rate, we performed measurements of solution conductivity as a function of initial Ag^+ and S^{-2} concentration. Assuming that the reaction is quantitative, the concentration can be related to the reaction conductivity according to (7,8):

$$c = [(\Lambda_0 - \Lambda)/\alpha]^2 \tag{4}$$

from which the reaction rate can be obtained The dependence of the reaction rate, as determined from conductivity measurements like the one displayed on Figure 2, on initial Ag^+ and S^{-2} concentration were further studied in this work with the purpose of establishing the form of the rate law or the reaction described by equation 1. Graphs of the $\ln(r_0)$ as a function of $\ln(Ag^+)$ and $\ln(S^{-2})$ are displayed in figure 6. From the slope of the plots displayed on Figure 6, we estimate that the reaction has a -1.1 order on Ag^+ and a $+1.0$ order in S^{-2}. The fact that these reaction orders are markedly different from the stoichiometric numbers described in equation 1 indicates that the reaction mechanism involves multiple steps.

Summary

In summary, we have employed optical absorption and conductivity measurements to study the formation of Ag_2S semiconductor nanoparticles. The kinetic data is consistent with a reaction mechanism involves multiple steps. Conductivity and optical absorption measurements indicate that the semiconductor, nucleation and coalescence of particles occur in a time scale shorter than 5 seconds after the flow is brought to a stop.

References

1. J. R. Lakowicz, I. Gryczynski, Z. Gryczynski, and C. J. Murphy, *J. Phys. Chem. B.* **1999**, *103*, 36, 7613-7620
2. C. B. Murray, D. J. Noms, and M. G. Bawendi, *J. Am. Chem. Soc.* **1993**, *115*, 8706-8715
3. A. van Dijken, E.A. Meulenkamp, D. Vanmaekelbergh, and A. Meijerink, *J. Luminescence* **2000**, *90*, 123-128

4. Sarkar, A., Kapoor, S., and Mukherjee, T., *J. Phys. Chem. B.* **2005**, *109*, 7698-7704.
5. Jana, N. R, Gearheart, L., and Murphy, C. J., *Langmuir* **2001**, *17*, 6782-6786.
6. Brühwiler, D., Leiggener, C., Glaus, S., and Calzaferri, G., *J. Phys. Chem. B.* **2002**, *106*, 3770.
7. Atkins, P. and de Paula J., *Atkins Physical Chemistry*, 7th edition (2002), Oxford University Press Inc., New York.
8. Bard, A. and Faulkner L., *Electrochemical methods fundamentals and applications*, 2nd edition (2001), John Wiley & Sons, Inc.
9. Kryukov, A.I., Stroyuk, A.L., Zin'chuk, N.N., Korzhak A.V.,. Kuchmii, S.Ya, *J. Molecular Catal. A: Chemical* **2004**, *221*, 209-221.

Ultrabright Fluorescent Silica Particles: Physical Entrapment of Fluorescent Dye Rhodamine 640 in Nanochannels

Sajo Naik[1] and Igor Sokolov[1,2,*]

Departments of [1]Physics and [2]Chemistry, Clarkson University, Potsdam, NY 13699

We have studied templated sol gel synthesis of fluorescent silica particles. Organic fluorescent dye Rhodamine640 (R640) was physically (non-covalently) entrapped inside closed type nanochannels. The assembly at different temperatures and concentrations of silica precursor were investigated. We also studied a possible leakage of R640 dye from the nanochannels and suggested a way to arrest the leakage by secondary vapor phase silica coating on the particles. This method will ultimately lead to the synthesis of ultra bright silica nanoparticles.

Introduction

Fluorescent particles have a broad application in tagging, tracing, and labeling (*1–5*). Fluorescence is typically made through incorporating either inorganic or organic fluorescent dyes into the particle's material. Inorganic dyes, being typically more stable, are rather restricted in choice and usually toxic. A large variety of commercial organic dyes makes them attractive for using in fluorescent particles. The problems are in the dye stability and typically its toxicity as well. Incorporation of dyes into silica matrix seems to be one of most promising approaches because of excellent sealing ability of silica and wide compatibility of with other, included bio-, materials. Numerous attempts to embed organic dyes into silica xerogels and zeolites have been known for long time (*6-15*). To prevent leakage of the dyes out of the porous matrix, dyes were

chemically bound to the silica matrix (*9,11,16-18*). While photostability of such materials was higher than stability of pure dyes, it did not prevent bleaching substances, including oxygen, from penetration inside such a composite material. In the case of xerogel, it is rather hard to use it for labeling because it doesn't produce well formed particles.

Uniform and well-ordered silica structure nano(meso) porous silica particles are gaining importance as micro-containers for storing dyes and other fluorescent molecules. Ozin and co-workers (*19-23*) have described synthesizing a zoo of well-formed mesoporous silica particles in the shape of discoids, spheres or fibers, collectively called as origami particles. These particles were synthesized at room temperature from $TEOS/CTACl/HCl/H_2O/HCONH_2$ sol and their formation mechanism involves polymerization-induced differential contraction of a patch of hexagonal silicate liquid-crystal film formed at the air-water interface, which can fold into particles by somewhat mimicking "origami" folding. Due to this unique formation mechanism, the particles have a closed type structure endowing it to be much suitable for storage of dye, fluorescent molecule or other molecules species of interest.

Recently it has been shown (*24*) that encapsulation of rhodamine 6G dye inside the channels of micron-size nanoporous particle makes those particles fluorescently ultra-bright. The particles have fluorescence about 170 times brighter than the similar size assembles of quantum dots. The synthesized particles are complex nanostructured objects that can be described as tightly packed arrays/bundles of silica nanochannels/nanotubes. The increase in fluorescence comes from two reasons: 1. Attaining higher concentrations of the organic fluorescent dye molecules inside the tubes without the dye dimerization (which would quench fluorescence); 2. Physical entrapment of the dye inside the silica nanotubes (which doesn't decrease quantum yield of each molecule).

Maintaining high concentration of the dye without dimerization can be explained by one-dimensional confinement of the molecules inside the tubes (the silica walls between the tubes/channels naturally do not let the dye molecules dimerize in perpendicular to the channels directions) and the presence of surfactant molecules inside the tubes, which can act as dispersants.

In this work we show that the above synthesis can be extended to rhodamine 640 fluorescent dye. The synthesis preserves high concentration of the dye inside the particles retaining high fluorescent activity of the dye. This means that we can report assembly of another sort of ultrabright fluorescent particles. Moreover, the effect of temperature on the synthesis of well-formed and ultra-bright fluorescent mesoporous silica particles will be investigated. The problem of slow dye leakage will be discussed. We will show that by providing secondary vapor phase silica coating the leakage of dye from the mesostructure could be arrested.

Experimental

A mixture of closed type mesoporous silica particles, mostly comprising discoids, together with fibers, spheres, etc. and collectively called as origami was synthesized using, tetraethyl orthosilicate, TEOS (98%, Aldrich) as the silica source, cetyltrimethylammonium chloride, CTAC (25 % aqueous, Aldrich) as the SDA in presence of hydrochloric acid (36% aqueous, J T Baker) and Formamide, $HCONH_2$ (98%, Aldrich). Rhodamine 640, R640 (Exciton Inc.) was added to the sol to be incorporated in the resulting particles.

The investigated molar sol composition range and temperature for the synthesis are shown in Table 1. Concentrated HCl was added to $CTAC/H_2O$ (resistance 18 M Ω cm, MilliQ ultra pure)/$HCONH_2$ solution taken in a high density polypropylene (HD-PP) bottle, and the mixture was magnetically stirred at 500 rpm for 10 min, and aged at room temperature for 2 h. TEOS was then added to the above sol under stirring, and the resulting sol was stirred for 1 minute at ambient conditions. The sol was then allowed to react at a fixed temperature under quiescent condition for 3-5 days. The sol is clear for a few minutes after mixing of the reactants, and then turbidity sets in after a few hours. The product was recovered by filtration using a Buckner funnel under vacuum, washed several times with distilled water and subsequently dried at 70 °C for 2 h.

To estimate the amount of dye from the discoids, a calculated amount of the particles were dispersed in 0.2 M ethanolic KOH solution under vigorous stirring for 24 h to disintegrate the particles and liberate dye in ethanol. After filtering out the remnant solid, the dye concentration in the clear solution was estimated by using a UV-VIS spectrophotometer (Ocean Optics, USB2000). A standard calibrations curve was prepared by dissolving known amounts of dye in 0.2 M ethanolic KOH to estimate accurately the dye trapped in the discoids. To measure fluorescence of the particles, a fluorescent spectrophotometer (Varian, Cary Eclipse) was used. To prevent the change of fluorescence because of particles' sedimentation, a magnetic stirring was used.

The powder x-ray diffraction (XRD) patterns on the particles were collected on an M03X-HF, Bruker AXS, instrument using CuKα radiation (40 kV, 40 mA) and in the range of 1.5− 8, 2 theta. The confocal laser microscopy (CLM) images of the fluorescent particles were taken on a Nikon, D-Eclipse C1-Microscope. The N_2 adsorption/desorption isotherms of the calcined mesoporous silica samples were measured at 77 K on NOVA 1200e, Quantachrome Co. instrument. Before the measurement, calcined samples were degassed at 350 °C and 10 Pa for at least 12 h. The Barett, Joyner and Halenda (BJH) method *(25)* considered the desorbed amount in two parts. First there is evaporation of pore cores corresponding to the Kelvin equation, which produced open pores with some remained adsorbed film. In addition, there is Nitrogen desorbed from the previously opened pores, which will correspond to a decrease of the adsorbed film thickness.

Results and Discussion

As was shown previously (*20,24,26*), the closed type mesoporous silica particles in the shape of discoids, spheres or fibers, origami particles are formed by a process involving folding of the mesoporous silica film formed at the liquid-air interface. Due to coiling of the film domains, ribbons (*26*) the resulting particles have close type structure facilitating retention of dye molecules. The zoo of shapes includes mostly discoids and fibers. Here we show that the synthesis is quite robust against the change over several parameters. The changes in molar sol compositions together with the synthesis temperature are summarized in Table 1. The synthesis sols show pH of 1.5–2. Formamide functions as a pH stabilizer preventing the pH variation during long synthesis hours.

Table 1. Molar Composition for the Synthesis of the Particles

Sample	Molar sol composition						$T\,^oC$	Morphology
	TEOS	HCl	CTAC	H_2O	$HCONH_2$	R640		
O-1	0.13	7.8	0.11	100	9.8	0.005	25	Origami
O-2	0.13	7.8	0.11	100	9.8	0.005	4	Origami
O-3	0.13	7.8	0.11	100	9.8	0.005	-17	No Shapes
O-4	0.13	7.8	0.11	100	9.8	0.005	65	Origami
O-5	0.05	7.8	0.11	100	9.8	0.005	25	Origami
O-6	0.3	7.8	0.11	100	9.8	0.005	25	Origami
O-7	0.8	7.8	0.11	100	9.8	0.005	25	Origami
O-8	1.2	7.8	0.11	100	9.8	0.005	25	No Shapes

From Table 1, it is clear that origami particles could be formed from the sol of molar composition TEOS 0.13: 7.8HCl: 0.11CTAC: 100H$_2$O: 9.8 HCONH$_2$, between the studied temperature range 0-65 °C. Origami particles were however not obtained at very low temperature (-17 °C). The CLM images of some of the particles, O-1 to O-4, are shown in Figure 1 (A) – (D), respectively.

Well-formed particles, mostly discoids and fibers, are seen for samples O-1, O-2 and O-4, synthesized at 25, 0 and 65°C, respectively. The sample O-3, synthesized at -17 °C did not show any special morphology. The lack of formation of origami particles at that low temperature could presumably be explained on the basis energy consideration for bending and folding of mesoporous silica film at very low temperatures.

To form a compact particle from a film mesoporous ribbon, some minimum of Brownian motion might be needed. This motion might not be enough for
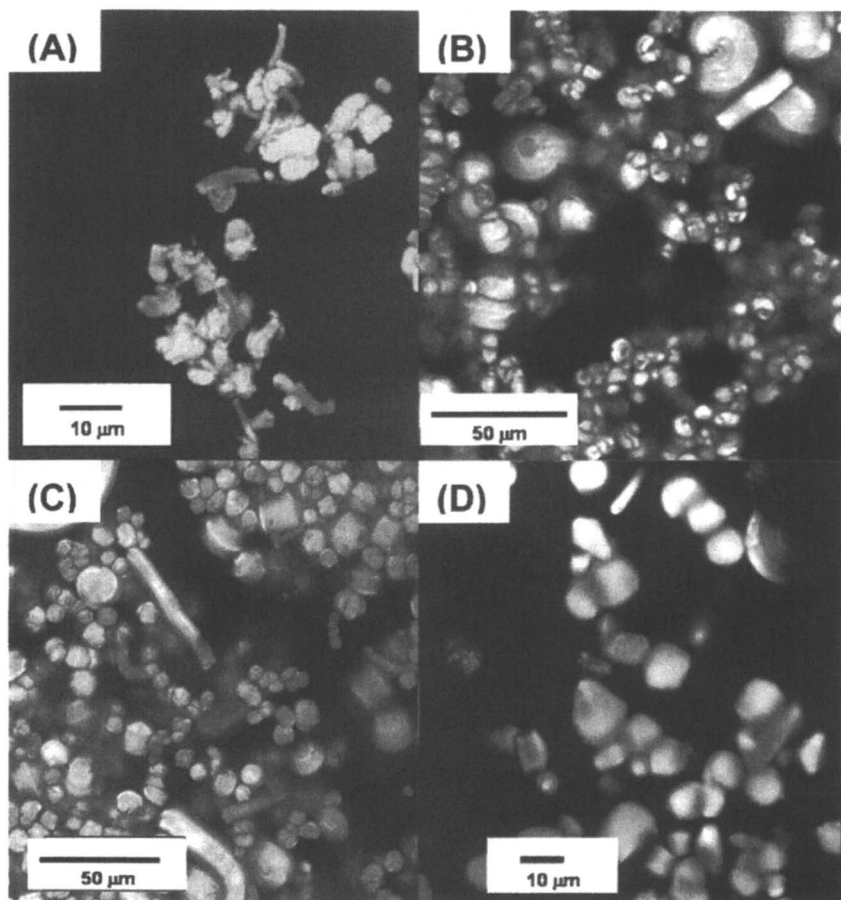
Figure 1. CLM images of ultra-bright fluorescent origami samples indicating the effect of temperature on their formation; images (A), (B), (C) and (D), correspond to samples O-3, O-2, O-1 and O-4, respectively, synthesized at temperatures, -17°C, 4°C, 25°C and 65°C, respectively. The samples were prepared from sol of molar composition 0.13 TEOS: 7.8HCl: 0.11CTAC: 100H₂O: 9.8 HCONH₂: 0.005 R640.

those low temperatures. At the low temperature is it ribbon bending and folding must have been considerably slower or could have been prevented altogether.

We found that all the samples showed mesoporous *p6mm* structure from XRD. A representative XRD image of O-1 is shown in Figure 2. The mesoporosity in the sample O-1 was confirmed from N_2 adsorption desorption isotherms measured for the calcined sample at -77 K and shown in Figure 3. This is a type IV isotherm with a step rise at ~ 0.2 P/P_0 and hysteresis that is typical of high quality mesoporous materials. The mesopore diameter of 2.4 nm was estimated from the adsorption branch of the isotherm according to the correlation obtained from BJH theory. The total pore volume was 0.85 cm^3/g and the BET surface area was 1200 m^2/g.

We also varied the TEOS concentration in the sol from 0.05 to 1.2 in the sol TEOS: 7.8HCl: 0.11CTAC: 100H_2O: 9.8 HCONH$_2$, forming samples O-5 to O-8, to study the formation of ultra-bright fluorescent origami particles. Well-formed particle could be obtained up to TEOS molar concentration of 0.8 in the sol, samples O-5 to O-7. Further increase in the concentration of TEOS did not yield origami particles as confirmed from CLM, highlighting the effective optimum TEOS/CTAC ratio for the obtainment of the particles.
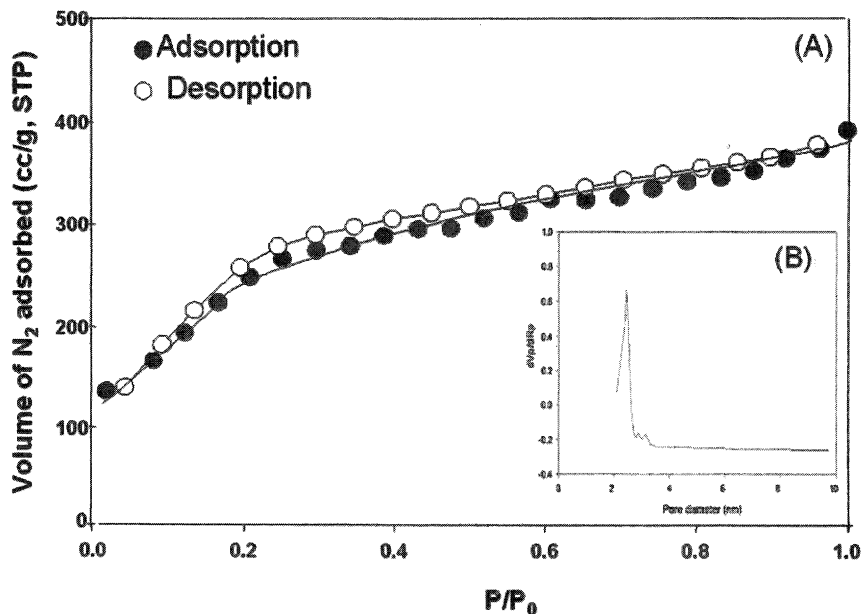
Figure 2. XRD patter of origami sample O-1, prepared from sol of molar composition 0.13TEOS: 7.8HCl: 0.11CTAC: 100H$_2$O: 9.8 HCONH$_2$ at 25°C.
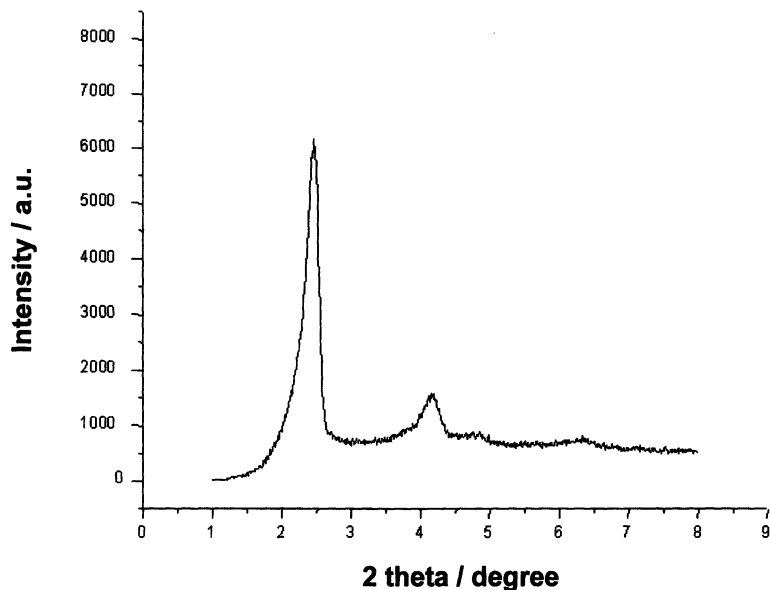
Figure 3. N₂ adsorption/desorption plot (A) measured at -77 K for calcined sample O-1. Insert (B) is the pore size distribution calculated using BJH correlation.

The ultra-bright fluorescent nature of these particles with rhodamine R6g dye molecules inside nanochannels has been recently reported (*24*). Similarly, we study the spectral behavior of the dye R640 after encapsulation in the channels. Figure4 shows the fluorescence emission for different excitation wavelengths for both free dye in water and the dye encapsulated in the particles. While the maxima of the fluorescence of the dye after encapsulation are slightly shifted, there is more explicit difference, the encapsulated dye can be excited more effectively for smaller wavelengths than the dye in water. Presumably it is related to partial dimerization of the dye. It will be investigated in future works. As was discussed in (*24*), the additional factor in the uncertainty of the experiment is related to the extinction of light by scattering by silica matrix. However even with all the uncertainty, we can conclude that our particles have ultra bright fluorescence, see below.

To find now how the particles are really bright, we need to find the amount of the dye retention in the origami particles. Sample O-1 was used as a representative for this study. The total amount of dye trapped inside the mesoporous structure was estimated to be 0.01070 g/g of dry silica, after thorough washing of the sample with deionized water to remove the loosely held dye on the exterior of the particle surface. This is similar to what was reported in ref.(*24*). Comparing these to the brightest so far 1.2-μm beads that contains 50,000 quantum dots (*27*), one can conclude that synthesized here particles
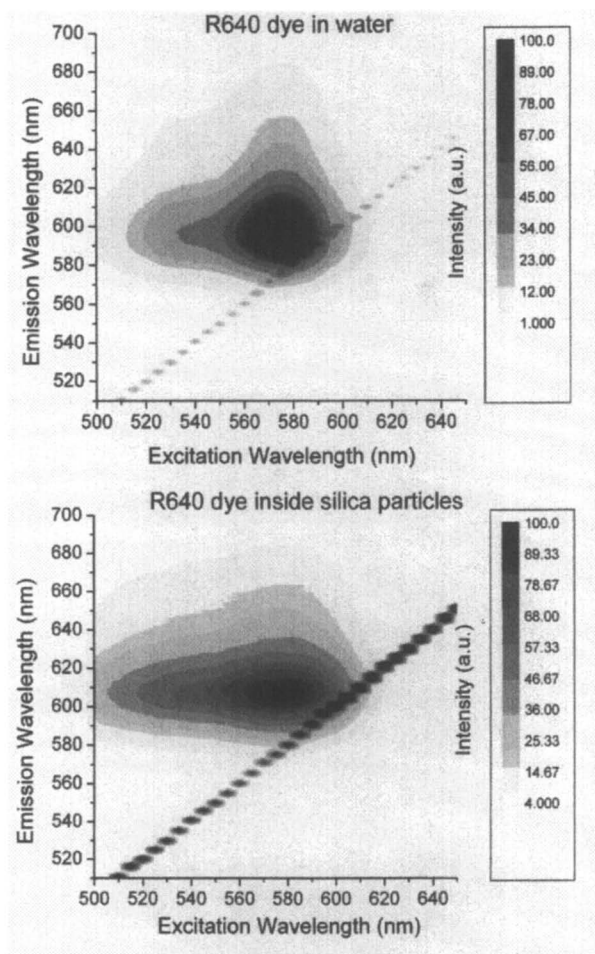
Figure 4. Fluorescence of R640 dye in water and encapsulated in the nanochannels of the particles

scaled to the same size can be ~ 120 times brighter. To find it, we used the ratio brightness between quantum dots and rhodamine 6G molecules 20:1 as found in ref.(*28*).The exact proportion depends on some other parameters, for example, on the refractive index of the particle itself (this determines how much light penetrates inside the particles). Placing known amount of particles in a cuvette, and measuring its fluorescence, we can compare to it to the fluorescence from water solution of the dye of known concentration. Thus, we can compare the amount of fluorescence per each molecule of the dye in water vs each molecule of the encapsulated dye. This was done for the maximum of the dye absorbance (575nm). We found that the dye in water produces about 3.7 times more

fluorescence than the dye inside the particles. Which portion of it is due to the scattering will be studied in the future works.

It is important to address the issue of a possible leakage of the dye molecules out of the synthesized particles. After initial washing the particles with the DI water by centrifugation (stopped after we observed no dye in the supernatant), we did not observe leakage of the dye when the particles are suspended in water. However, switching to an organic media, we did observe the leakage. For example, we found that ~75% of the dye was leaked out from the particles after dispersing in ethanol. Presumably, ethanol reacts with silica surface partially breaking open the coiled mesopores releasing the dye in the solvent. To circumvent this serious problem of dye leakage, we provided a secondary coating of silica onto the particle surface by vapor phase silica coating technique using the modification of the process developed by Nishiyama and co-workers (29).

The ultra-bright fluorescent origami particles were coated with CTAC sol, dried, and treated at 50 °C with TEOS vapor, in presence of HCl, in a closed vessel resulting in a thin secondary coating of silica on origami particles. The morphology, structure of the ultra-bright fluorescent origami particles did not change upon this treatment. The modified particles showed dye leakage of less than 10% markedly improving its capacity to retain dye in alcoholic solvents. Figure 5 shows visualization of the leakage of the dye out of the particles in a water solution of glycerol. A droplet of glycerol was placed on one side of a coverslip sitting on a microscope slide. Aqueous dispersion of the particles was between the slide and coverslip. This creates a gradient of the glycerol flow in the direction shown in the figure by an arrow. One can clearly see leakage of the dye out of the particles before coating and no leakage after the coating. As to the noted that the amount of leakage is really small, and can be clearly seen only in switching to "colorized grayscale" mode of the confocal microscope. We believe that this simple technique of providing secondary silica coating onto the particles is a very attractive approach for preventing the dye leakage from the nano-structures.

In conclusion, we will like to say that despite the definite interest in having micron size fluorescent silica particles; there is a strong interest in ultra bright fluorescent silica nanoparticles. We hope that the described synthesis will be extended to the synthesis of nanoparticles. This is possible simply because of the fact that the synthesis of large particles inevitably passes through the stage of nanosize. This idea has been used by us (29) to demonstrate feasibility of such synthesis.

Acknowledgements
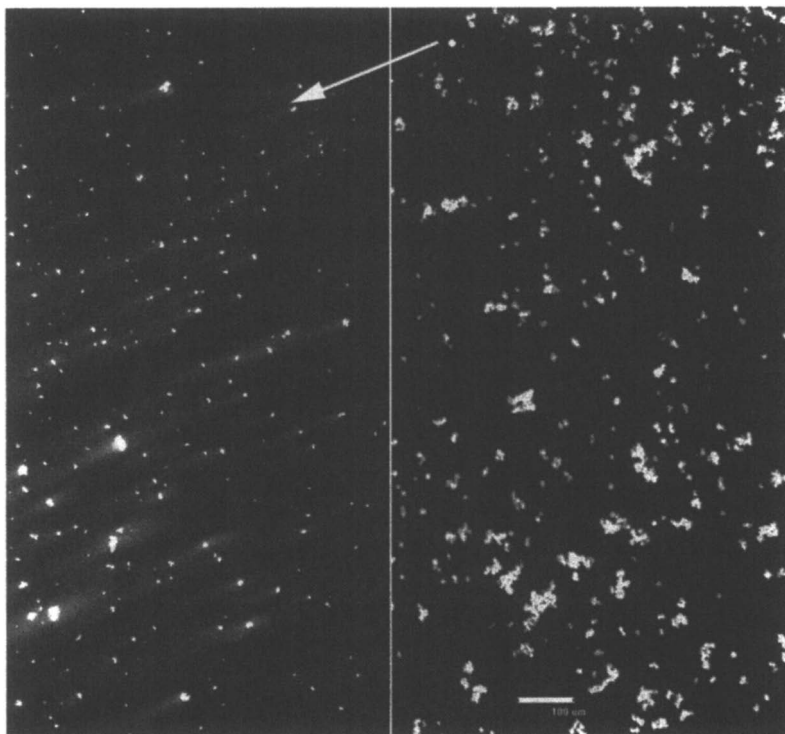
Figure 5. A collage of two confocal images of the particles in a gradient of glycerol flow. The arrow shows the direction of the flow. One can clearly see leakage of the dye from uncoated particles (left) and no leakage after the coating (right image). The scalebar is 100 microns.

References

1. Hasegawa, U.; Nomura, S. I.; Kaul, S. C.; Hirano, T.; Akiyoshi, K. *Biochem Biophys Res Commun* **2005**, *331*, 917-921.
2. Edwards, B. S.; Oprea, T.; Prossnitz, E. R.; Sklar, L. A. *Curr Opin Chem Biol* **2004**, *8*, 392-398.
3. Lizard, G.; Monier, S.; Prunet, C.; Duvillard, L.; Gambert, P. *Ann Biol Clin (Paris)* **2004**, *62*, 47-52.
4. Meldal, M. *Biopolymers* **2002**, *66*, 93-100.
5. Ohata, H.; Yamada, H.; Niioka, T.; Yamamoto, M.; Momose, K. *J Pharmacol Sci* **2003**, *93*, 242-247.
6. Rao, A. P.; Rao, A. V. *Materials Letters* **2003**, *57*, 3741-3747.
7. Klonkowski, A. M.; Kledzik, K.; Ostaszewski, R.; Widernik, T. *Colloids Surf. a-Physicochem.Eng. Asp.* **2002**, *208*, 115-120.

8. Deshpande, A. V.; Kumar, U. *J. Non-Crystalline Solids* **2002**, *306*, 149-159.
9. Leventis, N.; Elder, I. A.; Rolison, D. R.; Anderson, M. L.; Merzbacher, C. I. *Chem. Mater.* **1999**, *11*, 2837-2845.
10. del Monte, F.; Levy, D. *J. Phys. Chem. B* **1998**, *102*, 8036-8041.
11. Suratwala, T.; Gardlund, Z.; Davidson, K.; Uhlmann, D. R.; Watson, J.; Peyghambarian, N. *Chem. Mater.* **1998**, *10*, 190-198.
12. Calzaferri, G.; Huber, S.; Maas, H.; Minkowski, C. *Angew. Chem. Int. Ed.* **2003**, *42*, 3732-3758.
13. Ow, H.; Larson, D.; Srivastava, M.; Webb, W. W.; Baird, B.; Wiesner, U. *Abstracts of Papers of the American Chemical Society* **2003**, *225*, U639-U639.
14. Zhao, X. J.; Bagwe, R. P.; Tan, W. H. *Adv. Mater.* **2004**, *16*, 173-176.
15. Santra, S.; Xu, J.; Wang, K.; Tan, W. *J Nanosci Nanotechnol* **2004**, *4*, 590-599.
16. Frantz, R.; Carbonneau, C.; Granier, M.; Durand, J. O.; Lanneau, G. F.; Corriu, R. J. P. *Tetrahedron Lett.* **2002**, *43*, 6569-6572.
17. Baker, G. A.; Pandey, S.; Maziarz, E. P.; Bright, F. V. *J. Sol-Gel Sci. Technol.* **1999**, *15*, 37-48.
18. Lin, Y. S.; Tsai, C. P.; Huang, H. Y.; Kuo, C. T.; Hung, Y.; Huang, D. M.; Chen, Y. C.; Mou, C. Y. *Chem. Mater.* **2005**, *17*, 4570-4573.
19. Yang, S. M.; Yang, H.; Coombs, N.; Sokolov, I.; Kresge, C. T.; Ozin, G. A. *Adv. Mater.* **1999**, *11*, 52-55.
20. Yang, S. M.; Sokolov, I.; Coombs, N.; Kresge, C. T.; Ozin, G. A. *Adv. Mater.* **1999**, *11*, 1427-1431.
21. Yang, H.; Coombs, N.; Dag, O.; Sokolov, I.; Ozin, G. A. *J. Mater. Chem.* **1997**, *7*, 1755-1761.
22. Ozin, G. A.; Yang, H.; Sokolov, I.; Coombs, N. *Adv. Mater.* **1997**, *9*, 662-667.
23. Yang, H.; Coombs, N.; Sokolov, I.; Ozin, G. A. *Nature* **1996**, *381*, 589-592.
24. Sokolov, I.; Kievsky, Y.; Kaszpurenko, J. M. *Small* **2007**, *3*, 419-423.
25. Barrett, E. P.; Joyner, L. G.; P., H. P. *J. Am. Chem. Soc.* **1951**, *73*, 373.
26. Sokolov, I.; Kievsky, Y. *Studies in Surface Science and Catalysis* **2005**, *156*, 433-443.
27. Han, M. Y.; Gao, X. H.; Su, J. Z.; Nie, S. *Nature Biotechnology* **2001**, *19*, 631-635.
28. Chan, W. C. W.; Nie, S. M. *Science* **1998**, *281*, 2016-2018.
29. Nishiyama, N.; Tanaka, S.; Egashira, Y.; Oku, Y. *Chem. Mater.* **2005**, *15*, 1006.

Synthesis, Passivation, and Stabilization of Nanoparticles, Nanorods, and Nanowires by Microwave Irradiation

V. Abdelsayed, A. B. Panda, G. P. Glaspell, and M. S. El Shall[*]

Department of Chemistry, Virginia Commonwealth University, Richmond, VA 23284

In this chapter, we present several examples of the synthesis of high quality, nearly monodisperse passivated nano-structures of controlled size and shape. Specifically, we focus on the synthesis of II-VI semiconductors, TiO_2, rare earth oxides, CeO_2, metal and metal oxide nanostructures.

The synthesis and characterization of nanocrystals with controlled size and shape have attracted rapidly growing interest both for fundamental scientific interest and many practical and technological applications (*1-3*). The shape control and assembly of nanostructures into organized patterns provide valuable routes to the design of functional materials and to a variety of applications (*1-3*). Several methods based on physical and chemical approaches have been developed for the synthesis of controlled size and shape of nanostructures. Examples of these approaches include solvothermal methods, template-assisted, kinetic growth control, sonochemical reactions, and thermolysis of single-source precursor in ligating solvents (*1-7*).

Microwave Irradiation (MWI) methods provide simple and fast routes to the synthesis of nanomaterials since no high temperature or high pressure is needed. Furthermore, MWI is particularly useful for a controlled large-scale synthesis that minimizes the thermal gradient effects (*8-17*). Due to the difference in the solvent and reactant dielectric constants, selective dielectric heating can provide significant enhancement in reaction rates. The rapid transfer of energy directly to the reactants (faster than they are able to relax), causes an instantaneous internal

temperature rise. By using metal precursors that have large microwave absorption cross-sections relative to the solvent, very high effective reaction temperatures can be achieved. This allows the rapid decomposition of the precursors thus creating highly supersaturated solutions where nucleation and growth can take place to produce the desired nanocrystalline products. These conditions lead to the formation of very small nanocrystals since the higher the supersaturation the smaller the critical size required for nucleation. The growth of the newly formed nanocrystals can be effectively inhibited by the adsorption of ligating organic surfactants that bind strongly to the nanocrystals, thus stabilizing and passivating the surface. Furthermore, selective adsorption of the ligating organics can significantly slow down the growth of the nanocrystal in all but the favorable crystallographic plane thus resulting in a one dimensional (1D) structure. Since in MWI it is possible to quench the reaction very early on (~10 s), this provides the opportunity of controlling the nanostructures from small spherical nuclei to short rods to extended assemblies of nanowires by varying the MWI reaction time and the relative concentrations of different organic surfactants with variable binding strengths to the initial precursors and to the nanocrystals.

MWI methods have been demonstrated for the synthesis of a variety of high quality, nearly monodisperse semiconductor nanoparticles as well as one-dimensional nanostructures (8-17). In this chapter, we describe several examples of the application of MWI for the synthesis of a variety of passivated nanostructures of controlled size and shape.

Experimental

For the synthesis of sulfides, a single precursor, metal ethyl xanthate was used and for selenides, a mixture of metal acetate and selenourea precursors was used (16). Another method for the synthesis of CdSe and PbSe involved the use of a selenium solution prepared by dissolving Se powder in a mixture of trioctylphosphine (TOP) / trioctylphosphine oxide (TOPO) with octadecene as a solvent (18). In all cases, a solution of the metal precursor and the appropriate ligands [hexadecylamine (HDA), octadecylamine (ODA), oleic acid (OAc), oleylamine (OAm)] was placed in a conventional microwave oven (2.45 GHZ) with the power set to 60% of 650 W and operated in 30-s cycles (on for 10 s, off and stirring for 20 s) for reaction times that varied from 10 seconds to several minutes. In some cases, N,N-dimethylformamide (DMF) was added to ensure the solubility of all reagents and to avoid the formation of inhomogeneous solutions as, for example, a result of the poor solubility of selenourea in alkylamines.

For the synthesis of colloidal TiO_2, titanium butoxide + titanium tetrachloride were used as precursors and a mixture of OAc/OAm as ligating solvents (19). For the synthesis of rare earth oxides, metal acetate or metal

acetylacetonate was used as a precursor and a mixture of OAc/OAm as ligating solvents (17). For the synthesis of Au, Ag, Pt, Ni, and Co, the precursors used were HAuCl$_4$, silver acetate, platinum acetylacetonate, nickel acetylacetonate, and Co$_2$(CO)$_8$, respectively. After microwaving for the desired time, the synthesized nanocrystals were washed with ethanol, centrifuged, and re-dispersed in hydrophobic solvents such as toluene or dichloromethane.

The size of the nanocrystals is tuned by varying the concentration of the precursors and the MWI times, while the shape is controlled by varying the concentration and composition of the ligating solvents which stabilize the nanocrystals by passivating the surfaces. Table I summarizes the experimental parameters used for the synthesis of nanocrystals of controlled size and shape.

Results and Discussion

A. Semiconductor Sulfide and Selenide Nanostructures

TEM micrographs of the as-prepared spherical CdS, ZnS and PbS nanoparticles are displayed in Figures 1-a, 1-c and 1-e, respectively. These particles are prepared in a mixture of oleic acid and olylamine using short MW reaction times (1-3 min, Table I). However, after 3-4 min of MW irradiation using only olylamine; a mixture of rods, dipods, and tripods is obtained for CdS (Fig. 1-b). For ZnS and PbS short rods (Fig. 1-d) and cube-like or square plates (Fig. 1-f), respectively are obtained at longer reaction times.

Figure 2 displays TEM images of fully developed ZnS rods (Fig. 2-a), with an average diameter of 1 nm and an average length of 5±0.05 nm synthesized in ODA with a microwave reaction time of 2 min. The nanorods self-assemble into large arrays of highly ordered 2-D supercrystals. At longer reaction times (3-5 min), wires spontaneously form (Fig. 2-b) with the same narrow widths as the rods, and lengths of more than 350 nm (an aspect ratio of ~300). The growth mechanism of the rods involves the adsorption of the amines on both of the long side walls of the rods and only on one end of the head-to-tail spacing between the nanorod tips (20,21).

The XRD patterns of the spherical sulfide nanoparticles are shown in Figure 3. All the XRD patterns of the nanoparticles match well to the standard patterns of the corresponding bulk materials. The broadening of the XRD peaks is due to the small particle size consistent with the TEM images. In most cases, the particle size increases by increasing the MW reaction times.

The CdS nanoparticles exhibit the hexagonal (wurtzite) structure while the ZnS and PbS exhibit the cubic (zinc blende) and rock salt structures, respectively. For bulk ZnS, the cubic phase is more stable at room temperature while the hexagonal phase is more stable only at higher temperatures nearly

Table I. Experimental Parameters for the MW Synthesis of Nanocrystals

Nano crystals	Precursors / Ligating Solvents / Mole Ratio / MW Time	Shape
CdS	CdXn / OAm-OAc / (1:16:16) / 1-3 min	Spherical
	CdXn / OAm / (1:30) / 4-10 min	Tripods
	CdXn / ODA-DMF / (1:1) / 1-2 min	Tripods
ZnS	ZnXn / OAm-OAc / (1:16:16) / 1-4 min	Spherical
	ZnXn / OAm / (1:30) / 5-10 min	Rods
	ZnXn / ODA-DMF / (1:1) / 1-3 min	Rods
	ZnXn / ODA-DMF / (1:1) / 4-10 min	Wires
PbS	PbXn / OAm-OAc / (1:16:16) / 10-60 sec	Spherical
	PbXn / OAm-OAc / (1:16:16) / 2-10 min	Plates or Cubes
CdSe	$Cd(ac)_2$ – Se / TOP-TOPO / (1:5:29:55) / 1-2 min	Spheres + Short Rods
	$Cd(ac)_2$ – $SeC(NH_2)_2$ / ODA / (1:1:9) / 3-10 min	Rods + Tripods
ZnSe	$Zn(ac)_2$ / $SeC(NH_2)_2$ / ODA (1:1:9) / 1-2 min	Rods
	$Zn(ac)_2$ / $SeC(NH_2)_2$ / ODA (1:1:9) / 3-10 min	Wires
PbSe	$Pb(ac)_2$ / Se / TOP-TOPO / (1:8:41:78) / 1-2 min	Star-like + Belts
	$Pb(ac)_2$ / Se / TOP-TOPO / (1:8:41:78) / 3-5 min	Cubes + Belts
TiO_2	$TBO + TiCl_4$ / OAm-OAc / (4:15:9) / 5-10 min	Spherical
	$TBO + TiCl_4$ / OAm / (1:6) / 15-20 min	Rods
	$TBO + TiCl_4$ / OAm-OAc / (1:6:18) / 10-15 min	Cube-like + Plates
	$TBO + TiCl_4$ / OAm-OAc / (1:6:9) / 10-15 min	Star-like aggregates
Rare Earth Oxides	Acetate or Acetylacetonate / OAm-OAc / (1:17:17) / 3-10 min (1:22:14) / 3-10 min (1:27:9) / 3-10 min	Spherical Rods Cube-like + Plates
CeO_2	$Ce(ac)_2$ / OAm-OAc / (1:14:9) / 1-4 min	Spherical
	$Ce(ac)_2$ / OAm-OAc / (1:14:9) / 5-10 min	Rods
	$Ce(ac)_2$ / OAm-OAc / (1:14:9) / 15-20 min	Wires
	$Ce(ac)_2$ / OAm-OAc / (1:6:1) / 15-20 min	Cube-like + Plates
Au	$HAuCl_4$ / OAm-DMF/ (1:15) / 1-2 min	Spherical
Ag	Ag(ac) / OAm-DMF/ (1:15) / 1-3 min	Spherical

Table I. *Continued.*

Nano crystals	Precursors / Ligating Solvents / Mole Ratio / MW Time	Shape
Pt	Pt Acetylacetonate / OAm-DMF/ (1:15) / 1-2 min	Spherical
Ni	Ni Acetylacetonate / OAm-DMF/ (1:15) / 1-2 min	Facetted Particles
Co	$Co_2(CO)_8$ / OAm-DMF/ (1:15) / 1-2 min	Spherical + Plates
Metal Oxides	Metal Acetylacetonate / OAm-DMF/ (1:15) / 10-15 min	Spherical, Prisms (ZnO), Plates (In_3O_4)

NOTE: Xn = Xanthate, OAm = Oleylamine, OAc = Oleic acid, DMF = N, N-dimethylformaide, TOP = Trioctylphosphine, TOPO = Trioctylphosphine oxide, TBO = Titanium butoxide, ODA = octadecylamine.

above 1000 °C. However, for nanocrystals both the hexagonal and cubic phases may coexist at low temperatures depending on the experimental conditions that influence the degree of supersaturation, the nucleation rate and the growth kinetics of the two nanocrystal phases. These conditions include the decomposition rate of the initial precursors, the effective reaction temperature during the MW process, the reaction time, and the rates of adsorption of the organic ligands onto the nanocrystal surfaces. The relative binding energies of the organic ligands to the precursor molecules and to the newly formed nanocrystals also affect the nucleation rate (22). In general, ligands which bind weakly to the precursors increase the nucleation rate while ligands which bind weakly to the newly formed nanocrystals enhance the growth rate. If the ligands adsorb faster or preferentially on one site of the nanocrystal than the other sites, the growth in 1D could be enhanced thus leading to the formation of rods and wires.

Figure 4 displays TEM images of CdSe spherical (a) and tripods (b), and assemblies of ZnSe rods (c) and wires (d) prepared using different ligating solvents. For CdSe, the spherical nanoparticles are obtained using the ligating mixed solvents TOP-TOPO. The CdSe tripods and the ZnSe rods and wires are prepared using the ODA ligating solvent. The assembly of the ZnSe rods and wires into large arrays of organized structures clearly demonstrates that the rods are identical in length and width, and that the nanowires with similar width as the rods (Fig. 4-d) grow by the attachment of the individual rods.

Figure 5 displays TEM images of the PbSe nanostructures prepared using the TOP-TOPO system with different MWI times. At shorter times (1-2 min), star-like structures and long belts are observed as shown in Figures 5-a and 5-b. However, at longer MWI times (4-6 min) large cubes along with the long belts are observed. It appears that the star-like structures of PbSe are composed of
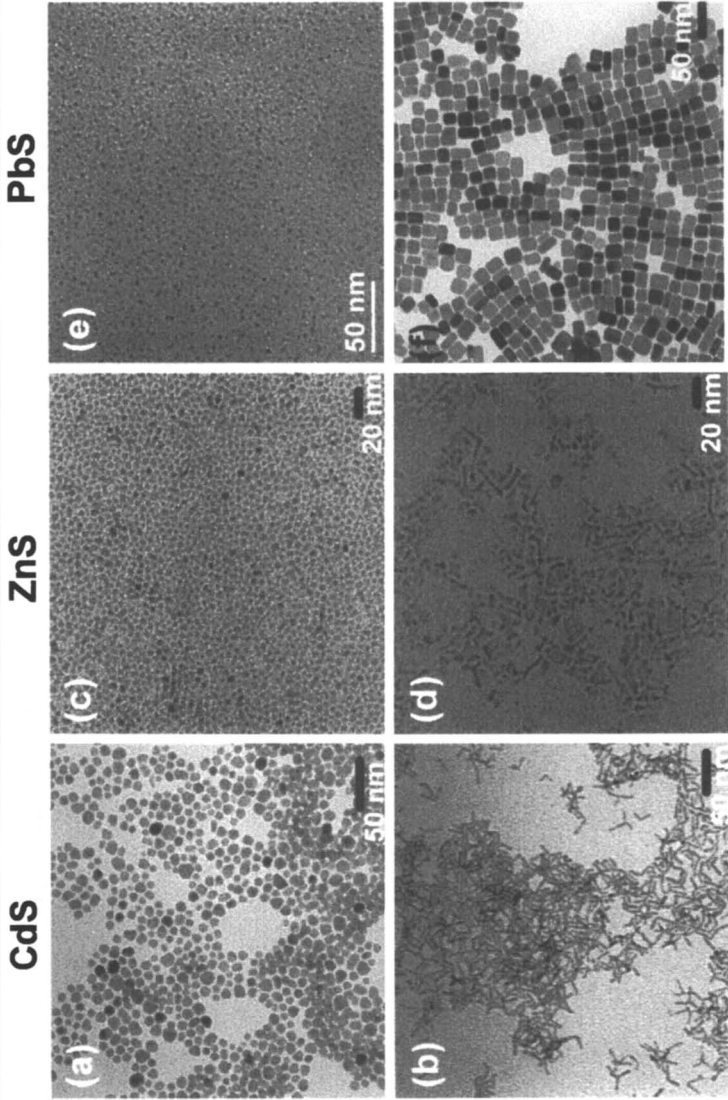
Figure 1. TEM images of: (a) CdS spheres, (b) CdS tripods, (c) ZnS spheres, (d) ZnS rods, (e) PbS spheres and (f) PbS cubes.

ZnS
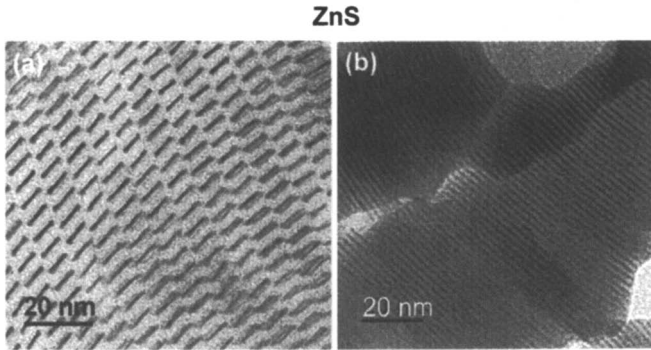
Figure 2. TEM images of: (a) ZnS rods and (b) ZnS wires prepared in ODA with MWI times of 2 and 6 min, respectively.
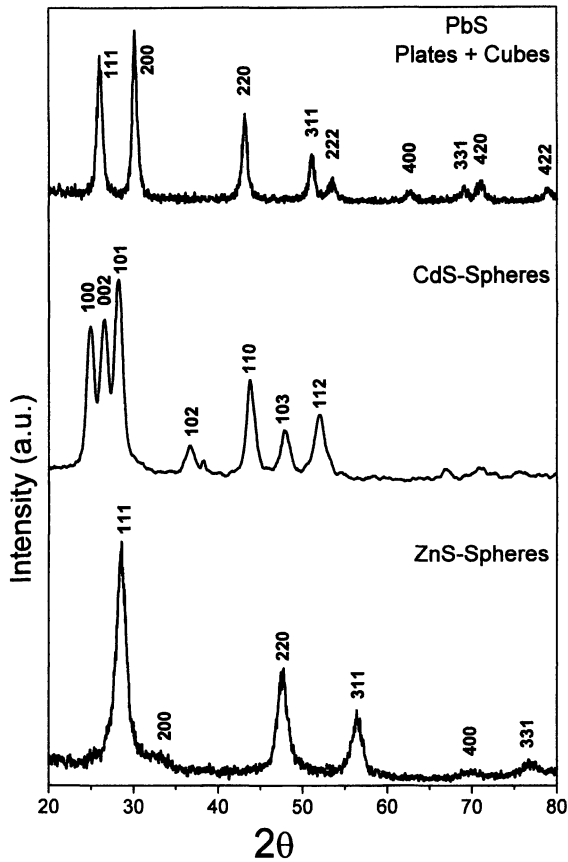
Figure 3. XRD patterns of PbS cubes, CdS spheres and ZnS spheres.

assemblies of aggregated rods, and these structures are transformed into large cubes at longer reaction times.

It is interesting to note that the long chain alkylamine (ODA) results in the formation of the hexagonal crystal phase of the CdSe tripods as evident from the XRD pattern shown in Figure 6. Similarly, the ZnSe rods prepared in alkylamines exhibit the wurtzite structure (the XRD pattern is shown in Fig. 6). The alkylamines are weak ligands to the initial precursors and therefore, the nucleation process can be very fast. This leads to the formation of many small nuclei which can combine in a secondary nucleation process to form the kinetically stable wurtzite phase in the form of rod shapes. Since the amines are likely to bind preferentially on the terminal metal end and on the mixed metal-Se sides of the nanocrystals, the 1D growth can be initiated through the Se end. On the other hand, the TOP-TOPO ligating solvents bind strongly to the initial precursors thus resulting in a slow nucleation process which favors the formation
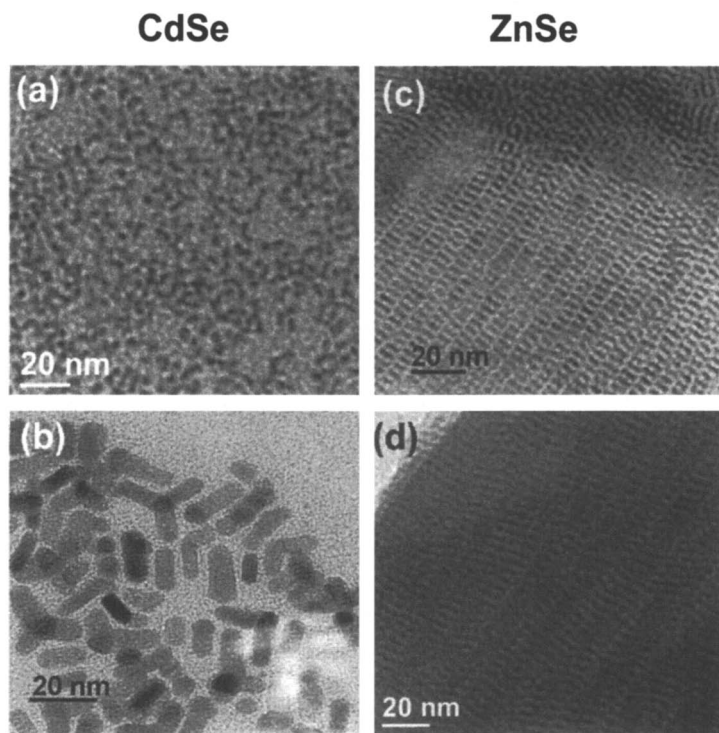
Figure 4. TEM images of: (a) CdSe spheres, (b) CdSe rods and tripods, (c) ZnSe rods and (d) ZnSe wires.

PbSe
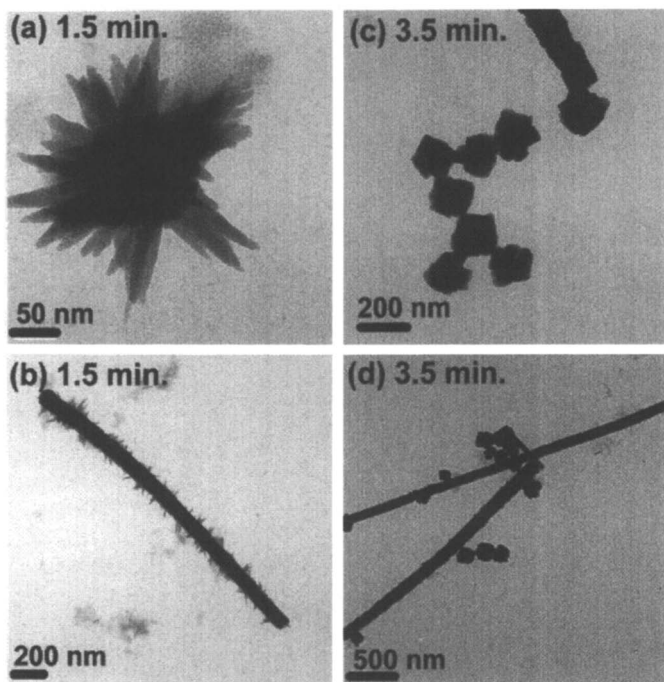
Figure 5. TEM images of PbSe nanocrystals with different shapes: (a) star-like, (b) belt, (c) cubes and (d) cubes and belts.

of the cubic phase of the spherical CdSe nanoparticles as shown from the XRD pattern in Figure 6.

Figure 7 illustrates the evolution of the UV-Vis absorption and the photoluminescence (PL) spectra of the spherical ZnS nanocrystals at different MWI times. The initially formed nuclei after 30 sec reaction time exhibit an absorption peak at 288 nm significantly blue-shifted from the bulk band gap of 3.6 eV (344 nm), thus confirming a high degree of quantum confinement in the synthesized nanocrystals (*16*). Similarly, the room temperature PL spectrum after 30 sec reaction time shows a band-gap emission at 315 nm, which again confirms the high degree of quantum confinement. Both the UV absorption and the PL spectra shift to longer wavelengths as the MWI reaction times increase as a result of increasing the size of the nanocrystals. These results demonstrate the ability of the MWI method to control the size of the nanocrystals by simply varying the reaction times.
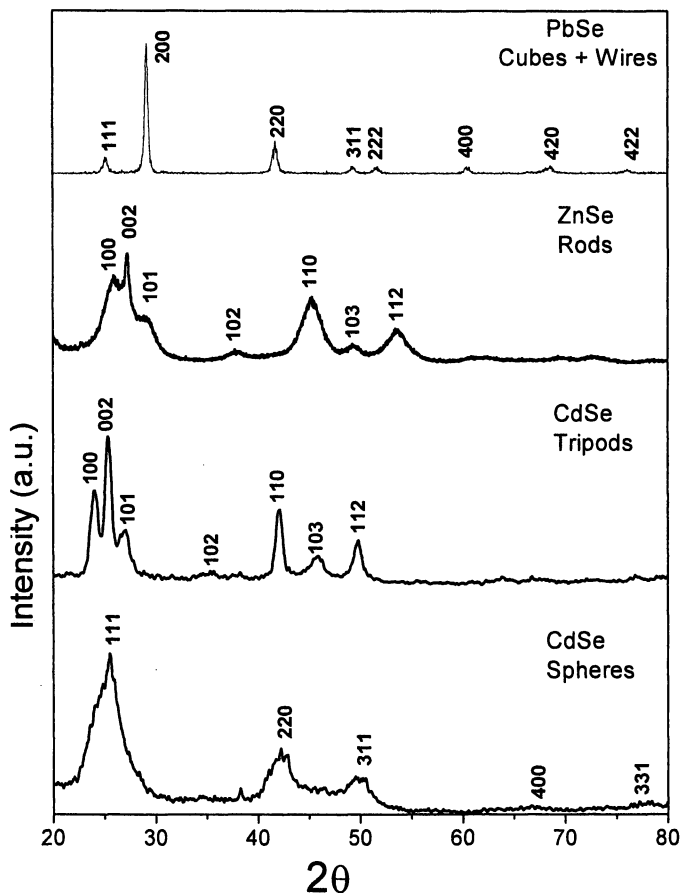
Figure 6. XRD patterns of PbSe cubes, ZnSe rods, CdSe tripods, and CdSe spheres.

Figure 8 displays the UV-Vis and the PL spectra of the synthesized ZnS, ZnSe, CdS and CdSe nanorods and nanowires dispersed in dichloromethane. The observed distinct absorption peaks at 285 nm, 301 nm, 465 nm and 551 nm for ZnS, ZnSe, CdS and CdSe, respectively are significantly sharper and blue-shifted relative to the corresponding bulk material (*16*). The room temperature PL spectra of the nanowires show narrow band-gap emission bands at 300 nm, 424 nm, 487 nm and 580 nm for ZnS, ZnSe, CdS and CdSe, respectively (*16*). The low energy emission bands, at 428 nm for ZnS; 486 nm, 505 nm, and 528 nm for ZnSe; and 586 nm for CdS are attributed to surface emissions, and possible metal vacancies in the nanorods and nanowires. The narrow spectral features are

ZnS Spheres
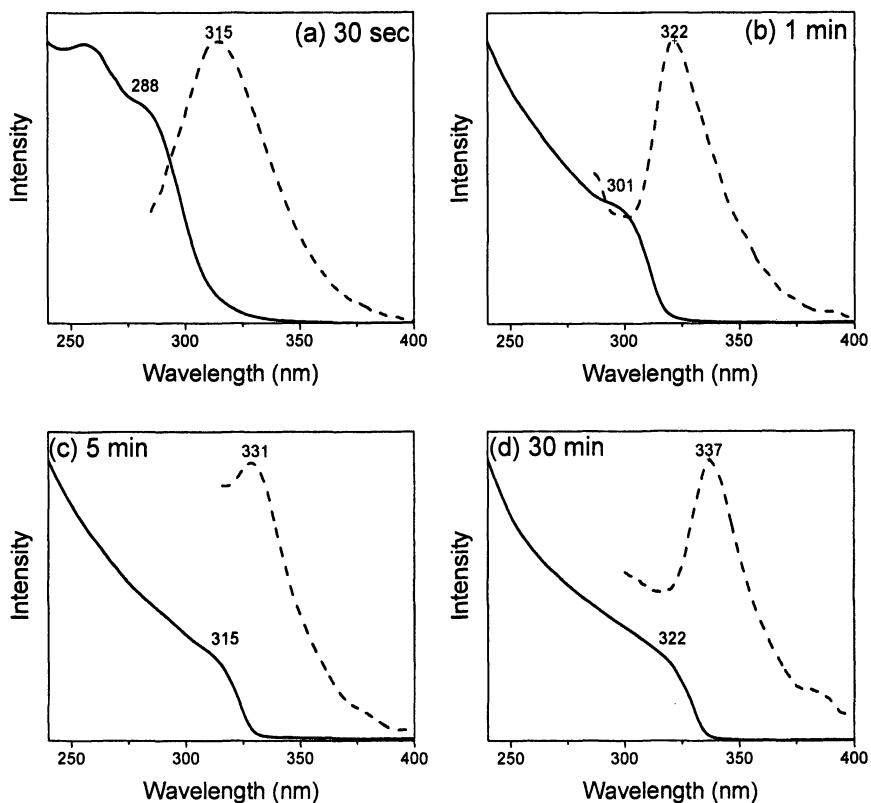
Figure 7. UV-Vis absorption (solid lines) and PL (dotted lines) spectra of ZnS spherical particles prepared at different MWI times.

attributed to high uniformity and ultra narrow width of the rods and wires and confirm the high degrees of quantum confinement in these nanostructures.

B. TiO₂ Colloidal Nanostructures

TiO₂ nanocrystals have attracted much interest due to their unique electronic, optical, catalytic, chemical, and photochemical properties which contribute to a wide variety of applications in solar cells, pigments, gas sensors, and photocatalysis (*23-28*). The synthesis of colloidal TiO₂ with controlled size, shape and crystal structure is essential for many of theses applications. Bulk TiO₂ has three crystalline phases, rutile is the high temperature phase, and both
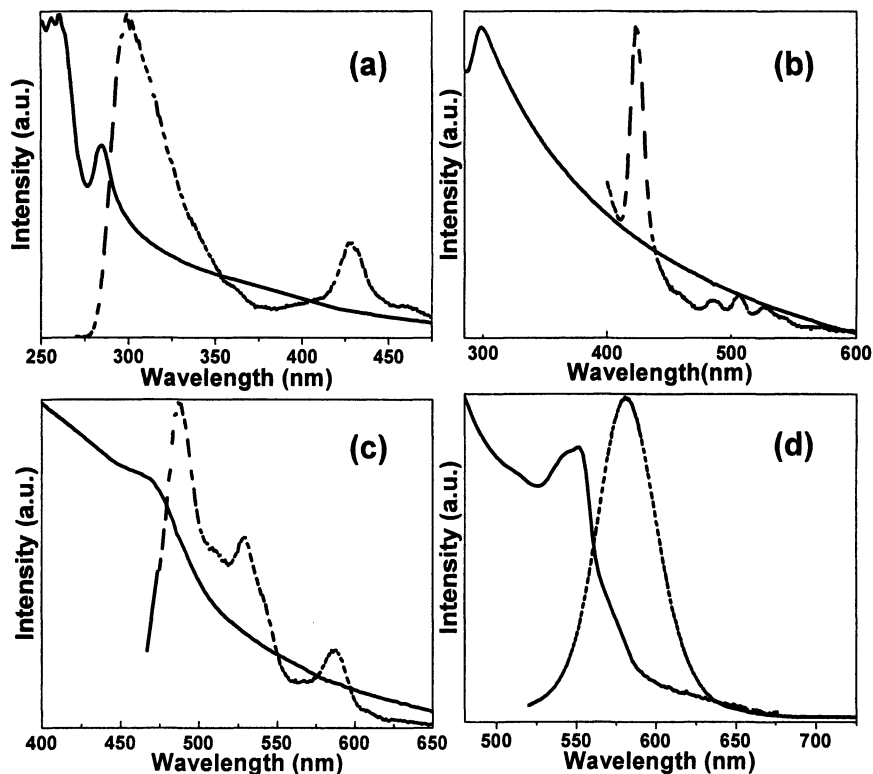
Figure 8. UV-Vis absorption (solid lines) and PL (dotted lines) spectra of (a) ZnS rods, (b) ZnSe wires, (c) CdS rods and CdSe rods. (Reproduced from reference 16. Copyright 2006 American Chemical Society.)

anatase and brookite are metastable phases and transform to rutile at high temperatures, around 700-1000 °C (*23-28*).

The TiO_2 nanocrystals are prepared using titanium butoxide + $TiCl_4$ as precursors and OAc-OAm as ligating solvents (*19*). Figure 9 displays TEM images of the TiO_2 nanocrystals prepared under different reaction conditions. When the mole ratio of the precursors to the OAm to the OAc is approximately 1:4:2 under short MWI times (5-10 min), small spherical or little elongated particles are formed (Fig. 9-a). Rods are obtained by using only OAm with a higher concentration relative to the precursor (6:1), as shown in Figure 9-b. Prolonging the MWI reaction time results in growth of the nanoparticles to form cube-like (Fig. 9-c) and star-like aggregated rods (Fig. 9-d). For example, using relative concentrations of the precursor to the OAm to the OAc of approximately 1:6:9 under long MWI times (10-15 min) results in orientationally aggregated rods around a central particle producing a star-like shape (Fig. 9-d). However, if

the concentration of the OAc is increased (precursor: OAm: OAc = 1:6:18, Table I), most of the nanocrystals display cube-like and bipyramid shapes (Fig. 9-c). The selective crystal growth with different shapes is due to the strong ligand binding and passivation of the oleic acid – oleylamine to the TiO_2 nanocrystal surfaces. The growth of cube-like and bipyramid shapes under high concentrations of oleic acid is consistent with its strong binding to certain surfaces of the anatase crystals (26, 27).
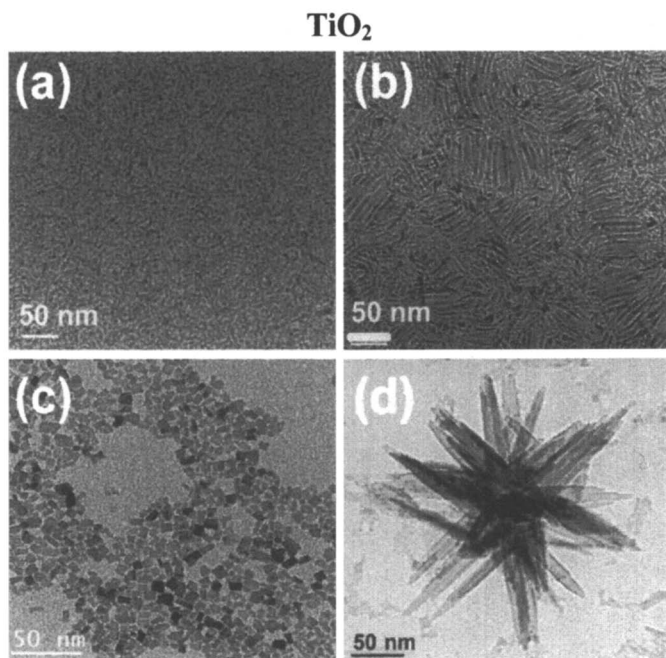
TiO_2

Figure 9. TEM images of TiO₂ nanocrystals with different shapes: (a) spherical, (b) rods, (c) cubes and (d) star-like shape.

The XRD pattern of the prepared TiO_2 nanocrystals, displayed in Figure 10-a, is consistent with the standard pattern of anatase (JCPDS 21-1272). No peaks are found at 27° or 31°, indicating the absence of rutile and brookite phases. However, the results indicate that depending on the precursor used, different phases of TiO_2 are obtained. For example, when titanium tetrachloride was used, a mixture of anatase and rutile was obtained.

The UV-Vis absorption and PL spectra are shown in Figure 10-b. The UV spectrum is typical for anatase (29, 30). The PL spectrum exhibits two peaks due to band-to-band transitions centered around 384 nm, and surface trap states at 425 nm. No peaks are observed between 600 and 800 nm, which are associated
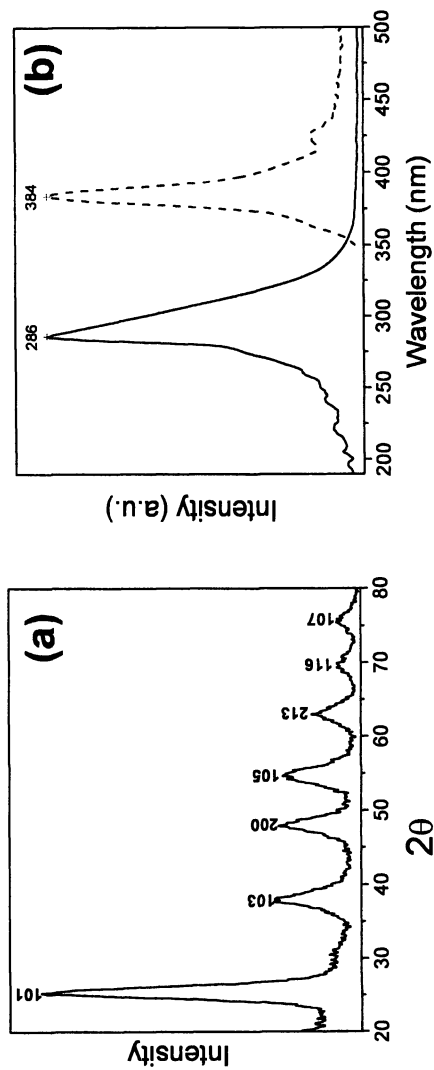
Figure 10. (a) XRD pattern and (b) UV-Vis absorption (solid line) and PL (dotted line) spectra of TiO₂ nanocrystals.

with transitions from conduction band edge to holes trapped at the interstitial Ti^{3+} site (28).

C. Rare Earth Oxide Nanostructures

Rare earth oxides with one dimensional structures represent a particularly interesting class of materials due to their unique electronic, optical, magnetic and catalytic properties arising from the confinement of the 4f electrons (17, 31-34). These properties are critical for many interesting applications involving, for example, optical displays, optical communication, UV shielding, medical diagnostics, and efficient catalysis for the oxidation of heavy oils, jet fuels and coal gasification (17, 31, 34).

Recently, we developed a rapid, simple and versatile MWI methodology for the synthesis of organically passivated uniform, single crystalline rare earth oxide (M_2O_3, M= Pr, Nd, Sm, Eu, Gd, Tb, Dy) nanorods (~1.2×4-5 nm), and cube-like or square nanoplates (6×6 nm) (17). Figure 11 displays representative examples of the TEM images of the as-synthesized Eu_2O_3, (spherical, rods and cube-like), Gd_2O_3 (wires), and Pr_2O_3 (wires).

The relative amount of rods and cube-like nanocrystals can be controlled by the MWI time, and the relative concentrations of the metal precursor, the oleic acid and the oleylamine. The competitive adsorption of oleic acid and oleylamine can effectively inhibit the growth of the nanocrystal in all but the favorable crystallographic plane where the growth is significantly enhanced thus resulting in a 1D structure (16,17). The crystal plane with a higher surface energy is expected to have a faster growth rate. By varying the relative concentrations of oleic acid and oleylamine in the MWI syntheses, the shape of the resulting nancrystals can be controlled. When the mole ratio of the metal precursor: OAc: OAm is 1: 17: 17, spherical particles are formed as shown in Figure 11-a for the Eu_2O_3 nanocrystals. This is consistent with the stronger binding capability of oleic acid relative to oleylamine, and therefore it binds strongly with the atoms of all the planes and the thermodynamic limit (3D) is approached in the presence of excess oleic acid. The nanorods are formed when the mole ratio of OAm: OAc is about 3:2. However, when oleylamine is present in excess, cube-like or square nanoplates are formed as shown for Eu_2O_3 in Figure 11-a. Repeated sets of experiments under the same MWI times, show that the nanorods and the cube-like (or square nanoplates) are predominantly formed when the mole ratios of the metal acetate: OAm: OAc are 1: 22: 14 and 1: 27: 9, respectively. These results demonstrate that by controlling the composition of the capping ligands good control over the shape of the resulting nanocrystals can be achieved during the growth process.

The XRD patterns of the rare earth nanorods are consistent with the cubic Ia3 space group and exhibit intensity enhancement of the (400) diffraction

(a) Eu$_2$O$_3$
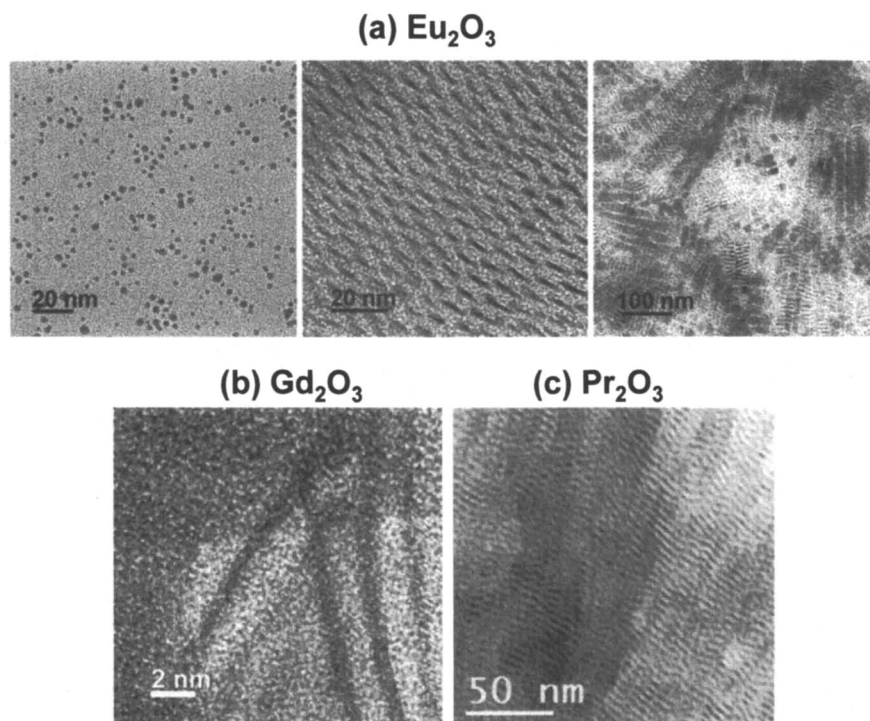
(b) Gd$_2$O$_3$ (c) Pr$_2$O$_3$

Figure 11. TEM images of: (a) Eu$_2$O$_3$ (spheres, rods and plates),
(b) Gd$_2$O$_3$ rods and (c) Pr$_2$O$_3$ wires.

compared to the standard patterns for the bulk rare earth oxides (*17*). This enhancement of the diffraction intensity from the (400) plane is unique to the nanorods since it is not observed in spherical or plate-like nanocrystals (*34*).

The high-resolution TEM images of the individual rods and wires show well-resolved lattice planes perpendicular to the long axis with an interplanar distance corresponding to the *d* spacing of the (400) plane of the cubic Ia3 space group (*17*). The assembly of the rods into ordered 2D supercrystals (Fig. 11-a, middle image) has been confirmed by the small angle XRD analysis (*17*).

The PL properties of the rare earth nanorods synthesized by MWI have been investigated (*17*). For example, the PL spectrum of the Eu$_2$O$_3$ nanorods shows strong split peaks at 612 and 620 nm which can be assigned to the $^5D_0 \rightarrow$ $^7F_{1,2,3,4}$ transitions of the Eu^{3+} ions (*17,35*). For spherical Eu$_2$O$_3$ nanoparticles, these peaks appear as a single broad band centered around 615 nm (*35*). The difference is probably due to different surface sites occupied by the Eu^{3+} ions in the nanorods.

D. CeO₂ Nanostructures

CeO₂ nanostructures have wide applications in many fields such as catalysis, fuel cells, surface modifications, lubrications, gas sensors, radiation protectors, and anode materials for lithium ion battery systems (*36-38*). The properties of CeO₂ nanocrystals are significantly different, and in most cases, superior to the properties of bulk ceria composed of micron-sized particles. For example, significant enhancement is found in the rate of CO oxidation on gold nanocatalysts supported on CeO₂ nanocrystals as compared to the same catalyst supported on micron-sized CeO₂ particles (*15*). Also, the electronic conductivity of CeO₂ nanocrystals is much higher than in large particles (*38*). It is expected that CeO₂ nanocrystals with different shapes would exhibit different quantum confinement effects, and therefore display different optical and PL properties.

For the MWI synthesis of CeO₂ nanocrystals, cerium acetate in a mixture of oleic acid and oleylamine is first heated to about 110 °C in order to remove the hydrated water and obtain a clear solution. The mixture is then transferred quickly to a conventional microwave for the desired amount of time. Different shapes of the CeO₂ nanocrystals can be obtained at different MWI times by using the mole ratio of 1: 14: 9 corresponding to Ce(ac)₂ : OAm: OAc, respectively. For example, at MWI times of (1-4 min), (5-10 min) and (15-20 min), spherical particles, short rods and wires, respectively are formed as shown from the TEM images of Figures 12-a, 12-b, and 12-c, respectively. The 1D orientational growth leading to the formation of rods and wires is induced by the presence of oleic acid which exhibits strong binding and selective adsorption to the surface atoms of the CeO₂ nanocrystals. Increasing the concentration of the precursor and decreasing the concentration of OAc produces cube-like nanocrystals as shown in Figure 12-d. This is consistent with the nonselective adsorption of oleylamine on the CeO₂ nanocrystals, and thus the growth occurs in 3D to produce the cube-like nanocrystals.

The evolution of the XRD patterns of the CeO₂ nanoparticles prepared after 10 min, 20 min and 30 min MWI times, respectively is shown in Figure 13-a. The patterns could be readily indexed to the face-centered cubic phase (space group: *Fm3m*, JCPDS #34-0394). There is considerable broadening in the XRD peaks since the CeO₂ nanoparticles are very small in dimension as shown from the TEM image in Figure 12-a. As the MWI times increase, the diffraction peaks become sharper consistent with the shape transformation from very small spherical particles to short rods and long wires or to cube-like nanocrystals.

Figure 13-b displays the UV-Vis and PL spectra of the CeO₂ cube-like nanocrystals. The UV-absorption shows a peak around 300 nm corresponding to a charge transfer transition from O to Ce in the CeO₂ nanocrystals. Extrapolation of the absorption edge of this band (335 nm) indicates a band gap of 3.7 eV, which confirms the strong quantum confinement in the prepared CeO₂ cube-like nanocrystals. This value is consistent with the reported band gap energies of
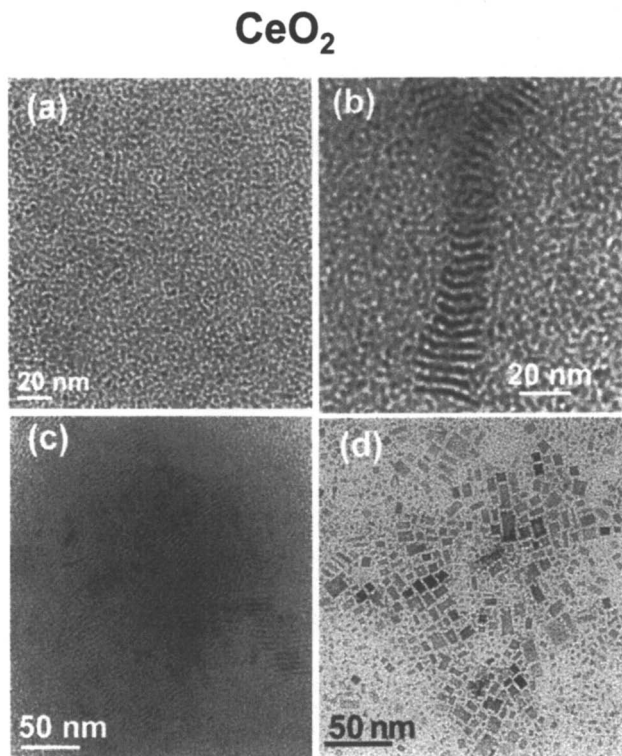
CeO₂

Figure 12. TEM images of CeO₂ nanocrystals with different shapes:
(a) spheres, (b) rods, (c) wires and (d) cubes.

ceria nanoparticles (3.03 to 3.68 eV) prepared using sonochemical synthesis and larger than the values (3.38 to 3.44 eV) reported for the particles prepared using reverse micelles (*39, 40*). The PL spectrum shows a major band around 430 nm, and two low energy bands which could be attributed to surface trap states. These bands could be related to surface modifications of the nanocrystals by the oleylamine passivation.

E. Metal and Metal Oxide Nanostructures

In this section, we demonstrate the application of the MWI method for the synthesis of nearly monodisperse metal and metal oxide nanocrystals. These syntheses are carried out by the MW decomposition of the metal precursors within the reducing environment of the oleylamine ligand. Figure 14 displays TEM images of Au, Ag, Co and Ni nanocrystals prepared with metal precursor
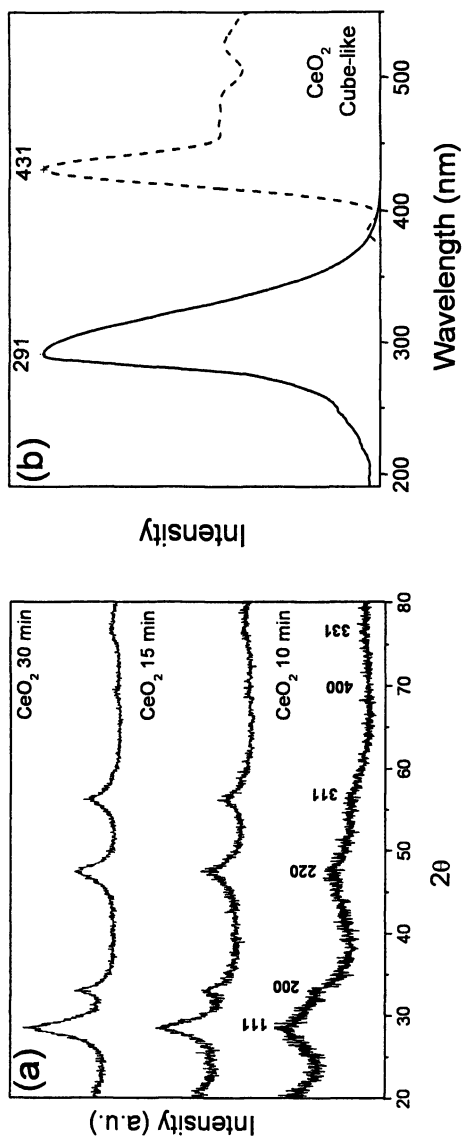
Figure 13. (a) XRD patterns of CeO₂ nanocrystals prepared at different MWI times.
(b) UV-Vis absorption (solid line) and PL (dotted line) spectra of CeO₂ nanocrystals.

to oleylamine ratio of 1: 15 within 1-3 min MWI times. Both Au and Ag produce uniform spherical nanocrystals while Co and Ni result in facetted particles. The size of the particles can be controlled by varying the MWI times, the metal precursor to ligand ratio, and the OAm to OAc ratio. The addition of a small amount of OAc results in smaller nanocrystals due to its strong binding to the nanocrystals which inhibits further particle growth. However, if higher concentrations of OAc are used, the reducing environment provided by the OAm decreases and metal ions may not be efficiently reduced. The XRD patterns (not shown) of the synthesized metal nanocrystals exactly match the patterns of the corresponding bulk metal powders thus confirming the purity of the nanocrystals and the absence of oxides.
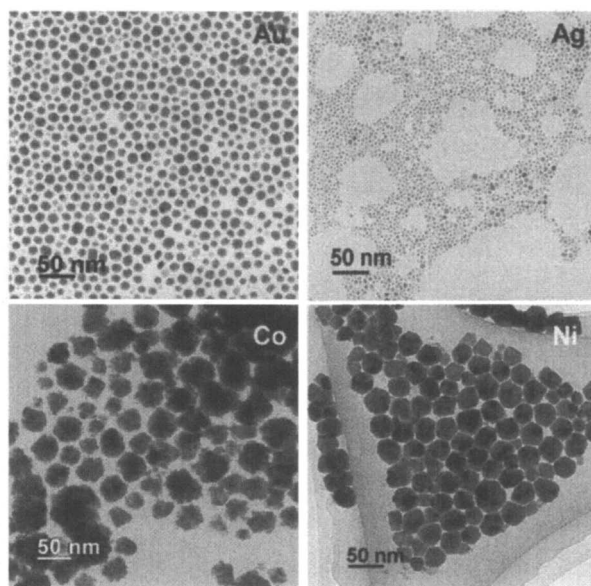
Figure 14. TEM images of Au, Ag, Co and Ni nanocrystals.

Figure 15 displays representative TEM images of the synthesized ZnO, Ga_3O_4, Mn_3O_4 and In_3O_4 nanocrystals. The compositions of the oxide nanocrystals have been confirmed by the XRD data. These nanocrystals are produced by the MW decomposition of the corresponding metal acetylyacetonate in oleylamine –DMF solutions (mole ratio of acetylacetonate: OAm is 1:15). Under these conditions, Ga_3O_4 and Mn_3O_4 nanocrystals form spherical particles while ZnO and In_3O_4 produce nanoprisms and nanoplates, respectively. We are currently exploring the use of mixed ligand systems such as OAm – OAc and ODA as well as different metal precursors in order to control

the composition of the oxide nanocrystals. For example, in addition to Mn_3O_4, MnO nanocrystals can be synthesized by adding a few drops of formic acid to the oleylamine liganding solvent which tends to increase the reducing environment necessary for the synthesis of MnO.
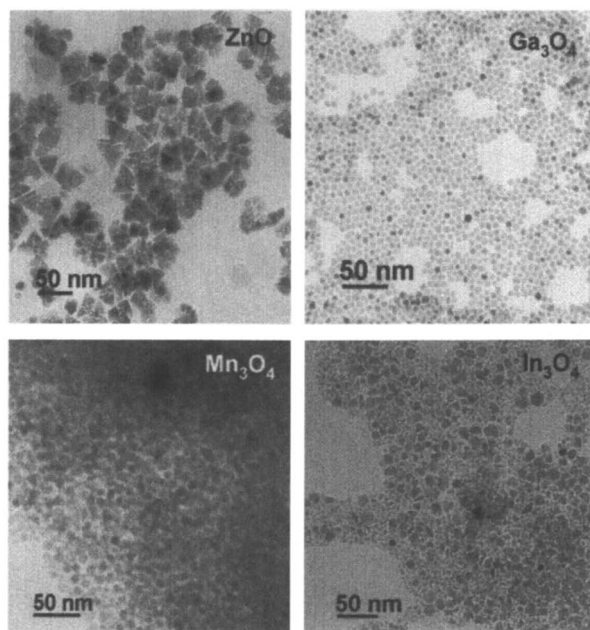
Figure 15. TEM images of ZnO prisms, Ga_3O_4 spheres, Mn_3O_3 spheres and In_3O_4 cubes.

It is clear from the above examples that by manipulating the nucleation and growth kinetics of the nanocrystals through the choice of the appropriate precursors, ligand systems, solvents and the MWI times, one can control the size, shape and composition of the resulting nanocrystals.

Conclusion and Outlook

In conclusion, the microwave irradiation method is simple, versatile and rapid. It allows the synthesis of a wide variety of semiconductor, metal, metal oxide and doped metal oxides with controlled size and shape. The important advantage of microwave dielectric heating over convective heating is that the reactants can be added at room temperature (or slightly higher temperatures)

246

without the need for high-temperature injection. The method allows the passivation of the nanostructures by ligating organic solvents of variable structures and surface properties. Passivated nanorods and nanowires can be synthesized by appropriate choice of the organic ligands and the experimental parameters.

Acknowledgments

References

1. *Nanoparticles from Theory to Application,* Schmidt, G.; Wiley-VCH, Weinheim, 2004.
2. Alivisatos, A. P. *J. Phys. Chem.* **1996**, *100*, 13226.
3. El-Sayed, M. A. *Acc. Chem. Res.* **2004**, *37*, 326.
4. Peng, Z.; Manna, W.; Wickham, J.; Scher, E.; Kadavanich, A.; Alivisatos, A. P. *Nature.* **2000**, *404*, 59
5. Park, J.; An, K.; Hwang, Y.; Park, J.-G.; Noh, H.-J.; Kim, J.-Y.; Park, J.-H.; Hwang, N.-M.; Hyeon, T. *Nat. Mater* **2004**, *3*, 891.
6. Li, Y.; Malik, M. A.; O'Brien, P. *J. Am. Chem. Soc.* **2005**, *127*, 16020.
7. Wang, X.; Zhuang, J.; Peng, Q.; Li, Y. *Nature* 2005, *437*, 121.
8. Zhu, J.; Palchik, O.; Chen, S.; Gedankan, A. *J. Phys. Chem. B.* **2000**, *104*, 7344.
9. Boxall, D.; Lukehart, C. *Chem. Mater.* **2001**, *13*, 806, 891.
10. Gallis, K.; Landry, C. *Adv. Mater.* **2001**, *13*, 23.
11. Liang, J.; Deng, Z. X.; Jiang, X.; Li, F.; Li, Y. *Inorg. Chem.* **2002**, *41*, 3602.
12. He, J.; Zhao, X. N.; Zhu, J. J.; Wang, J. *J. Cryst. Growth* **2002**, *240*, 389.
13. Patra, C. R.; Alexandra, G.; Patra, S.; Jacob, D. S.; Gedanken, A.; Landau, A.; Gofer, Y. *New J. Chem.* **2005**, *29*, 733.
14. Gerbec, J. A.; Magana, D.; Washington, A.; Strouse, G. F. *J. Am. Chem. Soc.* **2005**, *127*, 15791.
15. Glaspell, G.; Fuoco, L.; El-Shall, M. S. *J. Phys. Chem.B.* **2005**, *109*, 17350.
16. Panda, A. B.; Glaspell, G.; El-Shall, M. S. *J. Am. Chem. Soc.* **2006**, *128*, 2790.
17. Panda, A. B.; Glaspell, G.; El-Shall, M. S. *J. Phys. Chem. C.* **2007**, *111*, 1861.
18. Peng, X., *J. Am. Chem. Soc.* **2001**, *123*, 8844.
19. Trentler, T. J.; Denler, T. E.; Bertone, J. F.; Agrawal, A.; Colvin, V. L. *J. Am. Chem. Soc.* **1999**, *121*, 1613.

20. Pradhan, N.; Efrima, S. *J. Phys. Chem. B.* **2004**, *108,* 11964.
21. Panda, A. B.; Acharya, S.; Efrima, S. *Adv. Mater.* **2005**, *17,* 2471.
22. Yu, W. W.; Wang, Y. A.; Peng. X. *Chem. Mater.* **2003**, *15,* 4300.
23. Wang, C. C.; Ying, J. Y. *Chem. Mater.* **1999**, *11,* 3113.
24. Huang, W.; Tang, X.; Wang, Y.; Koltypin, Y.; Gedanken, A. *Chem. Commun.* **2000**, 1415.
25. Wilson, G. J.; Will, G. D.; Frost, R. L.; Montgomery, S. A. *J. Mater. Chem.* **2002**, *12,* 1787.
26. Gozzoli, P. D.; Kornowski, A.; Weller, H. *J. Am. Chem. Soc.* **2003**, *125,* 14539.
27. Jun, Y.; Casula, M. F.; Sim, J.; Kim, S. Y.; Cheon, J.; Alivisatos, A. P. *J. Am. Chem. Soc.* **2003**, *125,* 15981.
28. Ding, K.; Miao, Z.; Liu, Z.; Zhang, Z.; Han, B.; An, G.; Miao, S.; Xie, Y. *J. Am. Chem. Soc.* **2007**, *129,* 6362.
29. Zhu, H.; Lan, Y.; Gao, X. P.; Ringer, S. P.; Zheng, Z. F.; Song, D. Y.; Zhao, J. C. *J. Am. Chem. Soc.* **2005**, *127,* 6730.
30. Mao, Y. B.; Wong, S. S. *J. Am. Chem. Soc.* **2006**, *128,* 8217.
31. Yada, M.; Kitamura, H.; Ichinose, A.; Machida, M.; Kijima, T. *Angew Chem Int. Ed.* **1999**, *38,* 3506.
32. Stouwdam, J. W.; van Veggel, F. C. J. M. *Nano Lett.* **2002**, *2,* 733.
33. Kompe, K.; Borchert, H.; Storz, J.; Lobo, A.; Adam, S.; Moller, T.; Haase, M. *Angew. Chem. Int. Ed.* **2003**, *42,* 5513.
34. Si, R.; Zhang, Y. W.; you, L. P.; Yan, H. Y. *Angew. Chem. Int. Ed.* **2005**, *44,* 3256.
35. Bazzi, R.; Flores-Gonzalez, M. A.; Louis, C.; Lebbou, K.; Dujardin, C.; Brenier, A.; Zhang, W.; Tillement, O.; Bernstein, E. ; Perriat, P. *J. Lumin.* **2003**, *102,* 445.
36. Service, R. F. *Science* **1996**, *271,* 920.
37. Sun, Y.; Mayers, G.; Xia, B. Y. N. *Nano Lett.* **2003**, *3,* 675.
38. Zhou, F.; Zhao, X.; Xu, H.; Yuan, C. *J. Phys. Chem. C.* **2007**, *111,* 1651.
39. Yin, L.; Wang, Y.; Pang, G. Koltypin, Y.; Gendanken, A. *J. Colloid Interface Sci.* **2002**, *246,* 78.
40. Sathyamurthy, S.; Leonard, K. J.; Dabestani, R. T.; Paranthaman, M. P. *Nanotechnology* **2005**, *16,* 1960.

Chapter 18

Ion Transport in Sulfonated Nanoporous Opal Films

Joanna J. Smith and Ilya Zharov

Department of Chemistry, University of Utah, Salt Lake City, UT 84112

Nanoporous silica colloidal crystalline films (opals) containing ca. 35 layers of self-assembled 170-nm-diameter silica spheres have been surface-sulfonated by treatment with 1,3-propanesultone. The transport of ions through these films as a function of ion charge, pH and solution ionic strength has been studied using cyclic voltammetry in water. At neutral pH and low supporting electrolyte concentration the flux of anions through the opal film is blocked, while the flux of cations is increased, compared to the unmodified silica opal films. The permselectivity is pH dependent and is due to electrostatic repulsion/attraction that can be modulated by changing the ionic strength of the contacting solution.

There is a growing interest in functional nanoporous membranes with applications in separations, drug release and fuel cells. Silica colloidal crystals (opals) are promising candidates for such materials. Indeed, synthetic opals form via self-assembly (*1*), contain ordered arrays of three-dimensional interconnected nanopores, they are characterized by a diffusive flux that is only ca. 10 times smaller relative to the free solution value, independent of the size of the nanopores (*2*), and the chemical modification of the opal surface is facile (*3,4*).

Recently, we described amine-modified thin nanoporous opal films functioning as cation-selective pH-responsive membranes (*5,6*), modification of opal film surfaces with chiral selector moieties (*7*) and polymers brushes (*8*), as well as the preparation of suspended defect-free opal membranes (*9*). The potential of colloidal crystals as separation media has been also recently recognized by Ozin *et al.* (*10*) and Wirth *et al.* (*11,12*).

In the present report we describe the preparation and transport studies of surface-sulfonated opal films. We demonstrate the transport selectivity for both cations and anions based on electrostatic attraction/repulsion.

Experimental Section

Materials. Hexaamineruthenium (III) chloride, $Ru(NH_3)_6Cl_3$ (99%, Strem Chemicals), potassium chloride (99%, Mallinckrodt), potassium hexachloro-iridate (III), K_3IrCl_6 (98%, Aldrich), 1,1'-ferrocenedimethanol (98%, Aldrich), and 1,3-sultone (98%, Aldrich) were used as received.

Silica spheres were synthesized (*13–16*) by adding 0.2 M tetraethyl orthosilicate (TEOS) in absolute ethanol to a solution of 1.1 M ammonia and 17 M water in absolute ethanol. The mixture was stirred for 24 hours at room temperature. Silica spheres were collected and purified by repeated centrifugation in absolute ethanol. The diameter of the spheres was determined to be 440±11 nm using SEM.

Pt Microdisk Electrodes. Pt microdisk electrodes (25 μm in diameter) shrouded in glass were prepared by first attaching a 1.0 mm diameter Cu wire (Alfa Aesar) to a 25 μm diameter Pt wire using Ag paint (DuPont). The Pt wire was then flame-sealed in a glass capillary; the capillary was bent to a U-shape and the end cut orthogonal to the length of the capillary with a diamond saw to expose the Pt disk. The resulting electrodes were then polished with microcut paper discs (Buehler), from 240 to 1200 grit in succession, until the surface was free from visible defects.

Sulfonated Opal Films. Opal films were assembled on the electrode surfaces by placing the electrodes vertically (*17*) in a 1.5 wt% colloidal solution of the silica spheres in ethanol and letting the solvent evaporate for 2-3 days in a

Scheme 1
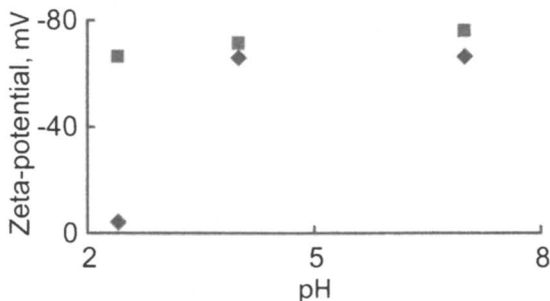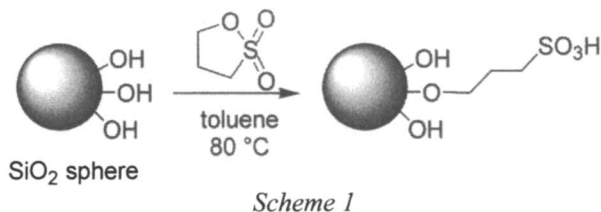
Figure 1. Zeta-potential of the unmodified (diamonds) and sulfonated (squares) 170-nm-diameter silica spheres in water at different pH.

vibration free environment. The 1.5 wt% silica spheres solution produced 35-layer films as was shown by SEM (5).

The surface of the spheres, after assembly into opal films on the Pt electrode, was modified with sulfonic acid groups by immersing the electrode under nitrogen in dry toluene containing 0.05 M of 1,3-propanesultone for 2 days at 80 °C (Scheme 1). After the modification, the electrodes were soaked and rinsed in dry acetonitrile.

Voltammetric Measurements. The flux of permeants across the opal film was measured voltammetrically using a 2-electrode cell and an Ag/AgCl reference/counter electrode. A Par Model 175 Universal Programmer and Dagan Cornerstone Chem-Clamp potentiostat were used to conduct the measurements. Data were recorded with a PC using programs written in LabView. Aqueous solutions were prepared using 18 MΩ·cm water obtained from a Barnstead "E-pure" water purification system. All solutions were purged with N_2 to remove dissolved O_2. pH was adjusted by the addition of acetic acid and sodium hydroxide.

Surface Charge and Composition Measurements. Dynamic light scattering (Brookhaven ZetaPALS) was employed to determine the Zeta-potential of the sulfonated silica spheres (Figure 1). X-ray photoelectron spectroscopy (Kratos AxisUltra DLD) was used to determine the degree of surface sulfonation.

Results and Discussion

Sulfonation of Opal Surfaces

The sulfonation of the silica spheres was conducted both in toluene colloidal solution (for surface charge and composition characterization) and in opal films using the reaction shown in Scheme 1. The presence of the sulfonic groups has been confirmed by XPS that showed a peak corresponding to sulfur atoms. In addition, the modified silica spheres possessed a much lower zeta-potential than unmodified silica spheres at low pH (Figure 1). Based on zeta-potential measurements we estimate that at least half of the silanol groups have been replaced by the sulfonic groups.

Effect of Opal Film Sulfonation on the Molecular Flux.

Figure 2 shows the voltammetric responses of 25 μm-diameter Pt microdisk electrodes carrying an opal film of ca. 35 layers 170 nm silica spheres in aqueous solutions containing three redox couples: a multiply charged anion, a multiply charged cation and a neutral molecule. The voltammetric responses for each redox couple display a sigmoidal shape characteristic of near steady-state radial diffusion of the redox species to a microelectrode (*18*).
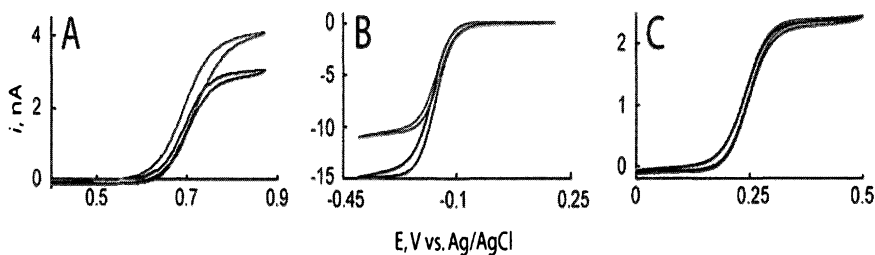
Figure 2. Representative voltammetric responses of an opal film electrode before (top curve) and after (bottom curve) surface sulfonation of the opal for (A) $IrCl_6^{3-}$, (B) $Ru(NH_3)_6^{3+}$, and (C) $Fc(CH_2OH)_2$ at neutral pH.

Permselective behavior is readily apparent in the voltammetric response of the electrode after covalent attachment of sulfonic acid groups to the silica spheres. At pH ~7 and 0.1 M KCl, the voltammetric limiting current, i_{lim}, corresponding to the one-electron oxidation of $IrCl_6^{3-}$ is diminished (Figure 2A), i_{lim}, corresponding to the one-electron reduction of $Ru(NH_3)_6^{3+}$ is increased (Figure 2B), while i_{lim} for the one-electron oxidations of $Fc(CH_2OH)_2$ remains approximately the same as before surface modification (Figure 2C). This result

is consistent with electrostatic attraction of the cationic species, $Ru(NH_3)_6^{3+}$, and electrostatic repulsion of the anionic species, $IrCl_6^{3-}$, by negatively charged surface sulfonic groups. These results have been reproduced on ten sulfonated opal electrodes, with the limiting current drop observed for $IrCl_6^{3-}$ was 28±6 % and the limiting current increase for $Ru(NH_3)_6^{3+}$ was 36±8 %.

To verify that the permselectivity results from the surface modification of the opal and not of the Pt electrode surface, we treated the bare Pt electrodes with 1,3-sultone in dry toluene at 80 °C. The treated electrodes did not show any permselective behavior.

pH Effect on Diffusion through Sulfonated Opal Films

The limiting current, i_{lim}, was used as a measure of the molecular flux through the opal films. Figure 3 shows the voltammetric responses of sulfonated opal electrodes in water to changes in pH.

As clearly seen in Figure 3, the diffusion of the positively charged species across the sulfonated opal film is further accelerated by increasing the pH of the
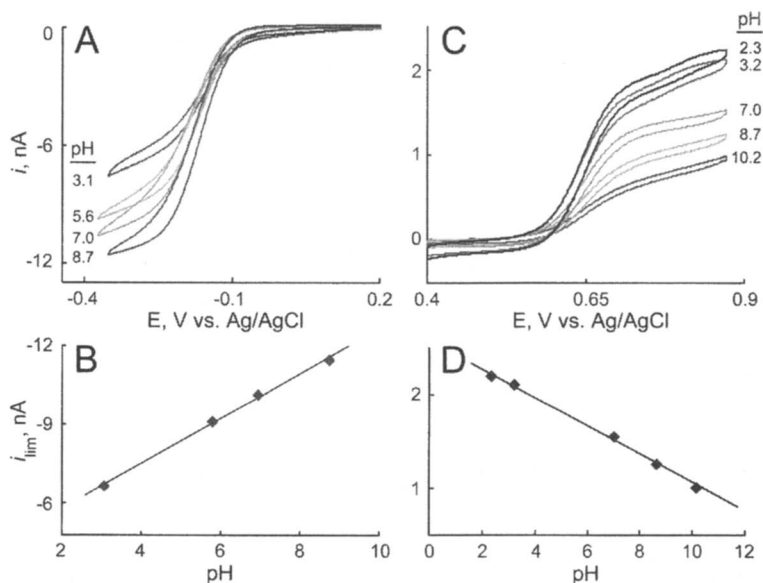
Figure 3. Voltammetric responses of the sulfonated opal electrode as a function of pH for $Ru(NH_3)_6^{3+}$ (A) with the corresponding limiting current dependence on pH (B), and for $IrCl_6^{3-}$ (C) with the corresponding limiting current dependence on pH (D).

contacting solution, which is likely the result of the further deprotonation of the surface sulfonic groups. In contrast, the flux of $IrCl_6^{3-}$ is further reduced as the pH of the contacting solution is increased.

Ionic Strength Effect on Diffusion through Sulfonated Opal Films

In order to demonstrate that the permselectivity in sulfonated opal films is electrostatic in nature, we studied the diffusion of $Ru(NH_3)_6^{3+}$ and $IrCl_6^{3-}$ through the films as a function of solution ionic strength, using KCl as the electrolyte at pH ~7 in water. Increasing the solution ionic strength reduces the diffusion rates for the positive species, $Ru(NH_3)_6^{3+}$ (Figure 4A-B), while the transport rate of negatively charged species, $IrCl_6^{3-}$, increases with the increasing ionic strength.
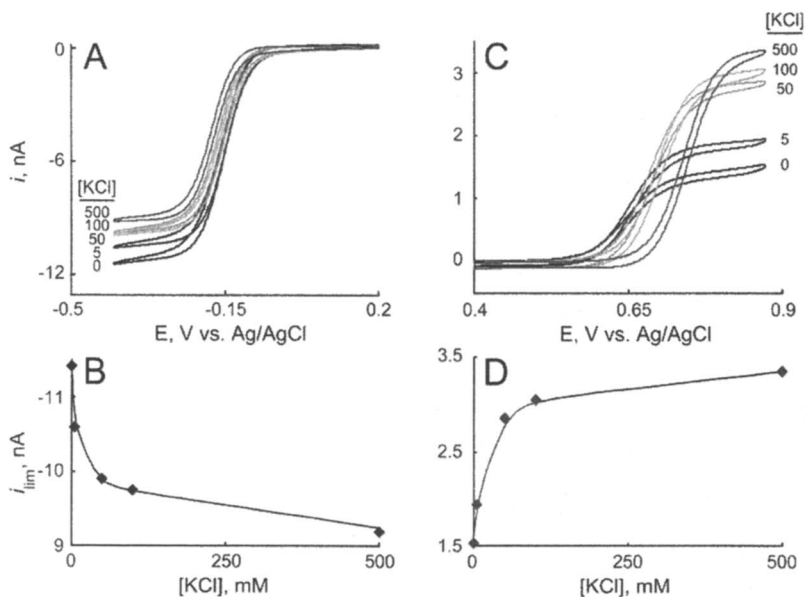
Figure 4. Voltammetric responses of the sulfonated opal electrode as a function of KCl concentration for $Ru(NH_3)_6^{3+}$ (A) with the corresponding limiting current dependence on [KCl] (B), and for $IrCl_6^{3-}$ (C) with the corresponding limiting current dependence on [KCl] (D).

These observations clearly demonstrate the electrostatic nature of the permselectivity. Indeed, as electrolyte is added to the solution, it screens the charge of the surface ammonium groups allowing diffusion of the positively charged species through the opal film.

Conclusions

We demonstrated that the surface of opals can be modified with sulfonic groups using 1,3-propanesultone. This leads to opal films with nigh negative surface charge in the wide pH range and results in accelerated transport of positively charges species and blocking of the negatively charged species. We showed that this permselectivity is pH and ionic strength dependent. Thus, it is based on electrostatic attraction/repulsion between the negatively charged opal surface and diffusing ions. The permselectivity is modulated by the Debye screening length of the electric field within the pores of the opal film.

Acknowledgment

References

1. Wong, S.; Kitaev, V.; Ozin, G. A. J. Am. Chem. Soc. **2003**, *125*, 15589.
2. Newton, M. R.; Morey, K. A.; Zhang, Y.; Snow, R. J.; Diwekar, M.; Shi, J.; White, H. S. Nano Lett. **2004**, *4*, 875.
3. Hanai, T. Adv. Chrom. **2000**, *40*, 315.
4. Ravoo, B. J.; Reinhoudt, D. N.; Onclin, S. Angew. Chem. Int. Ed. **2005**, *44*, 6282.
5. Newton, M. R.; Bohaty, A. K.; White, H. S.; Zharov, I. J. Am. Chem. Soc. **2005**, *127*, 7268.
6. Newton, M. R.; Bohaty, A. K.; Zhang, Y.; White, H. S.; Zharov, I. Langmuir **2006**, *22*, 4429.
7. Cichelli, J.; Zharov, I. J. Am. Chem. Soc. **2006**, *128*, 8130.
8. Schepelina, O.; Zharov, I. Langmuir **2006**, ASAP.
9. Bohaty, A. K.; Zharov, I. Langmuir **2006**, *22*, 5533.
10. Kamp, U.; Kitaev, V.; Von Freymann, G.; Ozin, G. A.; Mabury, S. A. Adv. Mat. **2005**, *17*, 438.
11. Zhang, H.; Wirth, M. J. Analytical Chemistry **2005**, *77*, 1237.
12. Zheng, S.; Ross, E.; Legg, M. A.; Wirth, M. J. J. Am. Chem. Soc. **2006**, *128*, 9016.
13. Van Helden, A. K.; Jansen, J. W.; Vrij, A. J. Colloid Interface Sci. **1981**, *81*, 354.
14. Stoeber, W.; Fink, A.; Bohn, E. J. Colloid Interface Sci. **1968**, *26*, 62.

15. Wang, W.; Gu, B.; Liang, L.; Hamilton, W. J. Phys. Chem. **2003**, *107*, 3400.
16. Bogush, G. H.; Tracy, M. A.; Zukoski IV, C. F. J. Non-Cryst. Solids **1988**, *104*, 95.
17. Jiang, P.; Bertone, J. F.; Hwang, K. S.; Colvin, V. L. Chem. Mater. **1999**, *11*, 2132.
18. Bard, A. J.; Faulkner, L. R.; Electrochemical Methods: Fundamentals and Applications, 2nd ed.; Wiley: New York, **2001**.

Chapter 19

Convectional, Sedimentation, and Drying Dissipative Patterns of Colloidal Dispersions and Solutions

Tsuneo Okubo[1,2]

[1]Cooperative Research Center, Yamagata University, Johnan 4–3–16
Yonezawa 992–8510, Japan
[2]Current address: Institute for Colloidal Organization, Hatoyama 3–1–112
Uji 611–0012, Japan

Convectional, sedimentation and drying dissipative structural patterns on a cover glass, a watch glass and others in the course of drying colloidal dispersions and solutions of simple electrolytes, polyelectrolytes, neutral polymers, bio-polymers, detergents and others, have been reviewed. Cell convections and convectional flow of solvent and solutes from central area toward outside edges along the bottom substrates are observed. Primarily sedimentation patterns are broad ring but vague microscopically. Sedimentary solutes moved in the balance between convectional flow and the sedimentation. Principal macroscopic drying patterns are broad rings and spoke-like ones. The microscopic patterns such as star-like, needle-like, street road-like, blanch-like, string-like, cross-like are formed. The stratified structures form from macro to micro scales. Importance of the shape and size of solutes on the dissipative patterns is clarified.

Generally speaking, most structural patterns in nature form via self-organization accompanied with the dissipation of free energy and in the non-equilibrium state. In this aspect, three dimensional colloidal crystals, which have been studied by the author, for example, is one of the self-organization but close to the energy conservative and the equilibrium state (1-7). Among several factors in the free energy dissipation of aqueous colloidal suspensions, evaporation of solvent molecules at the air-solvent interface and the gravitational convection are very important. In order to understand the mechanisms of the dissipative self-organization of the simple model systems instead of much complex nature itself, the authors have studied the convectional, sedimentation and drying dissipative patterns of suspensions and solutions as systematically as possible.

Several papers on the pattern formation in the course of drying the colloidal suspensions have been reported so far (8-23). Most of the papers, however, studied the liquid-like suspensions in the particle distribution. Electrostatic inter-particle interactions have been pointed out as one of the important factors for the dissipative structures. Hydrophobic and hydrophilic interactions are also demonstrated to be important in the drying processes (21-23). Gelbart et al. (11,12,14) examined the mechanism of solvent dewetting in broad rings formed by drying metal colloids on a substrate. Haw (24), Narita et al. (25) and Mahesh et al. (26) have studied the dynamic and phase transitional processes in dryness. Shimomura et al. and other researchers have studied intensively the dissipative patterns in drying polymer solutions (27).

In the author's laboratory drying dissipative patterns have been studied for suspensions and solutions of many kinds of colloidal particles (28-40), linear-type polyelectrolytes (41), water-soluble non-ionic polymers (42), biopolymers (43), gels (44) and detergents (45-47) on a cover glass. Recently the sedimentation dissipative patterns have been studied in the course of drying suspensions of colloidal silica spheres and green tea in a glass dish, a watch glass and others (34-36). Furthermore, convectional patterns were studied for Chinese black ink and the 100 % ethyl alcohol suspensions of colloidal silica spheres (30,33). The existence of the small circle-like cell convections, proposed by Terada et al., for the first time were supported (48-50).

Drying Patterns of Suspensions

Drying Patterns of Spherical Colloidal Suspensions Including Colloidal Crystals

Figure 1 shows the typical patterns formed in the drying a series of suspensions of colloidal silica spheres, their diameters ranging from 29 nm to 1.09 μm and at the concentrations of 0.0333 in volume fraction (31). The broad

rings and the spoke-like cracks were observed. There were quite few spheres in the central region, whereas broad ring-like region was occupied with many spheres. Clearly, the cracks were formed in the process of shrinking of the wetted films (*39*). Interestingly, the cracks were introduced in the final stage of drying the colloidal suspensions along the outer edges first, where the dryness proceeds in advance. The cracks curved and then developed straight toward the center of the film. It is impressive that the new cracks developed successively keeping the same angle with the adjacent elder cracks (*39*). Clearly, film is transparent and so many cracks are observed for small spheres. When sphere size increases, film becomes white and the number of the cracks decreases sharply. Increase in size will result in increase in the elastic modulus of the film and then in decrease in the crack number. It should be noted here that so many potential cracks are formed already in the suspension state by the cell convections and the convectional flow of spheres and solvents. The spoke-like cracks and the broad ring patterns were observed for almost all the suspensions and solutions examined so far.

A main cause for the broad ring is due to the convection flow of solvent and colloidal spheres. Especially, the flow of the colloidal spheres from the central area toward outside edges in the lower layer of the liquid drop is important, which was observed directly from the movement of the very rare aggregates of
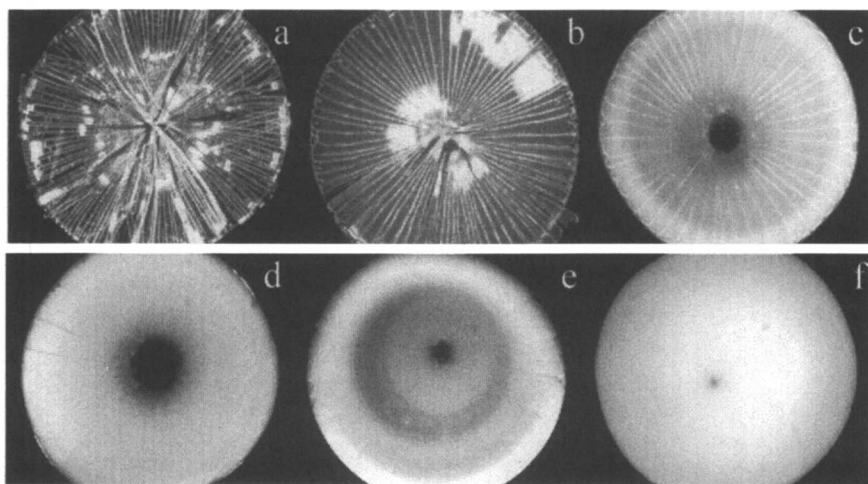
Figure 1. Drying patterns of colloidal silica spheres on a cover glass at 25 °C.
a CS22p (29 nm in diameter), b CS45 (56.3 nm), c CS82 (103 nm), d CS161
(183 nm), e CS301 (311 nm), f CS1001 (1090 nm), in water, φ = 0.0333,
0.1 ml, length of the bar is 5 mm.

the particles (*30*). The flow is enhanced by the evaporation of water at the liquid surface, resulting in lowering of the suspension temperature in the upper region of the liquid. When the spheres reach the edges of the drying frontier at the outside region, a part of the spheres will turn upwards and go back to the center region. However, the movement of most spheres may stop at the frontier region because of the disappearance of water. These processes must be followed by the broad ring-like accumulation of the spheres near the round edges. It should be noted here that the importance of the convectional flow of colloidal spheres in the ring formation has been often reported in the process of film formation (*16*).
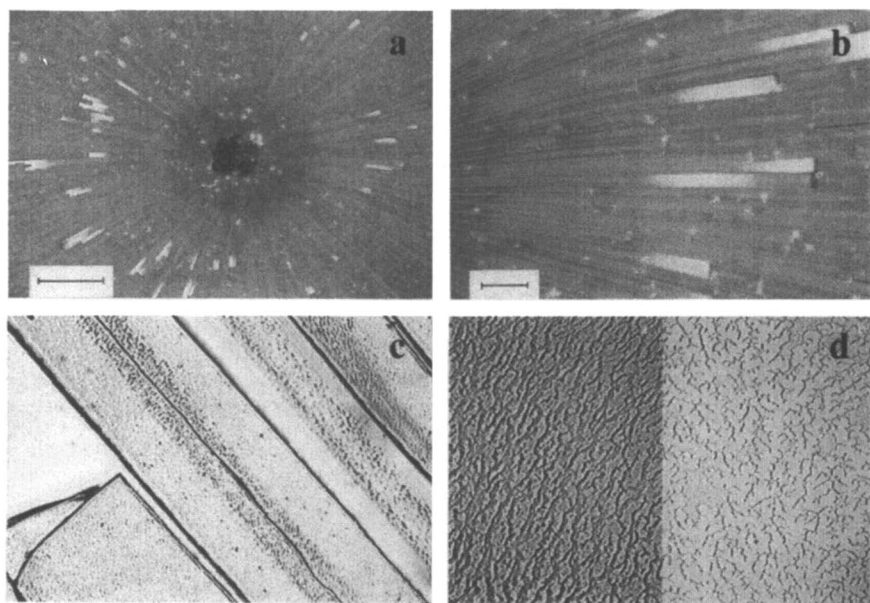
*Figure 2. Drying patterns of polystyrene spheres (D1W52, 88 nm in diameter) on a cover glass at 25 °C. In water, **a** $\phi = 0.011$, 0.2 ml, length of the bar is 1.0 mm, **b** 0.011, 0.2 ml, 0.2 mm, **c** 0.001, 0.1 ml, **d** (a) D1W52, 0.0000885, 0.1 ml, 10 μm, (b) CS82 (colloidal silica spheres, 103 nm in diameter), 0.00133, 0.1 ml, 10 μm.*

Figure 2 shows the drying patterns from macro- to micro-scale. Most extended micro-scale patterns of colloidal crystals of polystyrene and silica spheres are shown in Figures 2(d), left- and right-hand side, respectively. Clearly, the stratified structures form from macro to micro scales. These microscopic patterns must be made by the movement of spheres to associate with each other, especially in the final stage of drying processes. Branch-like fractal patterns were observed for a series of colloidal silica spheres ranging from 29 nm to 311 nm

and in the only limited conditions of sphere concentrations. The fractal dimensions of drying patterns of polystyrene and silica spheres were 1.45 (29) and between 1.3 and 1.9 (28), respectively.

Interestingly, the single crystals were observed during the dryness. The size of single crystals increased in the course of dryness, which clearly shows that the contamination of the suspensions with air, especially with carbon dioxide, progresses with time. It is well known that the crystal size becomes largest at the salt concentration of crystal melting (1,5). The crystal size began to decrease after passing the maximum as time proceeded. The single crystals were not recognized in the wet drying state. However, the peak appeared even for the wet film and for the completely dried film in the reflection spectroscopy. The peak wavelength at the beginning stage of drying shifted to the longer wavelengths, and then decreased with time, especially drastically in the final stage of drying (28).

Drying patterns of colloidal crystals of silica spheres in water, methyl alcohol, ethyl alcohol, 1-propyl alcohol, diethyl ether and in the mixtures of ethyl alcohol with other solvents have been studied on a cover glass (39). The broad rings were observed. Much distinct broad rings appeared in the inner area when solvents were ethyl alcohol, methyl alcohol and their mixtures. Profiles of the thickness of the dried films were sensitive to kind of the organic solvents, and explained well with changes in the surface tensions, boiling points and viscosities of the solvents. Drying patterns of the binary mixtures of colloidal silica spheres in a watch glass were composed of the outer broad ring of small spheres and the inner ring of large spheres, and the width ratio of the rings changed in proportion to the mixing ratio in volume fraction (51). On a cover glass the width of the broad rings of small spheres at the outside edges increased as the mixing ratio of small spheres increased. Clearly, observation of the sedimentation and drying patterns is one of the novel quantitative analysis techniques. Recently, the sedimentation and drying patterns of the ternary mixtures of spheres have been studied (52).

Drying Patterns of Non-spherical Colloidal Suspensions

Drying patterns of fractionated bentonite suspensions were studied (32). The broad rings were observed and their widths increased sharply as particle concentration increased. There appeared a hill in the center region in addition to the broad ring. These hills in the central area have not been observed for the suspensions of any kind of spherical particles. The rotational movement must be highly restricted for the anisotropic-shaped particles (plate-like ones here), and the sliding movement will be in major especially in the area close to the substrate. This restricted Brownian movement must be correlated deeply with the appearance of the hill in the center.

Figure 3 shows the pattern formation processes of the bentonite suspension. The drying frontier moves from right to left with time in the pictures. The border between the liquid and solid regions is the frontier zone of drying. Soon after setting the suspensions, vague wrinkle patterns appeared. As time elapsed, the drying frontier moved to the left side, and the vague patterns formed in the liquid phase became clearer and finer in the course of solidification. These observations suggest strongly that the patterns grow and are already fixed in the suspension phase. Broad ring patterns in the deionized suspensions shifted toward the single round hill pattern by the addition of sodium chloride. Association of the plate-like particles is highly plausible. Substantial decrease in the translational movement of the associated particles is one of the main reasons for the very interesting change in the patterns.
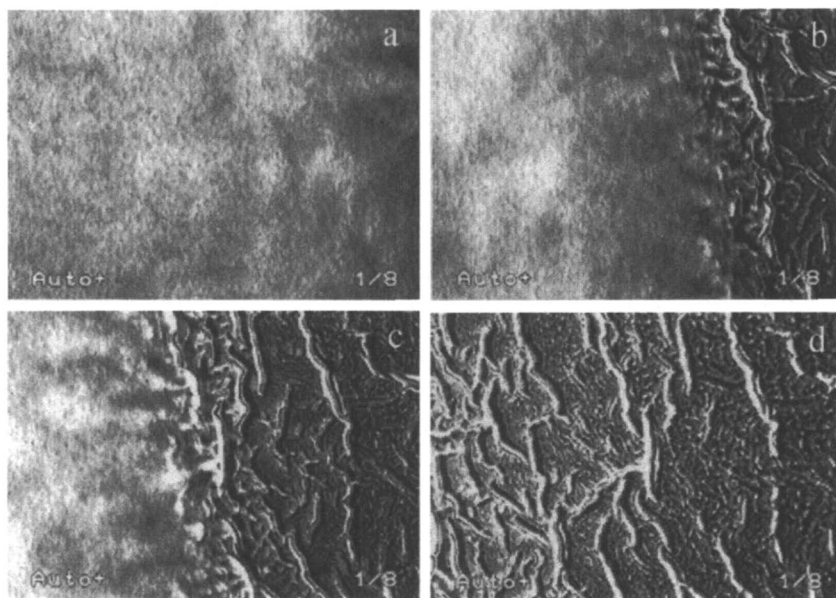
*Figure 3. Drying patterns of bentonite particles on a cover glass at 25 °C. In water, w = 4.6 mg/ml, 0.05 ml, **a** 46 min 30 s after dropping the suspension, **b** 48 min, **c** 48 min 45 s, **d** 49 min 50 s, length of the bar is 10 μm.*

Drying patterns of Chinese black ink on an unrinsed cover glass have been studied. The broad rings are observed at the outer edges irrespective of concentration. The width (*W*) of the broad ring regions increased when the concentration increased. The spoke-like hills appeared but cracks were not

observed. Chinese ink contains the glue component and the film must be strong enough to make cracks.

Drying Patterns of Solutions

Drying Patterns of Polymers Including Gels

Drying patterns of poly (allylamine hydrochloride), one of the cationic polyelectrolytes, were studied on a cover glass (41). Figure 4 shows the typical examples of the patterns. Fractal dimension increased from 1.2 to 1.6, as polymer concentration increased from 1×10^{-6} monoM to 0.01 monoM. Drying patterns of a series of poly (4-N-alkylpyridinium halide) were studied (53). The patterns were influenced significantly with the hydrophobicities of the polyelectrolytes. Drying patterns of aqueous solutions of biological polyelectrolytes, sodium poly (α, L-glutamate) and poly (L-lysine hydrobromide) were studied on a cover glass (43). Below the critical polymer concentration, m^* the dried patterns shrank only around the center area. Above m^*, on the other hand, drying area extended throughout the initial solution area. The macroscopic broad rings and the spoke-like crack patterns were observed. Microscopic patterns such as cross-like, rod-like, block-like and further city-road-like patterns appeared.

Drying dissipative patterns of thermo-sensitive gels of poly (N-isopropyl acrylamide) were studied on a cover glass (44). As the suspension temperature rose, the small size of drying area extended transitionally at the critical temperature ca. 35 °C. The principal patterns at 25 °C were the single or multiple broad rings of the hill accumulated with the gels. At 50 °C, on the other hand, the beautiful flickering spoke-like patterns were observed at the inner area of the broad ring (see Figure 5). These observations support that the extended gel spheres at low temperatures apt to associate weakly to each other, whereas the gels at high temperatures shrink and move rather freely with the convectional flow of water, though the very weak inter-gel attractions still remain. It should be mentioned that the flickering spoke-like patterns show the traces of the cell convection of water and gels.

Drying Patterns of Ionic and Non-ionic Detergents

Cationic surfactant of n-dodecyltrimethylammonium chloride (DTAC) was studied (45). At low concentrations the pattern area shrank in the center and the broad ring regions distributed roundly in the outer edges. At the highest concentration of 0.01 M a broad ring was observed. Clearly, the microscopic patterns of DTAC are cross-like irrespective of the location. The microscopic

patterns of DTAC coexisting KCl, CaCl₂ and LaCl₃ were also studied. When the concentrations of detergent and salt are comparable to each other, tree branch-like and arc-like patterns were observed, which are entirely different from those of the purely detergent or salt solutions. The patterns are also similar to the microscopic structures of poly (allylamine hydrochloride) *(41)*. These results suggest that the micelle structure of DTAC is in the form of a long rod in the solution just before the solidification. The drying patterns of a series of anionic ones of sodium *n*-alkyl sulfates were studies on a cover glass *(46)*. The broad ring patterns are formed. The microscopic patterns of the small blocks, star-like and branched strings are formed.
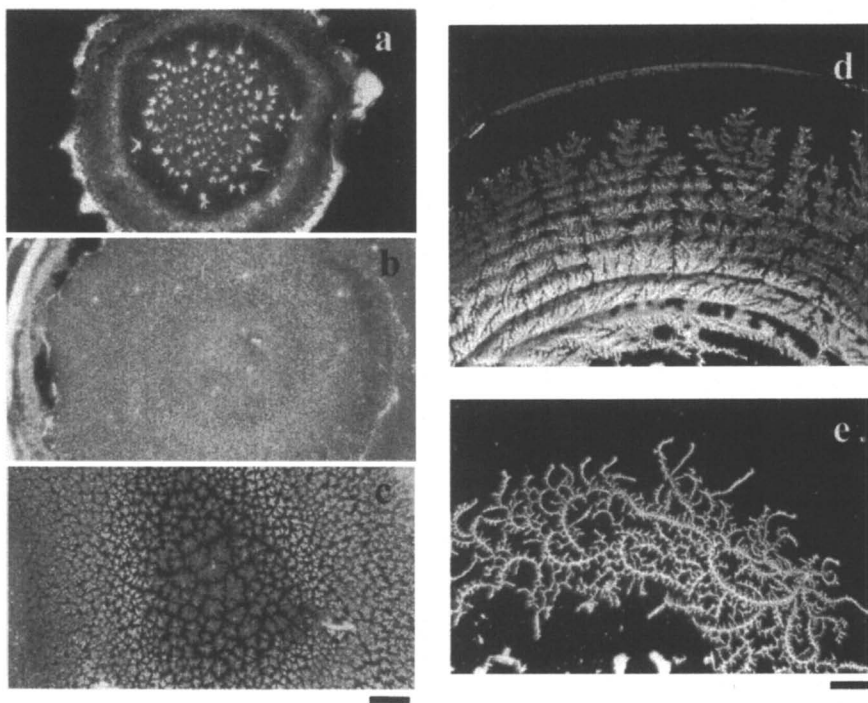
*Figure 4. Drying patterns of Poly(allylamine hydrochloride) on a cover glass at 25 °C. In water, 0.1 ml, length of the bar is 0.2 mm, **a** 1x10⁻⁷ monoM, **b** 1x10⁻⁶ monoM, **c** 1x10⁻⁵ monoM, **d** 1x10⁻⁴ monoM, **e** 1x10⁻³ monoM.*

The drying patterns of aqueous solutions of polyoxyethylene alkyl ethers have been observed *(47)*. The shift from the single round hill to the broad ring patterns occurs as the HLB (hydrophile-lipophile balance) of the surfactant

molecules increases. Microscopic patterns of small blocks, star-like patterns and branched strings are formed. Size and shape of the surfactant molecules and their micelles themselves influence the drying patterns. The pattern area and the time to dryness have been discussed as a function of surfactant concentration and HLB of the surfactants.
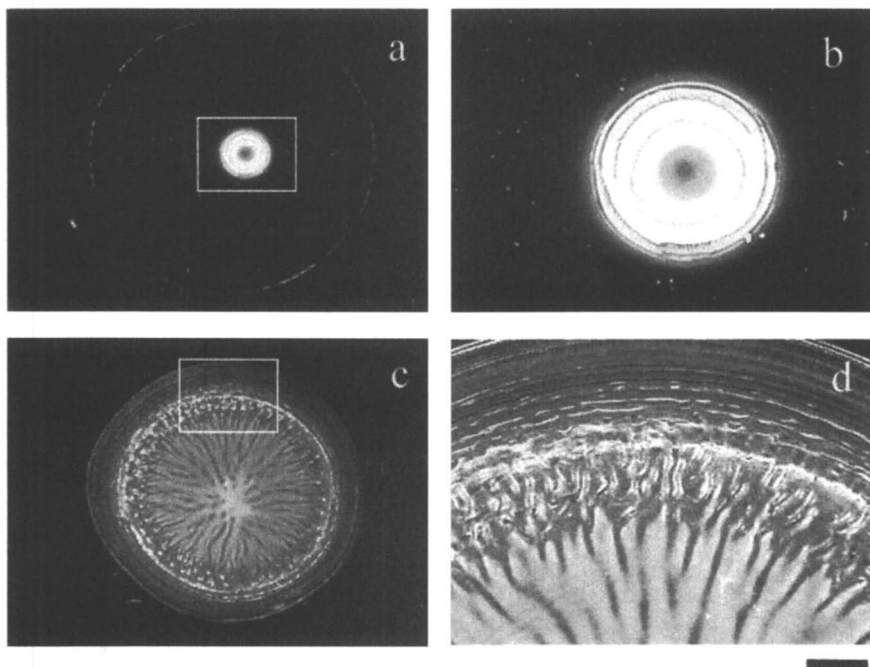
*Figure 5. Drying patterns of thermo-sensitive gels. In water, 0.05 ml, w = 0.01 g/ml, **a** 25 °C, length of the bar is 2.0 mm, **b** 25 °C, 0.5 mm, **c** 45 °C, 2.0 mm, **d** 45 °C, 0.5 mm.*

Drying Patterns of Dyes and Simple Electrolytes

Drying dissipative structural patterns formed in the course of drying ethyl alcohol solutions of rhodamine 6G, uranine, 7-hydroxy coumarin and 7-amino-4-(trifluoro methyl) coumarin were studied on a cover glass (*54*). The macroscopic broad ring patterns formed for all the solutions examined, which supported importance of the convectional flow of ethyl alcohol and dye solutes. Dried area increased as dye concentration increased above the critical dye concentration. Microscopic fine patterns including street-like, needle-like and flower-like

crystal structures were formed in the solidification processes. Change in the functional side group moieties of the dye gave the strong effect on the microscopic drying patterns even the main chemical structures are same. Kinetic aspect of the drying patterns was also studied. Drying patterns of KCl, NaCl, CaCl$_2$ and LaCl$_3$ and the binary mixtures among them were studied on a cover glass (55). Patterns were determined greatly in the process of the solidification, i.e., crystallization.

Sedimentation and Convectional Patterns of Suspensions

Sedimentation Patterns of Colloidal Dispersions

The author observed the sedimentation dissipative structures, which must play an important role for the drying patterns, for several kinds of colloidal suspensions. Frankly speaking, the author became aware of the importance of the convectional flow for the broad ring formation of Ocha (plate-like and colloidal size of Japanese green tea particles, ca. 7 μm in the largest axis) accumulating on the slope of the inner surface of an Ochawan (tea bowl) (34). The sedimentation patterns of broad rings have been always observed when Ocha was prepared by swing a tea bag in an Ochawan containing hot water. Formation of the broad-ring patterns were retarded when a tea cup is covered with a cap, which demonstrates the important role of convectional flow of water and tea particles. The sedimentary particles were suspended above the substrate of the cell and always moved by the convectional flow of water. The broad ring patterns became sharp just before the solidification occurs. Interestingly, the broad rings were formed even in an inclined glass dish, though the rings were transformed slightly, which demonstrates the strong convectional flow of tea particles. The drying broad rings and the microscopic fine structures were formed in the solidification processes on the basis of the convectional and sedimentation patterns in suspension state.

Systematic studies on the sedimentation patterns have been made for colloidal silica spheres of 1.2 μm and 305 nm in diameter on a glass dish, a watch glass and a cover glass (35,36,40). The macroscopic broad ring patterns were formed on the inner inclined watch glass in suspension state within a short time after suspension was set (35). It was clarified that the sedimentary spheres move toward upper and outer edges along the inclined cell wall by the cell convection and hence the patterns are formed by the balancing between the outside movement and the downward sedimentation of the spheres. Beautiful microscopic drying patterns were observed from the optical microscopy. It should be mentioned here that the drying patterns of the colloidal silica spheres containing NaCl were star-like ones, which strongly supports the synchronous

cooperative interactions between the salt and colloidal spheres in the suspension state. Figure 6 shows the typical examples of the dendritic drying patterns of silica spheres with coexistence of small amount of NaCl and the star-like patterns of NaCl surrounded by the dendrite patterns of silica spheres at high salt concentrations on a glass dish.
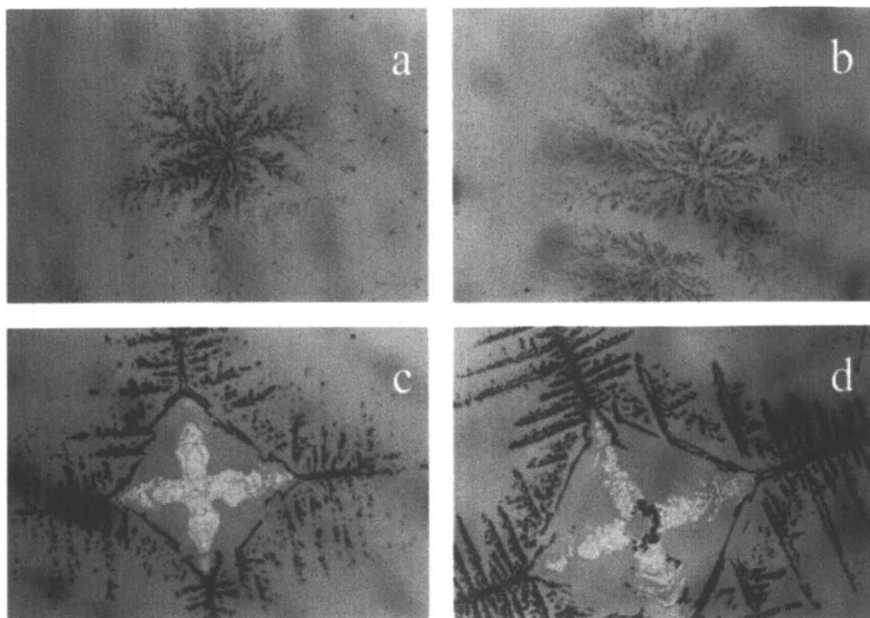
Figure 6. Microscopic drying patterns of silica spheres (1.205 μm in diameter) in a glass dish at 24 °C. φ = 0.00129, 10 ml, a [NaCl] = 0.0003 M, b 0.0006 M, c 0.001 M, d 0.003 M.

Convectional Patterns of Colloidal Dispersions

At the special experimental conditions on the convectional patterns of Chinese black ink, 0.001 g/ml at 25 °C, the convectional flow of the particles was visible with the naked eye (*30*). At 1 min after setting, the particles met together and the associated particles distributed at random. However, after 36 min, the particles started to orient themselves as a result of the convectional flow. Surprisingly, after 136 min, the spoke-like lines both in the liquid and in the solid phases just coincided with each other. This observation supports that the spoke lines were already formed in the suspension phase by the convectional

flow. The drying frontier at the border between gray (center part) and black regions (edges) moved inside with time. The clear-cut spoke lines appeared especially around the outside region of the liquid area.

A further study on the convectional flow in the course of drying was made using a large amount of the ink suspension in a glass dish on a hot plate keeping the suspension temperatures between 25 and 80 °C (*30*). (a) Cyclic cell convections around the outside edges of the suspension, (b) grain-like convection patterns and (c) smoke-like convection patterns were observed. The patterns of the dried films were spoke-like lines, fine circles and the surface patterns of the Japanese earthenware called "Shigaraki Yaki", respectively.
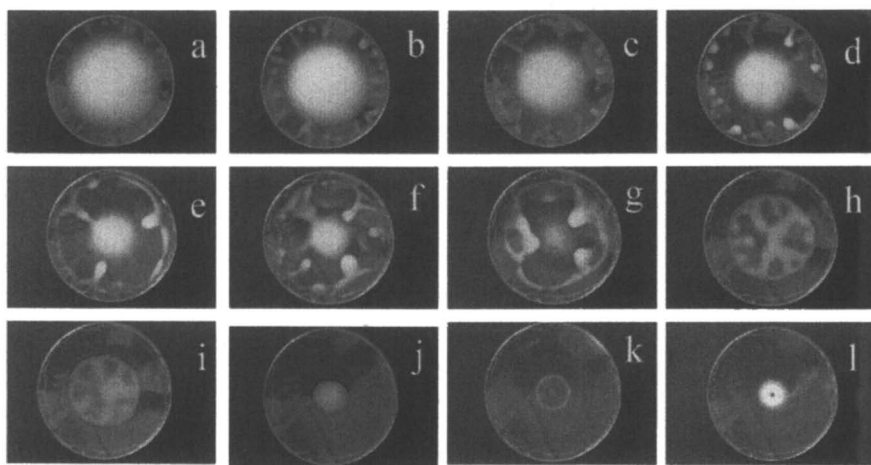
Figure 7. Convectional, sedimentation and drying patterns of 100 % ethanol suspensions of colloidal silica spheres (110 nm in diameter) in a watch glass at 25 °C. $\phi = 0.00427$, 4 ml, a after 7 min, b 25 min, c 40 min, d 50 min, e 60 min, f 62 min, g 65 min, h 70 min, i 75 min, j 90 min, k 122min, and l 125 min, dry.

Dissipative structural patterns formed in the course of drying ethyl alcohol suspensions of colloidal silica spheres (110 nm in diameter) were studied in a glass dish and a watch glass (*33*). Figure 7 is the typical examples showing the dynamic change of the patterns. Vigorous cell convectional flow was observed with the naked eyes, and the patterns changed dynamically with time. Within 50 min after suspension was set, the spoke-like patterns formed outside of the mother suspension in the central area. The suspension drops in the outer region were bridged sometimes with the mother suspension in the central area, disappeared when most of the suspension drops flow down to the mother

suspension, and then the suspension flow takes place from the mother suspension pool toward outside edges resulting in the appearance of the spoke-like suspension drops again. Between 60 min and 75 min, the mother suspension area decreased with time and the initial patterns changed drastically to the different kind of patterns like the section of lotus-root. After 90 min the suspension remained in the central area only, and the broad rings were formed in the final course of dryness. Broad-ring like sedimentation patterns were observed in the suspension state just before the suspension was dried up, and the principal macroscopic drying pattern was also broad-ring, though the colorful and fine microscopic structures were also observed from the microscopy.

Acknowledgments

References

1. Okubo, T. *Acc. Chem. Res.* **1988**, *21*, 281.
2. Okubo, T. *Prog. Polym. Sci.* **1993**, *18*, 481.
3. Okubo, T. *Macro-ion Characterization. From Dilute Solutions to Complex Fluids*; Schmitz, K.L., Ed.; American Chemical Society: Washington, DC, 1994; pp364-380.
4. Okubo, T. *Curr. Topics Colloid Interface Sci.* **1997**, *1*, 169.
5. Okubo, T. *Encyclopedia of Surface and Colloid Science*; Hubbard, A., Ed.; Dekker: New York, 2002; p1300.
6. Okubo, T. *Structural Colors in Biological Systems. Principles and Applications*; Kinoshita, S.; Yoshioka, S., Ed.; Osaka Univ. Press: Osaka, 2005; pp267-286.
7. Tsuchida, A.; Okubo, T. Molecular and Colloidal Electro-optics; Stoylov, S.; Stoimenova, M., Ed.; CRC Press: Boca Raton, 2006; pp447-455.
8. Vanderhoff, J.W.; Bradford, E.B.; Carrington, W.K. *J. Polym. Sci. Symp.* **1973**, *41*, 155.
9. Nicolis, G.; Prigogine, I. *Self-organization in Nonequilibrium Systems*; Wiley: New York, 1977.

10. Cross, M.C.; Hohenberg, P.C.; *Rev. Modern Phys.* **1993**, *65*, 851.
11. Ohara, P.C.; Heath, J.R.; Gelbart, W.M. *Angew. Chem. Intern. Ed. English* **1997**, *36*, 1078.
12. Ohara, P.C.; Heath, J.R.; Gelbart, W.M. *Langmuir* **1998**, *14*, 3418.
13. Uno, K.; Hayashi, K.; Hayashi, T.; Ito, K.; Kitano, H. *Colloid Polymer Sci.* **1998**, *276*, 810.
14. Gelbart, W.M.; Sear, R.P.; Heath, J.R.; Chang, S. *Faraday Discuss.* **1999**, *112*, 299.
15. van Duffel, B.; Schoonheydt, R.A.; Grim, C.P.M.; De Schryver, F.C. *Langmuir* **1999**, *15*, 957.
16. Maenosono, S.; Dushkin, C.D.; Saita, S.; Yamaguchi, Y. *Langmuir* **1999**, *15*, 957.
17. Brock, S.L.; Sanabria, M.; Suib, S.L.; Urban, V.; Thiyagarajan, P.; Potter, D.I. *J. Phys. Chem.* **1999**, *103*, 7416.
18. Nikoobakht, B.; Wang, Z.L.; El-Sayed, M.A. *J. Phys. Chem.* **2000**, *104*, 8635.
19. Ge, G.; Brus, L. *J. Phys. Chem.* **2000**, *104*, 9573.
20. Chen, K.M.; Jiang, X.; Kimerling, L.C.; Hammond, P.T. *Langmuir* **2000**, *16*, 7825.
21. Lin, X.M.; Jaenger, H.M.; Sorensen, C.M.; Klabunde, K.J. *J. Phys. Chem.* **2001**, *105*, 3353.
22. Kokkoli, E.; Zukoski, C.F. *Langmuir* **2001**, *17*, 369.
23. Ung, T.; Liz-Marzan, L.M.; Mulvaney, P. *J. Phys. Chem.* **2001**, *105*, 3441.
24. Haw, M.D.; Gilli, M.; Poon, W.C.K. *Langmuir* **2002**, *18*, 1626.
25. Narita, T.; Beauvais, C.; Hebrand, P.; Lequeux, F. *Eur. Phys. J. E* **2004**, *14*, 287.
26. Tirumkudulu, M.S.; Russel, W.B. *Langmuir* **2005**, *21*, 4938.
27. Shimomura, M.; Sawadaishi, T. *Curr. Opinion Colloid Interf. Sci.* **2001**, *6*, 11.
28. Okubo, T.; Okuda, S.; Kimura, H. *Colloid Polymer Sci.* **2002**, *280*, 454.
29. Okubo, T.; Kimura, K.; Kimura, H. *Colloid Polymer Sci.* **2002**, *280*, 1001.
30. Okubo, T.; Kimura, H.; Kimura, T.; Hayakawa, F.; Shibata, T.; Kimura, K. *Colloid Polymer Sci.* **2005**, *283*, 1.
31. Okubo, T.; Yamada, T.; Kimura, K.; Tsuchida, A. *Colloid Polymer Sci.* **2005**, *283*, 1007.
32. Yamaguchi, T.; Kimura, K.; Tsuchida, A.; Okubo, T.; Matsumoto, M. *Colloid Polymer Sci.* **2005**, *283*, 1123.
33. Okubo, T. *Colloid Polymer Sci.* **2006**, *285*, 225.
34. Okubo, T. *Colloid Polymer Sci.* **2006**, *285*, 331.
35. Okubo, T. *Colloid Polymer Sci.* **2006**, *284*, 1191.
36. Okubo, T. *Colloid Polymer Sci.* **2006**, *284*, 1395.
37. Okubo, T.; Nozawa, M.; Tsuchida, A. *Colloid Polymer Sci.,* **2007**, *285*, 827.

38. Okubo, T.; Kimura, K.; Tsuchida, A. *Colloids Surfaces B*, **2007**, *56*, 201.
39. Okubo, T.; Nakagawa, N.; Tsuchida, A. *Colloid Polymer Sci.*, submitted.
40. Okubo, T.; Okamoto, J.; Tsuchida, A. *Colloid Polymer Sci.*, **2007**, *285*, 967.
41. Okubo, T.; Kanayama, S.; Ogawa, H.; Hibino, M.; Kimura, K. *Colloid Polymer Sci.* **2004**, *282*, 230.
42. Okubo, T.; Yamada, T.; Kimura, K.; Tsuchida, A. *Colloid Polymer Sci.* **2006**, *284*, 396.
43. Okubo, T.; Onoshima, D.; Tsuchida, A. *Colloid Polymer Sci.*, 2007, 285, 999.
44. Okubo, T.; Itoh, E.; Tsuchida, A.; Kokufuta, E. *Colloid Polymer Sci.* **2006**, *285*, 339.
45. Okubo, T.; Kanayama, S.; Kimura, K. *Colloid Polymer Sci.* **2004**, *282*, 486.
46. Kimura, K.; Kanayama, S.; Tsuchida, A.; Okubo, T. *Colloid Polymer Sci.* **2005**, *283*, 898.
47. Okubo, T.; Shinoda, C.; Kimura, K.; Tsuchida, A. *Langmuir* **2005**, *21*, 9889.
48. Terada, T.; Yamamoto, R.; Watanabe, T. *Proc. Imper. Acad. Tokyo* **1934**, *10*, 10.
49. Terada, T.; Yamamoto, R.; Watanabe, T. *Sci. Paper Inst. Phys. Chem. Res. Japan* **1934**, *27*, 75.
50. Terada, T.; Yamamoto, R. *Proc. Imper. Acad. Tokyo* **1935**, *11*, 214.
51. Okubo, T.; Okamoto, J.; Tsuchida, A. publication in preparation.
52. Okubo, T.; Okamoto, J.; Tsuchida, A. publication in preparation.
53. Okubo, T.; Ogawa, H.; Tsuchida, A. publication in preparation.
54. Okubo, T.; Yokota, N.; Tsuchida, A. *Colloid Polymer Sci.*, in press.
55. Okubo, T.; Togawa, H.; Tsuchida, A., publication in preparation.

Chapter 20

Synthesis, Assembly, and Functionalization of Polymer-Coated Ferromagnetic Nanoparticles

Bryan D. Korth[1], Pei Yuin Keng[1], Inbo Shim[2], Chuanbing Tang[3], Tomasz Kowalewski[3], and Jeffrey Pyun[1,*]

[1]Department of Chemistry, University of Arizona,
1306 East University Boulevard, Tucson, AZ 85752
[2]Department of Nano and Electronic Physics, Kookmin University,
Seoul, Korea 136–702
[3]Department of Chemistry, Carnegie Mellon University, 4400 Fifth Avenue,
Pittsburgh, PA 15213

A novel, robust synthetic methodology has been developed to prepare and functionalize well-defined ferromagnetic cobalt nanoparticles. Polystyrene (PS) surfactants of precise molar mass were prepared using controlled radical polymerization and used in the synthesis of metallic cobalt nanoparticles by the thermolysis of dicobaltoctacarbonyl ($Co_2(CO)_8$). Transmission electron microscopy (TEM), scanning probe microscopy (AFM, MFM), x-ray diffraction (XRD) and vibrating sample magnometry (VSM) confirmed that uniform (D = 15 nm $\pm$ 1.5 nm, PS shell = 2 nm), face centered cubic (fcc) cobalt nanocrystals that were prepared and ferromagnetic at room temperature (M_s = 38 emu/g, H_c = 100 Oe). A ligand exchange strategy to functionalize ferromagnetic nanoparticles was developed with functional polymeric surfactants.

The preparation of organic/inorganic hybrid materials integrating inorganic magnetic colloids and organic macromolecules has been pursued for potential applications in biotechnology and microelectronics (1–4). Advances in polymer science have enabled synthetic routes to new materials possessing controllable mechanical, thermal and electroactive properties (5). However, the preparation of wholly organic polymers possessing inherently high magnetic moments and coercivity comparable to magnetic metals remains a challenge. A widely pursued approach to this problem has been the synthesis of nanocomposite hybrid materials with tunable organic and inorganic composition and functionality. The hybridization of inorganic and organic materials on the nanoscale is often the smallest domain size possible to retain useful properties similar to the bulk state (6–8).

Magnetic assembly of particles has been the subject of significant interest due to the directionality that is arises via dipolar attractions. This selective association has been utilized to organize iron oxide-loaded latex colloids and emulsion droplets (100 nm to 30 μm) into one-dimensional (1-D) ordered composite materials (9–17). Despite seminal work with larger dipolar colloids, the use of nanoparticles (1 nm to 100 nm) for hierarchical assembly remains largely unexplored. Magnetic assembly can be achieved by self-assembly, or field induced processes of ferromagnetic nanoparticles into two-dimensional arrays using a "bottom up" methodology (18,19). The use of magnetic nanoparticles is particularly intriguing, as organic polymers can be hybridized with inorganic colloids to form novel nanocomposite materials with synergistic properties (1,20,21). However significant challenges in the synthesis and functionalization of ferromagnetic nanoparticles has stifled further progress in this area.

Both small molecule and macromolecular organic compounds have been used as surfactants, or stabilizers to prepare magnetic nanoparticles. Polymeric surfactants offer distinct advantages as nanoparticle functionality can be modified by tuning the composition of polymers bound to colloidal surfaces via copolymerization, or post-functionalization strategies. The nanoscale dimensions of these surface bound polymers are well-suited to sterically stabilize magnetic colloidal dispersions that are strongly associative and readily agglomerate with small molecule surfactants.

The synthesis of well-defined ferromagnetic nanoparticles is intriguing, as the inherent dipolar associations between certain metallic colloids enables selective 1-D assembly. A number of methods have been reported for the synthesis of uniform magnetic nanoparticles that are superparamagnetic via thermolysis of metal carbonyl precursors, reduction of metal salts (e.g., "polyol methods", sodium borohydride), or oxidation of preformed metallic colloids (22,23). The preparation of ferromagnetic nanoparticles of iron (Fe) and cobalt (Co) have been reported using both polymeric and small molecule surfactant

systems (*24–35*). However, methods to synthesize ferromagnetic nanoparticles in a highly reproducible fashion that afford materials that can be easily processed (i.e., isolated as powders, redispersed in organic solvents) still remains an important challenge.

Herein, we will discuss our recent efforts to prepare well-defined polymer coated ferromagnetic colloids and functionalize via a ligand exchange methodology. Numerous techniques will also be described in the imaging and characterization of these hybrid nanoparticles.

Synthesis of Polystyrene Coated Cobalt Nanoparticles (*36*)

Synthesis of end-functional polystyrene surfactants. Low molecular weight polymers (M_n < 5,000 g/mol) with a single ligating end-group were synthesized using nitroxide mediated polymerization (NMP) (*37–40*) with functional alkoxyamines. The preparation of end-functional polymers bearing primary amines, carboxylic acids, or phosphine oxides was targeted to synthesize macromolecular surfactants that mimicked the functional of small molecule surfactants, such as, oleyl amine, oleic acid and trioctylphosphine oxide (TOPO).
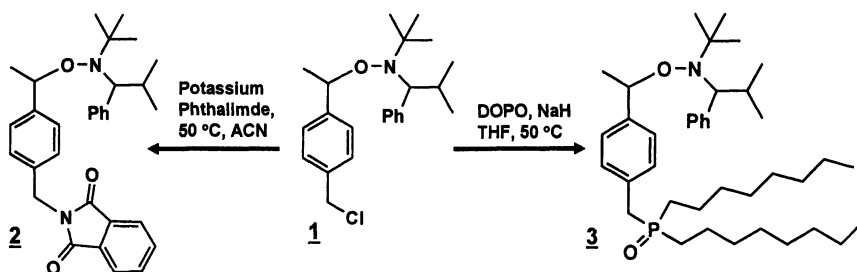
Figure 1. Synthesis of functional alkoxyamine initiators for the preparation of well-defined polystyrene end-functional surfactants.

In the initial steps of the synthesis, the well-established benzyl chloride functional alkoxyamine of Hawker (**1**) (*37,39,41,42*) was prepared and modified in a single step with either potassium phthalimide, or dioctylphosphine oxide (DOPO) affording alkoxyamines **2** & **3**, respectively (Figure 1). Protection of the amine functionality in **2** was required to suppress undesirable chain transfer reactions in the free radical polymerization step. The use of DOPO based ligands was inspired by the work of Emrick *et al.*, which was successfully applied to the functionalization of quantum dots with organic polymers (*43–46*). The synthesis of amine functional PS was achieved by the NMP of styrene (Sty)

using **2** as the initiator. Deprotection of the phthalimide group using hydrazine afforded a well-defined amine end-functional polystyrene (PS-NH$_2$, M$_{n\ SEC}$ = 4,900; M$_w$/M$_n$ = 1.09). Phosphine oxide terminal polystyrene (PS-DOPO, M$_n$ SEC = 5,100; M$_w$/M$_n$ = 1.10) was synthesized by the direct controlled polymerization of styrene (Figure 2).
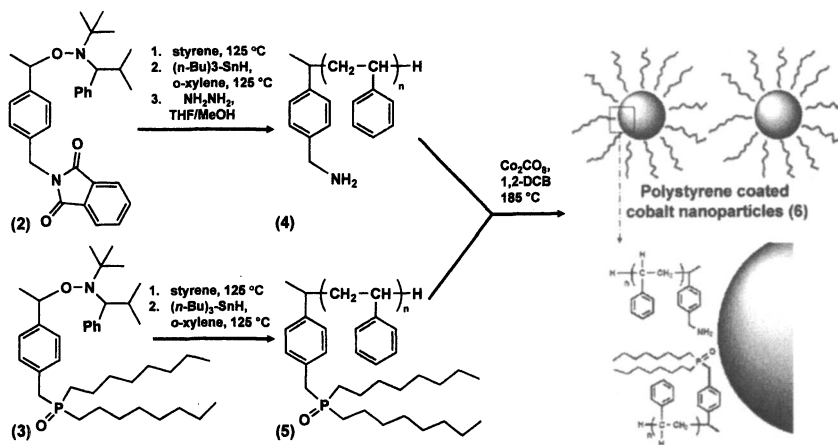
Figure 2. General synthetic scheme for the synthesis of amine, or phosphine oxide functional PS surfactants (M$_n$ = 5,000 g/mol; M$_w$/M$_n$ = 1.10) and thermolysis of Co$_2$(CO)$_8$ to form ferromagnetic PS-CoNPs. (Reprinted with permission from reference 29. Copyright 1999 American Chemical Society.

Polystyrene coated cobalt nanoparticles (PS-CoNPs) were then prepared using a 4:1 wt% mixture of PS-NH$_2$ and PS-DOPO end-functional polystrenes (Figure 2). In this system, the thermolysis of Co$_2$CO$_8$ was carried out at 185 °C yielding ferromagnetic nanoparticles, similar to a previously reported system by Alivisatos *et al.*, using aliphatic amines and TOPO (*30,31*). As observed for cobalt colloids prepared using small molecule surfactants, nanoparticle surfaces were ligated with amine and phosphine oxide end-groups, while the polymer chain formed a hairy corona that stabilized the nanoparticle with a sterically shielding shell while dispersed in organic media. The solid state particle size and morphology of PS-CoNPs were characterized using transmission electron microscopy (TEM). Samples for TEM were prepared by drop casting a colloidal dispersion onto a carbon coated copper grid both in zero-field and magnetic field-induced conditions. Low magnification TEM images reveal the formation of extended fiber-like assembling spanning several microns in length (Figure 3a). TEM images of these assemblies at higher magnification clearly demonstrate the

presence of individual cobalt nanoparticles (particle size ~ 15nm, Fig. 3b) organized into 1-D chains. The formation of chaining in these systems is a well-known signature of ferromagnetism arising from the magnetic dipolar associations of individual colloids. These chains are easily aligned into rigid rod-like structures using weak magnetic fields (100 mT) from standard horseshoe magnets. High resolution TEM clearly image the PS shell as a light corona around dark Co colloidal cores which was two nanometers in thickness. The retention of the polymer coating on the cobalt colloid was confirmed using x-ray photoelectron spectroscopy, as evidenced by the characteristic signature of pS with peaks at 284 and 288 ev.
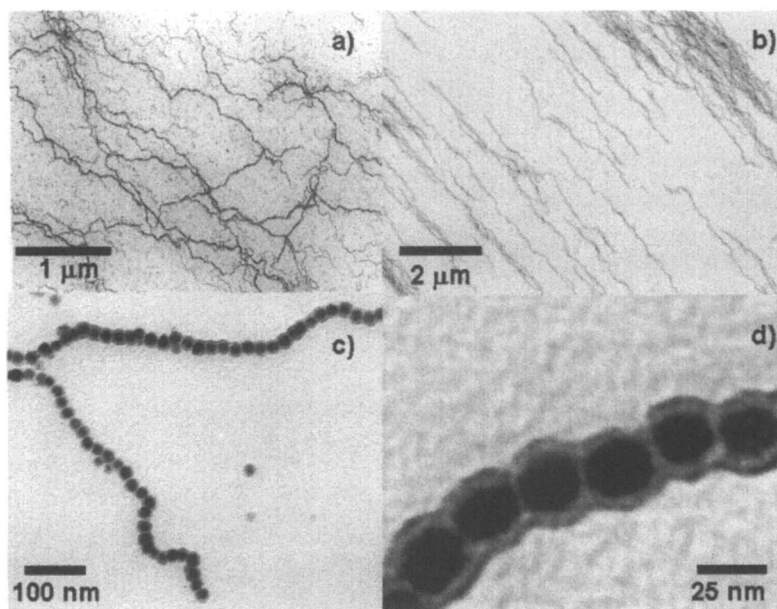
Figure 3. TEM images of ferromagnetic PS-CoNPs (a) self-assembled by deposition from toluene dispersions onto carbon coated copper grids, (b) cast from toluene dispersion and aligned under a magnetic field (100 mT), (c) self-assembled single nanoparticle chains, (d) high magnification image visualizing cobalt colloidal core (dark center) and pS surfactant shell (light halo). (Reprinted with permission from reference 29. Copyright 1999 American Chemical Society.)

Aligned chains of nanoparticles were also clearly evident in topographical tapping-mode AFM (Figure 4) images. PS-CoNP chains were imaged as thin-fiber like features composed of individual nanoparticle repeating units spanning

microns in length. These micron-sized chains were referred to as mesoscopic polymer chains, or simply "meso-polymers", drawing analogies to organic macromolecules on the nanoscale. PS-CoNP meso-polymers cast onto mica subtstrates were found to remain as 1-D assemblies under both "light" and "hard" tapping conditions in AFM imaging experiments, which was attributed to both dipolar associations and interdigitation of PS hairs between nanoparticles.
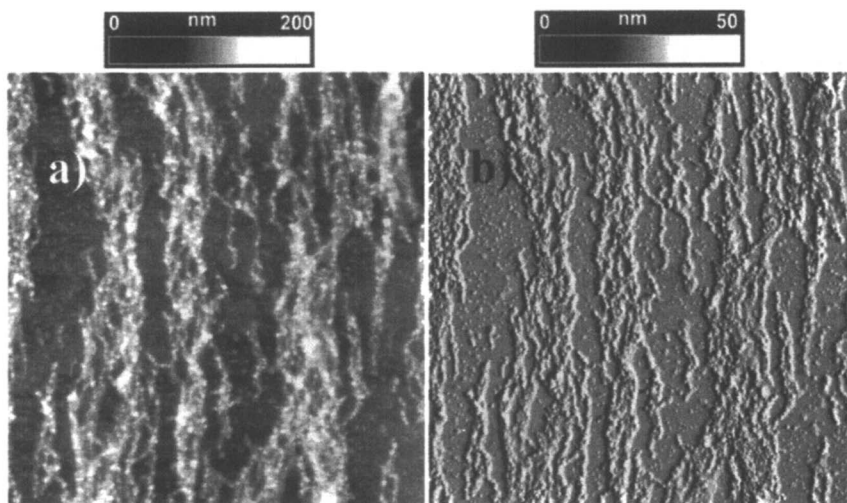
Figure 4. AFM topography (a) and amplitude (b) images (size 10 × 10 μm²) of PS-CoNP meso-polymer chains cast onto carbon-coated mica from toluene dispersion in the presence of external magnetic field (100 mT). (Reprinted with permission from reference 29. Copyright 1999 American Chemical Society.)

Due to the ferromagnetic nature of PS-CoNPs, magnetic force microscopy (MFM) in pure non-contact mode was conducted to interrogate the morphology of ultrathin films from aligned meso-polymer chains (Figure 5). All particles in MFM images appeared brighter than the nearby substrate surface, and the observed contrast did not depend on the direction of tip magnetization. Such behavior can be viewed as an indication that nanoparticle dipole moments were practically parallel to the surface. MFM images depict either the phase or frequency shift induced by the tip-sample force in the oscillating cantilever scanned at constant height above the previously recorded tapping mode-AFM topographic profile. For tip-sample forces perpendicular to the surface, the phase or frequency shift of the cantilever is a function of the gradient of tip-sample force and the brighter regions correspond to weaker attraction (or

stronger repulsion). Reversal of tip magnetization resulted in contrast reversal in MFM images. The absence of reversal indicates that the net tip sample force was dominated by the component which was neither repulsive nor attractive. Such a situation would correspond to the sample magnetization dominated by the component parallel to the surface.
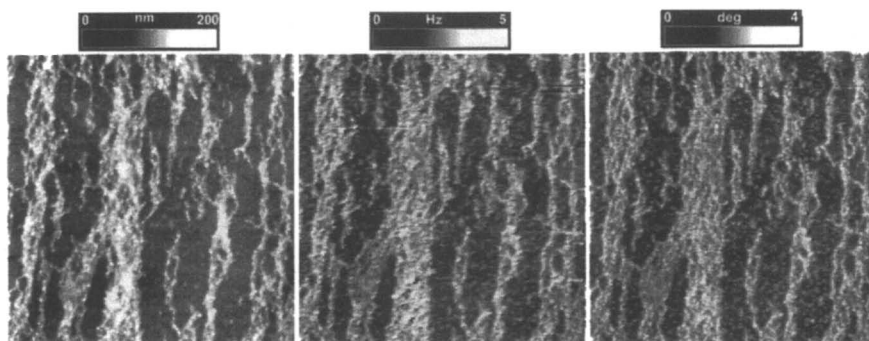
Figure 5. AFM Topography and MFM images (size 10 × 10 μm²) of PS-CoNPs cast onto carbon-coated mica in the presence of 100 mT magnetic field. Left: AFM, height; middle: MFM, frequency; right: MFM, phase. Indentical features imaged in all three modes of imaging provide compelling confirmation of 1-D morphology of assembled ferromagnetic nanoparticles. (Reprinted with permission from reference 29. Copyright 1999 American Chemical Society.)

The presence of end-ligating PS surfactants on CoNPs enabled isolation of hybrid nanoparticles as powders via precipitation and facile redispersion in a variety of non-polar organic solvents (e.g., toluene, THF, dichloromethane). PS-CoNPs possessing polymer hairs of sufficient molar mass ($M_n > 5000$ g/mol) were found to afford colloidal stable dispersion that remained dispersed under dilute concentrations (c ≤ 1 mg/mL) over a period of several months. Conversely, ferromagnetic CoNPs of similar size passivated with small molecular surfactants of oleic acid and TOPO flocculated out of solution in less than 24 hr. due to dipolar associations that could not be sufficiently screened with a short steric barrier around nanoparticles.

The solid state structure of inorganic cores of PS-CoNPs was determined using x-ray diffraction (XRD). The formation of the face centered cubic (fcc) phase of cobalt was confirmed, in addition to the presence of a thin cobalt oxide (CoO) passivating layer around the metal core. Observation of fcc, epsilon (ε), or hexagonal closed packed (hcp) has been reported for the preparation of magnetic cobalt nanoparticles under a variety of different conditions. Vibrating sample magnetometry (VSM) confirmed that these hybrid materials were weakly

ferromagnetic at room temperature (M_s = 38 emu/g, H_c = 100 Oe) and strongly ferromagnetic at 40 K (M_s = 38 emu/g; H_c = 2000 Oe). Significant enhancement of the magnetic coercivity (H_c = 340 Oe) was observed by aligning nanoparticle chains under a weak magnetic field at 300 K due to the coupling of magnetic dipole moments along the 1-D assembly (Figure 6).
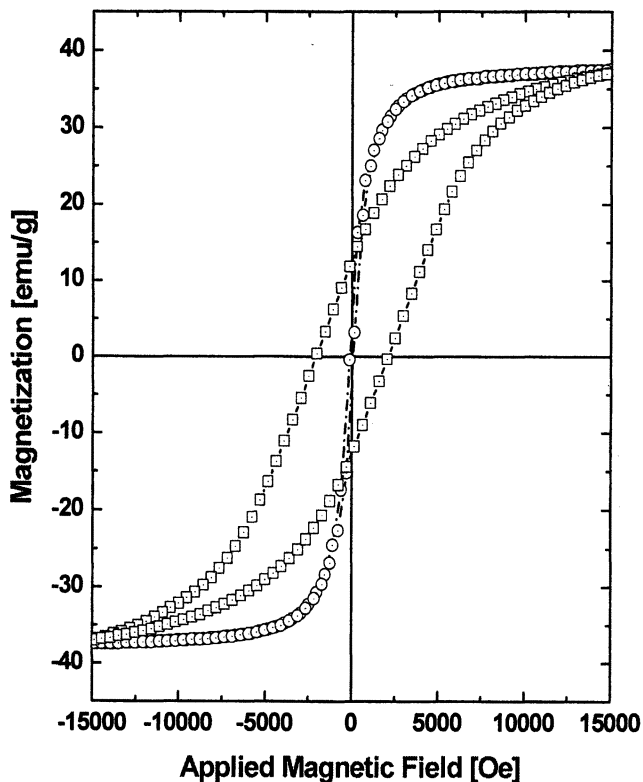
Figure 6. VSM spectra of polystyrene coated cobalt nanoparticle powder.
□ - 40 K, ○ – 300 K. (Reprinted with permission from reference 29.
Copyright 1999 American Chemical Society.)

The ability to decorate ferromagnetic CoNPs with polymers enables enhanced dispersion when blended with free linear polymers, in comparison to magnetic nanoparticles coated with aliphatic groups from oleic acid, TOPO, or other small molecular surfactant shells. The dispersion of ferromagnetic PS-CoNPs (PS shell, M_n = 5,000 g/mol) in blends with excess free linear PS (M_n = 15,000 g/mol) was conducted and evaluated using TEM (Figure 7). These experiments confirmed that nanoparticle chains assemble and remain dispersed

in the free PS matrix. This result indicates that while the polymer coating on nanoparticles enables dispersion in a free polymer matrix, depletion forces from the higher molecular weight polymer matrix, in combination with magnetic associations, force nanoparticles into 1-D assemblies.
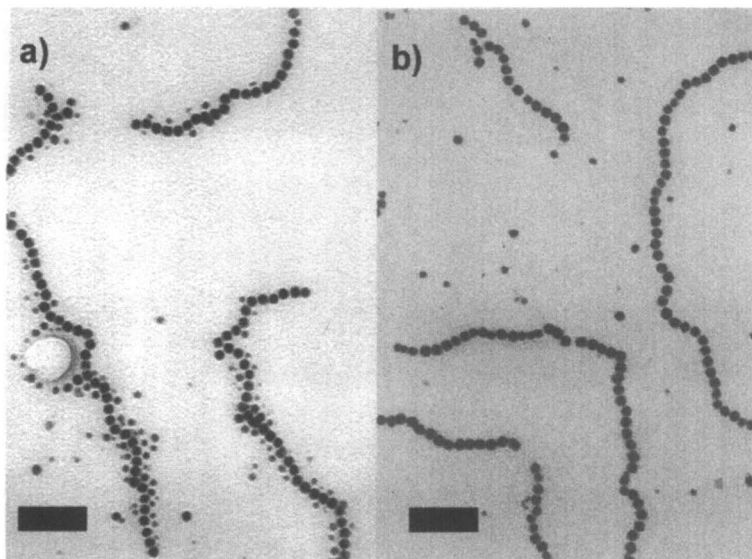
Figure 7. TEM of PS-coated ferromagnetic cobalt nanoparticle cast onto carbon coated copper grid. b) TEM of same PS-coated cobalt nanoparticle blended with 10-fold weight excess of free linear PS (Mn = 15,000 g/mol) cast onto carbon coated copper grid. PS coated nanoparticles capable of assembly when cast both neat (a) and into thin films (b). Scale bar = 100 nm.

Functionalization of Ferromagnetic Cobalt Nanoparticles

The versatile functionalization of ferromagnetic colloids has also been achieved using a ligand exchange process. While extensive work has been dedicated to the functionalization of gold (Au) (38,47–51) and cadmium selenide (CdSe) (43,52,53) quantum dots via ligand exchange reactions, synthetic methods to functionalize magnetic nanoparticles are lacking. Recent examples have demonstrated that superparamagnetic colloids can be functionalized using this approach, however, the preparation of functional ferromagnetic colloids from ligand exchange has not been reported (35,54–57).

This is presumably a major issue accounting for the limited use of magnetic colloids for hierarchical assembly and as 1-D templates in thin films. In the ligand exchange process, polystyrenic surfactants bearing amine and phosphine oxide end-groups are first used to prepare ferromagnetic nanoparticles and are then replaced with other functional polymers with end-functional ligands (i.e., -COOH) that possess a higher affinity for the colloidal surface (Figure 8). The major advantage of the ligand exchange process is the mild reaction conditions employed in the reaction (T = 25-50 °C) enabling a much wider range of functionality that can be introduced to the ferromagnetic colloid periphery, in comparison to conditions used to synthesize nanoparticles (T = 185 °C). This general methodology can be applied to prepare a tremendous range of functional magnetic colloids by simple end-functionalization of polymers, which can be extended to electronically active materials (i.e., conjugated polymers).

In our initial efforts with ligand exchange, carboxylic acid end-functional polymers were synthesized using atom transfer radical polymerization (ATRP)
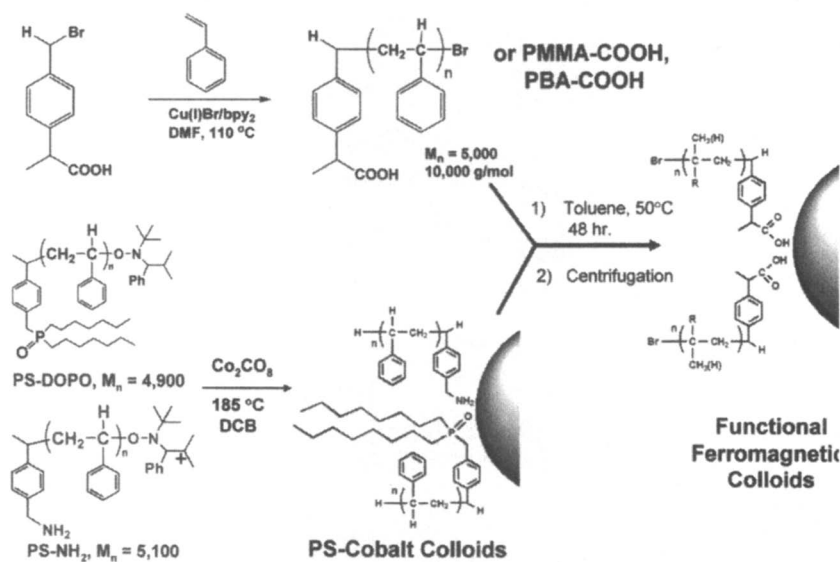
Figure 8. General synthetic scheme for the functionalization of ferromagnetic CoNPs using ligand exchange. Carboxylic acid (COOH) end-functional polymers of polystyrene, poly(methyl methacrylate), or poly(n-butyl) acrylate) were prepared using atom transfer radical polymerization (ATRP) with a COOH functional alkyl halide initiator. Ligand exchange of COOH terminated polymers with preformed PS-CoNPs is then conducted to displace existing PS surfactants.

(6,58–61) to prepare PS, poly(methyl methacrylate) (PMMA) and poly(*n*-butyl acrylate) (PBA) surfactants and functional ferromagnetic cobalt colloids. The key advantage of ATRP, NMP and other controlled radical polymerizations is the ability to control the molecule weight of macromolecules and dictate the placement/connectivity of functional groups along the polymer chain. Using copolymerization of comonomers, or modification of protected side chain groups on copolymers, a wide range of functionality will be introduced onto polymeric surfactants and ferromagnetic nanoparticles.

We have developed a straightforward analytical method to characterize the efficiency of ligand exchange by acidic degradation of metallic colloidal cores with mineral acids (e.g., HCl) and recovery of cleaved polymers. A critical development in this approach is the ability to cleanly isolate ligand-exchanged nanoparticles from free surfactants using centrifugation (e.g., 5,000 rpm, 20 min.) from good solvents (Figure 9).
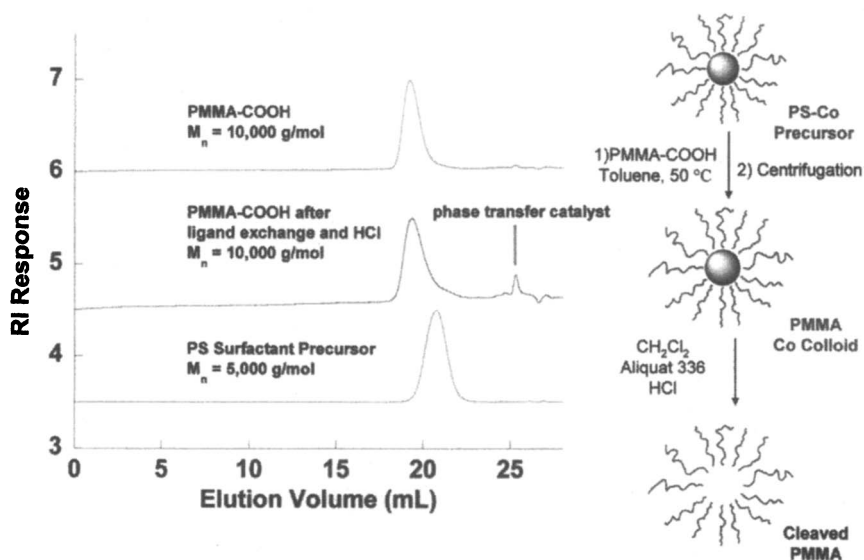
Figure 9. General scheme for ligand exchange (right) SEC characterization of ligand exchange processes (left). Beginning with a PS-CoNP, (PS surfactant, M_n = 5,000 g/mol; M_w/M_n = 1.10) ligand exchange with a PMMA-COOH surfactant (M_n = 10,000 g/mol; M_w/M_n = 1.18) yielded a PMMA-CoNP. HCl degradation of the metallic colloid and recovery of cleaved PMMA chains enables confirmation of ligand exchange via SEC.

Polymer coated cobalt colloids are difficult to characterize directly using traditional NMR spectroscopy, or laser light scattering due to both the ferro-

magnetic properties and the strongly absorbing nature of these materials. Thus, by cleavage and recovery of ligand exchanged polymeric surfactants, traditional techniques, such as, size exclusion chromatography (SEC) and NMR, can be utilized to characterize the structure/composition of organic nanoparticle shells (Figure 9).

Conclusions

A general and versatile methodology to synthesize and functionalize ferromagnetic cobalt nanoparticles with well-defined (co)polymers was achieved. The use of NMP and ATRP enabled the preparation of a wide range of polymeric surfactants of controllable molar mass, composition and functionality which were then used to decorate the surfaces of magnetic cobalt nanoparticles.

Acknowledgements

References

1. Leslie-Pelecky, D. L.; Rieke, R. D. *Chem. Mater.* **1996**, *8*, 1770-1783.
2. Dobson, J. *Nanomedicine* **2006**, *1*, (1), 31-37.
3. Sun, S. *Adv. Mater.)* **2006**, *18*, (4), 393-403.
4. Vatta, L. L.; Sanderson, R. D.; Koch, K. R. *Pure Appl. Chem.* **2006**, *78*, (9), 1793-1801.
5. Hawker, C. J.; Wooley, K. L. *Science* **2005**, *309*, (5738), 1200-1205.
6. Pyun, J.; Matyjaszewski, K. *Chem. Mater.* **2001**, 3436-3448.
7. Grubbs, R. B. *J. Polym. Sci., Part A: Polym. Chem.* **2005**, *43*, 4323-4336.
8. Glogowski, E.; Tangirala, R.; Russell, T. P.; Emrick, T. *J. Polym. Sci., Part A: Polym. Chem.* **2006**, *44*, 5076-5086.
9. Furst, E. M.; Suzuki, C.; Fermigier, M.; Gast, A. P. *Langmuir* **1998**, *14*, (26), 7334-7336.
10. Furst, E. M.; Gast, A. P. *Phys. Rev. Lett.* **1999**, *82*, (20), 4130-4133.
11. Biswal, S. L.; Gast, A. P. *Anal. Chem.* **2004**, *76*, (21), 6448-6455.
12. Cohen-Tannoudji, L.; Bertrand, E.; Bressy, L.; Goubault, C.; Baudry, J.; Klein, J.; Joanny, J.-F.; Bibette, J. *Phys. Rev. Lett.* **2005**, *94*, (3), 038301/1-038301/4.

13. Goubault, C.; Leal-Calderon, F.; Viovy, J.-L.; Bibette, J. *Langmuir* **2005**, *21*, (9), 3725-3729.
14. Mandal, S. K.; Lequeux, N.; Rotenberg, B.; Tramier, M.; Fattaccioli, J.; Bibette, J.; Dubertret, B. *Langmuir* **2005**, *21*, (9), 4175-4179.
15. Singh, H.; Laibinis, P. E.; Hatton, T. A. *Nano Lett.* **2005**, *5*, 2149-2154.
16. Singh, H.; Laibinis, P. E.; Hatton, T. A. *Langmuir* **2005**, *21*, 11500-11509.
17. Singh, H.; Hatton, T. A. *J. Magn. Magn. Mater.* **2007**, *315*, 53-64.
18. Sun, S.; Murray, C. B.; Weller, D.; Folks, L.; Moser, A. *Science* **2000**, *287*, (5460), 1989-1992.
19. Pileni, M.-P. *Adv. Func. Mater.* **2001**, *11*, (5), 323-336.
20. Grubbs, R. B. *Polym. Rev.* **2007**, *47*, 197-215.
21. Pyun, J. *Polym. Rev.* **2007**, *47*, 231-263.
22. Hyeon, T. *Chem. Commun.* **2003**, 927-934.
23. Cushing, B. L.; Kolesnichenko, K. L.; O'Connor, C. J. *Chem. Rev.* **2004**, *104*, 3893-3946.
24. Hess, P. H.; Parker, P. H., Jr. *J. Appl. Polym. Sci.* **1966**, *10*, (12), 1915-27.
25. Thomas, J. R. *J. Appl. Phys.* **1966**, *37*, 2914-2915
26. Griffiths, C. H.; O'Horo, M. P.; Smith, T. W. *J. Appl. Phys.* **1979**, *50*, 7108-7115.
27. Smith, T. W.; Wychick, D. *J. Phys. Chem.* **1980**, *84*, 1621-1629.
28. Platonova, O. A.; Bronstein, L. M.; Solodovnikov, S. P.; Yanovskaya, I. M.; Obolonkova, E. S.; Valetsky, P. M.; Wenz, E.; Antonietti, M. *Colloid and Polym. Sci.* **1997**, *275*, (5), 426-431.
29. Dinega, D. P.; Bawendi, M. G. *Angew. Chem. Int. Ed.* **1999**, 38, (12), 1788-1791.
30. Puntes, V. F.; Krishnan, K. M.; Alivisatos, A. P. *Science* **2001**, *291*, (5511), 2115-2117.
31. Puntes, V. F.; Zanchet, D.; Erdonmez, C. K.; Alivisatos, A. P. *J. Am. Chem. Soc.* **2002**, *124*, (43), 12874-12880.
32. Bao, Y.; Beerman, M.; Krishnan, K. M. *J. Mag. Mag. Mater.* **2003**, *266*, 1245-1249.
33. Diana, F. S.; Lee, S. H.; Petroff, P. M.; Kramer, E. J. *Nano Lett.* **2003**, *3*, 891-895.
34. Baranauskas, V. V., III; Zalich, M. A.; Saunders, M.; St. Pierre, T. G.; Riffle, J. S. *Chem. Mater.* **2005**, *17*, (21), 5246-5254.
35. Gravano, S. M.; Dumas, R.; Liu, K.; Patten, T. E. *J. Polym. Chem., Part A: Polym. Chem.* **2005**, *43*, (16), 3675-3688.
36. Korth, B. D.; Keng, P.; Shim, I.; Bowles, S. E.; Tang, C.; Kowalewski, T.; Nebesny, K. W.; Pyun, J. *J. Am. Chem. Soc.* **2006**, *128*, 6562-6563.
37. Benoit, D.; Chaplinski, V.; Braslau, R.; Hawker, C. J. *J. Am. Chem. Soc.* **1999**, *121*, (16), 3904-3920.
38. Boal, A. K.; Ilhan, F.; DeRouchy, J. E.; Thurn-Albrecht, T.; Russell, T. P.; Rotello, V. M. *Nature* **2000**, *404*, 746.

39. Hawker, C. J.; Bosman, A. W.; Harth, E. *Chem. Rev.* **2001**, *101*, (12), 3661-3688.
40. Lacroix-Desmazes, P.; Lutz, J. F.; Chauvin, F.; Severac, R.; Boutevin, B. *Macromolecules* **2001**, *34*, 8866-8871.
41. Hawker, C. J. *J. Am. Chem. Soc.* **1994**, *116*, (24), 11185-6.
42. Hawker, C. J. *Acc. Chem. Res.* **1997**, *30*, (9), 373-382.
43. Skaff, H.; Ilker, M. F.; Coughlin, E. B.; Emrick, T. *J. Am. Chem. Soc.* **2002**, *124*, (20), 5729-5733.
44. Sill, K.; Emrick, T. S. *Chem. Mater.* **2004**, *16*, 1240-1243.
45. Skaff, H.; Emrick, T. S. *Angew. Chem. Int. Ed.* **2004**, *43*, 5383-5386.
46. Skaff, H.; Ilker, M. F.; Coughlin, E. B.; Emrick, T. *J. Am. Chem. Soc.* **2002**, *124*, (20), 5729-5733.
47. Hostetler, M. J.; Green, S. J.; Stokes, J. J.; Murray, R. W. *J. Am. Chem. Soc.* **1996**, *118*, 4212-4213.
48. Templeton, A. C.; Hostetler, M. J.; Kraft, C. T.; Murray, R. W. *J. Am. Chem. Soc.* **1998**, *120*, 1906-1911.
49. Hostetler, M. J.; Templeton, A. C.; Murray, R. W. *Langmuir* **1999**, *15*, 3782-3789.
50. Frankamp, B. L.; Uzun, O.; Ilhan, F.; Boal, A. K.; Rotello, V. M. *J. Am. Chem. Soc.* **2002**, *124*, 892-893.
51. Shenhar, R.; Norsten, T. B.; Rotello, V. M. *Adv. Mater.* **2005**, *17*, 657-669.
52. Murray, C. B.; Norris, D. J.; Bawendi, M. G. *J. Am. Chem. Soc.* **1993**, *115*, 8706-8715.
53. Skaff, H.; Emrick, T. S. *Chem. Commun.* **2003**, 52-53.
54. Vestal, C. R.; Zhang, Z. J. *J. Am. Chem. Soc.* **2002**, *124*, (48), 14312-14313.
55. Wang, Y.; Teng, X.; Wang, J.-S.; Yang, H. *Nano Lett.* **2003**, *3*, 789-793.
56. Hong, R.; Fischer, N. O.; Emrick, T.; Rotello, V. M. *Chem. Mater.* **2005**, *17*, (18), 4617-4621.
57. Lattuada, M.; Hatton, T. A. *Langmuir* **2007**, *23*, 2158-2168.
58. Patten, T. E.; Xia, J.; Abernathy, T.; Matyjaszewski, K. *Science* **1996**, *272*, (5263), 866-868.
59. Matyjaszewski, K.; Patten, T. E.; Xia, J. *J. Am. Chem. Soc.* **1997**, *119*, (4), 674-680.
60. Patten, T. E.; Matyjaszewski, K. *Adv. Mater. (Weinheim, Germany)* **1998**, *10*, (12), 901-915.
61. Matyjaszewski, K.; Xia, J. *Chem. Rev.* **2001**, *101*, 2921-2990.

Chapter 21

Structural Characterization of Glassy and Rubbery Model Anionic Amphiphilic Polymer Conetworks

Gergely Kali[1,2], Theoni K. Georgiou[1], Béla Iván[2],
Costas S. Patrickios[1,*], Elena Loizou[3], Yi Thomann[4],
and Joerg C. Tiller[4]

[1]Department of Chemistry, University of Cyprus, P.O. Box 20537,
1678 Nicosia, Cyprus
[2]Department of Polymer Chemistry and Material Science, Institute
of Materials and Environmental Chemistry, Chemical Research Center,
Hungarian Academy of Sciences, P.O. Box 17, H–1525 Budapest,
Pusztaszeri út 59–67, Hungary
[3]Center for Neutron Research, National Institute of Standards
and Technology, Gaithersburg, MD 20899
[4]Freiburg Materials Research Center and Institute for Macromolecular
Chemistry, Department of Chemistry, University of Freiburg,
D–79104 Freiburg, Stefan-Meier-Strasse 21, Germany

The structure of two series of model amphiphilic polymer
conetworks based on the hydrophilic anionic methacrylic acid
was characterized by atomic force microscopy (AFM) and
small-angle neutron scattering (SANS). In the first series, the
hydrophobic component was the glassy poly(methyl meth-
acrylate), while the rubbery poly(2-butyl-1-octyl methacrylate)
constituted the hydrophobic segments in the second series.
Each series comprised conetworks in which the hydrophile /
hydrophobe ratio was systematically varied as well as
conetworks with different architecture of the linear chain:
ABA and BAB triblock and statistical. The AFM and SANS
measurements indicated nanophase separation in the triblock
copolymer-based conetworks and provided the spacing, size
and shape of the formed nanodomains.

Introduction

Amphiphilic polymer conetworks (APCNs) possess unique properties that are useful for different and important applications (*1,2*). These properties include the ability to interact and swell in polar and nonpolar solvents, good mechanical strength (compared to hydrogels), and the ability for nanophase separation (*1-15*). Several characterization methods have been used to investigate the nanophase separation in these materials: small-angle x-ray scattering (SAXS) (*5-8*), small-angle neutron scattering (SANS) (*9,10*), transmission electron microscopy (TEM) (*11*), solid state NMR (*8,12*), and atomic force microscopy (AFM) (*5-7,11,13,14*). However, there are not many literature reports where more than one of these methods were used to investigate nanophase separation and to give combined structural information.

In this report, we study two series of model anionic APCNs and we extensively investigate their swelling and structural properties. Methacrylic acid (MAA), a hydrophilic, negatively ionizable monomer, was the common component in the two series. In the first series, the simple, commercially available and inexpensive methyl methacrylate (MMA) constituted the hydrophobic component. However, PMMA is glassy (tough), and likely to result in fragile materials with non-equilibrium frozen structures. In contrast, the hydrophobic component in the second series was the non-commercially available 2-butyl-1-octyl methacrylate (BOMA), whose polymers are rubbery (soft) and likely to lead to APCNs that are mechanically more robust and present easily accessible equilibrium morphologies.

Experimental

Copolymer Synthesis

All the conetworks in this study were synthesized by group transfer polymerization (GTP) (*16*). The hydrophilic monomer MAA was introduced via the polymerization of tetrahydropyranyl methacrylate (THPMA, in-house synthesized from dihydropyran and MAA), followed by the removal of the protecting tetrahydropyranyl group by acidic hydrolysis after conetwork formation. From the two hydrophobic monomers used in this study, MMA was commercially available, while BOMA was in-house synthesized from the corresponding alcohol and methacryloyl chloride. 1,4-Bis(methoxytrimethyl-siloxymethylene)cyclohexane (MTSMC, in-house synthesized) and ethylene glycol dimethacrylate (EGDMA) were used as the initiator and the cross-linker for the conetwork formation, respectively. Figure 1 shows the chemical structures and names of the repeating units of all monomers and the EGDMA cross-linker.

Figure 1. Chemical structures and names of the monomer and cross-linker repeating units.

The conetworks were synthesized by sequential monomer / cross-linker additions (*17-20*). APCNs of different compositions were obtained by varying the comonomer feed ratio, while APCNs of different architectures were obtained by varying the order of reagents addition (monomers, cross-linker or initiator (*10*)). Before cross-linking, the linear copolymer precursors were sampled and were characterized in terms of their molecular weight (MW) and composition using gel permeation chromatography (GPC) and ^{1}H NMR spectroscopy, respectively. Figure 2 represents a typical structure of a model APCN.
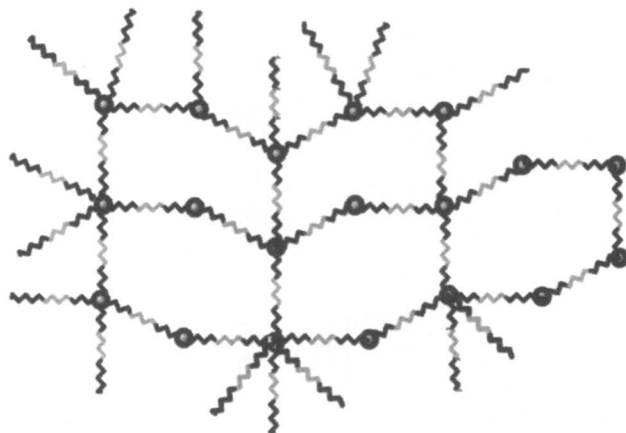
Figure 2. A probable structure of a typical model conetwork. The grey and black colors represent hydrophilic and hydrophobic chains, while the EGDMA cross-linkers are shown as black circles. The number of arms at the cross-links is around 30.

Dynamic Mechanical Analysis (DMA)

Investigations on the mechanical properties of hydrolyzed and uncharged conetworks were carried out using a Tritec2000 Triton Technologies dynamic mechanical analyzer. The measurements were performed in the compression mode at a single frequency of 1 Hz. The experiments were carried out at 25 °C and, during the measurements, the samples were immersed in water (pH ~ 8).

Measurements of the Degree of Swelling (DS)

The hydrolyzed conetworks were cut into small pieces and dried under vacuum for three days at room temperature. The dry conetwork mass was determined gravimetrically, followed by the transfer of the conetworks in water. Twelve samples were allowed to equilibrate for three weeks in milli-Q

290

(deionized) water, covering a pH range between 2 and 13 and the whole range of the degree of ionization (DI) of the MAA units. The DSs were calculated as the ratio of the swollen conetwork mass divided by the dry conetwork mass. After the measurements of the DSs in water as a function of pH, the water-swollen samples were dried in vacuum at room temperature for three days. A volume of 5 mL THF was transferred into the glass vials containing the dried conetwork samples, which were allowed to equilibrate again for three weeks. The THF-swollen mass of each conetwork was determined gravimetrically, from which the DS in THF was calculated.

Small-Angle Neutron Scattering (SANS)

All the (hydrolyzed) conetworks of this study were characterized using SANS in D_2O. The samples were in the uncharged state (pH ~ 8). SANS measurements were performed on the 30 m NG7 instrument at the Center for Neutron Research of the National Institute of Standards and Technology (NIST). The incident wavelength was $\lambda = 6$ Å. Three sample-to-detector distances, 1.00, 4.00 and 15.30 m, were employed, covering a q-range [q is the scattering vector, with $q = 4\pi/\lambda \sin(\theta/2)$, θ is the scattering angle] from 0.003 Å^{-1} to 0.60 Å^{-1}. The samples were loaded in 1 mm gap thickness quartz cells. The scattering patterns were isotropic, and, therefore, the measured counts were circularly averaged. The averaged data were corrected for empty cell and background. The distance between the scattering centers was estimated from the position of the intensity maximum, q_{max}, as $2\pi / q_{max}$.

Atomic Force Microscopy (AFM)

The surfaces of the dried samples (hydrolyzed and uncharged) were microtomed at room temperature with a diamond knife from Diatome and a Microtom ULTRACUT UCT from Leica, removing about 100 nm of the surface. AFM images of the microtomed samples were recorded with a Nanoscope III scanning probe microscope from Digital Instruments using Si cantilevers (tip radius about 5 nm) with a fundamental resonance frequency of approximately 200 kHz.

Results and Discussion

The sequential GTP of the monomers and the cross-linker resulted in model APCNs with linear copolymer chains between the cross-links (elastic chains) of well-defined MW and composition as it was confirmed by GPC and ^{1}H NMR measurements, respectively. The number-average MWs, M_ns, the polydispersity indices (M_w/M_n) and the compositions of all conetwork precursors for the two

series of conetworks are shown in Tables I and II. Copolymers of different compositions and architectures were prepared. For the model APCNs, ABA and BAB triblock as well as statistical copolymer chain architectures were synthesized. Schematic representations of these architectures as well as of that of the randomly cross-linked APCN are illustrated in Figure 3.

Mechanical Properties of the Conetworks

The elastic modulus in compression of the hydrolyzed conetworks in water at pH ~ 8 was determined using DMA. The elastic moduli of the model conetworks based on MAA_{10}-b-$BOMA_m$-b-MAA_{10} triblock copolymers ranged between 2.5 and 110 MPa, and increased with the MAA content because of the concomitant decrease in the BOMA soft component. The modulus of the randomly cross-linked conetwork was higher than that of its ABA triblock copolymer isomer due to the greater density of elastic chains in the former conetwork, resulting from the random distribution of the cross-linker in the conetwork. In contrast, in the triblock copolymer based conetworks, the cross-linkers were concentrated at the chain ends (4 cross-linker residues per chain end), leading to fewer elastic chains of higher MW. In the case of the MMA series, DMA characterization was more difficult because most of the conetworks broke during the measurements. These results support the initial hypothesis that the BOMA-based conetworks would exhibit improved mechanical properties compared to the MMA-based ones.

Effect of Degree of Ionization on Swelling

The experimentally measured DSs in water and in THF along with the DIs of two selected conetworks are plotted against pH in Figure 4. The DSs of the conetworks in the two solvents followed opposite pH dependencies. In water, the conetworks started to swell above pH 7 and the DSs increased with increasing pH, due to the ionization of the weakly acidic MAA units. The DI $vs.$ pH curves followed the respective aqueous DS $vs.$ pH curves, confirming the importance of electrostatics in swelling.

In THF, the conetworks showed the opposite behavior. In particular, the DSs in THF decreased as the DI of the MAA units in the conetworks increased. This was due to the incompatibility of THF with the ionized MAA units.

Effect of Conetwork Composition on Swelling

Figure 5 shows the dependence of the DSs on the composition of ABA (MAA end-blocks) triblock copolymer-based conetworks in the fully charged state and the uncharged state, both in H_2O and THF.

Table I. Molecular Characteristics of the Linear Copolymer Precursors to the MMA-THPMA Conetworks

Net. No.	Theoretical chemical structure [a]	Theoretical MW	GPC results		% mol THPMA	
			M_n	M_w/M_n	Theor.	^1H NMR
1	$T_{1.25}$-b-M_{32}-b-$T_{1.25}$	3825	5870	1.22	7	-
2	$T_{2.5}$-b-M_{32}-b-$T_{2.5}$	4250	5130	1.22	14	-
3	T_5-b-M_{32}-b-T_5	5100	5820	1.25	24	16
4	T_{10}-b-M_{32}-b-T_{10}	6800	8700	1.31	39	26
5	T_{15}-b-M_{32}-b-T_{15}	8500	9870	1.32	48	31
6	M_{16}-b-T_{20}-b-M_{16}	6800	9820	1.34	39	24
7	T_{20}-co-M_{32}	6800	9130	1.27	39	31
8	Random- random	----	N/A[b]	N/A[b]	39	N/A[b]
9	T_{10}-b-M_{20}-b-T_{10}	5599	5660	1.28	50	43
10	T_{10}-b-M_{10}-b-T_{10}	4598	5720	1.24	67	-

[a] T, M and b are (further) abbreviations for THPMA (MAA), MMA and *block*, respectively.
[b] N/A: Not applicable as it could not be determined due to the simultaneous copolymerizations of monomers and cross-linker.

Table II. Molecular Characteristics of the Linear Copolymer Precursors to the BOMA-THPMA Conetworks

Net. No.	Theoretical chemical structure [a]	Theoretical MW	GPC results		% mol THPMA	
			M_n	M_w/M_n	Theor.	^1H NMR
1	T_{10}-b-$B_{1.25}$-b-T_{10}	3740	6190	1.13	94	95
2	T_{10}-b-$B_{2.5}$-b-T_{10}	4080	7180	1.14	89	83
3	T_{10}-b-B_5-b-T_{10}	4750	10030	1.18	80	81
4	B_5-b-T_{20}-b-B_5	6100	6680	1.23	67	67
5	T_{10}-b-B_{10}-b-T_{10}	6100	15330	1.25	67	74
6	T_{20}-co-B_{10}	6100	16520	1.15	67	83
7	Random- random	----	N/A[b]	N/A[b]	67	N/A[b]

[a] T, B and b are (further) abbreviations for THPMA (MAA), BOMA and *block*, respectively.
[b] N/A: Not applicable as it could not be determined due to the simultaneous copolymerizations of monomers and cross-linker.

ABA triblock copolymer precursor

BAB triblock copolymer precursor

statistical copolymer precursor

randomly cross-linked structure
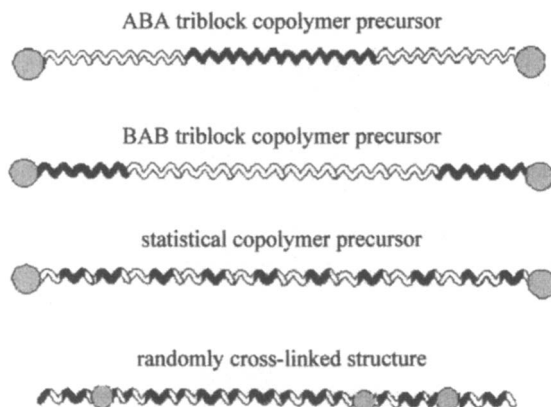
Figure 3. Architectures of the precursor chains between the cross-links of the conetworks. The white and black colors represent hydrophilic and hydrophobic chains, while the EGDMA cross-linkers are shown as grey circles.

Uncharged MAA. In this case, all the monomers, uncharged MAA, MMA, and BOMA, are compatible with THF. Thus, the DSs in THF for both conetwork series were high and depended only on the average MW between the cross-links, and not on the composition. In contrast, all the segments are only slightly compatible (uncharged MAA) or not compatible at all (MMA and BOMA) with water. Thus, the conetworks were collapsed, exhibiting very low DSs, and presenting no composition effect on swelling.

Fully Charged MAA. The DSs in water increased by increasing the MAA content, because of the full compatibility of the charged MAA segments with water. The DSs in THF remained low, because of the incompatibility of the charged MAA units with THF.

Effect of Conetwork Architecture on Swelling

Figure 6 illustrates the effect of conetwork architecture on the DS. All the conetworks whose DSs are presented in this figure are isomers, having the same composition, 39 mol % MAA in Figure 6(a) (see Table I) and 67 mol % MAA in Figure 6(b) (see Table II).

Uncharged MAA. No conetwork architecture dependence on swelling in THF or in water was observed when the MAA units were uncharged, because, as already stated, all monomer units were compatible with THF and incompatible with water.

(a) $(MAA_{10}$-b-MMA_{20}-b-$MAA_{10})$-*network*

(b) $(MAA_{10}$-b-$BOMA_{2.5}$-b-$MAA_{10})$-*network*
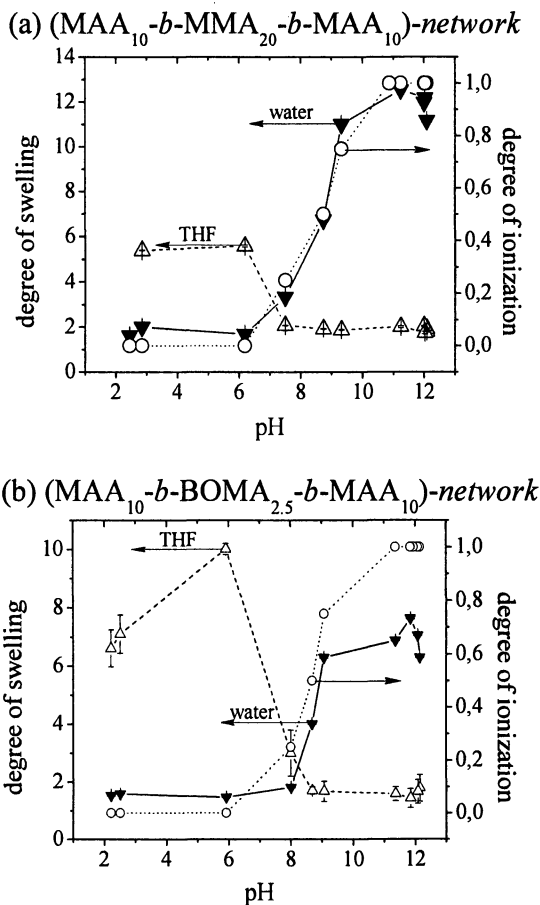
Figure 4. Degrees of swelling and degrees of ionization of selected (a) MMA- and (b) BOMA-containing conetworks as a function of pH.

Fully Charged MAA. In water, the conetwork architecture had a significant influence on the DSs. In particular, in each series, the statistical copolymer model APCNs swelled more than the other three types of conetworks. This was attributed to the inability of these conetworks to microphase separate due to the random distribution of the hydrophobic monomer repeat units along the elastic chains. This is to be contrasted to the block copolymer APCNs where microphase separation occurs because of the collapse of the solvent incompatible blocks (hydrophobic PMMA and PBOMA in water, and charged PMAA in THF). The APCNs based on the triblock copolymers with a hydrophilic (PMAA) inner (middle) block (BAB structure) presented lower aqueous DSs than the APCNs with the reverse architecture (ABA structure), probably due to the

(a) $(MAA_x\text{-}b\text{-}MMA_{32}\text{-}b\text{-}MAA_x)$-*network*

(b) $(MAA_{10}\text{-}b\text{-}BOMA_y\text{-}b\text{-}MAA_{10})$-*network*
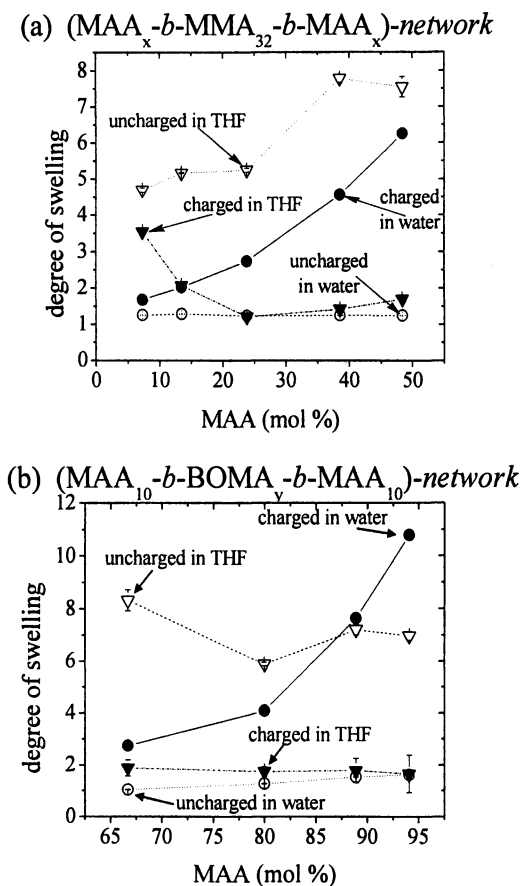
Figure 5. Effect of conetwork composition on the degrees of swelling of the conetworks in water and in THF at their uncharged and fully charged states. (Figure 5a is reproduced from reference 10. Copyright 2007 American Chemical Society.)

synergistic effect on microphase separation arising from the proximity of the hydrophobic units (MMA or BOMA) to the also hydrophobic EGDMA cores in the former type of APCNs. The randomly cross-linked statistical APCNs presented lower DSs than the statistical copolymer-based model APCNs due to the presence of shorter copolymer chains in the former type of APCNs arising from the random distribution of the cross-links.

Nanophase Behavior

In the following paragraphs, the nanophase behavior of the APCNs, as investigated using SANS and AFM, is discussed.

(a) MMA-MAA

degree of swelling

- charged in water
- uncharged in THF
- charged in THF
- uncharged in water

statistical copolymer network
randomly cross-linked copolymer network
ABA triblock copolymer network
BAB triblock copolymer network

(b) BOMA-MAA

degree of swelling

- uncharged in THF
- charged in THF
- charged in water
- uncharged in water

BAB triblock copolymer network
ABA triblock copolymer network
randomly cross-linked copolymer network
statistical copolymer network

Figure 6. Effect of conetwork architecture on the degrees of swelling of the conetworks in water and in THF at their uncharged and fully charged states. (Figure 6a is reproduced from reference 10. Copyright 2007 American Chemical Society.)

SANS. Figure 7 shows the SANS profiles of all the APCNs in the uncharged state in D_2O. In particular, Figures 7(a) and (c) show the results for the MMA-MAA conetworks, whereas Figures 7(b) and (d) show those for the BOMA-MAA conetworks. The effect of conetwork composition is illustrated in Figures 7(a) and (b), while Figures 7(b) and (d) illustrate the effect of conetwork architecture. Most SANS profiles exhibited single peaks, consistent with conetwork nanophase separation. The absence of higher harmonics could be attributed to the polydispersity of the scattering centers or / and to their short-range liquid-like order. Below, the four graphs in Figure 7 are discussed separately:

In Figure 7(a), as the MMA content decreased (or, equivalently, as the MAA content and the elastic chain length increased), the intensity of the peaks increased. Samples with very low MAA content did not present a peak, not necessarily due to lack of nanophase separation, but most likely due to the lack of sufficient contrast: the high conetwork hydrophobicity did not allow enough D_2O to swell the conetworks, resulting in a weak signal. The spacings between the scattering centers (calculated as $2\pi/q_{max}$) were quite similar (9-10 nm).

In Figure 7(b), as the BOMA content in the APCNs increased, the position of the peaks was shifted to lower q-values and their scattering intensity increased. The latter was in agreement with a more complete nanophase separation in the more hydrophobic conetworks (larger scattering centers), while the former indicated the greater separation between the scattering centers as the size of the conetwork elastic chains increased. In particular, the spacing between the scattering centers varied from 7.7 nm, to 7.6 nm, to 9.3 nm and to 12.8 nm as the M_n of the linear copolymer precursors to the conetworks increased from 6190 to 15330 g mol^{-1} (see Table II).

In Figure 7(c), from the four isomeric APCNs, the triblock copolymer-based ones presented clear correlation peaks, consistent with nanophase separation, whereas the weak correlation peak in the SANS profile of the statistical copolymer APCN was probably due to the EGDMA hydrophobic cores. The complete absence of a peak in the randomly cross-linked APCN was due to lack of nanophase separation and to the random distribution of the cross-linker units over the conetwork structure.

In contrast to the curves in Figure 7(c) (MMA-MAA series), all SANS profiles in Figure 7(d) (BOMA-MAA APCNs) presented a peak. For the triblock copolymer-based APCNs, the peaks were pronounced due to nanophase separation. The weaker peaks observed in the scattering curves of the statistical copolymer APCN and in the randomly cross-linked APCN were probably due to correlations between BOMA unimolecular micelles. The peaks of all four curves were located approximately at the same q-values, suggesting similar distances between the scattering centers.

AFM. Figures 8 and 9 display phase mode AFM images for isomeric model APCNs based on ABA triblock and statistical copolymers for the MMA-MAA and the BOMA-MAA conetwork series, respectively.
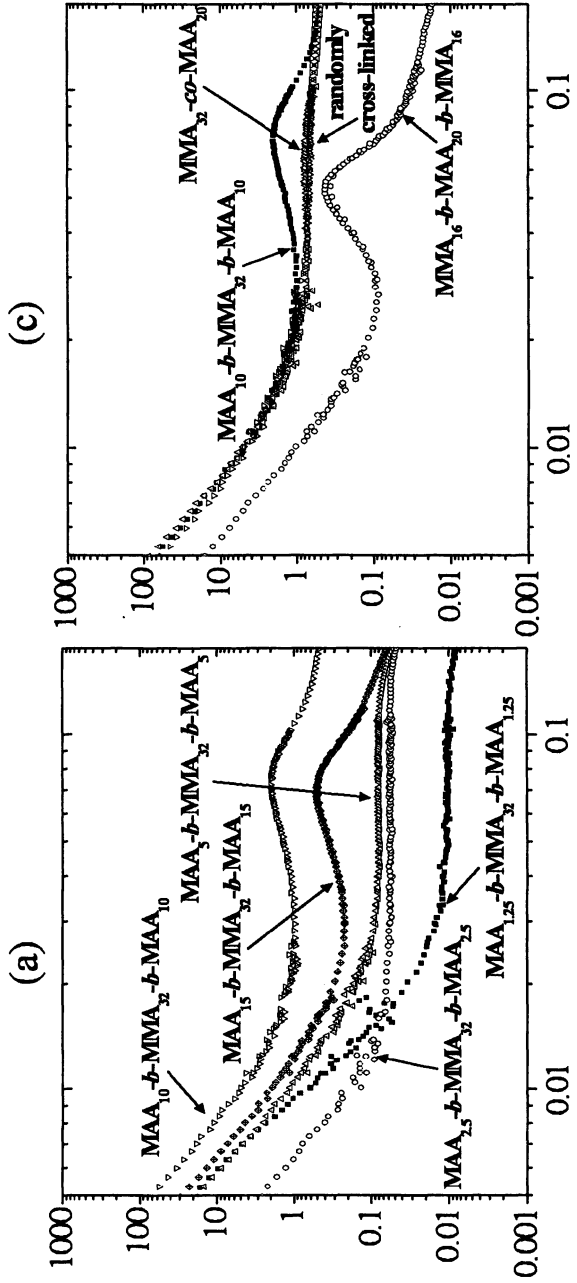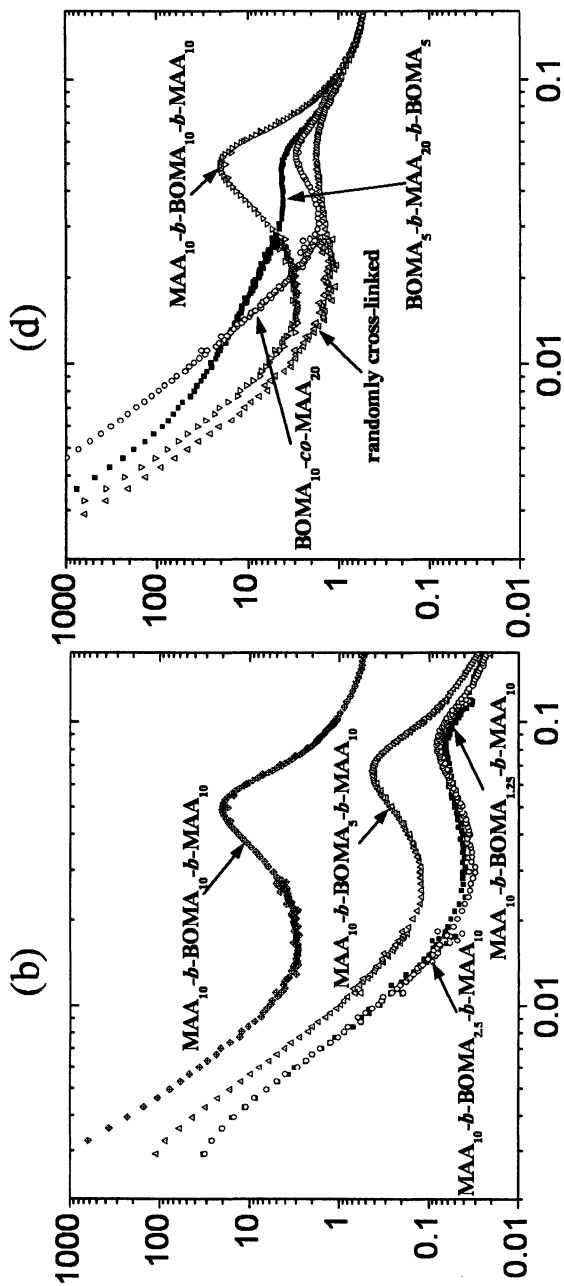
Figure 7. SANS profiles of all the APCNs in D_2O in the uncharged state. The vertical and horizontal axes are intensity in arbitrary units and q ($\mathring{A}^{-1}$). (Figure 7c is reproduced from reference 10. Copyright 2007 American Chemical Society.)
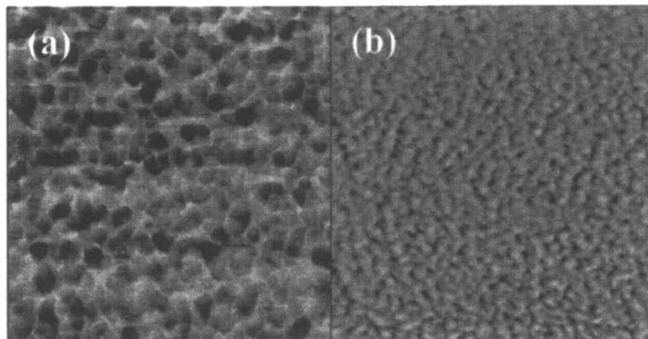
Figure 8. AFM phase mode images for (a) the ABA triblock copolymer-based and (b) the statistical copolymer-based MMA-MAA model conetworks. Each image has dimensions of 500 nm × 500 nm. (Reproduced from reference 10. Copyright 2007 American Chemical Society.)
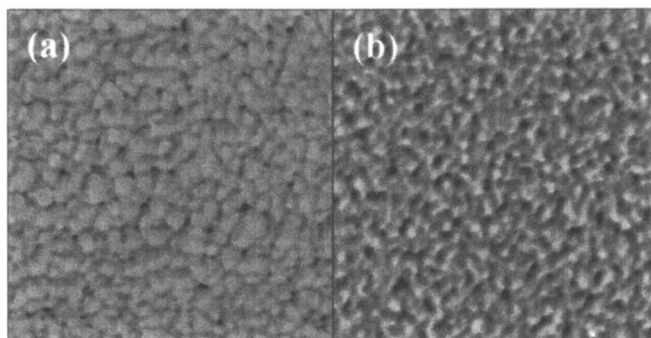
Figure 9. AFM phase mode images for (a) the ABA triblock copolymer-based and (b) the statistical copolymer-based BOMA-MAA model conetworks. Each image has dimensions of 500 nm × 500 nm.

The MAA_{10}-b-MMA_{32}-b-MAA_{10} triblock copolymer-based model APCN (Figure 8(a)) presented large spherical domains of a size of 40 nm, while its isomeric, statistical copolymer-based model APCN (Figure 8(b)) showed smaller and elongated domains of a broadly distributed size in a range of 4-20 nm (average 10 nm). The domain size of 40 nm in the triblock copolymer-based APCN was larger than the characteristic size of 9 nm determined by SANS. This might indicate that the contrast difference between the phases in AFM was not high enough to see distinguishable morphologies in the higher resolution. The average domain size of 10 nm in the statistical copolymer-based model APCN might correspond to the EGDMA cores, and this is in perfect agreement with the SANS measurements.

Figure 9(a) presents the phase mode AFM image for the model APCN based on the MAA_{10}-b-$BOMA_{10}$-b-MAA_{10} triblock copolymer. Similar to the corresponding MMA-based model APCN (Figure 8(a)), large spherical domains were established in the range of 28 to 55 nm (average 40 nm). The model APCN based on the statistical copolymer (Figure 9(b)) exhibited smaller and elongated domains (average 10 nm). The average domain size of the triblock copolymer model APCN (40 nm) was again greater than the characteristic size (13 nm) determined by SANS. The average domain size for the statistical copolymer-based model APCN was close to 10 nm, corresponding again to the size of the EGDMA cores in the conetwork structure.

Conclusion

Two series of model anionic APCNs with glassy and rubbery hydrophobic components were characterized in terms of their swelling and structural properties. The swelling depended on conetwork composition, degree of ionization, MW and architecture, and on the swelling solvent. Despite their different mechanical properties, the nanoscale structure of the two conetwork series was similar: the triblock copolymer-based model APCNs self-assembled into spherical domains with a size of 40 nm and subdomains with a size of 10 nm, while the statistical copolymer-based model APCNs exhibited elongated domains with a size of 10 nm.

Acknowledgements

References

1. Patrickios, C. S.; Georgiou, T. K. *Curr. Opin. Colloid & Interface Sci.* **2003**, *8*, 76-85.
2. Erdődi, G.; Kennedy, J. P. *Prog. Polym. Sci.* **2006**, *31*, 1-18.
3. Haraszti, M.; Tóth, E.; Iván, B. *Chem. Mater.* **2006**, *18*, 4952-4958.
4. Bruns, N.; Tiller, J. C. *Nano Lett.* **2005**, *5*, 45-48.
5. Scherble, J.; Thomann, R.; Iván, B.; Mülhaupt, R. *J. Polym. Sci., Part B: Polym. Phys.* **2001**, *39*, 1429-1436.

6. Howse, J. R.; Topham, P.; Crook, C. J.; Gleeson, A. J.; Bras, W.; Jones, R. A. L.; Ryan, A. J. *Nano Lett.* **2006**, *6*, 73-77.
7. Topham, P. D.; Howse, J. R.; Mykhaylyk, O. O.; Armes, S. P.; Jones, R. A. L.; Ryan, A. J. *Macromolecules* **2006**, *39*, 5573-5576.
8. Domján, A.; Erdődi, G.; Wilhelm, M.; Neidhöfer, M.; Iván, B.; Spiess, H. W. *Macromolecules* **2003**, *36*, 9107-9114.
9. Iván, B.; Almdal, K.; Mortensen, K.; Johannsen, I.; Kops, J. *Macromolecules* **2001**, *34*, 1579-1585.
10. Kali, G.; Georgiou, T. K.; Iván, B.; Patrickios, C. S.; Loizou, E.; Thomann, Y.; Tiller, J. C. *Macromolecules* **2007**, *40*, 2192-2200.
11. Bruns, N.; Tiller, J. C. *Macromolecules* **2006**, *39*, 4386-4394.
12. Lequieu, W.; Van De Velde, P.; Du Prez, F. E.; Adriaensens, P.; Storme, L.; Gelan, J. *Polymer* **2004**, *45*, 7943-7951.
13. Iván, B.; Haraszti, M.; Erdődi, G.; Scherble, J.; Thomann, R.; Mülhaupt, R. *Macromol. Symp.* **2005**, *227*, 265-273.
14. Bruns, N.; Scherble, J.; Hartmann, L.; Thomann, R.; Iván, B.; Mülhaupt, R.; Tiller, J. C. *Macromolecules* **2005**, *38*, 2431-2438.
15. (a) Vamvakaki, M.; Patrickios, C. S. *J. Phys. Chem. B* **2001**, *105*, 4979-4986. (b) Georgiou, T. K.; Vamvakaki, M.; Patrickios, C. S. *Polymer* **2004**, *45*, 7341-7355. (c) Karbarz, M.; Stojek, Z.; Patrickios, C. S. *Polymer* **2005**, *46*, 7456-7462. (d) Karbarz, M.; Stojek, Z.; Georgiou, T. K.; Patrickios, C. S. *Polymer* **2006**, *47*, 5182-5186.
16. Webster, O. W.; Hertler, W. R.; Sogah, D. Y.; Farnham, W. B.; RajanBabu, T. V. *J. Am. Chem. Soc.* **1983**, *105*, 5706-5708.
17. (a) Simmons, M. R.; Yamasaki, E. N.; Patrickios, C. S. *Polymer* **2000**, *41*, 8523-8529. (b) Patrickios, C. S.; Simmons, M. R. *Colloids and Surfaces A* **2000**, *167*, 61-72. (c) Vamvakaki, M.; Hadjiyannakou, S. C.; Loizidou, E.; Patrickios, C. S.; Armes, S. P.; Billingham, N. C. *Chem. Mater.* **2001**, *13*, 4738-4744.
18. Triftaridou, A. I.; Kafouris, D.; Vamvakaki, M.; Georgiou, T. K.; Krasia, T. C.; Themistou, E.; Hadjiantoniou, N.; Patrickios, C. S. *Polym. Bull.* **2007**, *58*, 185-190.
19. (a) Simmons, M. R.; Yamasaki, E. N.; Patrickios, C. S. *Macromolecules* **2000**, *33*, 3176-3179. (b) Triftaridou, A. I.; Hadjiyannakou, S. C.; Vamvakaki, M.; Patrickios, C. S. *Macromolecules* **2002**, *35*, 2506-2513. (c) Demosthenous, E.; Hadjiyannakou, S. C.; Vamvakaki, M.; Patrickios, C. S. *Macromolecules* **2002**, *35*, 2252-2260. (d) Loizou, E.; Triftaridou, A. I.; Georgiou, T. K.; Vamvakaki, M.; Patrickios, C. S. *Biomacromolecules* **2003**, *4*, 1150-1160. (e) Hadjiantoniou, N.; Triftaridou, A. I.; Georgiou, T. K.; Patrickios, C. S. *Macromol. Symp.* **2005**, *227*, 135-142. (f) Georgiou, T. K.; Patrickios, C. S.; Groh, P. W.; Iván, B. *Macromolecules* **2007**, *40*, 2335-2343. (g) Triftaridou, A. I.; Vamvakaki, M.; Patrickios, C. S. *Biomacromolecules* **2007**, *8*, 1615-1623.
20. (a) Georgiades, S. N.; Vamvakaki, M.; Patrickios, C. S. *Macromolecules* **2002**, *35*, 4903-4911. (b) Vamvakaki, M.; Patrickios, C. S. *Chem. Mater.* **2002**, *14*, 1630-1638. (c) Achilleos, D. S.; Georgiou, T. K.; Patrickios, C. S. *Biomacromolecules* **2006**, *7*, 3396-3405. (d) Georgiou, T. K.; Patrickios, C. S. *Macromolecules* **2006**, *39*, 1560-1568.

Polymer–Inorganic Nanocomposites from Si-Based Substrates: Applications of Ring-Opening Metathesis Polymerization

Jun-Hyun Kim[1], Joshua A. Kellar[2], Mark C. Hersam[2], and SonBinh T. Nguyen[1,*]

Departments of [1]Chemistry and [2]Materials Science and Engineering, Northwestern University, 2145 Sheridan Road, Evanston IL 60208

This contribution outlines four different ROMP-based (ROMP = ring-opening metathesis polymerization) approaches to prepare polymer overlayers possessing either hydroxyl or carboxylic acid functionalities on oxidized silicon surface or silica (SiO_2) nanoparticles. The morphology, elemental composition, and properties of these polymer overlayers can be characterized by X-ray photoelectron spectroscopy (XPS), scanning electron microscopy (SEM), atomic force microscopy (AFM), transmission electron microscopy (TEM), ellipsometry, and Fourier-transform infrared spectroscopy (FTIR).

Introduction

The controlled fabrication of well-defined organic overlayers on solid substrate has long been a key research focus in many technological areas including adhesion, lubrication, coatings, information storage, biomimetic materials, and electronics (*1–4*). Organic overlayers can endow the underlying substrates with additional mechanical, thermal, optical, and electrical properties that can subsequently be utilized in a synergistic fashion in microelectronics, microelectromechanical systems (MEMS) devices, and biological sensors (*5–7*) In particular, covalently attached polymer layers (e.g., brushes, films) on surfaces can facilitate the fabrication of complex architecture possessing multiple organic, biomolecular, and inorganic components, allowing for novel combination of properties and functions (*8*). In theory, such polymer overlayers can readily be prepared in a controlled manner from a wide range of functionalized monomers to yield multifunctional films that have tunable density and thickness (*9,10*). However, to construct these films, reliable synthetic methods that allow for uniform polymer growth as well as being tolerant to a variety of functional groups must be developed.

Typically, polymer overlayers can be fabricated by two different approaches: physisorption on solid substrates or covalent attachment to the substrate surface (*11*). The first strategy is widely practiced in industry and includes methods such as spin-coating, ink-jet printing, screen printing, and selective physisorption of block copolymers (*12,13*). Covalent attachment of polymers to surfaces is a newer methodology that can, in theory, offer films that are thinner but also thermally and solvolytically more stable (*14*). As such, it has received considerable attention, especially in the context of surface-initiated (SI) living polymerization where the molecular weight of individual polymer chains can be precisely controlled to give polymers with narrow polydispersity (*15,16*). Not only should this approach afford polymer films with tunable thickness, the directional growth of the polymer chain may allow for a reliable, controlled placement of many functional groups within the polymer overlayer and with respect to the surface (*8,17,18*). Thus, many researchers have attempted to develop SI living polymerization strategies, based on well-known solution techniques such as nitroxide-mediated controlled radical polymerization (*19–22*), atom-transfer radical polymerization (*15*), anionic (*22*), cationic (*23*), and ring-opening metathesis polymerization (ROMP) (*10,24,25*), to fabricate polymer overlayers (brushes) on solid substrates.

Among the aforementioned strategies, SI-ROMP stood out for its low activation energy (i.e. reactions can be carried out under ambient conditions) and ease of application, especially given the recent development of highly active, single-component olefin metathesis catalysts (*26*). Since 1999, SI-ROMP catalyzed by well-defined metal-alkylidene has been employed by several groups

(*10,27,28*) to prepare polymer films and nanopatterns on gold or oxidized silicon. In addition, as ruthenium catalysts for ROMP are known to be functional-group-tolerant and living in diverse solvents (from benzene to water), monomers containing a wide range of functionalities have also been incorporated into a number of surface polymer films (*10,22,26,27*). Unfortunately, back-biting or chain-transfer between neighboring ROMP polymer chains (Figure 1) still made it difficult to produce polymer overlayers with a wide rage of tunable thicknesses unless surface density of the initiating groups is carefully controlled. (*29*).
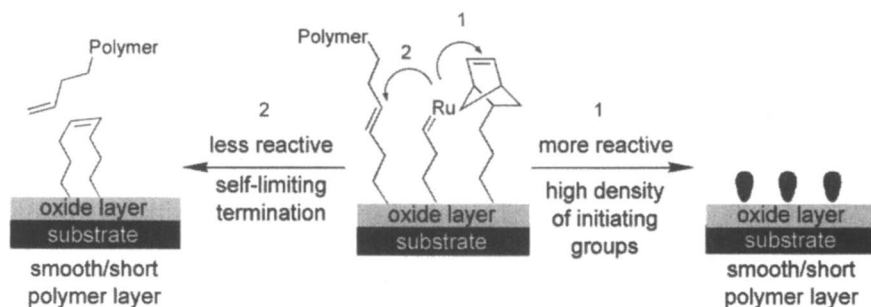
Figure 1. Schematic illustration of possible side reactions from surface initiated ring-opening metathesis polymerization (SI-ROMP) on an oxide substrate.

Our groups have had long-standing interests in integrating functional organic materials with silicon-based substrates for material and biological applications. To this end, we have explored four different ROMP-based approaches to prepare functionalized polymer films on oxidized Si(111) surface. We aimed to compare polymer overlayers obtained from two different SI-ROMP-based methods to those derived via *in-situ* polymerization and grafting processes. Through evaluating the different film morphologies, we have extended the two best strategies to the synthesis of discrete polymer-coated silica nanoparticles. These results are described herein.

Experimental Section

General Materials and Methods

Grubbs catalyst $(PCy_3)_2Cl_2Ru=CHPh$, 5-(bicyclo[2.2.1]hept-2-enyl) trichloro silane (NBE-SiCl$_3$), 5-norbornene-2-carboxylic acid (NBE-COOH), and bicyclo[2.2.1]hept-2-ene (NBE) were purchased from Aldrich and used as
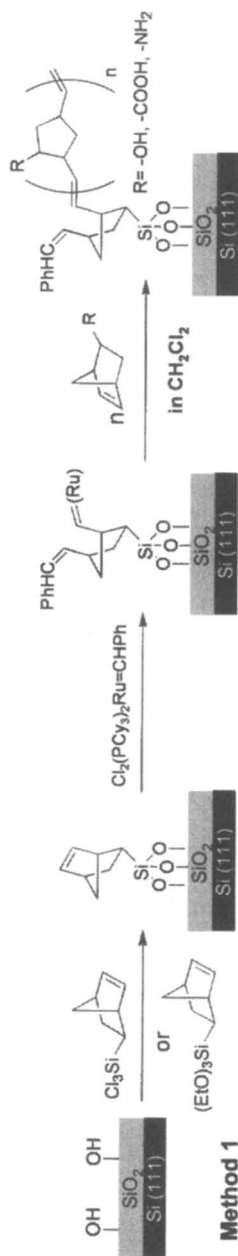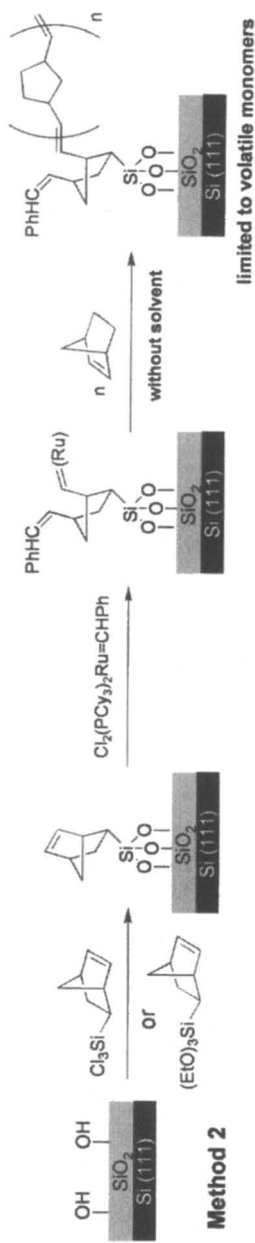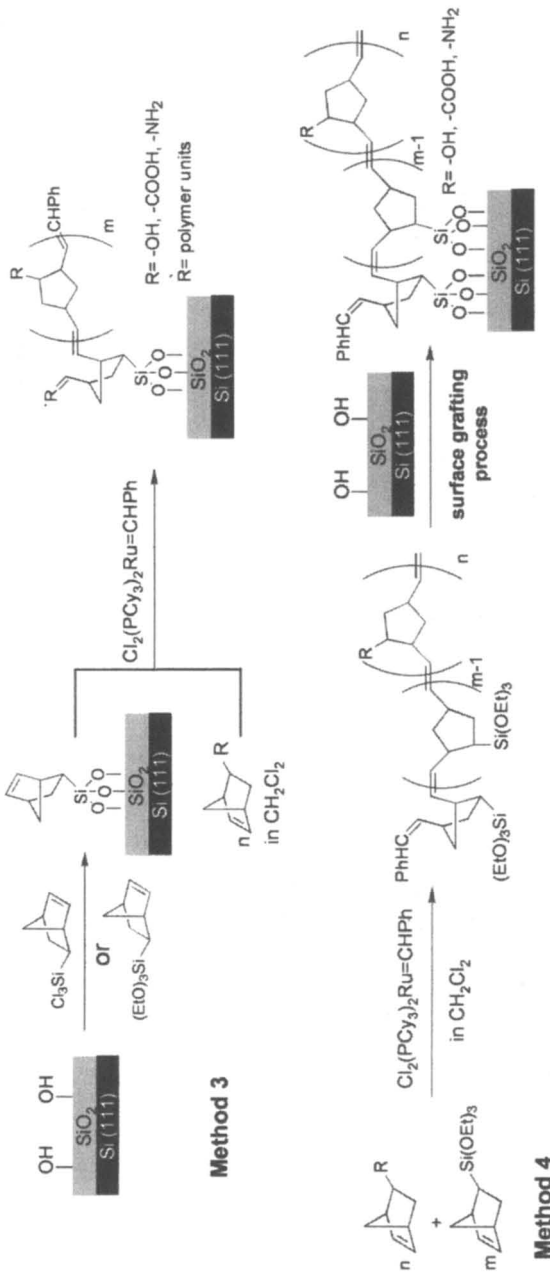
Figure 2. Schematic illustration of polymer film growth on oxidized Si(111) wafers using four different approaches

received. 5-(Bicyclo[2.2.1]hept-2-enyl)triethoxysilane (NBE-Si(OEt)$_3$) was purchased from Gelest and used as received. 5-*Exo*-norbornene-2-ol (NBE-OH) was prepared according to literature procedure (*28*). All solvents were dried over neutral alumina via the Dow-Grubbs solvent system (*29*). All polymerizations were carried out at room temperature either in a N$_2$-filled glovebox or using standard Schlenk techniques, unless otherwise noted. Si(111) substrates (~ 1.5 cm^2 in area, Virginia Semiconductor) were oxidized with piranha solution (3:1 conc. H$_2$SO$_4$:30%H$_2$O$_2$) following reported procedures (*30*) prior to the attachment of norbornenyl moieties (NBE-SiCl$_3$, NBE-Si(OEt)$_3$) (*31*). Figure 2 illustrates how we construct polymer brushes on oxidized Si(111) wafers utilizing ROMP methods.

Method 1 – Conventional SI-ROMP

A solution of NBE-SiCl$_3$ or NBE-Si(OEt)$_3$ in toluene (1% v/v) was prepared in a N$_2$-filled glovebox immediately before use. Oxidized Si(111) wafers were immersed in this monomer solution (0.1 mL in 10 mL of toluene) for 1 h (for NBE-SiCl$_3$ (or overnight for NBE-Si(OEt)$_3$)) to form norbornenyl moieties at the interface. The oxidized Si(111) wafers were then washed with toluene (2 x 4 mL) and methylene chloride (CH$_2$Cl$_2$, 2 x 4 mL) followed by submersion in a solution of Grubbs catalyst (17 mM in CH$_2$Cl$_2$) for 30 min to induce ring-opening of the surface-attached norbornenyl groups. Next, the oxidized Si(111) wafers were thoroughly rinsed with CH$_2$Cl$_2$ (3 x 4 mL) to remove any unbound and/or physisorbed catalysts. Surface growth of polymer brushes were then commenced by immersing the initiated wafers in a solution containing norbornene-based monomer (100 mM of NBE-COOH or NBE-OH in CH$_2$Cl$_2$) at room temperature for 30 minutes. (The polymerization reaction was believed to have started from the surface of Si(111) wafer where Grubbs catalysts were initially confined (*32*).) The samples were then removed from the glovebox and the polymerization was quenched with a few drops of ethyl vinyl ether. The wafers were then rinsed with CH$_2$Cl$_2$ (2 x 4 mL), sonicated (Fisher FS6 ultrasonic cleaner) in CH$_2$Cl$_2$ (4 mL) for 10 min, rinsed with CH$_2$Cl$_2$ (10 x 2 mL), and dried in a stream of nitrogen to remove any residual and physisorbed species prior to analyses.

Method 2 – Solventless SI-ROMP

In a N$_2$-filled glovebox, oxidized Si(111) wafers were functionalized with either NBE-SiCl$_3$ or NBE-Si(OEt)$_3$ monomer and then treated with Grubbs catalysts in the same manner as described in method 1. The wafers were then cleaned with CH$_2$Cl$_2$ (3 x 4 mL), dried in a stream of N$_2$ gas, and placed

separately in individual round-bottom flasks. In a separate Schlenk flask was placed a quantity of volatile NBE monomer (~0.032 g) and this flask was connected to the wafer-containing flask using a vacuum transfer manifold. The assembly was removed from the glovebox and connected to a Schlenk line. After three cycles of free-pump-thaw, the NBE monomer was vacuum-transferred over to the round-bottom flask containing the catalyst-immobilized Si(111) wafer to form polymer brushes on its surface. The round-bottom flask was kept at −78°C in an acetone-dry ice bath during the transfer, which took about 15 minutes. After the NBE monomer solid has all been transferred, the transfer valve was shut off, the cooling bath was removed, and the assembly was allowed to warm up to room temperature over the next hour. The wafer was then removed from the flask and cleaned using the same purification steps as described for method 1.

Method 3 – In-situ Copolymerization

In a N_2-filled glovebox, oxidized Si(111) wafer was treated with either NBE-SiCl$_3$ or NBE-Si(OEt)$_3$ monomer and rinsed twice each with toluene and CH$_2$Cl$_2$, as described in method 1. In a separate flask, a CH$_2$Cl$_2$ solution (1 mL) of Grubbs catalyst (0.0034 mmol) was injected into a CH$_2$Cl$_2$ solution (2 mL) of the desired norbornene monomer (0.34 mmol) to initiate polymerization. The NBE-functionalized Si(111) wafer was then quickly immersed in this polymerizing solution. After 30 min, a few drops of ethyl vinyl ether were then added to terminate the polymerization. Before analyses, the wafer was cleaned using the same purification steps as described for method 1.

Method 4 – Post-polymerization Attachment

In a N_2-filled glovebox, a CH$_2$Cl$_2$ solution (1 mL) of Grubbs catalyst (0.0034 mmol) was injected into a 1:1 mixture of NBE-OH and NBE-Si(OEt)$_3$ (0.34 mmol total) in CH$_2$Cl$_2$ (2 mL) to prepare random copolymers. After 30 min, a few drops of ethyl vinyl ether were added to the reaction to terminate the polymerization. An oxidized Si(111) wafer was then placed in this polymer solution overnight. Before analyses, the wafer was cleaned using the same purification steps as described for method 1.

ROMP on Silica Nanoparticles

Silica (SiO$_2$) nanoparticles of ~110 nm in diameter were prepared by the conventional Stobber method (*33*), and functionalized with NBE-Si(OEt)$_3$ overnight using a modified literature procedure (*34,35*). In essence, freshly

prepared SiO$_2$ nanoparticles in ethanol solution (100 mL, ~7 × 10^{14} particles/mL) is treated with NBE-Si(OEt)$_3$ (~50 μL, 0.28 mmol) overnight (with vigorous stirring) and then purified by centrifugation (Eppendorf centrifuge 5804R, 15 amp version, 5000 rpm for 30 minutes) to remove unreacted monomers, small SiO$_2$ nanoparticles, and any impurities. The resulting solution of NBE-Si(OEt)$_3$-functionalized SiO$_2$ nanoparticles were then treated with sodium sulfate for 15 minutes and then with activated 3Å molecular sieves overnight to remove any excess water before diluting in dry CH$_2$Cl$_2$ (1:40 v/v).

Subsequent polymerization of norbornene-type monomers (NBE-COOH or NBE-OH) on SiO$_2$ nanoparticles was carried out following the same procedures described above for methods 1 and 3. The diluted solution of the nanoparticles was mixed with NBE-COOH (or NBE-OH) monomer (0.34 mmol) and exposed to Grubbs catalyst (3.4 μmol) to initiate polymerization. The final solution was quenched with excess ethyl vinyl ether (~0.5 mL) after 1 h, concentrated to ~5 mL on a rotary evaporator, and combined with enough ethanol to make a 40-mL solution. The resulting colloidal solution was subjected to centrifugation (5000 rpm for 30 minutes) and the mother liquor was then decanted. To the settled nanoparticles were added ethanol (~ 40 mL) and the resulting mixture was sonicated for 2 minutes in a laboratory sonicator before being centrifuged one final time. After this final step, the particles were redispersed in ethanol (~10 mL) using sonication (~2 minutes).

Results and Discussions

Polymer Brushes on Oxidized Si(111) Wafers

We began by examining a variety of ROMP-based approaches for growing polymers of norbornene-derivatives from oxidized Si(111) surfaces. We aimed to find the best ROMP-based method(s) that would allow us to prepare functional polymer-inorganic composites of SiO$_2$ nanoparticles. Figures 3 and 4 show representative SEM (scanning electron microscopy, Hitachi S-4500) and AFM (atomic force microscopy, Autoprobe CP Research) images for ROMP-based polymer films grown on oxidized Si(111) surfaces using four different methods: conventional SI-ROMP, solventless SI-ROMP, in-situ copolymerization, and post-polymerization attachment.

In solutions of NBE-OH monomer with similar concentrations (~100 mM), all four of the aforementioned methods lead to polymer films on the surface of the oxidized Si(111) wafers; however these films have very different roughnesses. While methods 1 and 2 lead to the formation of smooth, thin polymer overlayers, methods 3 and 4 generated thick polymer films with rough surfaces (Table I, cf root-mean-square (rms) roughness). SEM images of the wafers prepared by methods 1 and 2 (Figures 3a-b, both side and top views)

show thin, relatively flat polymer films covering the entire Si(111) substrate. This is consistent with the corresponding AFM images (Figures 4a-b) where the top-down view shows surfaces that are uniformly covered with short brushes except for a few sporadic long spikes "sticking up" over the landscape. Presumably, this morphology is a consequence of the inherent high strain in our initiating moieties (NBE-SiCl$_3$ or NBE-Si(OEt)$_3$), which made these cyclic olefins more susceptible to crosslinking side reactions comparing to terminal-olefin initiating groups (Figure 1) (36). In addition, the height of the observed short polymer brushes is inversely affected by the surface concentration of the initiating moieties: the higher this density, the more likely polymer growth will be terminated via crosslinking/back-biting reactions (Figure 1). This latter characteristic is one of the main drawbacks in conventional SI-ROMP procedures when the catalyst is reactive enough to metathesize both strained and non-strained C=C bonds: the growth of ROMP-based polymer brushes on surfaces is usually self-limiting (36).

Previous studies from several research groups have suggested that the thickness of the polymer films in SI-ROMP can be controlled by adjusting the surface density and distribution of the initiating olefin moieties and by increasing the concentrations of monomer in solution (32,36,37). However, polymer growth often stops within 1 h due to either catalyst deactivation or backbiting reaction (Figure 1) (32,36,38). Consistent with these limitations, in our hands, methods 1 and 2 were less likely to produce long polymer brushes, presumably due to crosslinking between adjacent polymer chains within a polymer brush. Our attempts to evaluate the likelihood of these crosslinking events through measuring the surface density of the Ru-initiated monomers were unsuccessful due to overlaps of the Ru3d peaks with the C1s signals in the XPS spectra.

As a strategy, method 2 is rather limited: it requires a volatile monomer that can be vacuum-transferred onto a surface that has been modified with Grubbs catalyst. Presumably, the polymerization occurs as the monomer is deposited on the surface of the wafer. This method consistently give very thin polymer film (< 10 nm) on the substrate, regardless of the amount of deposited monomers (from 30 mg to 500 mg of NBE for an oxidized Si(111) wafer that is ~ 1.5 cm^2 in area). This data again supports a self-limiting polymer growth mechanism.

Methods 3 and 4 generated rough and thick polymer films as expected of a predominantly solution polymerization process where the catalyst is not bound to the surface and can access more monomer molecules in solution. In method 3, the catalyst in solution can incorporate surface-bound monomers into a growing polymer chain, giving polymer films that are thicker than those prepared by methods 1 and 2 but whose thicknesses vary significantly over the coverage area (Figures 3c and 4c). This variation is a consequence of the great discrepancy between solution polymer growth (fast) and surface incorporation (much slower) kinetics: as time progresses, the lengths of the most recently bound polymer chains will be much longer than those that become surface-bound at earlier
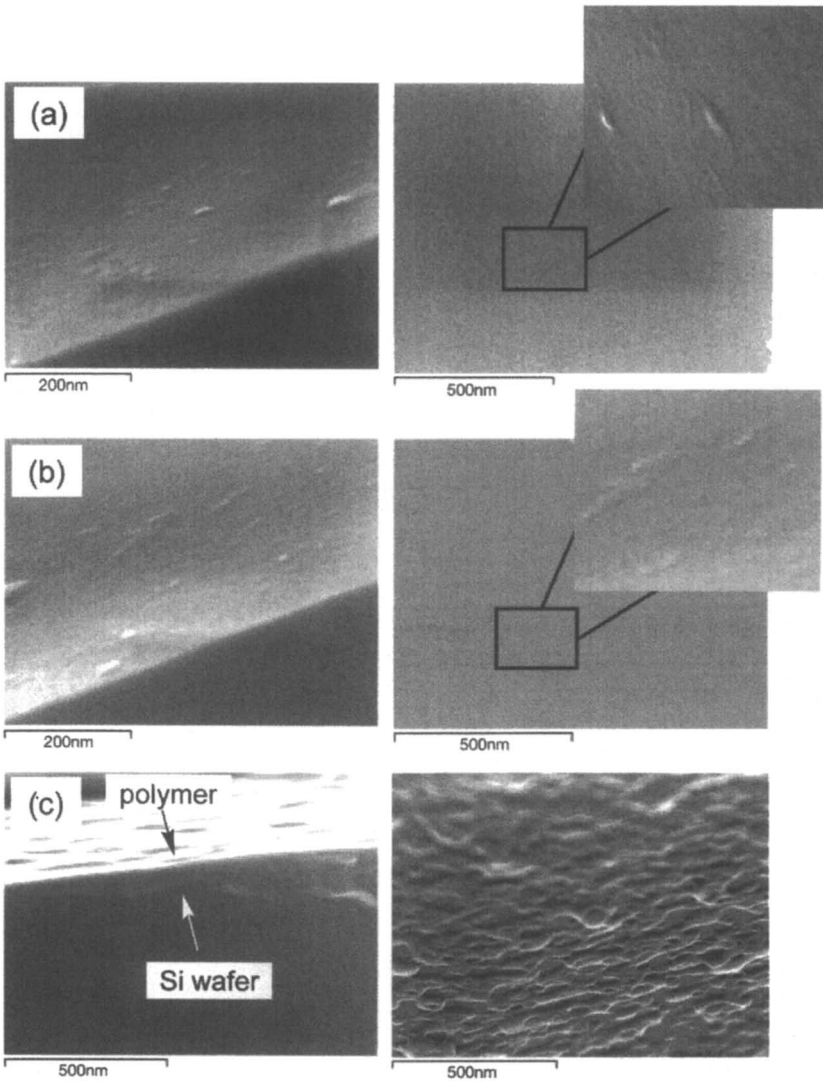
*Figure 3. SEM images of polymer films on oxidized Si(111) wafers.
(a-c) Side (left) and top (right) views of wafers that were subjected to methods
1- 3, respectively. (d) Side view of a wafer that was subjected to method 4.
(e) Side view of a bare oxidized Si(111) wafer.*
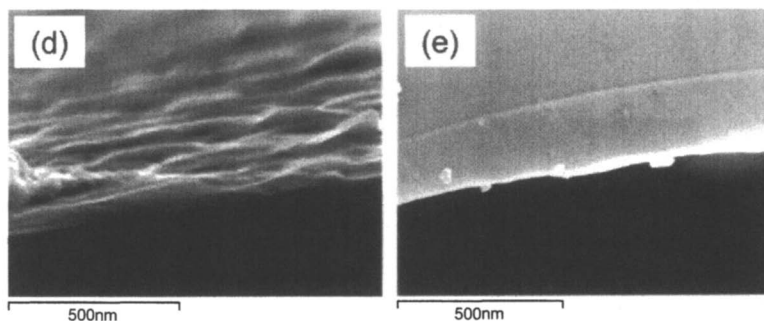
Figure 3. Continued.

Table I. Thicknesses and RMS Roughness of Polymer Brushes on Si-Wafers, Measured by Ellipsometry and AFM

Type of film	Conc.	Thickness in nm, from ellipsometry measurements (rms, from AFM measurements)			
		Method 1	Method 2	Method 3	Method 4
Monomer	1 vol%	1.4 ± 0.2 (NBE-Si(OEt)$_3$) or 2.1 ± 0.3 (NBE-SiCl$_3$)	N/A	N/A	
Catalyst + monomer	N/A	2.5 ± 0.3 (NBE-Si(OEt)$_3$) or 3.0 ± 0.3 (NBE-SiCl$_3$)	N/A	N/A	
Poly(NBE)	100 mM	N/A	5.8 ± 0.6 (0.55)	N/A	N/A
	300 mM	N/A	8.2 ± 0.8	N/A	N/A
Poly(NBE-OH)	100 mM	8.2 ± 2.7 (1.1)	N/A	21.5 ± 6.7 (9.2)	48.8 (25.5)
	300 mM	20.3 ± 6.9	N/A	52.1	N/A
Poly(NBE-COOH)	100 mM	9.9 ± 2.5	N/A	25.5	N/A
	300 mM	20.9 ± 14.7	N/A	N/A	N/A

rms = root-mean-square roughness, values are indicated in parentheses.

a)

b)
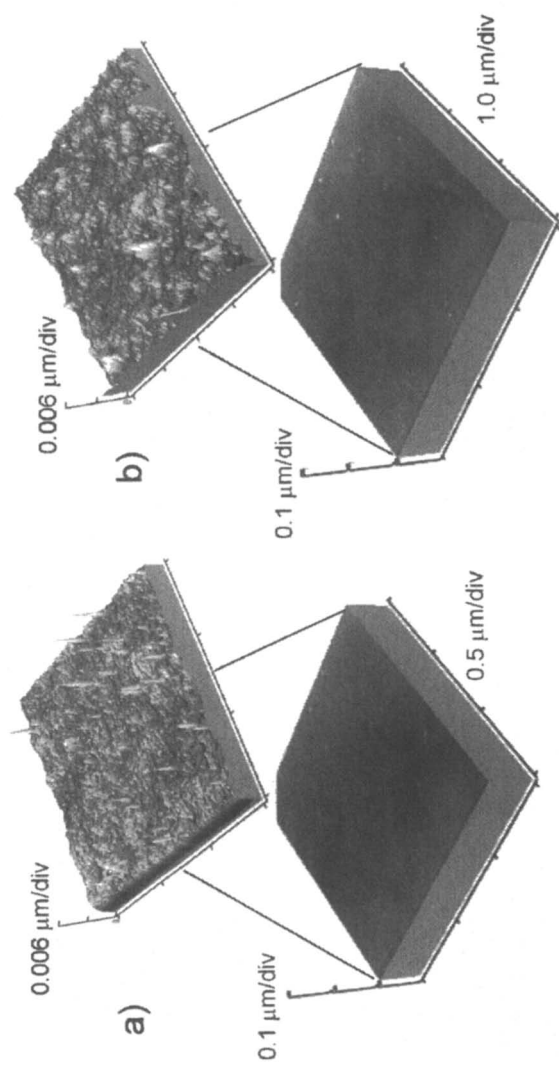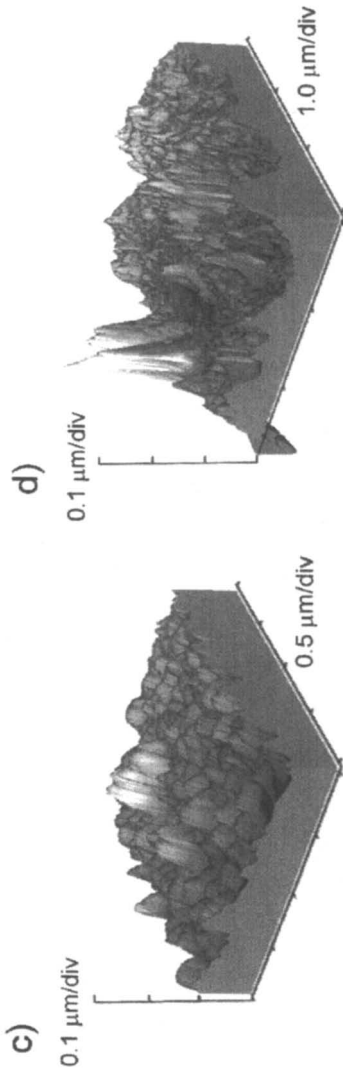
Figure 4. AFM images of polymer films on oxidized Si(111) wafers. a) Poly(NBE-OH) from method 1. b) Poly(NBE) from method 2. c) Poly(NBE-OH) from method 3. d) Poly[NBE-OH-r-NBE-Si(OEt)₃] from method 4.

times. The result is a rougher (Table I) but thicker polymer film comparing to those obtained with methods 1 and 2.

As a post-polymerization attachment strategy, method 4 requires ROMP-based polymers containing functional groups that can form covalent bonds with the surface of oxidized Si(111) wafers. Overnight treatment of such a wafer with a solution of a random copolymer of NBE-OH and NBE-Si(OEt)$_3$ (1:1 molar ratio) results in a very rough polymer film (Table I) as observed by AFM (Figure 4d) and SEM (Figure 3d). Presumably, the polymer attachment took place between the surface hydroxyl groups of the oxidized Si(111) wafer and the triethoxysilyl groups of the polymer. As this "exchange" reaction is fairly slow,[34] crosslinking of the free (i.e., not surface-bound) Si(OEt)$_3$ groups between adjacent side chains or neighboring polymer chains can also occur at the same time. Both of these processes can result in irregular and thick films possessing clumpy and rough morphologies.

The thickness of each organic/polymer overlayer and its uniformity, as measured by root-mean-square (rms) roughness, was determined using ellipsometry and AFM line profiling (Table I). All functionalized wafers were found to have increased thickness compared to a bare wafer (0.6 ± 0.6 nm), signifying the presence of an overlayer film. For wafers that were functionalized with NBE-Si(OEt)$_3$ and NBE-SiCl$_3$ monolayers, as well as those that were coated with thin polymer overlayers (methods 1 and 2), their film-coated surfaces are smooth and flat with low rms values that were consistent with SEM images. In contrast, wafers that were treated with methods 3 and 4 have thicker and rougher overlayers as indicated by their higher rms values. (To confirm the covalent growth of polymer overlayers in methods 1-3, oxidized but unfunctionalized Si(111) substrates (i.e., not treated with the initiating NBE-Si(OEt)$_3$ and (NBE-SiCl$_3$) monomers) were treated with solutions containing free monomers and Grubbs catalyst under the experimental conditions described for each method. Negligible thickness gains were observed after extensive cleaning to remove physisorbed materials.)

Figure 5 displays the attenuated total reflection (ATR) IR spectra (Thermo Nicolet, Nexus 870) of the poly(NBE-OH) films on oxidized Si(111) wafers prepared by methods 1-4. Both thin (<10 nm in thickness, prepared by methods 1 and 2) and thick (>20 nm in thickness, methods 3 and 4) polymer films show very strong v_{as} and v_s C-H stretches at 2927 and 2858 cm^{-1} from the norbornene polymer backbones, while the unfunctionalized oxidized Si(111) wafer does not exhibit any distinctive peaks in the aliphatic C-H region after the background correction.[14,32] All spectra of poly(NBE-OH)-coated Si(111) wafers are similar, suggesting formation of chemically analogous polymer overlayers.

The representative X-ray photoelectron spectroscopy (XPS, Omicron, ESCA Probe) survey scans of the poly(NBE-OH)-coated wafers are shown in Figure 6. The spectrum of oxidized Si(111) wafer exhibits core-level peaks characteristic of Si/SiO$_2$: Si2s at 151 eV, Si2p at 99 eV, and O1s at 532 eV, as

well as the C1s adventitious peak at 285 eV.[36,39] As polymer overlayers were grown on the surface using methods 1 and 2, the C1s peak intensity increased relative to those for the Si2s and Si2p peaks, consistent with the presence of carbon-rich films on the Si(111) substrate. The core-level peaks in the Si2p and Si2s regions almost completely disappeared for samples prepared by methods 3 and 4 where the polymer films are over 20-nm thick, as would be expected for substrates being covered with a thick insulating organic overlayer. Thus, surface growth of poly(NBE-OH) on oxidized Si(111) surface was evidenced by the attenuation of the underlying Si signals and the increase in intensity for the C1s signal in the XPS survey scans.

Polymer Overlayers on SiO$_2$ Nanoparticles

As methods 1 and 3 allow us to grow polymer overlayers with controlled thickness and relative uniformity on oxidized silicon substrates, we extend them to the construction of discrete polymer-coated SiO$_2$ nanoparticles having low polydispersity and good stability. The major advantages of using SiO$_2$ nanoparticles as core materials are: their ready availability, low polydispersities (e.g., less than 5%), tunable sizes, and easy surface modification chemistry with a variety of organic molecules.[33,34] We employed NBE-COOH and NBE-OH as monomers to demonstrate the preparation of polymer overlayers having chemical functionalities that can be easily manipulated.

Figure 7 shows the SEM images of [NBE-Si(OEt)$_3$]-functionalized SiO$_2$ nanoparticles as well as SiO$_2$ nanoparticles possessing poly(NBE-OH) and poly(NBE-COOH) overlayers prepared from methods 1 and 3. While method 1 yielded aggregations of particles (Figure 7b), method 3 produced discrete polymer-coated SiO$_2$ nanoparticles (Figures 7c and 7d), surprisingly. We suspect that the aggregated particles prepared by method 1 arise from the inter- and intraparticle cross-linking process during the centrifugation step used after catalyst treatment to separate the free catalyst molecules away form surface-captured catalysts.[40] Such centrifugation can decrease the average particle-particle distance and cause interparticle crosslinking via reactions between the surface-capture catalyst groups on one particle and unreacted norbornene groups on the neighboring particles. Interestingly, the particle diameters obtained from transmission electron microcopy (TEM) analysis were ~30% smaller than those obtained by SEM, possibly due to the desolvation of nanoparticles under the high vacuum and intense electron beam in TEM.

Conclusion

While norbornene-based ROMP polymers can be covalently attached to oxidized Si(111) surfaces using the four methods described in this manuscript,
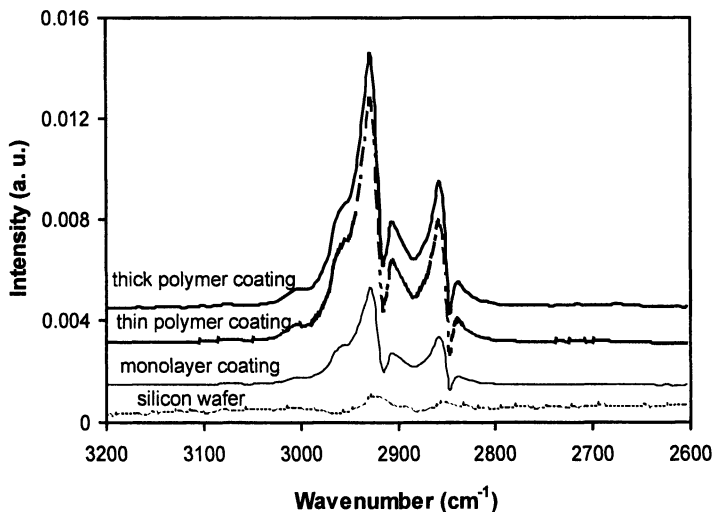
Figure 5. ATR-IR spectra of poly(NBE-OH) films on oxidized Si(111) wafers as well as a spectrum of the bare wafer. The sample with monolayer coating is obtained with NBE-SiCl₃. The sample with thin polymer coating is obtained through method 1. The sample with thick polymer coating is obtained through method 3.
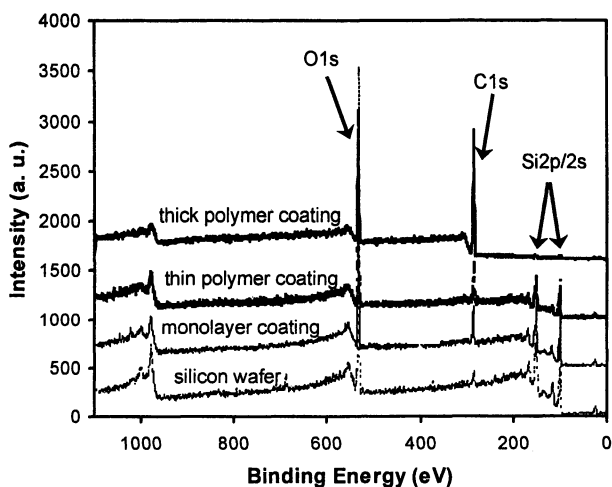
Figure 6. XPS survey scans of poly(NBE-OH) films on oxidized Si(111) wafers as well as a spectrum of the bare wafer. The sample with monolayer coating is obtained with NBE-SiCl₃. The sample with thin polymer coating is obtained through method 1. The sample with thick polymer coating is obtained through method 3.
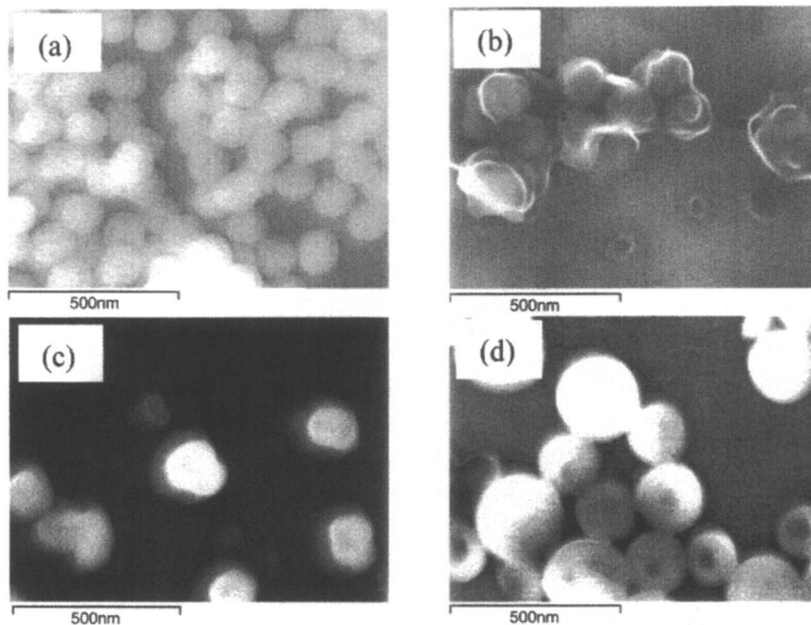
*Figure 7. SEM images of polymer-coated SiO₂ nanoparticles.
(a) NBE-Si(OEt)₃-functionalized. (b) Poly(NBE-COOH)-coated using method
1. (c) poly(NBE-OH)-coated using method 3. (d) Poly(NBE-COOH)-coated
using method 3.*

the resulting polymer films possessing very different thickness and morphology. If thin polymer films between 5-20 nm are desirable, SI-ROMP techniques are the most appropriate. However, *in-situ* polymerization seems to be the best strategy for achieving thicker, but still relatively uniform, polymer films on oxidized Si(111) surfaces as well as discrete polymer-coated SiO₂ nanoparticles. Post-polymerization surface attachment through alkoxysilane sidechains is perhaps the least controlled method in our hands, giving thick and highly irregular coatings. Detail studies of polymer films with tunable thicknesses on oxidized Si(111) surfaces and SiO₂ nanoparticles using method 3 are currently underway.

Acknowledgments

References

1. Sirringhaus, H.; Tessler, N.; Friend, R. H. *Science* **1998**, *280*, 1741-1744.
2. Lahann, J.; Mitragotri, S.; Tran, T.-N.; Kaido, H.; Sundaram, J.; Choi, I. S.; Hoffer, S.; Somorjai, G. A.; Langer, R. *Science* **2003**, *299*, 371-374.
3. Kim, J.; McQuade, D. T.; McHugh, S. K.; Swager, T. M. *Angew. Chem. Int. Ed.* **2000**, *39*, 3868-3872.
4. Sarikaya, M.; Tamerler, C.; Jen, A. K.-Y.; Schulten, K.; Baneyx, F. *Nature Mater.* **2003**, *2*, 577-585.
5. LeMieux, M. C.; McConney, M. E.; Lin, Y.-H.; Singamaneni, S.; Jiang, H.; Bunning, T. J.; Tsukruk, V. V. *Nano Lett.* **2006**, *6*, 730-734.
6. Dickinson, T. A.; White, J.; Kauer, J. S.; Walt, D. R. *Nature* **1996**, *382*, 697-700.
7. Madou, M.; Florkey, J. *Chem. Rev.* **2000**, *100*, 2679-2692.
8. Currie, E. P. K.; Norde, W.; Cohen Stuart, M. A. *Adv. Colloid Int. Sci.* **2003**, *100*, 205-265.
9. von Werne, T.; Patten, T. E. *J. Am. Chem. Soc.* **2001**, *123*, 7497-7505.
10. Weck, M.; Jackiw, J. J.; Rossi, R. R.; Weiss, P. S.; Grubbs, R. H. *J. Am. Chem. Soc.* **1999**, *121*, 4088-4089.
11. Boyes, S. G.; Granville, A. M.; Baum, M.; Akgun, B.; Mirous, B. K.; Brittain, W. J. *Surf. Sci.* **2004**, *570*, 1-12.
12. Kawase, T.; Sirringhaus, H.; Friend, R. H.; Shimoda, T. *Adv. Mater.* **2001**, *13*, 1601-1604.
13. Halik, M.; Klauk, H.; Zschieschang, U.; Schmid, G.; Radlik, W.; Webber, W. *Adv. Mater.* **2002**, *14*, 1717-1721.
14. Zhao, B.; Brittain, W. J. *Prog. Polym. Sci.* **2000**, *25*, 677-710.
15. Matyjaszewski, K.; Xia, J. *Chem. Rev.* **2001**, *101*, 2921-2990.
16. Chong, B. Y. K.; Le, T. P. T.; Moad, G.; Rizzardo, E.; Thang, S. H. *Mactromolecules* **1999**, *32*, 2071-2074.
17. Pyun, J.; Matyjaszewski, K. *Chem. Mater.* **2001**, *13*, 3436-3448.
18. Mori, H.; Seng, D. C.; Zhang, M.; Muller, A. H. E. *Prog. Coll. Polym. Sci.* **2004**, *126*, 40-43.
19. Prucker, O.; Ruhe, J. *Langmuir* **1998**, *14*, 6893-6898.
20. Husemann, M.; Morrison, M.; Benoit, D.; Frommer, J.; Mate, C. M.; Hinsberg, W. D.; Hedrick, J. L.; Hawker, C. J. *J. Am. Chem. Soc.* **2000**, *122*, 1844-1845.
21. Jones, D. M.; Huck, T. S. W. *Adv. Mater.* **2001**, *13*, 1256-1259.

22. Oosterling, M. L. C.; Sein, A.; Schouten, A. J. *Polymer* **1992**, *33*, 4394-4400.
23. Jordan, R.; Ulman, A. *J. Am. Chem. Soc.* **1998**, *120*, 243-247.
24. Watson, K. J.; Zhu, J.; Nguyen, S. T.; Mirkin, C. A. *J. Am. Chem. Soc.* **1999**, *121*, 462-463.
25. Matyjaszewski, K.; Patten, T. E.; Xia, J. *J. Am. Chem. Soc.* **1997**, *119*, 674-680.
26. Schwab, P.; Grubbs, R. H.; Ziller, J. W. *J. Am. Chem. Soc.* **1996**, *118*, 100-110.
27. Jordi, M. A.; Seery, T. A. P. *J. Am. Chem. Soc.* **2005**, *127*, 4416-4422.
28. Posner, G. H.; Ting, J. S.; Lentz, C. M. *Tetrahedron* **1976**, *32*, 2281-2287.
29. Pangborn, A. B.; Giardello, M. A.; Grubbs, R. H.; Rosen, R. K.; Timmers, F. J. *Organometallics* **1996**, *15*, 1518-1520.
30. Haller, I. *J. Am. Chem. Soc.* **1978**, *100*, 8050-8055.
31. Firestone, M. A.; Shank, M. L.; Sligar, S. G.; Bohn, P. W. *J. Am. Chem. Soc.* **1996**, *118*, 9033-9041.
32. Kim, N. Y.; Jeon, N. L. C.; I. S.; Takami, S.; Harada, Y.; Finnie, K. R.; Girolami, G. S.; Nuzzo, R. G.; Whitesides, G. M.; Laibinis, P. E. *Mactromolecules* **2000**, *33*, 2793-2795.
33. Stober, W.; Fink, A.; Bohn, E. *J. Colloid Interface Sci.* **1968**, *26*, 62-69.
34. van Helden, A. K.; Vrij, A. *J. Colloid Interface Sci.* **1980**, *78*, 312-329.
35. Pham, T.; Jackson, J. B.; Halas, N. J.; Lee, T. R. *Langmuir* **2002**, *18*, 4915-4920.
36. Harada, Y.; Girolami, G. S.; Nuzzo, R. H. *Langmuir* **2003**, *19*, 5104-5114.
37. *Handbook of Metathesis*; Grubbs, R. H., Ed.; Wiley-VCH: Germany, 2003; Vol 3, pp 2-66.
38. Juang, A. S., Scherman, O. A.; Grubbs, R. H.; Lewis, N. S. *Langmuir* **2001**, *17*, 1321-1323.
39. Lee, W.-K.; Caster, K. C.; Kim, J.; Zauscher, S. *Small* **2006**, *2*, 848-853.
40. Koenig, S.; Chechik, V. *Langmuir* **2006**, *22*, 5168-5173.

Chapter 23

Preparation of Polysaccharide-Covered Polymeric Nanoparticles by Several Processes Involving Amphiphilic Polysaccharides

M. Leonard[1], E. Marie[1], M. Wu[1], E. Dellacherie[1], T. A. Camesano[2], and A. Durand[1,*]

[1]Laboratoire de Chimie Physique Macromoléculaire, UMR 7568 CNRS-Nancy-University, ENSIC, BP 20451, 54001 Nancy cedex, France
[2]Worcester Polytechnic Institute, 100 Institute Road, Worcester, MA 01609

Polysaccharide-covered polymeric nanoparticles have potential applications in controlled drug delivery. Their properties can be adjusted by their surface coverage as well as by the chemical structure of the polymeric core. Engineering such nanoparticles with controlled properties can be achieved by designing the elaboration process. Several processes of nanoparticle preparation will be depicted, involving amphiphilic polysaccharides. In each case, the characteristics of the obtained nanoparticles will be correlated to their conditions of elaboration.

Introduction

Submicron nanoparticles find a wide number of applications in domains like medicine (drug delivery, diagnostic ...), cosmetics, food, etc. (*1-8*). Their properties are largely controlled by their surface characteristics and by the chemical nature of their core. We will limit to polymeric nanoparticles combining a hydrophobic core and a hydrophilic polymeric surface coverage. The important surface characteristics are the chemical nature of the covering material, the macromolecular architecture of this material (loops, brush, dendrimers...), the density of surface coverage and the thickness of the surface layer. The main characteristics of the polymeric core are its chemical nature, the average length of the chains and its size (*9*).

Polymeric surfactants are a very attractive class of compounds for nanoparticle surface coverage. The presence of macromolecular chains at the surface of colloidal particles offers significant advantages (*10*). First, they provide colloidal stability because of steric and eventually electrostatic repulsions (in the case of polyelectrolytes). Secondly, multi anchored polymers exhibit quasi-irreversible adsorption at interfaces (*11*). Finally, macromolecular chemistry allows preparing polymeric surfactants which combine other properties to their amphiphilic character: biocompatibility, biodegradability, specific interactions with some organs... convenient for specific applications.

Since the pioneering work of Landoll (*12*), hydrophobically modified polysaccharides have been largely studied as rheology modifiers in aqueous formulations (*13*). Their surface active properties and emulsifying ability have been also considered (*1-4*). For about 15 years, we have been using hydrophobically modified polysaccharides in the elaboration of polymeric nanoparticles with well-controlled surface characteristics (*5-9*).

Apart from the superficial layer, the chemical nature of the core of the nanoparticles is important for their suitability for drug delivery applications. Indeed, for drug encapsulation, compatibility should exist between the core material and the molecule to encapsulate. Moreover, the physical properties of the core can influence the kinetics of drug release through its rate of degradation in the release conditions or by changing the rate of drug diffusion. The chemical characteristics of the core of nanoparticles can be controlled by the use of well-designed processes of elaboration.

We will focus on four elaboration processes: two in which the polymeric core is obtained from previously synthesized macromolecules (emulsion/solvent evaporation and nanoprecipitation) and two others in which the polymeric core is synthesized from the monomer (emulsion and miniemulsion polymerization). All four processes have been well-studied in the literature but generally not with polymeric surfactants or rather recently.

In all processes, the surface properties of the nanoparticles are brought by the adsorption of polysaccharide surfactants. The density of surface coverage,

the thickness of the polymeric layer and the chemical nature of the superficial loops are closely related to the structure of the polymeric surfactants, the adsorption phenomena (fast or slow diffusion, macromolecular rearrangements...) and the process employed.

During miniemulsion polymerization (MP) and emulsion/solvent evaporation (ESE), an oil-in-water submicron emulsion, stabilized by polysaccharide surfactants, is first prepared. In MP the oil is essentially a monomer whose polymerization is initiated immediately after emulsification. The initiator can be dissolved either in the droplet or in the continuous aqueous phase. Because of the submicron size of the droplets and provided that the continuous phase contains no surfactant micelles, the nucleation occurs entirely in the droplets (strong difference with emulsion polymerization, see below) (*10, 11*). The oil droplets are then polymerized and lead to polymeric nanoparticles with a covering layer of polysaccharide surfactant. Varying the monomer structure allows obtaining a wide range of polymeric cores provided that their water solubility is not too high and the polymerization mechanism is compatible with emulsion conditions. In the case of ESE, the oil consists in a highly volatile solvent containing a dissolved polymer. After emulsification, solvent evaporation is performed under vacuum. Oil droplets are then converted into solid particles. The polymeric surfactants stabilizing the initial emulsion are supposed to remain at the surface of the final particles. The solvent must be easy to evaporate and compatible with the targeted application (ethyl acetate and dichloromethane are common examples). For MP and ESE, the average droplet size and stability of the initial oil-in-water emulsion is a fundamental aspect of the process for the resulting nanoparticles. This point can be optimized by studying separately the emulsifying properties of polysaccharide surfactants.

In the nanoprecipitation process (NP), the core material is first dissolved in a water-miscible solvent. Then the solution is dropped into a large excess of aqueous solution containing the polymeric surfactant. Due to exchange between the organic solvent and water, the polymer precipitates under the form of nanoparticles on which the polymeric surfactants progressively adsorb. The (rather low) amount of organic solvent present in the final suspension can be eliminated by a simple evaporation under vacuum. Generally, NP leads to very dilute suspensions of nanoparticles. No high energy input step is involved like emulsification in MP and ESE.

In emulsion polymerization (EP), nanoparticles are prepared by polymerizing a water-insoluble monomer following a free radical chain mechanism. Radicals are generated in the aqueous phase and nucleate aggregates formed by the amphiphilic macromolecules. The monomer in the droplets (with diameters generally of several microns) diffuses into the aggregates where polymerization takes place. Since the monomer droplets have sizes much higher than polymer aggregates, nucleation takes place only in the latter. This is the main mechanism difference between EP and MP but it has a lot of consequences

on the control of nanoparticles characteristics. Chain transfer reactions may occur between growing radicals and polymeric surfactants near the surface of the forming particle, leading to covalent anchoring at the surface. The consequence of such irreversible anchoring will be detailed below. Like in the NP process, the EP process does not need a high energy input step like ultrasound emulsification. This may be a real advantage when biological macromolecules are involved.

In what follows, the four previously cited processes will be applied to the elaboration of polysaccharide-covered nanoparticles. We will insist on the control of nanoparticle characteristics (size, composition and colloidal properties) through process conditions and try to compare the four processes.

Results and Discussion

Amphiphilic Polysaccharides for Nanoparticle Surface Coverage

Chemical Structure and Method of Synthesis

Dextran is an almost linear polysaccharide containing neutral repeat units (scheme 1). It is highly water-soluble and dissolves in some polar organic solvents: dimethylsulfoxide, ethylene glycol and formamide. The solution properties of dextran have been studied in water by viscometry and laser light scattering, leading to relations between the intrinsic viscosity (or the hydrodynamic radius) and the molar mass (Table I).

$R = CH_2-O-C_6H_6$ for $DexP_\tau$,

$R = C_6H_{13}$ for $DexC6_\tau$

$R = C_{10}H_{21}$ for $DexC10_\tau$.
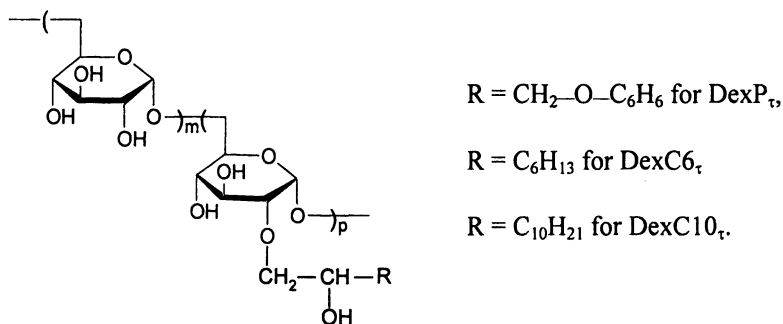
Scheme 1. Chemical structure of repeat units of dextran derivatives

Amphiphilic dextran derivatives were prepared from one commercial dextran sample T40® ($\overline{M}_n = 26,000 \, g/mol$, $\overline{M}_w = 40,000 \, g/mol$ as determined by size exclusion chromatography). For T40® we can calculate: $16.5 \leq [\eta] \leq$

Table I. Hydrodynamic Characteristics of Dextran in Water at 25°C

Experimental relation[a]	Reference
$[\eta] = 7.337 \times 10^{-5} \overline{M}_n^{0.533}$	(13)
$[\eta] = 5.628 \times 10^{-4} \overline{M}_w^{0.347}$	(14)
$R_h = 4.471 \times 10^{-2} \overline{M}_w^{0.464}$	(14)
$R_h = 4.328 \times 10^{-2} \overline{M}_w^{0.443}$	(15)

[a] $[\eta]$ is the intrinsic viscosity (L/g), R_h is the hydrodynamic radius (nm), $\overline{M}_n$ and $\overline{M}_w$ are the number-average and weight-average molar mass (g/mol) respectively.

22.2 mL/g and $4.7 \leq R_h \leq 6.1$ nm. Experimentally, we obtained $[\eta] = 20.0$ mL/g and $R_h = 4.9$ nm for that dextran sample (12).

Various amounts of hydrocarbon groups were attached onto the glucose units of dextran (scheme 1) using different epoxides: phenylglycidylether, epoxyoctane and epoxydodecane. Three families of amphiphilic dextrans were thus obtained, varying by the nature and the number of hydrophobes. The percentage of glucose units modified with one hydrocarbon group is called the degree of hydrophobic modification: $\tau = 100 \times y/(x+y)$ (see scheme 1). Since there are three hydroxyl groups in each repeat unit, τ could theoretically reach 300% (even higher values if the hydroxyl carried by the hydrocarbon tails reacts further as in the case of cellulose derivatives). Nevertheless, for amphiphilic dextrans used as polymeric surfactants, we will limit τ to 30% so as to keep a sufficient solubility in water.

The polymers will be named $DexP_\tau$, $DexC6_\tau$ and $DexC10_\tau$ according to the nature of hydrocarbon groups: phenoxy (P, with phenylglycidylether), $n-C_6H_{13}-$ (C6, with epoxyoctane) or $n-C_{10}H_{21}-$ (C10, with epoxydodecane). For all dextran derivatives, the degree of hydrophobic modification was calculated on the basis of ^1H NMR spectra in deuterated DMSO. The integrations corresponding to the hydrogen atoms of the hydrocarbon groups and that corresponding to the anomeric proton of the sugar rings were used. The chemical modification is detailed in previous papers (12,16).

Solution and Surface Active Properties

A detailed study of solution and interfacial properties of dextran derivatives is far above the scope of that paper. Only the essential aspects will be mentioned here. The interested reader is referred to more specialized papers (12,17).

Hydrophobically modified dextrans keep a significant water-solubility for degrees of substitution lower than 30%. When the ionic strength is increased, the solubility of dextran derivatives is strongly reduced, especially for $DexCn_\tau$ series (*17*).

In aqueous solutions, amphiphilic dextrans exhibit lower intrinsic viscosities than native dextran. On the contrary, Huggins coefficient increases with the degree of hydrophobic substitution (Table II). Both tendencies are related to the decrease of polymer-solvent affinity by the introduction of hydrocarbon groups along the polysaccharide chain. Similar trends have been evidenced for bile acid grafted dextrans (*18*). Light scattering experiments showed that these polymers are under the form of polymeric aggregates even in dilute solution. The number of macromolecules involved in the aggregates depends on the degree of hydrophobic substitution (*12, 19*).

Table II. Viscometric Parameters for Dextran Derivatives in Water and DMSO at 25°C.

Polymer	Solvent	$[\eta]$ (cm^3/g)	k_H
Dextran T40®	Water	20.0	0.6
	DMSO	28.5	0.6
$DexC6_{12}$	Water	16.8	1.1
	DMSO	27.4	0.7
$DexC6_{38}$	Water	8.0	3.7
	DMSO	25.9	0.6

In DMSO, $DexC6_\tau$ have intrinsic viscosities similar to that of native dextran. DMSO appears to be a good solvent for amphiphilic dextrans. Within that range of degree of substitution, the dilute domain extends up to approximately 35g/L in pure water. This range of concentrations is convenient for preparing submicron emulsions with oil volume fractions lower than 20% (see below). For higher polymer concentrations, a physical network is built through the formation of intermolecular interactions. This gives rise to an important viscosity increase. Similar effect has been reported for dextran esters prepared with valeric or benzoic acid.

At oil/water interfaces, hydrophobically modified dextrans lead to a significant decrease of interfacial tension. The kinetics of polymer adsorption at oil/water interfaces was examined (*8,17*). For polymer concentrations lower than 0.01g/L, the kinetics of decrease of interfacial tension appears to be controlled by macromolecule diffusion in the bulk solution. For higher concentrations, interfacial phenomena become limiting (conformational rearrangements, diffusion in the polymer layer close to the interface ...). Theoretical equations

were applied to experimental data obtained with amphiphilic dextrans in both concentration domains. Nevertheless, the values of physical parameters deduced from curve fitting should be considered with caution since theoretical equations were generally derived for molecular surfactants and not for polymeric ones.

Essential Aspects of Emulsification with Amphiphilic Polysaccharides

Amphiphilic dextrans can stabilize submicron oil-in-water emulsions (called miniemulsions) provided that the available amount of polymer in the aqueous phase and the energy input are high enough. Ultrasounds are used for miniemulsion preparation in what follows. Only the initial amount of surfactant will be considered as a process variable. A study of other operating parameters on emulsion characteristics is reported elsewhere (*17*). The relevant parameter
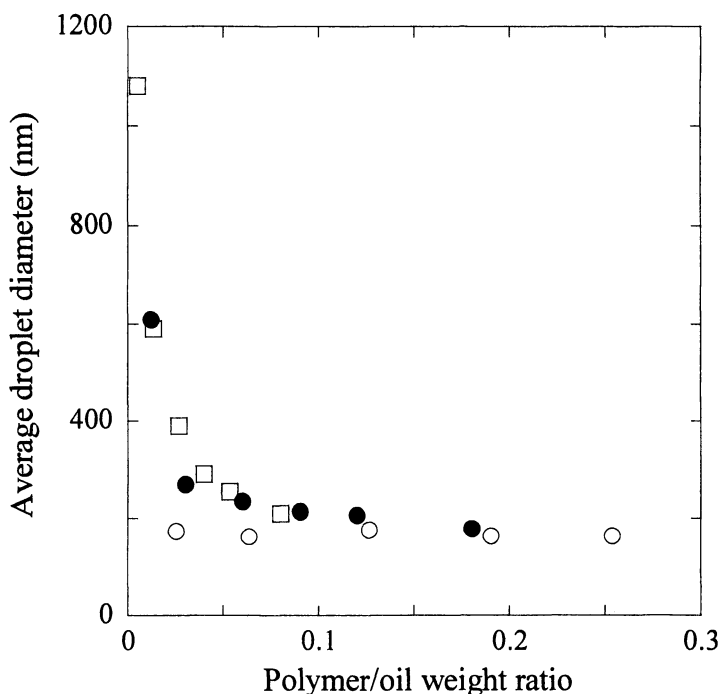
Figure 1. Variation of droplet size as a function of polymer-to-oil weight ratio for dodecane-in-water emulsions prepared in the presence of DexC6$_{38}$ at various concentrations in the aqueous phase (between 1 and 15g/L). Oil volume fraction: ○ 5%, ● 10% and □ 20%.

for the initial average droplet size is the weight ratio of amphiphilic dextran to oil. Using this ratio allows obtaining a unique curve combining experiments carried-out at various polymer concentrations and various oil volume fractions (Figure 1). For low values of that ratio (typically below 0.05), droplet diameter is a decreasing function of the initial amount of polymer. For higher values, the droplet diameter levels down, indicating that process conditions are limiting.

The surface coverage of oil droplets is also related to the weight ratio of polymeric surfactant to oil. For a given oil volume fraction, plotting the droplet surface coverage versus the excess polymer concentration in the aqueous phase leads to curves having the shape of usual adsorption isotherms. These curves are conveniently depicted using the Scatchard equation (8,20). As far as neutral dextran derivatives are considered, the range of droplet surface coverage obtained remains approximately unchanged whatever the number and nature of attached hydrocarbon groups. The minimum value obtained is generally around 1 mg/m^2. For high polymer concentrations, a maximum droplet surface coverage is reached which is around 4-5 mg/m^2. The exact analysis of these curves is complex since emulsification may occur under nonequilibrium conditions (2).

For miniemulsions stabilized by amphiphilic dextrans, it has been demonstrated that aging process follows Ostwald ripening mechanism (9). A spontaneous diffusion of oil from small droplets into the biggest ones takes place, giving rise to an overall displacement of the droplet size distribution towards higher dimensions. The dominant parameter for the rate of Ostwald ripening is the solubility of oil in water (21). A limited amount of hydrophobe (hexadecane) added to a more water-soluble oil (like toluene or styrene) is enough to strongly reduce the rate of Ostwald ripening (22). The use of rather water-soluble oils (dichloromethane...) gives rise to a very fast emulsion aging.

Materials for the Core of Nanoparticles

For ESE and NP processes, two polymers were used: poly(lactic acid) (PLA) and hydrophobically modified dextrans. PLA is a biocompatible polyester widely used for biomedical devices (23). A commercial atactic sample was used ($\overline{M}_w = 100,000\,g/mol$). The nanoparticles core is an amorphous material with a glass transition temperature around 43°C.

Hydrophobically modified dextrans were prepared by a similar method as that depicted for water-soluble amphiphilic dextrans. Nevertheless, the synthesis procedure was modified so as to limit the amount of water present in the reaction medium (16). Much higher degrees of hydrophobic modification were obtained. DexP$_\tau$ samples with τ above 80% exhibit a significant solubility in polar organic solvents like dichloromethane or ethyl acetate, provided that these solvents are saturated with water. Moreover, these polymers are readily soluble in

tetrahydrofuran (*16*). Varying the number and nature of hydrocarbon groups within dextran chains allows obtaining nanoparticles differing by the physical properties of their core (polarity, glass transition temperature ...).

For EP and MP processes, two monomers were employed: styrene and butylcyanoacrylate. Both monomers can be polymerized by a free-radical mechanism. Polymerization conditions should be optimized so as to ensure emulsion stability during the reaction. Butylcyanoacrylate undergoes rapid anionic polymerization in the presence of water (a strong enough base for that monomer). The pH of the aqueous phase should be adjusted so that the rate of spontaneous anionic polymerization remains low enough (*24*).

Emulsion-Solvent Evaporation Process

The applicability of different dextran derivatives containing various grafted hydrophobic groups (phenoxy, P; hexyl, C_6 or decyl, C_{10}) as emulsion stabilizers in the preparation of poly(lactic acid) (PLA) by an o/w emulsion/evaporation technique was extensively investigated (*6,7*). The feasibility of nanoparticles, with a hydrophobically modified dextran core instead of PLA, was examined. Dextran derivatives with high enough degrees of substitution were dissolved in the organic solvents. The stabilisation of droplets was achieved using low substituted dextran derivatives (see above).

The size and surface properties of PLA or dextran nanoparticles were significantly influenced by processing conditions. PLA nanospheres and $DexP_{130}$ nanospheres in the size range 150-300 nm were prepared by ESE using $DexP_{15}$ as stabilizer (Figure 2). In the case of PLA, the smallest particles were obtained with $DexP_{15}$ with concentrations of 1-1.5 g/L while the smaller $DexP_{130}$ particles with the smallest polydispersity index (0.2 ± 0.1) were obtained with $DexP_{15}$ for concentrations higher than 2.5g/L.

Interestingly $DexP_{130}$ particles can also be obtained without $DexP_{15}$ in the water phase, contrary to PLA (Table III). This result could be attributed to the solubility in water of a small $DexP_{130}$ fraction, providing surface active species in the aqueous phase at a concentration sufficient to stabilize the droplets.

The stability of colloidal suspensions with ionic strength was investigated. For biological use, particles should be stable at ionic strengths around 0.15M. The evolution of the zeta potential (ζ) of $DexP_{130}$ and of PLA particles versus the NaCl concentration is shown in Figure 3.

In all curves, ζ decreases with increasing NaCl concentration. Compared to uncoated PLA particles, it is clear that the $DexP_{15}$ layer at the PLA surface masks the COO$^-$ end groups of PLA chains, decreasing the zeta potential of particle surface. Unexpectedly, the surface of $DexP_{130}$ particles is also negatively charged, in spite of the fact that charged groups are not present on dextran. This

Table III. Size of Nanoparticles Prepared by Emulsion/Solvent Evaporation Process using Various Hydrophobically Modified Dextrans with or without DexP$_{15}$ in Water.

	Particle size (nm)	
Nanoparticle core	DexP$_{15}$ 5g/L in water	No DexP$_{15}$ in water
DexP$_{65}$	200	370
DexP$_{130}$	160	420
DexP$_{210}$	180	850
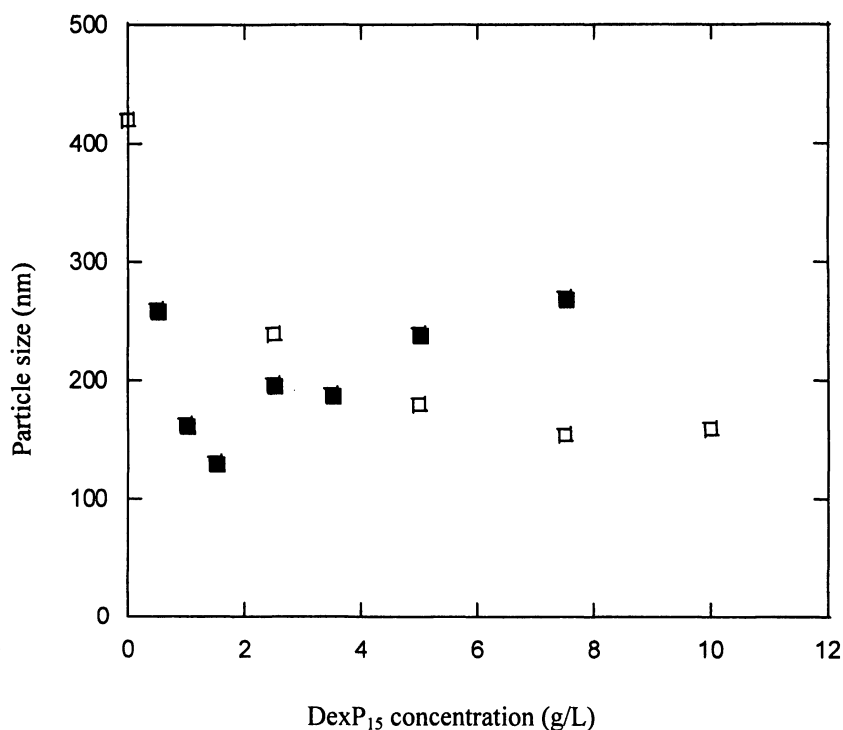
Figure 2. Particle size as a function of DexP$_{15}$ concentration following the emulsion/solvent evaporation process, for two different core materials.
□ *DexP$_{130}$ and* ■ *PLA*

result can be explained by the adsorption of ions on the particle surface. In both curves (corresponding to $DexP_{130}$ and $DexP_{15}$-coated $DexP_{130}$ particles), it can be observed that ζ decreases with increasing NaCl concentrations. Compared to $DexP_{130}$ particles obtained without $DexP_{15}$, it is clear that the effect of $DexP_{15}$ is also to reduce the zeta potential of particles. In addition, $DexP_{130}$ and PLA particles proved to be stable up to 1M NaCl when obtained in the presence of $DexP_{15}$ in the water phase (5g/l) while bare $DexP_{130}$ and PLA particles are destabilized in NaCl solution above 0.01 M. From these results, it can be accepted that the stabilization of particles obtained in the presence of $DexP_{15}$ is mainly due to steric repulsion of the $DexP_{15}$ polymer layer formed at the particle surface.

Both $DexP_{15}$ coated nanoparticles (PLA and $DexP_{130}$) proved to be stable in solution after a 7-day incubation period and most of them could also be easily resuspended in water after freeze-drying without cryoprotectant. These results clearly confirm the presence of a $DexP_{15}$ layer at the surface of nanospheres, providing a decrease of the extent of particle aggregation after freeze drying.

Nanoprecipitation

With the NP process, dextran nanoparticles of similar size were obtained with or without using $DexP_{15}$ as stabilizer. Contrary to the ESE process, particle sizes are quite independent of the surface active polymer added to the aqueous phase but are strongly related to the dextran concentration in the THF phase (Figure 4).

For colloidal stability, the results are similar to ESE; above 0.01 M NaCl, suspensions of particles with no $DexP_{15}$ shell are unstable and flocculate.

Miniemulsion Polymerization

Styrene-in-water miniemulsions were prepared in the presence of different dextran derivatives: $DexP_5$, $DexP_{13}$, $DexP_{16}$, $DexP_{23}$, and $DexP_{28}$. The relevant parameter is the initial weight ratio α = [polymer]/[oil]. The influence of the copolymer structure was far less pronounced. The droplet size was around 150 nm at maximal surface coverage for all the copolymers (Figure 5).

However drastic differences were observed during the polymerization step. The best results were obtained for τ higher than 10%. In these cases, the particle size was close to the initial droplet size and the coagulated amount was below 5 wt%. The particle size and amount coagulated strongly increased by decreasing τ below 10%. In the case of $DexP_5$, no latex was obtained.
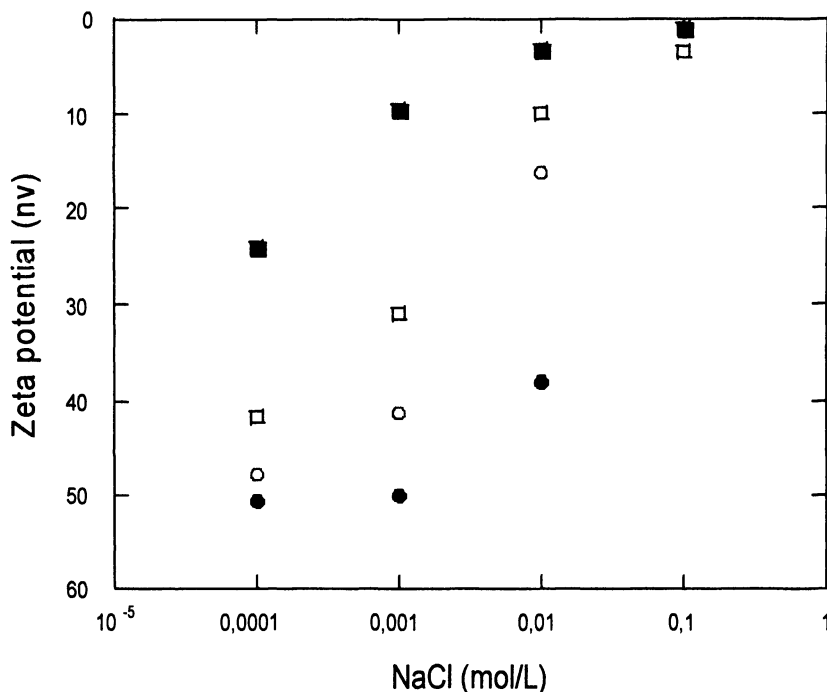
Figure 3. Zeta potential of polymeric nanoparticles at various ionic strengths.
● *bare PLA particles,* ■ *PLA particles coated with DexP$_{15}$,* ○ *bare DexP$_{130}$*
particles, □ *DexP$_{130}$ particles coated with DexP$_{15}$.*

Electrokinetic layer thickness was evaluated via Zeta potential measurements (*25*). It regularly increased with dextran concentration in the aqueous phase, to reach a maximum value of about 6 nm for all polymers.

The amount of non-adsorbed polymer remaining in the aqueous phase after polymerization was determined using the anthrone method (*26,27*). The maximum surface coverage was found to slightly increase with the modification degree of the polysaccharide starting from 3 mg/m² for DexP$_{13}$ and reaching 4 mg/m² for DexP$_{28}$.

The electrokinetic layer thickness linearly increased with the surface coverage of the particle (Figure 6). The slope of this variation decreased with the modification degree of the amphiphilic polysaccharide, suggesting the formation of a more compact layer. Indeed, the number of anchoring points increases with τ, thereby decreasing the polysaccharide layer thickness.
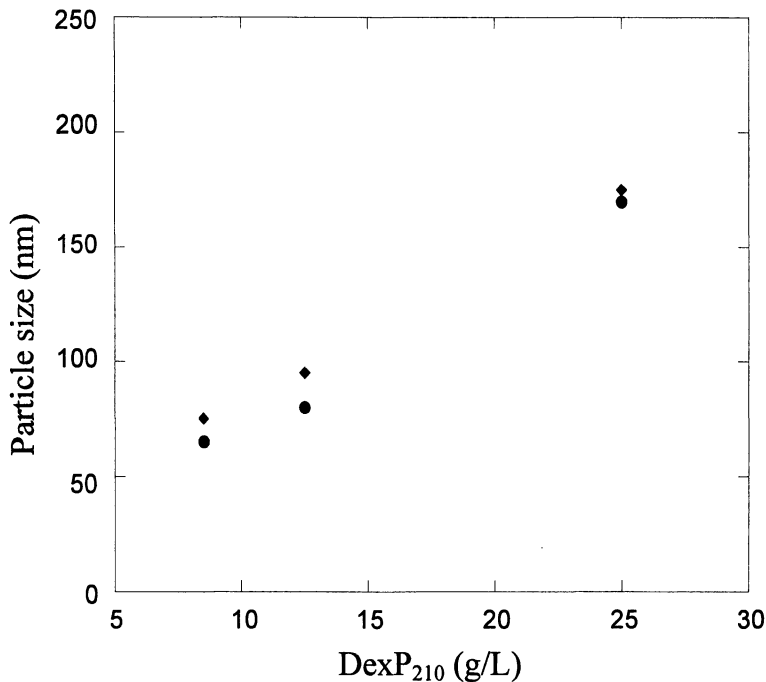
Figure 4. Size of DexP$_{210}$ nanoparticles prepared by nanoprecipitation as a function of DexP$_{210}$ concentration in THF, using DexP$_{15}$ as surface active polymer in the aqueous phase at 2.5g/L (◆) or without any surface active polymer in water (●).

Polystyrene nanoparticles were washed in SDS solutions with increasing surfactant concentrations in order to desorb the not tightly bound dextran derivatives. About 30% of the adsorbed polysaccharide could be easily washed from the nanoparticles. The other 70% remained linked to the surface of the nanoparticles even in the more concentrated SDS solutions (2 wt%). The polysaccharide layer is thus very stable.

In order to get biocompatible and biodegradable nanoparticles suitable for biomedical applications, styrene was replaced by butylcyanoacrylate. Very low pH values are required to avoid butylcyanoacrylate anionic polymerization during the emulsification step as water initiates the polymerization. Therefore, potential degradation of the amphiphilic derivatives was investigated. The degree of substitution remained unchanged in the polymerization conditions and dextran chain scission only occurred at high temperature and pH 1.

Emulsification conditions (sonication time and temperature) were optimized so as to minimize particle size and anionic polymerization of monomer at the
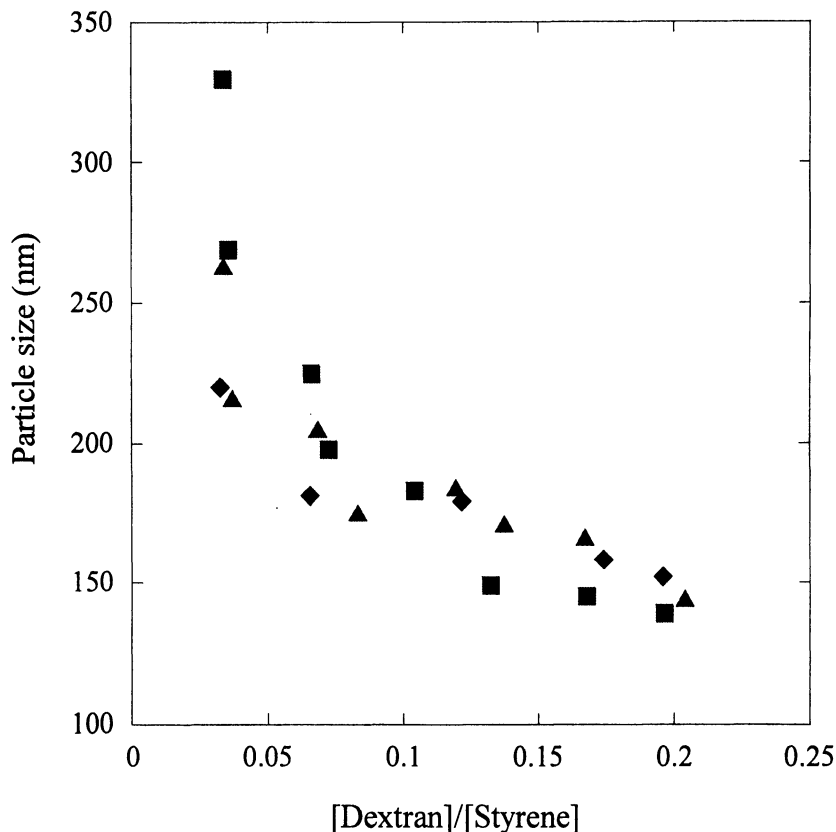
Figure 5. Variation of polystyrene particle size as a function of [dextran]/[styrene] mass ratio for miniemulsion polymerization stabilized by DexP$_{13}$ ◆, DexP$_{16}$ ▲ and DexP$_{28}$ ■

same time. Both radical and anionic polymerizations were studied. These results will be presented in details in a forthcoming paper. Briefly, the particles size was found to be in the same order of magnitude as in the case of styrene. Surface coverage was much higher. Indeed, alkylcyanoacrylate polymerization can be initiated by the hydroxyl groups of the polysaccharide backbone, thereby increasing the number of anchoring points. The polysaccharide layer was more compact as compared to polystyrene nanoparticles because of the increased number of anchoring points.

Miniemulsion polymerization stabilized by dextran derivatives thus allows the synthesis of polysaccharide-coated nanoparticles with a wide variety of chemical nature of the core.
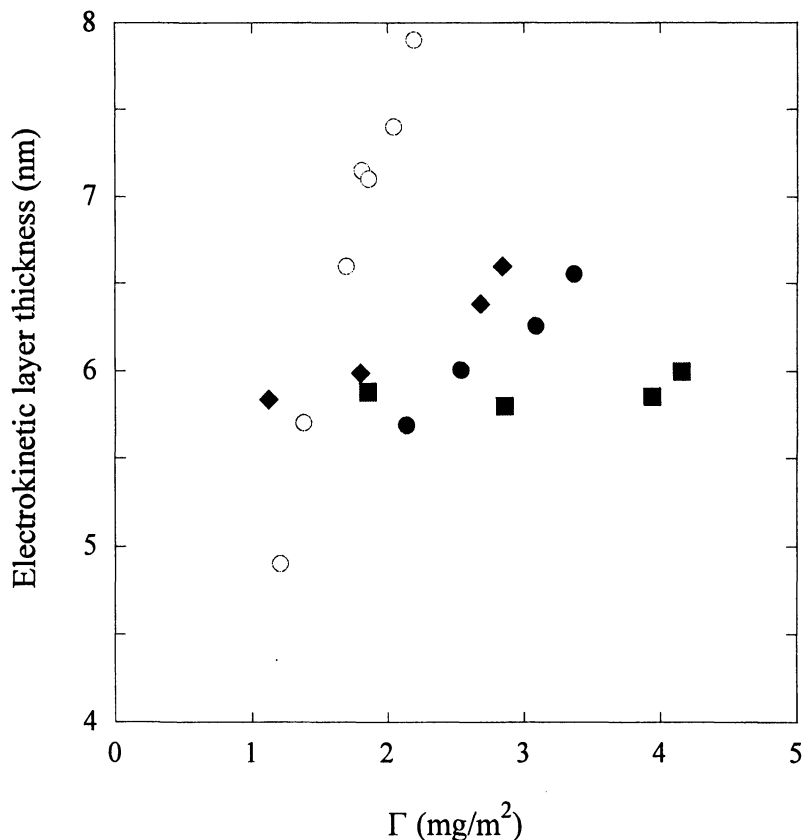
Figure 6. Electrokinetic layer thickness as a function of surface coverage for nanoparticles obtained by emulsion polymerization ○ or miniemulsion polymerization stabilized by DexP$_{13}$ ◆, DexP$_{23}$ ● and DexP$_{28}$ ■.

Emulsion Polymerization

Dextran-coated nanoparticles could be obtained by direct emulsion polymerization of styrene in the presence of native dextran. Although dextran is not a surfactant, stable particles with a permanently grafted dextran layer at their surface were obtained in a one-step procedure.

Chemical modification of the polysaccharide probably occurred in the early stage of the emulsion polymerization. Indeed, though conversion only reached a few percents, the reaction medium turned opaque after about one hour while the

organic layer totally disappeared. This speaks for the formation of a styrene in water emulsion, which is only possible in the presence of amphiphilic species. Furthermore, particle size was directly connected to the dextran concentration. As native dextran do not adsorb on polystyrene nanoparticles, this further suggest that the polysaccharide was modified.

The nature of the in-situ formed stabilizer was studied by NMR and MALDI-TOF. Graft copolymers are supposed to be formed, which are able to stabilize the emulsion polymerization of styrene (28).

Once more, it appeared that for a given dextran sample, the key parameter to control the final particle size was the initial weight ratio α = [dextran]/[styrene] (Figure 7). The molar mass of the dextran also had a great influence on final polystyrene particle size. Smaller particles were obtained for the dextran T500®, especially at low concentration. Particle sizes were only slightly higher than for miniemulsion polymerization of styrene.

However, the amount of dextran needed to stabilize the emulsion polymerization of styrene was relatively high. In the case of dextran T40®, the plateau value of particle diameter was obtained for a [polysaccharide]/[styrene] ratio of about 40%. By comparison, in the case of miniemulsion polymerization stabilized by amphiphilic derivatives of dextran, a [polysaccharide]/[styrene] ratio of only 5% is required.

Electrokinetic layer thickness regularly increased with dextran concentration in the aqueous phase, to reach a maximum of about 7 nm. This value is in agreement with the only one reported in the literature (29).

After washing the particles via centrifugation and redispersion in distilled water in order to eliminate the non adsorbed polysaccharide, the amount of remaining dextran at the surface of the particles was determined by direct titration of the particles and we get a maximum surface coverage equal to 2.5 mg/m^2 which is consistent with the literature (29).

The slope of the variation of the electrokinetic layer thickness as a function of the surface coverage was found to be much higher than for MP process. The formed polysaccharide layer is also far less compact. Indeed, the number of anchoring points is probably much lower.

Emulsion polymerization allows the chemical modification of native dextran and the synthesis of dextran-coated nanoparticles in a one-step procedure. Nevertheless, the hydrophobically modified dextrans cannot be isolated from the reaction mixture and characterized independently.

Conclusion

Polysaccharide-covered nanoparticles were produced by several methods involving amphiphilic polysaccharides. Using various processes, it is possible to
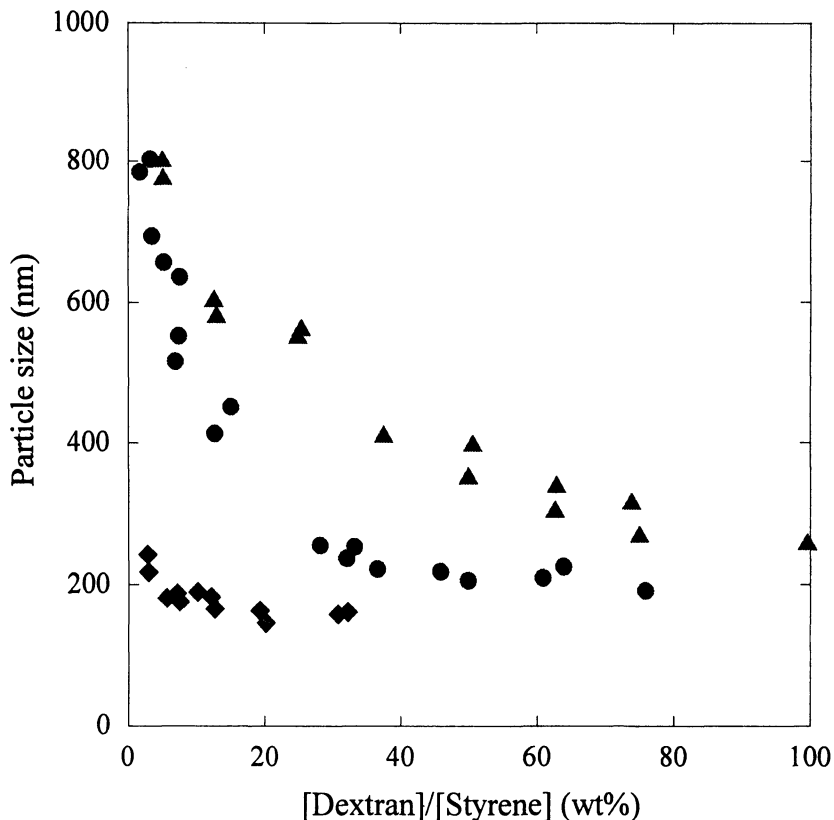
Figure 7. Particle size as a function of [dextran]/[styrene] mass ratio for emulsion polymerization of styrene with three dextran samples T6[R] ▲, T40[R] ● and T500[R] ◆, (average molar masses 6,430, 40,000 and 480,000 g.mol^{-1})

control the nature of the core material as well as the characteristics of the superficial polymeric layer. Even if only dextran is used here for surface coverage, it is possible to design other amphiphilic polymers based on different polysaccharides thereby leading to nanoparticles with specific surface interactions. Furthermore, using the wide variety of acrylic monomers, nanoparticles with polymeric cores having very different characteristics (polarity, glass transition temperature ...) can be prepared. Nevertheless, it is necessary to adapt miniemulsion conditions to polymerization requirements. Another way to vary the chemical nature of nanoparticle core is to prepare water-insoluble polymers that could be used in processes like nanoprecipitation or emulsion/solvent evaporation. Such topics are currently investigated in our laboratory.

Acknowledgements

References

1. Nilsson, L.; Bergenstahl, B. *J. Agric. Food Chem.* **2007**, *55*, (4), 1469.
2. Nilsson, L.; Bergenstahl, B. *Langmuir* **2006**, *22*, (21), 8770.
3. Karlberg, M., Thuresson, K., Lindman, B. *Colloids Surf. A* **2005**, *262*, 158.
4. Akiyama, E.; Kashimoto, A.; Fukuda, K.; Hotta, H.; Kitsuki, T. *J. Colloid Interface Sci.* **2005**, *282*, (2), 448.
5. Fournier, C.; Leonard, M.; Le Coq-Leonard, I.; Dellacherie, E. *Langmuir* **1995**, *11*, (7), 2344.
6. Rouzes, C., Durand, A., Leonard, M., Dellacherie, E. *J. Colloid Interface Sci.* **2002**, *253*, 217.
7. Rouzes, C., Léonard, M., Durand, A., Dellacherie, E., *Colloid Surf. B* **2003**, *32*, 125.
8. Rotureau, E., Léonard, M., Dellacherie, E., Durand, A., *J. Colloid Interface Sci.* **2004**, *279*, 68.
9. Rotureau, E., Léonard, M., Dellacherie, E., Durand, A., *Phys. Chem. Chem. Phys.* **2004**, *6*, 1430.
10. Landfester, K. *Topics Cur. Chem.* **2003**, *227*, 75.
11. Landfester, K. *An. Rev. Mat. Res.* **2006**, *36*, 231.
12. Rotureau, E., Chassenieux, C., Dellacherie, E., Durand, A., *Macromol. Chem. Phys.* **2005**, *206*, 2038.
13. Guner, A. *J. Appl. Polym. Sci.* **1999**, *72*, 871.
14. Ioan, C. E.; Aberle, T.; Burchard, W. *Macromolecules* **2000**, *33*, 5730.
15. Nordmeier, E. *J. Phys. Chem.* **1993**, *97*, 5770.
16. Durand, A.; Dellacherie, E. *Colloid Polym. Sci.* **2006**, *284*, 536.
17. Rotureau, E.; Leonard, M.; Marie, E.; Dellacherie, E.; Camesano, T. A.; Durand, A. *Colloids Surf. A* **2006**, *288*, 131.
18. Nichifor, M.; Carpov, A. *Eur. Polym. J.* **1999**, *35*, 2125.
19. Nichifor, M.; Lopes, A.; Carpov, A.; Melo, E. *Macromolecules* **1999**, *32*, 7078.
20. Scatchard, G. *Ann. N. Y. Acad. Sci.* **1949**, *51*, 660.
21. Taylor, P. *Adv. Colloid Interface Sci.* **1998**, *75*, 107.
22. Kabal'nov, A. S., Pertsov, A.V., Aprosin, Y.D., Shchukin, E.D. *Colloid Journal of the USSR* **1985**, *47*, 898.
23. Vert, M. *Encyclopedia of Biomaterials and Biomedical Engineering* **2004**, *2*, 1254.

24. Limouzin, C.; Caviggia, A.; Ganachaud, F.; Hemery, P. *Macromolecules* **2003**, *36*, 667.
25. Delgado, A. D. S.; Leonard, M.; Dellacherie, E. *J. Biomater. Sci. Polymer Edn* **2000**, *11*, (12), 1395-1410.
26. Scott, T. A.; Melvin, E. H. *Anal. Chem.* **1953**, *25*, 1656-1661.
27. Fournier, C.; Leonard, M.; Dellacherie, E.; Chikhi, M.; Hommel, H.; Legrand, A. P. *J. Colloid Interface Sci.* **1998**, *198*, 27-33.
28. Ladaviere, C.; Averlant-Petit, M.-C.; Fabre, O.; Durand, A.; Dellacherie, E.; Marie, E. *Colloid Polym. Sci.* **2007**, *285*, 621-630.
29. Chern, C. S.; Lee, C. K.; Tsai, Y. J. *Colloid Polym. Sci.* **1997**, *275*, 841-849.

<center>Chapter 24</center>

"Frozen" Micelles: Polymer Nanoparticles of Controlled Size by Self-Assembly

<center>R. Nagarajan</center>

<center>Molecular Sciences and Engineering Team, Natick Soldier Research, Development and Engineering Center, Kansas Street, Natick MA 01760</center>

Block copolymer micelles generated by spontaneous molecular self-assembly can serve as nanoparticles that are intrinsically passivated as well as stable, and with a controlled dispersion of size. But micelles are not "permanent" nanoparticles, because the equilibrium self-assembly process involves free exchange of block copolymer between the micelle and the surrounding solvent medium. However, micelles that are "frozen" in the kinetic sense can be prepared if one block of the copolymer has a high enough glass transition temperature or large enough hydrophobicity, so as to cause a large activation energy barrier for molecular exchange. In such systems, the nanoparticle preparation method involves the molecular dissolution of the block copolymer in a solvent common to both blocks, followed by the replacement of the common solvent by a selective solvent to cause the freezing of the micelle. In this work, we present a theory for predicting the size and shape of such "frozen" micelles in selective solvents, prepared using mixed solvents. We show that the resulting micellar properties are significantly different compared to those predicted based on the nature of the selective solvent alone, without considering the micelle preparation procedure.

Introduction

The preparation of passivated and stable nanoparticles of controlled size and shape is a problem of general interest to nanotechnology. A convenient way to achieve this goal for polymer nanoparticles is by self-assembly of amphiphilic polymers, possessing a block representing the nanomaterial of interest, to form micelles. This block forms the core of the micelle, serving as the desired nanoparticle and its passivation and stabilization are guaranteed by the presence of the other block forming the corona of the micelle.

The micelles formed by self-assembly are not permanent nanoparticles in the sense that free exchange of block copolymer molecules occurs between the micelles and the surrounding solvent medium. However, one can use the self-assembly process and create permanent nanoparticles if the core forming polymer block has a high glass transition temperature or is highly solvophobic with respect to the solvent medium in which the particle is to be dispersed. Consider, for example, the synthesis of polystyrene nanoparticles to be dispersed in aqueous medium. We can start with diblock copolymers of polystyrene-polyethyleneoxide (PS-PEO). Three key stages in the self-assembly process are schematically shown in Figure 1.
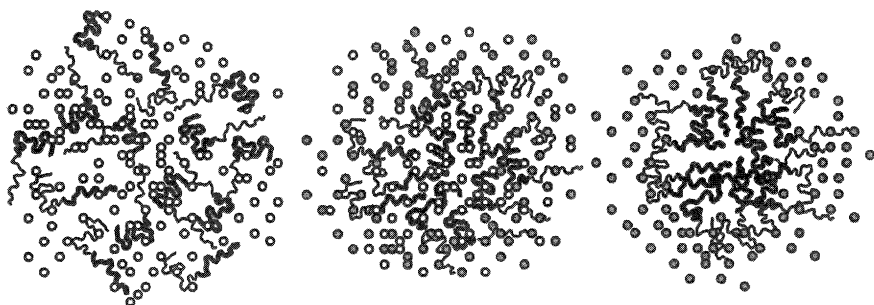
Figure 1. Process of forming block copolymer micelles. Thick and thin lines represent hydrophobic (PS) and hydrophilic (PEO) blocks. Open circles denote common solvent (THF) and filled circles denote solvent (water) selective to the hydrophilic block and non-selective to the hydrophobic block.

The block copolymer is first dissolved at the molecular scale in tetrahydrofuran (THF) which is a common good solvent for both PS and PEO blocks and no self-assembly takes place (Figure 1–left). Then water, which is a good solvent for PEO block and a very poor solvent for PS block, is added to the system, progressively replacing THF. The changing solvent composition induces the formation of block copolymer micelles in the solvent medium with a PS core

and a PEO corona (Figure 1-middle). The micelle core consists of PS and the common solvent THF since it is a good solvent for PS; but the selective solvent water is excluded from the core. The corona region consists of PEO blocks and the solvent mixture of THF and water, the same as the surrounding bulk solvent. The self-assembly process involves free molecular exchange, typical of an equilibrium process, since the PS blocks are in a liquid state under these conditions and pose no kinetic barriers to exchange.

As THF is progressively removed from the system by solvent substitution, the volume fraction of THF in the micelle core continues to decrease and reaches a critical volume fraction at which the PS block becomes glass. This critical volume fraction of diluent (THF, in this case) is a function of the temperature, molecular weight of the PS block and the molecular volume of the diluent. When the PS blocks become glassy, the micelle is considered frozen. The free exchange of block copolymer molecule is now forbidden. As THF continues to be removed from the system, the number of block copolymer molecules in the micelle (the aggregation number) will remain unaltered, since the block copolymer molecules are forbidden to enter or leave the micelle. The volume fraction of THF in the core continues to decrease and the conformation of the corona block PEO continues to change with changing solvent composition. Finally, when all THF is removed, the micelle is in pure water (Figure 1-right).

Indeed, we have great control over such a nanoparticle formation process by our ability to change the solvent composition gradually or abruptly. At any stage in the process, well before the volume fraction of THF in the core reaches the critical value, we can abruptly change the solvent composition by adding a large volume of water to the system causing the micelle to freeze at any bulk solvent volume fraction. Therefore, depending on the volume fraction of THF in the core (or in the bulk solvent) at which the abrupt change in solvent composition is caused, one can obtain a nanoparticle of different size.

A theoretical method to predict the size and shape of such frozen micelles currently does not exist in the literature. We develop such a predictive model here by implementing the following steps:

- First formulate a theory of micelle formation and solubilization in binary solvent mixtures (THF + water), allowing the common solvent (THF) to be also solubilized in the micelle core.
- Second, use the above theory to determine the volume fraction of THF in the core and the aggregation number of the micelle as a function of the volume fraction of THF in the bulk solvent medium.
- Third, freeze the micelle at a specific volume fraction of THF in the micelle core, thus freezing the aggregation number of the micelle. For this frozen aggregation number, determine the micelle core radius and the corona thickness when all THF is removed and only water remains as the solvent.

The theory developed here follows our previous treatments of micelle formation (*1*) and solubilization (*2*) in selective solvents and therefore the construction of

various free energy expressions are only briefly described here. We refer the reader to the earlier papers (1-5) for more descriptive information. The model developed here is applicable to all aggregate shapes and indeed calculations have been performed for both spherical and cylindrical micelles. However, only the results for spherical micelles are discussed here because of space limitations and the results for cylindrical micelles will be presented in a different publication.

Self-assembly in Binary Solvent Mixture

The size distribution of block copolymer micelles in a binary solvent mixture, with the common solvent solubilized in the micelle core, is given by

$$X_g = X_1^g \, a_T^j \, \exp - \left(\frac{g \, \Delta \mu_g^o}{kT} \right),$$

$$\Delta \mu_g^o = \frac{\mu_{gj}^o}{g} - \mu_1^o - \frac{j}{g} \mu_T^* , \quad \ln a_T = X_T \exp \left(\chi_{TW} X_W^2 \right)$$

(1)

Here, X_g is the mole fraction of the micelle with an aggregation number g and containing j molecules of the common solvent (solubilizate) in the micelle core, X_1 is the mole fraction of the non-aggregated block copolymer molecule (unimer), a_T is the activity of the common solvent (THF) that is also solubilized, μ_{gj}^o is the standard chemical potential of the micelle defined as that of an isolated micelle in the solvent mixture, μ_1^o is the standard chemical potential of the unimer, also defined as that of an isolated unimer in the solvent mixture, and μ_T^* is the standard chemical potential of the common solvent THF defined as that of a pure solvent. The variables X_T and X_W denote the mole fractions of THF and water in the bulk solvent medium and χ_{TW} is the interaction parameter between THF and water. To calculate the size distribution of micelles, one requires an expression for the standard free energy change on aggregation, $\Delta \mu_g^o$. Since this depends on the shape and size of aggregates, the geometrical variables describing the aggregates have to be defined as well.

Geometrical Relations for Aggregates

The symbols A and B represent the core and corona blocks. We use the variable R to denote the hydrophobic core dimension (radius for sphere or cylinder), D for the corona thickness, and a for the surface area of the aggregate

core per constituent block copolymer molecule. The numbers of molecules g and j, the micelle core volume V_C, and the corona volume V_S all refer to the total quantities in the case of spherical aggregates and quantities per unit length in the case of cylindrical aggregates. The volume fraction of the solubilizate molecules in the core is denoted by η. The concentrations of segments are assumed to be uniform in the core as well as in the corona, with φ_A standing for the volume fraction of the A segments in the core ($\varphi_A = 1 - \eta$), and φ_B for the volume fraction of the B segments in the corona. The geometrical relations describing spherical and cylindrical block copolymer aggregates are summarized in Table 1. If any three structural variables are specified all the remaining geometrical variables can be calculated through the relations given in Table 1. For convenience, R, D and η (or φ_A) are chosen as the independent variables.

Table 1. Geometrical Relations for Aggregates

Property	Sphere	Cylinder
$V_C = g\, N_A\, v_A + j\, v_T$	$4\pi R^3/3$	πR^2
V_S	$V_C\,[(1+D/R)^3-1]$	$V_C\,[(1+D/R)^2-1]$
g	$V_C\,(\varphi_A/v_A)$	$V_C\,(\varphi_A/v_A)$
a	$3\,v_A/(R\varphi_A)$	$2\,v_A/(R\varphi_A)$
φ_B	$(v_B/v_A)\,\varphi_A\,(V_C/V_S)$	$(v_B/v_A)\,\varphi_A(V_C/V_S)$
$\eta = j\,v_T/(g\,N_A\,v_A + j\,v_T)$	$1-\varphi_A$	$1-\varphi_A$

In Table 1, v_A, v_B, v_T and v_W, refer to the molecular volumes of A and B segments, the common solvent (which is also the solubilizate) and the selective solvent. The effective molar volume of the mixed solvent v_S is calculated by composition (mole fraction) averaging the molar volumes of THF and water. The characteristic lengths of K (= A, B) are defined as $L_K = v_K^{1/3}$. N_A and N_B are the number of segments of blocks A and B for both AB diblock and for the symmetric BAB triblock copolymers.

Standard Free Energy Change on Aggregation

The expression for the standard free energy change on aggregation is formulated by identifying all physicochemical changes accompanying micelle

formation. First, the transfer of the solubilizate and the singly dispersed copolymer to the micellar core is associated with changes in the state of dilution and the state of deformation of A block, including the swelling of A blocks in the core by solubilizate T. The corresponding free energy change is calculated using Flory theory for polymer solutions (6), Semenov theory for elastic deformations in constrained systems (7) and de Gennes theory for conformation of a collapsed polymer (8). Second, the formation of micelle is associated with the generation of an interface between the micelle core made up of A blocks and solubilizate T and the micelle corona consisting of B blocks and the mixed solvent S (mixture of T and W). The characteristic interfacial tension σ_{agg} between the core and corona regions is calculated based on the Prigogine theory for interfacial tension between solutions (9,10). Third, the B block of the singly dispersed copolymer is transferred to the corona region of the micelle and this transfer process also involves changes in the states of dilution and deformation of the B block. This is calculated using Flory theory for polymer solutions (6), Semenov theory for elastic deformations in constrained systems (7) and the Flory theory for swollen isolated polymer (6) with modification suggested by Stockmayer (11). Fourth, the formation of the micelle localizes the copolymer such that the A block is confined to the core while the B block is confined to the corona. This is calculated using a configurational volume restriction model. Fifth, in the case of a BAB triblock copolymer, there is a free energy contribution due to the folding or loop formation of the A block (which occurs to ensure that the B blocks at the two ends are in the corona while the folded A block is within the micelle core). This is calculated using the Jacobsen-Stockmayer model (12). Thus,

$$\Delta\mu_g^o = (\Delta\mu_g^o)_{A,dil} + (\Delta\mu_g^o)_{A,def} + (\Delta\mu_g^o)_{int} + (\Delta\mu_g^o)_{B,dil} + (\Delta\mu_g^o)_{B,def}$$
$$+ (\Delta\mu_g^o)_{loc} + (\Delta\mu_g^o)_{loop} \tag{2}$$

Expressions for each of these contributions are briefly presented below.

Change in state of dilution of block A

$$\frac{(\Delta\mu_g^o)_{A,dil}}{kT} = N_A \left[\frac{v_A}{v_T} \frac{1-\varphi_A}{\varphi_A} \ln(1-\varphi_A) + \frac{v_A}{v_T} (1-\varphi_A) \chi_{AT} \right] -$$
$$- N_A \left[\frac{v_A}{v_S} \frac{1-\varphi_{A1}}{\varphi_{A1}} \ln(1-\varphi_{A1}) + \frac{v_A}{v_S} (1-\varphi_{A1}) \chi_{AS} \right] \tag{3}$$
$$- \left(\frac{\sigma_{AS} L_A^2}{kT} \right) \frac{6 N_A^{1/2}}{\alpha_A}$$

The chain expansion parameter α_A and for the segment volume fraction φ_{A1} within the unimer in its standard state are calculated using the de Gennes theory for collapsed polymers (8) from the expressions:

$$\ln\left(1-\varphi_{A1}\right)+\varphi_{A1}+\chi_{AW}\,\varphi_{A1}^2 = 0, \quad \alpha_A = (6/\pi)^{1/3}\,N_A^{-1/6}\varphi_{A1}^{-1/3} \tag{4}$$

The interfacial tension σ_{AS} between block A and the binary solvent mixture is calculated using the Prigogine theory ($9,10$). The polymer-mixed solvent interaction parameter χ_{AS} depends on the composition of the bulk solvent. It is calculated from eq.(5), with the volume fractions φ_T and φ_W chosen as composition variables.

$$\chi_{AS} = \varphi_T\chi_{AT}+\varphi_W\chi_{AW}-\varphi_T\varphi_W\chi_{TW} \tag{5}$$

Change in state of deformation of block A

$$\frac{(\Delta\mu_g^o)_{A,def}}{kT} = \left[q\left(\frac{p\,\pi^2}{80}\right)\frac{R^2}{(N_A/q)\,L_A^2}\right]-\left[\frac{3}{2}\left(\alpha_A^2-1\right)-\ln\alpha_A^3\right] \tag{6}$$

Here, q = 1 for AB diblock and 2 for symmetric BAB triblock copolymers and p = 3 for spheres and 5 for cylinders.

Formation of core-solvent interface

$$\frac{(\Delta\mu_g^o)_{int}}{kT} = \frac{\sigma_{agg}}{kT}a, \quad \sigma_{agg} = \sigma_{AS}\,(1-\varphi_B)\,\varphi_A+\sigma_{AB}\,\varphi_B\,\varphi_A \tag{7}$$

Here, σ_{agg} is calculated recognizing that A interacts with the mixed solvent S (mixture of T and W) and the B block at the interface. σ_{AB} is estimated from the interaction parameter χ_{AB}.

Change in state of dilution of block B

$$\frac{(\Delta\mu_g^o)_{B,dil}}{kT} = N_B\left[\frac{v_B}{v_S}\frac{1-\varphi_B}{\varphi_B}\ln\left(1-\varphi_B\right)+\frac{v_B}{v_S}\,(1-\varphi_B)\chi_{BS}\right]-$$
$$-N_B\left[\frac{v_B}{v_S}\frac{1-\varphi_{B1}}{\varphi_{B1}}\ln\left(1-\varphi_{B1}\right)+\frac{v_B}{v_S}\,(1-\varphi_{B1})\chi_{BS}\right] \tag{8}$$

The chain expansion parameter α_B and the segment volume fraction φ_{B1} within the unimer in its standard state are calculated using the Flory theory for swollen isolated polymers (6) with the modification suggested by Stockmayer (11)

$$\alpha_B^5 - \alpha_B^3 = 0.88 \, (1/2 - \chi_{BS}) \, (N_B / q)^{1/2}$$

$$\varphi_{B1} = (6 / \pi) \, (N_B / q)^{-1/2} \, \alpha_B^{-3}$$

(9)

The polymer-mixed solvent interaction parameter χ_{BS} is calculated using the relation:

$$\chi_{BS} = \varphi_T \chi_{BT} + \varphi_W \chi_{BW} - \varphi_T \varphi_W \chi_{TW} \tag{10}$$

Change in state of deformation of block B

$$\frac{(\Delta\mu_g^o)_{B,def}}{kT} = q \left[\frac{3}{2} \frac{L_B R}{(a/q) \varphi_B} P \right] - q \left[\frac{3}{2} \left(\alpha_B^2 - 1 \right) - \ln \alpha_B^3 \right] \tag{11}$$

Localization of block copolymer

$$\frac{(\Delta\mu_g^o)_{loc}}{kT} = -q \ln \left[\frac{d \, L_B}{R \, (1 + D/R)^d} \right] \tag{12}$$

Here, $d = 3$ for spheres and 2 for cylinders.

Backfolding for a BAB block copolymer

$$\frac{(\Delta\mu_g^o)_{loop}}{kT} = \frac{3}{2} \beta \ln \left[N_A \right] \tag{13}$$

Here, the excluded volume parameter β is taken to be unity (12).

Molecular constants appearing in the free energy expressions

The molecular volumes of the repeating units are estimated to be $v_A = 0.1683$ nm^3 for PS and $v_B = 0.0646$ nm^3 for PEO while the molecular volume of tetrahydrofuran is $v_T = 0.1362$ nm^3 and that of water is $v_W = 0.030$ nm^3. The various Flory interaction parameters have been taken to be $\chi_{AT} = 0.25$, $\chi_{AW} = 6.0$,

χ_{BT} = 0.25, χ_{BW} = 0.2, χ_{TW} = 0.1, χ_{AB} = 0.1, based on available molecular information such as the solubility parameter data or UNIFAC group contribution data (*13-15*).

Results and Discussion

Illustrative calculations have been carried out for three polystyrene-polyethylene oxide diblock copolymers, PS(38)-PEO(90), PS(152)-PEO(557), and PS(301)-PEO(1164). The predicted volume fraction of THF in the micelle core as a function of the bulk solvent composition is shown in Figure 2 (left). The results for all three block copolymers practically collapse into a single curve. Based on Chow's thermodynamic model of glass transition in polymer-diluent systems (*15*), we have estimated the critical volume fraction of THF at which the liquid to glass transition occurs for the three block copolymers to be η_{crit} = 0.088, 0.143 and 0.152, respectively. When the THF volume fraction in the core reaches the critical value, the kinetic freezing of micelles occurs. Based on Figure 2, the volume fraction of THF in the bulk solvent at which the micelle freezing occurs is 0.58, 0.73 and 0.75, respectively. Obviously, the larger the molecular weight of the PS block more diluent (THF) is required to maintain the polymer in the liquid state.

The presence of the common solvent THF, both in the micelle core and the bulk solvent medium, influences two dominant free energy contributions, leading to two competing effects. First, THF present in the bulk solvent lowers the interfacial tension between the PS block and the bulk solvent (Figure 2 - right). This causes a decrease in the interfacial tension σ_{agg} between the micelle core and the corona and thus reduces the magnitude of the free energy of formation of the core-corona interface (Surface energy curve on Figure 3 - left). Such a free energy change favors an increase in the equilibrium area per molecule and a corresponding decrease in the micelle aggregation number. Second, THF present in the core provides a negative contribution to the free energy of aggregation (A block dilution curve on Figure 3 – left). This dominates the overall free energy change on aggregation ($\Delta\mu_g^o / kT - (j/g) \ln a_T$ curve on Figure 3-left) although the presence of THF in the core also causes an increase in the positive free energies associated with A block deformation, B block dilution, and B block deformation. It has been shown (*2*) that any solubilization in the micelle core will favor the micelle aggregation number to increase and the larger the amount solubilized, the larger will be the increase in the aggregation number. The net result of these competing effects on the predicted equilibrium area per molecule shows an increase in the area (Figure 3–right) and a corresponding decrease in the micelle aggregation number. This demonstrates that the decrease in core-corona interfacial tension caused by THF in the bulk solvent dominates the overall behavior of equilibrium aggregates formed.
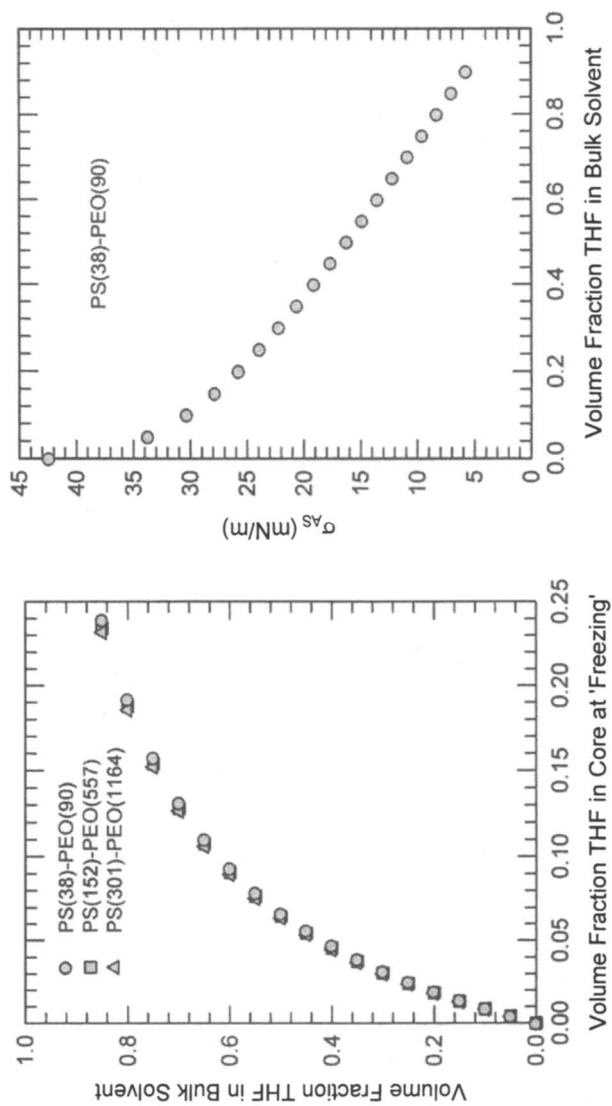
Figure 2. Predicted volume fraction of THF solubilized in micelle core as a function of the bulk solvent composition (left). Predicted dependence of interfacial tension between PS and mixed solvent on solvent composition (right).
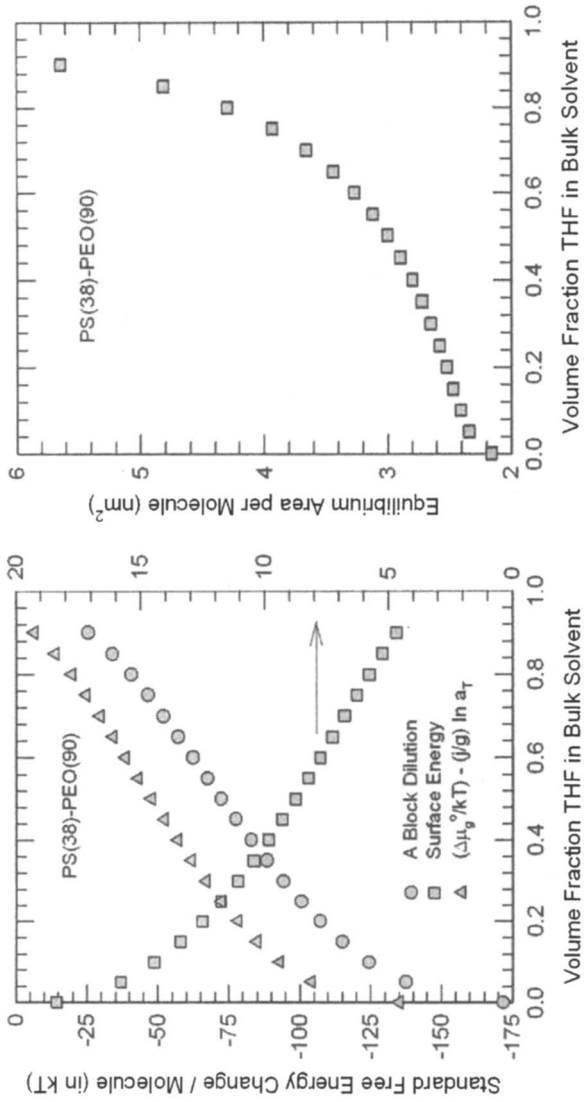
Figure 3. Free energy contributions representing THF solubilization in core (A block dilution), formation of core-corona interface (Surface energy) and the overall free energy change on aggregation (left). Predicted equilibrium area per molecule of the micelle with THF solubilized in the core (right).
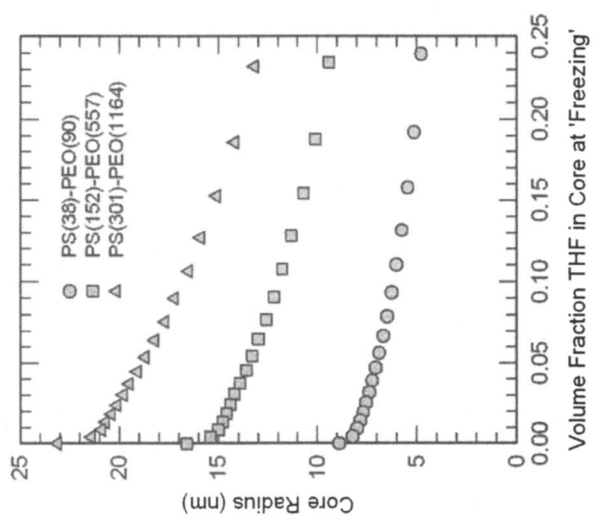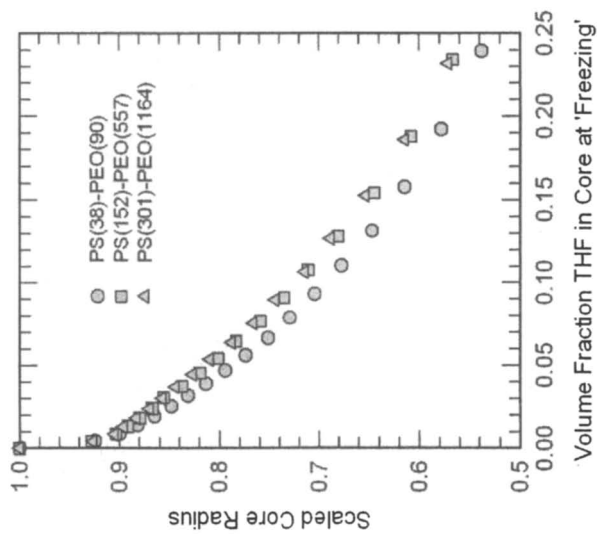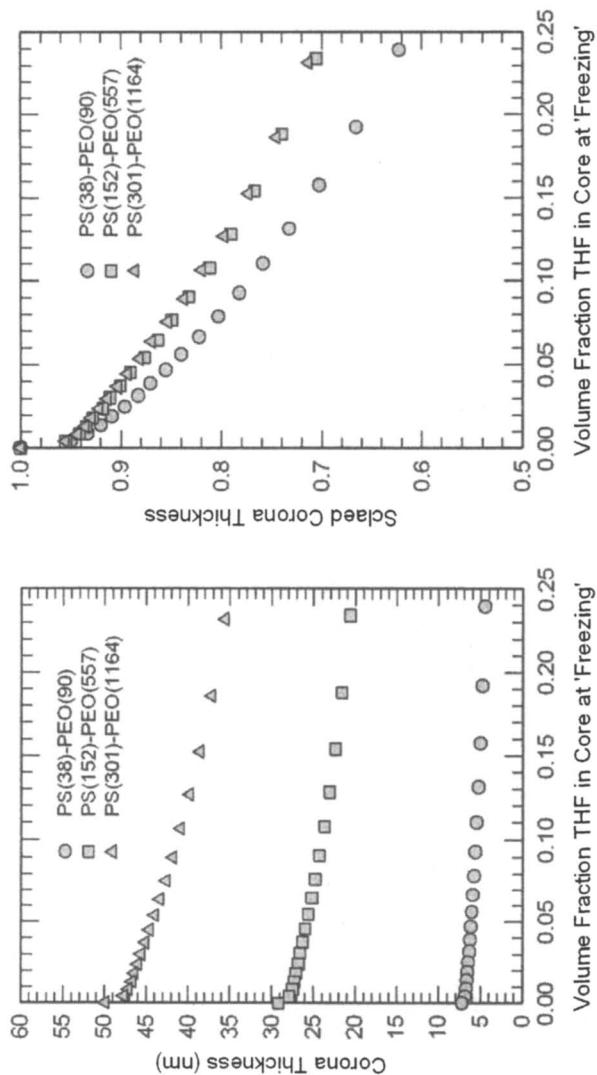
Figure 4. Predicted core radius and corona thickness of micelles (actual and scaled) as a function of the volume fraction of THF in the core when the core freezes.

In Figure 4, the predicted core radius and corona thickness of micelles are plotted against the volume fraction of THF in the core. These results correspond to micelles that would exist in water when all of the THF is removed from the system. The result plotted in Figure 2 allows the translation of the volume fraction of THF in the core at freezing to the volume fraction of THF in the bulk solvent.

Note that the region of volume fraction from $\eta = 0$ to $\eta = \eta_{crit}$ will not be attainable in this system since the PS block will be in glassy state over this domain. The scaled core radius and corona thickness nearly collapse together for all three block copolymers. There is a significant increase in both R and D as the amount of THF in the core decreases (this is the direction in which the micelle preparation occurs as THF is progressively being removed). The predicted aggregation number of the micelles is plotted in Figure 5. Again, the scaled aggregation numbers for all three block copolymer practically coincide. One can observe the significant growth in micelles as the micelle preparation method is pursued starting from pure THF.

In this work, we have considered THF as the common solvent. The choice of the common solvent affects the nature of nanoparticles produced in two important ways. One is the dependence of the critical volume fraction η_{crit} necessary to maintain the PS block in the liquid state. By selecting a different common solvent we can decrease η_{crit} and expand the binary solvent composition domain over which we can form nanoparticles using this approach. The second feature is the dependence of the PS block mixed solvent interfacial tension on the nature of the common solvent. Since this interfacial tension significantly influences the aggregation number and hence the size of the nanoparticle, we can obtain different patterns of aggregation number vs volume fraction of common solvent in core by different choices of the common solvent.

Conclusions

The micelle preparation approach using mixed solvents (of which one is a common solvent for both blocks of the copolymer) results in the formation of micelles smaller than what equilibrium calculations based on water as the solvent would predict. The size of the frozen micelle depends on the common solvent used and the solvent composition at which the 'freezing' takes place. Stable, passivated micellar nanoparticles in the size range from 2 nm to 100 nm are easily produced by this approach. The calculated results are shown here only for spherical particles but the same approach predicts cylinders for block copolymer compositions with larger PS to PEO ratios. Indeed both growth and shrinkage of cylindrical micelles is found to occur as the THF content in the micelle core changes, demonstrating the competing influence of THF as a solubilizate promoting growth and a solvent disfavoring the growth.
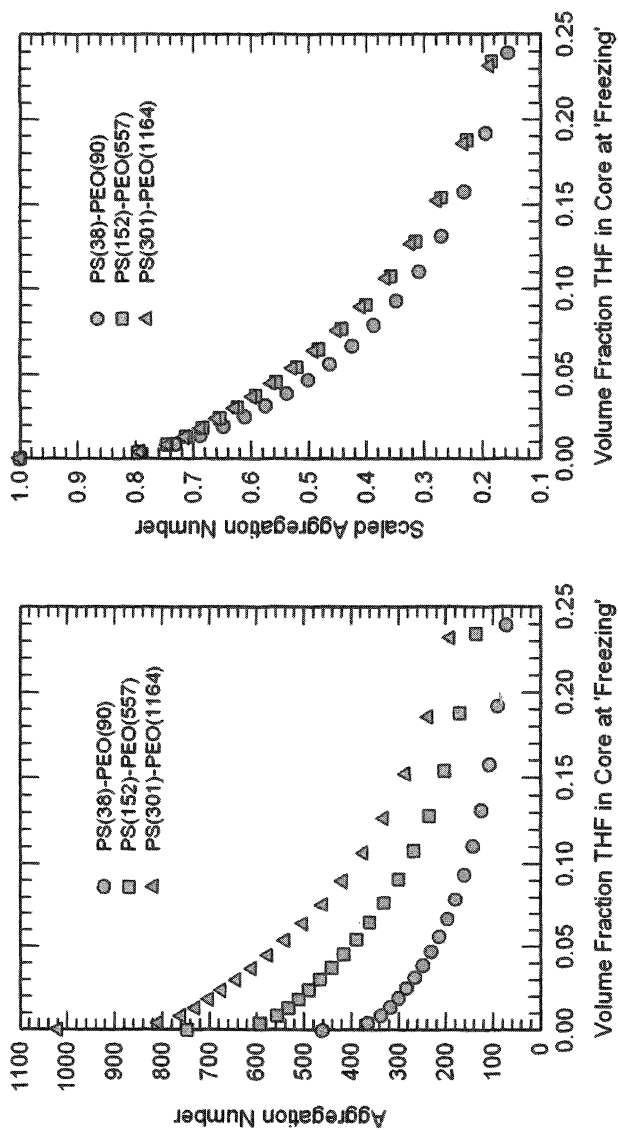
Figure 5. Predicted aggregation number of micelles (actual and scaled) as a function of the volume fraction of THF in the core when the core freezes.

Acknowledgements

References

1. Nagarajan, R.; Ganesh, K. *J. Chem. Phys.* **1989**, *90*, 5843.
2. Nagarajan, R.; Ganesh, K. *Macromolecules* **1989**, *22*, 4312.
3. Nagarajan, R. In *Solvents and Self-Organization of Polymers*, Webber, S.E., Munk, P., Tuzar, Z. Eds,; NATO ASI Series E: Applied Sciences, Vol 327, Kluwer Academic Publishers: Dordrecht, The Netherlands, 1996; p.121.
4. Nagarajan, R. *Colloids Surf. B. Biointerfaces* **1999**, *16*, 55.
5. Nagarajan, R. *Polym. Adv. Technol.* **2001**, *12*, 23.
6. Flory, P.J. *Principles of Polymer Chemistry*; Cornell University Press: Ithaca, NY, 1962.
7. Semenov, A.N. *Soviet Phys. JETP* **1985**, *61*, 733.
8. de Gennes, P.G. *Scaling Concepts in Polymer Physics*; Cornell University Press: Ithaca, New York, 1979.
9. Defay, R.; Prigogine, I.; Bellemans, A.; Everett, D.H. *Surface Tension and Adsorption*; Wiley: New York, 1966.
10. Siow, K.S.; Patterson, D. *J. Phys. Chem.* **1973**, *77*, 356.
11. Stockmayer, W.H. *J. Polym. Sci.* **1955**, *15*, 595.
12. Jacobsen, H.; Stockmayer, W.H. *J. Chem. Phys.* **1950**, *18*, 1600.
13. *CRC Handbook of Chemistry and Physics*; CRC Press Inc.: Boca Raton, FL, 1980. 60th Edition.
14. Barton, A.F.M. *Handbook of Solubility Parameters and Other Cohesion Parameters*; CRC Press: Boca Raton, FL, 1983.
15. Chow, T.S. *Macromolecules* **1980**, *13*, 362.

Chapter 25

Nanoparticles as Seeds for Organic Crystallization

Ruomiao Wang[1], Indika U. Arachchige[2], Stephanie L. Brock[2],
and Guangzhao Mao[1,*]

[1]Department of Chemical Engineering and Materials Science, Wayne State
University, 5050 Anthony Wayne Drive, Detroit, MI 48202
[2]Department of Chemistry, Wayne State University, 5101 Cass Avenue,
Detroit, MI 48202

This paper describes a seed-mediated nucleation strategy to
create a branched nano-hybrid by spin coating a mixed
solution of inorganic nanoparticles (thiol-capped CdSe) and
organic crystalline compound (arachidic acid) on graphite.
Both crystallization conditions and nanoparticle structure were
varied in order to understand the seed-mediated mechanism for
the control of molecular self-assembly and crystallization.
AFM, TEM, and *in situ* EDS were used for nanomaterial
characterization. Both the nanoparticles and the graphite
substrate affect arachidic acid crystallization competitively.
Nanoparticles were found to be effective nucleation agents for
fatty acids of different chain length.

Introduction

Nanomaterials are promising components for molecular electronics, sensors,
and thin film photovoltaic devices. In order to utilize and build on progress in
synthesis of monodisperse nanocrystals with well-defined morphologies such as
nanodots, nanorods, nano-plates, and nano-cubes (*1*), we investigate the
possibility of further functionalization of nanoparticles by forming
nanostructures directly on the nanoparticles, i.e. nucleation and crystal growth on
nanoparticle seeds. Nanocrystals that possess branched or other secondary

structures (2) add more complexity to structure, properties, and device design. For example, in the branched tetrapod CdTe nanocrystals, two crystal structures coexist in different domains of the same crystal (3).

In addition to geometric variation, hybrid nanomaterials, where different chemical functional units are integrated into one stand-alone structure, are attractive materials because they combine or even enhance the performance of individual units. For example, a multi-component nano-hybrid was synthesized by growing metal tips on semiconductor nanocrystals (4); Banni et al. reported the synthesis of asymmetric gold-tipped semiconductor nanoparticles and nanorods (5); Inorganic nanoparticles have been incorporated into polymeric materials by layer-by-layer deposition or by simply embedding the nanoparticles in a polymer matrix (6). Furthermore, hybrid photovoltaic devices have been constructed by combining ZnO nanowires with organic dye sensitizers (7) and by integrating semiconductor nanocrystals of TiO₂, an organic dye, and a hole transport material (8); Integration of inorganic semiconductor nanoparticles into organic thin film light-emitting devices was shown to enhance the performance of the device (9); A new polymer and inorganic nanoparticle hybrid design promises efficient laser emission and amplification in the eye-safe telecommunication window (10). As a final example, bioinorganic conjugates have been used as tracking tools in the tagging of biological entities (11).

This paper describes the formation of fatty acid nanorod crystals on CdSe nanoparticles during spin coating of the binary solution on highly oriented pyrolytic graphite (HOPG). We hypothesize a seed-mediated nucleation and crystal growth confinement mechanism for the formation of the nano-hybrid. The nano-hybrid was characterized by Transmission Electron Microscopy (TEM), *in situ* Energy Dispersive Spectroscopy (EDS), and Atomic Force Microscopy (AFM). The solution-based, room temperature crystallization process is attractive because it potentially allows the nanoparticle core and the nanorod branches to be tuned separately.

Experimental Section

Materials

All chemicals, including stearic acid (SA, Fluka, ≥99.5%), arachidic acid (AA, Sigma, ≥99%), behenic acid (BA, Aldrich, 99%), tetracosanoic acid (TA, Fluka, ≥99.0%), and hexacosanoic acid (HA, Sigma, ≥95%), methanol (Mallinckrodt Chemicals, 100%), ethanol (Pharmco, 100%), and 2-propanol (Mallinckrodt Chemicals, 100%), were used as received without any further purification. HOPG (ZYB grade, Mikromasch) was hand-cleaved with an adhesive tape just before film preparation until a smooth surface was obtained.

Film Fabrication via Spin coating

Binary solutions of AA and 11-mercaptoundecanoic acid capped CdSe (MUA-CdSe) nanoparticles were prepared in various short-chained alcohol solvents at room temperature. The synthesis and capping procedure of MUA-CdSe nanoparticles were adapted from literature (*12,13*) and have been described previously (*14*). The concentration of MUA-CdSe solutions was kept identical at 10^{-4} M unless specified. The concentration of AA was varied according to its solubility in the different solvents. 10^{-4} L of the binary solution was spin coated on HOPG. The spin rate and time were kept identical for all film preparation procedures at 3,000 rpm and 1 min, respectively.

Characterization

AFM (Dimension 3100, VEECO), high-resolution TEM (JEOL FastTEM 2010F), and *in situ* EDS (EDAX) attached to a Hitachi S-2400 Scanning Electron Microscope were used to characterize the nanoparticles and nanoparticle-containing films. TEM, operated in the bright field mode with an accelerating voltage of 200 keV, was used to determine the size of the inorganic nanoparticles. The average size was calculated based on manual measurements on 80 to 100 individual nanoparticles from different images. *In situ* EDS study provided elemental analysis of thiol-capped nanoparticles. Nanoparticles were sprinkled on carbon adhesive tabs placed on an aluminum stub, and EDS data were acquired at 25 keV in secondary electron mode. AFM was used to characterize the spin-coated films. AFM images of height, amplitude, and phase were obtained in tapping mode in ambient air using silicon probes (BS-Tap300, Nanoscience Instruments). Height images have been plane-fit in the fast scan direction with no additional altering operation. Sectional analysis and 2D fast Fourier Transform (2D FFT) data analysis were performed using Nanoscope software version 5.12 (VEECO).

Results

Nanoparticle Structure

MUA-CdSe nanoparticle size and elemental composition were characterized by TEM and *in situ* EDS. The average size of nanoparticles was determined to be 3.0 ± 0.5 nm. *In situ* EDS revealed a correlation between the elemental sulfur and cadmium ratio in the capped nanoparticles and the molar ratio of MUA to cadmium used in the synthesis (*14*). An increasing MUA:Cd synthesis ratio

results in a higher S:Cd ratio for the nanoparticle, which means that a higher number of capping agent molecules are attached to the nanoparticles. For example, the S:Cd ratio was determined to be 0.38:1 when MUA:Cd = 3:1 was used in the capping procedure. The S:Cd ratio was increased to 0.5:1 when MUA:Cd = 5:1 was used during synthesis. The MUA capping agent coverage on CdSe nanoparticles was found to influence the average number of branches grown on the nanoparticle.

Nano-Hybrid Thin Film Structure

This part summarizes our previous results on the structure of spin-coated films containing both MUA-CdSe nanoparticles and the fatty acid AA on HOPG and our hypothesis on its formation mechanism (*14*). AA itself forms a highly ordered stripe-like nanopattern on HOPG (Figure 1A), while MUA-CdSe does not deposit under identical film-forming conditions. The AA stripe phase is induced by the epitaxial match between the all-trans carbon chain of AA and the crystalline lattice structure of the HOPG basal plane (*15*). The periodicity obtained from 2D FFT analysis is 5.6 nm, exactly twice the AA molecular chain length. Therefore, one stripe is made of a row of parallel AA pairs. In each AA pair, the two AA molecules are arranged in the tail-to-tail configuration. When the binary solution of AA and MUA-CdSe was deposited on HOPG, the nano-hybrid structure was observed as exemplified by Figure 1B. The size of nanoparticles measured by AFM, 6.0 ± 2.2 nm in height and 18.5 ± 7.2 nm in width, is much larger than the TEM-measured values, possibly due to the photooxidation of MUA, which causes particle aggregation. Moreover, the size of nanoparticles is convoluted with the AFM tip and appears to be larger than its actual size. However, the AA nanorod branches exhibit remarkably uniform cross-sectional dimensions with height = 1.0 ± 0.1 nm (Figure 1C) and width = 5.4 ± 0.1 nm. The length has a wide distribution, as expected from the stochastic crystal growth process during spin coating. The cross-sectional dimensions of the nanorod match exactly the single unit cell dimensions of the (010) face of the C-form AA crystal. The C-form fatty acid crystal is monoclinic $P2_1/a$ with the following lattice parameters: $a = 0.9360$ nm, $b = 0.4950$ nm, $c = 5.0700$ nm, and $\beta = 128.250°$. Therefore, the rod axis should be along the <010> direction, which is perpendicular to the hydrocarbon chain of AA.

Based on AFM analysis and comparison to the AA crystal structure, the following kinetic events may have occurred during spin coating. Firstly, AA precipitates out to form a monolayer of the epitaxially oriented stripe phase on HOPG due to its low solubility. A closer scan of the flat area surrounding the nanoparticles shows the same stripe phase structure as Figure 1A. Secondly, the precipitation of the stripe phase facilitates the immobilization and uniform deposition of individual MUA-CdSe nanoparticles or their aggregates. Thirdly,
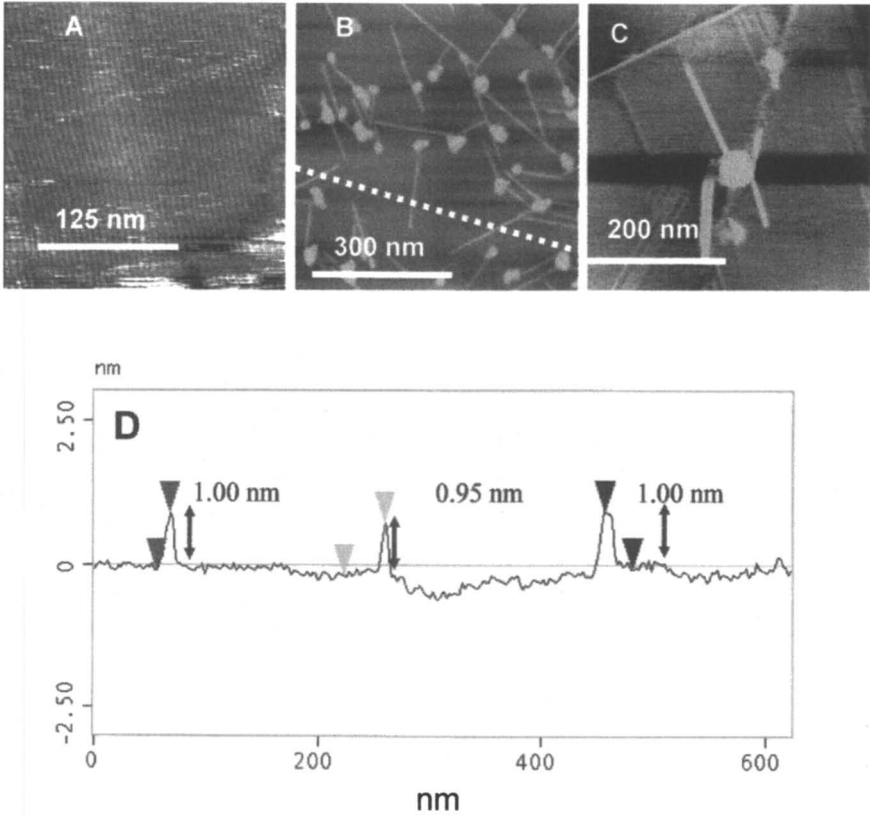
Figure 1. A) AFM height image of AA monolayer on HOPG; B) AFM height image of nano-hybrid structure formed on HOPG by spin coating MUA-CdSe and AA mixture in 2-propanol on HOPG. MUA-CdSe was made with a synthesis ratio MUA/Cd=3:1; C) Nanorods grow around nanoparticles, which are immobilized on top of AA monolayer. AFM height image, z range = 2 nm; and D) the height profile along the dotted line in B.

heterogeneous nucleation occurs preferentially at the nanoparticle surface, i.e. seed-mediated nucleation, due to the more favorable nucleation conditions provided by the nanoparticle. Finally, the crystallization conditions promote radial growth but inhibit tangential growth, i.e. confined crystal growth occurs, giving rise to radially oriented nanorods with single unit cell dimensions. Scheme 1 *(14)* illustrates the geometric relationship between the AA nanorod and the nanoparticle seed as well as the HOPG substrate based on the AFM images.
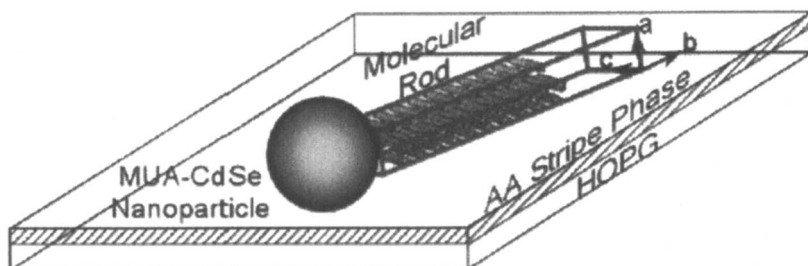
Scheme 1. AA crystallization on the MUA-CdSe nanoparticle. (Reproduced from Ref. (14) Copyright 2004 American Chemical Society.)

Effect of Crystallization Conditions

Supersaturation is a key parameter in crystallization. Here the standing time of the binary solution droplet on HOPG prior to spinning was varied to vary the degree of supersaturation. Instant spin coating with no standing time corresponds to the highest solvent removal rate and highest undercooling. Longer standing time allows partial solvent removal at a slow rate before the final freezing step. MUA-CdSe nanoparticles synthesized with MUA:Cd = 5:1 were dispersed in 2-propanol together with AA. The concentrations of MUA-CdSe and AA were kept at 0.1 mM. Only the standing time was varied while other spin coating conditions were the same as before. Figure 2 illustrates the progression in film structure from zero standing time, i.e. droplet was spun instantaneously, to standing time = 1 min. With longer standing time, more AA crystalline rods can be produced (Figure 2B). However, the influence of nanoparticles diminished with standing time as well. With no standing time, AA nanorods were induced predominantly by the nanoparticles seeds. This can be concluded both from the attachment of the nanorods on nanoparticles and the non-epitaxial orientation of the nanorods. On the other hand, there is a three-fold symmetry in the nanorod orientation in Figure 2B indicating the dominant influence of the HOPG substrate. No nanorods were observed when the standing time reached 1 min and

an irregular particulate structure, possibly due to nanoparticle aggregation, was observed. Due to the low solubility of AA in alcohols, it is believed that the nucleation of AA nanorods occurs during fast solvent removal, which is a crystallization condition far away from equilibrium. Spin coating removes solvent instantaneously and generates a steep temperature gradient or undercooling. It is hypothesized that far-from-equilibrium conditions, which can be achieved by high degree of supersaturation, favor the nanoparticle-templated crystallization over the HOPG-templated crystallization.

The effective supersaturation can also be varied by varying the relative crystallizing compound (AA) to seed molar ratio. The comparison between Figure 2B and Figure 3 shows this effect clearly. The film in Figure 3 was made with MUA-CdSe nanoparticles of MUA:Cd = 3:1 synthesis ratio in 2-propanol.
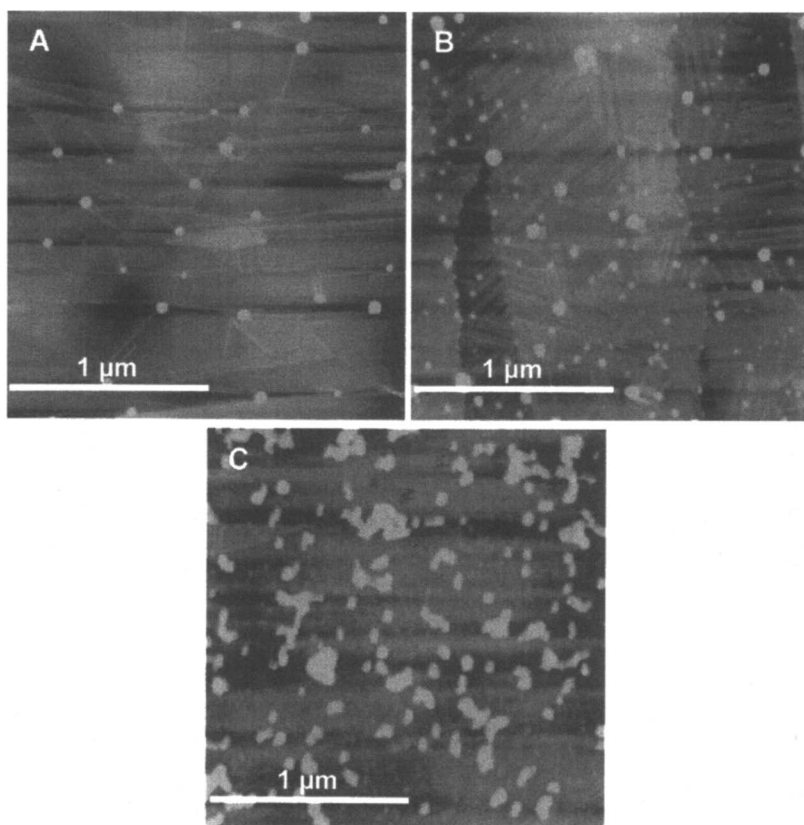
Figure 2. Effect of standing time. AFM height images of spin coated films from MUA-CdSe and AA in 2-propanol. A) Standing time = 0 s, z range = 8 nm; B) standing time = 15 s, z range =12 nm; C) standing time = 60 s, z range = 12 nm.

The AA concentration was maintained at 0.1 mM while the nanoparticle concentration was increased to 0.2 mM. The average number of rods per nanoparticle was determined to be 0.82, which is lower than the 1.9 rods/nanoparticle obtained when the CdSe concentration is 0.1 mM *(14)*. Moreover, the length of the induced nanorods was in the range 20–180 nm when MUA-CdSe = 0.2 mM as opposed to 50-250 nm when MUA-CdSe = 0.1 mM. More and longer nanorods can be produced by increasing the AA to MUA - CdSe seed ratio. Therefore, nanoparticle concentration provides a means to vary the nano-hybrid structure.
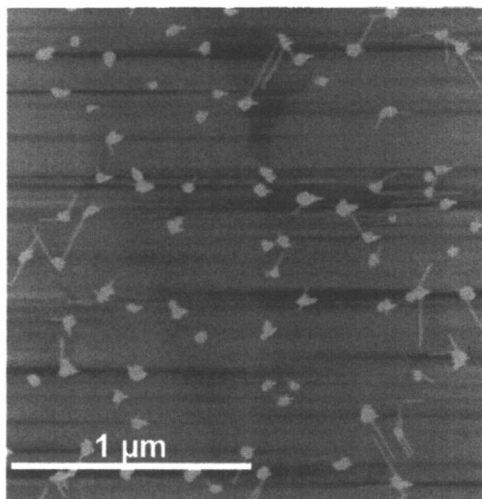
Figure 3. AFM height images of nano-hybrid formed from a mixture of 0.2 mM MUA-CdSe and 0.1 mM arachidic acid, z range = 5 nm.

Effect of Nanoparticle Seed Structure

When MUA-CdS nanoparticles were used instead of MUA-CdSe nanoparticles, we found the same nano-hybrid structure. This shows that the inner core of the nanoparticle is immaterial to the nano-hybrid formation.

To test the contribution of the surface capping group chain length on nucleation, films were prepared using CdSe nanoparticles capped by mercapto acids of different chain lengths. When 3-mercaptopropionic acid was used as the capping agent, the resultant MPA-CdSe nanoparticles did not distribute uniformly on the substrate. In addition, MPA-CdSe is ineffective in inducing AA nucleation. The relatively short hydrocarbon chain length of MPA reduces the

nanoparticle interaction with the substrate as well as the solvent, which prevents nanoparticle immobilization on the substrate and complete wetting by the solvent. It is expected that complete wetting of the nanoparticle surface by the crystallizing fluid is a pre-requisite for the templating effect. When 16-mercaptohexadecanoic acid capped CdSe (MHA-CdSe) nanoparticles were used, nano-hybrids were observed with identical AA nanorod dimensions. But the yield of AA nanorods per nanoparticle was lower for MHA-CdSe than for MUA-CdSe. The solvent and nanoparticle interfacial tension may be altered somewhat by the more hydrophobic MHA. The results show that the capping agents or the surface structure of the nanoparticle are important in the nanoparticle-templated crystallization process. It is conceivable that complete wetting of the nanoparticle surface by the crystallizing fluid is a prerequisite for nucleation on nanoparticles in order to overcome the high curvature of extremely small particles.

Effect of Fatty Acid Chain Length

We also tested the seed-mediated nucleation and confinement scheme against other fatty acids with different chain lengths, including SA, BA, TA, and HA. Spin coated films were prepared using both pure fatty acid solutions and their binary solutions with MUA-CdSe nanoparticles, similar to the AA film preparation procedures. AFM was used to characterize the film structures. The results are summarized in Table 1.

Table 1. Nanoparticle Effect on the Nucleation of Fatty Acids

Fatty aid	Carbon number	Periodicity (nm)	Nucleation on nanoparticles
SA	18	5.0	Yes
AA	20	5.6	Yes
BA	22	6.1	Yes
TA	24	6.6	No
HA	26	7.0	No

All the fatty acids studied self-assembled into the stripelike pattern on HOPG with the same 3-fold symmetric orientation. The stripe phase shows a linear increase in periodicity with increasing fatty acid chain length. Their periodicity is very close to the expected bilayer thickness. When these fatty acids were deposited in the presence of MUA-CdSe nanoparticles, the nanoparticles

again show a profound influence on their self-assembled structure. Nanorods with single unit cell cross-sectional dimensions were found to form directly from the nanoparticles for SA and BA only. In the case of TA, only the HOPG-induced stripe phase was detected. In the case of HA, we detected a tendency towards nanoparticle alignment along the stripe direction of the underlying HA stripe phase. In this case, the role of the fatty acid and nanoparticle is switched. The self-assembled fatty acid structure seems to influence the distribution of the nanoparticles. It is clear that nanoparticles and graphite could influence the crystallization of long-chained fatty acids in a competitive fashion. The larger bilayerlike pattern formed by the longer fatty acid may accommodate nanoparticles more easily, and the amphiphilic nature of the pattern may cause the partition of nanoparticles.

Conclusions

A novel method was used to crystallize organic nanorods as branches on inorganic nanoparticles. The nanorods were made of arachidic acid, a common fatty acid and the nanoparticles were made of cadmium selenide capped by mercaptoundecanoic acid. The nano-hybrids were made by spin coating of the binary solution on HOPG using various short-chained alcohol solvents. We hypothesize that a seed-mediated nucleation and crystal growth confinement mechanism is responsible for the nano-hybrid formation. AFM analysis concludes that the arachidic acid nanorods are only one unit cell in size in the cross-sectional area and the fastest growth direction is the <010> direction of the C-form crystal. Instantaneous solvent evaporation facilitates the seed-mediated crystallization process, while longer standing times cause nanoparticle aggregation. The average rod length can be increased by decreasing the relative amount of nanoparticles in solution. The nanoparticle surface structure and its interaction with solvent and substrate are important for the nano-hybrid formation, whereas the internal chemical composition of the nanoparticle plays no apparent role. We anticipate that this novel crystallization method will enable the incorporation of a variety of organic functional units onto pre-existing nanoparticles enabling a wide range of physical properties to be accessed.

Acknowledgements

References

1. Burda, C.; Chen, X.; Narayanan, R.; El-Sayed, M. A., *Chem. Rev.*, **2005**, *105*, 1025-1102.
2. Jun, Y.; Seo, J.; Oh, S. J.; Cheon, J., *Coordination Chem. Rev.*, **2005**, *249*, 1766-1775.
3. Manna, L.; Milliron, D. J.; Meisel, A.; Scher, E. C.; Alivisatos, A. P., *Nat. Mater.*, **2003**, *2*, 382-385
4. Cozzoli, P. D.; Manna, L., *Nat. Mater.*, **2005**, *4*, 801-802
5. Mokari, T.; Sztrum, C. G.; Salant, A.; Rabani, E.; Banin, U., *Nat. Mater.*, **2005**, *4*, 855-863
6. Yang, H.; Holloway, P. H., *J. Phys. Chem. B*, **2003**, *107*, 9705-9710.
7. Baxter, J. B.; Aydil, E. S., *Appl. Phys. Lett.*, **2005**, *86*, 053114-3.
8. Coronado, E.; Palomares, E., *J. Mater. Chem.*, **2005**, *15*, 3593-3597.
9. Coe-Sullivan, S.; Woo, W.; Steckel, J. S.; Bawendi, M.; Bulovic, V., *Organic Electronics*, **2003**, *4*, 123-130.
10. Le Quang, A. Q.; Zyss, J.; Ledoux, I.; Truong, V. G.; Jurdyc, A. M.; Jacquier, B.; Le, D. H.; Gibaud, A., *Chem. Phys.*, **2005**, *318*, 33-43.
11. Mattoussi, H.; Mauro, J. M.; Goldman, E. R.; Green, T. M.; Anderson, G. P.; Sundar, V. C.; Bawendi, M. G., *Phys. Stat. Sol. B*, **2001**, *224*, 277-283.
12. Aldana, J.; Wang, Y. A.; Peng, X., *J. Am. Chem. Soc.*, **2001**, *123*, 8844-8850.
13. Peng, Z. A.; Peng, X., *J. Am. Chem. Soc.*, **2001**, *123*, 183-184.
14. Chen, D.; Wang, R.; Arachchige, I.; Mao, G.; Brock, S. L., *J. Am. Chem. Soc.*, **2004**, *126*, 16290-16291.
15. Mao, G.; Dong, W.; Kurth, D. G.; Mohwald, H., *Nano Lett.*, **2004**, *4*, 249-252.
16. Rabe, J. P.; Buchholz, S., *Science*, **1991**, *253*, 424-427.
17. Cacciuto, A.; Auer, S.; Frenkel, D., *Nature*, **2004**, 428, 404-406.

Chapter 26

Synthesis and Characterization of Tobacco Mosaic Virus Templated Polymeric Nanomaterials

Zhongwei Niu[1], Siqi Li[1], Michael A. Bruckman[1], L. Andrew Lee[1], Byeongdu Lee[2], Sai Venkatesh Pingali[3], P. Thiyagarajan[3], and Qian Wang[1,*]

[1]Department of Chemistry and Biochemistry and Nanocenter, University of South Carolina, Columbia, SC 29208
[2]Advanced Photon Source and [3]Intense Pulse Neutron Source, Argonne National Laboratory, 9700 South Cass Avenue, Argonne, IL 60439

One-dimensional composite nanofibers were generated via the head-to-tail assembly of tobacco mosaic virus (TMV) as well as *in-situ* polymerization of polyaniline (PANI) on the surface of TMV. These composite nanofibers have very high aspect ratio and good processability. In addition, the morphology of the final composite materials can be modulated by the surface modification of TMV. The products were characterized with transmission electron microscopy, atomic force microscopy, and x-ray scattering techniques. This novel strategy of 1D nanomaterial synthesis could be utilized in the fabrication of advanced materials for potential applications including electronics, optics, sensing and biomedical engineering.

Developing one-dimensional (1D) functional structures on nanometer scales defines a new paradigm in the fabrication of novel biomedical, optical, acoustic, electronic, and magnetic materials and devices (*1-6*). In particular, using biological building blocks as templates in 1D materials synthesis is an exciting and emerging area of research at the interface of biology, chemistry and nanoscience (*7-12*). Among all biological scaffolds, viruses and viral like particles have attracted great attentions in the development of novel materials due to their well-defined structures and possibilities to be modified genetically and chemically without interfering the integrity and morphology (*8, 13-16*)
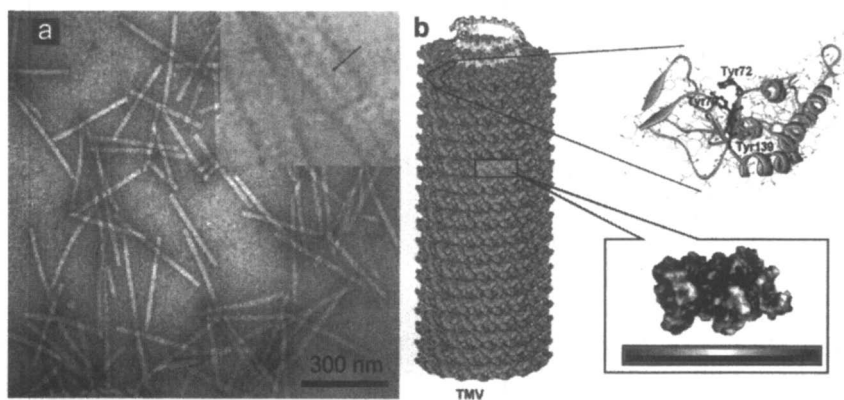
Figure 1. a) TEM image of wt-TMV. b) (left) Helical organization of TMV coat proteins. (right-top) A single subunit structure of coat protein is presented as ribbon diagram with the reactive tyrosines being highlighted, among which Tyr-139 (in red) can be accessed from the side, but Tyr-70 (in blue) and Tyr-72 (in green) can only be accessed from the top face of the TMV particle. (right-bottom) The surface charge distribution of the TMV coat protein dimers is also shown (blue: positive; red: negative) (See page 1 of color inserts.)

Tobacco mosaic virus (TMV) is a classic example of rod-like plant viruses consisting of 2130 identical protein subunits arranged helically around genomic single RNA strand (*17-20*). As shown in Figure 1a, the diameter of native TMV is around 18 nm. After negative staining with 2% uranium acetate, the 4 nm inner channel can be clearly visualized (Figure 1a, inset). The length of native TMV, i.e. 300 nm, is defined by the encapsulated genomic RNA that stabilized the coat protein assembly. It has been shown that the surface properties of TMV can be manipulated chemically or genetically without disrupting the integrity and

morphology of TMV capsids (*21-23*). The polar outer and inner surfaces of TMV have been exploited as templates to grow metal or metal oxide nanoparticles such as iron oxyhydroxides, CdS, PbS, gold, nickel, cobalt, silver, copper and iron oxides, and silica in many studies (*13, 24-30*). For example, by varying the conditions of the deposition, it has been shown that one can either specifically decorate the external surface with metallic nanoparticles via the chemical reduction of $[PtCl_6]^{-2}$ or $[AuCl_4]^{-1}$, or achieved controlled growth of Ag nanoparticles within the 4 nm internal channel present in the virus via the photochemical reduction of Ag salts (*31, 32*). Such kind of 1D structures have already shown great potential with applications in nanoelectronics (*33, 34*).

The aim of this chapter is to provide an overview of our current research in using TMV as template to synthesize 1D polymeric nanoassemblies. The morphology and the properties of final products are based on the controllable assembly as well as the surface modification of TMV. Three distinct assembly
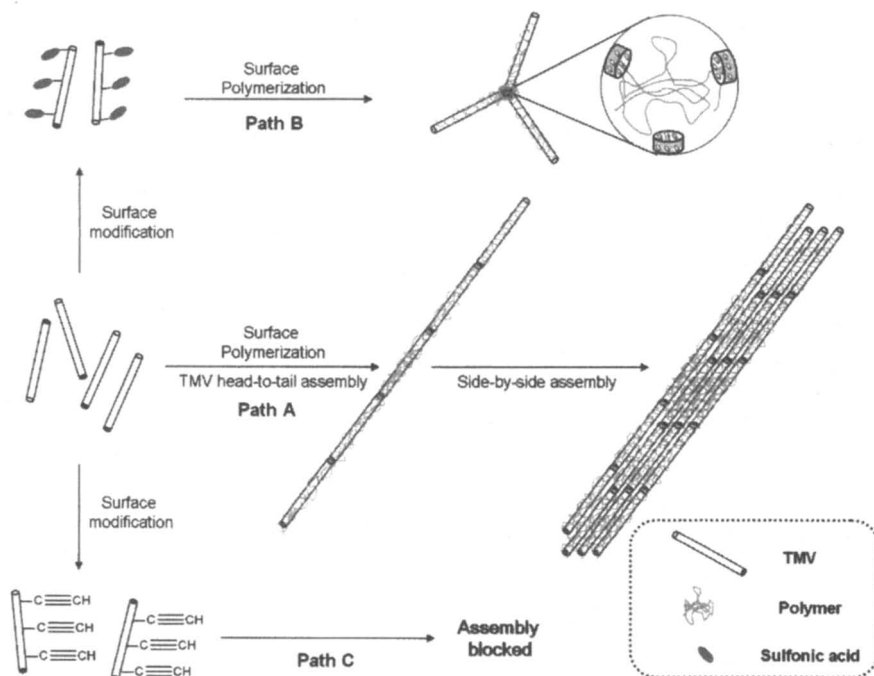
Scheme 1. Schematic illustration of the formation of TMV-templated nanoassemblies modulated by TMV surface modification and in situ surface polymerization. Path A: Linear TMV head-to-tail assembly assisted by aniline in situ polymerization and sequential side-by-side assembly; Path B: Branched TMV end-to-end assembly assisted by TMV surface sulfonation; Path C: Assembly was blocked by TMV surface modification with neutral groups.

pathways are depicted in Scheme 1, at near neutral pH, long 1D PANI coated composite nanofibers formed upon treating TMV with a dilute solution of aniline and ammonium persulfate (APS) (Path A). Polymerization of aniline on TMV surface was the key for stabilizing the 1D head-to-tail assembly of TMV nanofibers. The formation of highly-branched PANI at neutral reaction pH prevents lateral association of single PANI/TMV nanofibers due to the increase of steric repulsion. With extended incubation at low pH, these fibrous structures can further assemble in a side-by-side manner to generate long bundled structures (Scheme 1, Path A). When sulfonic acids or other acidic groups were covalently attached to the exterior surface of TMV, polymerization of aniline can induce TMV to form branched assembled structures with knot-like connections (Scheme 1, Path B). However, modification of TMV with uncharged groups can block the 1D assembly completely (Scheme 1, Path C).

Synthesis of 1D Nanofibers

A head-to-tail ordered assembly of wild type TMV has often been observed as very likely a product of complementary hydrophobic interactions between the dipolar ends of the helical structure (17). In particular, the 1D assembly is dramatically favored in an acidic environment due to the minimization of the repulsion between the carboxylic residues at the assembly interface (35). We hypothesize that monomeric molecules with amino group(s) or positive charged groups, such as aniline, can accumulate on the surface of TMV due to the electrostatic attraction or hydrogen bonding to the negatively charged surface residues of TMV. Therefore, the in situ polymerization should be able to produce a homogenous layer of polymers on the surface of TMV, and probably fix the head-to-tail assembled tube-like structure. Additionally, aniline is an ideal monomer to test this hypothesis because of the facile polymerization protocol (36) and the intrinsic anisotropic morphology that polyaniline (PANI) possesses (37-41).

In a typical experiment, distilled aniline (10 μL) was introduced into a 1 mg/mL pH 6.5 solution of TMV (5 mL), followed by addition of 10 mg APS (36). The reaction mixture was incubated at room temperature for 24 hours to form a yellow suspension. After centrifugation at 8000 g for 3 min, the pellet was removed and quickly rinsed three times with pure water, and resuspended in deionized water to afford the pure PANI/TMV composite. As shown by transmission electron microscopy (TEM) and atomic force microscopy (AFM), the length of the fiber can reach several micrometers (Figure 2). Upon PANI coating on its surface, the diameter of TMV increased to 20 nm which was measured with TEM (Figure 2b). The inner channel could not be detected even after negative staining and no visible gap can be detected from a long composite fiber (Figure 2d). This indicates that the head-to-tail protein-protein interaction

leads to the formation of fiber-like structures. Such interaction, in principle, is identical to the subunit interactions at any cross-section of the native TMV (*17, 42*). In addition, there is no solution PANI formed in the reaction. It is possible that the local concentration of aniline on the TMV surface is much higher than in solution; therefore, *in situ* polymerization should be able to produce a thin layer of polymers exclusively on the surface of TMV, and fix the head-to-tail assembled tube-like structure. The intrinsic anisotropic morphology of PANI at dilute polymerization conditions further assisted the 1D nanofibers formation. Therefore, there are two crucial factors that facilitate the formation of long 1D TMV-composite fibers: (1) accumulation and polymerization of monomers on the surface of TMV; and (2) prolongation and stabilization of TMV helices.
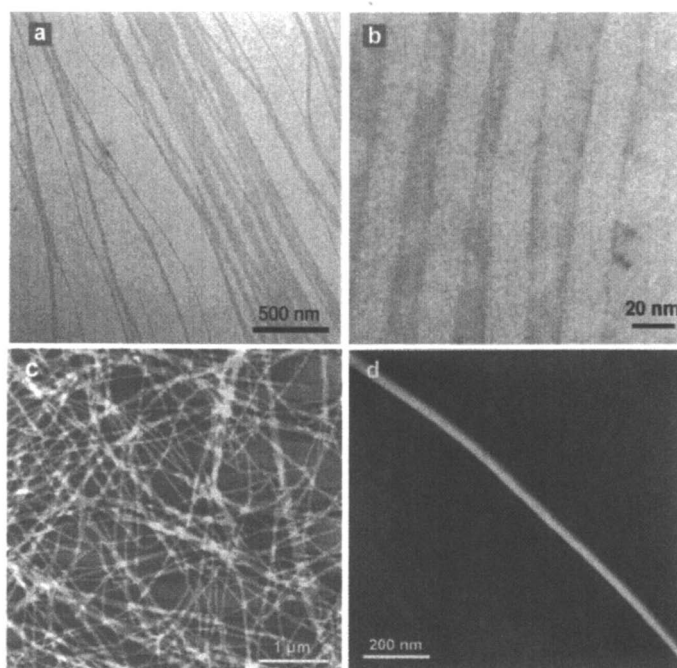
Figure 2. TEM images (a, b) and AFM images (c, d) of PANI/TMV nanofibers.

By combining electron microscopy (EM) and AFM, the length and surface morphology of TMV and composite fibers can be readily investigated. However, samples prepared on substrates for EM and AFM characterization upon drying can potentially alter both the diameter and surface morphology due to the interaction between the surface proteins and substrate (*43*). To complement the TEM data, small angle x-ray scattering (SAXS) and *in situ* time resolved SAXS

(TRSAXS) on solution samples were performed to understand the kinetics of PANI/TMV composite nanofiber formation(44). To illustrate the ability of SAXS to measure the growth of PANI on the TMV surface, we measured the SAXS of wild-type TMV and PANI/TMV after completion of the reaction. The difference in cross-sectional structure between wild-type TMV and PANI/TMV is revealed by fitting of the SAXS data using GNOM software as shown in Fig. 3 (45, 46). The largest dimension along the cross-section (D) obtained for TMV is ~18 nm which is consistent with the TMV crystal structure. For the PANI/TMV the maximum cross-sectional dimension is 30 nm and this increase in length scale can be attributed to the PANI coating of TMV.
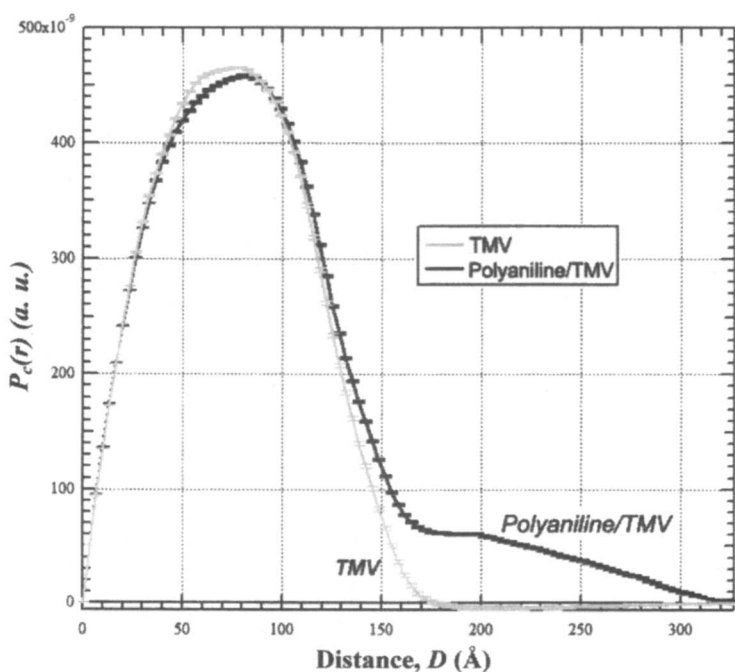
Figure 3. Fitted pair distance distribution function (PDDF) as a function of radial distance from center of the wild-type TMV and PANI/TMV obtained by fitting the SAXS data using GNOM (44).

Macroscopic Bundled Arrays

It is known that the pH of the polymerization reaction has great influence on the structure and conductivity of PANI. At near neutral reaction pH, long 1D PANI coated TMV single nanofibers formed upon treating TMV with a dilute

solution of aniline and APS. However, the nanofibers produced at near neutral reaction pH were not conductive likely resulted from the branched structures of PANI. In order to form conductive PANIs, polymerization reactions were performed under acidic conditions. As shown in Figure 4, at low reaction pH of 2.5 and 3.9, green PANI/TMV composites were observed after a 24 h reaction at room temperature indicating the formation of the emeraldine form of PANI. The color of the reaction mixture changed from dark yellow at reaction pH = 5.0 to bright yellow at reaction pH = 7.0. We attribute the color change to the formation of branched PANI or oligomers near neutral reaction pH.
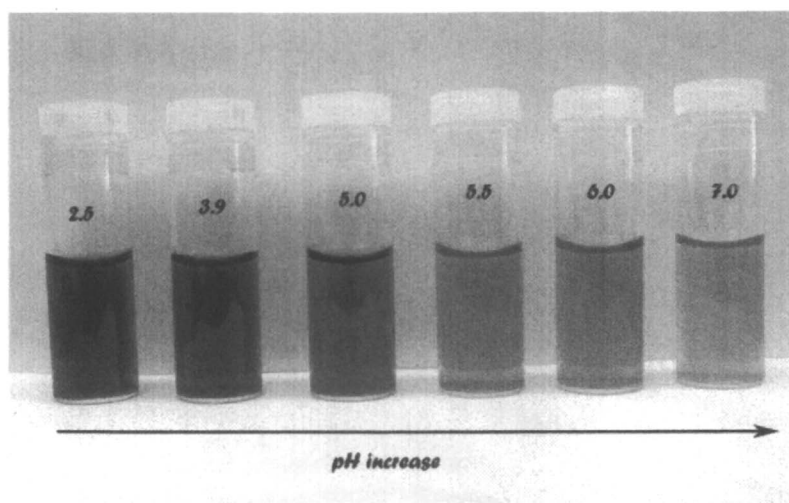
Figure 4. Color variation of the dispersions of PANI/TMV composite nanofibers in water as a function of reaction pH. (See page 1 of color inserts.)

TEM images of PANI/TMV composite nanofibers shown in Fig. 5 At a reaction pH of 5.0, bundled structures of nanofibers with lengths of several microns and widths of 1-2 microns were observed (Fig. 5a). Fig. 5b, an enlarged image of Fig. 5a, shows that the bundle consists of parallel arrays of nanofibers. Similar structures were observed for samples synthesized at reaction pH 4.0 and 5.5. There are two possible pathways that could lead to the formation of bundled arrays at low reaction pH: (1) TMV organizes laterally prior to the initiation of the aniline polymerization resulting in bundles; and (2) TMV assembles into long fibers through head-to-tail association followed by the aniline polymerization on the surface. Then the hydrophobic interaction mediated by the PANI on the surface of TMV nanofibers causes them to coalesce into bundles. In our view, the latter pathway (as shown in Scheme 1, Path A) is more plausible because the reactions were performed at low virus concentrations where TMVs

remain as individual particles. A series of time-dependent studies were performed at a reaction pH 5.0 to confirm the plausible mechanism. After a reaction time of 30 min (Fig. 5c), only short single nanofibers were observed. After 2 h (Figure 5d), higher population of long single nanofibers and a hint of long bundled nanofibers could be detected. However, after 4 hrs and beyond, only bundled structures were observed. The progress from single short nanofibers to long nanofibers is attributed to the head-to-tail assembly of TMV subunits. Time resolved SAXS study also confirmed our hypothesis (44).
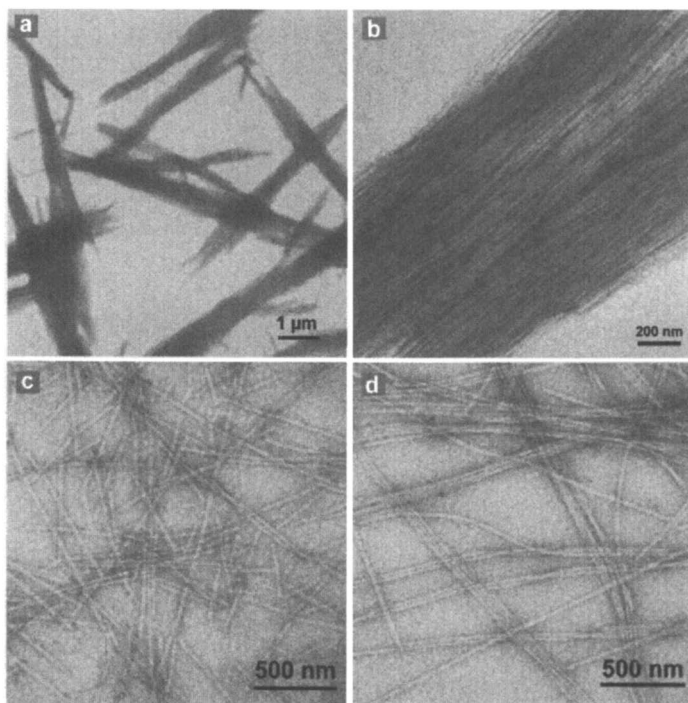
Figure 5. TEM images of PANI/TMV composites synthesized at pH 5.0: after 24 hrs (a & b), 30 min (c), and 2 hrs (d).

Standard four-probe method was employed to measure the conductivity of polyaniline/TMV composite nanofibers. At room temperature, the bulk DC conductivities measured were in the range of 0.01-0.1 $S.cm^{-1}$ for composite nanofibers synthesized at low reaction pH (2.5 and 4.0). This is comparable to the polyaniline nanofibers synthesized by other methods (47). No conductivity was observed for the composite nanofibers formed at a higher reaction pH.

Modulating the Assembly of PANI/TMV via Surface Modification of TMV

Due to the helical organization of TMV coat proteins, the head-to-tail protein-protein interaction led to the formation of the fiber-like structures (*17, 42*). If the cross-section of TMV (the face normal to the helical axis) is modified, such type of head-to-tail assembly should be twisted or blocked. To test this hypothesis, we further pursued the covalent surface modification of TMV. It has been shown that the phenol ring of Tyr-139 can be readily accessed with an electrophilic substitution reactions at the ortho-position of the phenol group in the presence of a diazonium salt (*22*). This reaction can be efficiently used to insert different functional groups using corresponding anilines in order to change viral properties such as solubility, surface charge or surface functionality. In addition, modification of Tyr-139 does not influence the *in vitro* assembly of the coat protein of TMV(*22*). On the other hand, although Tyr-70 and Tyr-72 cannot be accessed from the side surface of TMV, they are exposed on the top face (Figure 1). Therefore, for any rod-like particle, there could be about 33-34 phenol groups belonging to Tyr-70 and Tyr-72 can be modified from the top face. However, the proximity of Tyr-70 and Tyr-72 will lead to incomplete reactions. Still, such type of top face modification could modulate the assembly pattern according to the properties of attached groups.
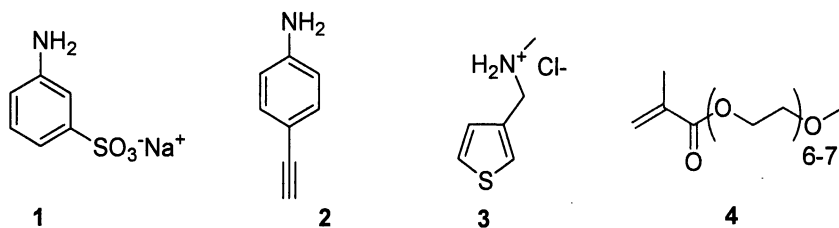
Scheme 2. Structures of starting materials

Using a modified protocol from literature (*22*), **1** and **2** were attached to the tyrosines of TMV through a diazo linkage (Figure 6a) (*48*). The reactions were monitored using UV-Vis spectroscopy. To force the modification of Tyr-70 and Tyr-72, large excess of diazonium reagents and extended reaction time were used. As shown in Figure 6a, *meta*-aminobenzosulfonic acid (msa) **1** was converted into a diazonium salt using sodium nitrite in acidic solution, which reacted with TMV after incubation in a pH = 9.0 buffer solution for 3 hr. The formation of the diazo bond was monitored by the appearance of a broad absorption peak at about 324 nm (Figure 6b).
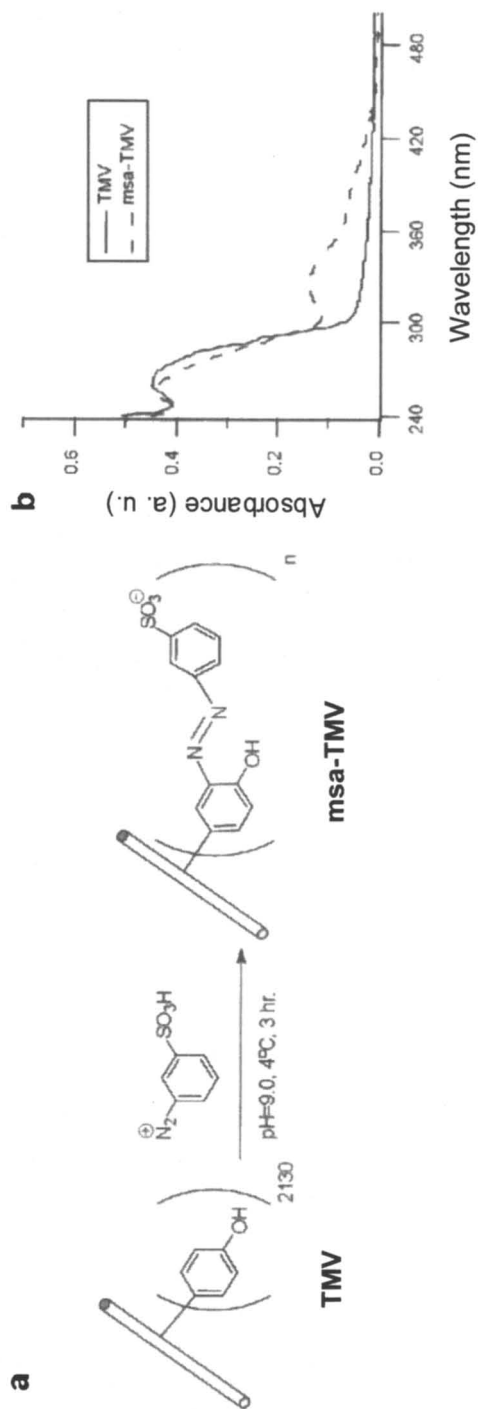
Figure 6. (a) Reaction scheme leading to msa-modification of TMV (msa-TMV). (b) UV-Vis spectra of wt-TMV and msa-TMV that shows characteristic absorbance peak at 324 nm.

Introducing sulfonic acid groups to TMV should have two effects on the final assembly: (1) negative charges on the surface of TMV increase leading to stronger binding of aniline to TMV and stronger nanofibers (*49, 50*); and (2) the modification of the tyrosine residues on the end-face of TMV will block the head-to-tail self-assembly since the newly attached groups will hinder the interaction between the subunits (*35, 51, 52*). As shown by TEM, the surface modification did not affect the integrity of the TMV particles (Figure 7a). However, treating with aniline and APS, no fiber-like structures were formed with msa-TMV as the starting material. The use of a negatively charged group did promote conglomeration at the ends of the particles. Branched structures with end-to-end knot-like connections were formed as the major morphology (Figure 7b). Although long 1D fibers could also be observed occasionally, they always appeared as bent structures with a gap between two TMV rods (Figure 7c). Clearly, the end-face modification of TMV prohibited the perfect match of the helical propagation as shown in Scheme 1 (Path A). Instead, the assembly of TMV/PANI adopted the Path B (Scheme 1). In addition, the additional acid groups on the end-face of TMV resulted in more PANI deposition, which served as the "glue" to connect TMV/PANI rods together.

When alkyne **2** was used to modify TMV particles, similar complete modifications have also been observed (data not shown). The uncharged alkyne group could not attract aniline or PANI as sulfonic acid groups did; therefore, it was difficult to have any PANI formed on the surface of alkyne tailored TMV particles. As shown in Figure 7d, the alkyne modified TMV, after treatment with aniline and APS, showed no difference from the initial condition. Obviously, the assembly was completely blocked by the surface modification (*48*).

TMV Templated Other Polymeric Assemblies

As shown in Figure 1, the exterior surface of TMV is highly charged and hydrophilic. In particular, the particles carry negative charges at neutral pH since the pI of TMV is around 3.5 (*53*). The formation of TMV/PANI composite fibers is facilitated by the attraction of aniline (and also PANI) to the surface of TMV at neutral pH. Therefore, the interaction between monomers and TMV is essential for the long fiber formation. For example, when thiophene was employed as the monomer under a similar polymerization condition, there was no formation of any fiber-like structures (Figure 8a), likely due to the much weaker interaction between thiophene and the surface of TMV. To further confirm it, an amino-functionalized thiophene salt, **3**, was synthesized (*48*). We hypothesized that the positively charged amino group will enhance the interaction of **3** with the negatively charged TMV surface. As shown in Figure 8b, 1D long fibers were readily formed when a mixture of TMV and **3** was treated with APS. Similarly, no visible gap can be detected in such poly(3-
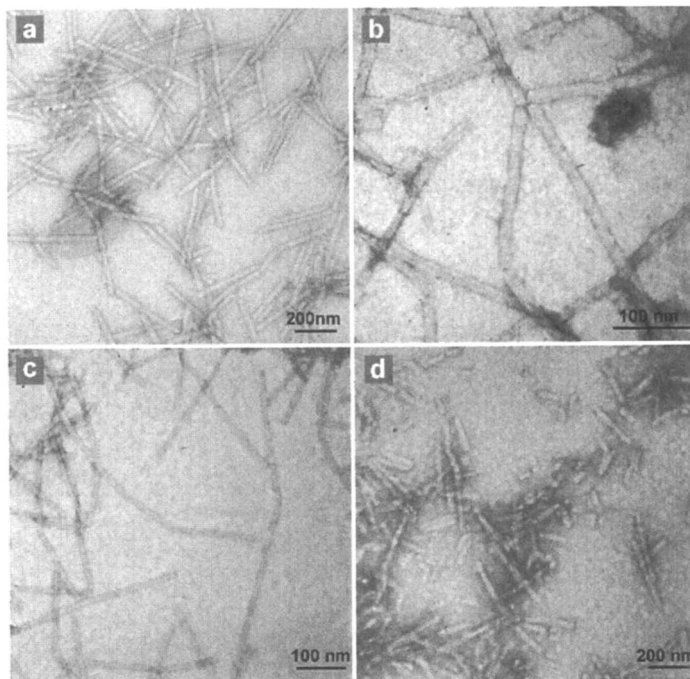
Figure 7. TEM images of (a) original msa-TMV, (b and c) TEM image of msa-TMV treated with aniline and APS, and (d) alkyne 2 modified TMV treated with aniline and APS.

aminothiophene)/TMV composite fibers (Figure 8c). In addition to electrostatic interaction, hydrogen bonding can also increase the surface adsorption of monomers to TMV. For instance, when the polyethylene glycol methacrylate (PEG-MA, **4**) was used as the monomer and APS as the initiator, similar fiber-like structures could also be obtained (Figure 8d).

Polypyrrole (PPy), a well known conductive polymer, has also attracted a lot of interest in developing functional materials due to facile polymerization conditions and the availability of the starting materials. Different templates, such as structurally well-defined "hard" templates and lyotropic liquid crystalline "soft" templates have been applied to synthesize nanostructured PPys (*54-56*). Similar to aniline, pyrole should also have strong interaction with the surface groups of TMV. Surprisingly, when using pyrole as starting material and APS as oxidant, the resulted composite PPy/TMV have a completely different morphology. As shown in Figure 9, both scanning electron microscopy (SEM) and TEM images show that the uniform spherical nanoparticles can be obtained. The average diameter of the particles is about 250 nm. The reaction pH value
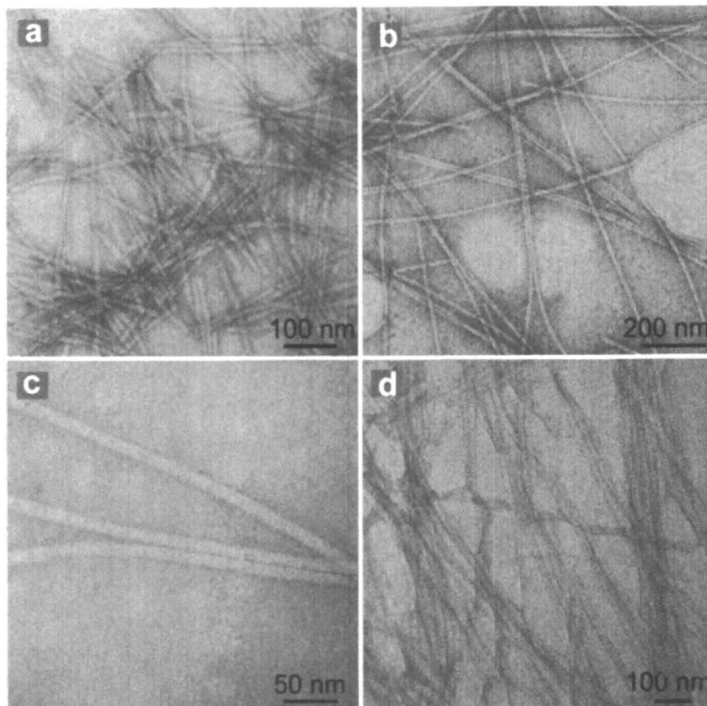
Figure 8. TEM images of (a) TMV treated with thiophene and APS, no long fiber can be observed; (b) long fibers formed by mixing TMV with amino modified thiophene 3 and APS; (c) an enlarged image of Figure 8b; and (d) poly(PEGMA)/TMV composite fibers using 4 as starting monomer.

and the concentration of starting materials have strong impact on the surface morphology of the PPy/TMV particles. The reason for the formation of spherical particles instead of fiber-like structures is still not clear, but more likely resulted from the faster polymerization process of pyrrole. For the same reason, fibrous structures are hardly seen when pyrrole is polymerized without 1D templates or using seedling method (47, 57). The bulk DC conductivities of PPy/TMV nanoparticles obtained by our method is comparable to PPy synthesized by conventional methods (56).

Conclusion

The well-understood structural information and the availability make TMV an attractive starting scaffold for novel materials development. We herein show
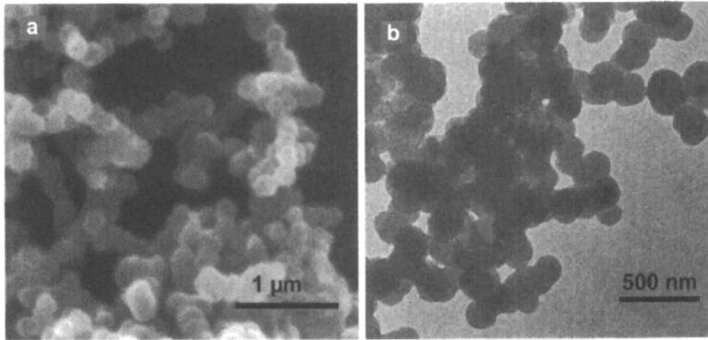
Figure 9. (a) SEM and (b) TEM images of PPy/TMV composites particles synthesized by a general protocol: To a solution of 50 µL distilled pyrrole in 3 mL nanopure H_2O at pH 2.5, 0.2 mg TMV in 0.1 mL H_2O and 50.2 mg APS in 1 mL H_2O were added at room temperature. After the mixture was stirred for half an hour, a black precipitant was collected by centrifugation at 14,000 rpm for 5 min. The pellet was resuspended in nanopure water and subjected to another run of centrifugation at 14,000 rpm for 5 min. The process was repeated 5 times and the final black pellet of fine powder was easily dispersed in 1 mL nanopure water, which was analyzed by SEM and TEM (58).

that 1D polymeric composite fibers could be formed by the polymerization of a variety of monomers on the surface of TMV at neutral pH. The ability of TMV coat proteins to form a regular helical array is the key that leads to the 1D head-to-tail assembly as demonstrated by our results. Two factors particularly contribute to the formation of long 1D TMV-composite fibers: (1) the ability of augmentation and polymerization of monomers on the surface of TMV; and (2) the possibility of propagation and stabilization of TMV helices. Such composite nanofibers have very narrow polydispersity in diameter, high aspect ratio and excellent processability. In addition, we demonstrate that the surface modification of TMV as well as the structure of starting materials will modulate the assembly pattern and dictate the structures of the final composites. This strategy highlights the merit of developing novel nanomaterials using biological building blocks as templates and will promote many potential applications in optics, electronics, and biomedical engineering.

Acknowledgements

References

1. Cui, Y.; Lieber, C. M., *Science* **2001**, *291*, 851-853.
2. Duan, X.; Huang, Y.; Cui, Y.; Wang, J.; Lieber, C. M., *Nature* **2001**, *409*, 66-69.
3. Tao, A.; Kim, F.; Hess, C.; Goldberger, J.; He, R.; Sun, Y.; Xia, Y.; Yang, P., *Nano Lett.* **2003**, *3*, 1229-1233.
4. Melosh, N. A.; Boukai, A.; Diana, F.; Gerardot, B.; Badolato, A.; Petroff, P. M.; Heath, J. R., *Science* **2003**, *300*, 112-115.
5. Busbee, B. D.; Obare, S. O.; Murphy, C. J., *Adv. Mater.* **2003**, *15*, 414-416.
6. Jana, N. R.; Gearheart, L.; Obare, S. O.; Murphy, C. J., *Langmuir* **2002**, 18, 922-927.
7. Niemeyer, C. M., *Angew. Chem. Int. Ed.* **2001**, *40*, 4128-4158.
8. Flynn, C. E.; Lee, S.-W.; Peelle, B. R.; Belcher, A. M., *Acta Materialia* **2003**, *51*, 5867-5880.
9. Seeman, N. C.; Belcher, A. M., *Proc. Nat. Acad. Sci. U. S. A.* **2002**, *99*, 6451-6455.
10. Seeman, N. C., *Chem Biol* **2003**, *10*, 1151-1159.
11. Caswell, K. K.; Wilson, J. N.; Bunz, U. H. F.; Murphy, C. J., *J. Am. Chem. Soc.* **2003**, *125*, 13914-13915.
12. Dujardin, E.; Mann, S., Bio-inspired materials chemistry. *Adv. Eng. Mater.* **2002**, *4*, 461-474.
13. Shenton, W.; Douglas, T.; Young, M.; Stubbs, G.; Mann, S., *Adv. Mater.* **1999**, *11*, 253-256.
14. Nam, K. T.; Kim, D. W.; Yoo, P. J.; Chiang, C. Y.; Meethong, N.; Hammond, P. T.; Chiang, Y. M.; Belcher, A. M., *Science* **2006**, *312*, 885-888.
15. Mao, C.; Solis, D. J.; Reiss, B. D.; Kottmann, S. T.; Sweeney, R. Y.; Hayhurst, A.; Georgiou, G.; Iverson, B.; Belcher, A. M., *Science* **2004**, *303*, 213-217.
16. Lee, L. A.; Wang, Q., *Nanomedicine* **2006**, *2*, 137-149.
17. Klug, A., *Philos Trans R Soc Lond B Biol Sci* **1999**, *354*, 531-535.
18. Stubbs, G., *Rep. Prog. Phys.* **2001**, *64*, 1389-1425.
19. Jeng, T. W.; Crowther, R. A.; Stubbs, G.; Chiu, W., *J. Mol. Biol.* **1989**, *205*, 251-257.
20. Butler, P. J. G.; Lomonossoff, G. P., *Biophys. J.* **1980**, *32*, 295-312.
21. Yi, H.; Nisar, S.; Lee, S. Y.; Powers, M. A.; Bentley, W. E.; Payne, G. F.; Ghodssi, R.; Rubloff, G. W.; Harris, M. T.; Culver, J. N., *Nano Lett* **2005**, *5*, 1931-1936.

22. Schlick, T. L.; Ding, Z.; Kovacs, E. W.; Francis, M. B., *J. Am. Chem. Soc.* **2005**, *127*, 3718-3723.
23. Miller, R. A.; Presley, A. D.; Francis, M. B., *J. Am. Chem. Soc.* **2007**, *129*, 3104-3109.
24. Fowler, C. E.; Shenton, W.; Stubbs, G.; Mann, S., *Adv. Mater.* **2001**, *13*, 1266-1269.
25. Fonoberov, V. A.; Balandin, A. A., *Nano Lett.* **2005**, *5*, 1920-1923.
26. Royston, E.; Lee, S. Y.; Culver, J. N.; Harris, M. T., *J. Colloid Interface Sci.* **2006**, *298*, 706-712
27. Knez, M.; Bittner, A. M.; Boes, F.; Wege, C.; Jeske, H.; Maiss, E.; Kern, K., *Nano Lett.* **2003**, *3*, 1079-1082.
28. Knez, M.; Kadri, A.; Wege, C.; Gosele, U.; Jeske, H.; Nielsch, K., *Nano Letters* **2006**, *6*, 1172-1177.
29. Knez, M.; Sumser, M.; Bittner, A. M.; Wege, C.; Jeske, H.; Martin, T. P.; Kern, K., *Adv. Funct. Mater.* **2004**, *14*, 116-124.
30. Knez, M.; Sumser, M. P.; Bittner, A. M.; Wege, C.; Jeske, H.; Hoffmann, D. M.; Kuhnke, K.; Kern, K., *Langmuir* **2004**, *20*, 441-447.
31. Lee, S. Y.; Culver, J. N.; Harris, M. T., *J. Colloid Interface Sci.* **2006**, *297*, 554-560.
32. Dujardin, E.; Peet, C.; Stubbs, G.; Culver, J. N.; Mann, S., *Nano Lett.* **2003**, *3*, 413-417.
33. Tseng, R. J.; Tsai, C.; Ma, L.; Ouyang, J.; Ozkan, C. S.; Yang, Y., *Nature Nanotechnology* **2006**, *1*, 72-77.
34. Kalinin, S. V.; Jesse, S.; Liu, W. L.; Balandin, A. A., *App. Phys. Lett.* **2006**, **88**, 153902.
35. Lu, B.; Stubbs, G.; Culver, J. N., *Virology* **1996**, 225, 11-20.
36. Niu, Z.; Bruckman, M. A.; Kotakadi, V. S.; He, J.; Emrick, T.; Russell, T. P.; Yang, L.; Wang, Q., *Chem. Commun.* **2006**, 3019-3021.
37. Huang, J.; Virji, S.; Weiller, B. H.; Kaner, R. B., *J. Am. Chem. Soc.* **2003**, 125, 314-315.
38. Huang, J.; Kaner, R. B., *J. Am. Chem. Soc.* **2004**, 126, 851-855.
39. Huang, J.; Kaner, R. B., *Chem. Commun.* **2006**, 367-376.
40. Li, D.; Kaner, R. B., *J. Am. Chem. So.c* **2006**, 128, 968-975.
41. Chiou, N. R.; Epstein, A. J., *Adv. Mater.* **2005**, 17, 1679-1683.
42. Butler, P. J., *Philos Trans R Soc Lond B Biol Sci* **1999**, 354, 537-550.
43. Lee, B.; Lo, C.-T.; Thiyagarajan, P.; Winans, R. E.; Li, X.; Niu, Z.; Wang, Q., *Manuscript submitted.*
44. Niu, Z.; Bruckman, M. A.; Li, S.; Lee, L. A.; Lee, B.; Pingali, S. V.; Thiyagarajan, P.; Wang, Q., *Langmuir* **2007**, 23, 6719-6724.
45. Svergun, D. I., *J. Appl. Cryst.* **1991**, 24, 485-492.
46. Svergun, D. I., *J. Appl. Cryst.* **1992**, 25, 495-503.
47. Zhang, X.; Manohar, S. K., *J. Am. Chem. Soc.* **2005**, 127, 14156-14157.

48. Bruckman, M. A.; Niu, Z.; Li, S.; Lee, L. A.; Varazo, K.; Nelson, T.; Lavigne, J. J.; Wang, Q., *NanoBiotechnology* **2007**. accepted.
49. Wei, Z.; Wan, M.; Lin, T.; Dai, L., *Adv. Mater.* **2003**, 15, 136-139.
50. Liang, L.; Liu, J.; Windisch, C. F.; Exarhos, G. J.; Lin, Y., *Angew. Chem. Int. Ed.* **2002**, 41, 3665-3668.
51. Lu, B.; Taraporewala, F.; Stubbs, G.; Culver, J. N., *Virology* **1998**, 244, 13-19.
52. Lu, B.; Stubbs, G.; Culver, J. N., *Virology* **1998**, 248, 188-198.
53. Wadu-Mesthrige, K.; Pati, B.; McClain, W. M.; Liu, G.-Y., *Langmuir* **1996**, 12, 3511-3515.
54. Wu, C. G.; Bein, T., *Science* **1994**, 264, 1757-1759.
55. Bocharova, V.; Kiriy, A.; Vinzelberg, H.; Moench, I.; Stamm, M., *Angew Chem Int. Ed.* **2005**, 44, 6391-6394.
56. Martin, C. R., *Acc. Chem. Res.* **2005**, 28, 61-68.
57. Chronakis, I. S.; Grapenson, S.; Jakob, A., *Polymer* **2006**, 47, 1597-1603.
58. Li, S.; Niu, Z.; Wang, Q., Unpublished results.

Chapter 27

Sensitivity and Selectivity Limits of Multiplex NanoSPR Biosensor Assays

Chenxu Yu and Joseph Irudayaraj

Department of Agricultural and Biological Engineering and Bindley Biosciences Center, Purdue University, West Lafayette, IN 47907

Gold nanorods (GNRs) of different aspect ratios were fabricated through seed mediated growth; partial and full functionalization procedures were developed to attach antibodies to the GNRs and yield Gold Nanorods Molecular Probes (GNrMPs). Multiplex sensing was achieved by the distinct response of the plasmon spectra of GNrMPs to binding events of up to three targets. A mathematical model formulated adequately described the ligand binding response of GNrMPs and concentrations of multiple targets were determined from experimental data. The GNrMP sensors were found to be highly specific and sensitive and the dynamic response was found to be in the range between 10^{-9} M and 10^{-6} M. Comparison of the experimental data with the theoretical model yielded an affinity constant $K_a=1.32\times10^7$ M^{-1} which was in agreement with the IgG-antiIgG binding affinity reported in the literature. The limit of detection (LOD) of GNrMPs was found to be in the low nano-molar range, and is a function of the binding affinity: for a higher probe-target affinity pair the LOD can be expected to reach femto molar levels. This technique can play a key role in developing tunable sensors for sensitive and precise monitoring of biological interactions.

Introduction

Gold nanoparticles possess optical properties that make them uniquely suitable for biosensing applications. Their optical properties strongly depend on both the particle size and shape and are related to the interaction between the metal conduction electrons and the electric field component of the incident electromagnetic radiation, which leads to strong, characteristic absorption bands in the visible to infrared part of the spectrum (*1*).

Fundamentally, a biosensor is constructed by coupling a ligand to its receptor complement via an appropriate signal transduction element (2). Various signal transduction mechanisms have been explored as biosensing schemes, including optical (*3,4*), radioactive (*5,6*), electrochemical (*7,8*), piezoelectric (*9,10*), magnetic (*11,12*), micromechanical (*13,14*), IR and Raman spectroscopic (*15,16*), and mass spectrometric (*17,18*). Although each of these methods has its individual strengths and weakness, optical sensors that utilize the surface plasmon resonance (SPR) phenomenon of planar gold surfaces have shown potential to become methods of choice in many biosensing applications (*4,19*).

Other than macro-scaled SPR sensors using planar gold surface, several research groups have begun to develop micro/nano scaled optical biosensors that utilize the unique optical properties of gold nanostructures (*20-29*). The optical properties of gold nano structures strongly depend on both the particle size and shape and are related to the interaction between the surface electrons and the incidental electromagnetic radiation, which leads to strong, characteristic absorption in the visible to infrared region of the spectrum (*1*). For gold nanorods in aqueous solution, two distinct plasmon bands, one associated with the transverse (~520 nm) mode and the other with the longitudinal mode (usually > 600 nm) of the surface electron oscillation could be observed (*1*). Biosensor applications (*20-30*) have been designed based on the fact that the wavelengths of these bands are affected by changes in the dielectric properties in the close vicinity of these structures (known as nanoSPR (*20*), or Localized Surface Plasmon Resonance (LSPR)) (*21*). These changes are induced by the binding of ligands to the receptor molecules (i.e. antibodies) immobilized onto the nanostructures through chemi- or physisorption.

The wavelength shift of the plasmon bands is solely determined by changes in the dielectric properties (i.e., refractive indexes) in the immediate vicinity of the nano structures. In the case of spherical particles, target-binding induced wavelength shift to single particles is small (2~3 nm), a sensor has to be designed based on the controlled aggregation concept (*28,31-34*). However, aggregation results in significant widening of the plasmon peak, and the resulting spectral resolution is too poor to distinguish multiple targets.

When anisotropic particles such as nanorods are used to fabricate Gold Nano-rod Molecular Probes (GNrMPs), single particle sensor could be devised. Recently we have demonstrated that GNrMPs made with gold nanorods of

different aspect ratios could be implemented in a multiplex mode to detect presence/absence of multiple targets simultaneously (*29*). However, in the earlier work the GNrMPs were only partially-functionalized and was prone to non-specific binding, and the detection of targets was not quantitatively interpreted.

In this research, we studied both partial and full functionalization strategies for making GNrMPs, and developed a scheme to implement the GNrMPs for specific detection of multiple targets. A systematic study of the response of GNrMPs to changes in dielectric properties (refractive indexes) in the vicinity is presented and quantitative analysis of binding events is provided. It is shown that these GNrMPs operate in a manner similar to macro SPR sensors and it is possible to transduce very small changes in refractive index near the surface of the GNrMPs into a measurable wavelength shift. The GNrMPs were found to be extremely sensitive and could measure the targets at low nano-molar level.

Experimental section

Materials

Hexadecyltrimethylammoniumbromide (CTAB, 99%) and benzyl dimethyl ammoniumchloride hydrate (BDAC, 99%), Sodium borohydride (99%), L-ascorbic acid, Gold (III) chloride hydrate (>99%) and Silver nitrate (>99%), gold atomic absorption standard solution, 11-mercaptoundecanoic acid (MUDA), were all purchased from Sigma-Aldrich (St. Louis, MO) and used without further purification. 1-ethyl, 3-(3-dimethylaminopropyl) carbodiimide (EDAC) and 4-(4-Maleimidophenyl) butyric acid *N*-succinimidyl ester (NHS), goat anti-human IgG, goat anti-mouse IgG, goat anti-rabbit IgG Fabs and human IgG, mouse IgG, rabbit IgG were all purchased from Pierce Biotechnology (Rockford, IL). Nanopure deionized and distilled water (18.2 MΩ) was used for all experiments.

Fabrication and Characterization of Gold Nanorods

A seed-mediated growth procedure modified from that suggested by Nikoobakht and El-Sayed (*35*) was used to fabricate gold nanorods with aspect ratio between 2.5 and 7. The details of the procedure were reported elsewhere (*29*).

The concentration of atomic gold in the solution of gold nanorods was determined by inductively coupled plasmon atomic emission spectroscopy (ICP-AES). The gold nanorods were then concentrated to 100 nM by centrifugation. All subsequent characterization, activation, and functionalization were conducted using these nanorods samples.

The yield and aspect ratios of gold nanorods was determined using Transmission Electron Microscopy (TEM), acquired with a Philips CM-100 TEM (Philips, Eindhoven, Netherlands). TEM grids were prepared by placing 1 µl of the nanorods solution in a 400-mesh formvar coated copper grid and evaporating the solution at room temperature. Images were then captured using a Tietz F415 slow scan digital camera at 4K resolution. At least 150~200 nanorods could be counted and measured per grid to provide an estimate of the mean aspect ratio of these nanorods after the synthesis step.

Absorption spectra of GNrMP samples through each stage of experiments were measured using a Jasco V570 UV-Vis-NIR spectrophotometer (Jasco, Inc., Easton, MD), in the wavelength range between 400 and 1500 nm. The measured spectra were normalized by rescaling the maximum absorbance of the longitudinal plasmon peak to 1.

Functionalization of Gold Nanorods to Synthesize GNrMPs

Once synthesized, the nanostructures were functionalized by biologically active agents and deployed as sensors. Biofunctionalization constitutes a two step process: in step 1, termed as the activation step, a chemical anchor layer was formed on the nanorods surface to provide active functional groups to which biological molecules (i.e., antibodies) can be covalently attached; and in step 2, the functionalization step, biomolecules were covalently linked to the anchor layer to produce GNrMPs for target specific sensing.

Partial activation of freshly-made gold nanorods was accomplished partially replacement of the CTAB capping. the CTAB capping at the {1,1,0}/{1,0,0} side faces of the nanorods is retained and the CTAB capping at the {1,1,1} side faces is replaced with an alkanethiol SAM, to which antibodies can be tethered through NH-CO bonds.

Partial activation of gold nanorods was achieved as follows: 0.5 ml of 20mM ethanol solution of MUDA was added to 5 ml of gold nanorods solution and stirred mildly for 24 hours under room temperature. Nanorods were then collected by centrifugation at 5000 rpm for 15 minutes and resuspended in a 0.005 M CTAB solution to yield a final concentration of ~100 nM.

Full activation of gold nanorods was achieved by the replacement of CTAB capping as in (37). The resulting solution was subjected to two rounds of chloroform extraction to remove the CTAB released from the nanorods. Nanorods were then collected by centrifugation at 5000 rpm for 15 minutes and resuspended in nano pure water (18.2 mΩ) to yield a final concentration of ~100 nM.

Once the MUDA SAM was formed, antibodies (goat anti-human, goat anti-mouse, goat anti-rabbit IgG Fabs) were then attached to the activated nanorods as follows: to a 5 ml of the activated nanorods (~100 nM), 1 ml of freshly prepared 0.4M EDAC and 0.1M NHS solution was added and sonicated for 25 minutes at 4°C. The resulting structures were then collected by centrifugation at

5000 rpm for 5 minutes and resuspended in 5 ml PBS buffer (pH=7.4). Antibodies suspended in PBS was then added to the resulting nanorods suspension (the concentration of antibodies was varied between 200~1000 nM) and then incubated for 1 h under constant sonication at room temperature. The functionalized nanorods were subsequently collected by centrifugation at 5000 rpm for 5 minutes and three rounds of vigorous washing and sonication in PBS solution for 10 mins. The supernatant was collected after each washing step and the cumulative protein content was measured using a Biorad Protein Assay (Biorad Laboratories, Hercules, CA) with bovine serum albumin (BSA) as a protein standard. The amount of antibodies bound to the nanorods was determined by subtracting the antibodies left in the supernatant from the original amount.

Implementation of the Gold Nanorods Molecular Probes

5 ml of the GNrMPs (20 nM) was mixed with 5 ml of targets (respective IgGs) with concentrations spanning from 10^{-6} M to 10^{-9} M for 30 mins under mild stirring to allow the probe-target binding to reach equilibrium and the sensor response to the probe-target binding depicted by a pronounced shift of longitudinal plasmon peaks, were measured using UV-Vis-NIR spectroscopy. For multiplex analysis, 3 GNrMPs with different aspect ratios were mixed at equal concentrations, and the target solution containing the respective complement (IgGs) at varying concentrations was prepared. Equal amount of GNrMP and target solutions were mixed and kept under mild stirring for 30 mins and the plasmon spectra of the mixture were then measured. The response of GNrMPs to target binding events was then quantitatively evaluated.

Results and Discussion

Nanorods Fabrication and Characterization

Gold nanorods of aspect ratios in the range between 2.8 and 7 were made following the single and double surfactant protocols discussed earlier. Figure 1 shows the absorption spectra of nanorods with aspect ratio of 2.8, 3, 4.5, 5.5, and 7, respectively. It can be clearly seen that small changes in aspect ratio introduce a significant red-shift in the longitudinal plasmon band of the GNR colloids, implying a significant potential for multiplexing. Within the range of this study, a linear correlation could be established between the aspect ratio of gold nanorods and the absorbance wavelength of the longitudinal plasmon bands; hence the aspect ratio of gold nanorods could be easily deduced from their plasmon spectra.
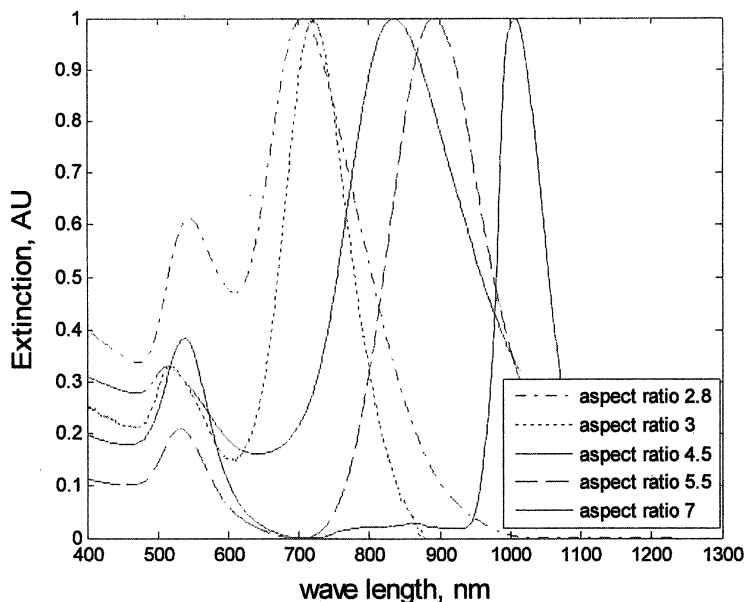
Figure 1. Absorption spectra of gold nanorods with different aspect ratios

Transmission Electron Microscope (TEM) imaging of nanorods of various aspect ratios confirmed yields of 93.5 to 98.5%. Typical TEM images of the Gold nanorods are shown in Figure 2. Another observation is that the width of nanorods (7~10 nm) remained approximately the same hence an increase in aspect ratio was predominately determined by elongation of nanorods.

It should be noted that as the ratio reaches 7, the longitudinal peak red-shifts to ~1011 nm, well beyond the visible and into the NIR region of the spectrum where biological samples such as cells have weak absorption and their interference with the plasmon signal is negligible. Hence these gold nanorods have a major advantage compared to the existing fluorescence and illumination labels where interferences due to sample autofluorescence could pose a significant problem in target detection.

The sensitivity factor, S, of the wavelength of the plasmon bands of gold nanorods to the refractive index of their surroundings, is proportional to the aspect ratio AR of the GNrMPs (*38*):

$$S = \frac{d\lambda_{res}}{dn_s} \propto \lambda_p \sqrt{Y} \propto \lambda_p AR \qquad (1)$$

where λ_p is the plasmon wavelength of bulk metal. Therefore, as the aspect ratio increases, the sensitivity of the GNrMPs will increase. Once aspect ratio is known, S can be readily determined.
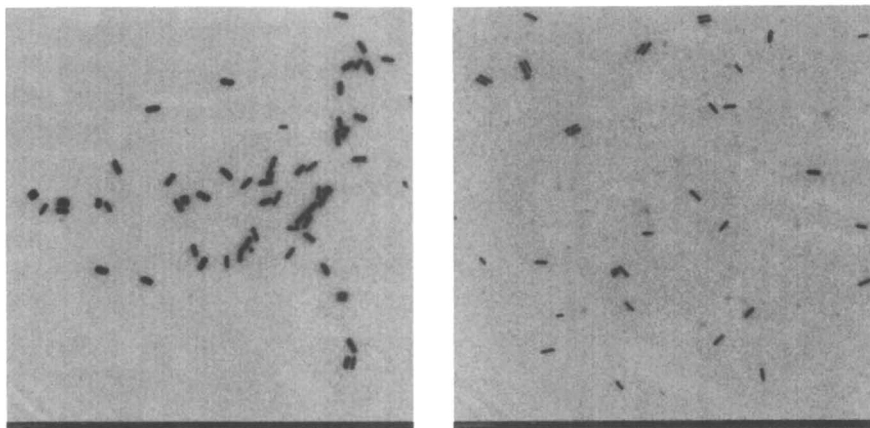
Figure 2. TEM micrographs of gold nanorods with mean aspect ratio 2.8 and 4.5

Functionalization of Gold Nanorods to Make GNrMPs

Functionalization of gold nanorods takes advantage of the well-known affinity between gold and thiol compounds. However, because the {1,1,0}/{1,0,0} side faces of the rods are densely covered by CTAB, only the {1,1,1} side faces are easily utilized by alkanethiols to form self-assembled monolayers (SAM) under ambient temperature, for the attachment of recognition agents (antibodies in this work). It should however be noted that the formation of alkanethiol SAM on the formerly more exposed {1,1,1} side faces introduces a red-shift in the plasmon peaks due to changes in the refractive index at the surface of gold nanorods.

When full activation is achieved, the CTAB layers on the side face of nanorods needs to be removed completely. It is known that the refractive index (RI) of the CTAB layer (RI=1.435 (*39*)) is smaller than the RI of MUDA (RI=1.463 (*21*)). However the CTAB layer is a bi-layer with a thickness of 4~5 nm (*37*), which is larger than the thickness of MUDA SAM (1.69 nm) (*21*). The effective local RI is then decreased due to the combined effect of the refractive index and thickness of the layers in the vicinity of each gold nanorods. Since the effective RI is higher before activation (1.414) a blue-shift of the plasmon bands is expected.

Once the MUDA SAM is formed, biomolecules can be covalently attached via the -NH$_2$ bond of the antibodies to the –COOH terminus of the MUDA SAM. A further red-shift of the plasmon peak can be observed due to antibody functionalization. After the attachment of antibodies these rods showed a significant shift (of up to 20 nm) compared to the unmodified rods. The

sensitivity of plasmon spectra to the attachment of molecular layers form the basis of molecular nanoSPR biosensors.

Although antibodies can only covalently attach to the MUDA activated sites, physisorption of antibodies to CTAB capped side faces is also possible for the partially activated rods. The isoelectric point for antibodies are ~6 (*40*), under the reaction pH (~7.4), the antibodies are negatively charged, and thus will bind to the positively charged CTAB cap due to electrostatic interaction.

Table 1 provides the binding ratio of antibodies to four different gold nanorods determined by measuring the concentration of antibody in the supernatant after the functionalized GNrMPs were collected by centrifugation. The binding ratio in this context is defined as the average number of antibody molecules attached to each individual gold nanorods. It was calculated as:

Binding ratio = (number of antibody bound to GNRs)/(number of GNRs)   (2)

At lower ratios (IgG:gold nanorods = 2:1), if the coupling efficiency is 100%, this binding ratio should be close to 2. For fully activated GNRs, the binding ratio was determined to be close to 2 (>1.89); for partially-activated gold nanorods, it is only 1.18 (from equation 4). The binding ratio is rather independent of the aspect ratio of gold nanorods at low IgG: gold nanorods ratios, under these conditions the gold nanorods are not saturated with respect to antibody binding, and the binding ratio is not restricted by the size of GNRs. However, when the antibody: gold nanorods ratio is high, larger gold nanorods allow more antibodies to bind and saturate at a higher binding ratio.

Table 1. Binding Ratio of IgGs to Partially and Fully Activated GNRs
IgG/GNR Ratio = 2 (n=3)

	GNrMP (aspect ratio 2.3)	*GNrMP (aspect ratio 3.5)*	*GNrMP (aspect ratio 4.5)*	*GNrMP (aspect ratio 6.5)*
Binding ratio (partial)	1.18 ± 0.08	1.1 ± 0.07	1.13 ± 0.08	1.15 ± 0.08
Binding ratio (complete)	1.89 ± 0.04	1.93 ± 0.07	1.95 ± 0.05	1.92 ± 0.08

A separate series of experiment was conducted to investigate the effect of increasing antibody concentrations and its attachment to activated nanorods

(aspect ratio 5.1, 20 nM), the antibody:nanorods ratio was increased from 2:1 to 20:1. For fully-activated GNRs, antibodies bind to the whole surface of the GNRs covalently through EDC-NHS mediated coupling; antibody-binding to partially activated nanorods are through two routes: EDC-NHS mediated covalent-coupling to the MUDA sites, and physisorption to the CTAB sites on the side faces; antibodies only bind to the in-activated gold nanorods through physisorption to the CTAB sites; if EDC-NHS mediated coupling was not used, antibodies do not bind to the MUDA SAM of the fully-activated GNRs due to the repulsion between MUDA⁻ and antibody⁻. Figure 3 shows the binding ratio for the GNRs, binding to fully-activated nanorods (~13.5) is consistently higher than to partially activated (~5.5) and non-activated rods (3.4); especially at high antibody:nanorods ratio. However, the number of antibodies bound to each nanorods, even for the fully activated gold nanorods, is still only about half of the number calculated based on a tightly-packed estimation, indicating the coupling efficiency of antibodies to the active carboxylic sites is only ~50%.
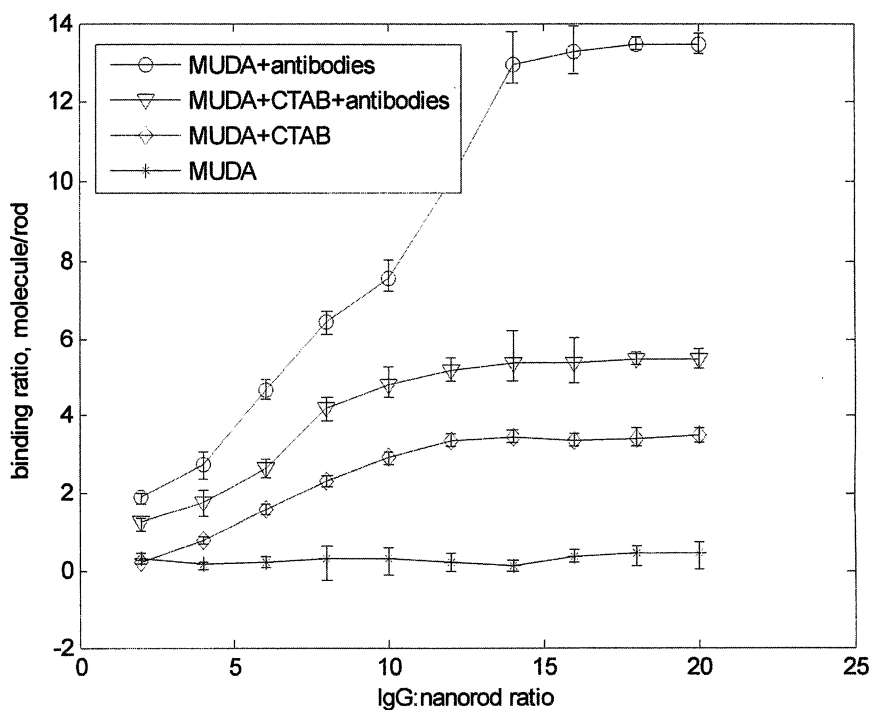
Figure 3. Target binding study on fully-functionalized and partially-functionalized GNrMPs

Responses of GNrMPs to Target Binding, as a Function of Target (anti-IgG) Concentration

Exposure of the GNrMPs of three different aspect ratios (1.5, 2.8 and 4.6) (20 nM) to targets (anti-IgGs) with different concentrations was conducted, the GNrMP responses were normalized against the maximum responses (ΔR_{max}) at saturation concentrations. $\Delta R/\Delta R_{max}$ are plotted against the concentrations of the targets and shown in figure 4 for the three GNrMPs. The concentration range was from 10^{-9} M to 10^{-5} M. This $\Delta R/\Delta R_{max}$ vs. concentration curve could be quantitatively interpreted using the steady-state binding kinetics model with the following assumptions: (i) Binding between solution-phased targets (IgGs) and particle-bound capturing agents (anti-IgG fabs) occurs by 1:1, with invariant affinities that were not affected by the antibody immobilization; (ii) The only operative GNrMP sensing mechanism is the change in the local refractive index caused by binding events; and (iii) The measured nanoSPR response, ΔR, is determined by the thickness, $d_{analyte}$, of the absorbed analyte layer, and its refractive index, $n_{analyte}$.
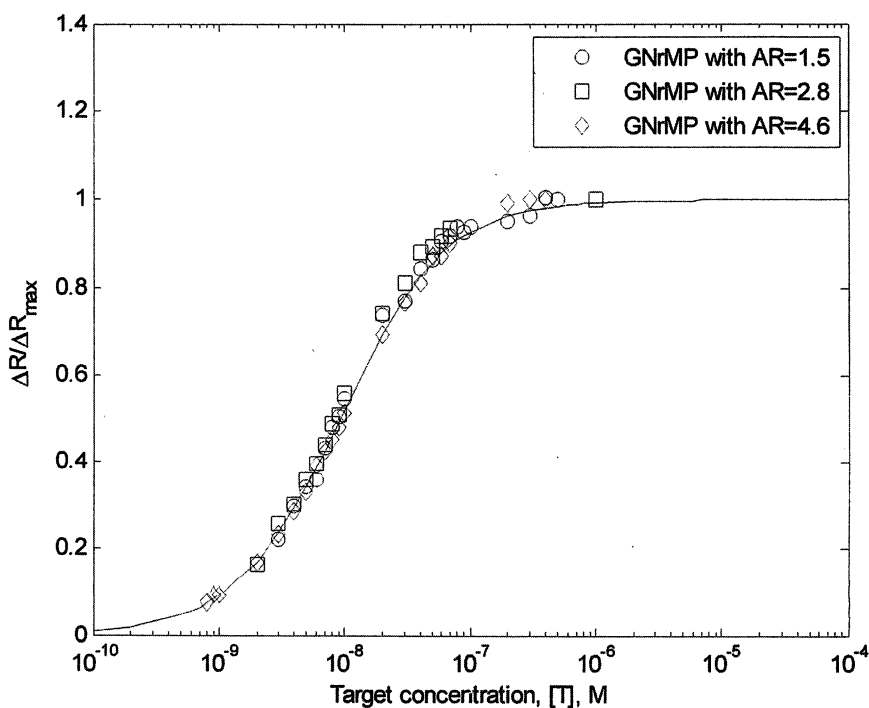
Figure 4. Normalized GNrMP response, $\Delta R/\Delta R_{max,}$ versus target concentration [T].

Treating each GNrMP as a single sensing platform, the equilibrium surface excess, $\Gamma_{targets}$ in molecules cm^{-2}, for 1:1 binding of IgG to particle-bound anti-IgG Fabs, is given by the Langmuir isotherm (41):

$$\frac{\Gamma_{target}}{\Gamma_{target}^{max}} = \frac{K_a[T]}{(1+K_a[T])} \tag{3}$$

where Γ_{target}^{max} is the saturation value of $\Gamma_{targets}$ (i.e., when every capturing agent (anti-IgGs) is saturated by the target (IgGs)), [T] is concentration of targets, and K_a is the apparent affinity constant for 1:1 binding of IgG to anti-IgG.

The nanoSPR response of GNrMPs, R, is given by

$$R = S(n_{eff} - n_{ext}) \tag{4}$$

where S is the sensitivity factor of GNrMPs, defined as the relative change in resonance wavelength with respect to change in refractive index (equation 1), n_{ext} is the bulk refractive index of the external medium ($n_{ext} = n_{water} = 1.33$), and n_{eff} is the effective refractive index of the quadralayer structure surrounding each GNrMP, as illustrated in figure 5.

GNR

MUDA anchor layer

capturing layer, anti-IgG fab

target layer, IgGs

Water layer

~ 30 nm
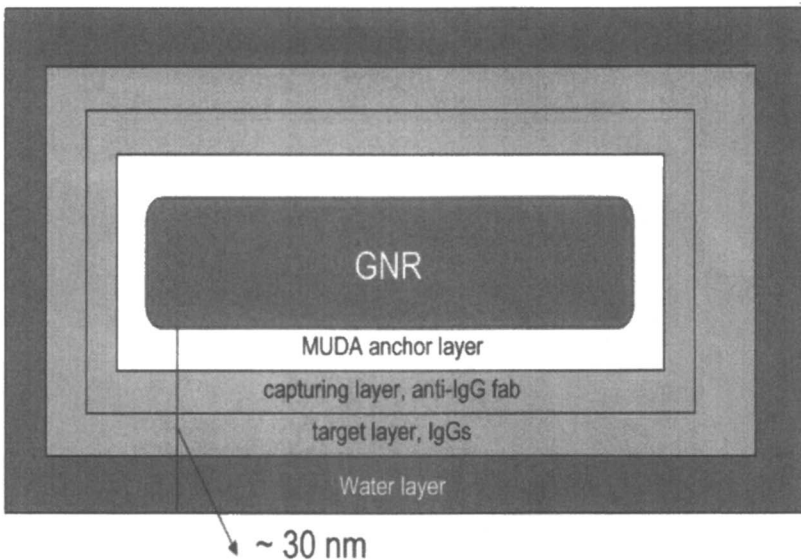
Figure 5. Micro-environment surrounding a GNrMP at target-binding mode

S is determined experimentally for each GNrMP. The effective refractive index of the quadralayer structure is determined by integrating the distance-dependent local refractive index, n(z), weighted by the square of the local electromagnetic field, E(z), from zero to infinity (41). E(z) is assumed to be only dependent on the local surface normal z, E(z) = exp(-z/l_d) (21), with l_d ~5 to 6 nm which was consistent with a saturation distance of ~30 nm. Hence, before and after target binding we have:

$$\Delta R = S(n_{IgG} - n_{water})e^{-\frac{2d_{sam}}{l_d}}(1 - e^{-\frac{4d_{IgG}}{l_d}})$$ (5)

where d_{target} ($d_{anti-IgG}$) is given by

$$\frac{d_T}{d_T^{max}} = K_a\frac{[T]}{1 + K_a[T]}$$ (6)

The thickness of the SAM layer, d_{SAM}, is approximated by (21)

$$d_{SAM} = ax + b$$ (7)

where x, the number of CH_2 units in MUDA = 10, a = 0.13 nm and b = 0.66 nm. $\Delta R/\Delta R_{max}$ ratio depicts the predicted normalized GNrMP response vs. d_T, which is directly related to target concentration, [T], through equation 6. K_a in equation 6 is the parameter to be optimized to best fit the experimental data.

In order to determine the best fit experimental data, the following experimentally determined values for the GNrMP-IgG system were used: S = 152.4*AR+19.17 nm/RIU, AR is the aspect ratio of the GNrMPs; n_{SAM}=1.463 (21), n_{water}=1.33, n_{IgG}=1.41 (44), l_d=6.0 nm, and d_{SAM}=1.96 nm, from saturation binding data of IgG to GNRs the parameter Γ_{target}^{max} was found to be 2.13×10^{-2} molecules/nm^2, which yield a d_T=d_{IgG}= Γ_{target}^{max} *V_{IgG}, V_{IgG} is approximated as 5.2 nm*5.2 nm*5.2 nm (45), so d_T = 2.98 nm. Using these parameters, for IgG-anti IgG binding, The $\Delta R/\Delta R_{max}$ vs. [T] data in figure 4 could be best fitted with a K_a = 1.32×10^7 M^{-1}. This K_a is consistent with the binding affinity reported in the literature for IgG-anti-IgG binding (45-47), suggesting that the immobilization of antibodies to gold nanorodss did not significantly reduce their binding affinity.

The LOD (limit of detection) for the IgG-anti-IgG complex can be estimated for GNrMPs with different aspect ratios; if AR=10, the LOD could reach ~1.8 nM. For a certain type of ligand-receptor pair, the LOD is determined by the size of molecules (thickness of the absorbed layers on the GNrMPs), the binding affinity, and the AR of GNrMPs.

398

It should also be noticed that the dynamic range of the GNrMP system for detecting IgG-anti-IgG interaction is 10^{-9} M to 10^{-7} M, within this range the response of the nanoscale probes increases exponentially with respect to target concentration. Therefore, the GNrMP scheme is an excellent system for detecting targets in the nano molar range and is comparable in sensitivity to fluorescence correlation spectroscopy (FCS) (*48*).

Quantitative Analysis of Multiple Targets Using GNrMPs in a Multiplex Fashion

A major advantage of the GNrMP scheme is its multiplexing capability. By using GNrMPs with different aspect ratios, multiple targets can be probed simultaneously. In this study, GNrMPs with aspect ratio of 1.5, 2.8, and 4.6 were used to measure a sample that containing three targets (50 nM human IgG, 20 nM rabbit IgG, and 20 nM mouse IgG), the measured results are shown in Table 2, a reasonable agreement with actual concentrations was reached, demonstrating that quantitative analysis of multiple targets could be achieved.

Table 2. Comparison of Measured Target Concentration to Real Values

	Target 1	*Target 2*	*Target 3*
Real value	50 nM	20 nM	20 nM
Measured value	51.23 nM	18.79 nM	17.86 nM

Conclusion

In this study we demonstrate a multiplex biosensor scheme for quantitative measurement of biological interactions. The limit of detection (LOD) for IgG-anti IgG interaction could reach nano molar range. The LOD of the GNrMP scheme is determined by four factors: the aspect ratio of GNrMP, the binding affinity of GNrMPs to its target, the molecular size of the ligand-receptors, and the dielectric properties of the ligand-receptor complex. It was found that the GNrMP based binding affinity calculations were close to the GNR-IgG-anti-IgG complex which is close to the binding of free IgG-anti IgG. This is a major improvement over the solid-substrate SPR sensor, where the motion of surface-immobilized capturing molecules is restricted and the binding affinity is reduced by 2-3 orders in magnitude. It has been demonstrated that the selectivity of the GNrMP scheme can be improved significantly by a full functionalization

protocol to minimize non-specific binding. The concept and methodology developed in this study can serve as the basis for developing multiplex assays with appropriate quantification models.

References

1. Perez-Juste, J., Pastoriza-Santos, I., Liz-Marz'an, L. M., Mulvaney, P. *Coord. Chem. Rev.* **2005**, *249*, 1870-1901.
2. Klotz, I. M. *Ligand Receptor Energetics: A Guide for the Perplexed.* Wiley, New York, **1997**.
3. Lee, H. J.; Goodrich, T. T.; Corn, R. M. *Anal. Chem.* **2001**, *73*, 5525-5531
4. Hall, D. *Anal. Biochem.* **2001**, *288*, 109-125.
5. Wang, J.; Cai, X.; Rivas, G.; Shiraishi, H.; Farias, P. A. M.; Dontha, N.; *Anal. Chem.* **1996**, *68*, 2629-2634.
6. Walterbeek, H. T.; vander Meer, A. J. G. M.; *J. Eniron. Radioact.* **1996**, *33*, 237- 254.
7. Thevenot, D. R.; Toth, K.; Durst, R. A.; Wilson, G. S. *Biosens. Bioelectron.* **2001**, *16*, 121-131.
8. Mascini, M.; Palchetti, I.; Marrazza, G. *Fresenius' J. Anal. Chem.* **2001**, *369*, 15-22.
9. Horacek, J.; Skladal, P. *Anal. Chim. Acta* **1997**, *347*, 43-50.
10. Ebersole, R. C.; Miller, J. A.; Moran, J. R.; Ward, M. D. *J. Am. Chem. Soc.* **1990**, *112*, 3239-3241.
11. Miller, M. M.; Sheehan, P. E.; Edelstein, R. L.; Tamanaha, C. R.; Zhong, L.; Bounnak, S.; Whitman, L. J.; Colton, R. J. *J. Magn. Magn. Mater.* **2001**, *225*, 156-160.
12. Chemla, Y. R.; Grossman, H. L.; Poon, Y.; McDermott, R.; Stevens, R.; Alper,M. D.; Clarke, *J. Proc. Natl. Acad. Sci.* **2000**, *97*, 26-29.
13. Raiteri, R.; Grattarola, M.; Butt, H.-J.; Skladal, P. *Sens. Actuators, B* **2001**, *B79*, 115-126.
14. Kasemo, B. *Curr. Opin. Solid State Mater. Sci.* **1998**, *3*, 451-459.
15. Yu, C.; Ganjoo, A.; Jain, H.; Pantano, C. J.; and Irudayaraj, J. *Anal. Chem.,* **2006**, *78*, 2500-2506.
16. Cao, Y. C.; Jin, R.; Mirkin, C. A. *Science* **2002**, *297*, 1536-1540
17. Natsume, T.; Nakayama, H.; Isobe, T. *Trends Biotechnol.* **2001**, *19*, S28-S33.
18. Polla, D. L.; Erdman, A. G.; Robbins, W. P.; Markus, D. T.; Diaz-Diaz, J.; Rizq, R.; Nam, Y.; Brickner, H. T.; Wang, A.; Krulevitch, P. *Annu. Rev. Biomed. Eng.* **2000**, *2*, 551-576.
19. Schuck, P. *Annu. Re. Biophys. Biomol. Struct.* **1997**, *26*, 541-566.
20. Nath, N. and Chilkoti, A., *J. Fluorescence* **2004**, *14*, 377-389.

21. Haes, A. and van Duyne, R. P., *J. Am. Chem. Soc.*, **2002**, *124*, 10596-10604.
22. Nath, N. and Chilkoti, A., *Anal. Chem.* **2002**, *74*, 504-509.
23. Yonzon, C. R., Jeoung, E. Zou, S. Schatz, G. C. Mrksich, M. Van Duyne, R. P., *J. Am. Chem. Soc.*, **2004**, *126*, 12669-12676.
24. Ghosh, S. K., Nath, S., Kundu, S., Esumi, K., Pal, T., *J. Phys. Chem. B*, **2004**, *108*, 13963-13971.
25. Dahlin, A., Zach, M., Rindzevicius, T., Kall, M., Sutherland, D. S., Hook, F., *J. Am. Chem. Soc.*, **2005**, *127*, 5043-5048.
26. Raschke, G., Kowarik, S., Franzl, T., Sonnichscen, C., Klar, T. A., Feldmann, J., Nichtl, A., Kurzinger, K., *Nano Lett.*, **2003**, *3*, 935-938.
27. Raschke, G., Brogl, S., Susha, A. S., Rogach, A. L., Klar, T. A., Feldmann, J., Fieres, B., Petkov, N., Bein, T., Nichtl, A., Kurzinger, K., *Nano Lett.* **2004**, *4*, 1853-1857.
28. Lee, S. and Perez-Luna, H., *Anal. Chem.*, **2005**, *77*, 7204-7211.
29. Yu, C. and Irudayaraj, J.; *Anal. Chem.* **2006**, in press
30. Millstone, J. E., Park, S., Shuford, K., Qin, L., Schatz, G. C., Mirkin, C. A., *J. Am. Chem. Soc.* **2005**, *127*, 5312-5313.
31. Englebienne, P., Van Hoonacker, A. and Valsamis, J., *Clin. Chem.* **2000**, *46*, 2000-2003
32. Elghanian, R., Storhoff, J. J., Mucic, R. C., Letsinger, R. L., Mirkin, C. A. *Science* **1997**, *277*, 1078 -1081.
33. Jin, R., Wu, G., Li, Z., Mirkin, C. A. and Schatz, G. C., *J. Am. Chem. Soc.* **2003**, *125*, 1643-1654.
34. Taton, T. A., Mirkin, C. A. and Letsinger, R. L., Science **2000**, *289*, 1757–1760.
35. Nikoobakht, B., El-Sayed, M. A., Chem. Mater. **2003**, *15*, 1957-1962.
36. Lee, K.; El-Sayed, M. A.; *J. Phys. Chem. B*, **2005**, *109*, 20331-20338
37. Murphy, C. J.; Sau, T. K.; Gole, A. M.; Orendorff, C. J.; Gao, J.; Gou, L.; Hunyadi, S. E.; and Li, T.; *J. Phys. Chem. B*, **2005**, *109*, 13857-13870
38. Lee, K.; El-Sayed, M. A.; *J. Phys. Chem. B,* **2006**, *110*, 19220-19225
39. Kekicheff, P.; Spalla, O., *Langmuir*, **1994**, *10*, 1584-1591
40. Kandimalla, V. B., Neeta, N. S., Karanth, N. G., Thakur, M. S., Roshini, K. R., Rani, B. E., Pasha, A., Karanth, N. G. *Biosens. Bioelectron.* **2004**, *20*, 903-906
41. Jun, L. S.; Campbell, C. T.; Chinowsky, T. M.; Mar, M. N.; Yee, S. S.; Langmuir, **1998**, *14*, 5636-5648
42. Jensen, T. R.; Kelly, K. L.; Lazarides, A.; Schatz, J. C.; *J. Cluster Sci.,* **1999**, *10*, 295-317.
43. Walczak, M. M.; Chung, C.; Stole, S. M.; Widrig, C. A.; Porter, M. D.; *J. Am. Chem. Soc.,* **1991**, *113*, 2370-2378
44. Vörös, J. *Biophys. J.* **2004**, *87*, 553-561

45. Murphy, R. M.; Slayter, H.; Schurtenberger, P.; Chamberlin, R. A.; Colton, C. K.; Yarmush, M. L.; *Biophys. J.,* **1988**, *54*, 45-56

46. Chevrier, M. C.; Chateauneuf, I.; Guerin, M.; Lemjeux, R. *Hybridoma Hybridomics,* **2004**, *23*, 362-367

47. Welschof, M.; Terness, P.; Kipriyanov, S. M.; Stanescu, D.; Breitling, F.; Dorsam, H.; Dubel, S.; Little, M.; Opelz, G.; *PNAS,* **1997**, *94*, 1902-1907

48. Schwille, P.; Meyer-Almes, F.-J.; Rigler, R.; *Biophys. J.* **1997**, *72*, 1878-1881

Investigation of Colloidal Suspension of SWCNT and γ-Cyclodextrin Using AFM and Molecular Dynamics Simulation

Minghui Chai[1], Srinivas Ravi[1], Mark P. Kujawski[2], and Leela Rakesh[3]

[1]Department of Chemistry, [2]Department of Engineering and Technology, and [3]Center for Polymer Fluid Dynamics and Department of Mathematics, Central Michigan University, Mt. Pleasant, MI 48859

Dispersal agents can increase the surface interaction between SWCNTs and water via coating themselves on the surfaces of SWCNTs, thus to solubilize and disperse SWCNTs in water. In this study, we have used γ-cyclodextrins (γ-CDs) to solubilize SWCNTs in water. A dark SWCNT-water colloidal suspension has been formed, while the system of SWCNTs alone in water looks like clear water with black precipitates. AFM images of SWCNTs prepared from the colloidal solution with γ-CDs clearly showed that γ-CD molecules decorated the surface of each SWCNT with a height around 4 nm. The images (in the same scanning range) also contain more SWCNTs than the ones of the SWCNTs alone (~ 18 nm in height, as a bundle structure). Force-distance curves (FDCs) have been measured to further probe the interaction between SWCNTs and γ-CDs. Molecular dynamics (MD) simulation has also been performed for understanding such interaction.

Introduction

Since the discovery of carbon nanotubes (CNTs) in 1991 by Sumio Iijima (*1*), a great deal of research has been performed on the properties of these special nanomaterials (*2,3*). Amazingly they are the strongest ever known material but with relatively low density. The main advantage of CNTs is that they have extraordinary physical properties based on their atomic structure (*4,5*) Among CNTs, single walled carbon nanotubes (SWCNTs) have the smallest cylindrical graphite structures with the diameter about 1 nm and the length ranging from nanometers to several millimeters (*6,7*). Each carbon atom in the SWCNT structure is covalently bonded to three nearest carbon atoms forming three σ-bonds using three of the four valence electrons; the fourth electron forms the delocalization of the π-bonds with neighboring carbon atoms. A planar configuration was expected for the trigonal sp^2 hybridized carbon atom. Based on the direction of rolling the graphite sheet into a tube, SWCNTs can be divided into three types namely 'armchair', 'zigzag', and 'chiral', characterized by two integers (n,m) that can be readily related to the diameter and chirality of each structure (*8*). Each SWCNT with a distinct (n,m) has a special electronic configuration. When n–m is divisible by three, that kind of SWCNT is metallic, while the rest are semiconducting (*9,10*). The strong structural dependence of SWCNT electronic properties drives potential applications of these nanoscopic materials for nanoscale electronics and optical sensors (*11,12*). Because of the structural sensitivity of their electrical characteristics, spectroscopic techniques such as Raman, UV/vis and NIR have been used to determine the structural properties of SWCNTs (*7*).

For most applications, CNTs need to be in solution form, especially for the biomedical applications, they have to be dispersible in water. It is well known that the dissolution of carbon nanotubes in water is rather difficult (*13*). Versatile functionalization strategies have further expanded the applications of carbon nanotubes to be used as vehicles for drug and gene delivery, *in vivo* imaging probes, biosensors, and tissue engineering (*14,15*). So far both physically mixing CNTs with dispersal agents (non-covalent functionalization) and chemical modification (covalent functionalization) of CNTs have been used to make them soluble or suspended in water (*16*). Non-covalent protocols (*17*) keep the structures of SWCNTs as they are, while covalent approach (*18*) makes structural changes to the nanotubes. There are many dispersal agents such as surfactants (*19-23*), polymers such as starch (*24,25*), poly(ethylene oxide) (*26*) and polypeptides (*27*), lipids (*28,29*), RNA (*30*), DNA (*31-33*) and proteins (*34-35*) used for the non-covalent functionalization. But there are only two ways of covalent functionalization, which are end and defect modification, and sidewall modification.

Distinct advantages of using cyclodextrins lie in that they are seminatural, produced from starch by an environmentally friendly technology; and they are very water soluble with a hydrophilic surface and a hydrophobic inner cavity or pocket. This leads to applications of CD as one of the active ingredients in drugs, foods, or cosmetics (*38*). A recent research report described the utilization of η-cyclodextrin (η-CD, with an inner diameter > 1 nm) to debundle and solubilize SWCNTs in water (*39*). By taking advantage of the larger hydrophobic inner pocket of the η-CDs, a long skinny SWCNT can penetrate through several CDs' center cavities like chaining the "rings" (η-CDs) through a "thread" (SWCNT). This strategy is just a physical inclusion, therefore belonging to the non-covalent functionalization.

In this presented research, γ-cyclodextrin (γ-CD, with an inner diameter about 0.95 nm) as a dispersal agent has been utilized to debundle and solubilize SWCNTs in water in a physical mixing manner. By means of this procedure, a dark SWCNT colloidal suspension can be clearly formed in water (Figure 1a), while SWCNT-alone system looks like clear water containing black precipitates (Figure 1c). In comparison, this method seems dispersing SWCNTs as equivalently as or even more efficiently than the one using the surfactant (i.e. SDS, sodium dodecyl sulfate, Figure 1b).

(a)   (b)   (c)
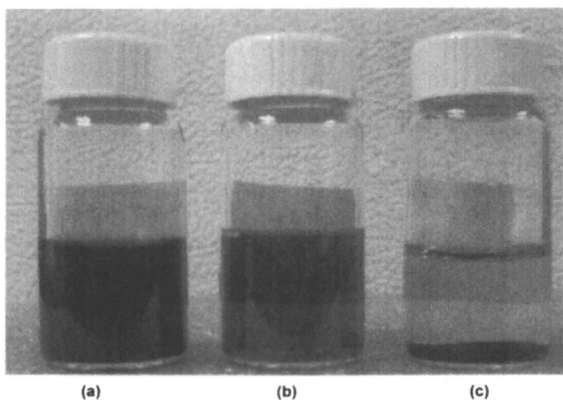
Figure 1. Different systems of SWCNTs in water: (a) SWCNTs mixed with γ-CDs; (b) SWCNTs mixed with SDS; and (c) SWCNTs alone

This aqueous colloidal system of γ-CDs and SWCNTs may expand the applications of SWCNTs in biomedical fields. Recently the characterization of the interaction of SWCNT and γ-CD was studied by using DSC thermal analysis, absorption and Raman spectroscopy (*40*). This study confirmed there is an interaction between γ-CD and SWCNT. However, it did not show how

they interact. The work in this paper aims at probing how γ-CDs interact with SWCNTs using AFM (atomic force microscopy). In order to further understand the interaction in theory, molecular dynamics (MD) simulation has also been used to characterize the molecular interactions in the water system of γ-CD and SWCNT.

AFM has been a powerful tool for probing the structural and physical properties of materials at a nanoscopic level, as well as providing information on the adhesive forces of the material surface with an AFM tip. Using topographic imaging, the surface nanostructures of materials can be directly visualized, including changes of surface morphology with the changes in environment. Force-distance curves measured by AFM can supply complementary information on surface properties of the materials including viscoelasticity and localized surface charge density and hydrophobicity. In this study, through AFM imaging and force-distance curve measurements, the interaction between SWCNT and γ-CD were investigated in order to understand how γ-CDs disperse and debundle SWCNTs in the aqueous solution to form the relative stable colloidal suspension, which may lead to some potential biomedical applications of SWCNTs.

Experimental

Materials and Sample Preparation

Single-walled carbon nanotubes were bought from Carbon Nanotechnologies Incorporated. These HiPco® SWCNTs, contain less than 35% of ash content. Recently it has been demonstrated that HiPco SWCNTs can be cut with the help of grinding in the presence of organic materials like γ-cyclodextrin. The γ-CD with an inner cavity diameter of 0.95 nm was used in this study, which was obtained from Wacker-Chemie. The sample was made by the grinding of γ-CD and SWCNT in the ratio of 30:1 in an agate mortar and pestle for approximately 2 hours with the addition of 1 ml of ethanol dropwise of the first 10 minutes. This results in the fine homogeneous mixture for the preparation of AFM samples. Deionized water (100 ml) was added to about 2 mg of the mixture in a plastic container and then the system was sonicated at 25°C for 30 mins to produce a quite stable suspension (~ 0.2 mg SWCNTs-γ-CD/ml water) (*40,41*). The suspension was further diluted (100 times) for AFM studies. The diluted sample (~0.002 mg SWCNTs-γ-CD/ml water) was put on a freshly-cleaved mica surface and was naturally dried at ambient temperature in clean chamber for half an hour. Then further drying (about 5 mins) was applied using a gentle N_2 flow from a compressed nitrogen gas tank to ensure there was no moisture on the surface of the sample.

AFM Imaging and Force-Distance Curve Measurements

All images were acquired in air with tapping mode on a PicoPlus SPM instrument from Agilent Technologies (formerly Molecular Imaging Co.) using 5.3.3.USB Picoscan software, a multi-purpose small scanner and silicon tips (Model PPP-NCHR, Al coated on detector side, thickness: 3.9 μm, length: 143 μm, width: 29 μm, resonance frequency: ca. 295 KHz, force constant: ca. 32 N/m and tip height 10-15 um (Nanosensor, Neuchatel, Switzerland)). Typically, a 2 lines/s speed was used for scanning on 2000 nm × 2000 nm areas, with a setpoint of 0.85 of the cantilever oscillation amplitude in free status. To avoid the hydrodynamic effect of thin air gaps, the resonance was carefully measured at a small tip - sample distance. All images were processed using SPIP (Scanning Probe Image Processor) software from the Image Metrology.

Force-distance curve measurements were obtained using unfunctionalized silicon probes (type PPP-CONTR, Al coated on detector side, thickness: 2 μm, length: 450 μm, width: 50 μm, force constant: ca. 0.1 N/m and tip height of 10-15 μm (Nanosensors, Neuchatel, Switzerland)) on mica prior and after the deposition of either SWCNTs, γ-CD or SWCNTS/γ-CD complex in deionized water. All measurements were performed using a Z-closed loop scanner with the Picoplus AFM instrument. Nearly 100μl of each sample was deposited on mica and then kept aside till air-dry. Then the mica with the sample was kept under the nitrogen gas until it became completely dry. Before measurement, the Z-closed loop scanner was calibrated for the standard proportional and integral gain on a mica surface using the protocols from the manufacturer. The slope of the force-distance curve measured on the mica was used to convert the measured cantilever deflection from relative units (V) to absolute units (nm). The Z-closed loop scanner can correct the hystereses typically existing between the approaching and retracting curves in calibration (42). Using the cantilever spring constant (K_c) in (N/m), the cantilever deflection (D_c) in (nm) was converted to force (F) in (nN) using Hooke's law (43). We used the company-provided values for the cantilever spring constants. The AFM force measurement plots were corrected for cantilever bending in order to quantify probe-sample separation. It should also be noted that, in these experiments, the radius of curvature of the probe was not able to be determined, and thus the probe-sample contact areas were estimated. Therefore, using SPIP software to process these measured force-distance curves, direct comparisons of forces were only made between those recorded with the same probe and those in which the probe-sample contact force was maintained at a constant value. To study probe-sample interaction by means of force-distance curves (43), the experiment was ramped along the vertical axis for 350 nm at a sweep duration of 1.0 second, and the cantilever deflection Dc was acquired.

An AFM force-distance curve is the result of two contributions: the tip-sample interaction F(D) and the elastic force of the cantilever. The tip sample

force is given by Hooke's law, $F = -K_cD_c$, where F is the Force in nano-Newton (nN), D_c is the cantilever deflection in nanometers (nm), and Kc is the cantilever spring constant in nN/nm. The distance controlled during the measurement is not the actual tip-sample separation distance (D) but rather the distance (Z) moved by the z-piezoelectric scanner. These two distances differ because of cantilever deflection D_c and sample deformation D_s. These four quantities are related as follows: $D = Z - (D_c - D_s)$.

Molecular Dynamics Simulation

MD simulations were carried out using a Forcite and Discover dynamic engine in MS modeling [Universal and Compass MS Modeling, 3.2 Materials Studio, Accelrys Inc., 2005], a second generation force field. The MD simulations are based on universal /compass force field for intermolecular interactions of small diameter (1Å) SWCNTs (10,10) with γ-CD molecules examined as a method of dispersion. The system of SWCNTs and γ-CDs in a ratio of 1:20 in the presence of water as the solvent was used for the simulation. The interaction was calculated via solving the Newtonian equations of motions using a predictor corrector method with a time step of one femtosecond. The calculation was carried out in canonical NVT ensemble using the Berendsen algorithm at 298K in all simulations. MD simulations ran for the system consisted of 5×10^6 time steps, that is, the simulation length was 1000ps. The trajectory images of the positions were recorded every 5000 time steps.

Initially the system containing one SWCNT with 20 γ-CDs and 50 water molecules was used for the simulation, Then the simulation was continued by adding 2, 3, 4 SWCNTs with 40, 60 and 80 γ-CDs in 100, 150 and 200 water molecules, respectively, to understand the complexation process of SWCNTs with γ-CDs in the aqueous solution.

Results and Discussion

Figure 2 shows two AFM images taken by the AC mode dry-scanning from different areas of the sample prepared from the colloidal suspension of SWCNTs and γ-CDs. From these images, it can be clearly see that each SWCNT like "chain" is coated with many γ-CDs "beads".

Because the SWCNT sample was grounded to improve miscibility and solubility in the sample preparation, the length of the nanotubes was measured in the range of 1 μm to 4.5 μm, with the width around 100 nm and the height below 10 nm on mica. (see Figure 3).

Scale bar = 200 nm Z scale = 2.5 nm   Scale bar = 150 nm Z scale = 1.5 nm
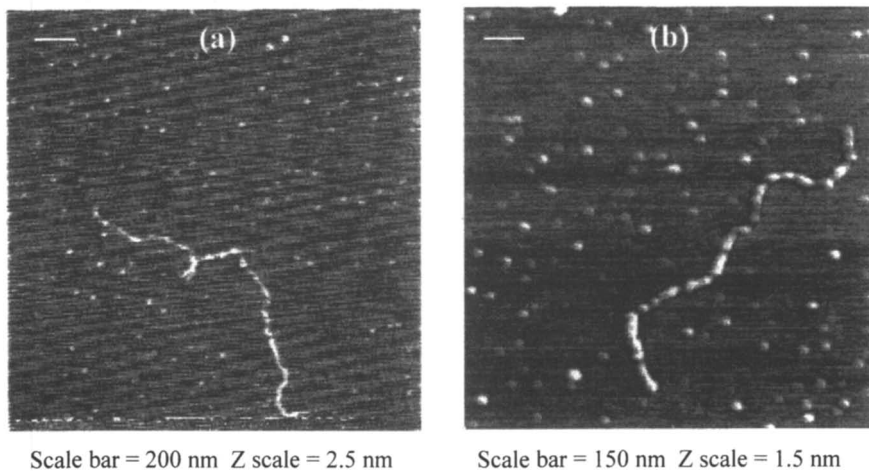
Figure 2. AFM images of SWCNTs mixed with γ-CDs in water obtained at different sample areas and shown at different scales.

Width: ~ 100 nm
Height: ~ 4.2 nm
Length: ~ 2.5 μm

Position [μm]

Scale bar = 100 nm Z scale = 1.5 nm
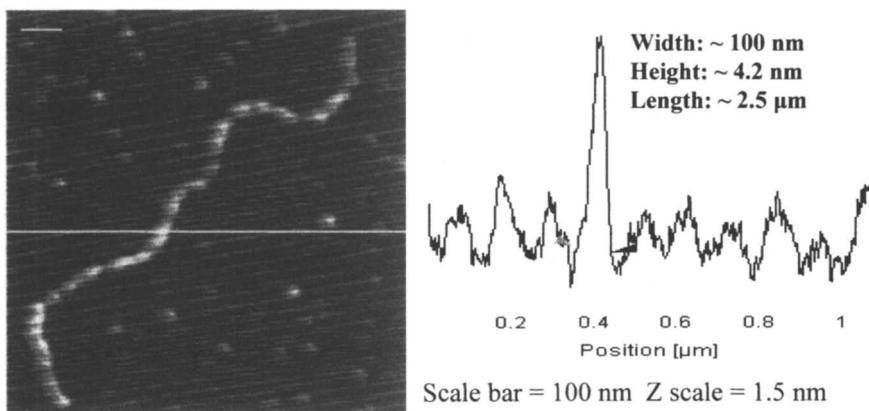
Figure 3. AFM Image of colloidal suspension of SWCNTs mixed with γ-CDs in water shown at 1μm × 1μm scale along with the size measurements

Figure 4 is the AFM image of the sample prepared from the SWCNT alone in water, taken by the AC mode dry-scanning. In comparison, the length of the SWCNTs alone was about 3.5 μm, similar to the one of the SWCNTs in the colloidal suspension system with γ-CDs. The width of the SWCNTs alone was nearly the same as the one of the γ-CD decorated SWCNTs, which may be due to the similar interaction with the mica surface for both types of SWCNTs.

Width: ~ 100 nm
Height: ~ 18 nm
Length: ~ 3.5 μm

Position [μm]

Scale bar = 200 nm Z scale = 35 nm
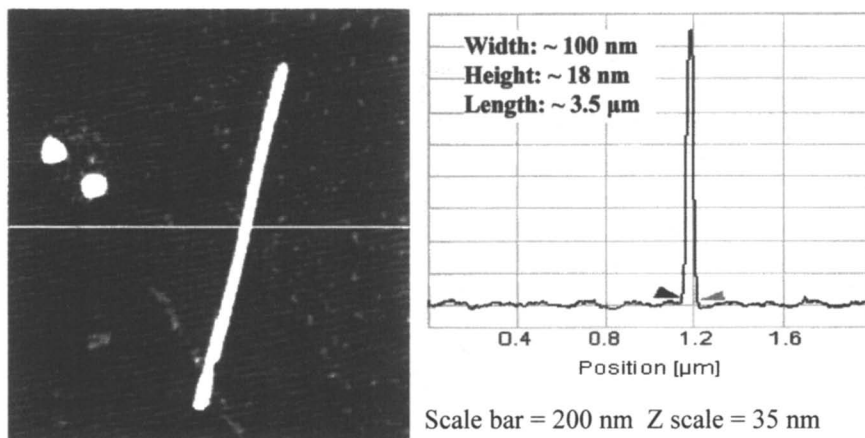
Figures 4. AFM image of the SWCNT alone in water shown at 2μm × 2μm scale along with the size measurements

However, in AFM topography, the height measurement often provides more accurate information on the size of the sample than the width measurement. Therefore, the height measurements were performed for both types of SWCNT systems. Interestingly the height of the SWCNT alone (~ 18 nm) was much greater than that of the γ-CD decorated SWCNTs (~ 4 nm). This indicates that the SWCNTs alone in water aggregate together forming "thick bundles", while the γ-CD decorated SWCNTs in water are more isolated individual SWCNTs in size plus the coating layer of γ-CDs. In addition, the AFM images also shows that the shape of the SWCNTs alone in water is more "rigid" and straight with a smooth edge, while the γ-CD decorated SWCNTs are more "flexible" and curved with a rough edge. These can be vividly shown in the 3D displays of the AFM images (see Figure 5). The rough edge of the γ-CD decorated SWCNTs in this AFM study is a direct experimental observation of the interaction of SWCNTs with γ-CDs in the colloidal suspension system, which is more visually advantageous than the previous Raman and thermal characterization of the interaction of SWCNTs with γ-CDs (41). Up to now, most of the reports on the imaging of SWCNTs have been

done by TEM (tunneling electron microscopy) and few AFM images have been reported (based on a search using SciFinder Scholar). The reported AFM images of the oxidized SWCNTs by Kovtyukhova *et. al. (44)* show a very similar feature as the ones of SWCNTs alone in this study.
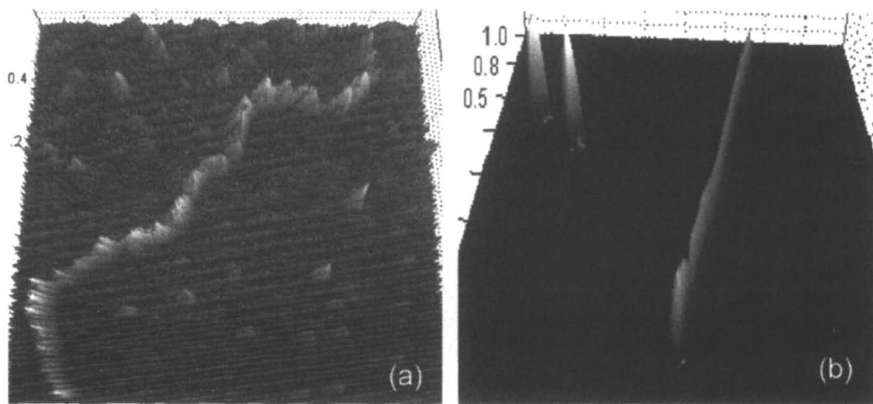
Figure 5. 3D Displays of tapping-mode AFM images for: (a) SWCNTs with γ-CDs, and (b) SWCNTs alone, both dried from water suspensions.

Force-distance curves reveal the forces of the AFM tip interacting with the sample surface on mica. So one can extrapolate information of the morphology of a material surface from a FDC. In this study, all the samples were dried on mica and FDCs were measured using the SiN tip. Figure 6a shown above is the FDC of the SWCNT alone, from the SPIP processing, the adhesion force was about 4.87 nN. This is because there was not much interaction between the "rigid" surface of the SWCNT bundle and the AFM tip. Figure 6b shows the FDC of the γ-CD alone. The adhesion force between the γ-CD surface and the tip was 5.27 nN. In comparison, the γ-CD alone surface is softer than that of the SWCNT alone, since γ-cyclodextrin has a strong attraction force with the tip. Figure 6c is the FDC of the mixture (or complex) of SWCNT and γ-CD. Its surface has an adhesion force of 4.99 nN with the AFM tip, which is right in-between the attraction forces of the SWCNT and γ-CD alone cases. This further demonstrates that the surface of the SWCNT and γ-CD complex system is decorated but not completely covered with γ-CD molecules, as shown in the AFM AC mode images. Such interaction between SWCNT and γ-CD molecules holds several γ-CDs close to the surface of each SWCNTs, at the mean time to debundle the aggregates of SWCNTs. Therefore in water, because of the high solubility of γ-CD, water molecules will easily solubilize the γ-CD coated
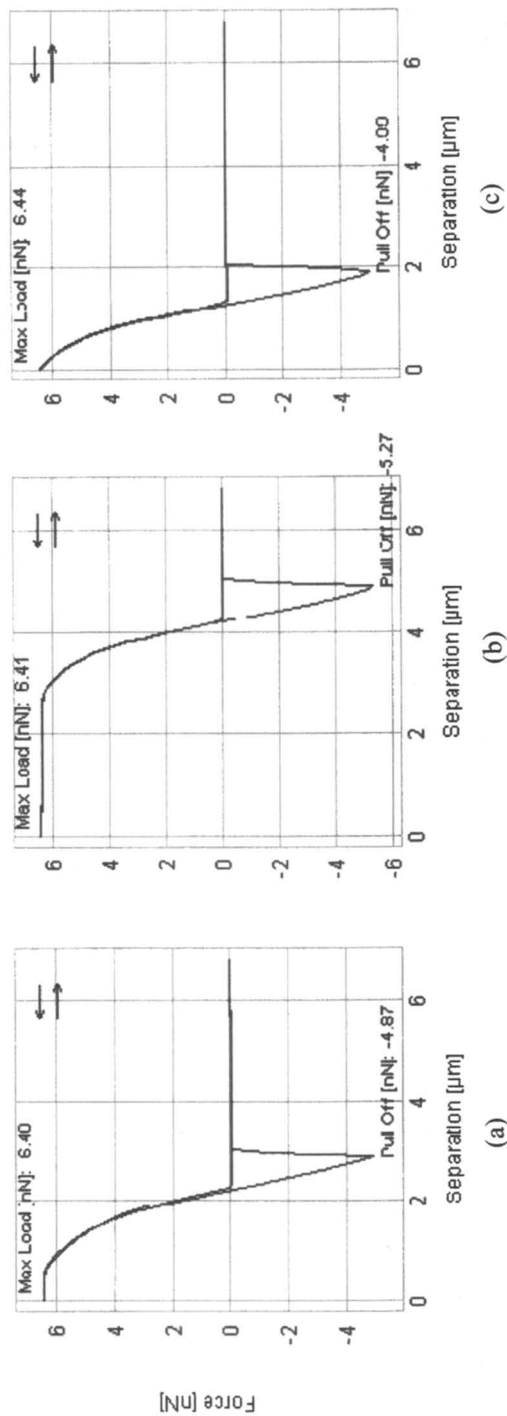
Figure 6. Force-distance curves (FDCs) of (a) SWCNT alone, (b) γ-CD alone, (c) SWCNT and γ-CD complex.

SWCNTs and further segregate SWCNT bundles into individuals. Thus the γ-CD molecules can interact with SWCNTs in water as an efficient dispersal agent to form a relatively stable colloidal suspension.

Figure 7 shows the energy minimized structure of the system containing 4 SWCNTs, 80 γ-CDs and 200 water molecules from MD simulation with 1500 ps simulation length per run. This structure clearly displays that the four SWCNTs are separated well by the γ-CD molecules in water, which is in consistence with the experimental observations in the AFM study. In addition, the initial distance between SWCNTs in the presence of γ-CDs prior to simulation was approximately 4.01 Å and after 1500 ps dynamics simulation, the distance between SWCNTs changed to approximately 6.00 Å. This quantitatively indicates that γ-CDs surround each of the SWCNTs and make them further apart.

In MD simulation, a radial distribution function (RDF), g(r), describes how the density of finding a particle changes as a function of the distance from a distinguished point. The radial distribution from the MD simulation (Figure 8) shows that the probability of finding γ-CD near (within 4 Å) SWCNT after 1500 ps is much greater than that after 500 ps.
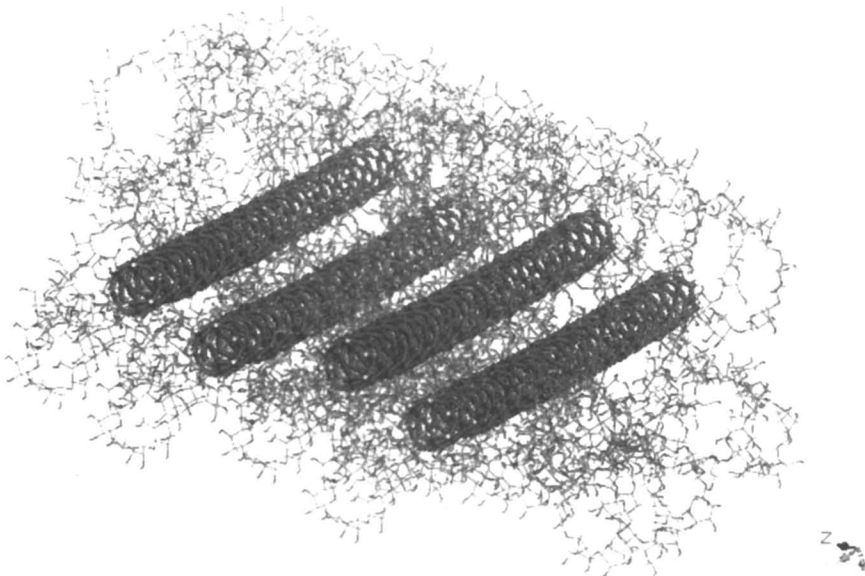
Figure 7. Energy minimized structure of the system containing 4 SWCNTs, 80 γ-CDs and 200 water molecules via MD simulation with 1500 ps simulation length per run (water molecules were deleted in the display for clarity).
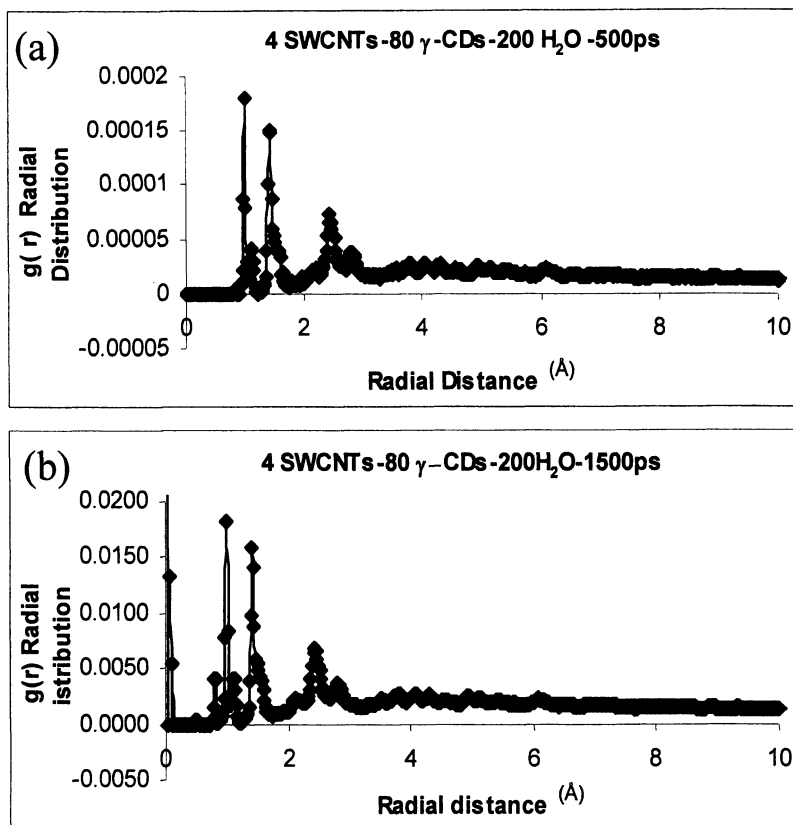
Figure 8. Radial distribution function [RDF, g(r)] plots of the system containing 4 SWCNTs, 80 γ-CDs and 200 water molecules via MD simulation: (a) with 500 ps simulation length and (b) with 1500 ps

Conclusion

This research demonstrates that AFM is a very powerful tool for studying nanostructures. AFM vividly show "pearl necklace" images for the SWCNT and γ-CD complex system, indicating that γ-CDs can decorate SWCNTs to segregate them from bundles to form a more homogeneous colloidal suspension in water. AFM force distance curve (FDC) measurements also show that the γ-CD decorated SWCNTs have more attraction force with the AFM tips in comparison with SWCNTs alone. The AFM results confirm that there is noncovalent interaction between γ-CD and SWCNT molecules. Such interaction permits

414

γ-CD to function as an efficient dispersal agent for debundling SWCNTs in aqueous solution, which may lead to more biological applications of these nanomaterials. The results from MD simulations for the SWCNT and γ-CD complex system are consistent with the ones from the AFM experiments.

References

1. Iijima, S. *Nature* **1991**, *354*, 56-58.
2. Piner, R., Ruoff, R. S., *Los Alamos National Laboratory, Preprint Archive, Condensed Matter* **2002**, 1-3.
3. Kinloch, I. A.; Eder, D.; Prehn, K.; Motta, M.; Moisala, A.; Li, Y.; Zhang, S.; Song, W.; Roberts, S.; Geng, J.; Johnson, B. F. G.; Singh, C.; Shaffer, M. S. P.; Boratynski, J.; White, A.; Emohare, O.; Brooks, R.; Best, S.; Walter, D. M.; Walker, G. S.; Scotchford, C. A.; Brown, D.; Stone, V.; Windle, A. H. *Prepr. Symp. - ACS, Div. Fuel Chem.* **2007**, *52*, 96-97.
4. Iijima,S.; Zhang, Y. Philosophical Magazine Letters **2000**, *80*, 427.
5. Belytschko, T.; Xiao, S. P.; Schatz, G. C.; Ruoff, R. S. *Phys. Rev.B* **2002**, 65, 235430/1-235430/8.
6. Strano, M. S. Prepr. Symp. - ACS, Div. Fuel Chem. **2007**, *52*, 120.
7. Hartschuh, A.; Pedrosa, H. N.; Peterson, J.; Huang, L.; Anger, P.; Qian, H.; Meixner, A. J.; Steiner, M.; Novotny, L.; Krauss, T. D. *ChemPhysChem* **2005**, *6*, 577-582.
8. Saito, R.; Dresselhaus, G.; Dresselhaus, M. S. *Physical Properties of Carbon Nanotubes*, Imperial College Press, London, 1999.
9. Odom, T. W.; Huang, J. L.; Kim, P.; Lieber, C. M. *Nature* **1998**, *391*, 62-64.
10. Wildoer, J. W. G.; Venema, L. C.; Rinzler, A. G.; Smalley, R. E.; Dekker, C. *Nature* 1998, *391*, 59– 62.
11. Lovat, V.; Pantarotto, D.; Lagostena, L.; Cacciari, B.; Grandolfo, M.; Righi, M.; Spalluto, Giampiero; P. M.; Ballerini L. *Nano Lett.* **2005**, *5*, 1107-1110.
12. Baughman, R. H.; Zakhidov, A. A.; de Heer, W. A. *Science* **2002**, *297*, 787-792.
13. Ausman, K. D.; Piner, .; Lourie, O.; Ruoff, R. S.; Korobov, M. *J. Phys. Chem.* **2000**, *104*, 8911-8915.
14. Kostarelos, K.; Lacerda, L.; Partidos, C. D.; Prato, M.; Bianco, A. *J. Drug Delivery Sci. Tech.* **2005**, *15*, 41-47.
15. Bianco, A.; Kostarelos, K.; Prato, M. *Curr. Opin. Chem. Bio.* **2005**, *9*, 674-679.
16. Hirsch, A.; Vostrowsky, O. *Top. Curr. Chem.* **2005**, *245*, 193-237.
17. Chen, R. J.; Dai, H. *PNAS J.* **2003**, *100*, 4984.
18. Banerjee, S.; Hemraj-Benny, T.; Wong, S. S. *Adv. Mater.* **2005**, *17*, 17-29.

19. Kocharova, N.; Aeaeritalo, T.; Leiro, J.; Kankare, J.; Lukkari, J. *Langmuir* **2007**, *23*, 3363-3371.
20. Niyogi, S.; Boukhalfa, S.; Chikkannanavar, S. B.; McDonald, T. J.; Heben, M. J.; Doorn, S. K. *J. Am. Chem. Soc.* **2007**, *129*, 1898-1899.
21. McDonald, T. J.; Engtrakul, C.; Jones, M.; Rumbles, G.; Heben, M. J. *J. Phys. Chem. B* **2006**, *110*, 25339-25346.
22. Matarredona, O.; Rhoads, H.; Li, Z.; Harwell, J. H.; Balzano, L.; Resasco, D. E. *J. Phys. Chem. B* **2003**, *107*, 13357-13367.
23. Moore, V. C.; Strano, M. S.; Haroz, E.H.; Hauge, R. H.; Smalley, R. E.; Schmidt, J.; Talmon, Y. *Nano Lett.* **2003**, *3*, 1379-1382.
24. Star, A.; Steuerman, D. W.; Heath, J. R.; Stoddart, J. F. *Angew. Chem., Int. Ed.* **2002**, *41*, 2508-2512.
25. Star, A.; Joshi V.; Han T.-R.; Altoe, M. V. P.; Gruner G.; Stoddart, J. F. *Org. Lett.* **2004**, *6*, 2089-2092.
26. Chatterjee, T.; Yurekli, K.; Hadjiev, V. G.; Krishnamoorti, R. *Adv. Func. Mater.* **2005**, *15*, 1832-1838.
27. Li, X.; Chen, W.; Zhan, Q.; Dai, L.; Sowards, L.; Pender, M.; Naik, R. R. *J. Phys. Chem. B* **2006**, *110*, 12621-12625.
28. Wu, Y.; Hudson, J. S.; Lu, Q.; Moore, J. M.; Mount, A.S.; Rao, A. M.; Alexov, E.; Ke, P. C. *J. Phys. Chem. B* **2006**, *110*, 2475-2478.
29. Qiao, R.; Ke, P. C. *J. Am. Chem. Soc.* **2006**, *128*, 13656-13657.
30. Jeynes, J. Charles G.; Mendoza, Ernest; Chow, David C. S.; Watts, Paul C. P.; McFadden, Johnjoe; Silva, S. Ravi P. *Adv. Mater.* **2006**, *18*, 1598-1602.
31. Karachevtsev, V. A.; Glamazda, A. Yu.; Leontiev, V. S.; Lytvyn, O. S.; Dettlaff-Weglikowska, U. *Chem. Phys. Lett.* **2007**, *435*, 104-108.
32. Zheng, M. *Science* **2003**, *302*, 1545-1548.
33. Cathcart, H.; Quinn, S.; Nicolosi, V.; Kelly, J. M.; Blau, W. J.; Coleman, J. N. *J. Phys. Chem. C* **2007**, *111*, 66-74.
34. Karajanagi, S. S.; Yang, H.; Asuri, P.; Sellitto, E.; Dordick, J. S.; Kane, R. S. *Langmuir* **2006**, *22*, 1392-1395.
35. Poenitzsch, Vasiliki Z.; Musselman, Inga H. *Microscopy Microanal.* **2006**, *12*, 221-227.
36. Bottini, M.; Cerignoli, F.; Tautz, L.; Rosato, N.; Bergamaschi, A.; Mustelin, T. *J. Nanosci. Nanotech.* **2006**, *6*, 3693-3698.
37. Matsuura, K.; Saito, T.; Okazaki, T.; Ohshima, S.; Yumura, M.; Iijima, S. *Chem. Phys. Lett.* **2006**, *429*, 497-502.
38. Szejtli, J. *Chem. Rev.* **1998**, *98*, 1743-1753.
39. Dodziuk, H.; Ejchart, A.; Anczewski, W.; Ueda, H.; Krinichnaya, E.; Dolgonos, G.; Kutner, W. *Chem. Comm.* **2003**, *8*, 986-987.
40. Chen, L.; Dyer, M. J.; Yu, M.-F. *J. Am. Chem. Soc.* **2001**, *123*, 6201-6202.
41. Chambers, G. ; Caroll, C. ; Farrell, F. G. ; Dalton, B. A. ; McNamara, M.; In Het Panhuis, M.; Byrne, H. J. *Nano Lett.* **2003**, *3*, 843-846.

42. Chen, X.; Davies, M. C.; Roberts, C. J.; Tendler, S. J. B.; Williams, P. M.; Davies, J.; Dawkes, A. C.; Edwards, J. C. *Ultramicroscopy* **1998**, *75*, 171-181.
43. Burnham, N. A.; Colton, R. J.; Pollock, H. M. *Nanotechnology* **1993**, *4*, 64-80.
44. Kovtyukhova, N. I.; Mallouk, T. E.; Pan, L.; Dickey, E. C. *J. Am. Chem. Soc.* **2003**, *125*, 9761-9769.

Author Index

Subject Index

A

Activated carbon, metal ion adsorption on tannic acid-coated, 91

Adsorption
  metal ion removal, 91
  See also Alkane adsorption

Ag_2S semiconductor nanoparticles
  Ag_2S in colloidal form, 208
  conductivity of equimolar reaction mixture, 208
  dependence of conductivity on time, 205, 207*f*
  dependence of molar conductivity on $AgNO_3$ and $(NH_4)_2S$ concentration, 205, 206*f*
  experimental, 204–205
  ion transport and colloidal nanoparticles, 210
  Kohlraush's law, 205
  molar conductivity of Ag_2S vs. colloidal Ag_2S concentration, 208, 210*f*
  molar conductivity of electrolytes, 205
  reaction mechanism for formation, 212
  real time-conductivity measurements, 204
  scanning tunneling microscopy (STM) of dry deposits of Ag_2S colloid, 208, 209*f*
  silver sulfide formation and concentration with time, 211*f*, 212
  tunneling current vs. gap voltage for, 208, 209*f*

Aggregation
  challenges in preventing, of nanoparticles, 42

geometrical relations for aggregates, 344–345
standard free energy change, 345–349
See also Frozen micelles

Alkane adsorption
  importance for study, 142
  isobutane on titanium dioxide nanotubes (TiNTs) and anatase thin films, 147, 148*f*
  See also Titanium dioxide (TiO_2)

m-Aminobenzosulfonic acid (msa), tobacco mosaic virus modification, 377, 378*f*

Ammonium persulfate (APS), tobacco mosaic virus (TMV) treated with thiophene and, 379, 381*f*

Amphiphilic polymer conetworks (APCNs)
  AFM (atomic force microscopy) method, 290
  AFM phase mode images, 297, 300–301
  architectures of precursor chains between cross-links, 293*f*
  characteristics of linear copolymer precursors to [2-butyl-1-octyl methacrylate]–[tetrahydropyranyl methacrylate] (BOMA–THPMA) conetworks, 292*t*
  characteristics of linear copolymer precursors to methyl methacrylate–THPMA (MMA–THPMA) conetworks, 292*t*
  chemical structures and names of monomer and cross-linker repeating units, 288*f*
  copolymer synthesis, 287, 289

I

J

Figure 26.1. a) TEM image of wt-TMV. b) (left) Helical organization of TMV coat proteins. (right-top) A single subunit structure of coat protein is presented as ribbon diagram with the reactive tyrosines being highlighted, among which Tyr-139 (in red) can be accessed from the side, but Tyr-70 (in blue) and Tyr-72 (in green) can only be accessed from the top face of the TMV particle. (right-bottom) The surface charge distribution of the TMV coat protein dimers is also shown (blue: positive; red: negative)
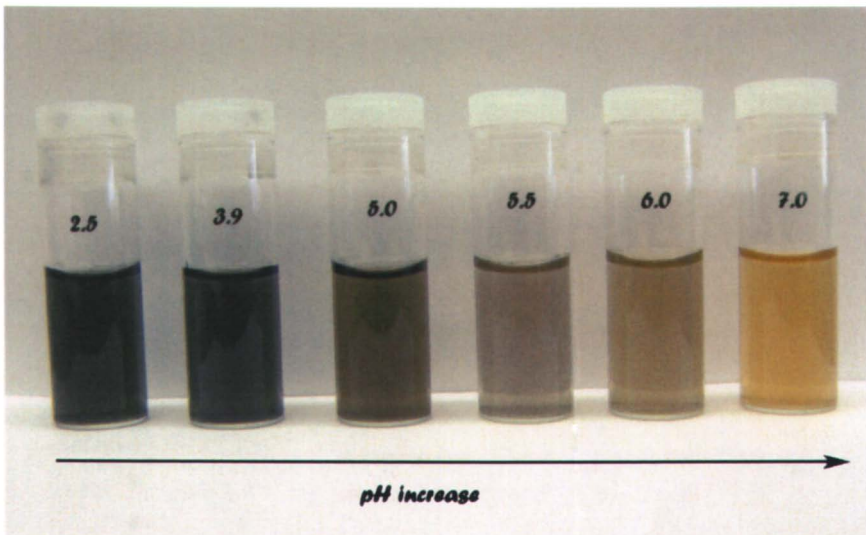
Figure 26.4. Color variation of the dispersions of PANI/TMV composite nanofibers in water as a function of reaction pH.